BULK-PIEZOELECTRIC TRANSDUCTION OF MICROSYSTEMS WITH APPLICATIONS TO BATCH-ASSEMBLY OF MICROMIRRORS, CAPACITIVE SENSING, AND SOLAR ENERGY CONCENTRATION SYSTEMS

A Dissertation

Presented to the Faculty of the Graduate School

of Cornell University

in Partial Fulfillment of the Requirements for the Degree of

Doctor of Philosophy

by

Serhan Mehmet Ardanuç

May 2010

BULK-PIEZOELECTRIC TRANSDUCTION OF MICROSYSTEMS WITH APPLICATIONS TO BATCH-ASSEMBLY OF MICROMIRRORS, CAPACITIVE SENSING, AND SOLAR ENERGY CONCENTRATION SYSTEMS

Serhan Mehmet Ardanuç, Ph.D.

Cornell University 2010

Electromechanical modeling, actuation, sensing and fabrication aspects of bulk-piezoelectric ceramic integration for microsystems are investigated in this thesis.

A small-signal model that describes the energy exchange between surface micromachined beams and bulk-lead zirconium titanate (PZT) actuators attached to the silicon substrate is presented. The model includes detection of acoustic waves launched from electrostatically actuated structures on the surface of the die, as well as their actuation by bulk waves generated by piezoelectric ceramics. The interaction is modeled via an empirical equivalent circuit, which is substantiated by experiments designed to extract the model parameters.

As a die level application of bulk-PZT, an Ultrasound Enhanced Electrostatic Batch Assembly (U2EBA) method for realization of 3-D microsystems is demonstrated. U2EBA involves placing the die in an external DC electric field perpendicular to the substrate and actuating the die with an off-chip, bulk-piezoelectric ceramic. Yield rates reaching up to 100% are reported from 8×8 arrays of hinged mirrors with dimensions of 180×100 μm^2.

U2EBA is later improved to provide temporary latching at intermediate angles between fully horizontal and vertical states, by using novel latching structures. It is shown that the micromirrors can be trapped and freed from different rotation

angles such that zero static power is needed to maintain an angular position.

The zero-idle-power positioning of large arrays of small mirrors is later investigated for energy redirection and focusing. All-angle LAtchable Reflector (ALAR) concept is introduced, and its application to Concentrated Solar Power (CSP) systems is discussed. The main premise of ALAR technology is to replace bulky and large arrays of mirrors conventionally used in CSP technologies with zero-idle-power, semi-permanently latched, low-profile, high-fill factor, micrometer to centimeter scale mirror arrays. A wirelessly controlled prototype that can move a 2-D array of mirrors, each having a side length of less than 5 cm, in two degrees of freedom to track the brightest spot in the ambient is demonstrated.

Capacitive sensing using bulk-piezoelectric crystals is investigated, and a Time-Multiplexed Crystal based Capacitive Sensing (TM-XCS) method is proposed to provide nonlinearity compensation and self-temperature sensing for oscillator based capacitive sensors. The analytical derivation of the algorithm and experimental evidence regarding the validity of some of the relations used in the derivation are presented.

This thesis also presents results on microfluidic particle transport as another application of bulk-PZT in microsystems. Experiments and work regarding actuation of micro-scale, fluorescent beads on silicon nitride membranes are described.

BIOGRAPHICAL SKETCH

Serhan M. Ardanuç received his B.S. degree in electrical engineering from Middle East Technical University, Ankara, Türkiye, in 2001. In the same year, he started his Ph.D. studies in the School of Electrical and Computer Engineering at Cornell University. In 2002, he joined *Sonic*MEMS Laboratory, where he completed his Ph.D. studies in 2010 with a minor in theoretical and applied mechanics. During the summer of 2006, he worked on failure analysis of micro-inkjet devices at Xerox Research Center in Webster, NY. His research interests include design and testing of micrometer and millimeter scale, wireless, reflector systems for large area beam-steering and solar concentration applications, mixed-signal circuit design, behaviorial and finite element modeling in microsystems, and ultrasonic applications of microelectromechanical systems.

To

my parents *İlker* and *Fernap*,

and

my sister *Sezin*

ACKNOWLEDGEMENTS

I was very fortunate to be supported by experts, friends, and family throughout my Ph.D. years. This thesis would not have been possible without them.

I can't thank Professor Amit Lal enough for the guidance, teaching, and mentorship he offered to me. The freedom that he provided was central to the completion of this thesis. His creativity, optimism, determination, patience, and early-morning e-mails continue to impress me even after having worked with him for close to eight years.

I send my special thanks to my committee members Professor Alan Zehnder and Professor Michael Spencer. It was a great relief to have their support and to know that they would be available when I needed them. I would like to thank Professor Sunil Bhave for generously sharing his group's facilities with me, for listening to my ideas, and for his invaluable comments on one chapter of my thesis. I would also like to acknowledge Professor Clifford Pollock for our stimulating and fun discussions.

I am grateful to the past and present members of *Sonic*MEMS Laboratory for being helpful, creative, and friendly: Kürşad Araz, Shankar Radhakrishnan, Hui Li, Xi Chen, Norimasa Yoshimizu, Chung-Hoon Lee, Rajesh Duggirala, Abhijit Sathaye, Alper Bozkurt, Hengky Chandrahalim, Shi-Herng Kan, Il-Seok Son, Abhishek Ramkumar, Hang Guo, Steven Tin, Siva Pulla, Ching-Ping Janet Shen, Ayesa Sinha, Yuerui Lu, and Kwame Amponsah. I also would like to thank Faisal Razi Ahmed, Sheng-Yu Peng, Karan Mathur, Jahan Dawlaty, Sunitha Bandla Ayers, Eugene Hwang, Tiffany Cheng, and Dana Weinstein.

I used the resources of many facilities for my research. I would like to thank the staff at Cornell Nanoscale Science & Technology Facility, Cornell Center for Materials Research, and Center for Nanoscale Systems. I thank Nathan Ellis for

training me in the machine shop and sharing his expertise on machining.

I would like to thank my parents Fernap Ardanuç and İlker Ardanuç, my sister Sezin Ardanuç, and my relatives in Türkiye. They were very supportive during the first decade of my Ph.D. studies. I bet they would keep supporting me even if I had to keep on pursuing this degree for another decade.

I thank to my friends who helped me enjoy "gorges" Ithaca even more: Kürşad Araz, Aycan Yurtsever, Ömer İlday, Özhan Özatay , Onur Tokel, Onur Kuzucu, Erdal Yılmaz, Turan Birol, Helena Silva, Ali Gökırmak, Uygar Avcı, Chris Liu, Alper Bozkurt, Hazer İnaltekin, Joshua Mark Rubin, Maria Oldiges.

Special thanks goes to Jessie Anna Childs, who has always supported me. I give thanks to Jo and Philip Childs for welcoming me into their home. I also thank the Visser family for the amazing meals we had together.

My acknowledgments would not be complete without thanking Professor Bradley Minch, Professor Edwin Kan, Professor Frank Wise, and Professor Alan Zehnder for their excellent classes on circuits, solid-state, and solid mechanics. I also thank Korhan Sevenler, Peter Gulvin, Andrew Hays, Donald Drake, and Peter Nystrom, whom I was fortunate enough to know during my summer internship at Xerox.

Last but not the least, I would like to acknowledge Professor Tayfun Akın and Professor Cengiz Beşikci of Middle East Technical University for inspiring me, when I was an undergraduate student, to pursue this path.

I am pretty sure that I am missing many people here. If you are one of those: "Thank you!"

TABLE OF CONTENTS

LIST OF TABLES

LIST OF FIGURES

CHAPTER 1

INTRODUCTION

The operation of all microsystems can be reduced down to one or more kinds of transduction (sensing and actuation) mechanisms. As such, it is hard to think that microsystem technologies would be ignorant of piezoelectric materials that provide a reciprocal platform for electrical to mechanical energy conversion.

While piezoelectric layers with thicknesses less than a few microns can be deposited using sputtering or sol-gel deposition, applications that require larger forces or strokes often require thicker layers. One of the fundamental limitations of using a common, *high-quality*, piezoelectric material such as lead zirconium titanium oxide ($Pb(Zr_{1-x}, Ti_x)O_3$, PZT) within a microsystem is the high sintering temperatures exceeding 1000°C required for PZT. At these high temperatures, severe reaction and diffusion occurs between PZT and silicon, which is one of the most common elements in microsystems. This limitation can be overcome by using off-the shelf high-quality bulk-PZT, which is optimally manufactured and sintered. Despite the challenges of bonding and hybrid integration, many microsystems such as medical ultrasonic imaging arrays, microfluidic mixers, separators, pumps, and ultrasonic motors commonly use bulk-PZT transduction.

In this thesis, electromechanical modeling, actuation and sensing functions of bulk-piezoelectric transduction were investigated within the context of their applications to microsystems. The next chapter uses a two-port, electrical circuit to model bulk-piezoelectric actuation of surface-micromachined, polysilicon beams with electrostatic actuation electrodes. Both piezoelectric and electrostatic actuation capability of the same beam supports bidirectional gain measurements as well as a comparison between the actuation performance of these two approaches.

The measurements were done in the vicinity of the resonance frequencies of the beams, which ranged from 200 kHz to 300 kHz. Bidirectional transduction gain measurements between piezoelectric and electrostatic domain are then used to extract model parameters under different operating conditions. Both the equivalent circuit and the experimental results are discussed in consideration of the reciprocity theorem.

Chapter 3 presents a method for non-contact, batch assembly of polysilicon micromirrors, using bulk-piezoelectric and electrostatic actuation. This method, Ultrasound Enhanced Electrostatic Batch Assembly (U2EBA), is demonstrated for permanent (i.e., one-time) and close-to-vertical assembly of 2-D arrays of high fill-factor, hinged micromirrors. One of the highlights of this effort is the yield rates reaching up to 100% reported on certain types of micromirror arrays. Subsequent efforts described in Chapter 4 employ novel lock-in structures in order to keep the assembled structures at intermediate rotation angles between 0° and 90° relative to the substrate surface. Furthermore, the new lock-in design supports semi-permanent latching of the micromirrors. In this type of assembly, the rotation angles of the mirrors can be modified during the operation, while still having zero-idle-power in the latched state.

The importance of the above attributes of U2EBA is emphasized within the framework of Concentrated Solar Power (CSP) applications. In a conventional implementation of one type of CSP, meter-scale heliostats (mirrors) are rotated with motors in order to track the sun and to reflect the incoming radiation to a central tower for energy generation. Availability of a zero-idle-power, out-of-substrate, non-contact, low cost assembly method, namely U2EBA, brings forth the possibility to use micrometer to centimeter scale mirror arrays in large-area,

beam-redirection applications. The large mirrors conventionally used for these applications do not lend themselves to low fill-factor, tile-level integration over the surfaces. Tile-level integration not only brings CSP to residential level and allows it to be used in densely populated urban environments, but also turns solar energy harvesting into a *pervasive* and *built-in* concept, as opposed to a utility-scale technology. The vision, applications and implications of pervasive, concentrated solar energy harvesting, beam redirection, and energy focusing are described in Chapter 5. This chapter substantiates many of the discussions with a working prototype of a high fill-factor, centimeter scale mirrors that can track the brightest spot in the ambient and can be wirelessly controlled.

On the sensing front of bulk-piezoelectricity, the focus of Chapter 6 is on the capacitive sensing via crystal oscillators. The sensing occurs via the shift in the mechanical resonance frequency of a quartz resonator in response to a change in electrical loading across the terminals of the crystal. Outstanding stability of quartz and decades long know-how to optimize its characteristics for time-control applications give quartz sensors a competitive edge in the low-cost, high-accuracy sensor arena. However, the use of an oscillating circuitry to lock into the mechanical resonance of the quartz resonator, introduces sources of variation, unless they are carefully controlled. More importantly, the intrinsic nonlinearity of a quartz oscillator as a capacitive sensor is problematic for large-dynamic range measurements. The main contribution of this chapter is a Time-Multiplexed Crystal based Capacitive Sensing (TM-XCS) method to compensate for circuit related nonlinearities and variations. It is proposed that the same method can also be used for self-thermometry measurement of the quartz resonator, eliminating the need for an external thermometer for temperature compensation. In addition, TM-XCS enables measurement of two or more capacitances using the same crystal, which

is especially important for many microsystems using differential capacitance measurement for higher common-mode rejection ratios.

Experiments and circuit simulations are performed to verify the models used in the derivation of the TM-XCS. Results of the experiments in conjunction with the published stability data from the literature are shown to be in agreement with the theoretical performance estimates regarding the minimum detectable level of capacitance.

Lastly, microparticle transport using bulk-piezoelectric actuation is demonstrated as an example of microfluidic applications in Chapter 7. Motion of five to ten micron beads is shown inside a microchannel that has, on one side, a 1-D array of SiN membranes deposited by LPCVD and released by KOH etching. Experiment results on the phased drive of PZT actuators that are coupled to different points along this channel are described. A process flow is given for the extension of 1-D concept to 2-D for localized, off-chip control of microsystems. Related fabrication challenges are discussed.

A summary of contributions of the thesis and a discussion of future work are given in Chapter 8.

CHAPTER 2

BULK-PIEZOELECTRIC TRANSDUCTION OF SURFACE MICROMACHINED BEAM RESONATORS THAT INCORPORATE ELECTROSTATIC ACTUATION ELECTRODES

2.1 Introduction

Electrostatic and piezoelectric transduction are common in microsystems: RF-MEMS [24–26], microfluidic pumps and valves [27,28], optical beam scanners and displays [29,30], medical ultrasound imaging [31,32], accelerometers [33,34], droplet generation for fluidic ejectors [35,36] can be listed just to name a few applications. In many cases, a microstructure is driven to resonance either by electrostatic or thin-film piezoelectric actuation to perform sensing, actuation or both. This structure can be a beam as in the case of electromechanical filter applications [37,38], or it can be a large diaphragm as in the case of microphone applications [39,40]. A comparative study of electrostatic and thin-film piezoelectric transduction of beam structures can be found in the literature [41,42]. This chapter focuses on excitation of microstructures by another type of piezoelectric actuation, "bulk-piezoelectric actuation", which makes use of bonded, millimeter scale, off-the-shelf, piezoelectric substrates[1].

Bulk-piezoelectric actuation of micro-resonators usually requires piece-by-piece assembly, and it is more commonly used at lower frequencies (< 5 MHz). Optical beam-scanners [44], ultrasonic motors [45], atomic force microscopes or resonant sensors with optical interrogation for frequency detection [46] are examples of microsystems using bulk-PZT actuation. The experimental method usually involves

[1]Part of the material presented in this chapter was published in reference [43].

clamping or adhesive bonding the bulk-piezoelectric ceramic, that is often made of lead zirconium titanate (PZT), to the bottom of the die that houses the resonator. The nature of energy coupling in these systems is fundamentally different than that of electrostatic (ES) or thin-film piezoelectric actuation. This is due to the excitation through the anchor and the substrate as opposed to the excitation by a distributed force or moment applied along the beam by locally generated forces.

It was recently reported that bulk-acoustic waves excited from a resonating microstructure could be detected by a piezoelectric ceramic attached to the die housing the resonator [47–49]. This is significant in a few ways. Firstly, it is a reminder that bulk-piezoelectric transduction is bi-directional despite the large difference in scales of bulk ceramic and the micro-resonators. Given the reciprocity of the piezoelectric effect, a piezoelectric ceramic on the backside could be used to detect part of the energy loss through the anchor. Secondly, ultrasonic detection of microstructure vibrations can allow measurements in situations where individual resonators cannot be electrically probed, but can be excited by magnetic or optical [50] means. In such cases, microstructure displacement can be monitored continuously by bulk-piezoelectric sensing without the need for any electrical pad and interconnects.

The microstructure mechanical coupling to bulk silicon is reminiscent of a microphone/speakerphone pair, one piezoelectric other electrostatic, interacting with each other through the substrate on which the resonator resides. Just like in large-scale, non-destructive testing or ultrasonic spectroscopy applications, the interaction between them carries the signature of the properties of the acoustic coupling medium. For example, Wong *et al.* recently suggested that this idea could be useful for the non-destructive assessment of the lifetime in RF-MEMS switches [51].

Earlier implementations of similar principles were used in dynamic, tip-based microscopy applications to map elastic properties on the surface of samples [52, 53].

The diverse applications of bulk-PZT to microstructure energy coupling need a model that can aid both in the design and interpretation of experimental results. Although Finite Element Modelling (FEM) can give desired levels of accuracy, first order equivalent circuits employing passive RLC components, dependent sources, and transformers are useful to convey the necessary insight about the magnitude (and phase) of the coupling. Also, an equivalent small-signal model can easily be integrated into circuit simulation software such as SPICE.

The goal of this work is to characterize acoustic wave coupling between resonators and bulk-PZT using a two-port, electromechanical model. Electrostatically actuated beams are employed as a benchmark in this effort. After describing the device under test in the next section, experimental results for the electrical characterization are given in Section 2.3. Section 2.4 introduces the equivalent electrical circuit and illustrates extraction of its parameters from the measurement results. It is followed by a discussion on reciprocity and comparison of bulk-PZT actuation to ES actuation. Section 2.5 concludes with a summary of key findings and future work.

2.2 Device description

The experiments were performed on surface-micromachined polysilicon beams, which were manufactured via PolyMUMPS® process from MEMSCAP [54]. All of the beams had poly-1 layer as the structural material and the top electrode, poly-0 layer as the bottom electrode. Beams were 10 μm wide, and they had a nominal

gap of 2 μm between poly-0 and poly-1. The devices were released in a supercritical point dryer after wet etching of the sacrificial layer between the electrodes. The experiments reported in this chapter were done on two different kinds of beams. One beam, also referred as *fixed-fixed beam*, was a conventional, bridge-like beam anchored at its two ends. The other beam, *fixed-fixed beam with tether*, was similar but with tethers close to the anchor. An SEM picture of the second type and an illustration of its paddle and tether regions are shown in Figure 2.1. At the bottom of the same figure, is a cross-section of the beam that highlights the electrodes and some of the layers used in the fabrication process. All tested beams were 200 μm long; Beam-A and Beam-B were fixed-fixed beams with tether, Beam-C was a fixed-fixed beam.

The coupling of the beam resonators to the bulk-PZT transducer was realized on a circuit board with a copper pad frame as shown in Figure 2.2. The piezoelectric ceramic used as the ultrasonic transducer was PZT-4 (Staveley NDT). Its bottom electrode was contacted via the top conducting surface of the underlying spacers. The spacers were also PZT-4, but with one electrode floating, making them inactive as mechanical transducers. The use of the spacers is optional, included here to decrease the energy loss due to ultrasound radiation to the circuit board. Silver paint was used to bond the spacer to the PZT plate since the interface between the two structures required electrical conduction. The most important bonding, the one between PZT and the silicon die, was done using cyanoacrylate (3M, Pronto CA-5). The same adhesive was used also to hold the spacers in place on the pad-frame.

The PZT rectangular bar was 5 mm wide, 25.4 mm long, and 0.5 mm thick. One design criteria was to have enough separation between the bulk resonance

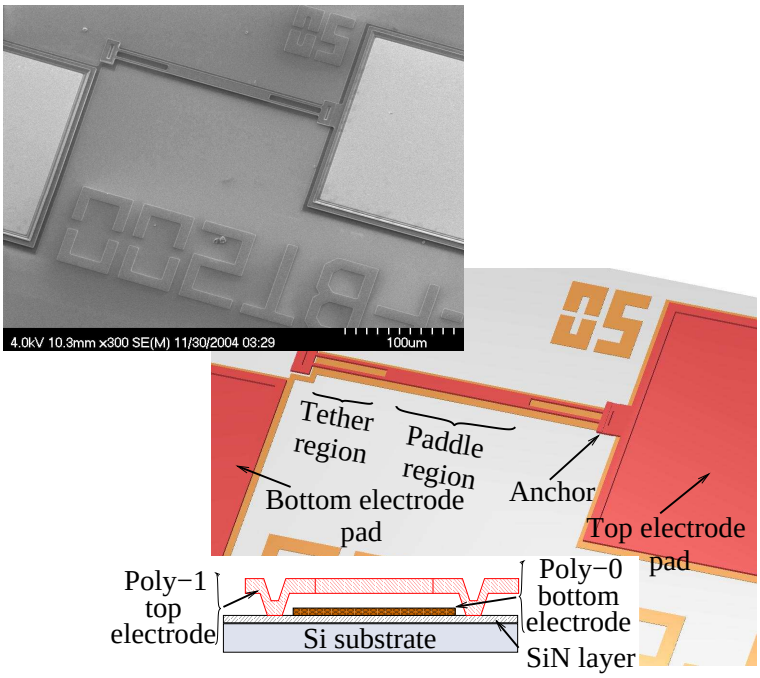

Figure 2.1: SEM picture (top), cross-section (bottom), and 3-D rendered illustration (background) of the **f**ixed-fixed **b**eam with **t**ether, *FBT-200*. The nominal gap between the top and bottom electrodes of the beam is 2 μm. The beam shown in the SEM has a 100 μm long paddle region and a pair of 50 μm long, 2 μm wide cantilever legs on each side in the tether region. Some of the tested *FBT-200* samples included variations in the length of the paddle regions.

frequencies of the PZT/Si stack and those of the beams to avoid co-resonant actuation. The electrical impedance of the PZT shown in Figure 2.3 is instrumental in this regard. The longitudinal mode along length is observed at 59.5 kHz and that along width is at 329.3 kHz; the ratio of which is within 10% of the width to length ratio of the PZT. After the bonding operation, the modes along the length and the width shifted to 64.5 kHz and 391.2 kHZ, respectively. As to be presented later, these frequencies are far from the resonance frequencies of the micromachined beams under test, which lie in the range from 210 kHz to 300 kHz. The inset in

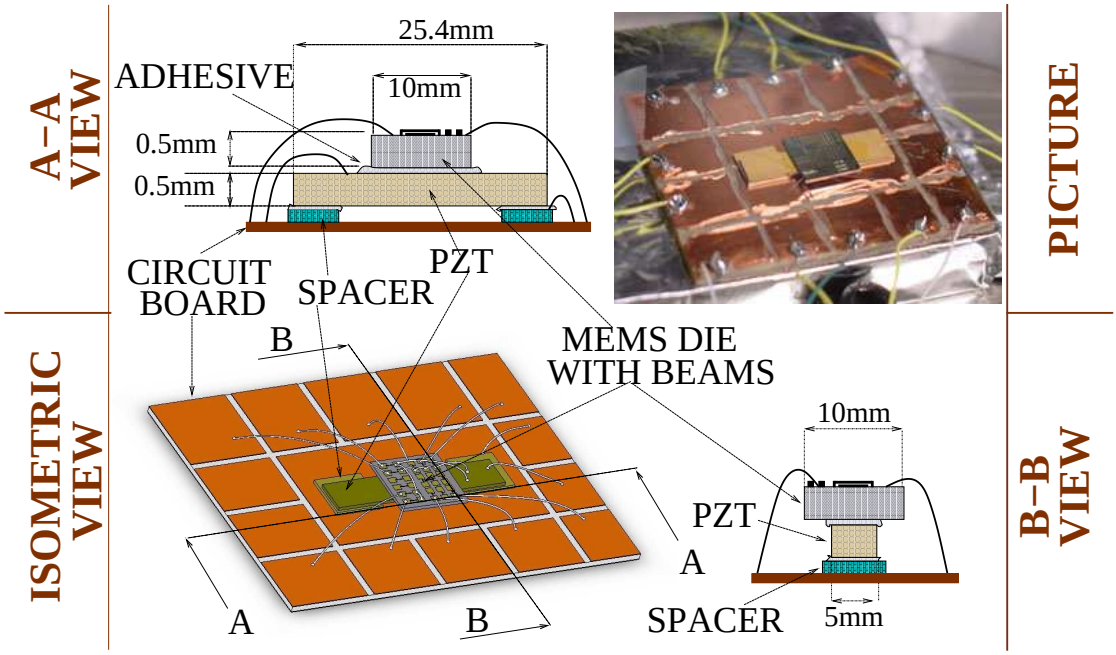

Figure 2.2: Illustration of the circuit board, PZT and MEMS die assembly. The isometric view is scaled (excluding the beams on the surface), but the cross-section views are not scaled for the sake of clearance. Note from "B-B view" that part of the silicon die hangs over the PZT bar. The individual beams are wirebonded to the pad frame along with the top and bottom electrodes of the PZT. The image on the top right shows the optical picture taken inside the vacuum chamber.

Figure 2.3 is the impedance amplitude in this frequency range and shows that no strong bulk resonance exists. However, the weak bulk resonance around 215 kHz that was present only in the bonded device had to be accepted, but numerically did not affect our analysis.

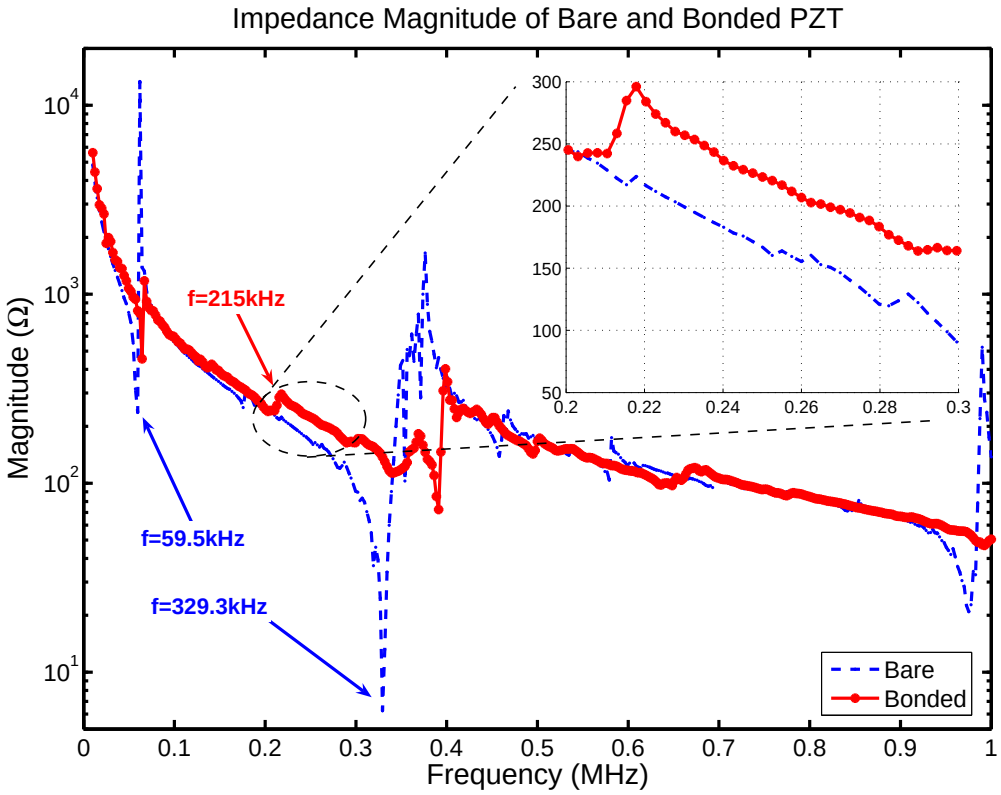

Figure 2.3: The impedance of the PZT bar measured using an HP4194 impedance analyzer before and after the assembly of the device. The resonance frequencies quoted in the text are indicated. The inset shows a zoomed view of the frequency range of operation that is of interest in this work.

2.3 Experiments

2.3.1 Forward and backward gain characteristics

The device under investigation has two electrical ports as shown in the schematic cross-section of Figure 2.4. The polysilicon electrodes of the electrostatically actuated beam constitute one port with its voltage and current defined as v_3 and i_3, respectively. This port is also referred as the "ES-port" throughout the text. The

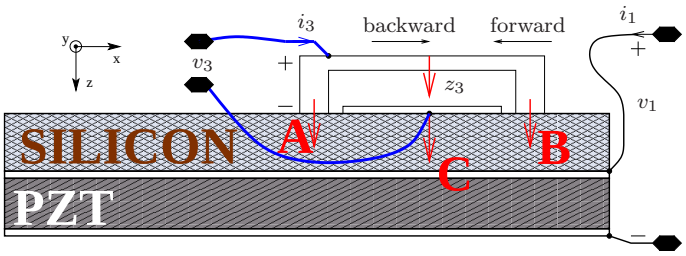

Figure 2.4: The physical schematic of a beam on a die coupled to a PZT plate underneath. The labels on top of the arrows show the naming convention used to refer to the gain experiments in this chapter.

second electrical port, named "PZT-port," is across the terminals of the PZT, and its associated voltage and current are labelled as v_1 and i_1, respectively. All of the mechanical coupling between the beam and the PZT/Si stack occurs across three regions which are indicated by letters 'A','B' and 'C' in the figure. 'A' and 'B' are used for anchors and 'C' for the bottom electrode region. The displacement of the center of the beam along z-axis, which is the mechanical variable of interest, is denoted by z_3.

The electrical characterization of the coupling between the beam and the PZT is done by bidirectional gain measurements. The direction of gain labelled as "forward" has PZT-port as the input and ES-port as the output, and the reverse direction is labelled as "backward." In a typical forward gain experiment, the PZT is excited and the displacement current of the beam is measured. As such, it can also be referred as the "piezoelectric actuation - ES pickup" experiment. Similarly, the backward one can be interpreted as "ES actuation - piezoelectric pickup." In addition, single port measurements of impedance at either port can be used for electrical characterization.

The electrical connections used for the forward and the backward gain mea-

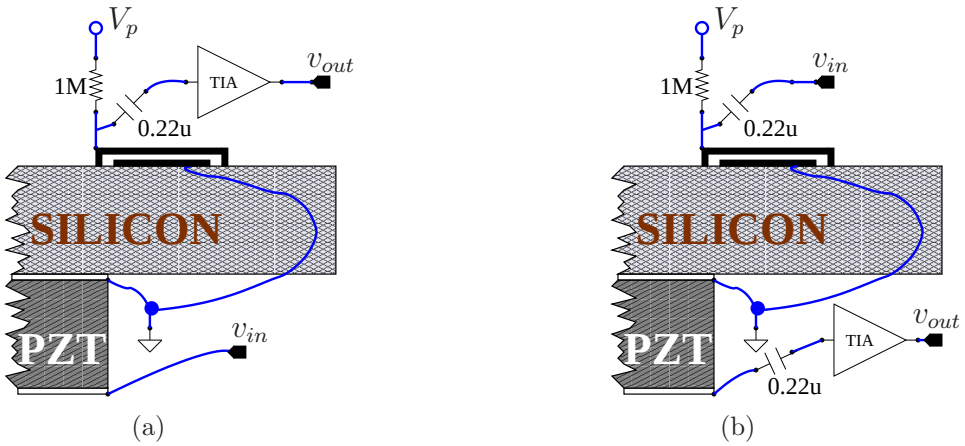

Figure 2.5: Wiring for (a) forward gain experiments: piezoelectric actuation & electrostatic pickup, (b) backward gain experiments: electrostatic actuation & piezoelectric pickup. In the backward case, the PZT presents a large capacitive loading at the input of the TIA, so attention must be paid while using its gain in the calculations. For Beam-C, the connections to the top and bottom electrodes of the beam were swapped for both the forward and the backward gain measurements.

surements are illustrated in Figure 2.5. Polarization voltage, V_p, is applied via a bias resistor of 1 MΩ. The output current in either case was measured by a transimpedance amplifier (TIA) that is AC-coupled to the output port of interest in series with a capacitor of 0.22 uF. Unless otherwise stated, all of the experiments involving beam excitation or motion sensing were performed at $80-100$ mTorr, at room temperature. The gain measurements were performed with an HP4194A network/impedance analyzer.

The amplitude of the measured forward gain is presented in Figure 2.6 for Beam-B at an input power level of $P_{in} = -30$ dBm. The peaks observed in the transfer characteristic correspond to the fundamental transverse resonance of the beam under test. A decrease in the peak transmission frequency as a result of an increase in V_p is clearly visible in the results. This behavior is typical of parallel-

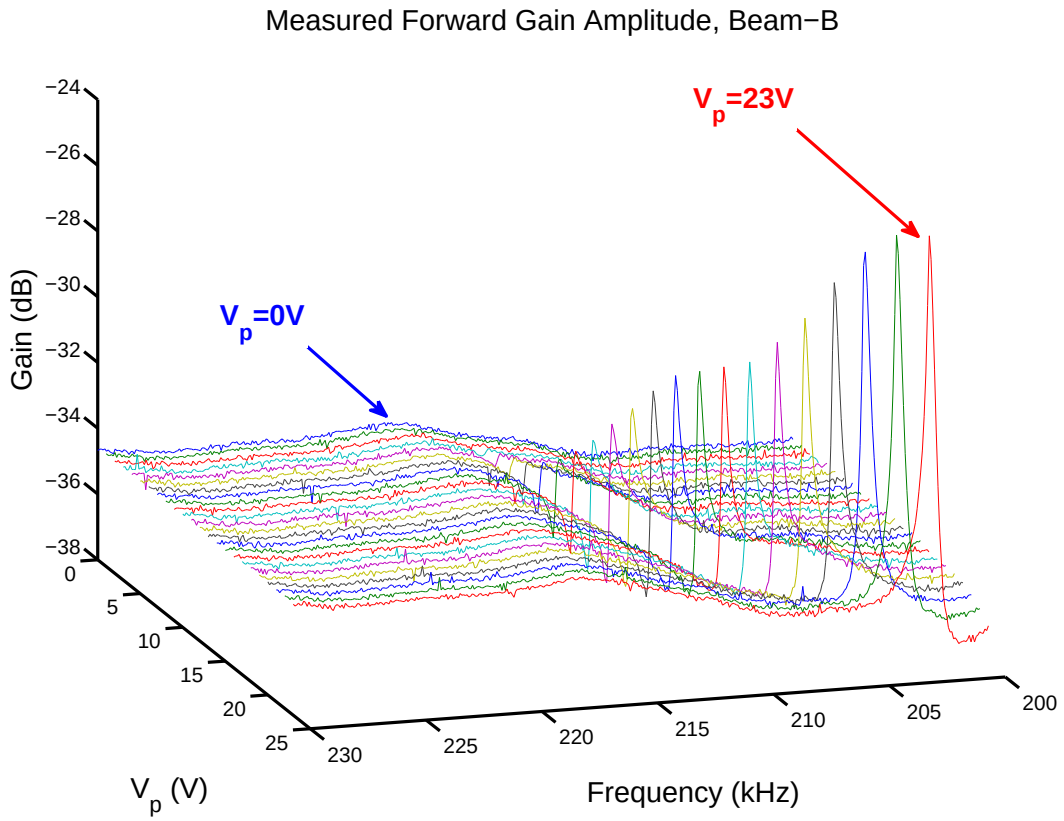

Figure 2.6: The forward gain amplitude for different V_p. The measurements are taken at $P_{in} = -30$ dBm with the setup shown in Figure 2.5(a).

plate, electrostatic actuators [55, 56], which is summarized in Appendix A. On the other hand, the rate of increase of the gain amplitude at resonance as a result of increase in V_p shows some irregularities.

Figure 2.7 gives the measured amplitude of the backward gain for the same beam and at the same input power level as that of forward gain. Backward gain characteristics depicts a much weaker signal, hence they are plotted for large V_p, that is only when the peaks in the gain response become distinguishable from the background signal level.

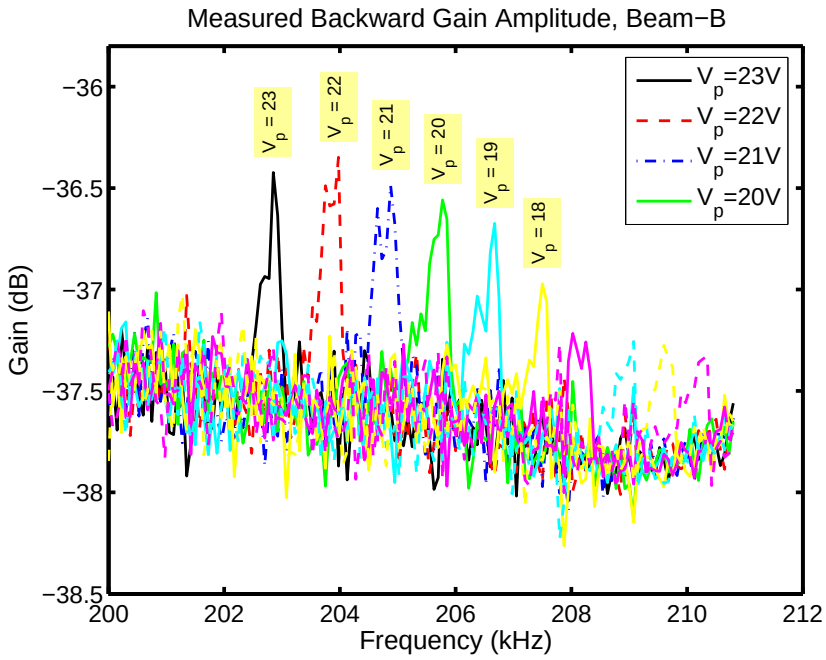

Figure 2.7: The measured backward gain at $P_{in} = -30$ dBm. Note the very small signal showing up only at large polarization voltages due to low SNR in the measurement setup.

The decrease in the peak gain frequency of the backward gain amplitude follows the same trends as that of the forward gain as the polarization voltage is changed. However, a consistent mismatch can be noticed between the peak gain frequencies of the forward and backward gain characteristics. The supporting data for this observation are presented in Figure 2.8. This mismatch originates from the nonlinearity of the fixed-fixed beam due to large vibration amplitudes, and it is explained in detail in the following section.

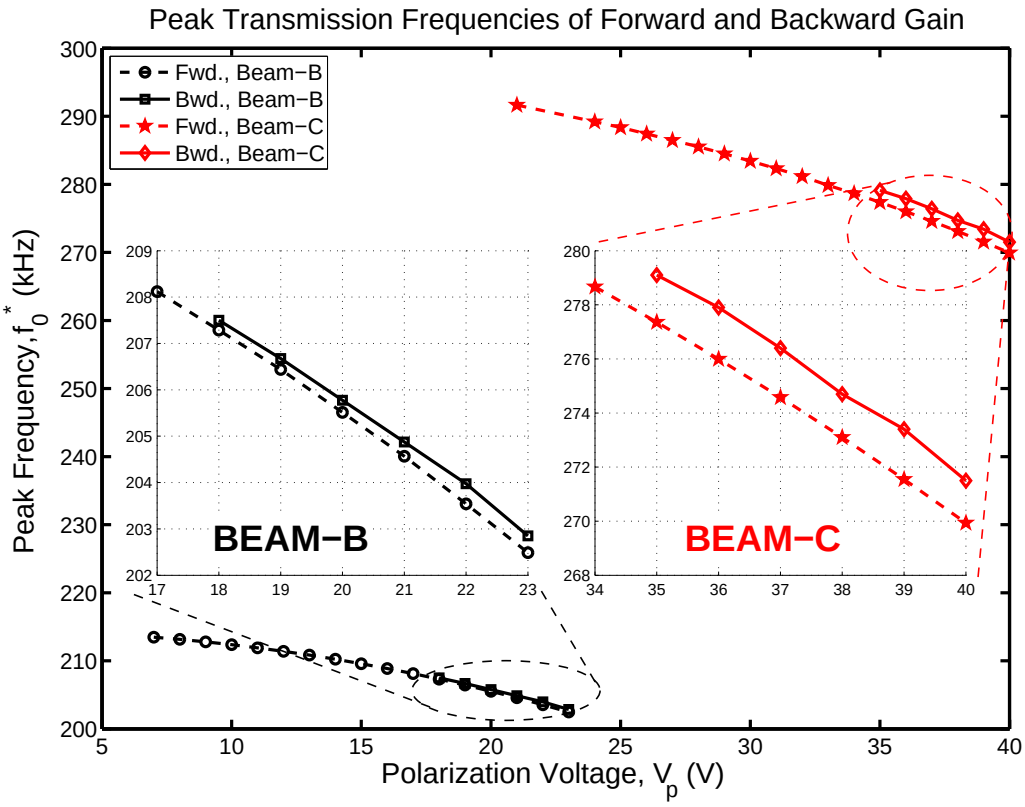

Figure 2.8: A comparison of peak transmission frequencies between forward and backward gain measurements for beams B and C. The insets give the zoomed views to highlight the difference.

2.3.2 Transduction nonlinearity

As the drive levels of resonators are increased, nonlinear effects become important [57]. The amount of nonlinearity for both the ES and the PZT actuation, as a function of the drive level, was quantified by the ES sensing of the beam displacement. The differential readout circuit and its wiring to the device in case of the ES actuation are illustrated in Figure 2.9(a). An instrumentation amplifier (AD621) followed by a gain stage was used to electrically subtract background signal from a similar but unpolarized beam. Measured gain amplitude and phase from this ES-actuation ES-detection experiment, $A_{ES-ES} = v_{out}/v_{in}$, were recorded at vary-

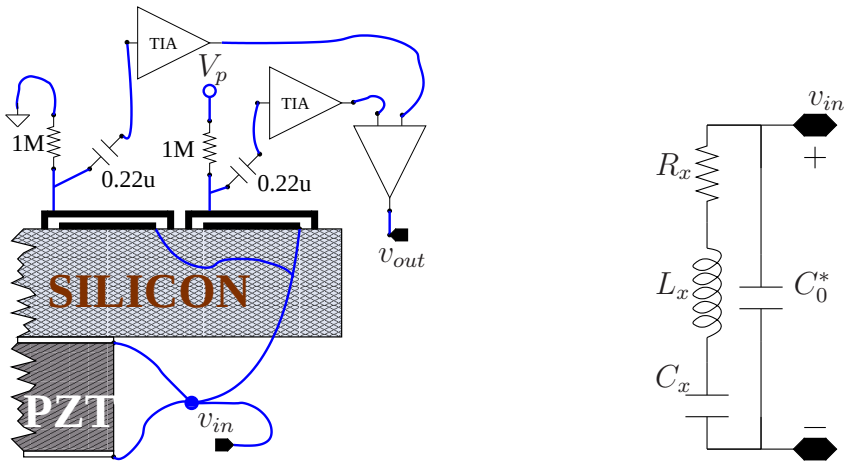

Figure 2.9: (a) Diagram showing electrical connections for the electrostatic gain A_{ES-ES} measurement. Bias resistances are 1MΩ, and AC coupling capacitances are 0.22μF. Shorting the terminals of PZT to the input signal not only eliminates PZT actuation, but also reduces stray capacitances between the beams and the top electrode of PZT. (b) Equivalent electrical circuit for the beam resonator (explained in Section 2.4.2).

ing input drive levels. The dual experiment, i.e., PZT-actuation ES detection, was performed using the same readout circuit to make a controlled comparison while having the rest of the connections as in Figure 2.5(a).

The limits of linear operation were tested on Beam-A[2] by increasing the oscillator level of the network analyzer from −40 dBm to −20 dBm. The PZT and the ES actuation results are given on the top and bottom plots, respectively, of Figure 2.10. They were all measured at $V_p = 20$ V and plotted after subtraction of $V_p = 0$ V data that was treated as a background signal.

The characteristic seen in both types of actuation in Figure 2.10 is typical in nonlinear resonators and is due to forced Duffing oscillations as a result of spring stiffening at large vibration amplitudes [57]. At the experiment conditions

[2]with Beam-B as the reference in Figure 2.9(a).

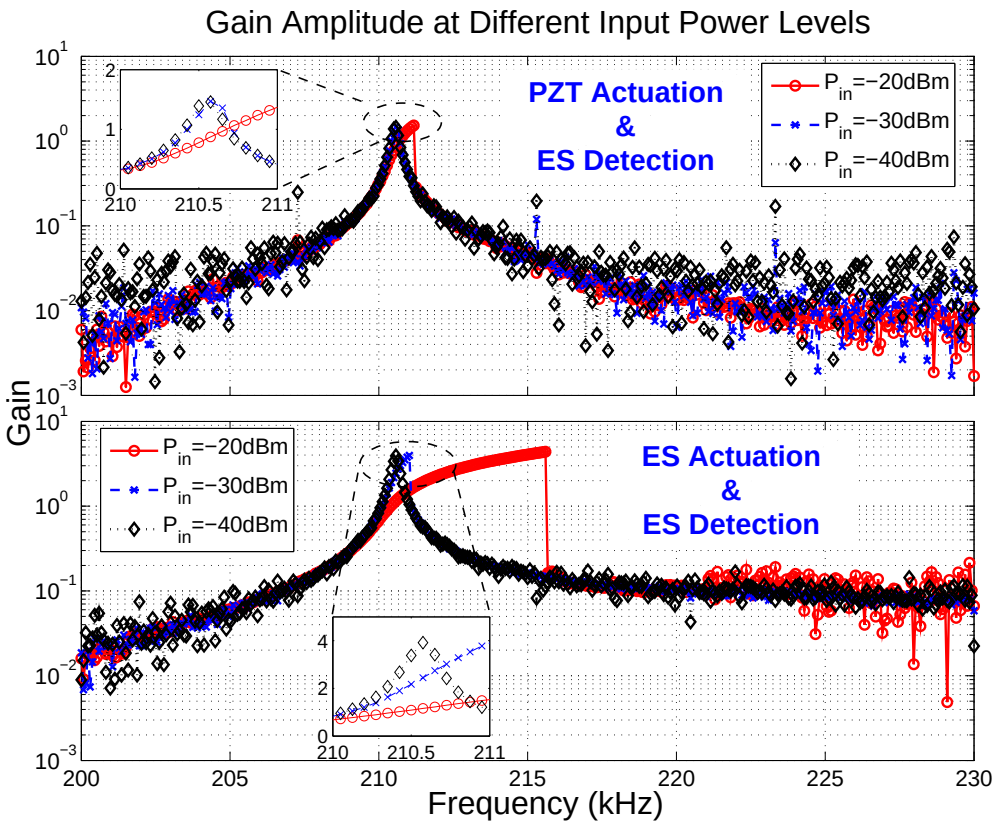

Figure 2.10: Gain amplitude from PZT (top) and ES (bottom) excitation measured from the Beam-A displacement current under different input power levels. The results are after background subtraction to better reveal that the PZT excitation remains linear while the ES excitation goes nonlinear when $P_{in} = -30$ dBm.

of $P_{in} = -30$ dBm, insets indicate that the ES actuation suffers from nonlinearity, while this is not apparent in the PZT actuation. This result shows that the ES actuation causes larger displacements than the PZT actuation at the same input power on the tested beams. A quantitative comparison of displacements between the ES and the PZT actuation is deferred until after equivalent circuit modeling is discussed in Section 2.4.1.

The stiffening of the spring due to nonlinear operation as in Figure 2.10 explains why the peak transmission frequencies from the backward gain measurements were

higher than those of the forward gain in Figure 2.8. In the forward gain experiments, PZT actuation at $P_{in} = -30$ dBm does not cause significant nonlinearity, while the ES actuation in backward gain experiments at the same power level causes significant nonlinearity. This nonlinearity leads to an increase in the measured resonance frequency of the beam at a given V_p as compared to the forward gain experiments.

On the other hand, decreasing the power levels to less than -30 dBm to minimize the nonlinearity, deteriorated the signal-to-noise ratio (SNR) of the backward gain experiments. In experiments used for model extraction, input power levels were kept in the range from -40 dBm to -30 dBm in consideration of conflicting requirements of SNR and nonlinearity.

2.3.3 Transimpedance amplifier characterization

The transimpedance amplifier (TIA) comprises the core of the detection circuitry to amplify the displacement current from the vibrating beam and also to convert the strain induced current on the PZT side.

In the forward gain configuration (as in Figure 2.5(a)), the input of the TIA is connected to the ES-port of a micro-scale beam that presents a shunt source capacitance on the order of femto-Farad. In the backward gain configuration (as in Figure 2.5(b)), on the other hand, the PZT-port terminals present a shunt capacitance on the order of nano-Farad to the input of the TIA. Consequently, the characterization of the frequency response of the same TIA under different loading conditions at its input is critical from a modelling standpoint. An analytical treatment of the effect of input capacitance on the TIA performance in terms of

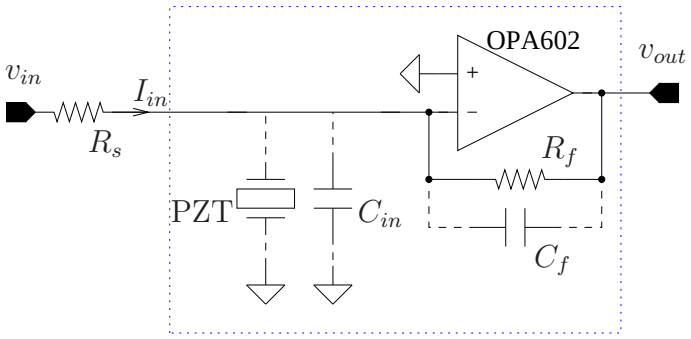

Figure 2.11: Schematic view of the transimpedance amplifier is shown with possible configurations that replicate the wiring setup in the forward and the backward gain experiments. R_f was fixed at 100 kΩ for all measurements.

op-amp specifications is given elsewhere [56].

Figure 2.11 shows the schematic of the TIA used in this work. This circuit, which was designed to have a low frequency transimpedance gain amplitude of 100 kΩ, was constructed on a breadboard using a high-speed, precision operational amplifier, OPA602[3]. The elements shown with dashed wiring in Figure 2.11 are added on demand to test under conditions encountered in the experiments. C_{in} and C_f represent the input and compensation capacitors, respectively.

The amplitude of the frequency response of the amplifier under different connection scenarios is shown in Figure 2.12. A broad peak in the amplitude response is obtained if none of the dashed elements in Figure 2.11 are connected. This peak is suppressed with the addition of a compensation capacitor of 5 pF, which was used for all the other experiments reported in this chapter. The 3 dB-bandwidth with the compensation capacitor was measured as 415 kHz.

The impact of a large capacitor at the input on the amplifier characteristic can

[3]Vendor specified nominal input bias current and unity-gain bandwidth are 1 pA and 6.5 MHz, respectively.

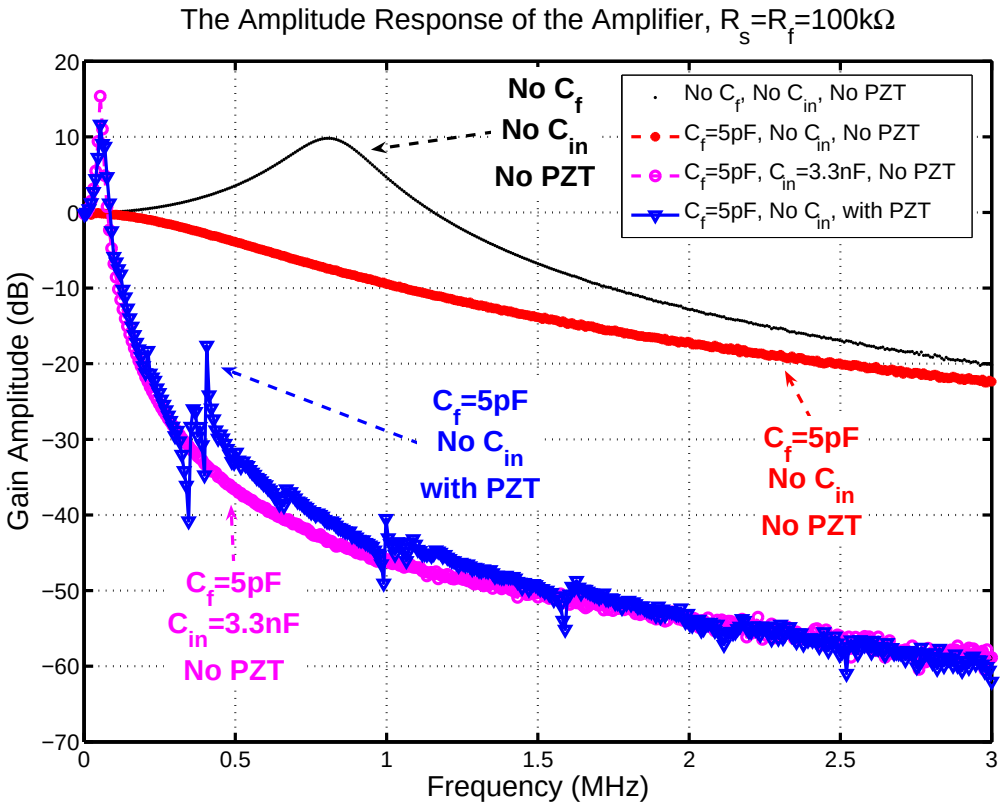

Figure 2.12: Amplitude response of the TIA amplifier at $P_{in} = -40$ dBm with source resistance , $R_s = 100$ kΩ. Curves are labelled with lists of used elements shown dashed in Figure 2.11. Measurements were done with an HP4194A network analyzer.

be seen in Figure 2.12 for the case of $C_{in} = 3.3$ nF. This particular value was picked in order to emulate the capacitive nature of the PZT impedance with the help of Figure 2.3 and after some finetuning. As seen in the figure, the general effect of addition of PZT from our bonded device is sufficiently modelled by an external capacitance. The extra peaks in the case of the PZT at the input of the TIA stem from the bulk resonances of the PZT/Si stack, one of which is also apparent in Figure 2.3.

2.4 Electrical equivalent circuit and parameter extraction

Prediction of die-level surface vibration amplitudes and their coupling to resonator microstructures via their anchor is challenging without FEM. However, 3-D FEM of devices from micrometer scale to centimeter scale often requires demanding meshing algorithms or abstraction of boundary conditions. As an alternative to FEM, one can approximate the stress and displacement for thickness mode resonators using 1-D equivalent circuits that use transmission lines and transformers. Although these models can provide us with a starting point, the boundary conditions of the real life problem often limit one-to-one applicability of this analytical approach. This is true for our case, in which 1 cm^2 silicon die with polysilicon beams on top is partially excited by the PZT from bottom.

An intuitive empirical tool in similar complex problems is to isolate the complex part of the system from the well understood part. In our case, bidirectional substrate to beam coupling is the complex part of the system, whereas the ES transduction of the beam is well understood. The extraction of the parameters of the model associated with the complex part can then help in identifying patterns of variation in substrate to beam coupling among beams with similar ES transduction characteristics. This section introduces an empirical, small-signal equivalent circuit and illustrates the parameter extraction process using mostly the results of Section 2.3.

2.4.1 Small-signal electrical equivalent circuit

Like its physical counterpart, the equivalent circuit should have two electrical ports, the ES-port and the PZT-port. At this stage there are two lines of attack; the first one is a more intuitive approach that models the PZT-to-beam interactions with the Mason equivalent circuit for 1-D thickness mode vibrations [58, §1.4]. This approach was described by Ardanuc and Lal in [43]. The second line of attack, which is described in this subsection, is a more rigorous one, and it mainly uses only first order principles.

The ES-port excitation and the beam dynamics are modelled with the Mass-Spring-Damper (MSD) description of the parallel plate ES actuator given in Appendix A [55, 56]. In this model: k is the mechanical spring constant, m is the mass, b is the damping constant, V_p is the DC polarization voltage applied to the moving plate, C_0 is the parallel plate capacitance with no applied voltage, g_0 is the parallel plate gap at its undeformed state, z_0 is the static displacement of the moving plate due to the polarization voltage, and η_{es} is the electromechanical transduction factor.

The illustration in Figure 2.13(a) takes the model in Appendix A one step further by assuming the equivalent mass of the beam being connected to the anchors via half of the system spring constant. Damping element is also divided symmetrically between the two anchors where z_1, z_2 represent the displacements, and F_1, F_2 represent the reaction forces. The displacement of the center of the beam is named as z_3.

Electrostatic force is added via a transformer of turns ratio η_{es} as shown in Figure 2.13(b) after replacing k by k^* to account for the electrostatically modified

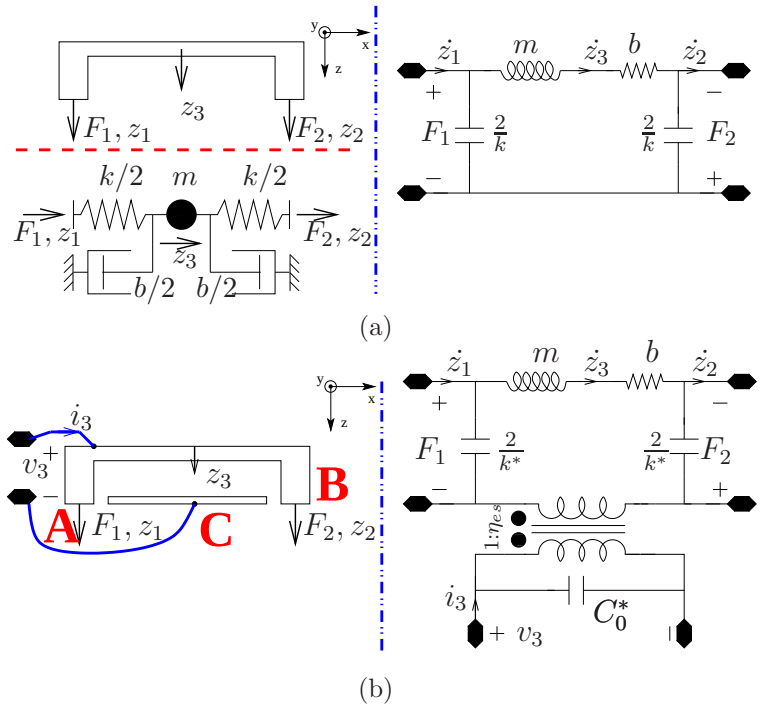

Figure 2.13: (a) On the left is the beam modeled as a mass spring system with anchor excitation force-displacement pairs given by (F_1, z_1) and (F_2, z_2). The displacements of mass and damper elements are represented by z_3. On the right is its equivalent circuit. (b) Electrostatic force can be added via a transformer of turns ratio η_{es} and by replacing k with k^*.

system spring constant. Similarly C_0^* represents the value of the static parallel plate capacitance, C_0, modified due to applied DC polarization voltage, V_p. All of the coupling between the beam and the PZT-Si stack occurs across three regions, each of which are indicated by letters 'A','B' and 'C' in the figure. 'A' and 'B' are used for anchors and 'C' for the bottom electrode region. Given the large size of the silicon die as compared to these regions of coupling, the reaction forces are assumed to be applied at their respective center.

Figure 2.14 describes the PZT side of the modelling problem. Figure 2.14(a) illustrates the circuit symbol used to represent the PZT-Si stack without the micro-beam. Electrical impedance of this element would be similar to that shown in

Figure 2.3 but with the micro-beam under test removed; in other words, with the coupling points under mechanically *free* boundary conditions.

Coupling to the PZT-Si stack at an arbitrary point on the die and its modelling are illustrated in Figure 2.14(b). The port labelled with v_1 on the left is PZT port, whereas the one on the right labelled with F_2 is the mechanical port representing the point of contact on the silicon surface atop PZT. The analogy between force-velocity pair to voltage-current pair is used. The sign convention is as shown on the bottom left picture in Figure 2.14(b) by F_2 and z_2. A two-port network, here represented in a hybrid (H)-parameter form, is picked as the *coupler element* to model the electromechanical interaction between the ports [59, §18.2]. Its symbol is shown at the bottom right of the same figure, with a highlight of the four elements that it comprises. The point of contact is indicated by L_{force} as a reminder that its parameters are a function of the position of the coupling point on the die. The terminal equations for the coupler element are given as:

$$i_{H1} = H_{11} v_{H1} + H_{12} i_{H2} \tag{2.1-a}$$

$$v_{H2} = H_{21} v_{H1} + H_{22} i_{H2}. \tag{2.1-b}$$

Here H_{22} is the ratio of the applied force to the velocity at the point of contact, with PZT terminals shorted. It has units of specific acoustic impedance multiplied by area, kg/sec. H_{22} gives a measure of the elastic stiffness seen from the point of contact. H_{12} and H_{21} are coupling parameters between different energy domains with units of N/V. H_{11} has units of Mho and is defined by the constraint that under no-force (free) conditions (i.e., $v_{H2} = F_2 = 0$), equivalent circuit of Figure 2.14(b) reduces to the symbol in Figure 2.14(a). A simple calculation shows that this requires the determinant of the H matrix to vanish, whereby uniquely

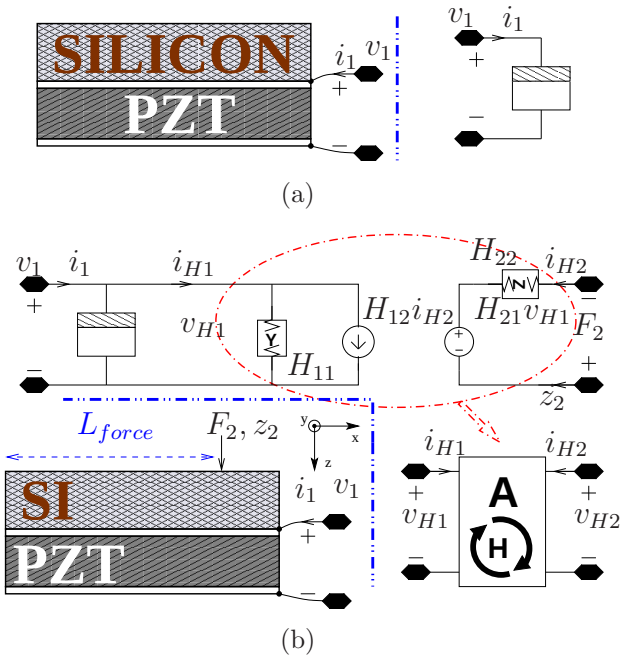

Figure 2.14: (a) To the left of the dashed curve is the picture of PZT-Si stack. To the right is the circuit symbol used to represent this structure. (b) Bottom left picture shows the application of a point force, L_{force} away from one side. The circuit to the right and above of the dashed line illustrates the coupling of this force to PZT ports via a two-port network using "H-parameters." The circuit symbol is given at the bottom right, and its parameters depend in general on L_{force} and frequency.

defining H_{11} to be[4]:

$$H_{11} = \frac{H_{12}H_{21}}{H_{22}}. \tag{2.2}$$

It can be shown that for a lossless, inhomogeneous media that includes piezoelectric materials, coupled electromagnetic and piezoelectric equations satisfy a reciprocity relation [60, 61]. From a circuit-theoretical point of view, this requires $H_{12} = -H_{21}$ [59]. However, we do not impose this constraint at this stage in order to avoid any confusion in the description of experiments by which their values are separately extracted and then compared.

[4]Finite current and voltage pairs can satisfy Equation (2.1) even when H matrix is singular.

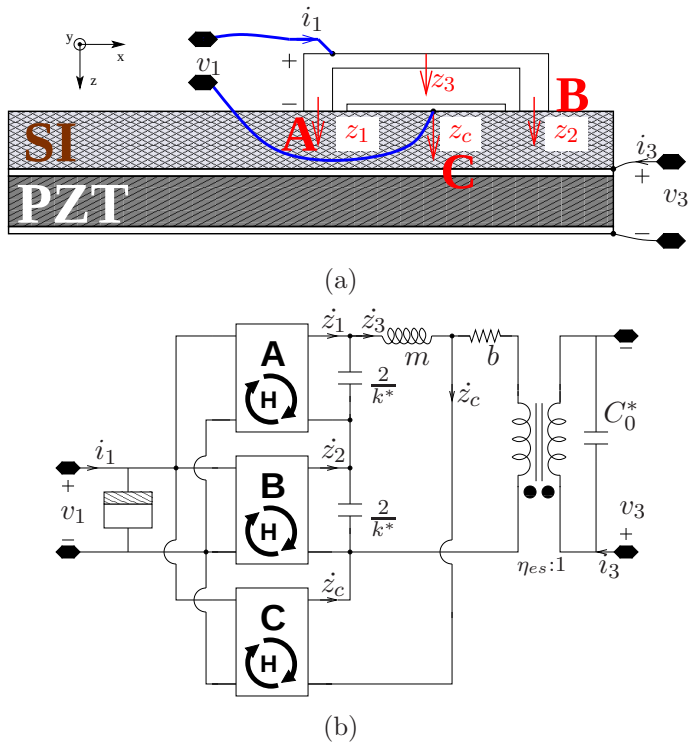

Figure 2.15: (a) Physical schematic of a beam on a die coupled to a PZT plate underneath. Displacements of anchors, the center of the beam, and the center of the ground electrode are as labelled. (b) Equivalent circuit which makes use of the coupler network defined in Figure 2.14(b).

Next step in building the equivalent circuit is to insert a coupler element at the points of interaction represented by 'A' to 'C' and with corresponding coupling parameters, $H_{pq,r} \mid p, q \in \{1, 2\} \wedge r \in \{A, B, C\}$. This is illustrated in Figure 2.15(a) and is similar to the receptance matrix approach used by Park *et al.* in the frequency domain [62, Equation 32]. The resulting circuit is given in Figure 2.15(b), where couplers are tagged with their corresponding point labels to emphasize that they are not identical. Furthermore, b in the figure is assumed to represent only squeeze film damping that is proportional to relative velocity of the beam center measured with reference to the ground electrode on the substrate. Displacement of the center of the ground electrode is represented by z_c.

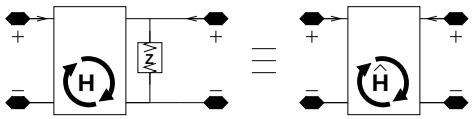

Figure 2.16: The coupler with a shunt load impedance of Z_L at the second port is represented by another coupler of modified parameters as given by Equation (2.3).

At this step, we need the circuit equivalence relation illustrated in Figure 2.16 and described by Equation (2.3). This simplifies the case when a shunt load impedance of Z_L is connected at the second port of the coupler, and it is used to dissolve out the $\frac{2}{k^*}$ capacitors in Figure 2.15(b) by taking $Z_L = \frac{k^*}{2\mathbf{s}}$. Here, $\mathbf{s} = \mathrm{j}\,\omega$, $\mathrm{j} = \sqrt{-1}$, and the angular frequency of excitation is ω. This operation generates $\hat{H}_{pq,r}$ from $H_{pq,r}$, allowing transformation of the shunt connection to an equivalent series connection.

$$\hat{H}_{11} = H_{11} - \frac{H_{12}H_{21}}{H_{22} + Z_L} \tag{2.3-a}$$

$$\hat{H}_{22} = \frac{H_{22}Z_L}{H_{22} + Z_L} \tag{2.3-b}$$

$$\hat{H}_{12} = \frac{H_{12}Z_L}{H_{22} + Z_L} \tag{2.3-c}$$

$$\hat{H}_{21} = \frac{H_{21}Z_L}{H_{22} + Z_L} \tag{2.3-d}$$

After applying Equation (2.3) to the coupler elements at the anchors, we can derive the forward gain that is the short circuit current in response to a voltage excitation from the PZT side. This gain is expressed as

$$\begin{aligned} A_{for} &= \left.\frac{i_3}{v_1}\right|_{v_3=0} \\ &= \frac{\eta_{es}}{H_{22,C}+b}\left[\frac{\left(\hat{H}_{21,A}+\hat{H}_{21,B}\right)H_{22,C}-(Z_{sr}-b)\hat{H}_{21,C}}{Z_{sr}-\frac{b^2}{b+H_{22,C}}}\right], \end{aligned} \tag{2.4}$$

where $Z_{sr} = m\mathbf{s} + \hat{H}_{22,A} + \hat{H}_{22,B} + b$.

At frequencies much lower than the fundamental thickness mode resonance of the PZT, the beam sees a very stiff spring looking into the substrate. For example, consider an imaginary silicon pillar along the thickness of the substrate that has a cross section comparable to the anchor of the beams under investigation. In this case, $l_{bar} = 500$ μm long of silicon pillar with a cross section of $A_{bar} = 10 \times 10$ μm^2 leads a spring constant of $k_{bar} = E_{Si}A_{bar}/l_{bar} = 32$ kN/m, where Young's modulus of silicon, E_{Si}, is taken as 160 GPa. This is much larger than the typical values for beam spring constants ($k < 50$ N/m) that are of interest in this work. Similar can be said for k^*. Then, we have:

$$|H_{22,r}| \gg \frac{k^*}{2\mathbf{s}}, \mid r \in \{A, B, C\}. \tag{2.5}$$

This assumption lets us approximate the values of $\hat{H}_{22,A}$ and $\hat{H}_{22,B}$ in Equation (2.3) as in Equation (2.6) after taking $Z_L = k^*/(2\mathbf{s})$.

$$\hat{H}_{22,A} \approx k^*/(2\mathbf{s}) \approx \hat{H}_{22,B}. \tag{2.6}$$

Let us further assume that the beam has a high quality factor Q, and we are only interested in frequencies close to the resonance frequency of the beam. This assumption yields $Z_{sr} \approx b$. Similarly, with the help of Equation (2.5) and the relation $b = \sqrt{km}/Q$, we get simplifications for some of the terms in Equation (2.4):

$$H_{22,C} + b \approx H_{22,C} \quad , \quad Z_{sr} \approx b \gg \frac{b^2}{b + H_{22,C}} = b\frac{b}{b + H_{22,C}}. \tag{2.7}$$

This puts the forward gain into the following form:

$$A_{for} = \eta_{es}\frac{\left(\hat{H}_{21,A} + \hat{H}_{21,B}\right)}{Z_{sr}}. \tag{2.8}$$

By using the same approximations that brought us to Equation (2.8), one can show that $\frac{\dot{z}_c}{\dot{z}_3} \propto \frac{1}{Q}$, hence $\dot{z}_c$ being negligible with respect to $\dot{z}_3$. This is expected since the center of the beam moves much more than the ground electrode close to the

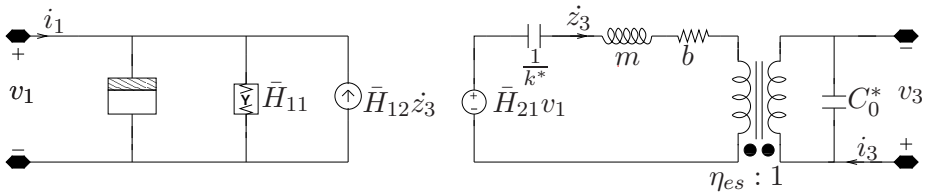

Figure 2.17: Schematic of the circuit in Figure 2.15(b) obtained after expanding the coupler elements of Figure 2.15(b)

resonance. In other words, for the circuit of Figure 2.15(b), the current through the wire splitting between the resistor and the inductor, $\dot{z}_c$, can be taken as zero. This brings us to Figure 2.17. The parameters for this circuit are given in Equation (2.9) that makes use of Equation (2.2) for the derivation of $\bar{H}_{11}$.

$$\begin{aligned}\bar{H}_{11} &= \hat{H}_{11,A} + \hat{H}_{11,B} + H_{11,C} \qquad \text{(2.9-a)}\\ &\cong H_{11,A} + H_{11,B} + H_{11,C} - \frac{H_{12,A}H_{21,A}}{H_{22,A}} - \frac{H_{12,B}H_{21,B}}{H_{22,B}}\\ &\cong H_{11,C}\end{aligned}$$

$$\bar{H}_{12} = \hat{H}_{12,A} + \hat{H}_{12,B} \cong \frac{H_{12,A}}{H_{22,A}}\frac{k^*}{2\mathbf{s}} + \frac{H_{12,B}}{H_{22,B}}\frac{k^*}{2\mathbf{s}} \qquad \text{(2.9-b)}$$

$$\bar{H}_{21} = \hat{H}_{21,A} + \hat{H}_{21,B} \cong \frac{H_{21,A}}{H_{22,A}}\frac{k^*}{2\mathbf{s}} + \frac{H_{21,B}}{H_{22,B}}\frac{k^*}{2\mathbf{s}} \qquad \text{(2.9-c)}$$

The resulting circuit in Figure 2.17 can be made more symmetric with the definition of new parameters. Taking $m_{23} = -\eta_{es}$, $\bar{H}_{21} = -m_{21}$, $\bar{H}_{12} = m_{12}$, $i_b = -\dot{z}_3$, and merging the first two parallel elements at the PZT port to form a different one with a crystal symbol, we finally come to the circuit of Figure 2.18. Here η_{es} is the electromechanical transduction factor described in Appendix A, and the component values are:

$$C_b = \frac{1}{k^*}, \quad \text{(2.10a)} \qquad L_b = m, \quad \text{(2.10b)} \qquad R_b = b. \quad \text{(2.10c)}$$

This circuit is reciprocal given the individual coupler elements are so, i.e., $\bar{H}_{12} = -\bar{H}_{21}$.

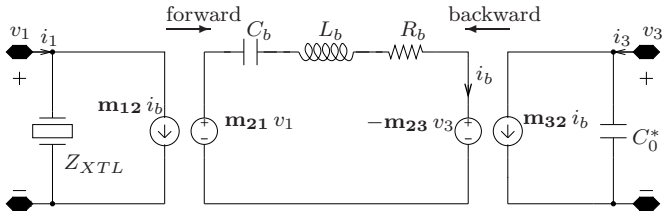

Figure 2.18: Small-signal equivalent circuit for the bulk-PZT actuation of a MEMS resonator modelled as a mass-spring-damper system. When power flow is from piezoelectric (left) to beam (right) side, its direction is referred as "forward" throughout the text. "Backward" is for the reverse direction.

The impedance block, Z_{XTL}, at the PZT-port in Figure 2.18 is different from an ordinary capacitor in that it accounts for the complex impedance due to structural resonances from the PZT/Si stack. When the effect of these resonances are negligible in the frequency range of interest, one can replace it with a capacitor as in the Mason equivalent circuit. Strictly speaking, it represents the admittance of the PZT/Si stack when the beam on top is forced to be stationary, i.e., $i_b = 0$.

Electrostatic coupling constants, $\mathbf{m_{32}} = \mathbf{m_{23}}$, root from the ideal transformer in Figure 2.13(b) being decomposed into dependent sources. They are given as:

$$\mathbf{m_{23}} = \mathbf{m_{32}} = -\eta_{\text{es}} = -\frac{V_p C_0^*}{g_0 - z_0}, \tag{2.11}$$

where g_0 is the parallel plate gap at its undeformed state, and z_0 is the static displacement of the moving plate in the MSD system due to applied polarization voltage, V_p. ES coupling constants have units of (N/V) along with the piezoelectric coupling constants, $\mathbf{m_{12}}$ and $\mathbf{m_{21}}$. An analytical expression for the latter pair is not available, whereas reciprocity arguments in elastic and piezoelectric media require their equivalence (i.e., $\mathbf{m_{12}}$=$\mathbf{m_{21}}$) just like the electrostatic pair. This would reduce the dependent sources on the piezoelectric side to an ideal transformer that implicitly implies reciprocity. In this case, the circuit would topologically be

similar to the one used to model thin-film piezoelectric actuated and sensed beams given by Humad *et al.* [63]. However, in order to facilitate independent extraction by forward and backward gain experiments and later to check how well they satisfy the reciprocity condition, we make no assumption about the equality of $\mathbf{m_{12}}$ and $\mathbf{m_{21}}$ at this stage. If the piezoelectric coupling coefficients are not equal (i.e., $\mathbf{m_{12}} \neq \mathbf{m_{21}}$), there would be an extra power dissipation term other than that modelled by R_b. The average value of this power dissipation can be described as

$$\mathrm{P}_{\mathrm{avg,dependent}} = \Re\left(\frac{(\mathbf{m_{12}^{\dagger}} - \mathbf{m_{21}})i_b^{\dagger}v_1}{2}\right), \tag{2.12}$$

where dagger represents the complex conjugate and $\Re$ denotes "the real part of."

Unlike the piezoelectric counterparts, the electrostatic coupling coefficients are never taken to be different in this work. The decomposition of the ideal transformer originating from the MSD model in the appendix to dependent sources was carried out to make the ES-side analogous to the PZT-side.

As for anchor losses; if they are not negligible as compared to squeeze film effects, it turns out that b in the final circuit of Figure 2.18 is not the same as the b in the starting circuit, Figure 2.15(b). Loss terms in the H parameters of the coupler elements, which are complex in general, also ends up having a contribution.

For the system of Figure 2.13(b) the anchor losses vanish if the anchor displacements are zero, $z_1 = z_2 = 0$. This would be the case if the substrate were infinitely stiff (i.e., $H_{22,A}$ and $H_{22,B}$ were infinite). By Equation (2.9-b) and Equation (2.9-c), piezoelectric coupling coefficients would vanish in this case, i.e., $\bar{H}_{21} = -m_{21} = 0$, $\bar{H}_{12} = m_{12} = 0$. With this point of view, piezoelectric coupling coefficients give a measure of *anchor losses* for a resonator. By the same token, we expect that among two resonators of similar type on the same die, the one which is actuated more by bulk-PZT is expected to have more anchor losses.

If reciprocity is imposed on the piezoelectric coupling coefficients, then there remains two sources of lossy components in the described equivalent circuit. The first one is the resistor of the MSD system that models most of the radiation-losses from the anchor of the beam as well as the squeeze-film and material losses in the beam. Secondly, any real part of Z_{xtl} can contribute some loss unless the PZT terminals are shorted. The real part of Z_{XTL} can be due to dielectric losses in the PZT or due to the radiation loss to the supports of the PZT plate and the surrounding air.

Results of Section 2.3.2 have shown that beams can easily be driven into nonlinear operation. The circuit in Figure 2.18 does not model any nonlinearities observed in the experiments. So, an error is introduced if results of experiments that involve operation in nonlinear regime are used for the data analysis.

An intuitive way of interpreting the circuit of Figure 2.18 is possible via two basic questions it aims to answer. First is: "what is the effective force amplitude and phase from the PZT actuation that couples to the resonator modelled as a mass-spring damper system and vice versa?" Second is: "how does this coupling compare to that of the electrostatic transduction?"

The series of experiments, assumptions, and calculations to get the piezoelectric coupling coefficients, $\mathbf{m_{21}}$ and $\mathbf{m_{12}}$, were as follows, and they are described next.

1. Perform ES-actuation and ES-pickup experiments (Figure 2.9(a)) to extract the values of m, k, and b.
2. Assume the theoretical values given in Equation (2.11) for the electrostatic coupling coefficients.
3. Calculate the piezoelectric coupling coefficients from the results of the for-

ward (Figure 2.5(a)) and the backward (Figure 2.5(b)) gain experiments, which are measurements of the short circuit current at one port due to a voltage excitation at the other.

2.4.2 Electrostatic actuation - electrostatic detection for lumped model parameter extraction

The MSD system parameters, k, b, and m, of the beams can be extracted from their electrical impedance without any piezoelectric transduction. Due to the slightly different notation used in this work, the important parts of this model are summarized in Appendix A. The wiring for this experiment was similar to the one used in Figure 2.9(a), with which we measured the frequency response of the beam as the polarization voltage, V_p, was changed. The amplitude of the measured gain from this only electrostatic transduction, A_{ES-ES}, is plotted in Figure 2.19. The remaining offset at the output of the differential readout circuitry was eliminated during the data analysis by subtracting '$V_p = 0$' case from the data. To minimize the nonlinearity, measurements were done at the lowest input power levels allowed by the minimum detectable signal level.

With the PZT plate terminals shorted as in Figure 2.9(a), the equivalent circuit in Figure 2.18 reduces to a series RLC in parallel with a capacitor, also shown in Figure 2.9(b). With the help of Equation (2.10), Equation (2.11), and Appendix A, the component values can be expressed as in Equation (2.13), where $\gamma = g_0/z_0$ is the ratio of the initial gap to the static displacement due to V_p. Note that, initially when $V_p = 0$ V, γ goes to infinity.

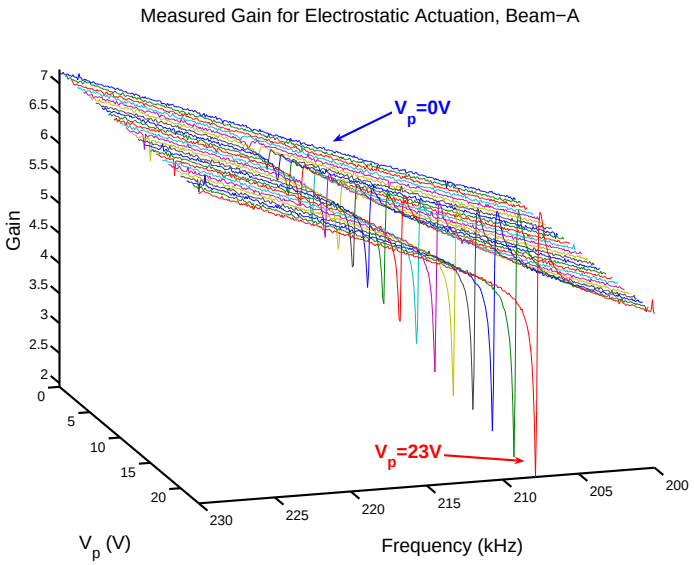

Figure 2.19: Amplitude of the gain from the ES actuation and ES pick-up experiment of Beam-A. The differential measurement configuration shown in Figure 2.9(a) was implemented with Beam-B as the unexcited reference. The input power level was -40 dBm @50 Ω.

$$C_0^* = \frac{\gamma C_0}{\gamma - 1} \qquad (2.13\text{-a})$$

$$R_x = \frac{b}{\eta_{es}^2} \qquad (2.13\text{-b})$$

$$C_x = \frac{2C_0^*}{\gamma - 3} \qquad (2.13\text{-c})$$

$$L_x = \frac{m}{\eta_{es}^2} \qquad (2.13\text{-d})$$

The first step in the extraction of the model parameters is to get the spring constant, k, from the resonance frequency change due to the electrostatic softening. Let us call the resonance frequency at any given V_p as $f_0^*(V_p)$, and its value at zero bias to be $f_0 = f_0^*(0)$. Then, rewriting Equation (A.3) and Equation (A.5), we get:

$$\left(\frac{f_0^*}{f_0}\right)^2 = \frac{k^*}{k} = \frac{\gamma - 3}{\gamma - 1} \qquad (2.14)$$

$$k = \frac{\epsilon A {V_p}^2 \gamma^3}{2(\gamma - 1)^2 g_0^3}. \qquad (2.15)$$

Resonance frequencies for Beam-A and Beam-B were extracted from the data

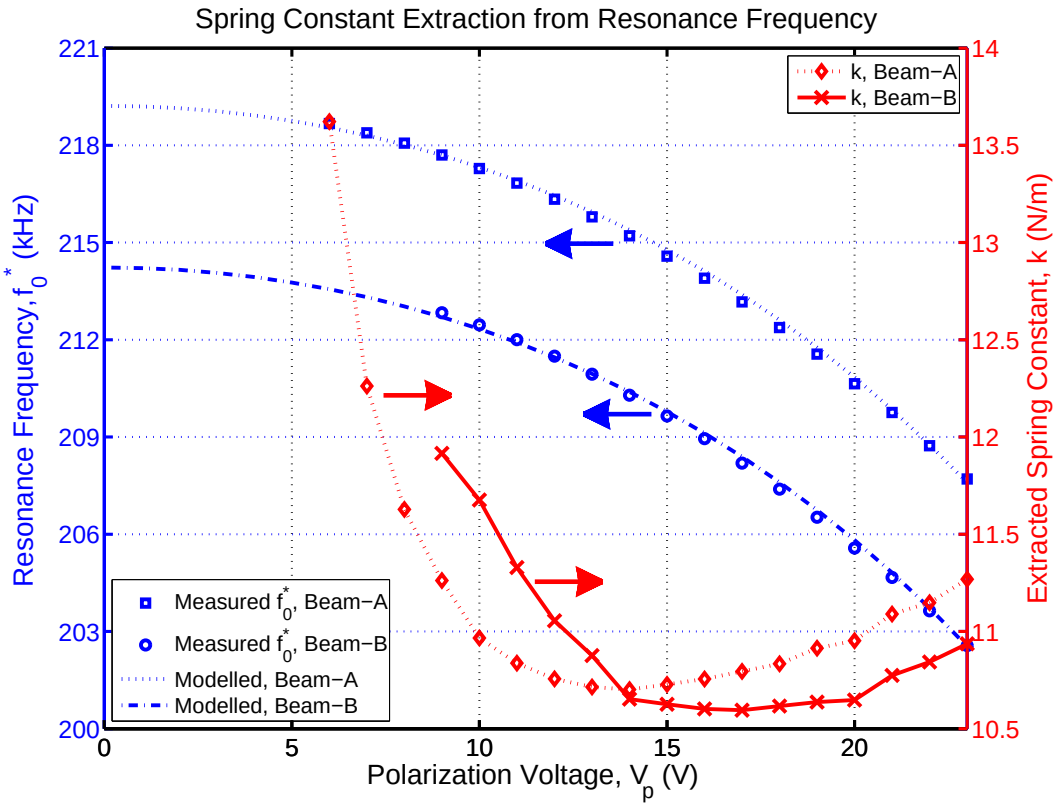

Figure 2.20: The left axis gives the resonance frequency versus polarization voltage for beams A and B. This data is later used in Equation (2.15) to extract mechanical spring constant, k. The right axis presents the results from this calculation. The final value for k was taken to be the average of the extracted value at different polarization voltages. The prediction of the model for the variation of resonance frequency, f_0^*, is plotted by dashed curves on the left axis.

in Figure 2.19, and they are plotted on the left axis of Figure 2.20. The part of the data at low V_p that do not support strong enough a signal to measure the quality factor was not considered in the calculations. Therefore, f_0 was extracted by a quadratic fit of the form $f_0^*(V_p) = A_0 + A_1 V_p + A_2 V_p^2$, where A_0, A_1, and A_2 are fit coefficients. Later f_0/f_0^* ratio was used to extract the spring constant, k, in light of Equation (2.14) and Equation (2.15). k, unlike k^*, is a system constant and must ideally be independent of V_p. Our calculations pointed to some variation in k as

a function of V_p, indicating some deviation from the ideal MSD model. However, variation from the mean was rather small ($\sigma < 0.07\mu$) for both of the beams; therefore the mean of the extractions at different polarization voltages was taken to be the value for k. Extracted values of the spring constant before the averaging operation are presented on the right axis of Figure 2.20. Predictions of the model for f_0^* with the known values of k and f_0 are plotted in dashed lines on the left axis to compare with the measurement data. The good match between the model and the experiment justifies the averaging operation performed to get a constant value for k.

The quality factor, Q, was extracted by fitting a Lorentzian with constant background signal to the data of Figure 2.19 at the lowest V_p possible.

Table 2.1 summarizes the MSD model parameters for the two beams, which will be used to calculate the piezoelectric coupling coefficients in the next section. Also listed are the expected values for m, k, and f_0 from physical dimensions, and FEM assuming nominal values for the process parameters [54]. For each measurement set, the type of measurement circuitry used and the extracted value of the quality factor at the indicated V_p are listed. Looking at the resonance frequencies extracted from the two experiments on Beam-B, one with ES excitation, the other with PZT excitation, we see that they match to within 8 ppm. On the other hand, the chamber pressure was not strictly controlled between experiments, and it was somewhere between 80 to 100 mTorr depending on the time elapsed from the pump-down. The large change in b ($> 16\%$) for these two experiments can be due to the effect of pressure on squeeze film damping [64].

A non-ideal experimental fact regarding the tested devices is due at this point. Sample availability issues forced us to use devices that were released about seven

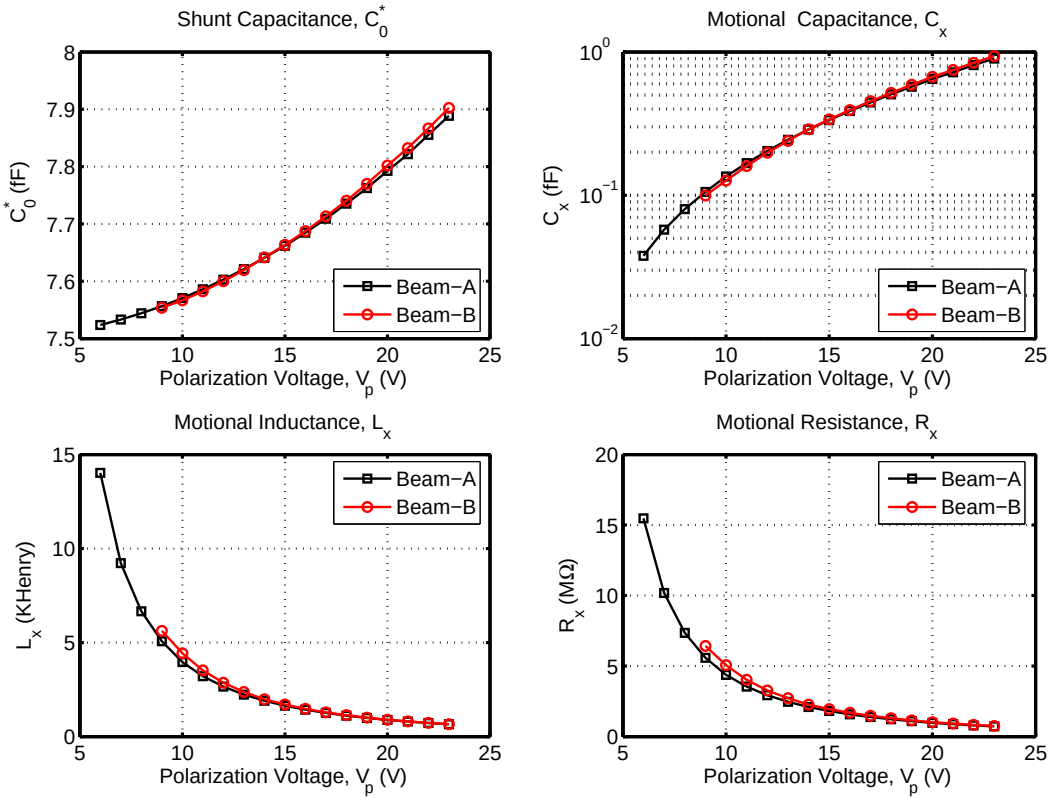

Figure 2.21: The calculated component parameters for the equivalent circuit of Figure 2.9(b) plotted as a function of V_p.

months before the time of the experiments. We are aware that this long dormant period can introduce variation/contamination on the surface of the beam. As such, it can be a nuisance for the prediction of resonance frequencies and quality factors. This point could have contributed to the measured values of fundamental resonance frequencies and spring constants significantly lower than those predicted by the FEM and theoretical values as Table 2.1 lists. Variations in beam thickness, Young's modulus, and compressive residual stress [54] in the process are possible contributors to the large mismatch. We have not delved into the exhaustive list of reasons for the mismatch, since effective mass and spring constants of the beams to be presented were all derived from measurement results. For this reason, they

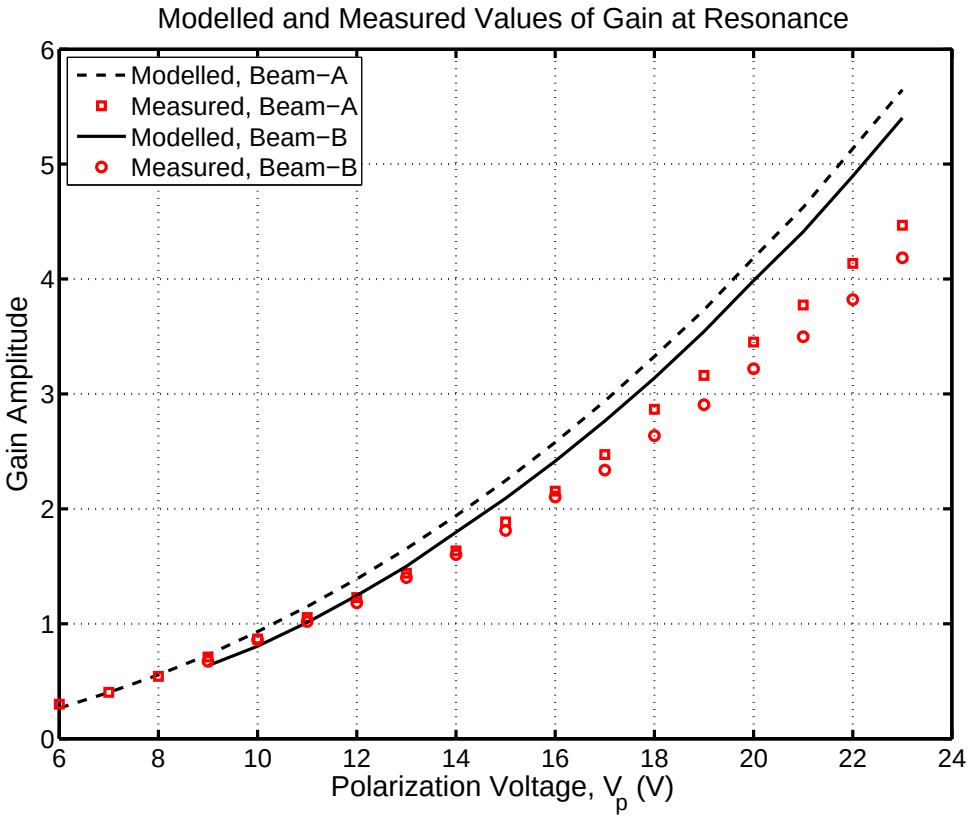

Figure 2.22: Comparison of the theoretical gain calculated from the equivalent circuit of Figure 2.9(b) and the gain from Figure 2.19.

are valid irrespective of the resonance frequency deviations due to any kind of mass-loading or contamination on the beam.

With all the parameters and Equation (2.13) at hand, calculation of the component values in Figure 2.9(b) is just a substitution away, and they are plotted in Figure 2.21. R_x of Beam-A, for instance, changes from 15.48 MΩ to 0.72 MΩ as V_p changes from 6 V to 23 V.

It is vital to check the validity of the model by quantifying the discrepancy between its predictions and experimental results for all ranges of V_p. This comparison can be done with the help of Figure 2.22, which plots the theoretical peak gains

from the equivalent circuit of Figure 2.9(b) and measured peak gains extracted from Figure 2.19 after background subtraction.

The good match for low V_p in Figure 2.22 is not surprising since the value of the quality factor, hence b, in the model was extracted from the data for the lowest V_p. Rather large mismatch of 21% at $V_p = 23$ V between the theory and the data indicates that an error was introduced with the assumption of constant b. The change in squeeze film damping for decreased gaps at large V_p could be one reason. Assuming the beams were tested at around 100 mTorr, Knudsen number, the ratio of the mean free path of molecules in the gas to the gap, was on the order of a few hundred. In this regime ambient gas is characterized by low number of collisions rather than as a viscous continuum. If we take a first order dependence of damping coefficient on the gap in this regime [65], we can only account for 5% of the 21% mismatch[5]. However note that, the matching of the analytical expressions for squeeze film damping to the experimental data in an ambient of rarefied gas, is an ongoing research effort [64, 66].

2.4.3 Coupling coefficients

This section will describe the details of the extraction of the electrostatic and the piezoelectric coupling coefficients with the sign conventions as defined in Figure 2.18. The ES coupling coefficients can be calculated using Equation (2.11). The piezoelectric coefficients can be determined by conducting forward and backward gain experiments for different V_p as suggested by Figure 2.18.

During the forward (backward) gain experiment as in Figure 2.5(a) (Fig-

[5]The calculated static displacement, z_0, is about 100 nm at $V_p = 23$ V, about 5% of the zero bias gap, $g_0 = 2$ μm.

Table 2.1: Calculated lumped model parameters. † ‡

Beam ID	m (kg$\times 10^{-12}$)		k (N/m)		f_0 (kHz)		b (N sec/m$\times 10^{-9}$)	Q @ V_p	P_{in} (dBm)	Circuitry & Detection Type ‡
	FIT	THY□	FIT	THY◊	FIT	THY△	FIT	FIT	—	—
A	5.89	7.90	11.18	25.72	219.2183	287.12	6.50	1248 @ 6 V	-40	Diff., ES-act., ES-pickup
B	6.03	7.90	10.92	25.72	214.2302	287.12	6.89	1177 @ 9 V	-40	Diff., ES-act., ES-pickup
B	6.02	7.90	10.91	25.72	214.2319	287.12	8.26	981 @ 7 V	-30	SE., PZT-act., ES-pickup
C	6.97	9.32	24.33	52.39	297.3488	377.36	9.38	1388 @ 21 V	-40	SE., ES-act., ES-pickup

† All beams are 200 μm long, 10 μm wide, 2 μm thick fixed-fixed beams. Beams A and B have a tether region as shown in Figure 2.1.

‡ FIT: Results from fit to the experimental data, THY: Nominally expected value from geometry of the device and FEM using ANSYS© .

‡ Diff.: Differential readout similar to Figure 2.9(a) SE.: Single-ended readout similar to Figure 2.5 ES: Electrostatic act.: actuation

□ $m = \rho_{Si} vol_{beam}$, where $\rho_{Si} = 2330$ kg/m^3 and vol_{beam} is the volume of the beam.

◊ $k = (2\pi f_0)^2 m$

△ FEM value with realistic anchors. Young's modulus and Poisson's ratio are taken as 158 GPa and 0.22, respectively.

Table 2.2: The transimpedance amplifier gains for the unloaded case, $Z_{TIA,fwd}$, and the PZT loaded case, $Z_{TIA,bwd}$, at the input.

Frequency (kHz)	$\mathbf{Z_{TIA,fwd}}$ ($\Omega \times 10^5$)	$\mathbf{Z_{TIA,bwd}}$ ($\Omega \times 10^5$)
≈ 203	-0.9 dB $\angle\, 148°$	-21.0 dB $\angle\, 15°$
≈ 272	-1.5 dB $\angle\, 139°$	-26.2 dB $\angle\, 5°$

ure 2.5(b)), the electrostatic (piezoelectric) port is expected to be a virtual ground forced by the TIA. This is a good approximation for the forward gain experiment. In this case, there is only 1 MΩ bias resistor at the input of the TIA that is much larger than the input impedance of the feedback amplifier. Therefore, it does not cause a significant loading. However, in the case of backward gain, large capacitive loading by the PZT plate at the input of the TIA distorts amplifier's operation for large frequencies as was shown in Figure 2.12. For this reason, we distinguish between the forward and the backward gain of the TIA as $Z_{TIA,fwd}$ and $Z_{TIA,bwd}$, which indicate the unloaded and the loaded cases, respectively. The gain of the TIA, amplitude of which is given in Figure 2.12, is listed in Table 2.2 at two frequencies typical for the resonance of beams B and C at large V_p.

The piezoelectric coupling coefficients can then be derived from Figure 2.18 as in Equation (2.16).

$$\mathbf{m_{21}} = -\frac{A_{fwd}}{Z_{TIA_{fwd}}} \frac{\mathbf{1}}{\mathbf{m_{32}}} \left(m\mathbf{s} + \frac{k^*}{\mathbf{s}} + b \right) \tag{2.16a}$$

$$\mathbf{m_{12}} = -\frac{A_{bwd}}{Z_{TIA_{bwd}}} \frac{\mathbf{1}}{\mathbf{m_{23}}} \left(m\mathbf{s} + \frac{k^*}{\mathbf{s}} + b \right) \tag{2.16b}$$

Here $\mathbf{A_{fwd,(bwd)}}$ is the forward (backward) gain in accordance with the arrows shown in Figure 2.18, and $\mathbf{s}$ is the Laplace transform variable. The minus sign in the above equations is a result of maintaining the convention used to define

Table 2.3: Coupling coefficients of Beam-B & Beam-C.

Beam ID	**Frequency** (kHz)	$\mathbf{m_{12}}$	$\mathbf{m_{21}}$	$\mathbf{m_{32} = m_{23}}$
		$(\mathrm{N/V} \times 10^{-7})$		
B	≈ 203 $@V_p = 23V$	$0.18 \angle 117°$	$0.33 \angle 95°$	$0.96 \angle 180°$
C	≈ 272 $@V_p = 40V$	$0.06 \angle 20°$	$0.11 \angle -37°$	$2.08 \angle 180°$

$Z_{TIA} = v_{out}/i_{in}$ in Figure 2.11; it has phase equal or close to 180° at low frequencies.

In our experiments, the measured frequency of peak transmission was not exactly the same for a given beam between different experiments, namely:

- the ES actuation - ES pickup, Figure 2.9(a),
- the PZT actuation - ES pickup (forward gain), Figure 2.5(a),
- the ES actuation - PZT pickup (backward gain), Figure 2.5(b).

The mismatch in the resonance frequency for the forward and the backward gain experiments was shown in Figure 2.8, and it was connected to nonlinear operation in backward gain measurements. Although the equivalent circuit of Figure 2.18 is valid only for linear operation, we proceed with the calculation at the expense of introducing an error, as low SNR during backward gain experiments made some nonlinearity inevitable.

The complication due to even small mismatches in the resonance frequencies measured from different gain experiments is that they cause large errors when substituted in Equation (2.16) due to the large quality factor of the beams ($Q >$

500). To get around this artifact, they are evaluated and reported only at the peak values of the respective gain responses using:

$$\mathbf{m_{21(12)}} = -\frac{A_{fwd(bwd)}}{Z_{TIA,fwd(bwd)}} \frac{b}{\mathbf{m_{32(23)}}} \tag{2.17}$$

The simpler form in Equation (2.17) leans on the assumption of operation close to the series resonance, therefore casting out the frequency dependent '**s**' terms in parenthesis in Equation (2.16).

The results of the numerical evaluation of Equation (2.11) and Equation (2.17) to calculate all the coupling coefficients are given in Figure 2.23 for beams B and C. The values of the coupling coefficients at their largest, respective V_p that was tested are listed in Table 2.3. Unlike the electrostatic coupling coefficients, the phase of the piezoelectric ones are a strong function of the polarization voltage. Furthermore, the dip in $|\mathbf{m_{21}}|$ of Beam-C around $V_p = 32$ V illustrates how different the trends can be among the piezoelectric and the electrostatic actuation.

The optical interferometry of the substrate vibrations were conducted to reveal the out-of-plane displacement field on the die. The experimental setup and results are presented in Appendix B and Appendix C, respectively. These measurements have verified that the spatial period of the standing wave patterns of transverse displacement of the substrate is much larger than the beam dimensions. The displacement field is mostly dictated by the cantilever like behavior of the overhang part of the die over the PZT in Figure 2.2. As the resonance frequency of the beam decreases with increasing V_p, the nodes and anti-nodes of the displacement field shift, thereby affecting the superposition of the net force applied to the beam through the anchors. We believe that the dip in $|\mathbf{m_{21}}|$ of Beam-C is a result of this die-level response of the beam that is dictated by its position on the die and mounting of the die on the PZT. However, this explanation is still not rigorous and

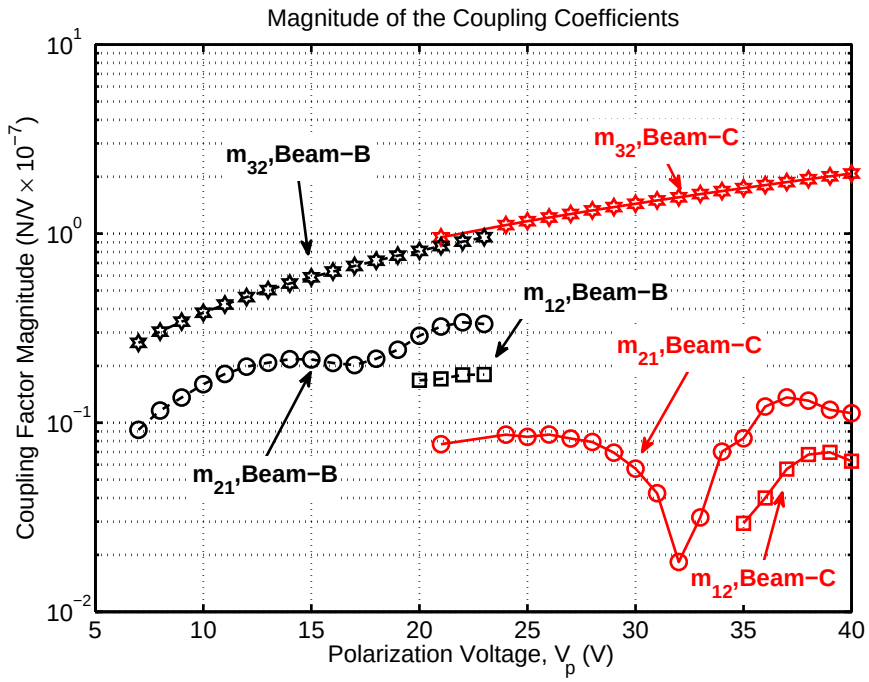

(a)

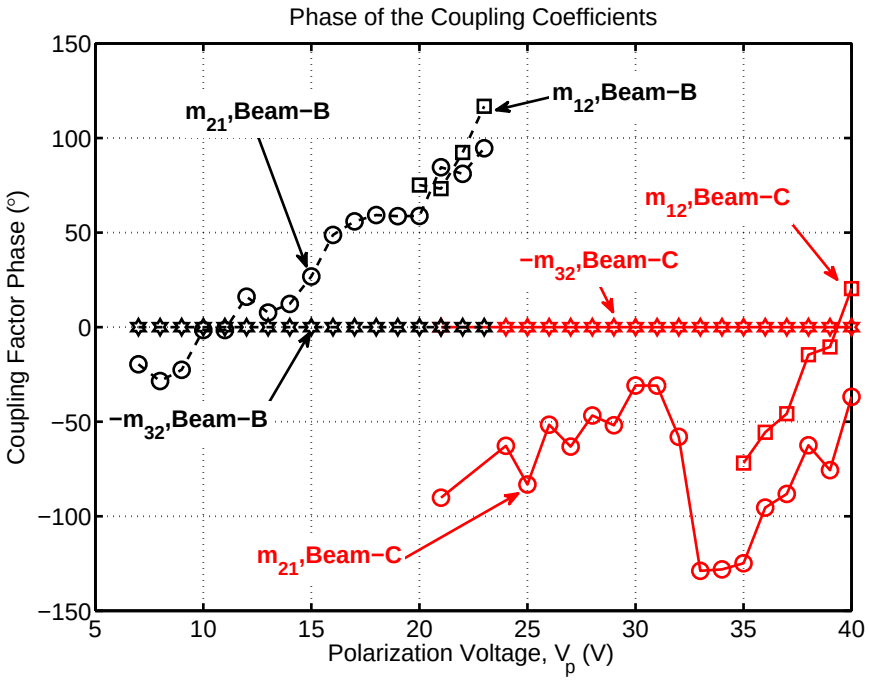

(b)

Figure 2.23: (a) Amplitude and (b) phase of the coupling coefficients calculated for Beam-B and Beam-C as a function of the polarization voltage at an input excitation of −30 dBm.

the relationship between the beam coupling and the die-level substrate vibrations as a function of the position of the beam requires more investigation.

Given the low levels of signal in backward gain experiments, an important concern is the possibility of electrical interference as opposed to a mechanical pickup. The motional impedance of the beam hits to a minimum at the resonance. This means that the transmission of the input excitation signal through the parasitic and fringing capacitances can also max out, unless the ground layer impedance in Figure 2.5(b) is low. This possibility was ruled out by a set of measurements that suggested for the maximum possible electrical feedthrough to be at least 5 dB less than the measured signal for R_x typical to our experiments, 0.5 MΩ $< R_x <$ 16 MΩ. These measurements are detailed in Appendix D.

Next, we present the comparison of the experimental gain characteristics to those obtained from the equivalent circuit model. Figure 2.24 shows the net signal after the background subtraction and the prediction of the model for Beam-B at $V_p = 23$ V. The background signal and the measured signal are also given for completeness. The calculation takes m, k, and b values from the second row of Table 2.1, and $\mathbf{m_{12}}$, $\mathbf{m_{21}}$ values from the first row of Table 2.3. k^* and $\mathbf{m_{32}} = \mathbf{m_{23}}$ are calculated from equations Equation (2.11), Equation (2.14), and Equation (2.15). The TIA gain is modelled as listed in Table 2.2. Figure 2.24(a) shows that the forward gain characteristic is well described with the model presented. The modelled backward gain characteristic in Figure 2.24(b) slightly underestimates the resonance peak due to nonlinearity issues (Section 2.3.2), whereas matching of the peak amplitude is satisfactory, thanks to the empirical nature of the model extraction.

We should emphasize that Figure 2.18 is an approximate equivalent circuit. The

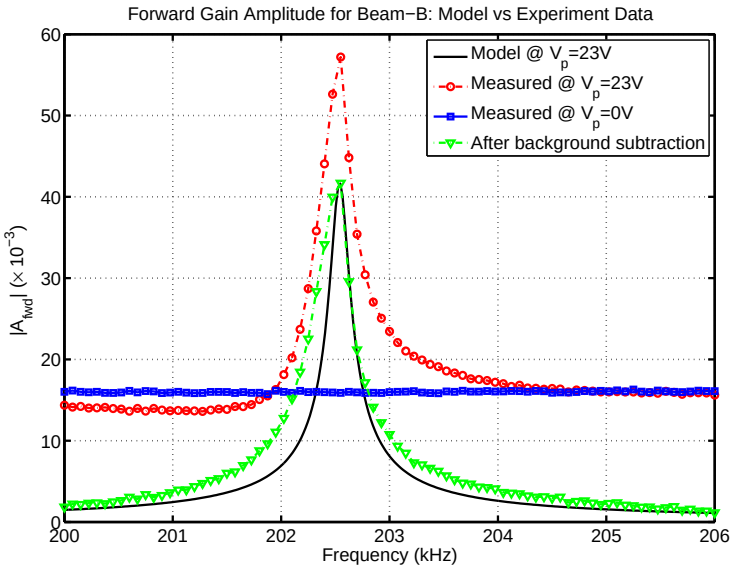

(a)

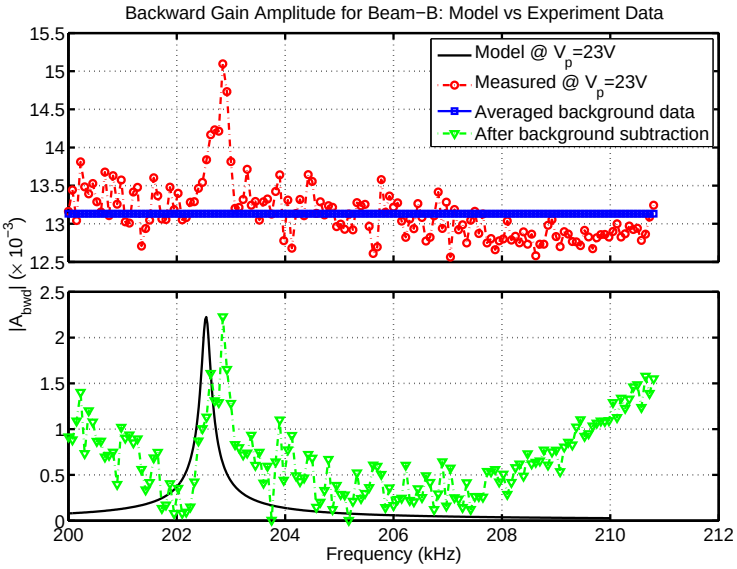

(b)

Figure 2.24: Comparison of (a) forward and (b) backward gain characteristics between the experimental and the modelled versions. The forward characteristic takes $V_p = 0$ case as the background signal, while the backward characteristic assumes a constant background noise calculated by averaging during the data analysis. In either case the actual characteristic to be modelled is calculated by subtraction of the background signal from the measurement results.

calculation at different polarization voltages were done by Equation (2.17) using the fixed value of b listed in Table 2.1 and obtained from the ES actuation-ES pickup experiments. So variation in b as a function of V_p due to the change in squeeze-film damping was disregarded. All of the coupling coefficients were extracted from the maximum amplitude values of the gain characteristics at different polarization voltages. Strictly speaking, they are valid *only* at those frequencies.

2.4.4 Discussion on reciprocity

Backward gain experiments are essentially the detection of ultrasonic waves emitted from the anchor of the resonator. The PZT ceramic acts like a microphone listening to the vibrations of the beam. With this point of view, *reciprocity* argument, which is very often employed in microphone calibration, requires that $\mathbf{m_{21}} = \mathbf{m_{12}}$ [61,67]. In other words, the short circuit current measured at one port due to the input voltage at the other must be the same no matter which port is excited in Figure 2.18; piezoelectric or electrostatic. This theorem is applicable to a linear viscoelastic medium [68, §6.5], as well as to linear, lossless, inhomogeneous multiregions [60]. Referring to the results in Table 2.3, $\mathbf{m_{12}}$ amplitude is about 55% of $\mathbf{m_{21}}$ amplitude for both of the beams. This result seems to be in contradiction with the reciprocity theorem. However, as noted, once the nonlinear effects become significant, an error is introduced when using Equation (2.17) to extract $\mathbf{m_{12}}$.

A better approximation can be obtained if one uses a different damping coefficient, b, in the numerator of the same equation. From a resonator point of view, given the distorted shape of the spectral response, Duffing behavior causes the bandwidth and the peak transmission frequency to increase. The bandwidth

increase can be modelled by a larger b. Since this parameter is in the numerator in RHS of Equation (2.17), a higher value for $|\mathbf{m_{12}}|$ could be obtained if one had used this higher value of b during backward gain calculations. Hence, extracting a lower coupling coefficient than that required by the reciprocity theorem can be explained by backward gain experiments' forcing beams into nonlinear operation. Another contributor to the mismatch between $\mathbf{m_{21}}$ and $\mathbf{m_{12}}$ could be the low SNR in backward gain calculations that was used to extract the latter.

Due to the described complications in the extraction of $\mathbf{m_{12}}$ that were not present in that of $\mathbf{m_{21}}$ we quote the value of $\mathbf{m_{21}}$ as the piezoelectric coupling coefficient. With this choice, Table 2.3 indicates, for beams B and C, that the ratio of magnitude of the piezoelectric coupling factors to the ES coupling factors are $0.33/0.96 = 0.34$ and $0.11/2.08 = 0.05$, respectively at their indicated V_p.

2.4.5 Electrostatic and bulk-piezoelectric actuation comparison

An important attribute of the equivalent circuit in Figure 2.18 is to let the bulk-piezoelectric coupling coefficients to be directly compared to the electrostatic ones that depend on neither the frequency of operation nor the position of the beam on the die. As such, it gives a reference frame for understanding of the coupling between microstructures and bulk-PZT.

In this section a comparison is made by keeping the detection method the same while varying the actuation method on the same beam. In other words, the maximum displacements from the ES actuation - ES pickup are compared to those from the PZT actuation - ES pickup for different V_p.

The peak displacement can be calculated from

$$z(\mathbf{s}) = -\frac{Y_{motional} V_{in}}{\mathbf{s}\,\mathbf{m_{23}}}, \tag{2.18}$$

where

$$Y_{motional} = \begin{cases} \frac{A_{fwd}}{Z_{TIA}} & : \text{ PZT actuation} \\ \frac{A_{ES-ES}}{Z_{TIA}} - \mathbf{s}C_0^* & : \text{ ES actuation} \end{cases} \tag{2.19}$$

is the motional transconductance reflected to the ES-port, A_{ES-ES} is the gain measured from the ES actuation - ES pickup experiment (Figure 2.9(a)), and A_{fwd} is the gain from the PZT actuation-ES pickup experiment (Figure 2.5(a)).

The results of the calculation are plotted in Figure 2.25. It shows a difference in the piezoelectric actuation due to its position dependence, although the beams have pretty much the same amount of displacement for the ES actuation. For the beams tested, the ES actuation gives two to three times larger displacement than the PZT actuation for large V_p. On the other hand, the ES actuation is expected to fall behind the PZT actuation at low enough V_p from a natural interpolation of the curves in Figure 2.25. This argument also follows by considering that the electrostatic force is proportional to V_p, unlike that of the PZT actuation.

The displacement comparison could directly be made from the piezoelectric and electrostatic coupling coefficients as well. For the presented experiment results, however, one should also consider the discrepancy reported in Figure 2.22 for large V_p.

The results of the above comparison that predict the same order of magnitude actuation for both ES and bulk-PZT actuation correspond to the case when beam and PZT/Si stack resonances do not overlap. If one assumes a typical PZT/Si quality factor of hundred, co-resonant actuation, which was not investigated in this chapter, becomes very attractive for future research. This task is simplified

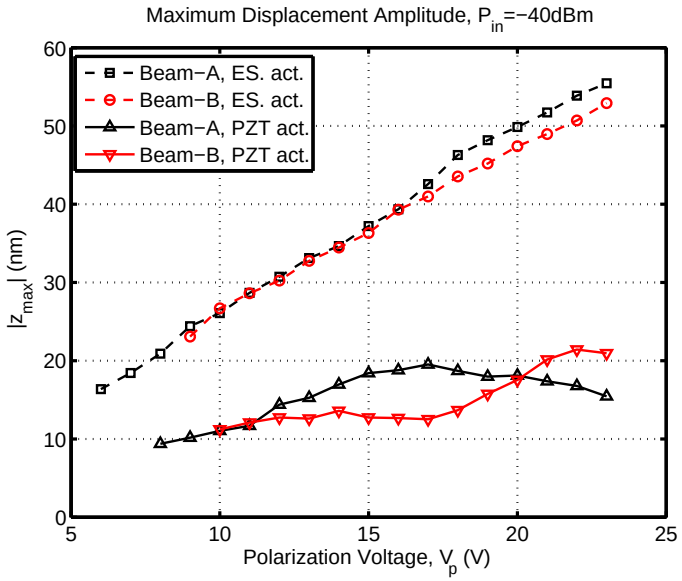

Figure 2.25: The maximum (small-signal) displacement amplitude for the ES and the PZT actuation @ $V_{in} = 6.32$ $\mathrm{mV_p}$. The ES actuation for two beams can be very close for two beams, whereas for the PZT actuation it is dependent on the position of the beams on the die.

further by the relatively high bandwidth of the PZT and the tunability of ES resonators.

2.4.6 Sensitivity of backward gain experiments

As one detects the vibration of an oscillating structure by an external bulk-piezoelectric element, the sensitivity of the PZT output voltage to a unit displacement at the resonator is of interest. We call this figure the *backward sensitivity* and denote it as S_{bwd}. In general, it can be defined either for the transverse or lateral displacement depending on the resonator type.

Wong *et al.* [49] performed experiments in a configuration similar to the one

in Figure 2.5(b), but with comb resonator structures as opposed to beams. They reported S_{bwd} of 25.2 mV/μm. The important difference between our and their work is that they used a preamplifier followed by an oscilloscope at the PZT-port for data acquisition, instead of a TIA used in this work.

We can calculate an *unamplified* version of S_{bwd} assuming that a typical oscilloscope with an input resistance of 1 MΩ and an input capacitance of 10 pF is connected at the PZT-port. In that case the backward sensitivity can be derived from Figure 2.18 as

$$S_{bwd} = \frac{|v_{out}|}{|z_3|} = \frac{|v_1|}{|z_3|} = \left| \frac{\mathbf{m_{12}} i_b \left(Z_{XTL} \mathbin{\backslash\backslash} Z_{osc} \right)}{i_b/\omega} \right|, \tag{2.20}$$

where Z_{XTL} is the impedance of the crystal symbol in Figure 2.18, Z_{osc} is the input impedance of the oscilloscope, ω is the angular frequency of operation and we have $i_b = -\dot{z_3}$.

A measurement of the input impedance when the beam electrodes are shorted in Figure 2.18 should yield the parallel combination of Z_{XTL} and the motional branch reflected to the PZT port. Strictly speaking, Z_{XTL} can be calculated from this measurement once the equivalent circuit component parameters are all known.

For our choice of experimental parameters, the above procedure is not fully necessary. As seen in the input impedance in Figure 2.3, the PZT/Si stack has no major resonances in the frequency range of interest. It can therefore be approximately modelled as a capacitor of $C_{PZT} = 3.3$ nF. Such a large capacitance dominates over the oscilloscope impedance reducing Equation (2.20) to

$$S_{bwd} \approx |\mathbf{m_{12}}| / C_{PZT} = |\mathbf{m_{21}}| / C_{PZT},$$

where we assumed $\mathbf{m_{12}} = \mathbf{m_{21}}$. Using the largest amplitude of $\mathbf{m_{21}}$ in Table 2.3 leaves us with a maximum *unamplified* sensitivity of $S_{bwd} = 8.8$ V/m. This value

is much smaller than the unamplified version of $S_{bwd} = 129$ V/m in [49] measured from the lateral mode comb resonators, given their reported preamplifier gain of 196.

2.5 Summary and conclusions

The energy transfer between the bulk-PZT and electrostatically actuated resonant micro-beams is explained via a simple equivalent circuit under the following assumptions:

- linearity,
- beam with a high quality factor,
- frequency of operation smaller than the fundamental thickness mode of the bulk structure, but at the same time in the vicinity of the beam resonance.

Three out of four possible types of experiments to extract the parameters of this circuit were described, namely the ES excitation-ES pickup, the PZT excitation-ES pickup, and the ES excitation-PZT pickup. The importance of the third type of experiment, which is the detection of sound waves launched from structures in motion, is highlighted in terms of the non-electrical resonance frequency detection for sensors and the anchor loss characterization for resonators. The fourth type of experiment, which was *not* addressed in this work, is the PZT excitation-PZT pickup. Such an effort could study the change in the PZT input impedance due to the existence of the beam or as a function of the polarization voltage applied to the beam [69]. It requires though, a backward gain SNR much larger than what was demonstrated in this work. A smaller bulk-PZT to minimize capacitive loading,

and a TIA with a higher gain-bandwidth product will be needed for parameter extraction.

The comparison of piezoelectric and electrostatic coupling coefficients that describe the net force on the beam exerted per unit of applied voltage is presented as a function of the polarization voltage. Typical amplitudes measured for piezoelectric coupling coefficients were less than 0.30×10^{-7} N/V. In the range of polarization voltages studied, electrostatic counterparts turned out to be larger.

Although the extracted values of the forward and the backward piezoelectric coefficients are not in full agreement with the reciprocity of the energy coupling, we attributed this to the nonlinearity that showed up during the ES excitation-PZT pickup experiment. Low SNR was also credited as a possible part of the cause. We showed that the bulk-PZT actuation of two beams of the same type can be considerably different despite their well-matched electrostatic actuation characteristics. Another unique attribute of the bulk-PZT actuation-ES detection is the dependence of the phase of the coupling coefficients on the polarization voltage.

A future work related to investigating the effect of the substrate modes on the bulk-PZT actuation of beams can be to look at the variation of the beam displacement with the beam position on the die. Experiments on a 2D array of identical beams can give a useful insight in this respect to understand the relation between the standing wave pattern on the silicon die and the piezoelectric coupling coefficients. In addition, quantifying the amount of correlation between the anchor loss and the piezoelectric coupling coefficients can complement the experiments presented in this work.

CHAPTER 3

ULTRASOUND ENHANCED ELECTROSTATIC BATCH ASSEMBLY

3.1 Introduction to microassembly and its applications

Over the years, many different microassembly methods emerged that apply to applications requiring large aspect ratio, out-of-plane structures, and significant 3-D complexity with different structural materials. These are also called *microassembly* methods and often involve large-scale displacement of one or more structures on the die. The transformation from one state to another can be done once or it can be reversible. In the latter case, where the structures are assembled reversibly, the distinction between large-displacement actuation and microassembly disappears. However, the speed at which the assembly is done is usually small compared to those required in actuation applications. In this chapter, the term *microassembly* is used in the context of out-of substrate erection of on-chip structures, rather than 2-D or 3-D positioning of small scale, free-to-move structures [70, 71].

Stereolithography or similar multilayer, 3-D fabrication methods are alternative technologies to one-time microassembly, which can have arbitrary 3-D complexity. However, they often fall short of offering the resolution, cost, throughput, surface smoothness, and variety of material options available in planar technologies that are used to fabricate microassembled structures.

As for the application areas of microassembly, optical MEMS is usually the fore-runner. The goal to miniaturize optical systems, which require expensive instruments as well as large amount of space on bulky optical tables, into a centimeter

size system-on-chip (SOC) is clearly well justified. Figure 3.1 illustrates some applications of microassembly on free-space optical systems on chip. A refractive lens like the one in Figure 3.1(a) provides a broad-band alternative to diffraction based planar version (Fresnel lens) [1, 72]. Figure 3.1(b) shows a surface-micromachined Fourier Transform Infrared Spectrometer (FTIR) [2], which is an important leap towards miniaturizing commercial FTIR systems.

Fast growth of the fiber optic based telecommunication networks towards the end of the millennium had justified research on micro optical-switches. Two designs, one that translates the whole mirror up and down [3], and another that uses hinge based rotation to flip the mirror up and down [4] are shown in Figure 3.2(a) and Figure 3.2(b), respectively. An example of how microassembly can be used to enhance the maximum rotation angle of surface micromachined, scanning mirrors is shown in Figure 3.3 [5].

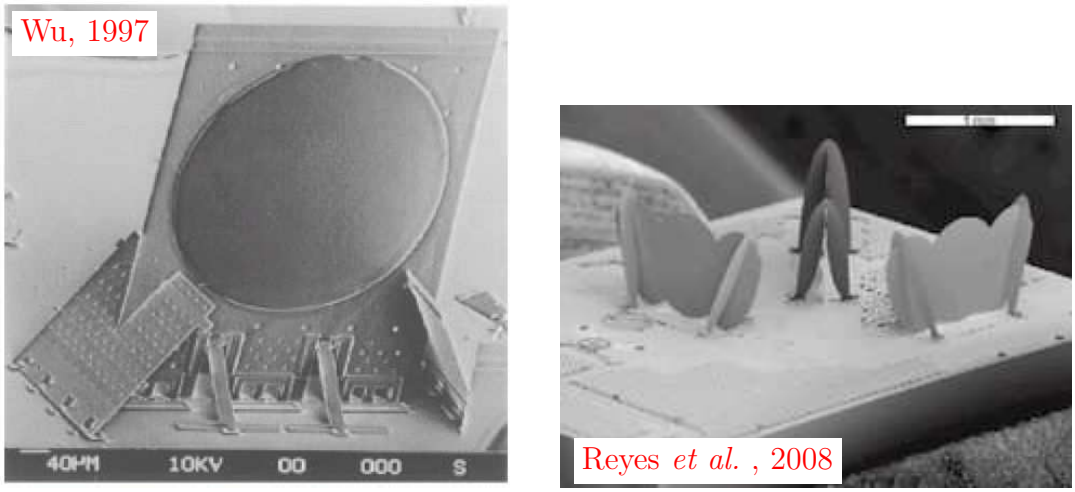

(a) (b)

Figure 3.1: Illustration of microassembled optical components and systems on chip. (a) A refractive lens formed on the surface micromachined plate with a central hole by reflowing resist [1]. (b) A surface micromachined FTIR system based on a Michelson interferometer capable of light modulation using a movable mirror platform [2].

In addition to optical applications, microassembly has also been of interest in RF-MEMS. One method of fabrication of inductors relies on coil-by-coil assembly by motor controlled microgrippers [6]. SEM picture of a device formed in this manner is given in Figure 3.4(a). Reference [7] describes inductors that are self-assembled after release using the built-in stress in the structural layers.

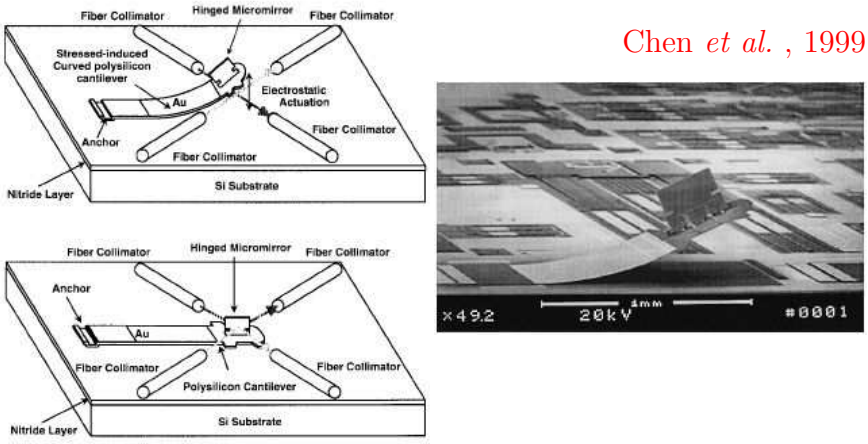

(a)

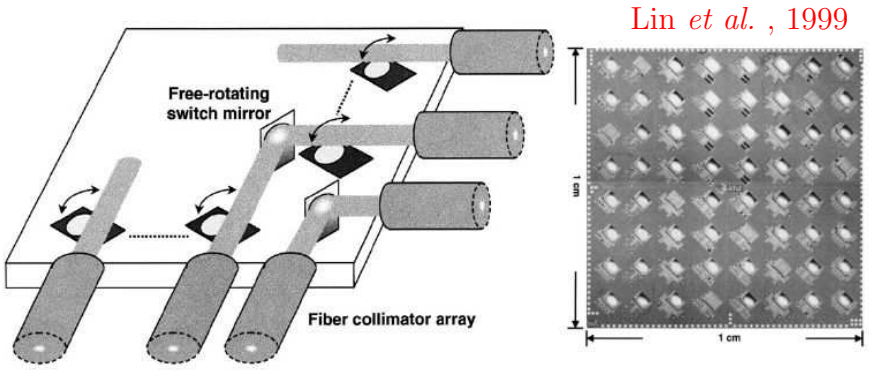

(b)

Figure 3.2: Optical switches operating as shutters are critical for fiber-optic networks. (a) A switch using a wide beam with residual stress is used to shuttle the mirror on top using electrostatic actuation [3], (b) A 8×8 free-space micromachined optical switch that uses scratch-drive-actuators [4].

Fan *et al.* , 1999

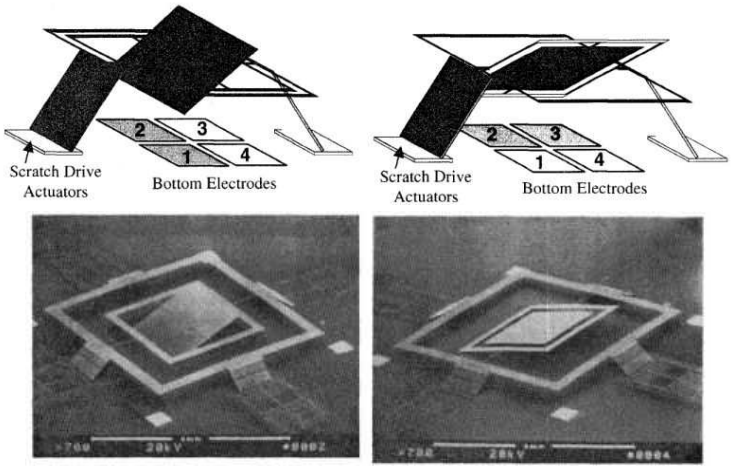

Figure 3.3: Illustration of raising of the 2-D tiltable mirror platform to increase dynamic range of scanning angle [5].

Dechev *et al.* , 2004

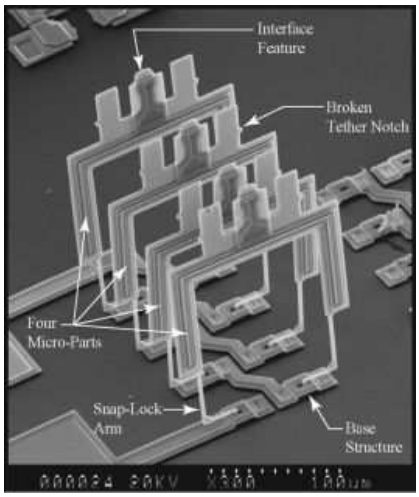

(a)

Lubecke *et al.* , 2001

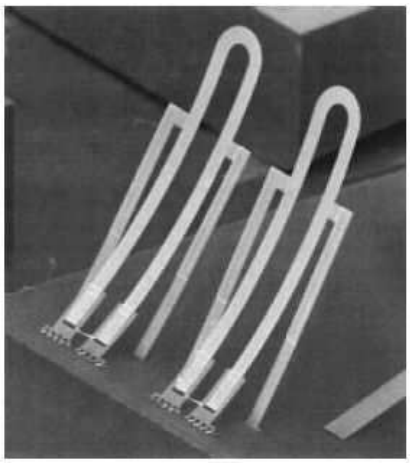

(b)

Figure 3.4: Illustration of microassembled RF coils. (a) SEM picture of the inductor realized by assembling individual coils using a passive microgripper [6], (b) SEM picture of self-assembled coils due to the residual stress in the layers [7].

3.2 Overview of microassembly methods

Various applications with different concerns have triggered some of the assembly methods available today in the literature. Surface tension based assembly uses the reflow of solder or resist like materials [73]. Depending on the process, the residual stress in the thin-layers forming the structures can serve as a convenient assembly method. The self-assembled RF coils in Figure 3.4(b) are erected based on this principle [7]. Deposition of special magnetic layers on the structures to be assembled and actuation under external magnetic bias is reported in reference [74].

Assembly using electrostatic, thermal, or similar forces generated by *on-chip* actuators is another common method. For example, the device shown in Figure 3.2(b) and Figure 3.3 use electrostatic forces [4,5]. In reference [75], centrifugal forces are employed by spinning the die to be assembled at high RPMs. This method is an example of an *off-chip* actuation, or *non-contact* method as no electrical or mechanical connection to the die is necessary. Assembly using microgrippers offer precision, but it is usually a serial process. The devices pictured in Figure 3.4(a) is an example of this approach [6].

A recent assembly method developed in Sonic*MEMS* laboratory is thermokinetic actuation, which exploits forces due to more energetic gas molecules emanating from a heated substrate, as well as ultrasonic actuation for stiction reduction [76]. Operation under vacuum and substrate heating are keys to this off-chip assembly method.

The assembly method to be described in this chapter inherits the superior properties of thermokinetic batch assembly such as large forces per unit area and ultrasonic lubrication for adhesion/friction reduction during the initiation and course

of the movement. The central difference is the use of electrostatic forces instead of thermokinetic actuation as the pull-up force. The combination of electrostatics and ultrasonic actuation is used by Bohringer *et al.* to trap and assemble surface-mount circuit components on patterned electrode surfaces [70]. In our process, which we call *Ultrasound-Enhanced, Electrostatic Batch Assembly (U2EBA),* initially uniform electric field applies on all parts to bring them closer to the top electrode. The structures of interest are connected to the substrate either by compliant structures or hinged staples. The following section is devoted to a detailed investigation of U2EBA starting from a brief description of surface-micromachining.

3.3 Ultrasound-Enhanced Electrostatic Batch Assembly (U2EBA)

3.3.1 Surface micromachined hinges

As unveiled by the examples of the previous section, surface micromachining technology is a common platform for microassembly operations. Planar mirror surfaces, hinges, compliant beams, and sliders are readily implemented. Figure 3.5 shows the fabrication of a hinge with a process using two structural polysilicon layers [1, 77]. Phosphosilicate glass (PSG) is used as the sacrificial layer. Dimples, are formed by a partial etch into the sacrificial PSG layers, and subsequent conformal polysilicon deposition. They are included generally to reduce stiction of the released microstructures to the substrate.

The devices to be mentioned in this chapter are fabricated by PolyMUMPs©

[54] and Sandia SUMMiT V^{TM} [78]. The standard release procedure involves 49% HF wet etch, followed by critical point drying.

3.3.2 Description of the method

Main parts of the apparatus and principle of operation for U2EBA are shown in Figure 3.6 [10, 79]. A DC-voltage V_{DC}, applied between the chuck holding the die and the global top electrode works to pull the microstructures away from the surface of the die. An ITO-coated glass-electrode is used to keep the mirror surfaces optically accessible, so that the motion of the structures can be recorded and analyzed later. A periodic voltage V_{AC}, applied across the piezoelectric ceramic (PZT[1]) underneath the die generates stress waves that reach to contacting inter-

[1]Following the convention, the term PZT is used both as an abbreviation for *piezoelectric* and *Lead Zirconate Titanate*.

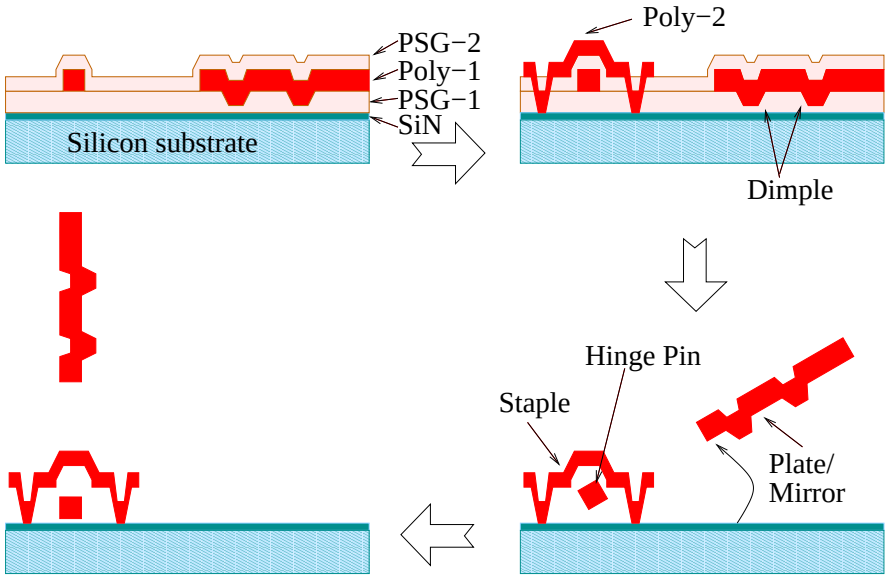

Figure 3.5: Cross-sectional illustration of the surface-micromachining of a hinge element, its release, and subsequent assembly [1, 77].

faces at the hinges, stuck parts or sliding surfaces. The stress waves modulate the tribological gap between the surfaces in contact. This modulation acts as an anti-stiction agent as well as an effective lubricant reducing the friction forces. The reduced friction and stiction enable the external forces such as electrostatic force to rotate the plate to an angle ϕ [80]. As a further tool against stiction, the heater used under the experimental setup works to mitigate humidity related capillary forces. In order to ensure good mechanical coupling between the *PZT* and *the MEMS die*, the latter is attached to the former with the help of a vacuum chuck. The frequency of V_{AC}, is linearly swept at the instrument level in order to excite the time-varying[2] structural resonances during the assembly process to improve actuation efficiency.

A general microstructure with a rotational degree of freedom, experiences moment M_ϕ, due to gravitational, electrostatic and surface adhesion forces that are in general a function of the angle of rotation ϕ. Further details about the experimental setup and specifications of the instruments used to generate AC voltage to drive PZT, and DC voltage to bias the top glass electrode are described in the experimental section.

Equivalent electrical circuit of the experimental setup is shown in Figure 3.7. R_{air1} and C_{air1} model the electrical impedance of the air between the assembled structures and the global top electrode. Similarly, R_{air2} and C_{air2} model the impedance of the remaining gas region in between the top electrode of the PZT plate and the glass electrode. Substrate resistance and capacitance are modelled by R_{sub}, and C_{sub}, respectively. No electrical connections are made to the die directly, but to the electrodes of the PZT and the top global electrode. One shortcoming of

[2]Deforming and moving structures introduce changes in boundary conditions, which alter the structural resonance frequencies.

this convenience is that, all of the applied voltage is not utilized for assembly due to capacitive voltage division. If we call the actual voltage across the microstructures and the top electrode as $\acute{V}_{DC}$, then during normal operation away from air breakdown:

$$\acute{V}_{DC} = \frac{C_{sub}}{C_{air1(\phi)} + C_{sub}} V_{DC}. \tag{3.1}$$

Fortunately, typical gaps used in U2EBA are in the range $1 - 5$ mm, i.e., larger than typical substrate thicknesses. Moreover, the dielectric constant of silicon, 11.7, is much larger than that of air which is practically unity. These two factors result in C_{sub} being at least an order of magnitude larger than that of C_{air}, when $\phi = 0$ initially. Therefore, only less than 10% of the applied voltage drops across the substrate; the rest appearing across the air-gap on top of the microstructures,

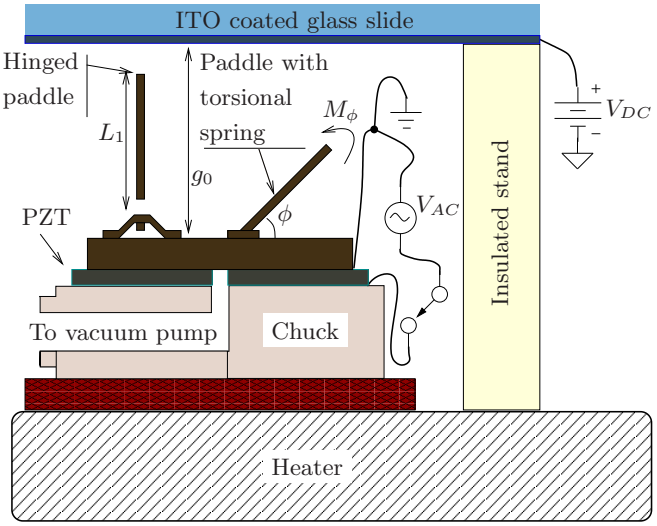

Figure 3.6: Experimental apparatus for ultrasound-enhanced, electrostatic batch assembly (U2EBA). The structures are subjected to an out-of plane electrostatic field in the presence of ultrasonic actuation by the piezoelectric actuator under the die. The total moment M_ϕ on a microstructure, has electrostatic, gravitational, and capillary components that depend on the value of the rotation angle ϕ.

as desired. This small drop across the substrate is neglected in the forthcoming analytical and FEM discussions, and $\acute{V}_{DC} \approx V_{DC}$ is assumed. This significantly simplifies the electrostatic problem. In practice however, the ϕ dependence of C_{air1} should be kept in mind *during* the assembly, as the validity of the approximation ($\acute{V}_{DC} \approx V_{DC}$) can be questionable for $\phi \gg 0$.

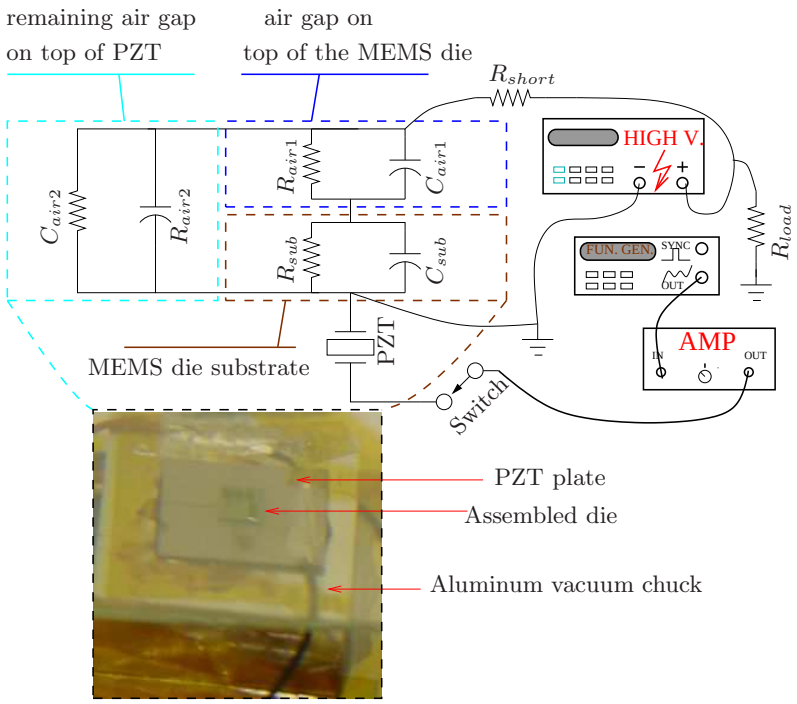

Figure 3.7: Electrical equivalent circuit of the assembly setup with nonlinear resistors and capacitors. An optical picture of the vacuum chuck is shown as well.

3.4 Investigations of the forces involved

In order to understand the assembly process, forces acting on the movable structures on the die need to be examined separately and then compared. Following types of forces can be identified for a hinge structure as the one illustrated in Fig-

ure 3.5: gravitational, ultrasonic, electrostatic [81, 82], friction, surface adhesion forces (van der Waals forces, capillary forces, electrostatic attraction forces, etc.), thermokinetic [76], and restoring elastic (spring) force of the compliant structures.

Some of the forces listed above are straightforward to calculate, some require numerical or finite element methods, and some are very complex, depending on many factors, characterization of which require dedicated effort. Examples for these factors are: surface contamination, material roughness, asperity statistics, and water contact angle.

What follows is a description of forces in-action during U2EBA of compliant or hinged microstructures.

3.4.1 Ultrasonic, friction, adhesion, and contact forces

Many people can relate to the effect of ultrasonic actuation as a motion-starting or lubrication agent. For example when tapping and jiggling the rice bag as we pour rice to a beaker for cooking, or after accidentally bumping to a table that results in dropping of a cup standing at the edge, or when using an ultrasonic toothbrush. Despite such common place, the quantification of this effect still takes the attention of researchers as there is a drive for ultrasonic machining tools and motors to scale down and operate more efficiently and for longer lifetimes [8, 83].

In the coming subsections, ultrasonic actuation of stationary objects and moving objects are investigated separately, and some important results from the literature are summarized. It is seen that the effect of ultrasonic forces is related closely to the frictional forces and surface adhesion/contact forces. In the case of sliding/moving objects, ultrasonic actuation manifests itself as a reduction in the

friction coefficient μ [8, 83]. In the case of stationary objects [20, 80], investigating the interactions of an AFM tip with a substrate yields us the quantitative and qualitative explanation for the "anti-stiction" forces that is crucial to U2EBA.

3.4.1.1 Ultrasonic actuation on moving objects: Change in frictional forces

The problem of sliding friction in the presence of ultrasonic vibration is pictured in Figure 3.8 [8]. The relative velocity of the object with respect to the base plate is taken to be

$$\nu_{ref} = \nu_o \overrightarrow{e_x} + \nu_u \cos(\omega t) \overrightarrow{e_y} = \nu_u \left(\zeta \overrightarrow{e_x} + \cos(\omega t) \overrightarrow{e_y}\right).$$

Here, the first component of the vector represents the relative velocity of the object in the absence of ultrasonic vibration (i.e., the principal component), and the harmonic term represents the ultrasonic component. $\zeta = \frac{\nu_o}{\nu_u}$ is the ratio of the principal speed to ultrasonic speed. Figure 3.8 illustrates the problem for the case when the ultrasonic vibration velocity vector is perpendicular to the principal velocity vector and the normal of the base-plate. An analogues treatment is given by Littmann *et al.* when the ultrasonic velocity vector and the principal velocity are parallel to each other [83]. In general, the principal and the ultrasonic components can be arbitrarily oriented to each other on a plane. However, the parallel and perpendicular cases constitute two practical constellations easy to model and test.

$\overrightarrow{F_R}$ in Figure 3.8 represents the sliding friction force, and F_N represents the amplitude of the normal force. Storck and Littmann *et al.* suggest the validity of *Coulomb's* friction law, as opposed to looking for a "special" theory [8]. As such,

the authors write the friction force as in Equation (3.2).

$$\overrightarrow{F_R} = -\mu F_N \frac{\nu_{ref}}{|\nu_{ref}|} = F_{rx}\overrightarrow{e_x} + F_{ry}\overrightarrow{e_y} \tag{3.2}$$

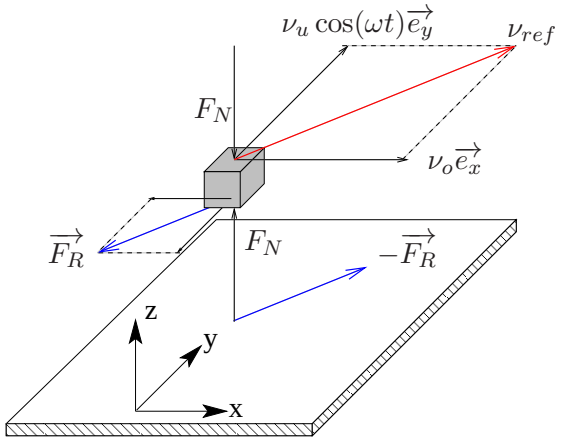

Figure 3.8: Body diagram of a moving object on a vibrating table from the reference frame of the table [8]. For this illustration, the body and the table are taken to be moving in orthogonal directions in the absolute reference frame.

After calculating the time average of the friction force in the direction of the principal velocity vector $\bar{F}_{R,principal}$, Storck and Littmann *et al.* show that, ultrasonic actuation lends itself to an effective friction coefficient different than the original value without ultrasound. If we call this modified friction coefficient as χ and the original friction coefficient as μ, the change is expressed with the help of a scaling factor $\mu_{perpendicular}$ ($\mu_{parallel}$) for the perpendicular (parallel) case. The relation among different friction coefficients is given by Equation (3.3).

$$\frac{\chi}{\mu} = \begin{cases} \mu_{perpendicular}(\zeta) & : \quad \text{for the perpendicular case [8]} \\ \mu_{parallel}(\zeta) & : \quad \text{for the parallel case [83]} \end{cases}. \tag{3.3}$$

The theoretical variation of the friction coefficients as a function of ζ along with the experimental results are given in Figure 3.9. The reduction in friction

is clearly seen in both the perpendicular and the parallel cases for low values of principal speed with respect to the ultrasonic speed, i.e., for low values of ζ. The kink at $\zeta = 1$ and saturation for large values of ζ in the parallel case are contrary to the perpendicular case where there is still some reduction in friction coefficient even for large values of ζ. The experimental results of Storck *et al.* are also in reasonable agreement with the theory, which verifies the lubrication effect of ultrasonic vibration for sliding/rubbing bodies.

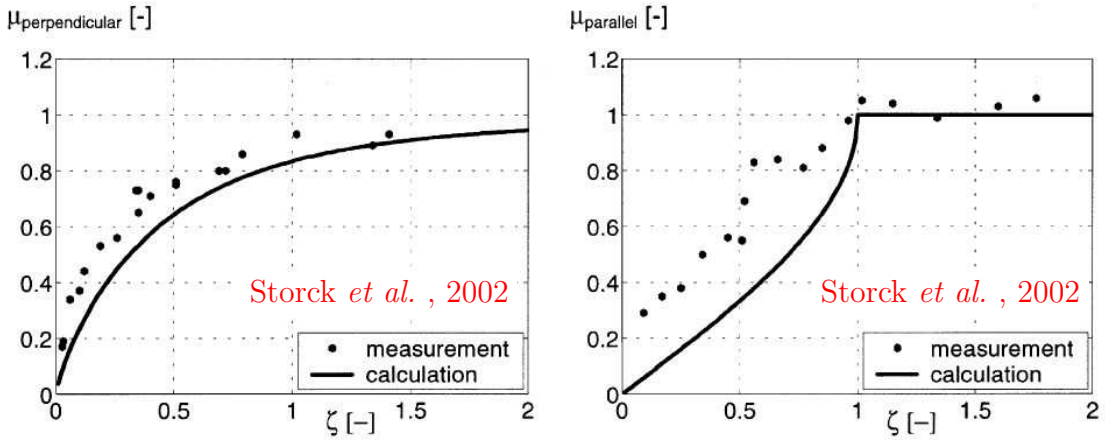

Figure 3.9: Theoretical and experimental values from Storck *et al.* for the reduction in effective friction coefficient as a function of ζ, which is the ratio of the principal speed to the ultrasonic velocity amplitude [8]. The left plot is for the case when the principal velocity is perpendicular to the ultrasonic vibration amplitude, and the right plot is for the parallel case.

3.4.1.2 Ultrasonic actuation on stationary objects: Nonlinear surface forces of adhesion and contact

Right after release, hinged structures are often stuck to the substrate over the large-area paddle region. If dimples are included as in Figure 3.5 with sufficient density, it is expected that the contact area is determined lithographically by dimples.

However, since the paddle of a hinge is a freely moving structure within the staple, it is quite possible that there is some contact of the pin to the staple, or other neighboring structures in general. Figure 3.10 shows optical pictures of two hinged plates without dimples taken after critical point drying. The pin in Figure 3.10(a) is nicely situated under the staple region, whereas the one in Figure 3.10(b) is displaced considerably from its central position, and the paddle is almost stuck underneath a neighboring beam used for latching after assembly.

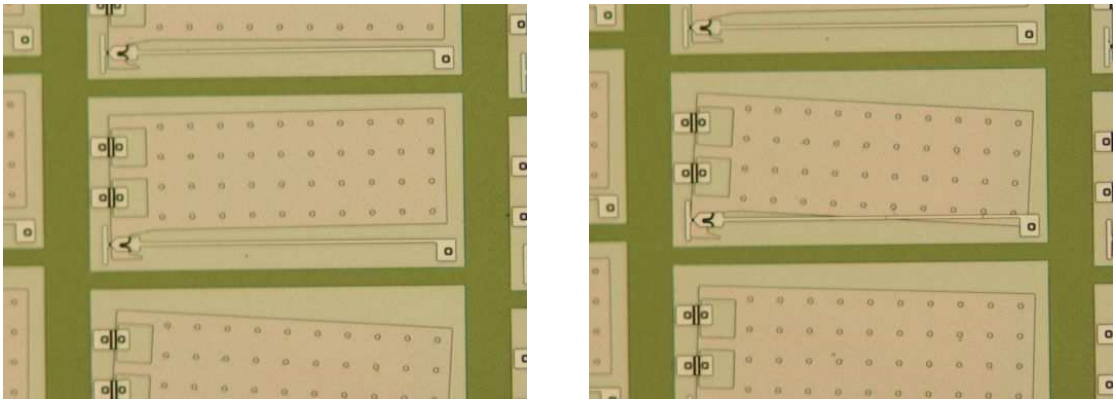

(a) (b)

Figure 3.10: Optical pictures of a hinged paddle structure right after critical point drying. Random nature of the wet release and critical point drying process can cause freely-moving paddle regions to be (a) aligned or (b) displaced with respect to their intended, CAD-level positions.

In order to investigate the effect of ultrasound on the tribology of stationary microstructures, first the surface forces on the microstructures need to be studied. Adhesion and stiction in MEMS are complex phenomena, originating from different sources, such as capillary, electrostatic, and van deer Waals forces [81, 84]. The employment of special on-chip test structures and contact angle measurements proved to be very instrumental to characterize adhesion between different surfaces [81, 85]. In addition to this, use of Atomic Force Microscope (AFM) and its derivative methods allowed easy investigation of surface forces at the nanometer

scale [9, 80, 86].

Figure 3.11 shows two force curves taken using an AFM (Dimension 3100). It traces the displacement of a cantilever tip as it extends and retracts from a stationary substrate. During the extension (solid curve), as the tip comes close to the wafer surface (z decreasing), the adhesion forces start to kick in and cause a slight change in the magnitude. This is followed by a small dip that indicates the touch down and the initial contact. Further motion of the AFM tip, causes almost a linear deflection due to the soft AFM cantilever as compared to the hard surface of the substrate. During retraction (dashed curve), the hysteresis in pull-off distance is a clear indication of surface attraction forces.

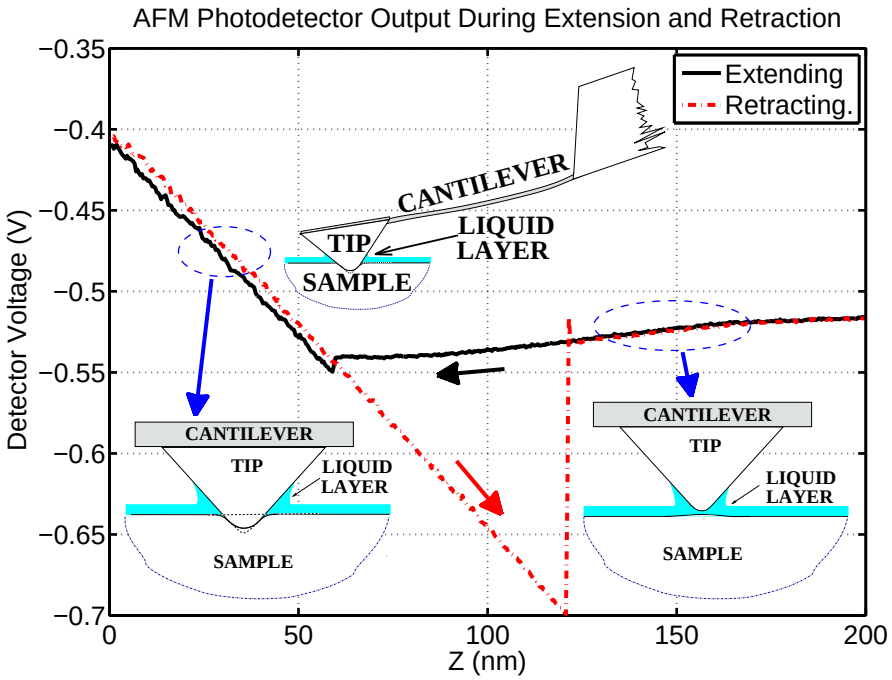

Figure 3.11: Force displacement curves measured on a wafer using a commercial AFM and tip. The inset on top is an illustration of the AFM cantilever in contact with the sample surface. The bottom insets highlight conception of the tip and surface with an intermediate liquid layer with and without contact.

Next, an argument about the origin of the ultrasound induced "anti-stiction" force on a structure that is stationary on a surface is given. For this argument, a qualitative version of the force-distance curve as sketched in Figure 3.12 is instrumental [9, 53, 87]. The equilibrium point, where total force on the object vanishes is denoted by P_0. If we superimpose an ultrasonic vibration along the z-axis, which denotes the separation between the structure and the substrate surface, then the force applied on the object is also modulated at the same frequency. These modulations on respective axes are shown by double-headed arrows in Figure 3.12.

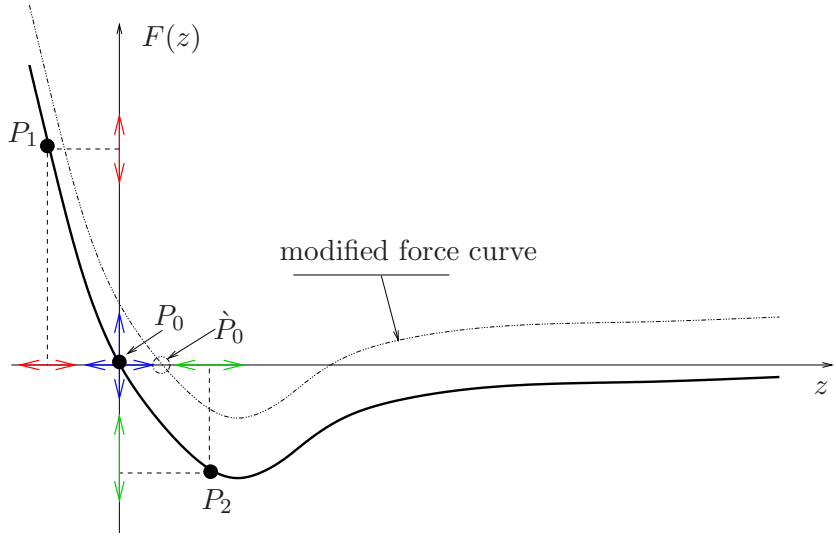

Figure 3.12: Illustration of a typical force-distance curve between an object and the surface. When the distance between the object and the surface is modulated due to the ultrasonic vibration of the surface, local nonlinearity of the force-distance curve determines the time-averaged force on the object [9]. In the figure, local nonlinearity is highest at point P_2 and lowest at point P_1. This force changes the apparent equilibrium point, by shifting the force-distance curve to the dashed position.

If the original force-distance curve is locally linear[3], then the time average of this modulated force on the object is zero [9]. On the other hand, any nonlinearity

[3]By "locally linear", it is assumed that the second and higher order derivatives with respect to independent variable are negligibly small.

causes a net average force to be exerted on the body. In Figure 3.12, the effect of nonlinearity can be seen from the asymmetry of the projection of the modulation on the force axis for point P_0. If the equilibrium point is taken to be P_2, the net average force due to ultrasonic vibration is larger. This is not true for P_1, where the force-distance curve is almost linear. When the time averaged force is significant, the static force-distance curve effectively shifts to right, causing the equilibrium point to occur at a larger value, shown by $\grave{P}_0$. This extra force and corresponding motion away from the substrate constitute the majority of the "anti-stiction" effect mentioned in this chapter.

The above phenomenon of having ultrasound induced repulsion forces away from the substrate due to nonlinearity of the force-distance curve is also analytically exemplified in Appendix E [20]. That treatment assumes a piecewise linear force-distance curve and neglects adhesion forces, viscoelastic, and other time-dependent phenomena. As the ultrasound vibration amplitude exceeds a threshold value, which takes the force-distance curve into a nonlinear operating regime, an increase in the time averaged value of the distance between the structure and the vibrating substrate can be calculated.

3.4.2 Gravitational, elastic spring, and thermokinetic forces

The calculation of gravitational moment is straightforward for the case of a rotational structure as in Figure 3.13. Here, L_p and L_0 are the length of the paddle and moment arm, respectively. Width of the paddle is b_p, the voltage difference between the top electrode and the paddle is V_a. L_1 is the distance between the outer

side of the plate and the moment center, i.e., $L_1 = L_0 + L_p$. The paddle region is taken to be supported by a torsional beam of rotational spring constant k_{rot}, to make the problem more general. Neglecting frictional forces, hinged structures become a special case for which $k_{rot} = 0$.

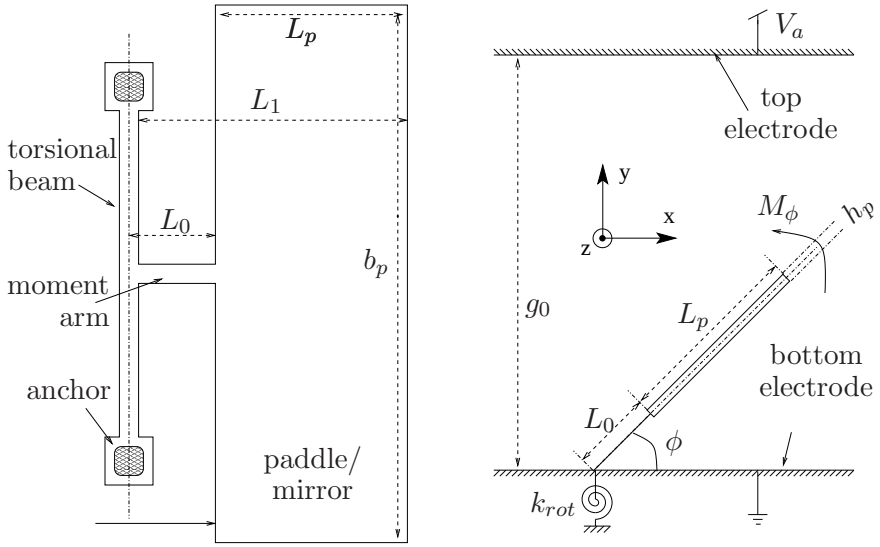

Figure 3.13: Undisplaced top view of a paddle in between two electrodes is shown on the left. Right schematic gives the electromechanical model at a rotation angle of ϕ.

The gravitational component of the moment on the paddle $M_{\phi,Gravity}$, assuming that the plate region can be treated as a rigid plate during deformation, is

$$M_{\phi,Gravity} = (0.5L_p + L_0)\,(L_p h_p b_p)\,\rho_{polySi}(g)\cos(\phi), \tag{3.4}$$

where g is the gravitational acceleration amplitude, ρ_{polySi} and h_p are the density and the thickness of the polysilicon layer, respectively.

Elastic spring component of the moment, without considering non-linearities, is

$$M_{\phi_{rot}} = k_{rot}\phi, \tag{3.5}$$

where the rotational spring constant k_{rot} can be determined by linear elasticity analysis of the structure or from documented tables of equations. For example, a 500 μm long polysilicon beam of 1.5 μm $\times$ 1.5 μm cross section with a shear modulus of $G_{polySi} = 70$ GPa yields $k_{rot} \approx 4 \times 10^{-10}$ Nm [88, Table 20, pp. 348]. However, for large-angle assembly or torsional springs of complex geometry, FEM can be necessary to reliably account for geometrical and material nonlinearities. It is also crucial to make sure that yield strain/stress of the material is not reached during the torsional deformation with a reasonable safety factor.

Lastly, thermokinetic forces become important at vacuum levels for which the mean free path of the gas molecules are comparable or larger than the characteristic length of the structures to be assembled. Kaajakari and Lal give expressions to estimate these forces [76]. Here, only in air operation of U2EBA is considered, so thermokinetic forces are neglected.

3.4.3 Electrostatic forces

At micron scale gaps and small-angle rotation angles, parallel plate approximation works well. It is widely used to model resonators' motional impedance, forces generated by electrostatic actuators (both linear and torsional), and pull-down behavior of the same [56, 89, 90]. A common aspect of these applications is the large ratio of electrode characteristic length to electrostatic actuation gap. In other words, if one uses the naming introduced by Figure 3.6, so that L_1 is the typical device or electrode size, and g_0 is the characteristic electrostatic gap, then many on-chip electrostatic actuation applications has the ratio $r_{ES} = L_1/g_0$ larger than 10 [90], or even 100 [89]. On the other hand, for U2EBA illustrated in Figure 3.6, the electrostatic gap should be kept larger than the largest of the micro-structures

to be assembled in order to be able to support 90° assembly, i.e., $r_{ES} = L_1/g_0 < 1$. Unfortunately, a fundamental problem with large gaps is the requirement for higher DC voltages for assembly.

From the design point of view, the condition of $r_{ES} < 1$ causes a significant error in parallel-plate approximation due to fringing fields. Moreover, very large rotation angles during the assembly hinder the use of small-angle approximations, further crippling the applicability of analysis methods used for on-chip electrostatic actuators that do not rotate more than a few degrees. Appendix F shows the inapplicability of parallel-plate approximation for the electrostatic field analysis of U2EBA. Although at small angles ($\phi \approx 0$) parallel-plate approximations can give a rough estimate of the electrostatic moment $M_{\phi,ES}$, the predictions are unrealistic for large angles of rotation.

As the structures rotate in U2EBA, they change the electric field around them, and field crowding occurs near the edges of the structures especially for large rotation angles. 3-D Laplace equation needs to be solved in order to accurately model the electrostatic moments during U2EBA. The coming subsection summarizes the finite element modelling work aimed at calculating the electrostatic moment on a rigid plate under a global top electrode.

3.4.3.1 Finite element analysis of the electrostatic problem

A numerical solution of the electric field is necessary to calculate the moment applied on the paddle and to determine maximum electric field intensity in the gap. Figure 3.14 shows the electrode and paddle configurations modelled in a commercial FEM package, ANSYS©.

For a compliant structure as in Figure 3.13, which is rotated away from the substrate surface far enough not to be affected by surface adhesion (i.e., $\phi > 0$), the equilibrium angle is determined by spring restoring force, gravity and the electrostatic moment. In the case of a hinged-paddle, there is no torsional spring force, but friction forces in the staple region of the hinge. Common to both hinged and compliant assembly using U2EBA, is the problem related to electrostatic moment on a paddle that makes a known angle of ϕ with the plane of the subsbtrate. This is equivalent to having a structural material of infinite Young's modulus in Figure 3.13. A simpler method is to use electrostatic elements that do not have structural degrees of freedom. 3D electrostatic element, `SOLID123`, was used for this purpose. The forces and the moments are calculated using the `EMFT` subroutine in ANSYS©. The simulations were repeated at three different gaps, namely 0.6, 1, and 1.5 mm, to study the effect of electrode separation for

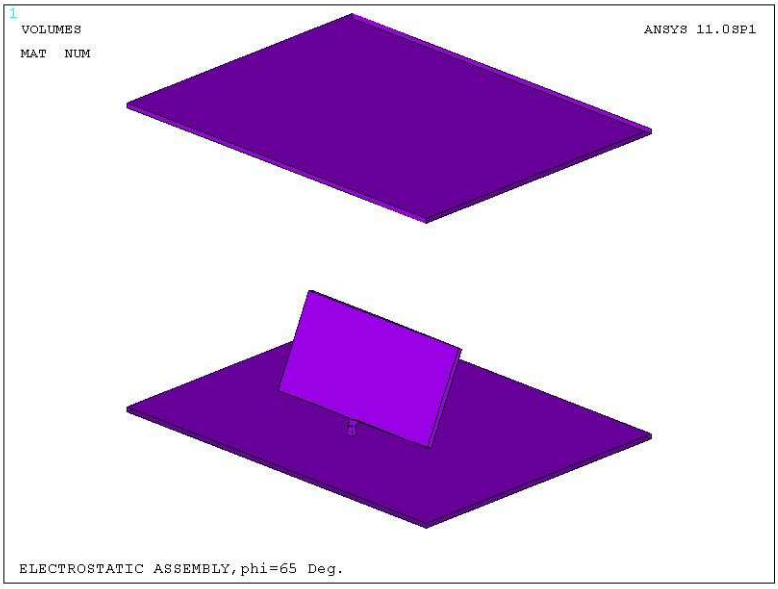

Figure 3.14: Finite element model (FEM) model in ANSYS© at a gap of $g_0 = 1500$ μm and a rotation angle of $\phi = 65°$.

different values of ϕ[4]. The geometrical parameters used in the FEM are listed in Table 3.1. The simulations were performed in a rectangular block with dimensions: 2 mm $\times$ 1.525 mm $\times$ g_0. Additional details about the simulation can be tracked down from the command-line version given in Appendix G.

Table 3.1: Geometrical parameters used in FEM.

Parameter	**Value**
h_p	25 μm
b_p	1000 μm
L_p	500 μm
L_0	25 μm
g_0	0.6, 1.0, 1.5 mm

The meshing of milimeter scale volumes in the presence of micron scale structures often results in a large number of elements. Being limited by the maximum number of elements allowed by the educational license of the software, the thickness of the polysilicon layer was taken as 25 μm, about an order of magnitude larger than its actual value.

Figure 3.15 shows contour maps of the electric field amplitude in the air region at $V_{DC} = 1$ V bias and at a rotation angle of $\phi = 65°$. The plots give a section view from the symmetry plane of the paddle in Figure 3.14. In each case, the maximum electric field is around the edges, since sharp points tend to cause field crowding.

The electrostatic moment on the paddle region from FEM is plotted in Figure 3.16(a) for different gaps along with the gravitational moment that is calculated from Equation (3.4). Although each simulation is performed at $V_{DC} = 1$ V, the

[4]In the FEM, the gap is defined to be the distance between the top surface of the paddle and the bottom of the top electrode. In other words, the thickness of the paddle and the height of the anchors are not included.

results are later scaled to the DC voltages as indicated in the legend of the figure. The DC voltage for each gap is chosen such that the electrostatic moment is equal to the gravitational moment for $\phi = 0$. This can be seen by the intersection of all moment curves on the y-axis. As such, the scaled voltages reported in Figure 3.16(a) also present a lower limit for the paddles to start moving due to electrostatic forces, in the absence of adhesion forces. Since the thickness of the paddle is small as compared to the gap, the electrostatic moment scales roughly

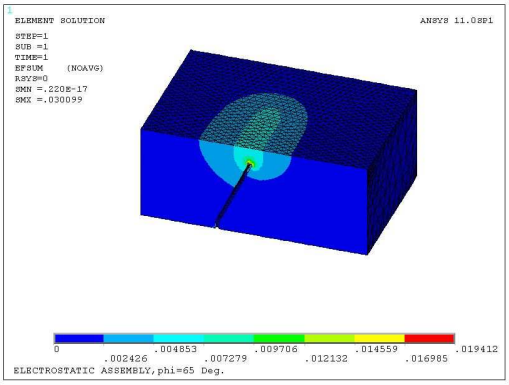

(a) $g_0 = 0.6$ mm, $V_{DC} = 1$ V

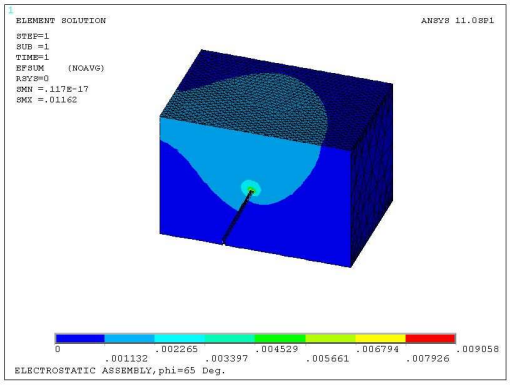

(b) $g_0 = 1.0$ mm, $V_{DC} = 1$ V

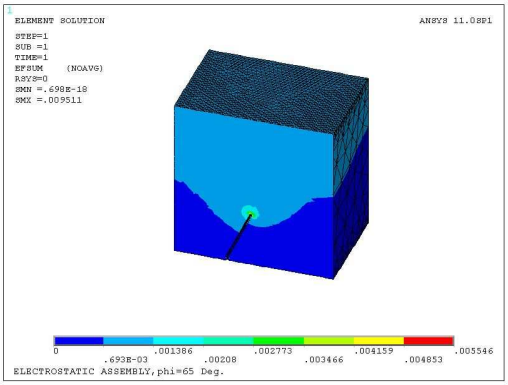

(c) $g_0 = 1.5$ mm, $V_{DC} = 1$ V

Figure 3.15: FEM solutions for the amplitude of the electric field in the air gap region at $\phi = 65°$, for a gap of (a) 0.6 mm (b) 1.0 mm (c) 1.5 mm. The maximum electric field amplitudes that are marked with red contours in the color version of this document are 0.019, 0.009, and 0.005 V/μm.

with $(V_{DC}/g_0)^2$ for $\phi = 0$. Consequently, the DC voltages after scaling end up being approximately proportional to the electrostatic gap.

An important observation from Figure 3.16(a) is that the rotation angle for which the moment reaches its maximum value depends on the gap. In addition, the relatively small change of the moment curves when the gap is decreased from 1.5 mm to 1 mm is noteworthy, and it is a sign that $(V_{DC}/g_0)^2$ proportionality for the electrostatic moment is still a good approximation. A further decrease in the gap down to $g_0 = 0.6$ mm, on the other hand, causes a significant change in the moment versus rotation angle characteristic.

For very large rotation angles $\phi \approx 90°$, the electrostatic moment values in Figure 3.16(a) suggest slightly negative values, instead of the expected zero moment. This is believed to be an artifact of the finite volume used in the FEM. As the paddle rotates, it separates the simulation space into two asymmetric regions as can be inferred from the contour plots of Figure 3.15. This asymmetry causes slightly more force on one side, yielding negative values at perpendicular position.

In the next section, which discusses the electrostatic force limit of U2EBA due to breakdown of air, the magnitude of the maximum electric field in the air-gap region will be important. This entity is plotted in Figure 3.16(b), where the marker points are FEM simulation results, and the solid lines are polynomial fit to the data. The dashed curves give the theoretical results when parallel-plate approximation is employed, disregarding the field crowding at the tip region. It is calculated using $E_{max,THY} = V_{DC}/(g_0 - L_1 \sin(\phi))$, which follows from Figure 3.13. However, analytical calculations using parallel-plate approximation underestimate the maximum electric field significantly, as they do not take field crowding and fringing fields into consideration. These observations, which are also in agreement

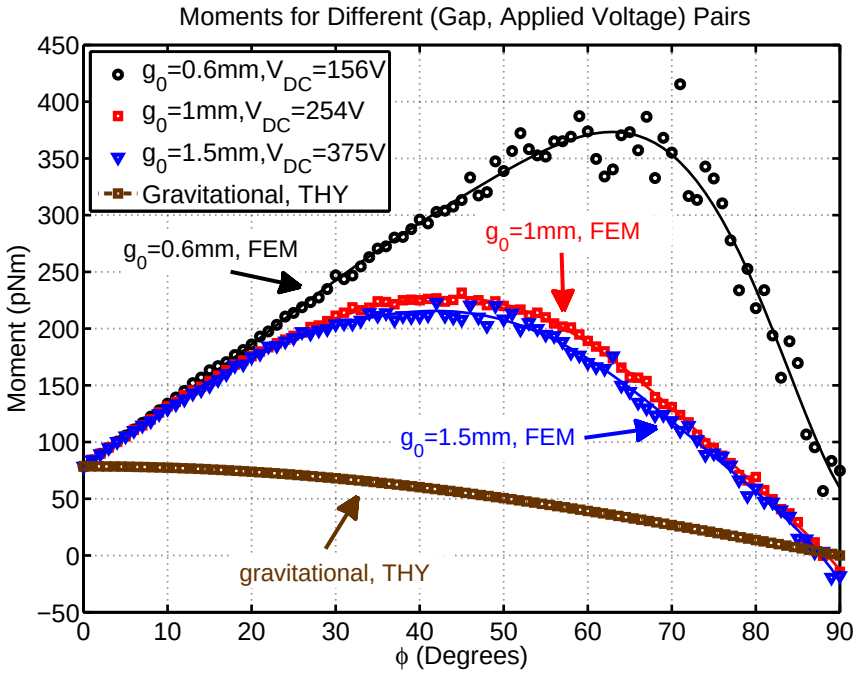

(a)

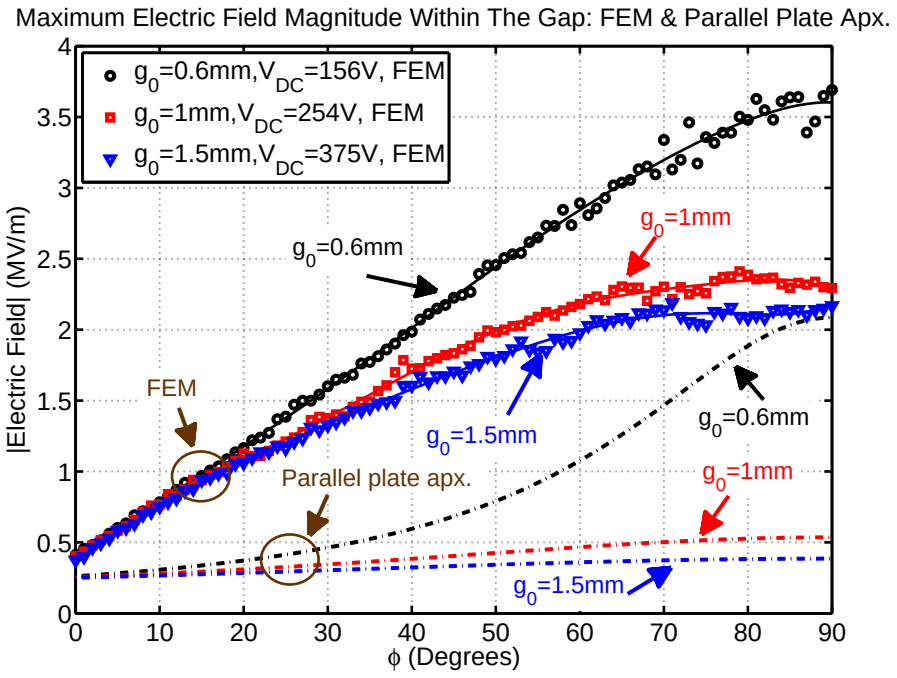

(b)

Figure 3.16: FEM solutions at different gaps as a function of the rotation angle for (a) electrostatic moment on the paddle, $|M_{\phi,ES}|$, and (b) maximum electric field magnitude in the air region, $|E_{max}|$. The DC voltage is scaled so that the electrostatic moments are equal to the gravitational moment at $\phi = 0$.

with the results of Appendix F, are quantified in Table 3.2. This table compares the FEM results to that from parallel plate theory. When the paddle is parallel to the top electrode, the match between the parallel plate theory and ANSYS© improves at smaller gaps for the electrostatic moment. An analogous statement regarding the accuracy of the parallel-plate approximation as a function of electrode separation can also be made numerically from the microstrip line theory [91, Equation 3.211].

Table 3.2: Comparison of FEM results to analytical values calculated using parallel plate approximation for a horizontal paddle (i.e., $\phi = 0$).

		Moment, $\lvert M_{\phi,ES}\rvert$			**Electric Field,** $\lvert E_{max}\rvert$		
g_0	V_{DC}	ANSYS©	THY.	Ratio	ANSYS©	THY.	Ratio
mm	V	pNm	pNm	—	V/m	V/m	—
0.6	156.48	78.5	37.5	2.093	412863	260799	1.583
1.0	254.41	78.5	35.7	2.200	402204	254408	1.580
1.5	375.96	78.5	34.6	2.267	374170	250641	1.492

3.4.3.2 Limit on electrostatic forces due to breakdown of air

In U2EBA setup shown in Figure 3.6, the air on top of the structures to be assembled is subjected to electric fields at high temperatures. The maximum attainable electrostatic moment available is limited by the breakdown of air. Furthermore, large aspect ratio, out-of-plane structures that erect during the assembly are going to introduce sharp regions and smaller electrostatic gaps. These regions cause, in their vicinity, high electric field and strong non-uniformity, as was apparent in the FEM simulation results of Figure 3.15. The same regions are potential corona discharge spots that might cause local damage to thin, polysilicon microstructures.

Results of Figure 3.16(b) and Table 3.2 have shown that, analytical prediction

of the maximum electric field point is not accurate, except for the initial case of $\phi = 0$. Besides, higher temperature of operation, which is used in U2EBA in order to reduce capillary forces, is known to decrease the electrical strength of air [92,93]. Owing to these complications, corona discharge voltage calculation for U2EBA is carried out below under some assumptions.

An empirical formula for the spark breakdown voltage in the case of *uniform electric field* with 50 Hz excitation is given by Powell and Ryan over a large temperature range ($20°\text{C} < T < 900°\text{C}$) as [93]:

$$V_{BD,s} = 24.49(\delta d) + 6.61\sqrt{(\delta d)} \qquad \text{(kV)}, \tag{3.6}$$

where d is the gap in cm and δ is the gas density relative to normal temperature and pressure as expressed below [92]:

$$\delta = \frac{P}{101.3 \text{ kPa}} \frac{273 + 20}{273 + T}. \tag{3.7}$$

Here P is the ambient pressure in Pascal and T is the temperature in °C.

Although vacuum operation of U2EBA is possible, all of the experiments to be reported are performed in atmospheric pressure. Then, the breakdown voltage from Equation (3.6) is $V_{BD,s} = 3160$ V at an operation temperature of 200°C and gap of $d = g_0 = 1$ mm. Being on the conservative side, the magnitude of the breakdown field is taken as $|E_{BD}| = 1300$ V/mm for the sake of estimation. Considering the $\phi = 0$ case that has a relatively uniform electric field distribution, the maximum initial electrostatic force per unit area is calculated to be [10]

$$\left|\bar{F}_{ES,max}\right| = 7.5 \ \mu\text{N/mm}^2.$$

This value is lower than some other assembly methods [75, 94], but it is complemented by ultrasonic radiation and lubrication forces.

It should be emphasized that the quoted value of 7.5 μN/mm^2 for the electrostatic pressure neglects surface material dependence [95] and the onset of corona discharge that occurs as assembled structures form regions of high electric field during the assembly, i.e., when $\phi \neq 0$. In those cases, coupled electromagnetic, structural, and Monte-Carlo simulations that accurately model the electron and ion dynamics as well as the physics of atomic level collisions and surface emissions can be necessary for realistic estimation of the breakdown voltage.

3.4.3.3 Friction forces due to electrostatic interactions

The change in the effective value of friction forces in the presence of ultrasonic vibrations was described in Section 3.4.1.1. Since electrostatic forces result in normal forces on the rotating and rubbing parts such as the staple region of the hinge, they will contribute to the frictional forces. These frictional forces are of the same order of magnitude as the normal component of electrostatic forces, as they are related to each other by an effective coefficient of friction. However, the length of the moment arm associated with friction of the staple region of the hinges is much smaller than the paddle dimensions. As such, moment associated with the friction is expected to be negligible as compared to the electrostatic moment. This is not true for more complex assemblies, where the point of contact and/or rubbing is far from the axis of rotation [2]. In those cases, friction is dependent on electrostatic forces, and therefore should be incorporated into FEM. Yet, performing a multi-physics FEM simulation, allowing large-angle, structural, electrostatic and contact problems is a challenging task, both from programming and computational view points.

3.5 Experimental

3.5.1 Ultrasound-Enhanced Electrostatic Batch Assembly fixture

The setup used in the experiments was explained in Figure 3.6. This section details the instruments used in the set-up and some important physical parameters.

The bulk PZT actuator has dimensions 12.5 mm $\times$ 12.5 mm $\times$ 0.5 mm (Staveley NDT). It is bonded on top of a custom-made, aluminum chuck using a conductive silver epoxy (Epoxy Technologies, H20E). A center-through hole of diameter 1 mm on the ceramic is aligned to the hole on the chuck manually before bonding to allow vacuum suction of the die on the ceramic. Wiring to PZT electrodes is also done using a conductive epoxy instead of the regular SnPb solder, in order to avoid thermal reflow during high-temperature experiment conditions.

A glass microscope slide (SPI Supplies®, 06400-CF) that has its bottom surface coated with Indium Tin Oxide (ITO) is used as a global top electrode and spaced $1 - 5$ mm above the substrate. In practice, any metal electrode works, but transparency is a plus as it allows optical monitoring of the assembly experiment. Electrical contact to the metal coated side of the glass slide is made with a copper tape and 30 AWG wiring. This wire is connected to the positive terminal of a high voltage DC power supply (EC Apparatus Corp., EC4000P / Series 90). A short circuit protection resistor of 10 MΩ is used at the output of the DC supply. A resistor of the same value is also used as a fixed shunt load at the output. Both of these resistors are shown in the electrical equivalent circuit of the setup in Figure 3.7. The top electrode of the PZT is kept at the ground potential, shielding

AC electrostatic actuation of the microstructures on the die. Although this could be a mode of operation, it is not pursued in this work.

Frequency-swept sinusoidal voltage from a function generator (Agilent- 33120A) is used to drive the PZT actuator. When more drive power was necessary, a power amplifier (Piezo Systems, EPA-102) was used with a nominal, low-frequency voltage-gain of 20. Frequency response characterization of both the loaded and unloaded amplifier along with that of the function generator are given in Appendix H.

The measurement of the displacement of a sample die placed on top of the assembly fixture was performed using Doppler interferometry setup described in Appendix B. The results are plotted in Figure 3.17 for 4 V_{pp} excitation of the PZT. Maximum displacement measured was around 25 nm and occurred around 85 kHz. The same figure shows the vibration characteristics on the die, when there is no vacuum suction. Reduced coupling in this case causes one to two orders of magnitude reduction in the out-of-plane displacement amplitude.

The assembly fixture, which is illustrated in Figure 3.6 and used in most of the reported experiments, has PZT ceramic bonded on top of the vacuum chuck. This order of assembly was chosen based upon its superior performance as compared to the previous version of the fixture that had PZT ceramic under the chuck. The relevant vibration spectra data, which were used as the basis of comparison, are given in Appendix I.1 for both of the setups.

The assembly fixture is mounted on a heater that allows experiments around 200°C to partially eliminate humidity-related stiction[5]. Impedance measurements of the PZT actuator at elevated temperatures showed that the sharpness of the

[5]The temperatures reported are the set temperature of the heater stage on which the U2EBA fixture is situated. The air temperature in the electrostatic gap was not measured separately. It is expected to be lower than, but close to the set temperature of the heater element.

resonance peaks has not changed considerably as compared to room temperature measurements. These results are given in Appendix I.2.

As another way of mitigating stiction, all the samples are kept in a nitrogen-purged container at temperatures 200-250°C until the experiments. Often times the dies were *seasoned* before starting the experiment by keeping them on the assembly fixture for a few minutes with ultrasonic actuation on, but without any DC bias. This operation was observed to yield slightly better assembly rates. Detailed information on the tested structures are given next.

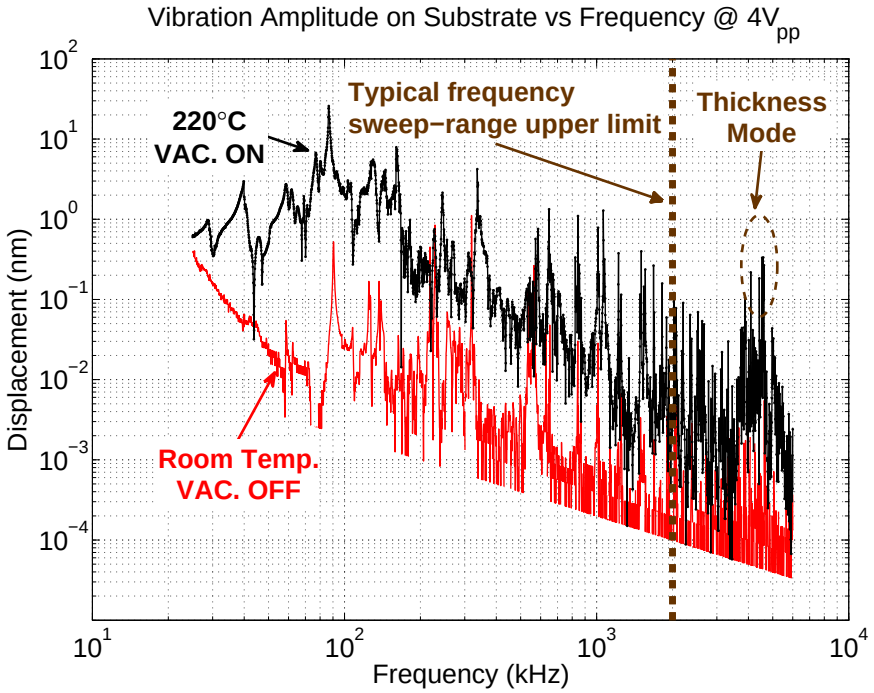

Figure 3.17: The displacement amplitude results calculated from measurements of surface velocity using a Doppler interferometer.

3.5.2 Tested surface-micromachined structures

One set of devices were fabricated in 75th PolyMUMPs^{TM} run in 2006 [54], whose process can support hinged structures with dimples that were illustrated by Figure 3.5. One quarter of the 1×1 cm^2 die shown in Figure 3.18(a) was reserved for assembly test structures. This 5×5 mm^2 region shown separately in Figure 3.18(b) involves 5 arrays of different hinge designs. Geometrical parameters, structural attributes and the optical picture of the hinge arrays are summarized in Table 3.3.

The second set of devices were designed by Block MEMS LLC [2] and fabricated in SUMMiT V^{TM} [96]. These devices were provided to us for assembly characterization. They involved compliant structures that had butterfly shaped paddle regions attached to the substrate with two torsional beams of varying lengths, namely 66, 88, 110, 133, 155, 200 μm. Figure 3.19 shows the device with 133 μm long beam. Two flaps on the sides are lock-in structures that constrain the central flap once it is assembled.

3.5.3 Assembly results on surface micromachined hinges

This section presents results from two different sets of dies which were manufactured in the same PolyMUMPs^{TM} run, but released at different times. Sets of dies are named as *set-A* and *set-B*, and each die in a given set is referred by a unique number from 1 to 5, prefixed by the set identifier, 'A' or 'B'. As shown in Table 3.3, each of these dies had five arrays of micro-hinges with permanent lock-in structures that prevented the collapse of hinges once they are assembled. Samples of assembled hinged structures are shown in Figure 3.20 and Figure 3.21.

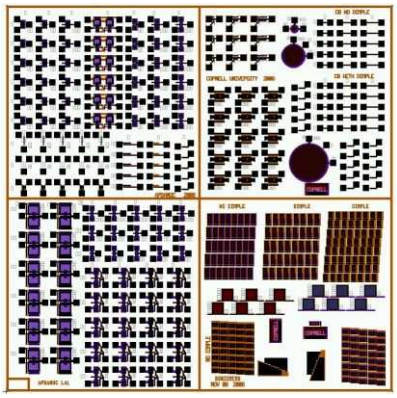

(a)

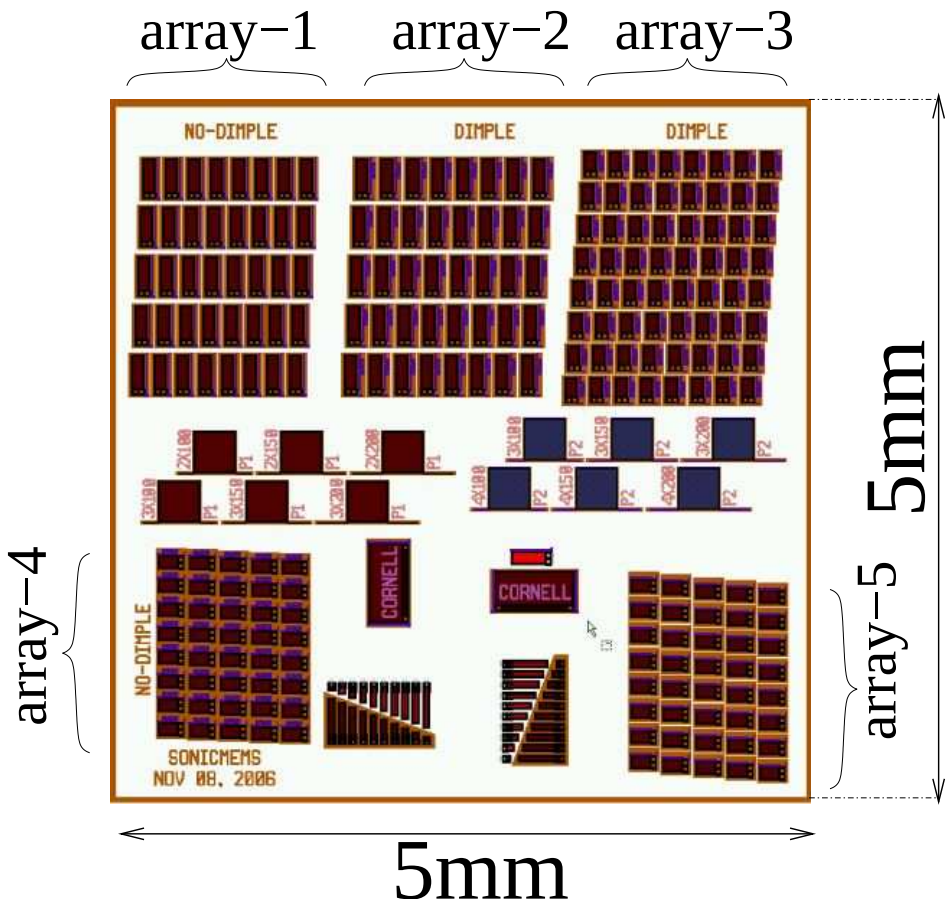

(b)

Figure 3.18: CAD layout of (a) die fabricated in PolyMUMPs^{TM} in 2006, (b) detailed view of the lower-right quadrant of the die that were used in U2EBA experiments.

Table 3.3: Listing of the attributes of the hinged arrays in the fabricated PolyMUMPs^{TM} die.

Array Index	**Description (Dimple, Length, Spring Type)**	**Array Size**	**Paddle Size WxL** (μm $\times$ μm)	**Picture**
1	No dimple, Long, Straight	5×8	97×279	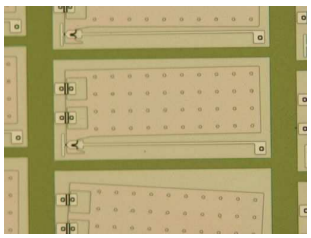
2	With dimple, Long, Serpentine	8×8	97×279	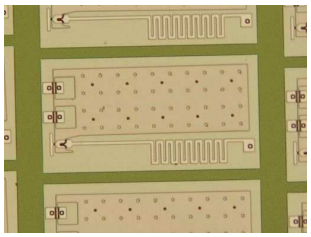
3	With dimple, Short, Serpentine	8×8	97×180	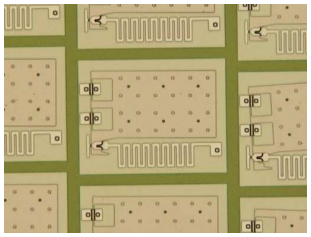
4	No dimple, Short, Serpentine	5×8	97×180	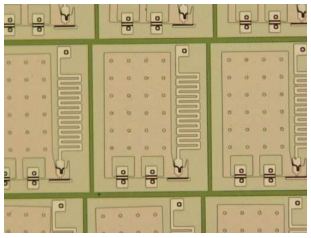
5	With dimple, Short, Straight	5×8	97×180	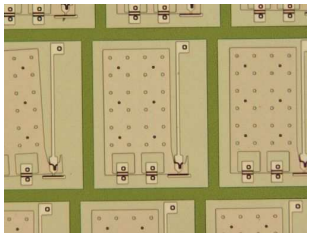

The experiments to be reported were performed at a gap of $g_0 = 2.45 \pm 0.3$ mm, with either the heater surface temperature set at 220°C, or with the heater turned off so that the experiment was at room-temperature (RT). Often times "hinge array-3" gave the highest yield of assembly. For this reason, the yield of the same array is picked as a benchmark parameter to assess the effect of any change in the control parameters of the experiments.

Table 3.4 and Table 3.5 tabulate most of the experiments performed and conditions at which they were performed. Some of the dies such as *die-A1* and *die-B2* went through consecutive experiments under different conditions. For those dies, assembly yield is reported in a cumulative manner, i.e., all of the experiments except the first one operated on a partially assembled die depending on the success of the previous experiments on the same die. The maximum drive amplitude of the PZT depends on the drive amplitude of the function generator, and whether a power amplifier is used or not, both of which are indicated in the tables. For

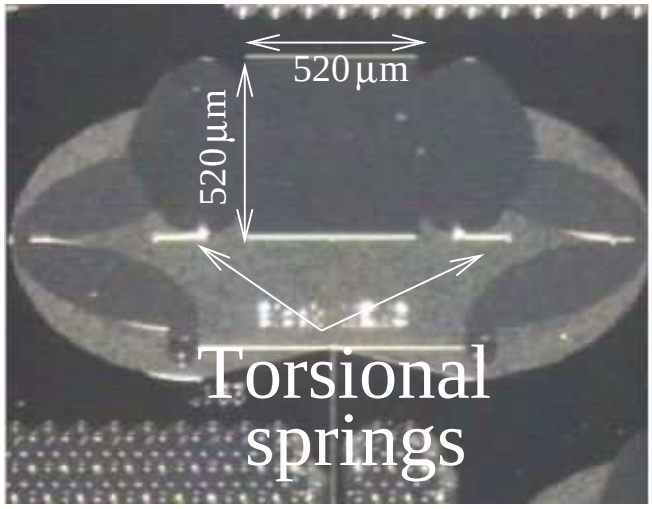

Figure 3.19: Optical picture of a mirror that is supported by two 133 μm long torsional beams, fabricated in SUMMiT V^{TM} process by Block MEMS LLC.

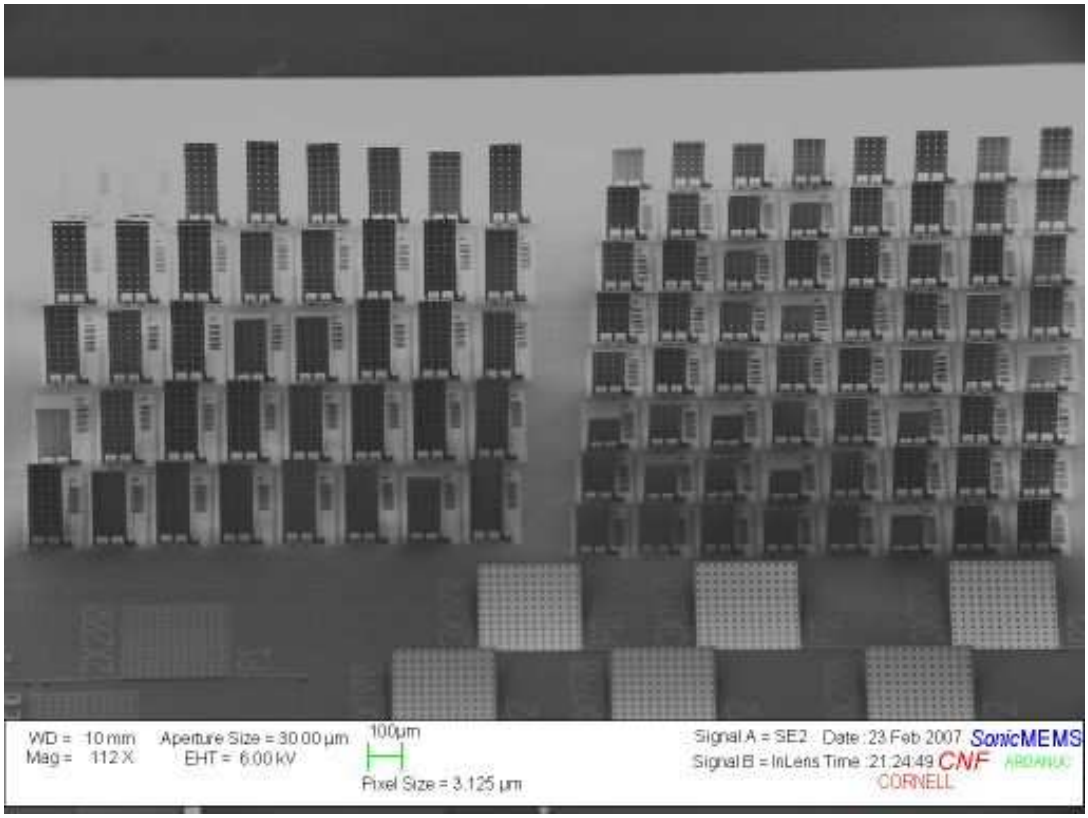

(a)

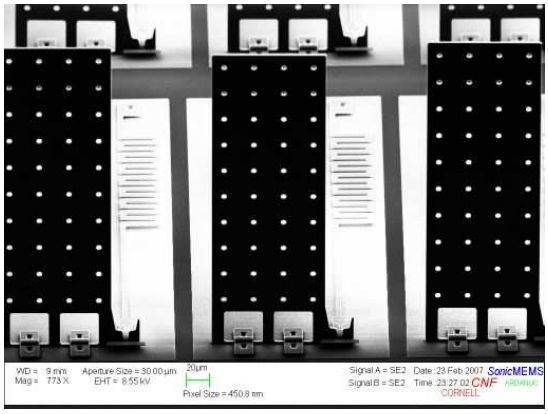

(b)

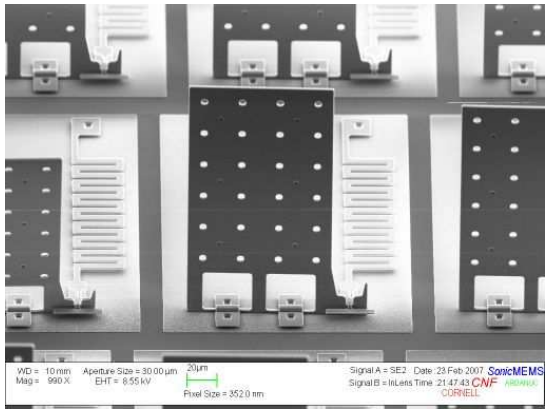

(c)

Figure 3.20: SEM pictures of the *die-A2* after U2EBA experiments: (a) with array-2 on left and array-3 on right, (b) array-2 hinges, (c) array-3 hinges.

example, if a function generator drive amplitude of 1 V_{pp} @ 50 Ω is used and followed by the power amplifier, then amplifier output at high impedance load is about 40 V_{pp}, given the amplifier nominal gain[6] of 20.

Following sections discuss the results of the U2EBA experiments on the hinged structures.

[6] The normalized frequency characteristic of the power amplifier is given in Appendix H.

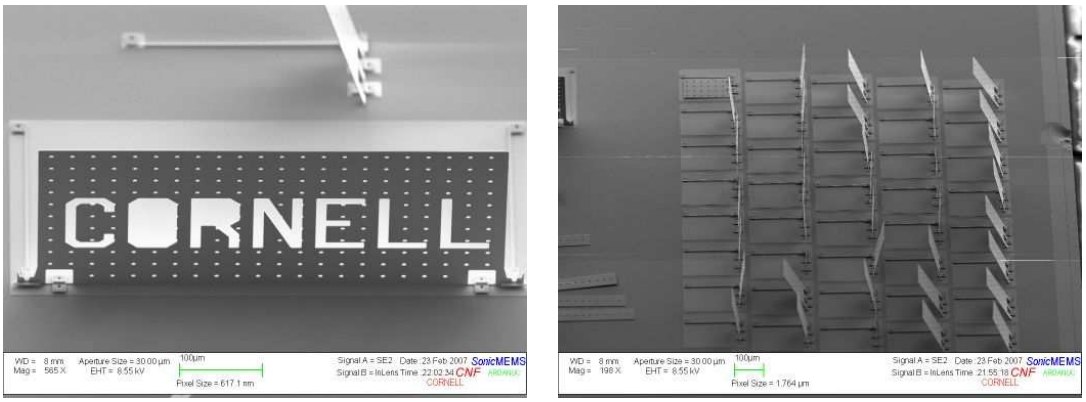

(a) (b)

Figure 3.21: SEM pictures of the *die-A2* after U2EBA experiments: (a) "Cornell" letters [10], (b) array-5 side view.

Table 3.4: Listing of the main experiment conditions for the first set of dies tested using U2EBA. ‡

Die Label	**Exp. No.**	**Frequency Sweep Start**	**Stop**	**Period**	**Max. fun. gen. output‡**	**Power amp.**	**Temp.†**	**Time btw. release & exp.**	**Array-3 assembly yield**	**Comment**
		MHz		sec	V_{pp}		°C	day		
A1	1	2	10	**10**	10	×	220	< 1	20/64	breakdown @ $V_{DC} = 3250$ V
	2	2	10	**60**	10	×	220	< 1	20/64	
	3	2	10	**2**	10	×	220	< 1	20/64	
	4	**0.5**	**2**	**10**	10	×	220	< 1	26/64	
A2	1	**0.01–0.1**	2	10	**1**	✓	220	< 2	64/64	
A3	1	0.01–0.1	2	10	1	✓	220	< 2	63/64	
A4	1	0.01–0.1	2	10	**1.4**	✓	220	< 2	62/64	some break
A5	1	0.01–0.1	2	10	**1**	✓	220	< 2	43/64	

‡ Maximum function generator output @ 50 Ω before power amplifier, if used.
† Set temperature of the hotplate which is in contact with the 0.5 mm thick silicon wafer under the chuck in Figure 3.6.

Table 3.5: Listing of the main experiment conditions for the second set of dies tested using U2EBA. ♯

Die Label	**Exp. No.**	**Frequency Sweep** Start	Stop	Period	**Max. fun. gen. output**‡	**Power amp.**	**Temp.**†	**Time btw. release & exp.**	**Array-3 assembly yield**	**Comment**
		MHz		sec	V_{pp}		°C	day		
B1	1	3	6	10	10	✗	RT	< 3	32/64	breakdown
B2	1	0.1	2	10	10	✗	RT	< 3	6/64	@
B2	2	**3**	**6**	10	10	✗	RT	< 3	6/64	$V_{DC} > 3750$ V
B2	3	3	6	10	10	✗	**220**	< 3	23/64	
B2	4	**0.1**	**2**	10	10	✗	220	< 3	31/64	
B2	5	**0.01**	2	10	10	✗	220	< 3	37/64	
B2	6	**0.1**	2	10	1	✓	220	< 3	48/64	
B2	7	**0.01**	2	10	1	✓	220	< 3	52/64	
B3	1	0.01– 0.1	2	10	1	✓	220	< 3	63/64	
B4	1	**3**	**6**	10	1	✓	220	< 3	7/64	
B4	1	0.01– 0.1	**2**	10	1	✓	220	< 3	64/64	
B5	1	0.1	2	10	1	✓	**RT**	$< \mathbf{4}$	63/64	

‡ Maximum function generator output @ 50 Ω before power amplifier, if used.
† Set temperature of the hotplate under assembly fixture. "*RT*"≡room temperature.

3.5.3.1 Quantifying the effect of ultrasound on the yield of assembly

Figure 3.22 gives a series of snapshots from an U2EBA experiment on *die-A3* with heater turned on [10]. The experimental procedure was as follows. The die was first exposed to increasing levels of electrostatic forces in the absence of ultrasonic actuation. The PZT actuator was switched on at $V_{DC} = 3000$ V, starting with a low amplitude drive, and then the drive voltage was gradually increased to the peak-to-peak amplitude that is specified in Table 3.4. After the PZT is switched on, a jump in the number of assembled flaps was observed. This sudden increase in the yield of assembly shows the anti-stiction effect of ultrasound. SEMs of the fully assembled array-3 and 96% assembled array-2 on *die-A2*, as well as close-up views of the hinged-flaps from their respective arrays are shown in Figure 3.20.

Similar experiments were performed on all of the dies of sets A and B. Snapshots from the assembly experiment of *die B-5* are shown in Figure 3.23. *Die-B5*, which was assembled at *room temperature*, achieves 63/64 assembly yield like *die-A3*, which was assembled at 220°C. Small but non-zero initial number of assembled flaps on *die-B5* even before the experiment, at $V_{DC} = 0$ V, stems either from assembly due to static charging during handling, or turbulence during wet release.

The numbers of assembled hinges as a function of V_{DC} before and after the PZT turned on were recorded for *dies A3*, *A4* and *B5*. This data are plotted in Figure 3.24. The large increase in the assembly yield after turning the PZT on is common to all. As this data shows, an electrostatic only approach can also work for assembly. Such an approach is previously presented by Johnstone *et al.* [97]. Yet, the yield enhancement in the assembly with ultrasound cannot be underestimated.

The inset in Figure 3.24 graphs a yield-histogram based on the results of *dies*

A2-A5, die B3-B4, all of which were tested at 220°C with the power amplifier. These attributes were chosen in order to include the largest number of samples among the reported dies in Table 3.4 and Table 3.5 [7].

Generally speaking, it was experimentally observed that high temperatures of operation yielded higher assembly rates, despite reducing the breakdown voltage. Second and third experiments on die *die-B2* in Table 3.5 show the increase in the assembly yield due to an increase in the temperature. In this respect, high assembly rate of *die-B5* **at room temperature**, deserves special attention. The

[7] *die-A1* is excluded as this sample was not tested with power amplifier, which was crucial for high-yield.

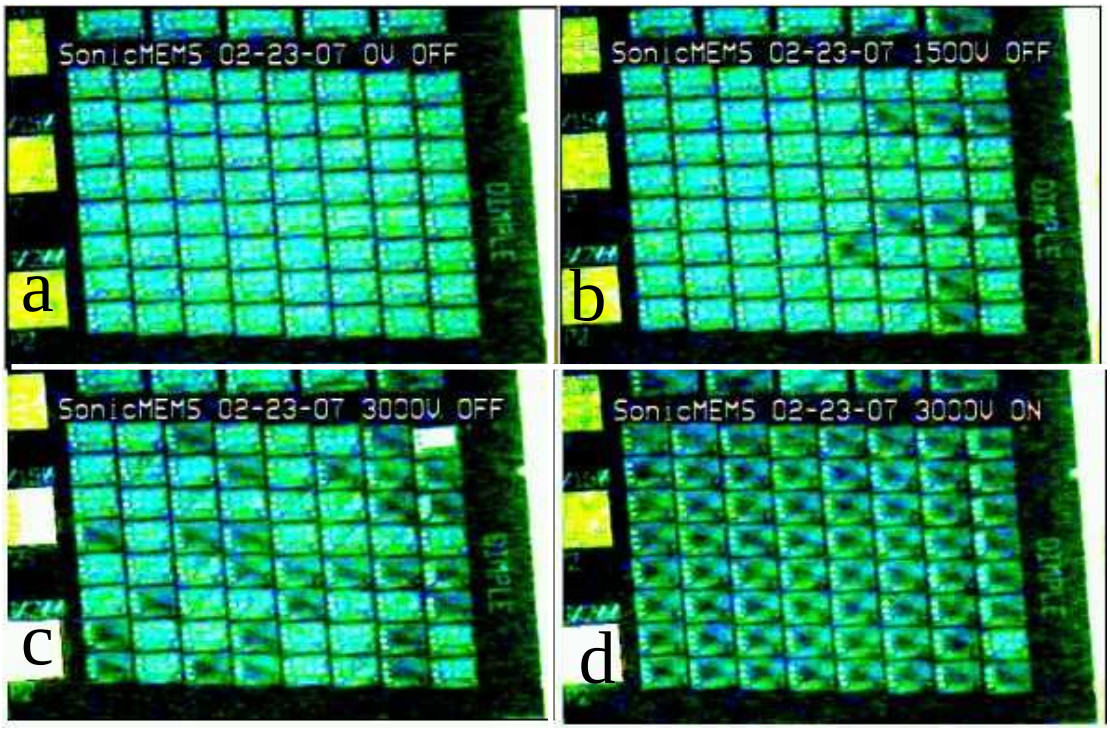

Figure 3.22: Snapshots from the assembly of array-3 in *die-A3* performed with heater set to 220°C. [10]. DC voltages are (a) 0V, (b) 1500V, and (c) 3000V with the PZT switched off. The last snapshot (d) is taken after the PZT is switched on at 3000V and has 63 of 64 flaps assembled.

experiments show that high temperature operation for antistiction is **not** a required condition for high-yield results in U2EBA. Nonetheless, since the reported samples were maintained at elevated temperatures ($> 200°C$) till the assembly experiments, even samples experimented at room-temperature might have benefited from exposure to high temperatures before the experiments.

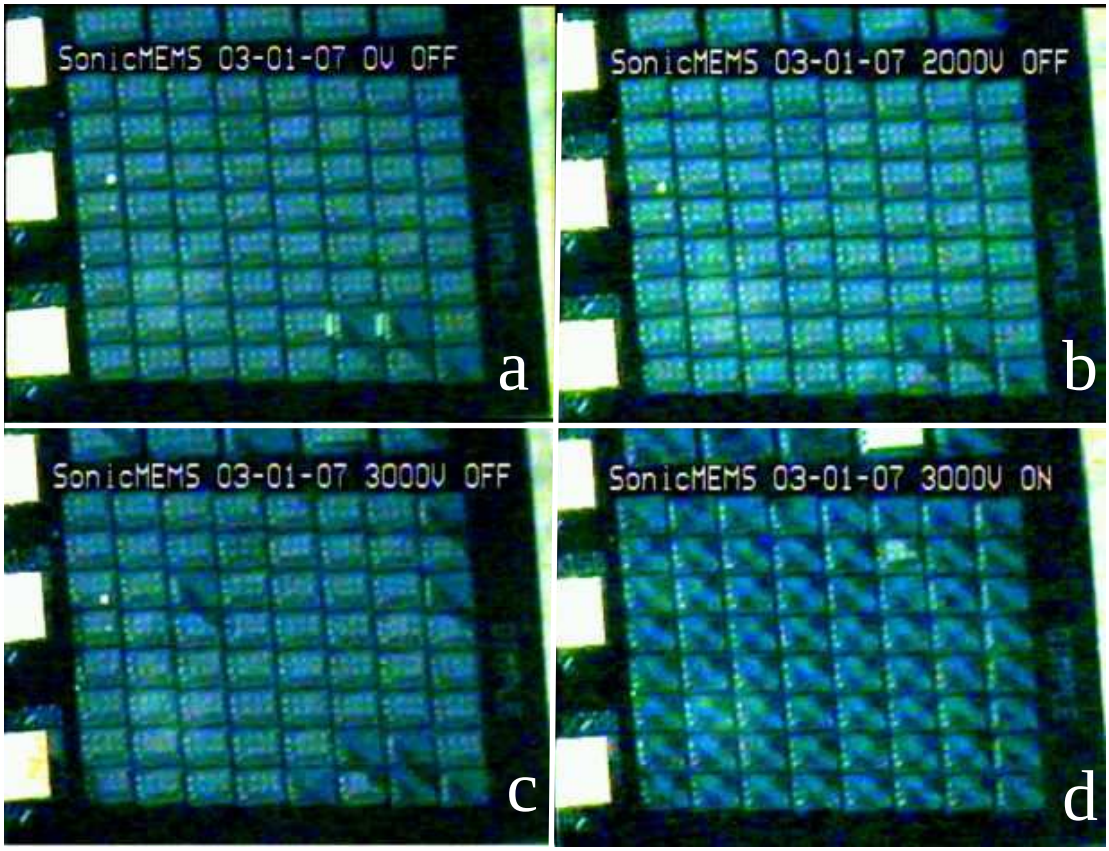

Figure 3.23: Snapshots from the assembly of array-3 in *die-B5* performed at room temperature on the third day after the release [10]. DC voltages are (a) 0V, (b) 2000V, and (c)3000V with the PZT switched off. The last snapshot (d) is taken after the PZT is switched on at 3000V and has 63 of 64 flaps assembled, just like the array in Figure 3.22.

3.5.3.2 Comparing the yields of different hinge structures on the same die

Five arrays listed in Table 3.3 were made using five different hinges of arrays, each being different than the other in one or more of the following attributes:

1. *Existence of dimples* of size 4×4 μm^2 with a repetition length (i.e., pitch) of 50 μm in both dimensions.
2. *Length of the paddle* to study the effects of area increase in the assembly

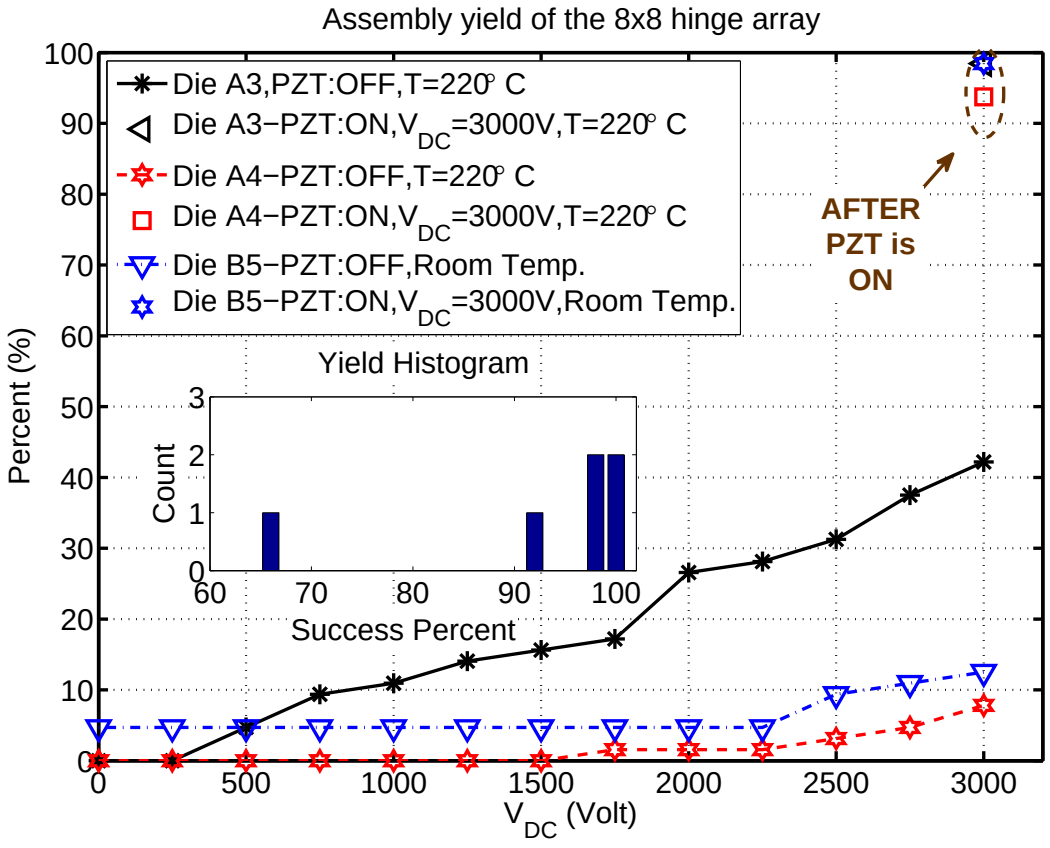

Figure 3.24: The assembly yield of array-3 on some of the tested samples as a function of V_{DC} applied. *Die-A3* and *die-A4* were tested at an elevated temperature whereas *die-B5* was tested at room temperature.

yield. The width of all of the hinge structures was fixed around 100 μm.

3. *Spring type* of the lock-in structure. The hinge itself is in principle free to move. However, there is a restoring force associated with the lock in structure. This force decreases if the beam of the lock-in structure right next to the paddle is changed from a *straight* design to a *serpentine* design.

Table 3.6 details the assembly yields of different types of hinged arrays that were listed in Table 3.3. For all of the reported samples in this table, array-3 results in a significantly better assembly yield than array-4. Therefore, one can conclude that dimples improve the assembly yield. A similar observation can be made about array-2 and array-3, both of which have identical hinge attributes except for the length of the paddle. Array-3, which has shorter paddles but the same width as array-2, showed better assembly yield. This result is contrary to the initial electrostatic moment being larger for the longer paddle due to its longer moment arm length at the same electrostatic pressure[8]. It can be that, as the structures get larger and the number of dimples increases, it becomes less probable to separate all of the dimples at once from the substrate at a given frequency of excitation. In other words, the increased paddle length decreases the antistiction effect of ultrasound more than it increases the electrostatic moment per unit area. Instead of a frequency-swept harmonic excitation, pulsed ultrasonic actuation [98] can be more effective in separating the structures from the surface due to its broadband nature. This hypothesis is not tested in this work.

Comparing the attributes of array-3 and array-5, the advantage of having a lock in design with a serpentine beam becomes apparent. Serpentine design provides a lower spring constant, which eases the assembly and contributes to array-3's higher

[8]See Equation (F.4).

yield of assembly

All of the above observations regarding, spring constant, effect of dimples and paddle length, are verified independently by comparing array-1 and array-3. As mentioned before, array-3 resulted in the best assembly yields in the experiments. On the other hand, array-1, which has exactly the opposite attributes of array-3 (i.e., no-dimples, long paddles, and a lock-in structure with a straight beam), has either the worst or one of the worst assembly yields for every die on Table 3.6.

Table 3.6: Yield of assembly of the hinge arrays from the tested dies of sets A and B.

		Array No				
		1	2	3	4	5
Attribute	Dimple	✗	✓	✓	✗	✓
	Paddle Length	long	long	short	short	short
	Spring Type	straight	serpentine	serpentine	serpentine	straight
SET A	A2	9/40	38/40	64/64	20/40	39/40
	A3	6/40	36/40	63/64	35/40	38/40
	A4	13/40	32/40†	62/64	23/40	40/40
	A5	15/40	19/40	43/64	37/40	35/40
SET B	B1	3/40	18/40	32/64	3/40	21/40
	B2-Exp. 1	0/40	2/40	6/64	0/40	9/40
	B3	7/40	38/40	63/64	28/40	39/40
	B4-Exp. 1	0/40	2/40	7/64	0/40	4/40
	B4-Exp. 2	4/40	39/40	64/64	26/40	39/40
	B5✠	14/40	31/40	63/64	37/40	39/40

† One structure is broken.
✠ Array-1 and array-2 have broken hinges.

For any successful assembly, free-to move structures like hinged paddles should first come to a favorable position with the help of ultrasonic actuation so that there

is not any mechanical hinderance, bump, stopper or alike along the path of assembly. Due to random nature of stiction, and random position of hinge pins in the staple regions, it took a few frequency sweep cycles before the hinges got assembled in our experiments. The time required to get the assembly yields reported in this work, with a frequency sweep period from $1 - 10$ sec, varied from seconds to a few minutes. Once, the hinged paddle structures were released from the substrate, they instantaneously moved close to vertical positions under the effect of electrostatic forces. The associated time scale is determined by the structure mass, damping, friction, spring constant, etc. This small time scale was not characterized as the frame rate of the standard camera used in the experiments was not fast enough.

The clearance associated with lock-in and hinge structures, as well as other non-idealities resulted in considerable variation from the fully-vertical ($\phi = 90°$) position, as shown by the side view of an array assembled with %96 yield in Figure 3.21(b). However, this variation can be minimized by careful design, alternative assembly structures, or process changes [2, 99].

3.5.3.3 Damage to devices which are subject to large ultrasonic vibration and/or large electric fields

The previous section showed qualitatively the improvement in the assembly yield due to ultrasonic excitation. However, damage to the hinge structures was observed at large PZT drive amplitudes. The damage was even more pronounced at lower frequencies, where the substrate vibration amplitude was larger as shown by interferometry results of Figure 3.17. The rate of the frequency sweep was also observed to affect the damage possibility during U2EBA. This characteristic, while not quantified, can be ascribed to the time spent around the resonance frequen-

cies, at which high amplitudes of vibrations occur. In some of the experiments, at large drive amplitudes and at certain frequencies, the whole die could be visibly displaced in spite of the vacuum suction.

Figure 3.25 shows SEM pictures of some of the damaged structures. It is interesting that the damaged regions are more like melted or exploded as opposed to a static fracture. This can be a signature of extreme heating of the rubbing parts inside the staple region due to ultrasonic excitation. The undamaged, stand-alone anchor regions next to the damaged staple regions in Figure 3.25(b) also supports this hypothesis.

Another way the structures fail occurs via breakdown of air, or in particular, via corona discharge from the assembled structures. Maximum electric field in the gap increases as the rotational angle ϕ increases, and the structures go towards the vertical position (i.e., $\phi = 90°$). The discharge is often times visible to the naked eye in terms of continuous or intermittent, blue light, accompanied by arcing sounds.

Room temperature experiments support larger breakdown voltages than those at elevated temperatures. This point is noted in Table 3.4 and Table 3.5 for *die-A1, B1, B2*, and it is in agreement with the theoretical discussions of Section 3.4.3.2.

Due to the stochastic nature of stiction and position dependence of ultrasonic vibrations on the die during the frequency-sweep, the assembly of hinges of the same type in the same array do not happen at the same time. The ratio of the characteristic length to the electrostatic gap, $r_{ES} = L_1/g_0$, first mentioned in Section 3.4.3, plays an important role in terms of the corona discharge limit. Larger the r_{ES}, easier it becomes for the assembled or actuated structures to crowd the electric field around them and make it harder for the unassembled structures to get

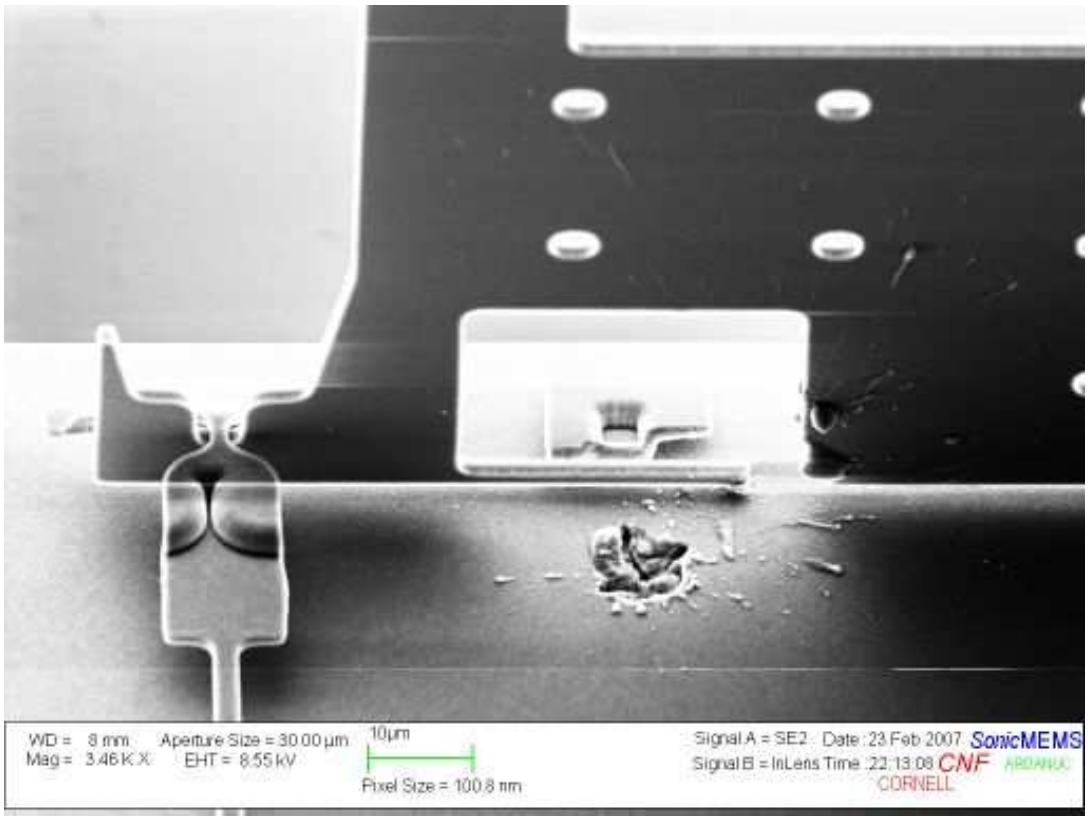

(a)

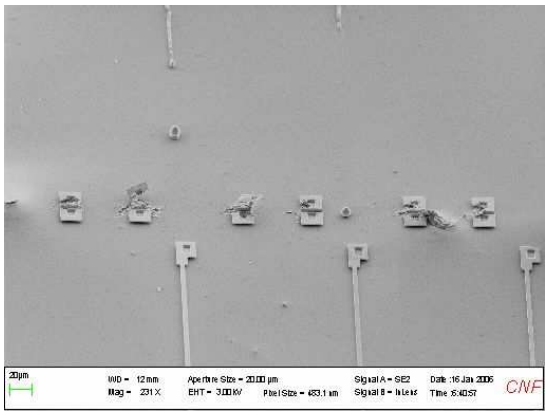

(b)

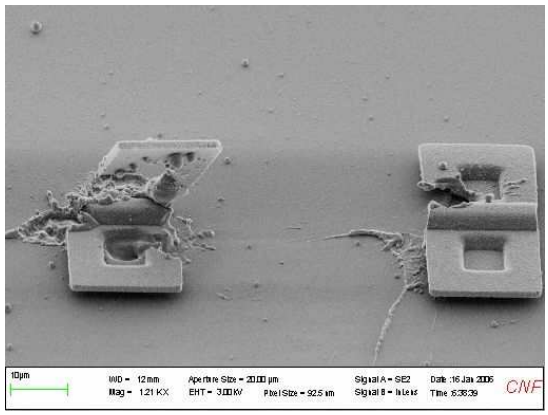

(c)

Figure 3.25: SEM pictures from some dies where hinges were damaged: (a) shows a damaged staple region from *die-A1*, (b) and (c) show large scale and zoomed versions of damaged structures from an earlier chip design tested using the first version of the assembly fixture, which had chuck-on-top of the PZT actuator.

their share of force/moment from the electrostatic field. This concept is referred as "field-starvation" [10]. Large values of r_{ES}, therefore, aggravates the limitation due to corona-discharge. This can be seen from the decrease in the maximum electric field amplitude for larger gaps in Figure 3.16(b). On the other hand, smaller r_{ES} values have the disadvantage of requiring larger DC voltages because of relatively large gaps. Many of our experiments favored the latter option in this tradeoff. As a result of this choice, V_{DC} voltages on the order of thousands were typical in most of the reported experiments.

Field starvation, also strongly depends on how close the structures to be assembled are. It is harder to assemble a given structure when there are already lots of assembled structures in the close vicinity. This becomes especially important during the assembly of complex 3-D microsystems as described in Section 3.5.4.1.

3.5.3.4 Failure of assembly due to trapping of the hinge-pin in the staple region

A very frequent reason of failure of assembly in dies that gave poor assembly yield of the hinges was identified to be the trapping of the rotation pin inside the staple [10]. This situation is illustrated in Figure 3.26 with an SEM of a hinge from *die-A5* that has one of the lowest assembly yields for the array-3 among the reported dies. Figure 3.10 shows similarly misplaced flaps right after wet-etch release. Therefore, one has reasons to believe that they are particular to neither electrostatic nor ultrasonic actuation. The trapping/stucking problems of the same nature and process remedies to overcome those are described by Hui *et al.* [99].

3.5.4 Results on assembly of compliant structures

The compliant structures tested were fabricated in SUMMiT V^{TM} by Block MEMS LLC (MA, USA) and were described in Section 3.5.2. These devices used secondary structures on the side for permanent lock-in after getting assembled to almost vertical position [2].

Figure 3.27 plots the static response of paddles of different torsional stiffness to applied DC voltage. Snapshot for one of the paddles is given by Figure 3.28. The angular rotation response as a function of V_{DC} is qualitatively in agrement with FEM calculations of the electrostatic moment on rigid structures plotted in Figure 3.16(a). In other words, the slope of the moment versus ϕ curves increases starting from $\phi = 0$, then reaches to a maximum, and finally goes to zero for

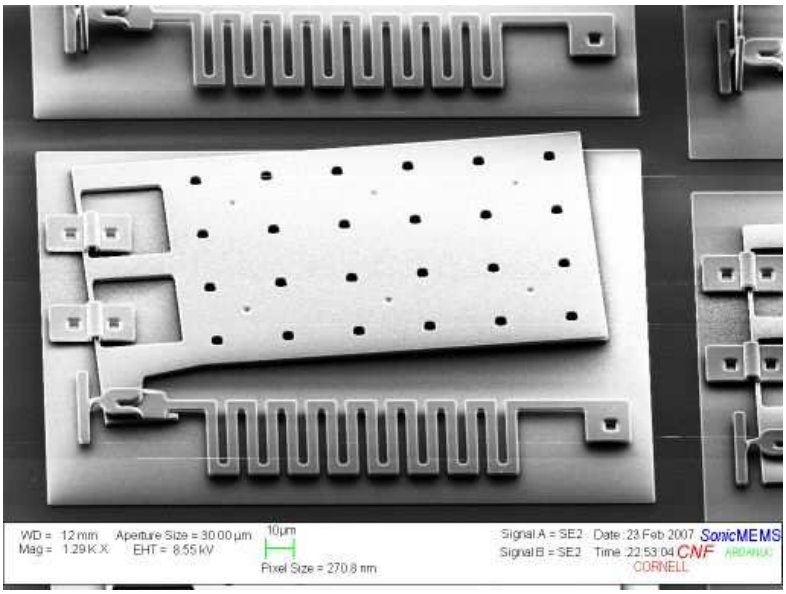

Figure 3.26: The SEM of the sample die with the worst yield for array-3 among tested samples with amplifier. The rotation bar is trapped near the anchor of the staple region, preventing any rotation of the hinge-pin around its axis.

$\phi \approx 90°$.

Experimental results, which were measured at 1 V_{pp} excitation, without power-amplifier, at 150°C, using the first prototype of the assembly fixtures indicate a threshold value for V_{DC}. The threshold phenomena is more likely to be related to SNR than to adhesion forces, since the value of the threshold voltage seems to decrease for paddles of the same geometrical shape but higher torsional stiffness. Nonetheless, if the SNR of the optical angle measurements is improved, then U2EBA can potentially be used to characterize adhesion forces of different surfaces or structures, thanks to the well-understanding of electrostatic forces.

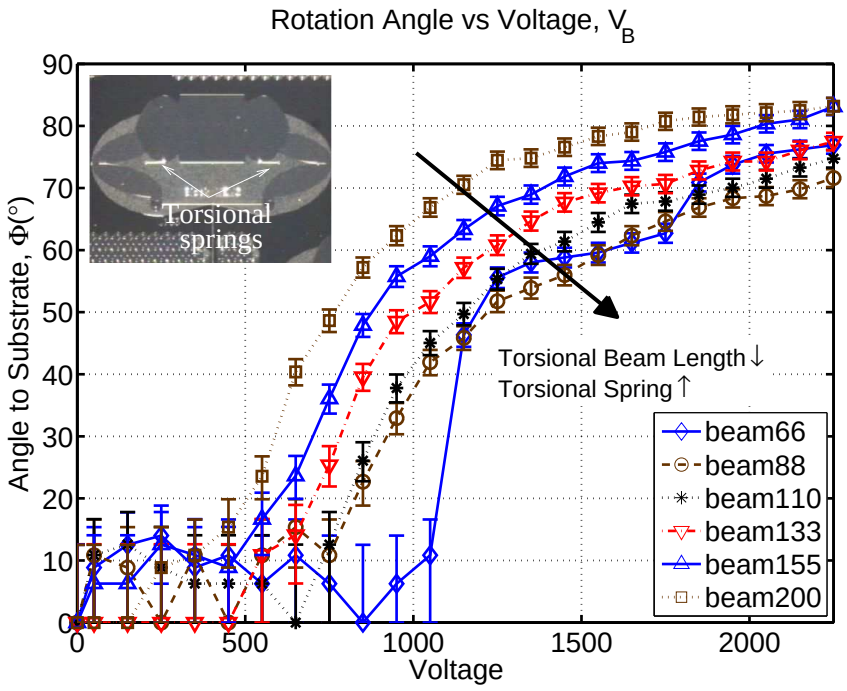

Figure 3.27: Angle of rotation versus applied DC potential on the top electrode for paddles anchored to substrate by torsional beams of different lengths. The inset shows the paddle geometry and position of the torsional beam springs in either side for the sample "beam-133" that has 133 μm long beams.

The largest angle measured in Figure 3.27 is $82 \pm 3°$ at 2250 V for the paddle

labelled as "beam-200". The maximum angle of rotation in compliant structures, is limited by the torsional stiffness and the breakdown voltage of air, and therefore never reaches fully vertical state when the top electrode is parallel to the die surface. This can be restrictive for free-space applications, that require vertical assembly of mirrors in accuracies of less than a degree.

Tilting of the top electrodes was shown to be effective to get actuation angles of more than 90°. Figure 3.29 compares the rotation angle of the same sample with parallel and tilted electrode configurations. The angle of rotation at 3000 V was measured as 88.8° and 93.3° for parallel and tilted configurations, respectively.

3.5.4.1 Experiments on assembly of complex free-space optical systems

U2EBA experiments were performed on micro FTIR spectrometer samples from Block MEMS LLC [10]. Figure 3.30 shows SEM pictures of some samples that could be partially assembled. Field starvation is believed to be the main obstacle towards full-assembly. Employing structures with higher compliance (lower stiffness) or patterning of the global top electrode can be promising for future U2EBA studies.

Figure 3.28: A series of snapshots for the actuation experiment of a paddle anchored to substrate with torsional polysilicon springs of 155 μm long. The voltage from left to right is (a) 0V, (b) 550V, (c) 2250V.

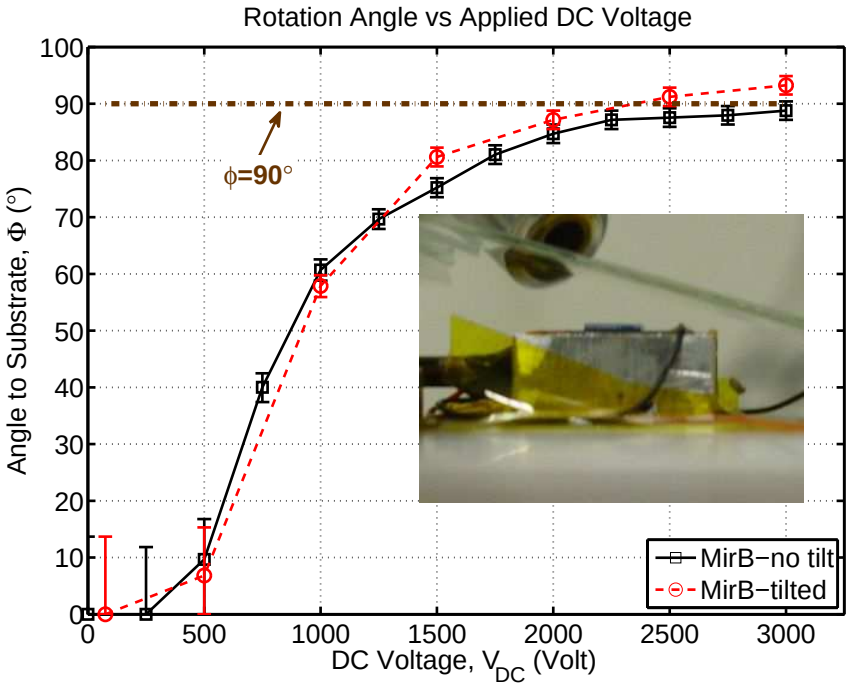

Figure 3.29: The angle of rotation of a compliant paddle as a function of the DC potential on the top electrode. The inset shows the side-view of the experimental setup when the top electrode is tilted.

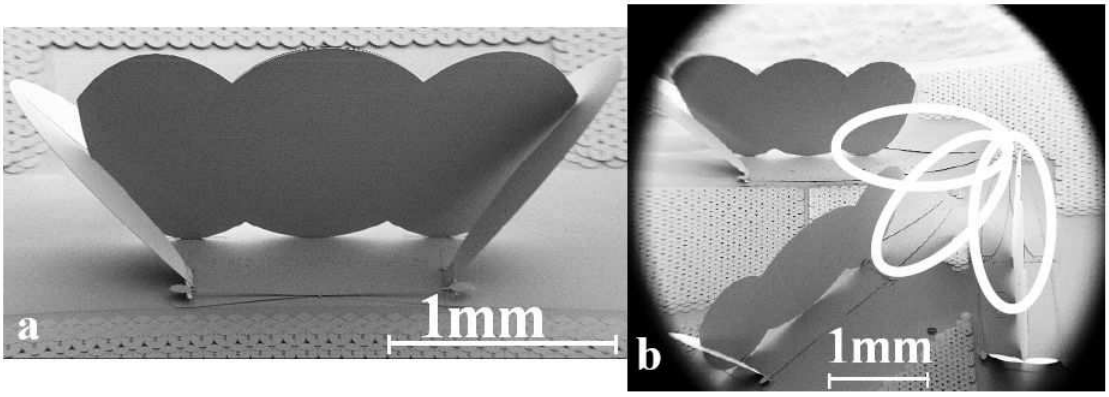

Figure 3.30: Partial assembly of parts of a micro FTIR spectrometer, which is in development by Block MEMS LLC, was demonstrated.

3.6 Summary and discussion

Ultrasound enhanced electrostatic batch assembly (U2EBA) is a simple, off-chip, method of micro-assembly that does not require, on-chip real estate, special layers, or additional steps in the process flow. This chapter described U2EBA and reported experiments with some samples reaching up to 100% assembly yield. Lack of on-chip actuators and wire-bonding to assembled structures enable high-fill-factor assembly of densely packed arrays of microstructures.

The forces involved in U2EBA, such as gravitational, electrostatic, and surface adhesion forces were investigated. FEM simulations were performed to predict electrostatic moment on rotating structures, as analytical predictions using parallel plate approximation significantly underestimated the forces. Effect of ultrasonic actuation on stationary objects and moving objects were described in view of the nonlinearity of the surface adhesion forces and modification of the friction coefficients, respectively.

Two assembly fixtures for U2EBA were considered, and their response to ultrasonic excitation were compared by measurements of transverse surface velocity. Experiments performed on micro-hinge arrays of different attributes quantified the enhancement in assembly yield due to ultrasonic actuation, dimples, and variations in the lock-in structure spring beam design.

Assembly angles in excess of 90° were demonstrated by experiments on compliant structures using a tilted electrode configuration. In addition, partial assembly of complex free-space optical components was shown as a promising first step towards off-chip, low-cost, batch assembly of commercial products.

The assembly forces are limited by the breakdown of air and predicted to be

conservatively around 7.5 μN/m^2 for a structure initially parallel to the die surface. The maximum amplitude for ultrasonic drive is mainly determined by the delicacy of the structures to be assembled. Tailoring harmonic frequency sweep attributes, namely amplitude, frequency range, and time of sweep might be necessary to prevent damage to the devices. Pulsed drive, whose broad band nature can have significantly different antistiction performance due to simultaneous excitation of multiple resonances, was not investigated in this work.

For structures which are stuck to the substrate, the speed of assembly is determined by how long it takes them to separate from surface so that attractive forces are not significant. This can be a slow process depending on U2EBA parameters, and it took from a few seconds to a few minutes in our experiments. For other structures, which are free to move under the effect of electrostatic field, the process is much faster, determined by the system parameters such as mass, damping, and spring constants of the structures.

Room temperature and in-air assembly aspects of U2EBA shown in this chapter distinguish it from the thermokinetic-batch assembly method, introduced by Kaajakari and Lal [76]. Succinctly speaking, neither vacuum nor high-temperature operation is a required condition for U2EBA. Although, high temperature operation was clearly observed to improve the yield of assembly, an assembly yield higher than 98% was also realized at *room temperature*.

Low-cost experimental fixture, in air operation, off-chip attribute requiring no electrical wiring separate U2EBA from alternative approaches. U2EBA can especially be useful for the one-time assembly of large arrays of simple structures such as microneedles or electron emitters.

CHAPTER 4

OFF-CHIP ACTUATION FOR ANGULAR POSITION CONTROL OF MEMS MIRRORS

4.1 Introduction to semi-permanent latching

One-time assembly of hinged and compliant, polysilicon plates with lock-in structures using Ultrasound-Enhanced, Electrostatic Batch assembly (U2EBA) was explained in Chapter 3 [10]. Unlike the *permanent* assembly work of that chapter, this chapter focuses on *semi-permanent* assembly of similar microstructures by proper control of ultrasonic and electrostatic fields during U2EBA[1] [79]. In this approach, the mirrors can be trapped and freed from different rotation angles such that zero static power is needed to maintain a desired angular position.

The application space of semi-permanent latching is similar to that of U2EBA described in the previous chapter. However, the focus is not on one-time assembly to a given target state, but assembly/actuation to an arbitrary state as part of the regular operation of the device. Favorable attributes of U2EBA such as off-chip actuation, batch assembly, and simple experimental setup still remain applicable.

One relatively new application area for semi-permanent, zero-idle power angular, positioning of small size mirrors ($< 10 \times 10$ cm^2) is Concentrating Solar Power (CSP). The main premise of CSP is to focus the incoming solar radiation on a central collector [100]. Higher concentration opens room for higher efficiency[2] [21,101]. Furthermore, cost per unit area of reflector surfaces can be lower than cost per unit

[1] The most trivial use for a flat plate surface in the context of micro-optical systems is to serve as a mirror. As such, "plate" and "mirror" words are sometimes used interchangeably in this chapter.

[2] See Appendix J.

area of photovoltaic (PV) modules. As such, many utility scale solar power stations employ CSP technologies such as central tower based systems, parabolic troughs, dish shaped collectors, and concentrated PV implementations [102].

Minimal power consumption to maintain mirror position is crucial for CSP. In CSP, large heliostats or collectors, with areas measured in m^2 have been used for decades, because of easy, off-the-shelf mirror and actuator technology. The scaling of mirrors down to cm, mm or even μm scale has potential to offer unique advantages as well[3]. For instance, Viereck *et al.* have previously considered using large-area MEMS fabrication technologies for solar light redirection. Curtains with adjustable transparency and active interior lighting control in residential buildings were proposed as other applications by the authors [13,103]. However, Viereck *et al.* do not mention the concept of zero-idle power and semi-permanent latching[4], which can be critical for energy scavenging at very low input light levels. This capability of zero-idle power is central theme of this chapter.

One can make an analogy between the temporary latching of a moving mirror at a particular position and multivalued, nonvolatile, mechanical memory elements. Previous implementations of micro-mechanical memory elements made use of buckling [104] and stiction [12]. Both of these phenomena only allow two states. For more states, stepped drive can be used with friction and stiction. Scratch drive actuators on chip [5], vibromotors both on-chip and off-chip [71, 105], and ratchet actuators on-chip [2] are some examples. In our case, U2EBA is used to position the mirror at multiple positions.

The actuation method and the experimental fixture used in this work are illustrated in Figure 4.1. The setup is the same as the one described in Figure 3.6

[3] See Chapter 5.

[4] In contrast, they report a leakage power of 0.1 W/m^2.

for U2EBA. The reader can refer to Section 3.3.2 for a detailed description of the assembly fixture. However, the lock-in concept used in micromirrors to enable semi-permanent latching is new. Figure 4.1 pictures some aspects of this lock-in structure, which is explained in detail in the next section.

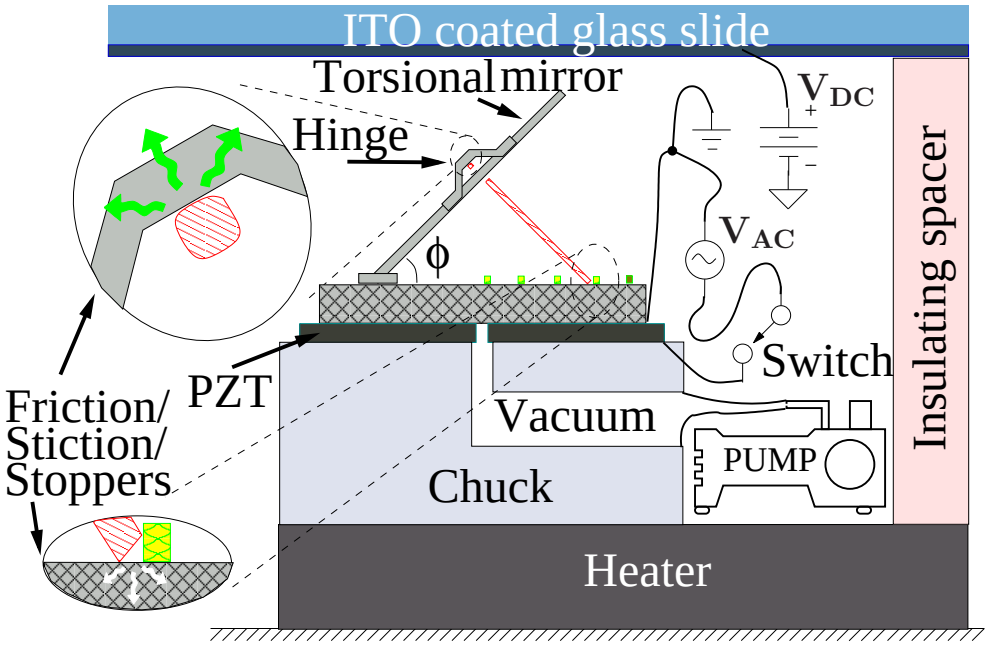

Figure 4.1: Schematic view of the experimental setup. Microstructures are actuated fully off-chip under the influence of electrostatic forces due to applied DC potential (V_{DC}), and ultrasonic forces due to applied AC potential (V_{AC}) on the piezoelectric ceramic.

4.2 A new lock-in structure for semi-permanent latching

The new lock-in structure relies on stiction and friction forces in the presence of a periodic array of mechanical bumps and stops to get semi-permanent assembly at multi-valued rotation angles [79]. 3-D rendering of the device and its cross-section are shown in Figure 4.2. The device comprises of a large mirror region that can rotate around a torsional rod anchored at its two ends. Figure 4.3 shows SEM pic-

tures of an assembled device and its important parts. The devices were fabricated by SANDIA SwIFT^{TM} process, which is an extension of the five-layer polysilicon surface-micromachining process, SANDIA SUMMiT V^{TM}, with additional silicon nitride layers. However, the reported devices were made exclusively of polysilicon layers, so SUMMiT V^{TM} or any similar surface micromachinging processes can also be used.

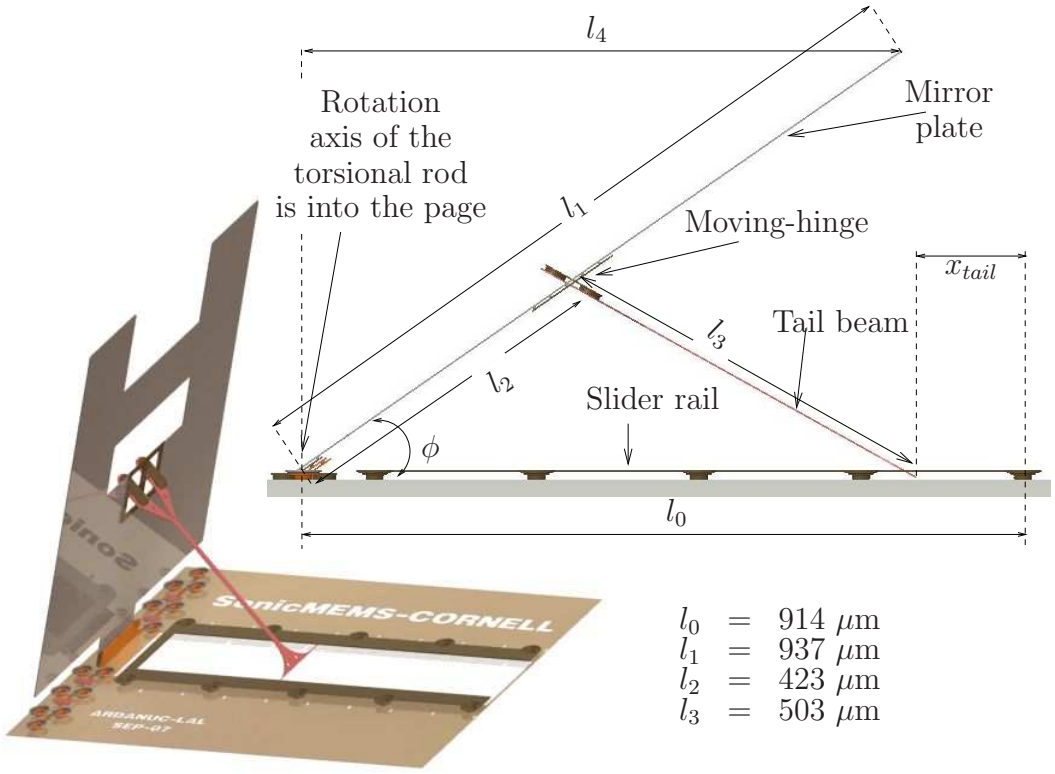

Figure 4.2: Illustration of the hinge with semi-permanent lock-in. Important geometrical design parameters and parts of the device are shown. Value of x_{tail} depends on ϕ, and its initial value at the unassembled state ($\phi = 0$) is $x_{tail} = -13$ μm.

The mirror region of the device has a rectangular footprint of 937 μm$\times$784 μm, and the total area of each device is 1003μm $\times$875 μm . There were unfilled regions over the mirror to enable optical measurements on underlying structures during

the experiments. The mirror can rotate around a torsional rod that is constrained to rotate in the plane of the substrate with bridge-like staples that go around the rod.

The mirror is connected to the *slider-rail* on the substrate by a beam, which is named as the *tail-beam*. The tail-beam is attached to the mirror via a moving-hinge, which is 423 μm away from the rotation axis of the torsional rod. The other end of the tail-beam is in sliding contact with the substrate, and it is forced to move along a line on the substrate, constrained by the slider-rail. The slider-rail is populated with a periodic array of bumps at a 6 μm pitch. These bumps act

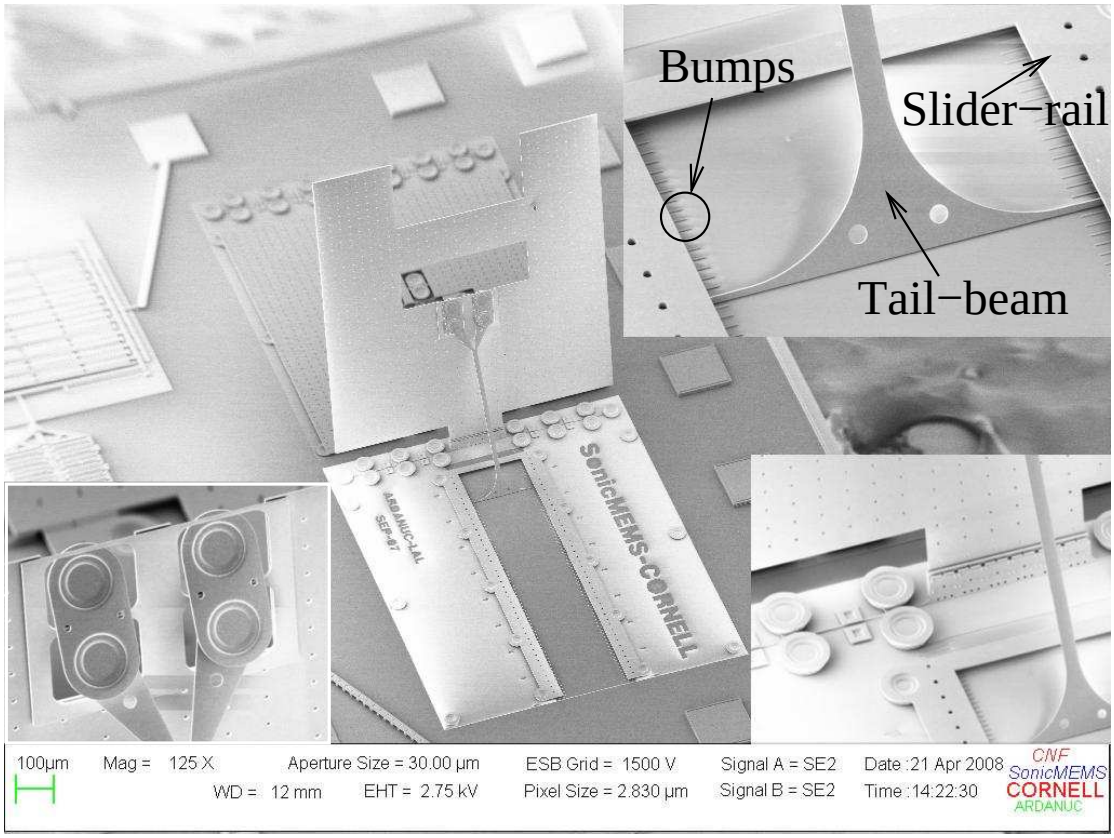

Figure 4.3: SEM pictures from an assembled device. The scale bar at the bottom left is only valid for the background image.

as mechanical stoppers and friction-enhancers as the tail-beam slides along the slider-rail, providing temporary lock-in/latching without any power consumption. The torsional rod of the mirror plate and the gravity force on the plate acts to push one end of the tail-beam against the substrate, providing the normal force for the friction.

The top right inset in Figure 4.3 shows the slider-rack and part of the tail-beam. Note the periodic bumps on the floor to enhance locking/latching at a particular state in the absence of ultrasonic vibration. The inset at the bottom right shows part of the torsional rod with the clamps and motion limiters that keep the rod in place in the presence of ultrasonic and electrostatic forces. The inset on the bottom left highlights the moving-hinge, where the tail-rod is connected to the mirror.

Definitions and values of some of the geometrical entities of the design are shown in Figure 4.2. l_0, l_1, l_2, l_3 are constants, whereas x_{tail} changes depending on the rotation angle ϕ, of the mirror. Figure 4.4 gives SEM pictures from a successfully assembled die.

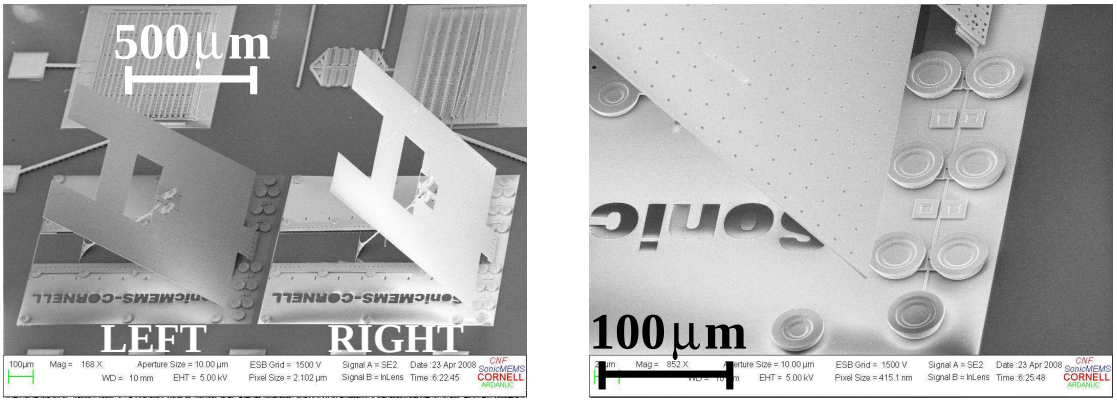

(a) (b)

Figure 4.4: (a) Die level SEM of two assembled devices, (b) SEM of the torsional mirror and the staples around it.

Table 4.1: Typical experimental conditions.

Parameter	Value	Unit
Sweep start frequency	50	kHz
Sweep stop frequency	2000	kHz
Sweep time	3	sec
Sweep type	linear	kHz
Piezo amplifier cutoff	≈ 800	kHz
Temperature	220	°C
PZT drive amplitude	< 20	V_{pp}

4.3 Experimental results

The typical actuation parameters pertinent to the experimental setup of Figure 4.1 are listed in Table 4.1. A hotplate set at 220°C is used as a heater to drive water off of the die surface for the experiments carried out in an unregulated room ambient. After the wet release, the samples are kept in a nitrogen purged ambient at around 200°C till the time of the experiment. As mentioned in Section 3.5, higher assembly yield could generally be obtained by keeping the samples on the experimental fixture for a few minutes before the experiment, with ultrasound on and DC voltage off.

4.3.1 Semi-permanent latching and stepped position control

One can assemble and deassemble the mirrors, hence realize semi-permanent latching, by controlling the application of ultrasonic and electrostatic fields. The asso-

ciated experimental procedure is described below.

When the DC-bias is applied between the global top electrode and the chuck in the presence of ultrasound, the tail-beam moves over the bumps along the slider-rail, allowing the rotation of the mirror. If ultrasound is turned off at this point, the mirror keeps its position even in the absence of a DC electric field, thanks to the static friction/stiction and contact forces on the substrate-side of the tail-beam. This sequence of controlling can be called a "SET" operation. The mirror can then be moved in the reverse direction by a "RESET" operation, which occurs when ultrasound is turned on in the absence of DC-bias such that the torsional restoring force and gravity pull the plate down. Likewise, the mirror can be switched between rotated and relaxed positions by successive SET and RESET operations. Measurements of the rotation angle and actuation signals as a function of time are plotted in Figure 4.5 for an experiment, over which a series of SET and RESET operations are applied to the device under test. Data for both the LEFT and RIGHT mirrors on the die are presented.

Video recordings from a CCD camera facing perpendicular to the die through the top glass electrode were used for the data analysis. The relations given by the left and right side of Equation (4.1) describe the two methods that were used to extract the mirror rotation angle ϕ. The first method requires the measurement of l_4, and the second one requires the measurement of x_{tail}.

$$\arccos\left(\frac{l_4}{l_1}\right) = \phi = \arccos\left(\frac{(l_0 - x_{tail})^2 + l_2^2 - l_3^2}{2l_2(l_0 - x_{tail})}\right), \tag{4.1}$$

The values of ϕ calculated from both methods were within 5° of each other. Yet, the latter is reported here since the rotating tip of the mirror could go out of focus and be blurred in the camera view during the assembly, whereas the sliding tip of the tail beam always stays at the substrate level, regardless of the value of

ϕ, providing an accurate measurement of position.

The two plots on top of Figure 4.5 give the state of the PZT excitation (on / off) and the value of the DC voltage applied. DC voltages of up to 2000 V are applied across gaps close to 2.8 mm. In this case, the applied voltage is less than the breakdown voltage calculated from the Paschen Curve, which is around 10 kV[5]. The snapshots of the die *before the first SET operation* (@ $t = 44$ sec),

[5]The sparking potential for air at atmospheric pressure and uniform field is approximately $V_s = 30d + 1.35$ (kV) for a gap d on the order of mm, and expressed in units of cm [106, pp. 163].

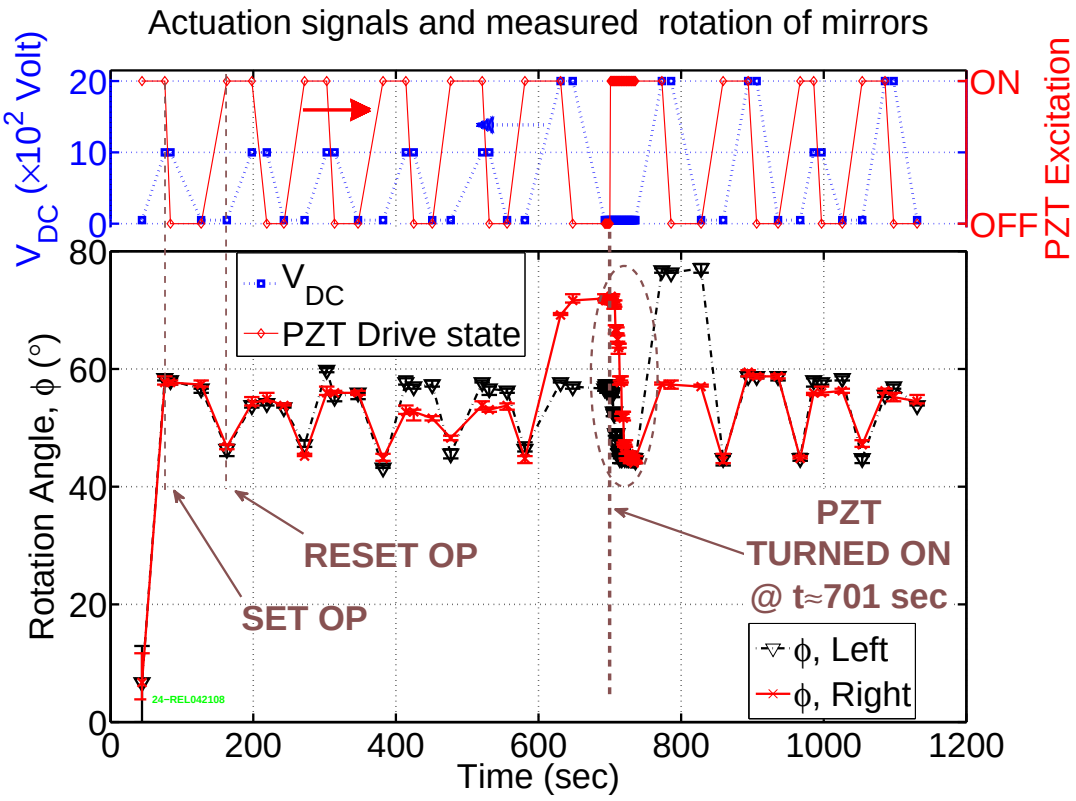

Figure 4.5: The top plot gives, on the left axis, the applied DC voltage on the global electrode. The right axis plots the state of the manual toggle switch that controls the ultrasonic actuation. The bottom plot gives the optically measured angular position of the mirrors as a function of time during a series of SET and RESET operations that are explained in the text. First SET and RESET operations are indicated in the figure.

after the first SET operation (@ $t = 76$ sec), and *after the first RESET operation* (@ $t = 163$ sec) are shown in Figure 4.6.

The latching operation is verified from Figure 4.5, by noting that following a SET operation, the mirror maintains its angular position after the DC voltage is removed, until PZT is turned on. Although one expects the reset position of the mirror to be close to the horizontal state, that is $\phi = 0°$, it is measured to be around 45° for both of the mirrors. Angular position $\phi > 30°$ was seen to be the case exclusively after RESET operations on the tested samples. This occurrence can be due to trapping of the pin in the staple region of the moving hinge, which connects the tail beam to the mirror plate.

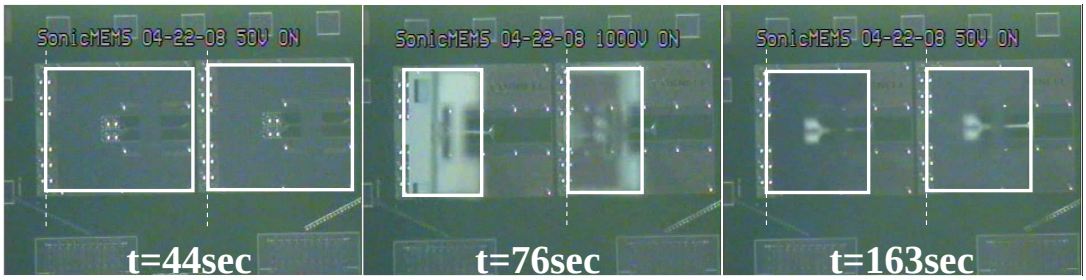

Figure 4.6: The snapshots of the die taken during the experiment, whose results are reported in Figure 4.6. The left, center, and right pictures give the initial, after the first SET, and after the first RESET states of the device, respectively. For the sake of clearness, boundaries of the mirrors are framed with white lines.

Another peculiarity in Figure 4.5 is around $t = 600$ sec, when the DC voltage applied during the SET operation was raised from 1000 V to 2000 V. The operation predicted at the design level was that the rotation angle would increase due to the increased electrostatic force, hence yielding semi-permanent latching at an

For $d = 2.8$ mm, at STP, this formula yields $V_s = 9.75$ kV. This value matches closely with the prediction using Equation (3.6) that yields $V_{BD,s} = 10.35$ kV.

arbitrary angle during the SET operation. On contrary, the increase in the rotation angle at 2000 V as compared to its value at 1000 V was observed only once. Successive SET operations at 2000 V yielded angles close to its value during the SET operation at 1000 V.

In addition, pre-breakdown failure at $V_{DC} = 3000$ V was observed in two samples tested. After this voltage, RESET operation stopped working, although no indication of a breakdown such as arcing sound, light, or physical damage was observed. The highest voltage at which SET and RESET operations worked as described above was 2000 V and 2500 V for the two mirrors of Figure 4.5. Another unusual response observed on one sample was failure of latching after the SET operation in the middle of a series of SET-RESET operations. However, the sample returned to normal operation after the failed cycle.

The SEM of the assembled device in Figure 4.4(a) and the data of Figure 4.5 show differences in the rotation angle response of two identical mirrors on the same die. We connect these differences to the position dependence of the piezoelectric actuation, the stochastic nature of friction/stiction, and different initial states of hinge pins in the staples. Stepped operation for both of the mirrors on the die could be observed during the RESET operation, which occurs in the absence of DC voltage. The supporting data for this observation is given in Figure 4.7. It shows a magnified version of the highlighted region around $t = 700$ sec in Figure 4.5. Figure 4.7 reveals that one of the mirrors can be made to hold position at seven different angles between 72° and 45°. The duration of the motion during stepped actuation is about 3 sec, which is equal to the period of the frequency sweep of the ultrasound. As such, certain resonances of the involved structures can be more effective in releasing the semi-permanent latch.

4.3.2 Anti-stiction with PZT actuation

Anti-stiction effect of U2EBA was shown in Chapter 3 using PolyMUMPs^{TM} process. A similar experimental result is presented in Figure 4.8 to support that conclusion with SwIFT^{TM} process. The experiment starts with PZT *off*. As the V_{DC} is increased up to 1000 V gradually, there is no considerable rotation in the mirror. However as soon as the PZT is turned *on* at $t = 121$ sec, both of the devices on the die go to SET mode with angles around $\phi = 65°$ for the "left" mirror, and

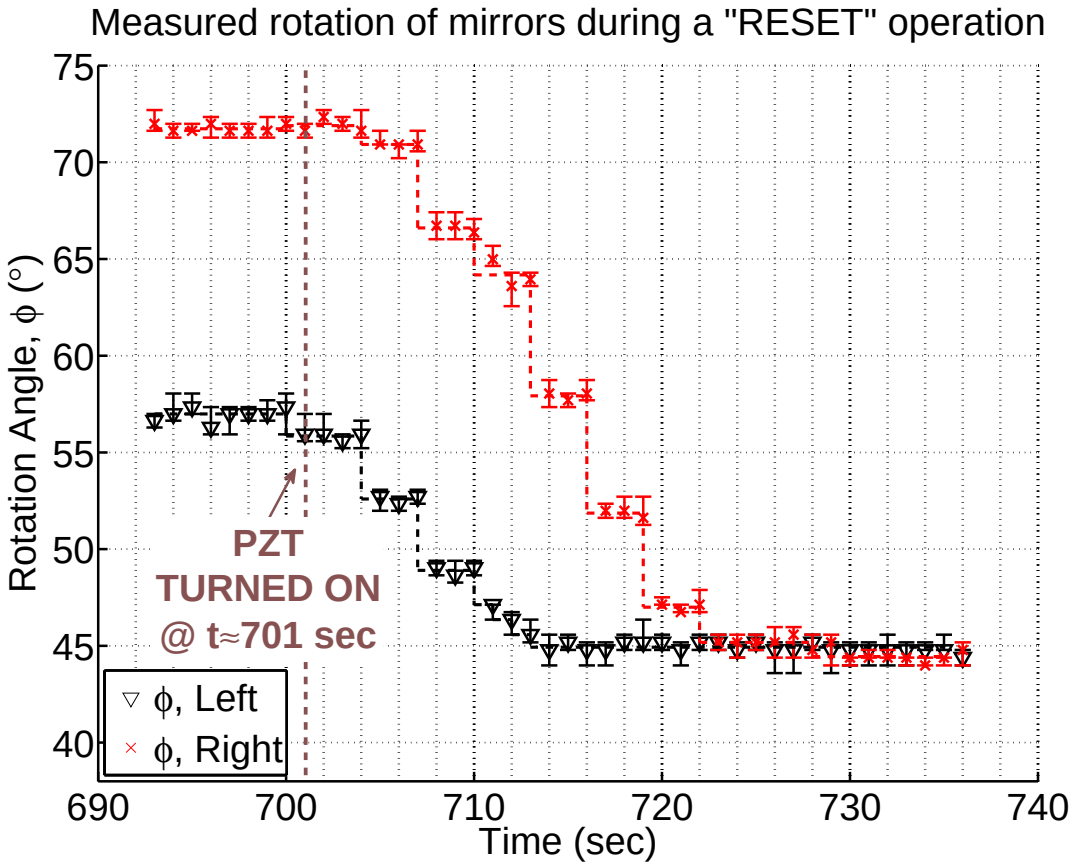

Figure 4.7: Angular position of the two mirrors on the die during the reset operation performed around t=701 sec. Stepped operation with a period of about 3 seconds can be identified. This duration is equal to the period of the frequency sweep of the PZT drive.

$\phi = 60°$ for the "right" mirror. As usual once the PZT is turned off and V_{DC} is reduced down to 50 V, they maintain their state., i.e., they are semi-permanently latched.

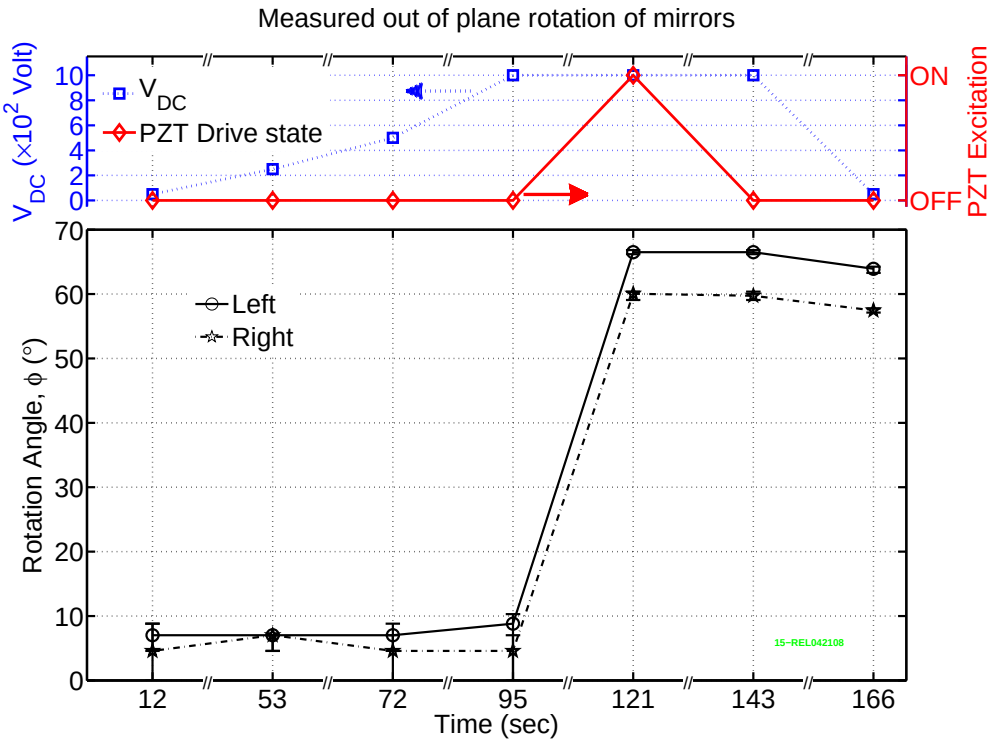

Figure 4.8: Measured rotation angle and control signals during a U2EBA experiment. The data shows the anti-stiction effect of PZT on samples from SwIFT^{TM} process.

4.4 Summary and conclusions

This chapter targeted applications that require or benefit from:

1. **Semi-permanent positioning with zero-idle power:** Once the structures are latched to a desired position, no external field or power supply

should be necessary to sustain the assembled position. In this idle position, the assembled structure have enough holding force to be able to maintain its position against gravity, and possible mechanical or thermal shocks.

2. **Batch-assembly:** The assembly of large arrays of a given micro-structure at the same time should be possible.
3. **Ability to support large density of micro-structures:** The solution should allow high fill-factor arrays without additional structural layers on the die to be assembled.
4. **Analog position control:** Angular position of the mirror can be controlled at discrete positions and continuously between these positions.

It was shown that ultrasonic-enhanced electrostatic batch assembly can be used for off-chip, angular position control of plane mirrors in a stepped fashion using a mechanism that is reminiscent of a scissor-lift. This mechanism employs a linear-slider populated with an array of mechanical bumps/stoppers, as well as a tail-beam attached to the mirror structure. The duration of the steps of angular displacements was shown to be approximately equal to the period of the frequency-sweep of the ultrasonic actuation. Therefore, angle control at higher precision can, in principle, be achieved by tailoring the ultrasonic drive parameters like sweep type and drive amplitude. Moreover, presented method facilitates high fill-factor rotation control without any on-chip actuator or any wirebonds on the die, since the ultrasound is applied from the bottom, and the electrostatic force from the top of the die.

DC voltages used during U2EBA, as presented here, are very large for deployment in real products. However use of compliant structures, at smaller gaps can potentially reduce the operating voltages in the future. On the positive side,

semi-permanent latching ensures zero-idle power, eliminating not only the leakage across dielectrics or air-gaps, but also power consumption due to high-voltage drive electronics. The presented method can be useful for modular, solar-concentrator applications, where the actuation speed requirements are very relaxed, while fill-factor and cost per unit area are extremely important.

CHAPTER 5

ALL-ANGLE LATCHABLE REFLECTOR FOR SOLAR ENERGY CONCENTRATION AND BEAM REDIRECTION

Foreword

Enough energy from the sun falls on earth everyday to power our homes and businesses for more than 15 years.

It was more than a century ago, when Thomas Edison said he wanted to make electricity so cheap that only rich could afford to burn candles. Today, for many of us, electricity is rather cheap. However, we have started to realize that the cheapness of electricity over the past decades came at the expense of disturbed ecological balance and has become a serious threat for the future of the next generations. On the other side of the coin, 1.5 billion people in the world do not even have access to electricity [107]. This means that more than 20% of the people in the world lack access to proper lighting, health services, refrigeration, education, and communication. Lack of such vital services perpetuates the vicious cycle of poverty, illiteracy, and neediness; making the problem only worse.

Keys to correcting the above problems are realizing that we are all in the same boat, and that **now** is a good time to rock the boat. I can therefore claim, with peace of mind, that one of the finest pursuits of contemporary science is to provide sustainable, green, and pervasive technologies to make energy inexpensively available to every nation in the world. With all my respect to Thomas Edison, this pursuit compels us to make electricity from solar and wind energies so cheap that only the rich can afford electricity from non-renewable sources.

Serhan Ardanuç

December 12, 2009

5.1 Introduction

It is the mark of a *new era* or a *big bubble* when everybody starts talking about the same technology. *Renewable Energy* is one such technology, often believed to deserve the former label rather than the latter. Government subsidies, frequent news of planned utility scale solar and wind plants, ambitious political and economic goals for carbon footprint reduction, outstanding residential and industrial demand for green energy all around the world are clear signs of collective action and implementation of renewable energy technologies. For solar energy harvesting, for instance, market reports and roadmap publications are populated with promising plots, tables and predictions[1].

Concentrated Solar Power (CSP) technologies, is expected to enjoy a steady growth driven by the outlook portrayed above. The main premise of this technology is the concentration of solar radiation by lenses and/or mirrors on an energy conversion, storage, or distribution structure. Often times the radiation collecting structures track the sun in one or two degrees of freedom to minimize the angle of incidence from the sun, and hence maximize the power output from the system. Some thermodynamical background and a few references to the literature can provide extra motivation for CSP, which is a key application in this chapter. This material is presented in Appendix J.

There are different types of CSP, such as central tower based systems with independently moving heliostats, parabolic trough systems, linear Fresnel lenses, dish engine systems [102]. Tower based CSP is one of the central themes in this chapter and is illustrated in Figure 5.1(a). A picture of a 11 MW thermal solar

[1]See for instance: REN21-Renewables 2007 Global Status report, Trends In Photovoltaic Applications (International Energy Agency), EREC Renewable energy technology roadmap up to 2020, Shell Energy Scenarios to 2050, 2008.

plant in Spain, PS10, is shown in Figure 5.1(b). PS10 is "the worlds first solar thermal power plant based on tower and heliostat field technology" to generate electricity in a stable and commercial way [11].

European Commission Pub., 2007

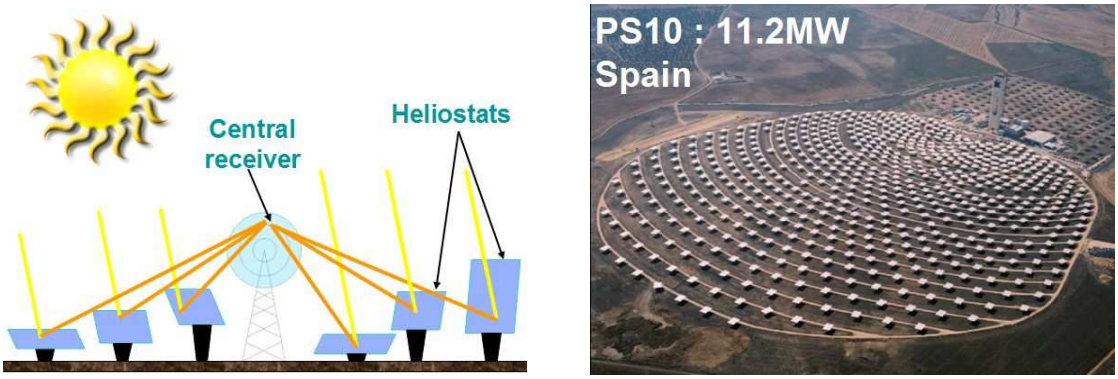

(a) (b)

Figure 5.1: (a) Schematic illustration of a Concentrated Solar Power (CSP) system with the central tower and sun-tracking heliostats. (b) A picture of PS10 thermal power plant in Spain with a nominal power generation capability of 11 MW [11].

Tracking CSP systems use *large-area* mirrors mounted on motorized stages or platforms. Use of large area mirrors maximizes the area subject to solar radiation for a given motor, which can be a significant contributor to the cost of the system. On the other hand, it also implies that the height above the mounting base is comparable to the dimensions of the *large-area* mirror to allow its rotation.

The geometrical asperity due to a large mirror above the base of the tracking unit implies, depending on the location, aesthetic and space issues on the surface of implementation. Furthermore, wind-loading, structural rigidity, and vibration induced fatigue considerations can complicate the design and force costly implementations. More importantly, structural loading can be a concern for large-area heliostats especially if they are to be installed on an existing infrastructure. It can be argued that these are among the reasons why solar harvesting by planar,

low-profile, photovoltaic modules is much more common on the roofs and walls of residential buildings as opposed to heliostat based central tower systems.

Here, a scaling argument is presented that suggests covering of large surfaces with small-size, sun-tracking, mirrors of cm to μm scale, whereby keeping the total out of plane motion comparable to the thickness of photovoltaic (PV) cells ($< 1 - 2$ cm). In other words, CSP can be enabled on a given surface with form factors comparable to the conventional tiles used on walls/floors or that of thin-film PV cells. If this tile level integration of large number of steerable small area mirrors and their control are done in a self-powered and wireless manner, not only large scale concentration can be possible over very small regions, but also costly installation process of conventional large scale heliostats can be eliminated.

The main function of the tile, namely beam/energy/wavefront redirection from a given source point to a target point, enables a large variety of other exciting applications. While mostly CSP applications are emphasized throughout the chapter, motivation, specifications, benefits, performance, possible limitations and manufacturing methods are considered for different applications as well. A prototype is developed that can track the brightest spot in an ambient and can be wirelessly operated using an IR remote control. Ray tracing simulation results regarding optical collection efficiency and angular error of beam redirection are presented. The chapter concludes with key observations about the technology and the roadmap to the development of reflector tiles in the near-future.

5.2 Scaling of mirrors for light redirection

Most of the concentrated solar tower plants employ large-area (> 10 m^2) heliostats [11, 108]. This fact is in agreement with the findings of a heliostat cost reduction study by Kolb *et al.* [109]. The following is a quote from the conclusion section of a report on the same study:

> A detailed analysis of capital, O&M, and installation costs of heliostats that measure a few m^2 up to a few-hundred m^2 indicates an optimum size of 150 m^2 or more. However, less-detailed data suggest that similar costs might be achieved with heliostats as small as 50 m^2.

Figure 5.2 presents an alternative view of scaling that considers orders of magnitude smaller sizes for the mirrors than the status quo. At very small mirror dimensions, diffraction of light is important. More aggressive scaling to very thin but relatively large-area mirrors should also consider the effects of radiation pressure of sun light on earth's surface. When features become comparable to wavelength of the light, micro(nano)-mirror array turns into an active diffraction grating or an active photonic-bandgap structure.

Figure 5.2 also highlights the main premise of a *low-profile* solar-tile integrated with moving μm to cm mirrors on top. Such a *tile-level technology* makes CSP much more portable and light-weight than the current implementations. Furthermore, if these solar-tiles can be wirelessly controlled and self-powered by means of a tiny PV-cell and/or battery on the tile, novel applications can be possible. Wirelessly controlled reflective displays for large-area billboards, automatic snow removal by

melting using focused sun light[2], and dynamic wallpapers for indoor decoration are some example applications.

If the moving mirrors are to be scaled down in order to fit in a tile with dimensions, for example, $20 \times 20 \times 0.7$ cm^3, then *MEMS* or *toy-scale* manufacturing technologies (injection molding, casting, machining, CNC, and so on) need to be used depending on the mirror-size. Using microscale mirrors for large-area applications such as CSP is off-the boundaries of the applications discussed in a typical MEMS textbook. For this purpose, large-area, reliable microfabrication processes needs to be developed on low-cost substrates such as glass or plastic, unlike the conventional silicon substrates. This might be a long-term goal considering the cost competitiveness of PV and large-area heliostat technologies. As such, *toy-*

[2]A numerical example regarding the absorbtion of concentrated sun-light by ice is available in Appendix J.3.

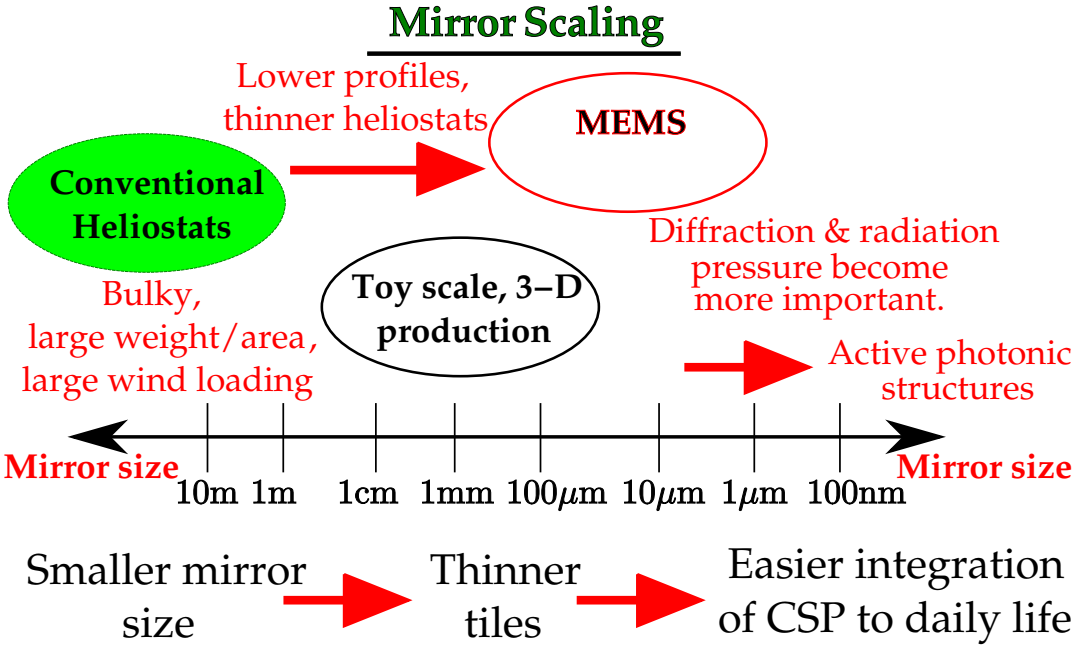

Figure 5.2: Overview of scaling of mirrors for solar tiles from tens of m^2 to (nm)^2 and relevant technologies.

scale manufacturing of tiles with mirror dimensions on the orders of milimeter to centimeters can be a more feasible and nearer-term goal. Tiles of this scale are referred as *mesoscale* implementations in this chapter.

The argument presented above, *by no means*, suggest the dismissal of MEMS technologies from future consideration. To the contrary, application of low-cost, large-area MEMS technologies to solar-tiles can provide more incentive for their development. There are already some very promising results from academic research institutions as well as tangible interest from industry for *thin-film MEMS on low-cost substrates*. A research group in Portugal has demonstrated basic surface-micromachining using radio-frequency plasma enhanced chemical vapor deposition (RF-PECVD) of amorphous silicon (a-Si:H) on both glass and flexible, transparent, polyethlene terephthalate (PET) substrates [110]. In addition, Qualcomm™ has commercialized a surface-micromachining on glass process for their Mirasol® displays that work by interferometric modulation (IMOD) [111, 112].

There are a couple of industrial research efforts that pursue scaling down the heliostats, contrary to the common practice [113]. "eSolar" and "BrightSource Energy" are two companies which develop smaller-area heliostats. As such, a consensus on scaling does not seem to be available yet. Even for a tile-based approach, production-cost, shadowing, and requirements for a specific application need to be carefully understood in order to determine the mirror size. Once a mirror-array is scaled down enough to fit within a few milimeters-thick tile, it may not be advantageous to scale down any further as thinner tiles can be very fragile.

All of the above issues, make the mirror scaling for light redirection applications an open-ended problem that deserves attention from both industry and academy. Section 5.3 and Section 5.4 present the solar-tile vision and a prototype,

respectively, developed to address this problem.

5.3 All-angle LAtchable Reflector (ALAR) tiles

Being able to control the reflection angle of light at an arbitrary surface by covering it with thin, wireless tiles that are self powered, can transform our roofs, pavements, outdoor walls into optimal, solar concentration surfaces that can *track the sun* to optimize collected amount of solar energy. The tiles used for this purpose have plurality of centimeter to nanoscale mirror surfaces, whose normal angle of reflection or diffraction can be changed independently of, or in parallel with other mirror pixels on the same tile. By virtue of continuous angular position control of mirror pixels and their ability to latch semi-permanently at a particular position, the described solar reflector-tile concept is called *All-angle LAtchable Reflector* (ALAR) technology. Depending on the size of the mirrors and wavelength of propagation, the reflectors can be used to modify the wavefront or redirect sound waves as well as electromagnetic radiation. ALAR tiles can potentially be used in applications such as residential CSP systems, indoor lighting control, dynamic architectural components, reflective billboard displays, adaptive antennas and directional speakers.

5.3.1 General aspects of an ALAR tile

A schematic illustration of a generic ALAR tile is given in Figure 5.3. The central concept of the technology is to miniaturize heliostats/reflectors so that they can fit in a tile that is as thin as a few milimeters or centimeters. The small size of

the mirrors allow rotation/steering within the low-profile of the tile. Every mirror pixel includes a reflector surface that can move and/or rotate continuously in one or more dimensions, to provide required steering and beam-redirection. In general, motion in two dimensions is necessary to redirect light coming from an arbitrary direction to another arbitrary direction. 3-D motion may also be necessary for phase critical wavefront modification applications with coherent sources [114].

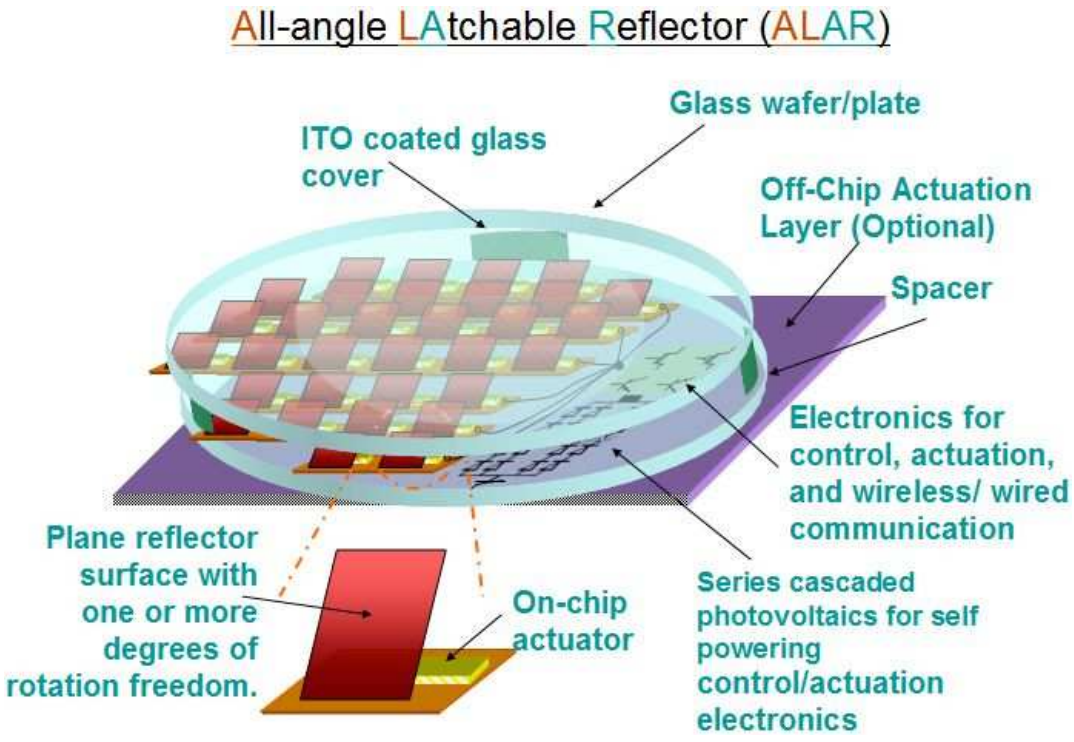

Figure 5.3: A pictorial illustration of All-angle LAtchable Reflector (ALAR) tile concept. The tile houses an array of mirrors that can vary from centimeters to micrometers in size. Each of these mirrors can move in one or more axes independently of other mirrors, or in parallel with other mirrors, in order to perform light redirection. The application space includes wall-to-wall coated, concentrated solar power generation with solar tracking, and zero-idle-power, reconfigurable architectural elements.

The steering motion of the pixel mirrors can be controlled by on-wafer actuators such as comb drives or scratch drive actuators. Off-chip actuation and assembly

methods such as Ultrasound Enhanced Electrostatic Batch Assembly (U2EBA) [10, 79] can also be used. Figure 5.4 gives SEM pictures of the devices assembled by U2EBA in *Sonic*MEMS Laboratory at Cornell University (Chapter 3).

Figure 5.3 shows elements for both on-chip and off-chip actuation to avoid loss of generality. For instance, included ITO layer on the top glass cover and the actuator substrate under the tile can be used for off-chip actuation. In this case, on-wafer actuators highlighted in the figure may not be needed. Actuator layer under the tile can also include a rotary motor to enable azimuthal rotation as an extra degree of freedom for the steering of the mirrors. The transparent cover on

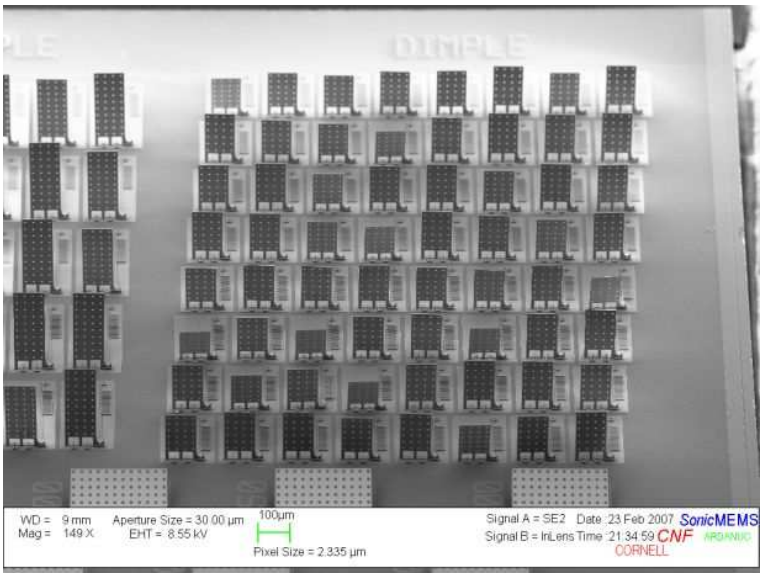

(a)

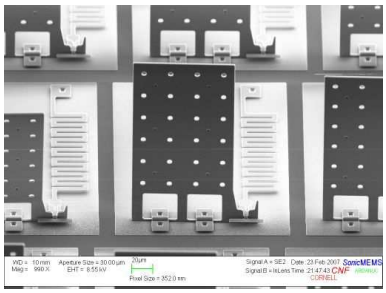

(b)

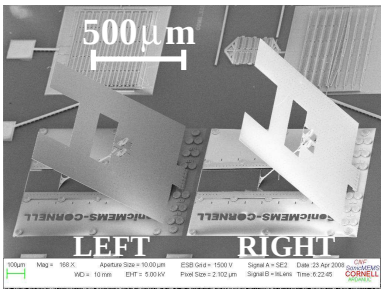

(c)

Figure 5.4: SEM pictures of hinged micromirrors assembled by U2EBA

top of the tile provides protection from environmental effects such as sand, dust, wind and rain.

For acoustic applications of ALAR, a rigid cover constitutes an obstacle and may need to be discarded or replaced by a thin diaphragm possibly with orifices. However, this type of exposure of reflector pixels to the environment, requires that they are manufactured to sustain environmental effects. For acoustic applications, the amount of *mismatch* in acoustic impedance seen by the traveling wave as it is incident on the reflector surface is important. The thickness and the bulk acoustic properties of the reflector should be considered along with the relevant elastic boundary conditions to design efficient acoustic reflector tiles.

Components such as antennas for wireless communication, speakers for acoustic triangulation at the towers, or GPS chipsets are not shown in Figure 5.3. These components and alike might be necessary depending on the communication, computation and tile positioning approaches pursued.

Important desired characteristics of the planar, mirror array integrated on the tile can be listed as:

1. 2-axis mirror positioning,
2. large angle of rotation $> 100^{\circ}$ in each axis (both separately and simultaneously at both axis), and continuous tunability,
3. minimum curvature/bending over the reflector surface for different rotation angles,
4. high fill factor,
5. semi-permanent latching and zero-idle-power consumption.

It is important to clarify that, "latchable" aspect of the mirrors lends itself to zero-idle-power operation such that when all the power fed to the tile[3] is removed, the tile still continues to redirect light in the desired manner. "Latchable" aspect ensures that the tile does not consume any power during regular operation, but only when it moves from one position to another. In other words, many of the statements made in this chapter for an ALAR tile can be available from a system that is not latchable. However, the efficiency in this case would be lower, since the tile would consume power to remain at a given rotation angle (i.e., in the idle state) while performing its radiation redirection operation.

5.3.2 Synchrony of mirror pixels: Free-latticed and parallel-latticed tiles

It is beneficial to distinguish between two extreme cases of operation regarding the synchronicity of the pixels with respect to each other. The first case occurs when the motion of the mirror pixels on the tile can be controlled independently of each other. In this scenario, each pixel needs a dedicated actuator mechanism and a communication link to provide motion in one or more degrees of freedom for steering. If an off-chip actuator mechanism is to be used, it should have the ability to be localized to a given pixel. For instance, in case of U2EBA, this might be possible by pixelating the top global electrode and addressing each electrode separately. Tiles that support independent motion of each reflector on the tile are named as *free-latticed ALAR tiles*.

[3]The power can be available to the tile either internally from a battery, externally from sunlight, microwave transmission, power cable, vibration, temperature differences, or other energy harvesting devices.

One example of a free-latticed design is described next to discuss the challenges related to getting high fill-factor, large angle of rotation, and 2-axis operation, all at the same time at microscale. The tile and the mirror-pixel are shown in Figure 5.5. The picture only shows 3×3 sub-array for the sake of clarity, and tile level components such as control circuitry and photovoltaic units on the tile are not shown[4]. The pitch length of the array can be assumed to be ≈ 1 mm in order to keep the discussions in the context of tiles with micrometer sized mirrors. The operation of the pixel is based on out-of-plane electrostatic assembly of a mirror on a rotary platform [115, 116]. The rotary motor is assumed to be driven by scratch drive actuators (SDA). The second degree-of-freedom of the mirror comes from the electrostatic actuation from the top global electrode formed on the top glass cover as ITO patterns [79, 97]. Note that routing to each one of the electrodes on top of the pixels is not shown, nor is the routing to the SDAs of the pixels.

The tile of 5.5(b) is a free-latticed tile in both axes as each pixel can move independently. The most significant handicap of an ALAR technology based on this tile structure would be the fill-factor. A simple calculation shows that the maximum theoretical fill-factor is $\pi/8$ or 39%. Although one can claim, that the rest of the power would be used to power the tile by the included PV cells, 61% of the incoming solar power is too much for this purpose. A less severe handicap is that the mirrors are not latchable. So an electrostatic voltage needs to be applied on the top electrode to keep the tiles at the desired state.

The second case to consider regarding the synchronicity of the pixels is when two or more pixels share a degree-of freedom of motion. Tiles whose pixels have dependent degrees-of-freedom are called *parallel-latticed ALAR tiles*. If this approach is implemented all over the tile, one can obtain two-axis steering with only

[4]These components are shown in the more generic illustration given in Figure 5.3.

two actuators. The prototype to be described in Section 5.4 is an example for this particular case, where all of the reflector pixels on the tile move in parallel to each other.

One can, in principle, assign *free-latticed* or *parallel-latticed* attributes for each degree-of-freedom that the mirrors have. So the same tile can be free-latticed for one DOF, while it is parallel-latticed for the other DOF. There can also be

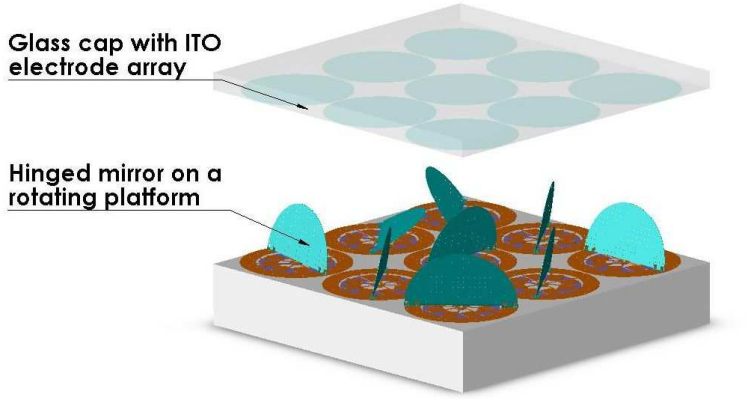

(a)

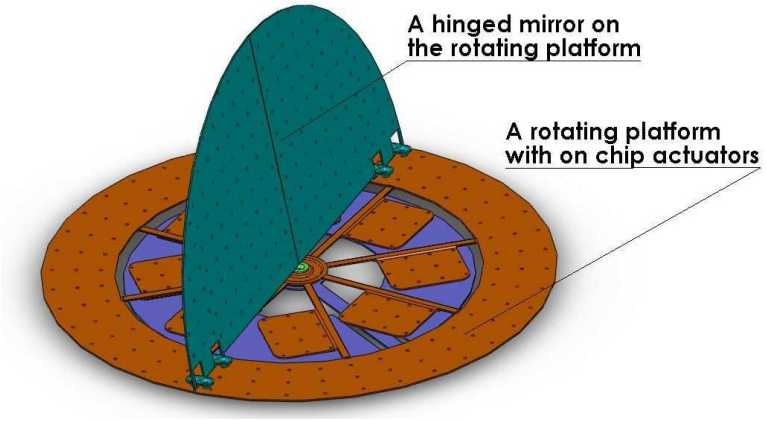

(b)

Figure 5.5: (a) Illustration of a free-latticed, ALAR tile with hinged micromirrors each of which is actuated on a rotating platform, (b) close up view of the the pixel structure including a hinged mirror and a scratch driver based rotary stage under the micromirror. Etch holes required for the release of large surface-micromachined structures are visible.

other combinations that lie in between the two constellations of free-latticed and parallel-latticed. For instance mirrors within a sub-array can move in parallel, while each sub-array can move independently. These cases will in general be referred as *hybrid-latticed ALAR tiles*. Although *free-latticed tile* may appear to be the most general case, its realization is also more challenging as each pixel requires dedicated actuation. On the other hand, parallel-latticed ALAR tiles simplify the problem tremendously, allowing many pixels to be steered from the same actuator or motor; an idea that is used in parabolic trough type CSP plants.

Whether one might need the resolution offered by *free-latticed ALAR tiles* or not is a very application dependent concern. For an indoor dynamic wall-tile application, where one spends most of his/her time looking at the tiles on average from 1 m away, free-latticed ALAR tiles would be preferred, and their extra cost might be justified. On the other hand, if the ALAR tiles are intended for use in a billboard application, where the average audience is 50 m far, then each ALAR tile with a dimension of 20×20 cm^2 may serve well enough as a pixel on the billboard display.

5.4 Description of a prototype of an ALAR tile

Two mesoscale prototypes of an ALAR tile, which can support the 2-D steering motion of a rectangular array of mirrors in parallel to each other (i.e., parallel-latticed), are demonstrated at Cornell University. The first prototype, which was was built by Professor Amit Lal, included an array of hinged mirrors over a tile-level, rotating platform as shown in Figure 5.6 [117, Figure 11.3(d)]. Tile-level rotation supports parallel-latticed operation unlike the microscale, free-latticed

version in Figure 5.5, which employs pixel-level rotary stages. After the success of the first prototype, the second prototype that used a *pivoted-pixel* design was built in early 2009. The *pivoted-pixel* version is described in the following sections.

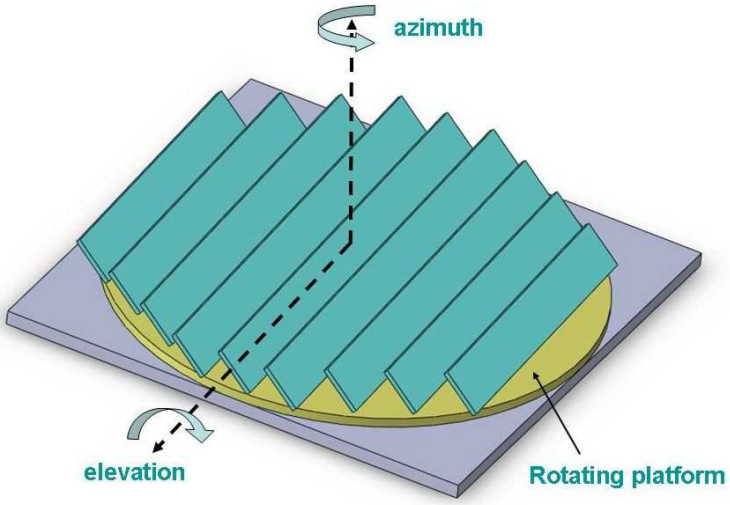

Figure 5.6: A mesoscale ALAR tile implementation that relies on hinged mirrors on a tile-level rotating platform in order to realize 2-axis mirror steering.

5.4.1 Overview of the prototype with the pivoted-pixel design

One way to choose an operating mechanism for the tile is to take an already existing large scale mirror array design [117, Figure 11.3] and miniaturize it. The shortcoming of this approach is that the final fill-factor of some of the large scale implementations are not high when they are considered for tiling in a rectangular fashion. For instance, the fill-factor for a design using the principle shown in Figure 5.6 is topologically limited to $\pi/4 \approx 79\%$, unless smaller tiles are used to fill-up the empty spaces in the larger ones.

The operating principle used in the prototype described here is based on pivotal steering of individual mirrors coupled to a common platform that ensures parallel operation of all of the reflector pixels on the tile. Figure 5.7 is instrumental to understand the operation in the simpler case of 1-D steering. This figure shows the side-view of a planar mirror surface connected to a rod. If any point along the rod is displaced with respect to the bottom point that is pivoted, this motion translates into a rotation of the mirror surface.

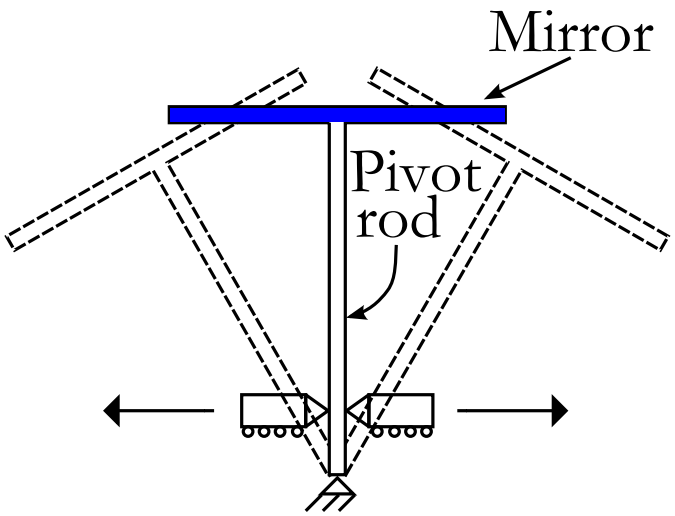

Figure 5.7: A rigid mirror and a rod structure forms a pivot and it can be rotated around a pinned support.

A more general mechanical model for the 1-D version of the tile is presented in Figure 5.8 for both unrotated and rotated states of the mirrors. The center of the mirror of each pixel is connected to a pivot-bar which is coupled to two, tile-level platforms. It is due to this coupling that the relative in-plane motion of the platforms with respect to each other results in steering of the mirror in two degrees of freedom. Depending on the implementation method, this relative displacement can be generated by moving one or both of the platforms. As these two platforms are common to all of the pixels, all of the mirrors on the tile are steered towards

the same direction, i.e., they move in parallel. In Figure 5.8(a), k_{r1} (k_{t1}) and k_{r2} (k_{t2}) represent the rotational and translational spring constants that model the elastic coupling of the pivot-rod to the platforms. The bottom and top platforms are labeled as "level-1" and "level-2" platforms, respectively.

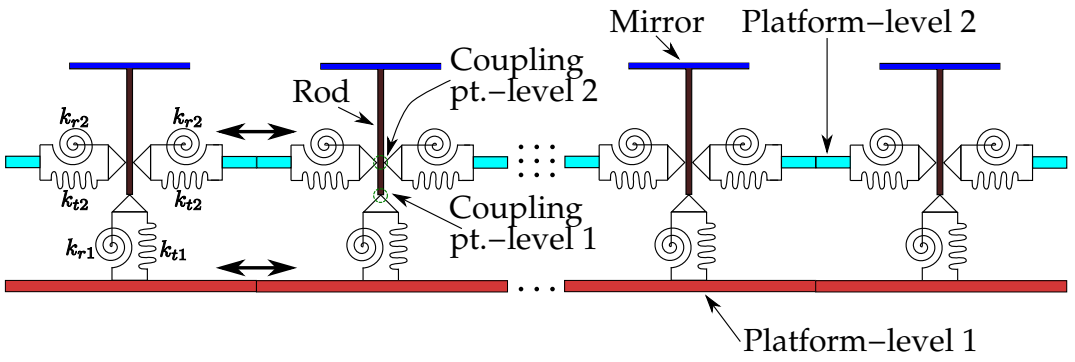

(a)

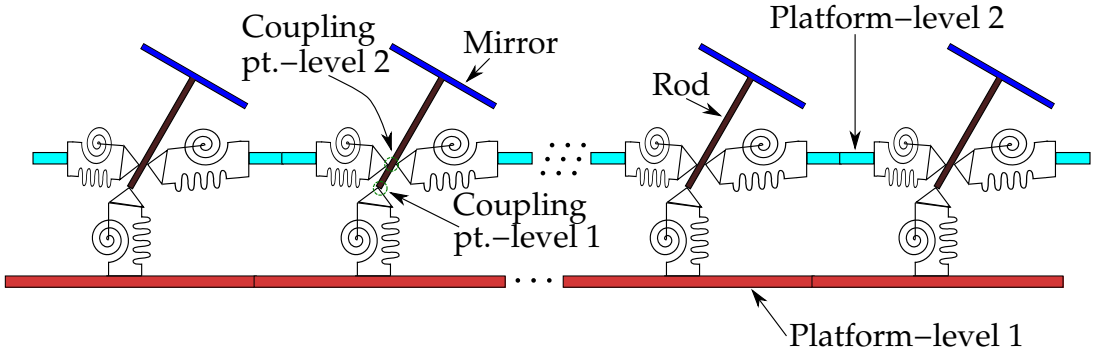

(b)

Figure 5.8: Elastic modeling of the 1-D tile with pivoted mirror pixels captured in (a) unrotated and, (b) rotated states. A rotational and translational spring is used to model the coupling of the reflector pixel to the platforms.

Generally speaking, coupling of the pivot-bar to the platforms does not have to be through elastic coupling. The coupling can be by other means such as Hertzian contact, sliding friction, or even via non-contact magnetic or electrostatic interactions. The way the coupling is handled is an important factor on the force required to steer the mirrors to a given position. As such, the coupling method of

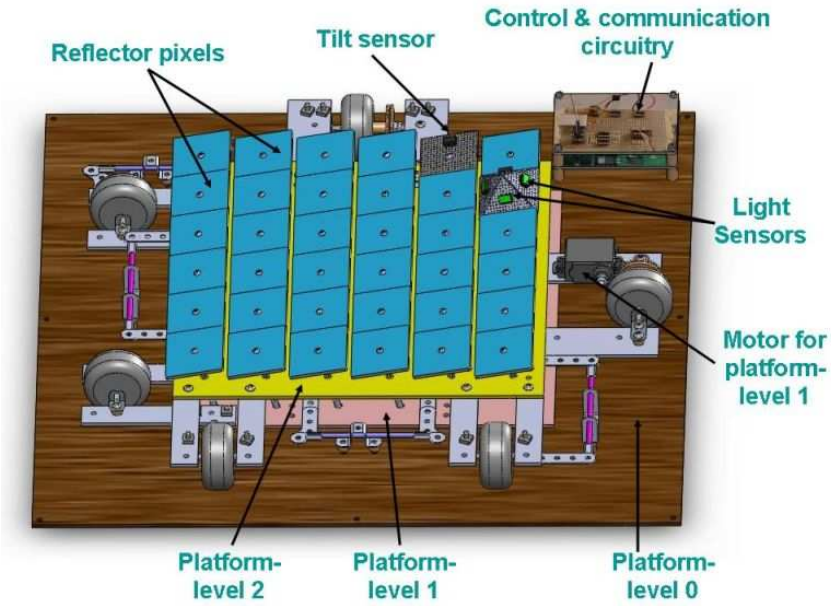

(a)

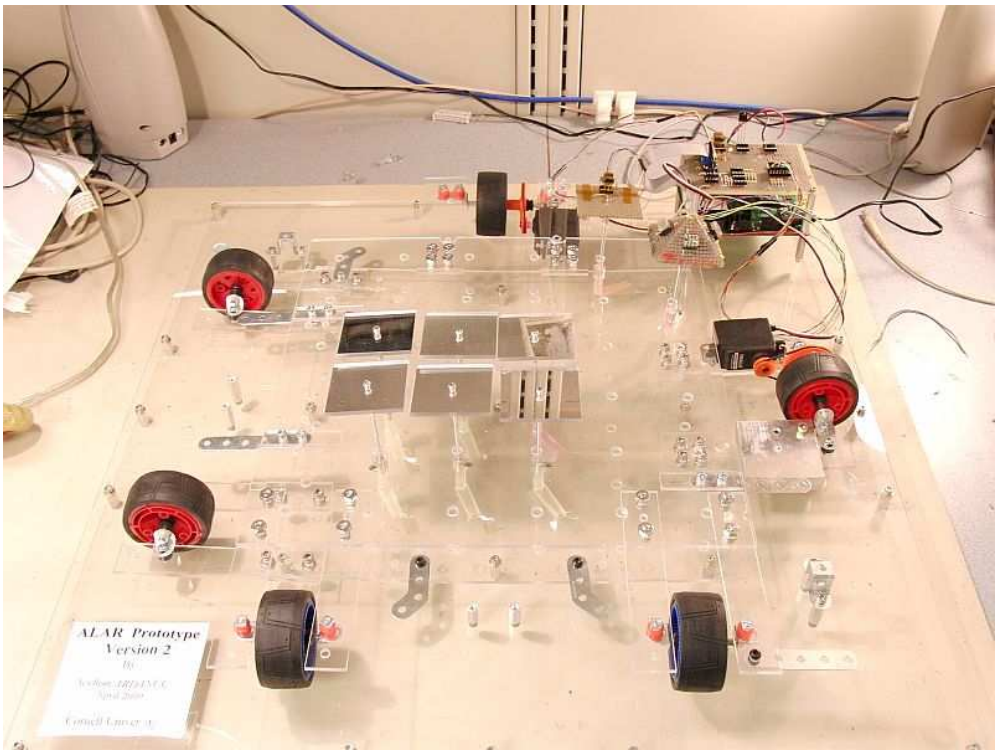

(b)

Figure 5.9: (a) CAD model and (b) optical picture of the prototype.

pixel-rods to the tile-level platforms is one of the central decisions for the design of an ALAR tile with pivoted pixel structure.

The CAD model of the prototype is shown in Figure 5.9(a). The prototype is designed to support a rectangular array of 6×6 array of mirrors within a foot square area. The pitch length of the mirror array is 2.0 inch, and mirrors on top of the pixels are squares with a side-length of 1.9 inch. This yields a fill-factor of more than 90%, for the mirror-array. Most of the parts are manually machined from transparent, acrylic plastic, except nuts and pivot-bars that were metal. Rolling on wheels is the method of choice for translating the platforms due to its simplicity. Each platform is supported by three wheels, the front of which is connected to a servo-motor to translate the platform back and forth along a line. An additional platform (level-0), is shown under platform-level 1. This platform, not being crucial to the operation, provides a common reference over which servo-motor controlled wheels of platform-level 1 and platform-level 2 can rotate.

The directions of linear travel for platform-level 1 and platform-level 2 are orthogonal to each other. Any relative displacement between the platforms as a 2-D vector translates to a unique amount of wheel rotation for either of the platforms as measured from their initial (unrotated) state[5]. Furthermore, elastic problem in Figure 5.8 governs a one-to-one mapping in two dimensions from the relative displacement between the platforms to the normal vector of the pivoted mirror surfaces. As such, one can calculate the required relative displacement of the platforms in order to steer the normal vector of the mirrors to a desired direction. Latchable aspect of the mirrors stem from rolling and sliding friction mechanisms involved in the operation of the tile, as well as the holding force of the servos once they are turned off at a particular position of the mirrors.

[5]assuming there is no slip.

The picture of the prototype constructed is shown in Figure 5.9(b). Only eight of the 36 pixels are populated for prototyping purposes. Six of the pixels have mirror surfaces, and two of the pixels are used for light and tilt sensing. The mirrors on the tile can track the brightest spot in the ambient using a pyramidal, four-quadrant, light sensor array mounted in place of one of the pixels as highlighted in Figure 5.9(a). This serves as a proof-of-concept feature for sun-tracking applications. A microcontroller (Basic Stamp, Parallax Inc.) is used to control the actuation of the platform servos in closed-loop operation. Figure 5.10 shows the system level architecture of the prototype. Microcontroller manages all of the actuation, communication, peripheral sensing (light & tilt), and control activities on the tile.

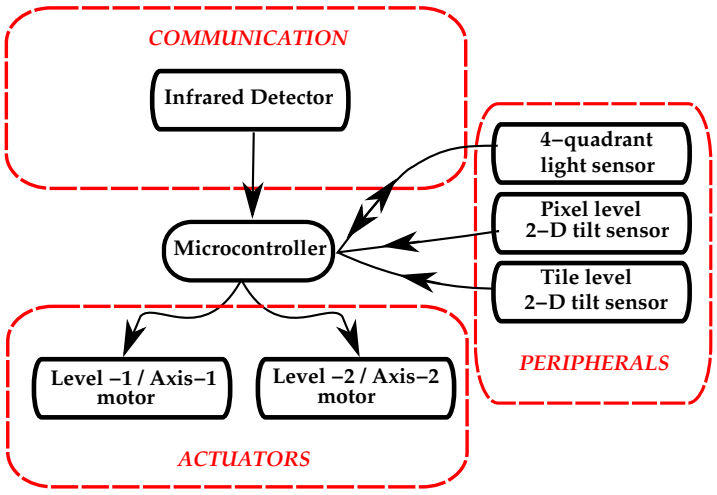

Figure 5.10: System level architecture of the prototype.

The angular position sensing of the mirror surfaces for the closed-loop control is performed by measuring the 2-D tilt of the reflector planes using a dual-axis accelerometer. Necessary commands to the prototype are communicated wirelessly using an IR remote control. Other capabilities of the prototype include an auto-

matic demo mode, homing of the platforms to bring the mirrors into a position parallel to the tile plane, autoscaling of light sensors, and remote manual steering of the mirrors. An additional accelerometer was included to measure the tilt of the tile-plane. Important parts of the prototype are detailed in Section 5.4.2.

Self-powering and minimization of the tile thickness were not pursued in this version of the development work. Integration of these aspects as well as wireless protocols such as ZigBee® will be considered during the future prototyping efforts. Although the pivoted design is extremely suitable for high fill-factor tile designs, choice of a wheel-based translation mechanism and employment of large wheels resulted in plenty of unused space on the tile. Despite 12×12 inch^2 square mirror region, the dimensions of the platform-level 0 is $\approx 21 \times 21$ inch^2. Future work will consider improved translation mechanisms to reap the benefits of high-fill factor capability offered by the pivoted design.

5.4.2 Description of the peripheral components of the prototype

Two pixels on the tile were used to sense entities that depend on the direction of the normal vector of the mirrors. Any pixel on the tile can be used as locations of directional sensing, thanks to the parallel-latticed operation. First pixel used in this manner measures the two-axis tilt of the reflector mirror surfaces on the tile using a dual axis accelerometer (MEMSIC 2125). This tilt sensor, which is indicated in Figure 5.9(a), is central to the closed loop control of the positions of the mirrors on the tile.

The second pixel-level, directional sensing on the tile is used to determine the

direction of the brightest spot in the ambient. Operation principle of the custom-assembled, light-sensing pixel structure for the simpler, 1-D case is illustrated in Figure 5.11(a). If a light source is not positioned symmetrically with respect to the light sensor pair, a difference signal is created at the outputs of the sensors. This difference signal can be used to rotate the triangular support structure housing the sensors until the tip of the triangle faces towards the light source, i.e., the sensors are symmetrically positioned with respect to the light source. At this point, the incident light on the sensors are equal. Extension of this idea to 2-D tracking resulted in a pyramidal shaped pixel structure with a light sensor (TSL230) on each one of the four faces. Pictures of the assembled pixel structure before the placement of sensor chips are shown in Figure 5.11(b). The microcontroller can quantify the

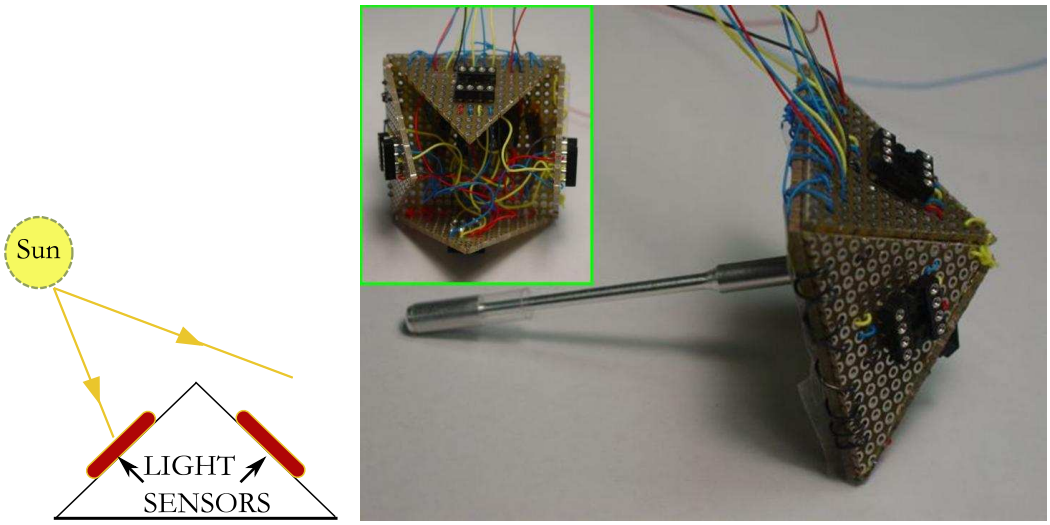

(a) (b)

Figure 5.11: (a) The operating principle of the light tracking pixel in 1-D, (b) optical picture of the light tracking pixel with pivot-bar. DIP sockets for the light sensors are visible at the center of each face.

position of the brightest spot in conjunction with the output of the tilt sensor. A feedback algorithm implemented in the microcontroller ensures that the pyramidal light sensing pixel is steered to a position where the gradients between the outputs

of the light sensors on opposing faces of the pyramid are below a certain threshold value. Two snapshots taken during the operation of the prototype in light tracking mode are shown in Figure 5.12.

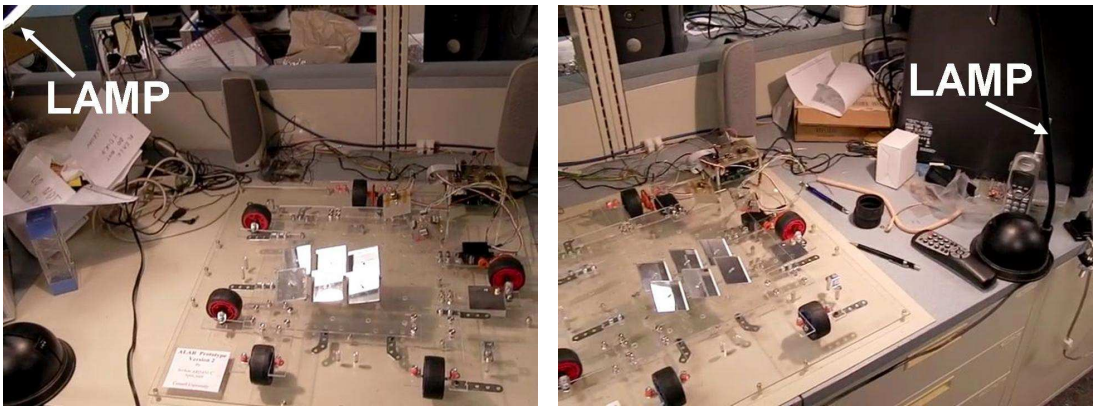

(a) (b)

Figure 5.12: Two pictures taken during light tracking-mode of operation of the prototype, when a desk lamp is used as a bright light source in the ambient. The pixels of the prototype face towards the lamb when the lamp is placed to the (a) left, and (b) to the right of the prototype.

The sensitivity and the settling speed of the closed-loop control can be controlled by changing certain parameters in the microcontroller program. Microcontroller can also run an autoscaling routine to adjust the sensitivity of the light sensors (TSL230) to ensure proper operation at varying background light levels.

5.4.3 Geometrical implications of the pivoted-pixel design

Pivoted operation of a parallel latticed tile can be analyzed to derive simple relations for the maximum angle of rotation and a lower limit on the tile thickness. Maximum relative displacement between the platforms of Figure 5.8(a) that is necessary for a given rotation angle can also be estimated under some assumptions.

The model to be used is shown in Figure 5.13(a). This basic model only considers pivoted motion of the pixels in synchronicity with each other, and the model neglects the coupling to different platforms. The pivot connection is assumed to be through a friction-less, pinned connection. Here L_x is the length of the reflector surface, d_x is half of the spacing between neighboring reflectors, L_z is the length of the pivot-bar, and

$$P_x = L_x + 2d_x \tag{5.1}$$

is the pitch length of the mirror array.

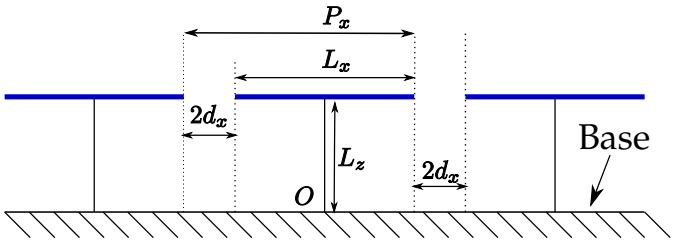

(a)

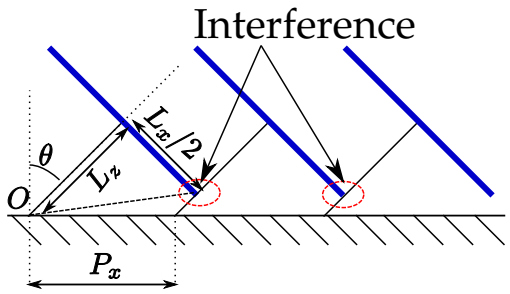

(b)

Figure 5.13: (a) Simplified side view of reflector pixels on a parallel-latticed tile, (b) deformed state when there is interference between the neighboring pixels, which limits the rotation angle θ.

Figure 5.13(a) considers only a single platform that is labeled as "base", unlike the model in Figure 5.8, which shows two platforms. All of the pivot points of the pixels are assumed to lie on the plane of the base-platform, similar to the case for platform-level 1. The negligence of the second platform is pursued in order to

simplify the calculation of the maximum-rotation angle for the mirror pixels on the tile. The implications of this assumption are addressed later in this section.

The maximum angle of rotation in 1-D is limited by the interference of the pixel structure to either the *neighboring pixels* or to the *base-platform*. The former case is illustrated in Figure 5.13(b). Here, θ is the angle of rotation from the initial unrotated state ($|\theta| \leq \pi/2$), at which reflector surfaces on top of the pixels are parallel to the tile plane. Maximum value of θ as limited by neighbor interference is denoted with $\theta_{max,ni}$, and it is expressed in Equation (5.2).

$$\theta_{max,ni} = \begin{cases} \arccos\left(\frac{L_x}{2P_x}\right) = \arccos\left(\frac{1}{2} - \frac{d_x}{P_x}\right) & : \quad \text{if} \quad L_z^2 \geq P_x^2 - \frac{L_x^2}{4} \\ \pi/2 & : \quad \text{otherwise} \end{cases} . \tag{5.2}$$

Note that for an interference by a neighboring pixel to happen, the length of the pivot-bar should be larger than a critical value, which can be calculated by considering a right-angled triangle with side-lengths L_z, $L_x/2$, and a hypothenuse of P_x. Equation (5.2) shows that $\theta_{max,ni}$ is larger than 60° by virtue of d_x being positive. This corresponds to an optical rotation angle (2θ) of at least 120° due to neighboring pixel interference[6]. However, base-platform interference should also be considered to deduce the overall limit on rotation.

Maximum value of θ due to base-platform interference, $\theta_{max,bi}$, is given by Equation (5.3).

$$\theta_{max,bi} = \arctan\left(\frac{2L_z}{L_x}\right). \tag{5.3}$$

The overall limit for rotation, θ_{max}, is then the smaller of limits imposed by neighbor and base-platform interference.

$$\theta_{max} = min(\theta_{max,ni}, \theta_{max,bi}) \tag{5.4}$$

[6]If negative values of θ are also considered, optical rotation angle is 240°.

Therefore, the model of Figure 5.13(a) supports a maximum rotation angle of at least $2\theta_{max} \geq 120^{\circ}$ provided that $L_z \geq (\sqrt{3}L_x/2)$. A lower limit on the thickness of the tile can be expressed considering the largest distance between the edge of the mirror and the pivot point O in the pixel of Figure 5.13(b):

$$t_{tile} \geq \sqrt{L_z^2 + \frac{L_x^2}{4}}. \tag{5.5}$$

The simple model in Figure 5.13 neglected the existence of two platforms. Consideration of interference to another platform *above* the base platform (i.e., above the plane of the pivot points of the pixels) can change θ_{max} due to an additional argument to the $min(\cdots)$ function in Equation (5.4). Since the additional argument would be smaller than $\theta_{max,bi}$, θ_{max} value can potentially be reduced. An alternative approach to consider interference due to another platform *above* the base platform is to use a smaller value for L_z to reflect the reduced distance between the mirror plane and the closest platform under the mirrors.

Consideration of another platform *below* the base platform (i.e., below the plane of the pivot points of the pixels) can not introduce a smaller argument to the $min(\cdots)$ function in Equation (5.4), so θ_{max} would be unchanged in this case.

The maximum relative displacement between level-1 and level-2 of Figure 5.8 can be estimated, if one calculates θ_{max} as described above. If the platform-level 2 is coupled to the pivot-bar at a distance $h_{12} < L_z$ above the platform-level 1, then the limit for the maximum travel range of platforms, denoted by $u_{max,1D}$, is:

$$u_{max,1D} = h_{12} \sin(\theta_{max}). \tag{5.6}$$

Equation (5.6) implies that the required displacement can be made very small by simply decreasing h_{12}, the distance between the platforms. Since the maximum angle of rotation only depends on length ratios, pivoted design also supports scaling

and use of smaller stroke actuators without sacrificing from the large angular travel range. On the other hand, operating mechanisms that rely on tile level rotations (as in Figure 5.6) need to traverse around the whole tile regardless of the pixel size. This may be disadvantageous since the on-time for the motors, and hence the power consumption of the tile do not scale down with the pixel size.

In practice, one can use a complex 3-D structure for the platforms to overcome some of the interference limitations as well as to decrease weight per unit area. Simultaneous rotation/displacement on both axis is likely to be limited by the interference of one corner of the mirror to a neighboring structure or one of the platforms. Therefore, detailed design for the pivoted ALAR tile mandates a 3-D analysis and consideration of the shape of the reflector of the pixel.

5.4.4 Some advantages of the pivoted-pixel design

Pivoted-design of the tile supports manufacturing of the bulk of the tile from a single piece, if the coupling of the pivot rod is made via an elastic joint as shown in the model of Figure 5.8. In this case, a single-piece, compliant structure can be used to implement majority of the tile, namely, platforms, pivot-bars, and supports for planar reflector of pixels.

The concept of a single-piece, pivoted-pixel is illustrated with a sample design in Figure 5.14. Although pivoted operation can be implemented both at micro and mesoscale, the discussions of this section focus mostly on the mesoscale version. The two platforms spaced very closely to each other at the bottom of the pixel can be identified in Figure 5.14(a). Low distance between the tile-level platforms can reduce the stroke required by the actuators as described in Section 5.4.3.

Figure 5.14(b) shows the realization of an elastic joint to act as a pinned coupling between the pivot-bar of the pixel and the platform-level 1. Platform-level 2 spring coupling is realized by four rectangular bars that go through a deformation when the two platforms are displaced. The total force needed to displace the platforms is mostly determined by the spring constant associated with the deformations of the rectangular bars as well as that of the elastic joint. Use of softer materials within the deforming regions helps to reduce the total force required to steer the mirrors, but this approach complicates the manufacturing. Figure 5.14(c) and Figure 5.14(d) show arrayed views of the sample design.

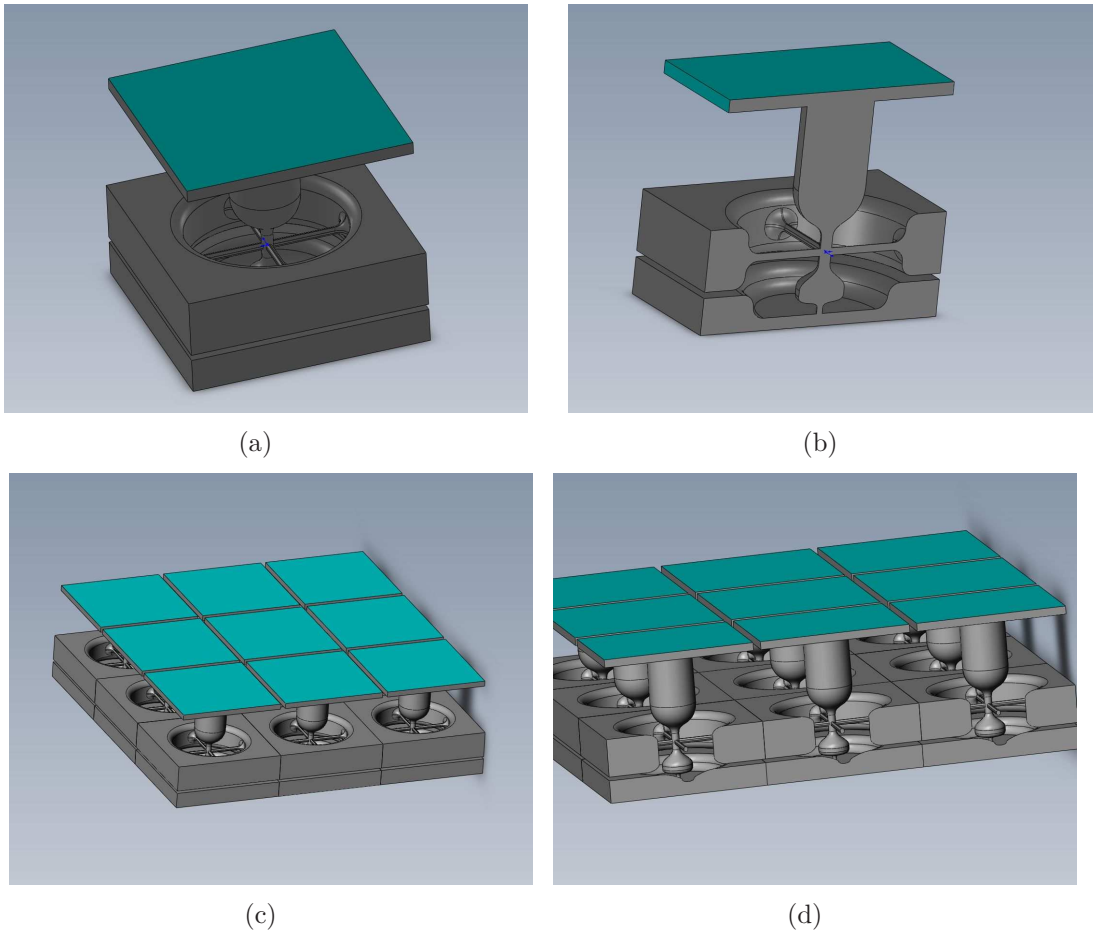

(a) (b)

(c) (d)

Figure 5.14: Schematic illustration of a sample, pivoted-pixel design for the tile. Isotropic and cross-section views of both the pixel and the array are shown.

Figure 5.14 does not show a latching mechanism to enable zero-idle-power operation of the tile by maintaining the positions of the deformed structures against the restoring spring-forces. The incorporation of a latching mechanism, for which tile-level or pixel-level implementations are possible, is not a straightforward task, but could be done by latching motor actuators.

One can consider more compliant spring structures to minimize the total force. However, minimum feature size that can be realized during 3-D manufacturing process can be a limit on how compliant the structures can be made. Additionally, stress intensity factors at the joints and around the coupling-bars should be considered to increase robustness against material fatigue and fracture. Fabrication of the structure in Figure 5.14 in two or more layers, and then bonding of these layers can enable use of a larger set of manufacturing tools, given the involved 3-D complexity of the tile.

Having a high quality optical surface is important for solar applications of ALAR. The technology used to create complex 3-D structures of the form in Figure 5.14 may not allow optically smooth surfaces. So evaporation or spray coating of a metal on top may not yield a good quality reflector tile. Therefore, lamination of reflective thick films followed by laser cutting can be a viable solution. In this case, the top of the compliant structure acts as a support for the reflector surface that is attached on top at a later stage. Likewise, pick-and-place assembly of different reflectors, optical filters, actuators or passive modules can realize the applications to be mentioned in Section 5.9.

Single-piece designs greatly reduce the assembly effort, and they can potentially lower the cost of manufacturing. This is a significant advantage as compared to other mechanical operation principles that require hinged components or mounting

of many small parts on the tile in precise locations with respect to each other.

Pivoted design can lend itself to very light-tiles if proper materials with low densities can be identified. The minimization of the weight can be more of a challenge when components with possibly different materials are used in the tile. The volume of the bulk material used can also be decreased by trussed or meshed implementations of the platforms, helping further with the reduction of the weight per unit area.

Another advantage of a compliant, pivoted design as in Figure 5.14 is the reduction of energy loss mechanisms due to friction. Furthermore, the inherent elastic energy storage capability ease the task of actuating the platforms about half of the time the motors are on, thanks to the work done by the spring restoring forces. While this might complicate the design of the latching mechanism due to holding force considerations, it can also reduce the power consumption of the tile.

5.5 Optical modeling of the basic tile operation

5.5.1 Problem definition

The main problem at hand for the ALAR tile is to reflect light from a certain *source-point* $\boldsymbol{F_s}$ to a *target-point* $\boldsymbol{F_t}$ via an array of densely-packed mirrors. In order to specify the problem to a more tractable level, only pivoted-design described in Section 5.4 is considered. The picture of this problem that was given in Figure 5.7 is redrawn in Figure 5.15 with source and target points. The polar coordinates of source and target points are (R_{src}, θ_{src}) and $(R_{tgt},\ \theta_{tgt})$, respectively. The

problem is trivial if the length of the pivot-rod is zero, i.e., $L_z = 0$. Then the mirror always rotates around its center point $\boldsymbol{D}$ as illustrated in Figure 5.16. Incident and reflected unit vectors, labeled respectively as $\hat{\boldsymbol{r}}_{\boldsymbol{i}}$ and $\hat{\boldsymbol{r}}_{\boldsymbol{r}}$, can readily be calculated as $\boldsymbol{F_s}$, $\boldsymbol{F_t}$, and $\boldsymbol{D}$ are known.

$$\hat{\boldsymbol{r}}_{\boldsymbol{i}} = \frac{\boldsymbol{F_s} - \boldsymbol{D}}{|\boldsymbol{F_s} - \boldsymbol{D}|} \qquad (5.7a) \qquad\qquad \hat{\boldsymbol{r}}_{\boldsymbol{r}} = \frac{\boldsymbol{F_t} - \boldsymbol{D}}{|\boldsymbol{F_t} - \boldsymbol{D}|} \qquad (5.7b)$$

Normal unit vector of the mirror $\hat{\boldsymbol{n}}$[7] and the corresponding rotation angle θ is calculated by Equation (5.8) [118, Equation 5.13].

$$\hat{\boldsymbol{n}} = \cos(\gamma)\hat{\boldsymbol{e}}_{\boldsymbol{x}} + \sin(\gamma)\hat{\boldsymbol{e}}_{\boldsymbol{y}} = (\hat{\boldsymbol{r}}_{\boldsymbol{i}} + \hat{\boldsymbol{r}}_{\boldsymbol{r}})\,(2 + 2\hat{\boldsymbol{r}}_{\boldsymbol{i}}\cdot\hat{\boldsymbol{r}}_{\boldsymbol{r}})^{-0.5}\,, \qquad (5.8)$$

where $\hat{\boldsymbol{e}}_{\boldsymbol{x}}$ and $\hat{\boldsymbol{e}}_{\boldsymbol{y}}$ are the unit basis vectors, and $\gamma = \pi/2 + \theta$ is the angle between the mirror normal and the x-axis.

The solution above for $L_z = 0$ can serve as a good approximation also for cases when source and target locations are far from the tile, i.e., when $L_z \ll R_{src}$ and $L_z \ll R_{tgt}$. While this may be the case for many outdoor solar applications, a

[7] Unit vectors are indicated with a ˆ symbol.

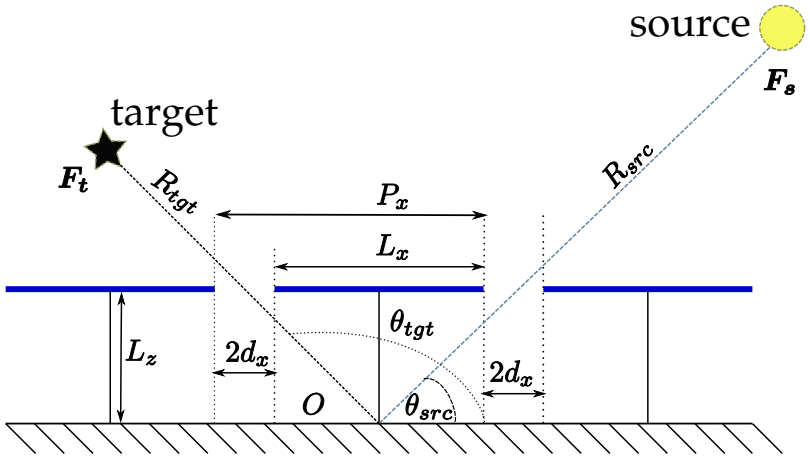

Figure 5.15: Model for the pivoted pixel design used in analytical ray-optics calculations.

rigorous derivation for $L_z \neq 0$ is needed for other applications of the tile such as indoor lighting control and dynamic wallpapers. The analysis for this case is lengthy, and it is presented in Appendix K. The equations derived are then used to sketch the mirrors of the parallel-latticed and the free-latticed tiles in Figure K.2.

5.5.2 Self-shadowing and light trapping as efficiency loss mechanisms

Two important phenomena in arrays of small mirrors are shadowing and light trapping. The shadowing occurs when part of a given pixel is not illuminated by the source due to obstruction by the neighboring pixels. Trapping of light occurs when the incident light makes it on the pixel, but then reflected light gets obstructed by the neighboring pixel before it leaves the tile. Shadowing and trapping are

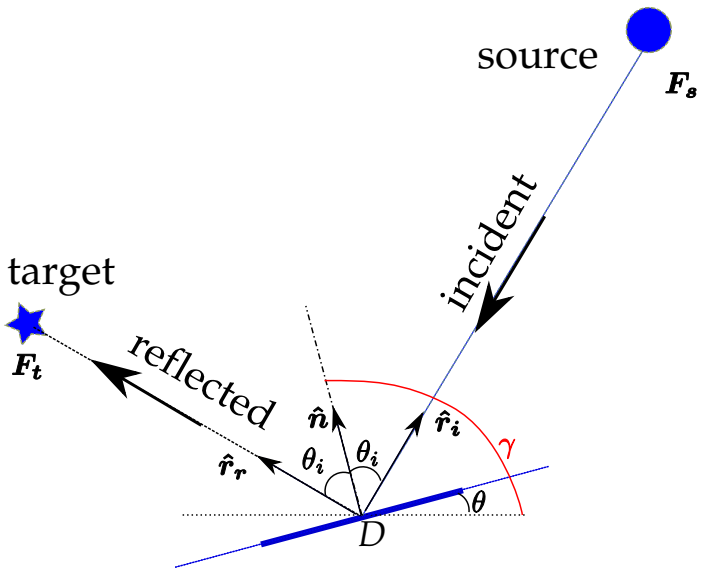

Figure 5.16: Calculation of the mirror normal vector in case of vanishing pivot length, i.e., $L_z = 0$.

illustrated in Figure 5.17.

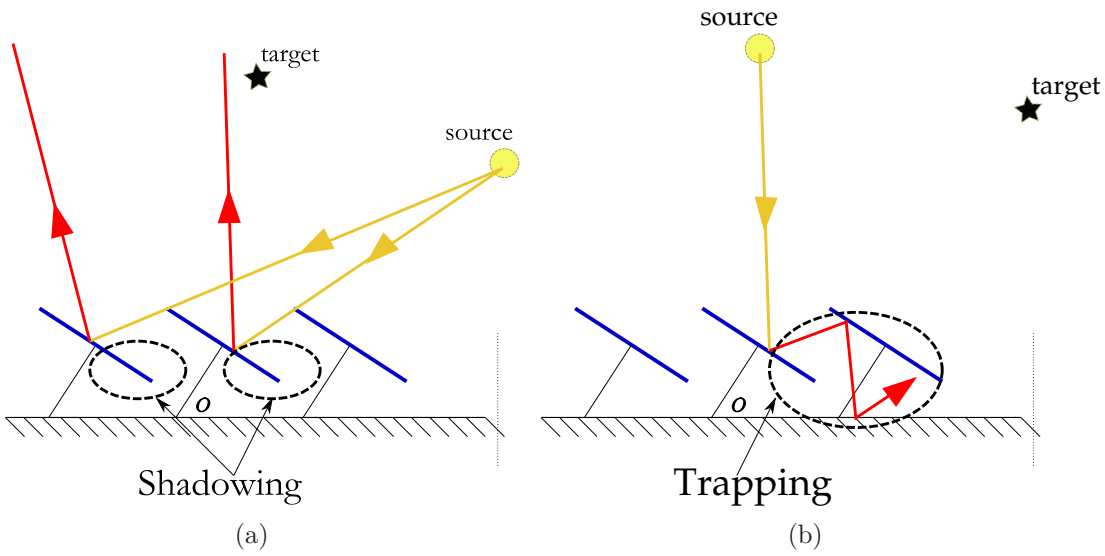

Figure 5.17: Illustration of (a) shadowing, and (b) light trapping on an ALAR tile.

Light trapping in ALAR tiles can be useful in some applications to adjust the heat absorbed by a surface or to adjust the transmitted light when used with transparent substrates for controlled shading applications [13]. It should be emphasized that the optical modeling of the tile presented in this section assumes target and source points to be on the same side of the half-space as determined by the plane of the reflectors. Therefore, models may need to be modified to handle the cases where light is transmitted through the tile.

Both shadowing and light-trapping within the tile act as efficiency loss mechanisms when considered for central-receiver based CSP applications. As such, three different optical collection efficiencies can be identified: First efficiency, which is named as *best-efficiency* (η_{best}), indicates the ratio of the illuminated light over the mirror region of the pixel to its pitch, assuming the given pixel is isolated and there is no neighboring pixels. This efficiency is determined by the fill-factor of

the mirror pixel. For the 2-D model in Figure 5.15:

$$\eta_{best} = \frac{L_x}{P_x}. \tag{5.9}$$

The second efficiency is *illuminated-efficiency* (η_{ill}). This is the ratio of the illuminated region of the pixel in consideration of the shadowing from the neighboring pixels. If we call the length of the illuminated region in Figure 5.15 as $L_{illuminated}$, then

$$\eta_{ill} = \frac{L_{illuminated}}{P_x}. \tag{5.10}$$

The last efficiency definition to consider, *reflected-efficiency* (η_{ref}), is determined by the amount of light remaining from the illuminated region after part of the light is trapped. If we call the length of the region over which light reflects off towards the target without any shadowing or trapping as $L_{reflected}$, then

$$\eta_{ref} = \frac{L_{reflected}}{P_x}. \tag{5.11}$$

One can express a relation between illuminated, reflected, shadowed and trapped regions of the mirror surface as in Equation (5.12).

$$L_x = L_{illuminated} + L_{shadowed} = L_{reflected} + L_{trapped} + L_{shadowed}, \tag{5.12}$$

where $L_{trapped}$ is the length of the region over which light incident within the illuminated part of the mirror gets trapped, and $L_{shadowed}$ is the length of the region of the mirror, over which neighboring pixels obstruct the incoming light.

The relations between best, illuminated, and reflected efficiencies described above are summarized in Figure 5.18.

Simulations were carried out in MATLAB® in order to calculate the best, illuminated, and reflected efficiencies for tiles of arbitrary dimensions and arbitrary

source and target locations. Since η_{best} is only dependent on the array geometry (independent of source and target locations), it serves as a convenient benchmark for reflected and illuminated efficiencies when source or target locations are swept during a simulation. The simulation efforts are described in Section 5.6.

5.5.3 Quantifying the error in targeting of the incoming light

In Section 5.5.1 and Appendix K, analytical and numerical calculations of mirror rotations were carried out assuming that the reflection of light from the source point to the target point occurs precisely at the center of the mirror. Consequently, reflection of light off of different points on the mirror introduces an error. Quantification of this error, which is a measure of the optical concentration efficiency of the tile, is necessary to answer the following question: "How much of the reflected light reaches within a given radius of the target point?"

One method that is useful for answering the raised question above is illustrated

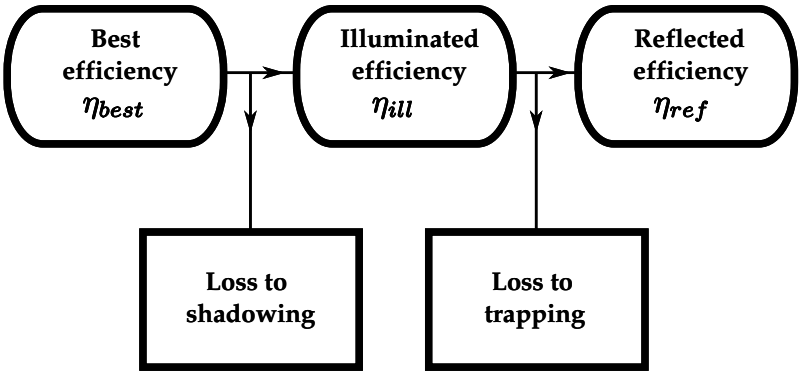

Figure 5.18: Relations between best, illuminated, and reflected efficiencies.

in Figure 5.19. This method, which quantifies the error in the process of reflecting of light from a source point to a target point, is used in the simulations to be presented later in this chapter. It also serves as a yardstick to evaluate optical concentration performance of different tile designs.

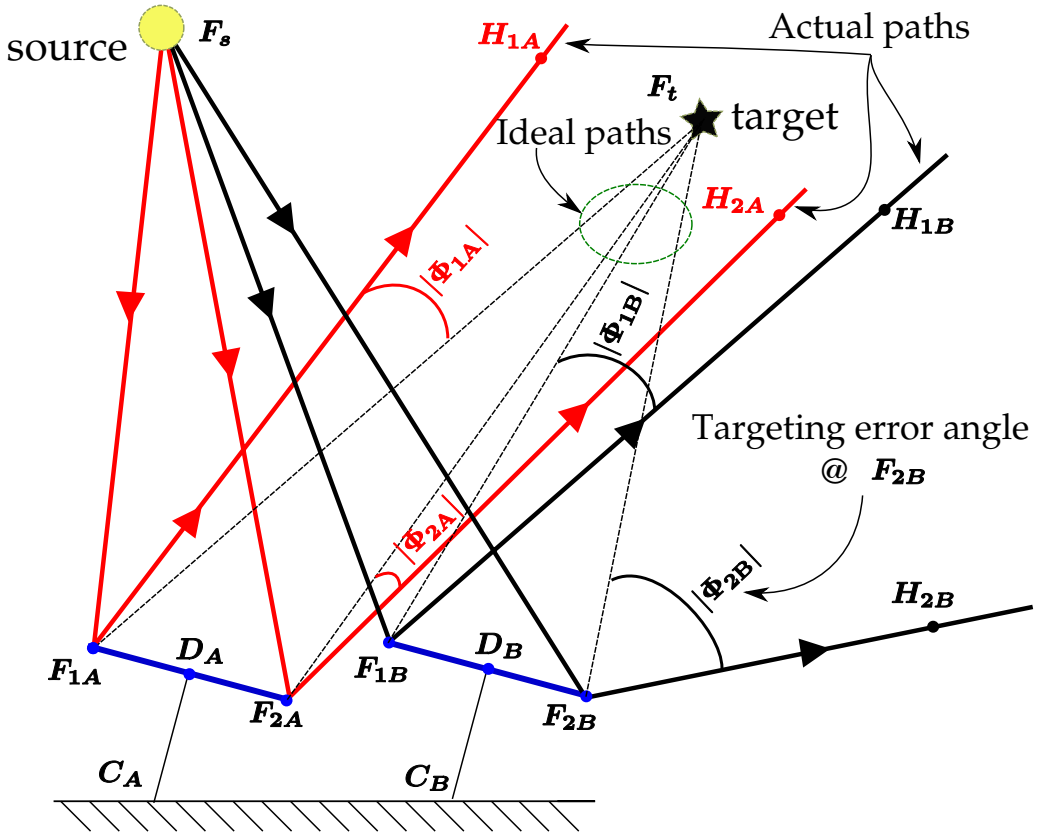

Figure 5.19: Quantification of the error in the targeting operation. The mean value of absolute values of error angles calculated using the actual and ideal reflection paths is used to estimate the targeting error.

Two mirrors, tagged with ID's 'A' and 'B', are shown in Figure 5.19. An error angle Φ is calculated at the boundary points of the region over which light is reflected successfully towards the target, i.e., without either shadowing or light-trapping. Φ is calculated from the difference between the polar angles of the ideal

and the actual paths of reflected light. Actual path is the one that follows from simple ray optics, whereas the ideal path goes from the point of interest on the mirror to the target point. Figure 5.19 indicates a pair of error angles for each mirror: Φ_{1A}, Φ_{2A} for mirror-A, and Φ_{1B}, Φ_{2B} for mirror-B.

For example, the error angle for the point $\boldsymbol{F_{2B}}$ in Figure 5.19 is shown to be the angle between the ideal ray path $\overline{\boldsymbol{F_{2B}F_t}}$ and the actual ray path $\overline{\boldsymbol{F_{2B}H_{2B}}}$. The average error angle calculation for mirror-B is performed using the following equation.

$$\Phi_B = 0.5\left(|\Phi_{1B}| + |\Phi_{2B}|\right). \tag{5.13}$$

As Equation (5.13) exemplifies, only absolute value of the error angles are used at every point. Such a procedure is employed in order to avoid erroneous cancelation of error angles with opposite signs at either sides of the reflected regions on the mirror[8].

Average error angle Φ calculated for a given reflector pixel can be used to estimate the average spot size of the image of the source formed around the target using the relation:

$$r_{spot} \approx |\boldsymbol{F_t} - \boldsymbol{D}|\,\Phi, \tag{5.14}$$

where r_{spot} is the estimated radius of the spot on the target and $\boldsymbol{D}$ is the center point of the mirror as shown in Figure 5.19.

The error angle calculation is carried out only at the boundaries of the mirrors in Figure 5.19 since shadowing and light-trapping is not a concern for the given geometrical arrangement of mirrors, source and target locations. Generally speaking, shadowing and light-trapping should always be considered in simulations such as the one described next.

[8]Other sign-insensitive statistical measures such as root-mean-square can also be used.

5.6 Simulation results

The simulations, which are implemented in MATLAB®, consider pivoted-pixel ALAR tiles of free-latticed and parallel-latticed types, with identical mirror-array properties such as mirror size and pitch. First the optimum angle of rotation of the mirrors are calculated for both types of tiles using the specified source and target locations. For the free-latticed tile (i.e., the one with mirrors moving independently of each other) rotation of each mirror on the tile is individually optimized using the algorithm described in Appendix K. Whereas for the parallel latticed tile, the algorithm is run only once by assuming that the reflection happens at the pivot point of the central pixel[9]. Then, all of the mirrors on the parallel-latticed tile are rotated by the same amount based on this calculation. By virtue of this operation, parallel-latticed tiles can never achieve smaller targeting error angles than their free-latticed counterparts, although they can come close under some circumstances.

After the position of each mirror on the tile is calculated based on the tile-type, the simulation calculates the amount of shadowing and light-trapping for a given arrangement to yield the best, reflected and illuminated efficiencies. Targeting error angles are also calculated both at the pixel-level and at the tile-level as an average. A basic level of interference detection between the pixels is implemented in the simulation code to alert against pixel rotations that are not physically possible.

Two different cases are simulated regarding the distance of the source point to the tile. In the "*FAR*-case" the distance of the source to the tile is orders of magnitude larger than the tile size as in solar applications. The same distance is comparable to the size of the tile for the "*NEAR*-case", which can be applicable to

[9]This operation is done using Equation (5.8).

indoor-applications. The values and descriptions of the parameters for both cases are summarized in Table 5.1.

There can be many interesting configurations to simulate. The parameter, which was used as the sweep-variable in the simulations to be presented, was θ_{src}. It was swept from 1° to 179° with 1° step size. Changing θ_{src} can emulate the day period from sunrise to sunset for the *FAR*-case, or an indoor-lamp whose position is changed for the *NEAR*-case.

Table 5.1: Model parameters used in the simulations.[a]

Symbol	Description	Value		Unit[b]
		FAR-case	*NEAR*-case	
R_{src}	Norm of $\boldsymbol{F_{src}}$	10^5	30	AU
R_{tgt}	Norm of $\boldsymbol{F_{tgt}}$	25	25	AU
θ_{src}	Polar angle of $\boldsymbol{F_{src}}$	1–179	1–179	°
θ_{tgt}	Polar angle of $\boldsymbol{F_{tgt}}$	80	80	°
L_x	Reflector length	1	1	AU
$2d_x$	Clearance between reflectors	0.04	0.04	AU
P_x	Array pitch	1.04	1.04	AU
N_{pix}	Number of pixels	11	11	–

[a] The origin is at the pivot point of the central-pixel.
[b] "AU" represents an arbitrary, consistent length unit. The results are applicable to both microscale and mesoscale tiles.

5.6.1 Results for a given source point

Figure 5.20 shows the *FAR*-case simulation results for $\theta_{src} = 154°$. The figure shows six plots in three rows and two columns. The first (left) column of the figure is reserved for the free-latticed tile results, and the second (next) column is reserved for the parallel-latticed results. X-axis for all of the plots represents the positon on the tile, which spans a distance of $L_{tile} = (N_{pixel} - 1)P_x + L_x$. The first

row of plots show a snapshot of the mirrors on the tile in their rotated state. The insets in the same row show the tile, source and target points at a larger scale. The second row of plots show the best, reflected, and illuminated efficiencies for each of the pixels on the tile. The last row of plots show the average targeting error angle in radians, $|\gamma_{error}| = |\Phi|$.

For the efficiency plots of the *FAR*-case in Figure 5.20, the best, reflected and illuminated efficiencies of the (first) pixel closest to the source point are all equal, indicating neither shadowing nor light-trapping as expected. The rest of the pixels on the tile have illuminated-efficiencies that are considerably smaller than their best-efficiencies indicating shadowing. Furthermore, the efficiencies of all of the pixels besides the first one are the same within the scale of the plots.

None of the pixels on the tile has a difference between the reflected and the illuminated-efficiencies. The lack of difference indicates lack of light-trapping. This is expected from the positioning of mirrors shown in Figure 5.20.

The efficiency results for both the free-latticed and the parallel-latticed cases are practically the same, whereas the error angles in targeting are considerably different. The free-latticed tile results in much better targeting performance as expected.

5.6.2 Comparison of different efficiency parameters as a function of the polar angle of the source point

Tile level averages of efficiency parameters are plotted in Figure 5.22 for the *FAR*-case and the *NEAR*-case. Operation with close to the maximum efficiency is

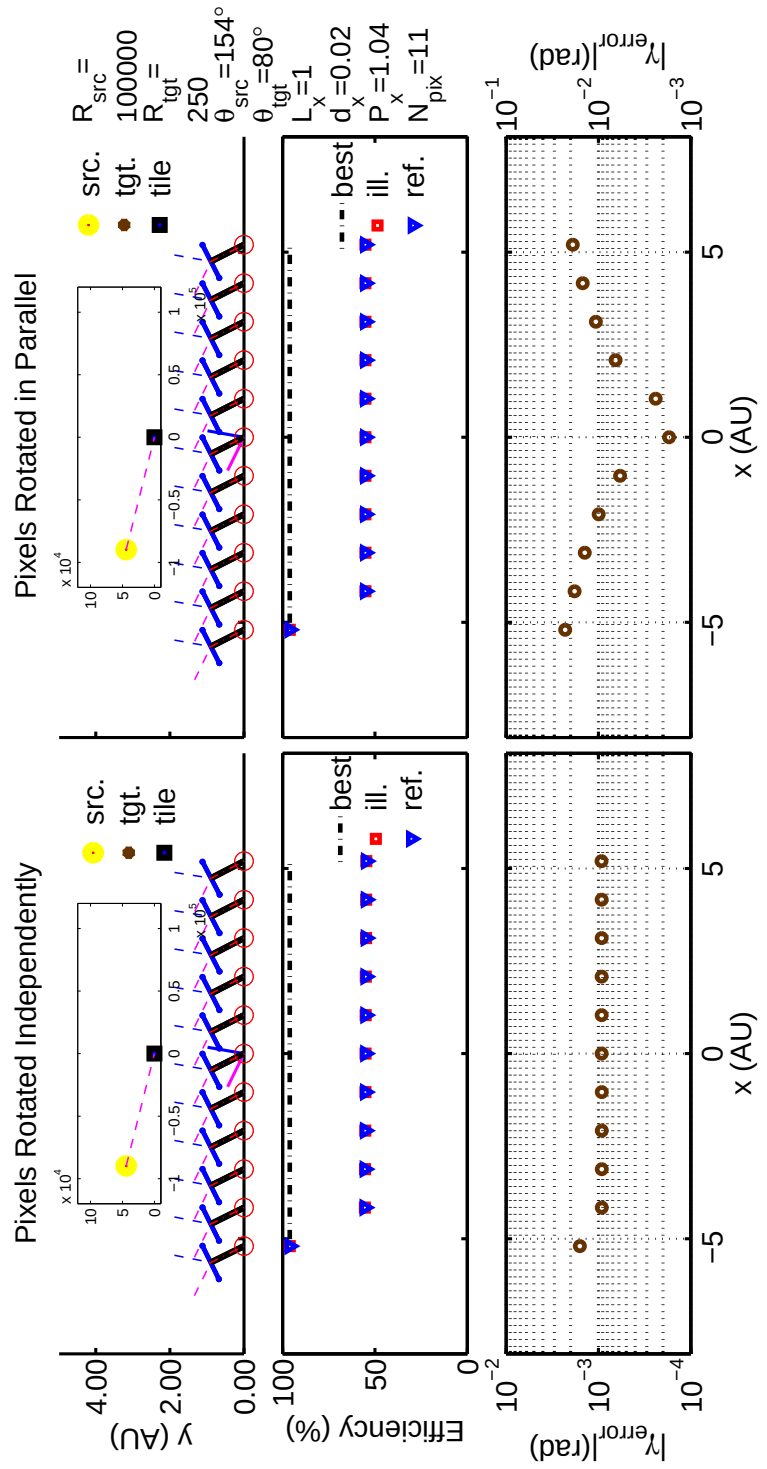

Figure 5.20: Simulation results when the source is far but the target is close to the tile.

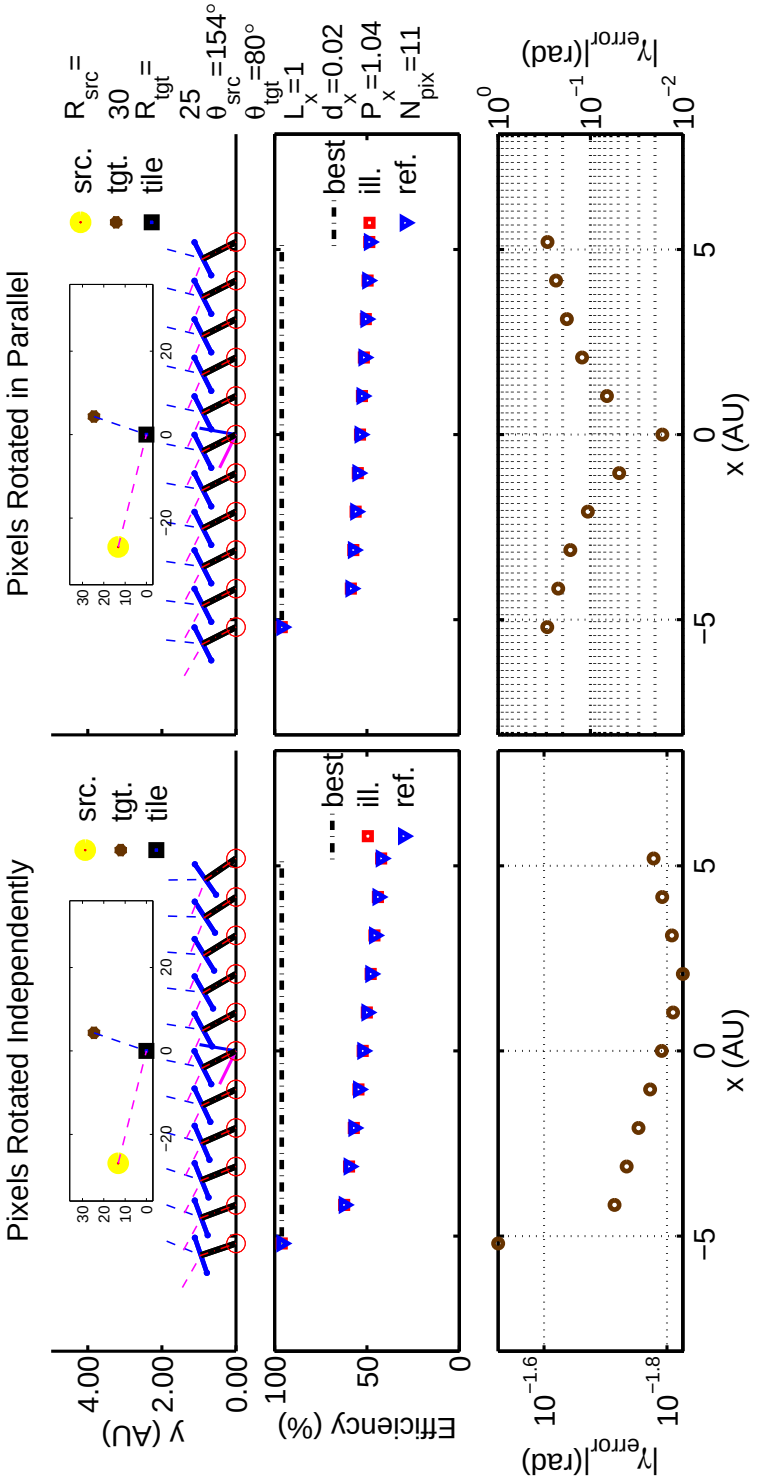

Figure 5.21: Simulation results when both source and target are in the vicinity of the tile.

possible only over a certain range of values of θ_{src}. As θ_{src} approaches to either $\theta_{src} = 1°$ or $\theta_{src} = 179°$ limits, the reflected-efficiency can drop to as low as 10%[10]. While the tiles may not need to be operated under such extreme angles, the results clearly show that optimization of self-shadowing can be crucial to increase tile-level efficiencies.

Efficiency due to light-trapping can be observed for the *NEAR*-case in Figure 5.22(b), which shows a few percent of difference between illuminated and reflected efficiencies for the independently-rotated pixel case (i.e., free-latticed). The same figure also shows that the efficiency of free-latticed tile is slightly less than the parallel-latticed tile. This is a bit counter-intuitive as one expects that independent rotation of the pixels is the optimum configuration for solar collection. The reason becomes clear with a close look at the mirror rotations in Figure 5.23, which shows the simulation results for $\theta_{src} = 118°$. Here, it is seen from the efficiency plot and the sketch of the mirror positions that free-latticed operation cause shadowing especially for the mirrors on the right hand side of the pixel (i.e., the side away from the source point).

5.6.3 Targeting error angle

Figure 5.24 plots the simulation results for the tile level averaged values targeting error, $|\gamma_{error}| = |\phi|$ as a function of θ_{src}. Free-latticed operation clearly does a much better job of beam redirection in both the *FAR*-case and the *NEAR*-case. Targeting error angles in the *FAR*-case were simulated to be about an order of magnitude less than that of the *NEAR*-case.

[10]Note that the lowest value is determined by the number of pixels $N_{pix} = 11$, because the mirror at the edge that is closest to the source point shadows the rest of the mirrors on the tile.

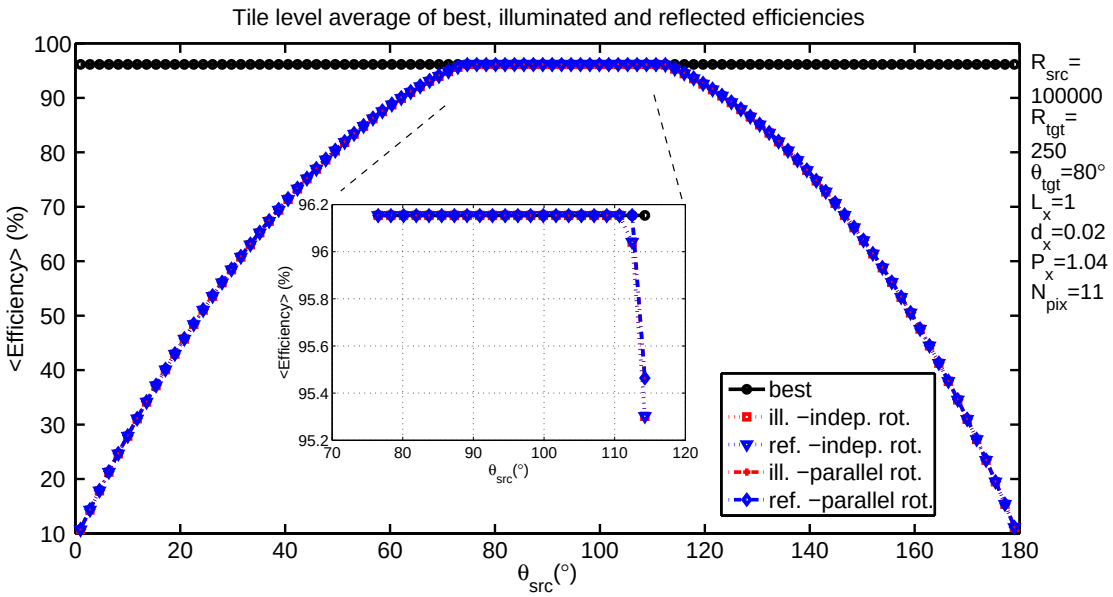

(a)

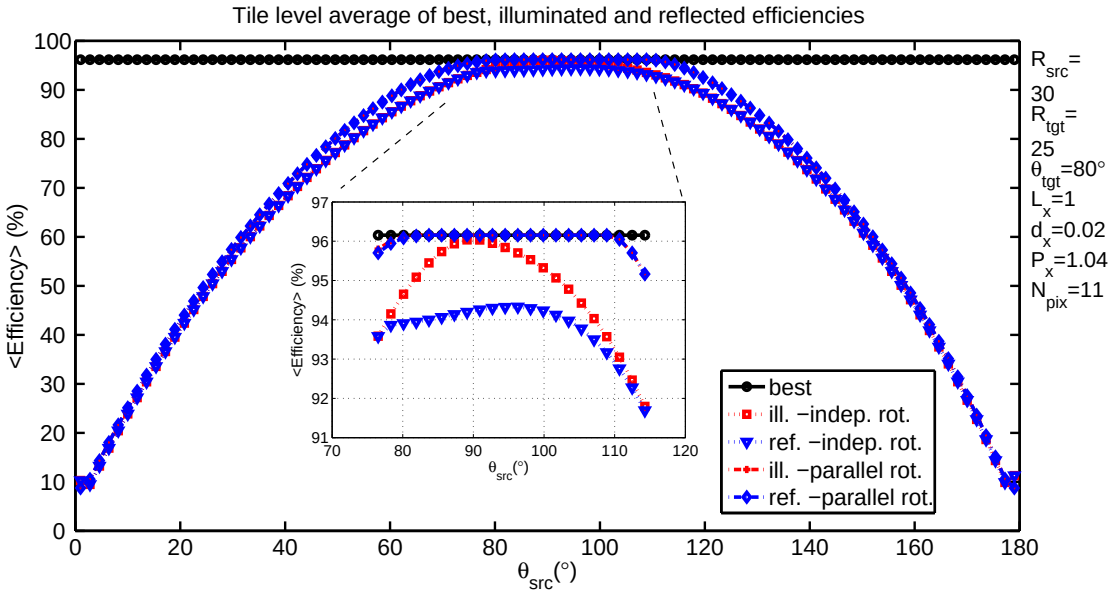

(b)

Figure 5.22: Tile-level efficiency results of parallel-latticed and free-latticed (i.e., independently rotating pixels) tiles for $1^\circ \leq \theta_{src} \leq 179^\circ$: (a) *FAR*-case, and (b) *NEAR*-case. The insets show the close-up views for $75^\circ \leq \theta_{src} \leq 115^\circ$. The horizontal line on top is the best efficiency in both of the plots.

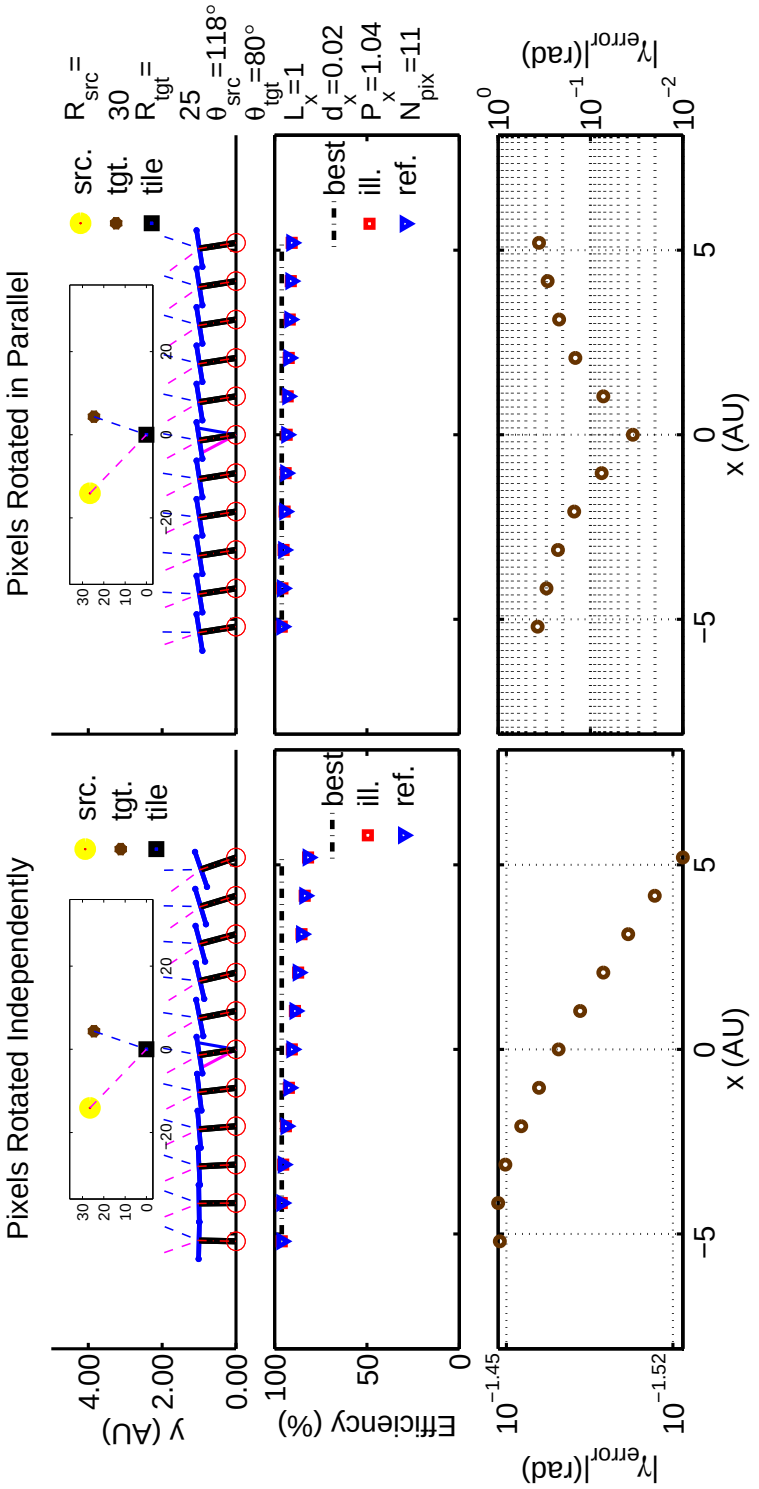

Figure 5.23: Simulation results of the *NEAR*-case when $\theta_{src} = 118°$. Tile-level average of the free-latticed tile is less than that of the parallel-latticed tile due to self-shadowing.

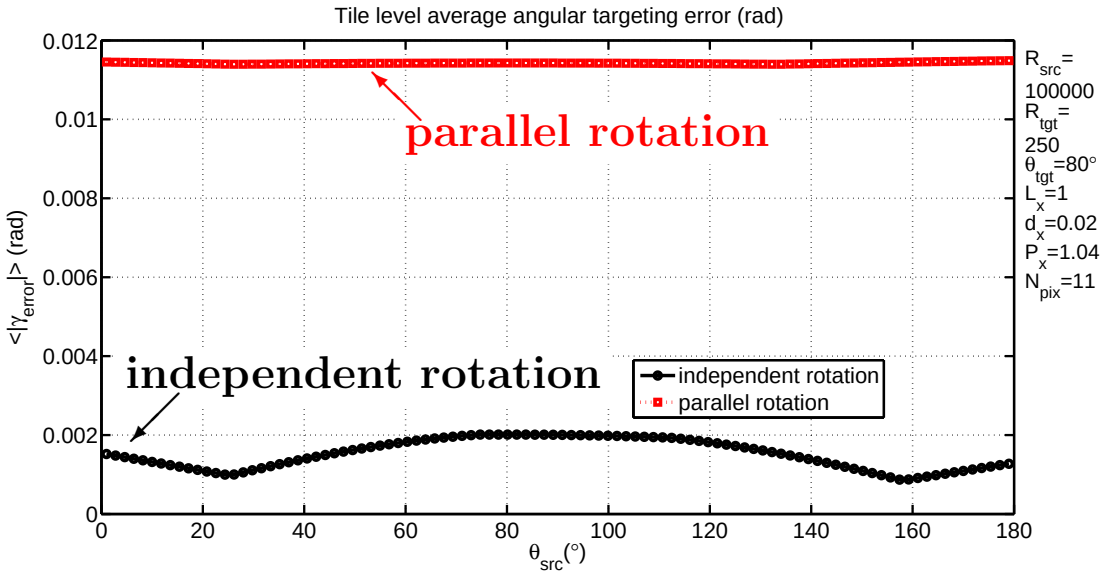

(a)

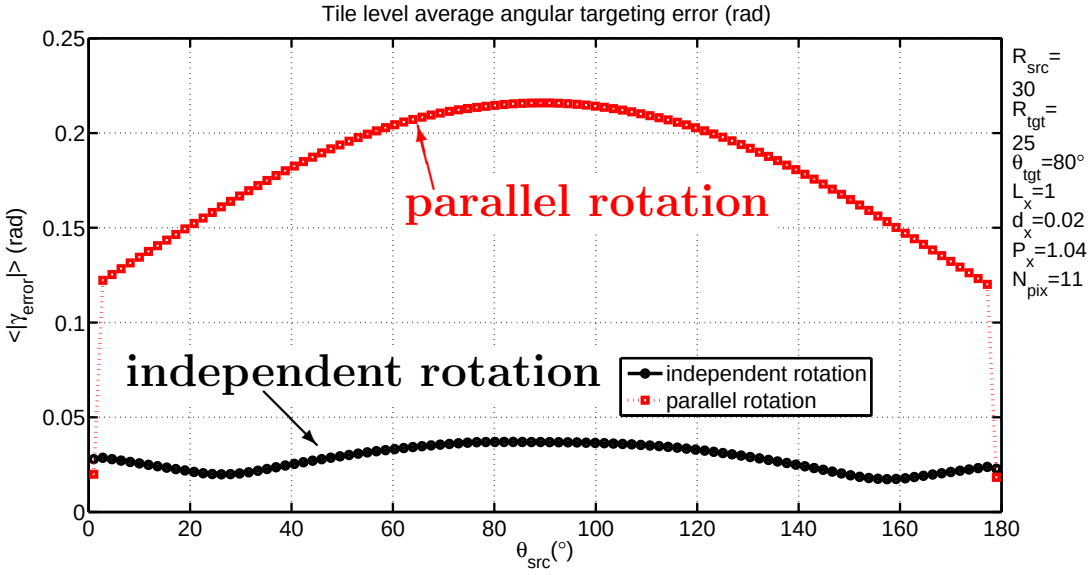

(b)

Figure 5.24: Tile-level, angular targeting error results of the parallel-latticed and the free-latticed (i.e., independently rotating pixels) tiles for $1^\circ \leq \theta_{src} \leq 179^\circ$: (a) *FAR*-case, and (b) *NEAR*-case.

5.7 Power consumption of the tile

Power consumption of the tile is expected to be only a very small fraction of the total solar power incident on the tile that has a typical surface area of 20×20 cm^2. Therefore, "self-powered" aspect of the tile can practically be satisfied with only a small percent of the tile area. Solar tracking applications do not require fast actuators in general. As such, different components of the tile such as circuitry, wireless transmission, and actuators can be operated in a time-multiplexed manner to relieve the maximum power requirement of the tile. A numerical example regarding the power dynamics of the tile is given next.

Let us assume that maximum power requirement of a 20×20 cm^2, zero-idle-power ALAR tile is 100 mW at times of motor actuation. Let us also assume that, the tile has a 2×4 cm^2 silicon solar cell with 20% efficiency[11]. Note that the area of the solar cell is only 2% of the tile area, and that the cell can be stacked on top of the control, communication, and drive electronics (e.g., microprocessor, motor drivers) to maximize mirror-area (i.e., fill-factor) of the tile. The tile is assumed to operate $1/100^{\text{th}}$ of the time, leading to about 7 min of operation over 12 hr day period and a corresponding average daily power consumption of 1 mW. Total energy consumption of the tile over the day time is calculated as $E_{total,tile} \approx 43.2$ J. Average power supplied from the solar cell ($\eta = 20\%$) on the tile with an average global radiation of 340 W/m^2 over the day is 54 mW. This is much larger than the average power consumption of the tile (1 mW), leaving plenty of room for night time usage provided that the extra energy is stored in a battery or a super-

[11]These specs for the solar cell are available commercially from a RadioShack® silicon solar cell: Model: 276-124 — Catalog ♯: 276-124 . The solar cell is specified to deliver about 0.3 A at 0.55 VDC in full sunlight, yielding an output power of > 150 mW. 2×4 cm^2 surface area at 1000 W/m^2 global normal irradiance [119] yields an input power of about 800 mW. The overall efficiency is therefore $\eta_{cell} = 100 \times 165$ W/800 W $\approx 20\%$.

capacitor.

The capacitance requirement for storage of 43 J of total daytime energy at 5 V operation can be calculated to be ≈ 3.5 F. Super-capacitors of similar specifications are available commercially[12], with > 50000 cycles of charge-discharge cycle, yielding an expected lifetime of seven decades if charged twice a day.

5.8 Pervasive solar power: Tile-level concentrated solar power harvesting

ALAR technology aims to make solar-energy harvesting a pervasive practice, in which addition of extra power generation capacity is so simple and low-cost that even arbitrary surfaces can be seamlessly involved in a ubiquitous network of solar harvesters. This requires a portable and low-weight solar harvesting technology, whose extension does *not* require any overhead such as down-time for the existing system, additional electrical wiring, inverters, tubing, support frame, or charge control circuitry.

Following thought experiment is instrumental in understanding this vision[13]: *The end user goes to a local hardware store and buys* 0.7 cm *thick,* 20×20 cm^2 *ALAR tiles that consist of a large number of small mirrors. Each tile is self-powered to steer its mirrors and reflect the incoming light to an arbitrary direction. The user comes home and drops these tiles on his/her backyard, patio or roof. Next, he/she opens up his/her internet browser, enters a password, and chooses his/her*

[12]Heter Battery Technology Co., Ltd - SuperCapacitors 5.5 V 4 F. Available online: http://www.globalspec.com/FeaturedProducts/Detail/HeterBattery/SuperCapacitors_55V_1F_55V_4F/76551/0.

[13] ALAR vision as a similar thought experiment was first phrased by Professor Amit Lal.

personal central solar tower among the list of detected ones in the neighborhood. Within seconds, each tile positions its mirrors to reflect the incident solar energy on it towards the specific collection tower selected. He/she then checks out the display of his/her smart-grid meter and starts enjoying the extra kWh's produced from the solar energy collected by the tiles.

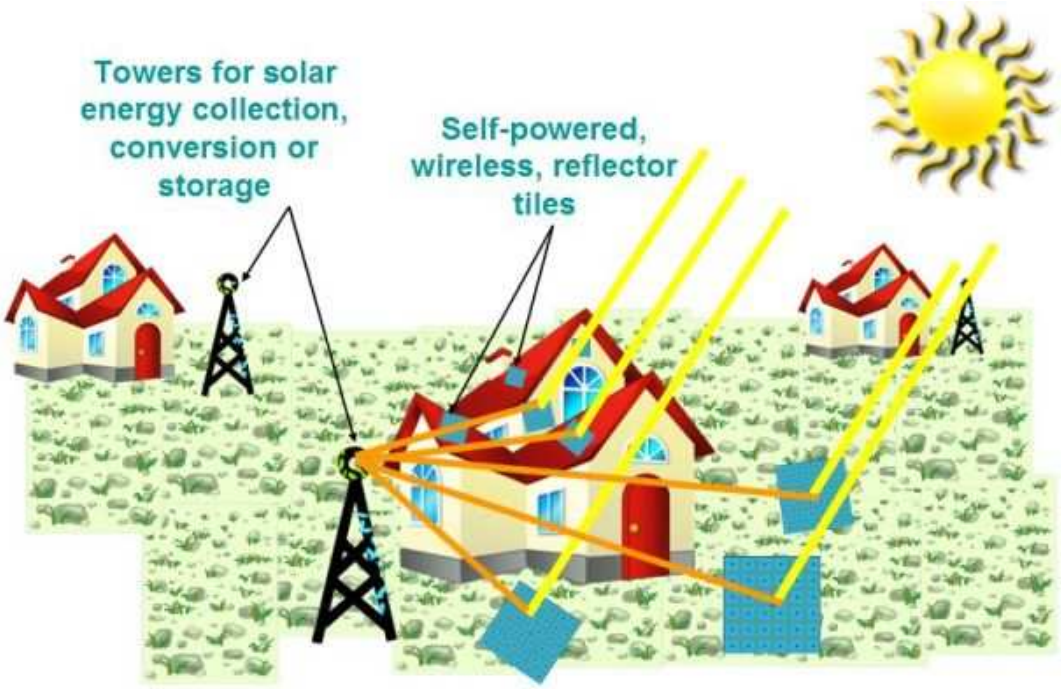

Figure 5.25: Illustration of pervasive solar harvesting with wireless, reflector tiles each of which contains mirrors that can be positioned in a self-powered manner to reflect incoming solar radiation to a desired direction.

An illustration of the described thought experiment is given in Figure 5.25. ALAR tiles are inspired by tower based CSP technology that are used most commonly in utility scale power plants, where efficiency and cost issues are extremely critical given the large amounts of investments made. On the other hand, ALAR technology differs from the conventional CSP in terms of scale, low-profile implementation, portability, and control. In fact, these are the traits that yield ALAR

technology many additional benefits and applications as described next.

Minimal installation for extension of solar harvesting: ALAR tiles can steer its mirrors to a required position autonomously, or as communicated to the tile wirelessly as soon as the tile is dropped at its location. This capability requires the tiles to be self-powered or self-charging with built in photovoltaics or other kind of energy harvesting devices. It is also possible that the tiles are powered with wires. However, this would require electrical connections for each tile as in PV modules, and manual wiring is in general undesired as it requires assembly time and material.

Each tile can incorporate an energy storage device such as a battery or a super-capacitor to provide the necessary power for operation during night-time or when the incident solar radiation on the tile is not at the required level. The life time of tiles that include battery will be limited by that of the battery for night-time operation (e.g., applications other than solar). Day-time operation should be possible even past that point.

Installation and facilities requirements can be reduced as compared to the PV technology as wiring is eliminated. The end-user can do the installation by simply nailing the tile on the desired surface, literally tiling it on the wall, or perhaps leaving it unanchored. The installation of grid-connected PV, on the other hand, might involve electrical wiring that may be a safety concern for the end-user.

Support for operation with minimal installation, while being extremely beneficial, can require additional components on the tile. Additional cost may not be justifiable for a tile, which is installed on a roof and is never moved again over its lifetime.

ALAR tiles minimize energy-loss when solar energy can directly be used for lighting and heating applications without intermediate steps of solar to DC and DC to AC conversion: Each time a light powered by a PV module is turned on during day-time, light emission from the bulb involves many lossy energy conversion processes. Firstly, the solar energy is converted to a DC voltage via the PV cell with 10–30% efficiency. The DC voltage is then converted to AC via an inverter with typically 85–95% efficiency. Finally the AC voltage is used to drive a bulb with an optimistic efficiency of 60%. Technologies like light-pipes and light-tubes installed in the house can eliminate this inefficient energy loop by simply using the sun light itself. Similar arguments can be made for solar ovens and water heating systems. It is therefore desired to have a technology that not only can use solar to generate electricity, but also one that can efficiently transfer the incoming solar radiation to other systems employed for heating, water sanitation, lighting, cooking, gardening, UV cleaning, catalyzing, cutting, and so on.

The direct use of solar energy for the tasks listed above can be supported by ALAR tiles. This point is illustrated in Figure 5.26 for a residential house that is densely integrated with ALAR tiles. The same figure is also instrumental in visualizing the paradigm shift offered by the ALAR technology. Summer and winter operations are depicted on left and right sides of the figure, respectively. The house is tiled with ALAR technology on the exterior and the interior walls as well as the roof.

All of the central collection towers in Figure 5.26 are pictured on the roof of the house. This is different than the case pictured in Figure 5.25, which shows towers to be separate from the houses. ALAR tiles on the roof reflect the incoming radiation to one of the collection towers. One tower on the roof provides the basic solar to

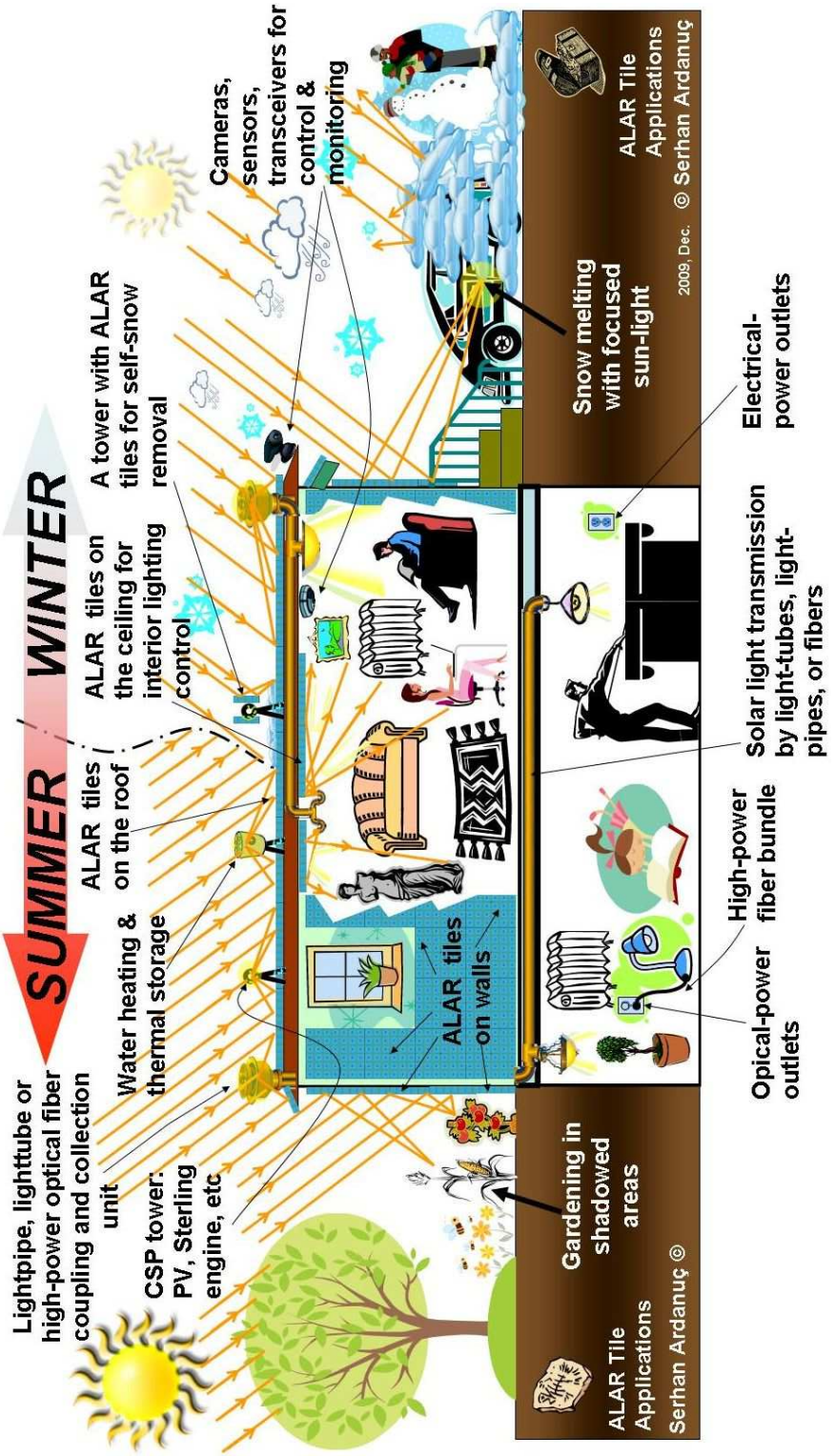

Figure 5.26: Some residential applications of solar tiles during summer and winter.

electrical energy conversion. It can incorporate means such as PV technology, steam generators, and Sterling engines for energy conversion.

Two of the structures on either end of the roof are for collection and transfer of solar light into the house via existing and/or emerging technologies such as light-tubes, light-pipes or high-power fiber optic bundles[14]. This way, one can replace electricity based lighting during the day time with solar lighting. Planting in rooms without windows, such as basements or closets is one of the applications pictured in the figure. Moreover, one can imagine that in the future, houses can come equipped with *optical* power-outlets as well as electrical ones. This way one can simply plug the optical-fiber extension of an instrument into the optical outlets, and perform operations such as lighting or solar cooking without conversion to or from electricity at any stage. This idea is entertained in Figure 5.26, where a person reads a book via a special table-lamp that uses the solar light provided from such an optical power outlet.

Figure 5.26 pictures two other types of towers on the roof. One of them is for water heating, or thermal-storage applications. The function of the other one, which is shown on the winter-side of the picture, is less straightforward. This tower itself, incorporates ALAR tiles that are positioned perpendicular to the ground in order to focus light on different parts of the roof to melt the snow. This lighthouse like operation, ensures that ALAR tiles on the roof can function without being obstructed by the snow on top[15].

Snow melting operation by concentrated solar light can be an important appli-

[14]See, for example, the technologies offered by companies such as Parans, Solatube and Himawari.

[15]This argument assumes that the lighthouse-like tower responsible from melting the snow on the roof does not get obstructed by snow. This is plausible as perpendicular surfaces get much less snow accumulation than the roof which is horizontal.

cation for colder cities that spend significant amount of money on snow plowing and removal. The ALAR tiles on the sidewalls of the buildings can be used for this purpose. Melting of snow on the car in this manner is exemplified in Figure 5.26. The tiles on the exterior surfaces of the building can also be used for distributing light to shadowed regions. For example, in the same figure, some of the ALAR tiles are used to shine light on a garden that would otherwise be under shadow during most of the day owing to the tree and the house around it.

The interior tiles are used to distribute light non-uniformly on desired objects or places where residents perform daily activities. Motion sensors, thermal cameras, and optical cameras can be used to gather required information about occupation and activity. The control can be full-automatic or semi-automatic with some human interaction involved in determining amount of solar light to be distributed on items such as statues and paints. The overall behavior of all of the tiles can be controlled wirelessly from a central command area depending on the demand on heating, lighting or electricity by adjusting the ratio of tiles that focus light on a given central structure such as towers or light tubes.

ALAR tiles make a solar investment that is almost-technology independent: Due to the large number of players in the solar market, the competition to get the best solar-to-grid efficiency is extremely tough. While this competition brings the costs down and drives the research on higher efficiency systems[16], it also brings up a dilemma to the potential solar-power user of today, who is, for instance, interested in getting PV modules installed all over the roof of his/her house. There is no guarantee that his/her PV technology is not going to be outdated 10 years from now, and produce only 70% of what his/her neighbor's new PV system can.

[16]See Figure J.3 to see the advancement of research cell efficiencies over the years.

Updating all of the modules will be almost as costly as buying and installing a brand new system from scratch. As such, he/she will probably stick to what (s)he has although the situation keeps getting worse over the years.

For a tower based CSP approach such as the ALAR technology, there is only one main generator unit at the tower to be updated. As the tiles do not need to be replaced, the amount of material and labor used for the technology update are significantly less than those of PV systems, where each module needs to be replaced to make the most out of the new, higher-efficiency technology. As such technology update of *only* the tower reduces the long-term cost of ownership of having a high-efficiency solar to electrical energy conversion technology.

Another common selling point for tower based concentrated solar power systems is the fact that photovoltaic cells, which are exclusively made on expensive substrates for decent efficiencies ($> 15\%$), are replaced by mirrors that are made by coating glass with commodity materials like aluminum or silver. This offers a cost advantage without decreasing the available input energy, while possibly paving the way to higher efficiencies as described in Appendix J. The cost of the ALAR tile will still need to compete with PV cells.

Concentrated solar harvesting in urban areas and sustainable agriculture in cities: Concentrated solar power (CSP) systems are widely used in utility-scale, solar power harvesting due to their lower cost per Watt attribute. Incredible savings to the economy can be possible by building concentrated solar power systems on unused, non-windowed regions of buildings. However, installation of these structures in highly dense, packed, urban areas is not feasible due to very large area heliostats or parabolic mirrors currently used in these systems.

Figure 5.27(a) illustrates the awkward picture that would arise from using conventional, large-area heliostats on building roofs and sidewalls. The cost of installation, the extra weight incurred in the support, wind loading concerns of the buildings, large space consumed, and unattractive architectural look are some of the fundamental concerns. Therefore, there is an unmet need in bringing utility scale CSP systems to cities, buildings, skyscrapers, roads, in short to our daily lives.

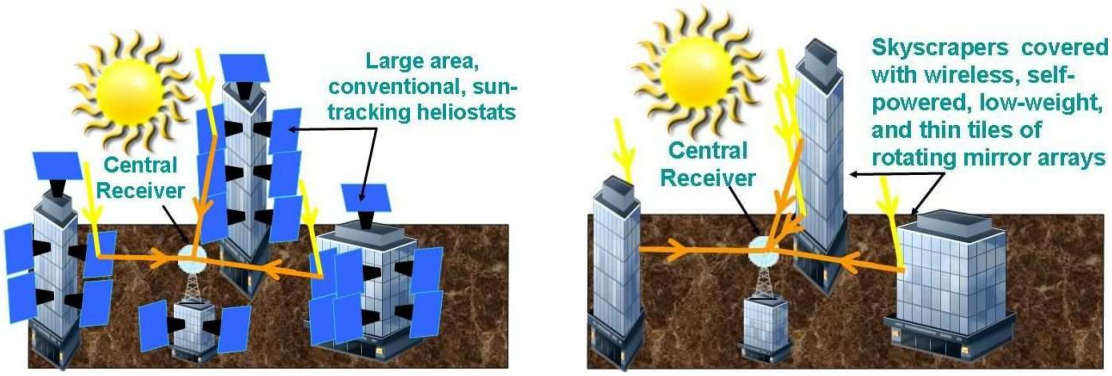

(a) (b)

Figure 5.27: Comparison of CSP in cities between implementations with (a) large area, solar-tracking heliostats, and (b) ALAR tiles. In both cases, central solar collection towers are implemented on the roofs of neighboring buildings.

Thin, small form-factor, lightweight and easy installation attributes of ALAR technology solve the above problems of large-area heliostats. This is pictured in Figure 5.27(b). ALAR tiles merge the cable-less installation attribute of the heliostat based CSP technology, with coatable and lightweight attributes of the photovoltaic technology. It essentially provides a smart surface coating to any structure. ALAR technology, enables integration of arrays of very small-area, sun-tracking, self-powered mirrors into thin tiles so that CSP aspect can be entrenched into building walls or roofs almost seamlessly. Tile-level integration on the building sidewalls does not cause shadowing over windows as conventional heliostats would

do in the case portrayed in Figure 5.27(a).

A distinguishing aspect of these tiles is that they can communicate wirelessly, so that the angle of incidence from a given surface can be controlled remotely, when a given application requires more than automatic sun tracking. For instance, every tile can act as a pixel for a very large-area, reflective display for which slow refresh rates are acceptable. This makes a unique application area for ALAR tiles, as any surface could be turned into a large, low-power, billboard with straightforward installation, without any wiring. While one side of the building which faces the sun most directly at a given time of the day is used for energy harvesting by CSP, the other faces can be used for display applications.

The efficiency of renewable energy technology is more crucial in crowded cities, where infrastructure surface area per capita is less due to large number of apartments and skyscrapers. The support of ALAR technology for high efficiency electrical generation, with minimal cost of technological update is invaluable in this regard. It is also important to be able to store the energy produced since *intermittency* or large and long-lasting fluctuations in the power output of a renewable technology is problematic for grid connected systems. There is significant amount of research and development in batteries, thanks to the drive for electric vehicles. Until that time comes when everybody can point to an economic and environmental energy storage technology as the winner, support of ALAR technology for well-established *thermal-storage* practices is very appealing.

Given the carbon emission from gasoline motors during the transport of food and the requirement on freshness of food, it is interesting to note the similarity between electricity and food consumption. Both are more sustainable when they are local and freshly harvested/produced. As described above and illustrated in

Figure 5.26, ALAR tiles also allow indoor agriculture with the help of a network of optical-fibers or technologies like solar tubes and pipes. In this respect, ALAR technology has a significant potential to make our urban-life more sustainable. However, possible health concerns related to unintended exposure to concentrated sunlight should be investigated.

The above scenarios of CSP integration into cities allows sustainable generation of electricity: *closest to the place where it is consumed, and at the time it is consumed*. The generation of electricity in such a way relieves the requirements on transmission and storage of electricity. On the other hand, we do not see utility scale power plants in downtown areas, where the consumption of electricity is significant. The dangers, environmental and health implications of having a nuclear plant or a coal plant in a densely populated region are obvious. Furthermore, often times these plants are not even welcome by people living in the neighborhood even if they live miles and miles away. As such, renewable, pervasive, and green technologies like ALAR provide an outstanding opportunity to redefine the environmental footprint of living in crowded cities.

5.9 Applications of ALAR tiles

Some of the main application areas of ALAR tiles are as follows:

1. Collection of radiation at a central tower or location for subsequent heat, electricity, or power production unit such as photovoltaic cells, Sterling engines, heat storage plants or steam turbines. These application are explained in detail in the previous section and are illustrated in Figure 5.25, Figure 5.26, and Figure 5.27(b).

2. The focused or redirected light can be targeted to a certain point to perform desired tasks of large-scale burning, heating, curing, catalyzing, reacting or transforming such as water sanitation, snow melting, cooking, chemical charging of a battery, or photosynthesis.

3. Concentration of light on different optical components such as lenses, beam splitters, beam collimators, and expanders for subsequent large-scale, light processing or optical/wireless power transfer.

4. Concentration of light on light pipes, fibers or other optical waveguides for distribution.

5. Replacement of mirror surfaces of the tile with small-area modules such as photovoltaic cells or thermoelectric generators (possibly with microfluidic and electrical connections to the tile) in order to add tracking, steering and directional functionality to a given application within a tile-like, thin profile.

6. Individual pixels can be manufactured with different sub wavelength diffraction gratings to appear at different colors, at different viewing angles for display applications in billboards and active architectural components.

7. Generation of different light effects that can be observed on the tiled surface itself or any target location through diffraction, reflection, interference for display, projection, and optical spectrum filtering. These effects can be dependent on the observer's location with respect to the tile, as well as the optical spectrum the observer is responsive to. ALAR technology can have potential use in 2-D and 3-D (volumetric) displays, holography, and 3-D optical scanning in this manner.

8. Similarly, the cover of the tile can be coated with different color filters to yield large scale zero-idle-power displays.

9. Concentration of light on certain volumes of gas, or on certain parts of a photosensitive material for 3-D lithography, chemical activation or thermal mobilization of molecules.

10. Replacement of mirror surfaces with sensors, actuators, and energy sources such as condenser microphones, acoustic reflectors, light emitting diodes, solid state laser diodes, directional RF antennas lets scaling of small scale devices to larger scale versions with added benefit of directional control, actuation, and sensing.

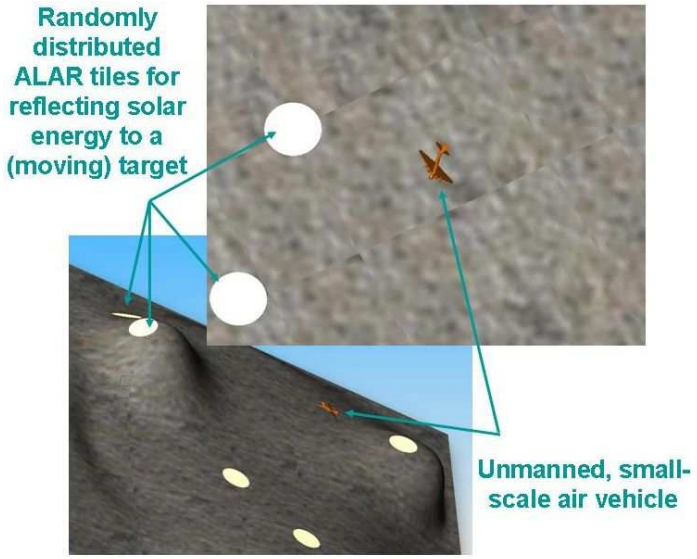

Figure 5.28: Wireless power transmission as an application of ALAR tiles.

11. Wireless power transmission to (moving) objects whose surface area is not large enough for powering only by unconcentrated sun. ALAR tiles randomly distributed on a territory can provide concentrated solar power to PV structures on the object. Powering of unmanned, small scale air vehicles with integrated PV on their wings is one example of such an application, and this specific case is illustrated in Figure 5.28

A recent report by The Royal Society entitled "Geoengineering the climate: science, governance and uncertainty" is referenced in order to mention one last example of an application for the ALAR technology [120]. This document reviews solar radiation management (SRM) methods to fight against global warming. Covering a part of earth's surface with reflectors to modify the surface albedo is among the reviewed methods for SRM.

One can imagine ALAR tiles being used to reflect the light back into the space for part of the day, while they get engaged in a myriad of other applications as itemized above for the rest of the day. ALAR tiles can, in this way, provide additional economic incentives for the realization of large-area, surface albedo modification projects at both governmental and residential level. Otherwise, covering large areas of land with reflective mirrors, only to reflect the solar radiation back into the space, involves great obstacles regarding funding and timescales of implementation.

5.10 Methods of manufacture: From micrometer to centimeter scale

Section 5.2 on scaling of mirrors mentioned two scales of manufacturing technologies for ALAR tiles. One is the microfabrication processes on low-cost substrates (microscale), and the other is mesoscale manufacturing. While there is not a strictly defined boundary in this distinction of scale[17], the transition can be assumed to occur around a mirror side-length of ≈ 1 mm.

It is possible that an operating principle for steering the pixels in one or more

[17]By the term "scale", characteristic side length of the mirror is referred, not the thickness.

dimensions can be implemented both in microscale and mesoscale. However certain actuation methods might be more suitable for one scale than the other. For instance electrostatic assembly at mesoscale is not feasible due to high volume to surface area ratios, while it is very useful at microscale.

Availability of low-cost, mass-production methods as in the toy industry is an important motivation for mesoscale implementations of ALAR tiles. These are more likely to be parallel-latticed, given the challenge of integrating hundreds of actuators within a thin tile. On the other hand, microscale mirror-size might be more suitable for free-latticed tiles.

There is a rich literature, in the field of optical microsystems and adaptive optics, on how to make large arrays of movable/steerable micro-reflectors [4,121–126]. The following section reviews some of the existing micromirror technologies for *tile-level*, large-area, beam redirection applications and comments on their suitability based on the mirror specifications listed on page 136.

5.10.1 Comments on using available micro-mirror technologies for ALAR tiles

One of the best known examples of a micromirror array is DLP^{TM} from Texas Instruments [127]. Schematic and SEM pictures of this device are shown in Figure 5.29 [12]. DLP^{TM} microchip functions as a reflective digital light switch for projection displays. Operation of every pixel on the chip relies on the electrostatically actuated motion of a micromirror connected to a torsional hinge. This technology, with underlying CMOS circuitry and numerous proprietary techniques developed for its reliable operation, is often quoted as a milestone in the develop-

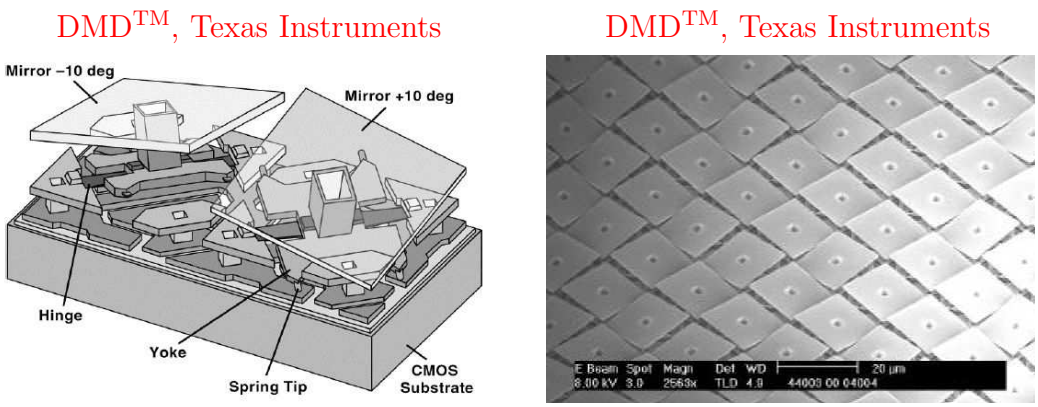

Figure 5.29: (a) Schematic and (b) SEM views of the Digital Micromirror Device (DMD™) from Texas Instruments [12].

ment of complex microelectromechanical systems.

The mirror pitch of DMD™ can be made smaller than 15 μm [12], thanks to the resolution offered by optical lithography. However, surface micromachining and electrostatic actuation limit the maximum optical rotation angle (2θ) to less than 50°. This level of rotation is sufficient for on-off type light switching applications, but it becomes a significant limitation of dynamic range, if one is interested in applications like solar concentration. In addition, digital nature of DLP necessitates bistable operation, which is not really suitable for the analog (i.e., all-angle) operation necessary in beam redirection and concentration applications.

DMD™ does not have 2-DOF steering capability. ALAR tiles, on the other hand, should be able to support 2-DOF motion of the mirrors for a general solar tracking or beam redirection operation. There are gimble-less [126, 128] and with-gimble [121] approaches to getting 2-axis and 3-axis steerable mirrors. Many such microsystems implementations, however, do not have the large-angle rotation capability. Even when large angle rotation of individual axes is achieved on a device, simultaneously supporting large-angle rotation along both axis is an addi-

tional challenge. Raising the plane mirror above the substrate and electrostatically actuating it from that raised state is very useful to obtain relatively large-angle rotations in surface micromachined devices [5]. But, lack of latching after mirror rotation and low-fill factor remain to be weak aspects of this approach.

Single-axis rotation angles of more than 120° are reported from mirror structures with thermal actuators [129], yet they suffer from large power consumption, changing curvature of reflector surface, and low fill factor.

Planar micromirrors erected and latched on top of rotary-stages yield $> 360°$ azimuthal rotation capability and ability to maintain the mirror's position in the absence of electrical power [18] [115, 116, 130]. These 1-axis designs are promising for future micro-scale implementations of 2-axis ALAR tiles.

None of the above referenced work was intended to be used for an application such as CSP, so it might be the case that the extension of the above work to satisfy CSP requirements might be straightforward. However, at the time of writing, the author is not aware of a micro scale replacement for large heliostats as used in utility scale CSP, with mirror-array attributes listed on page 136.

5.10.2 MEMS for Concentrated Solar Power: The current state

The only research effort on using steerable micro-mirror arrays for large area solar applications, to the author's best knowledge, is from University of Kassel in Germany [13, 14, 103, 131, 132]. They mention applications such as heat protection,

[18] In other words, mirrors support zero-idle-power operation.

room lightning, and solar concentration on PV modules. Their work, about which the author became aware after ALAR tile development efforts started in his research group, relies on electrostatic actuation of micromirrors that are located at the tip of cantilever beams. SEM and schematic illustration of these mirrors are shown in Figure 5.30 at open (left) and closed (right) positions [13]. These beams are self-assembled due to the residual stress of the thin-films. Consequently, the mirrors are positioned close to vertical in the absence of an actuation voltage (left column of images in Figure 5.30). When a voltage is applied between the cantilevers and the substrate, electrostatic force works to move the cantilevers toward the substrate (right column of images in Figure 5.30). This results in 1-axis steering of the mirror region at the free-end of the cantilever.

Optical pictures of the mirrors developed in University of Kassel are shown in Figure 5.31(a) and Figure 5.31(b), with and without actuation, respectively. Their fabrication process is simple, as required for any future implementation of a low-cost, large area CSP or indoor light-redirecting application. However, there can be some fundamental limitations stemming from using only on-wafer, cantilever-like, electrostatically actuated mirror structures and residual-stress based self assembly. Some of these are limited rotation range due to electrostatic pull-down, dielectric charging possibility, focusing behavior that depends on radius of curvature, and bending of the composite beam due to thermal mismatch of the structural layers as a function of the incident power-level.

MEMS on low cost substrates for large-area solar applications is an exciting new idea, and it offers many interesting applications as described in Section 5.8. However, the realization of a few milimeter thick, *free-latticed* ALAR tile with *microscale* mirrors may have to wait until a reliable and complex surface micro-

Viereck *et al.* , University of Kassel - 2007

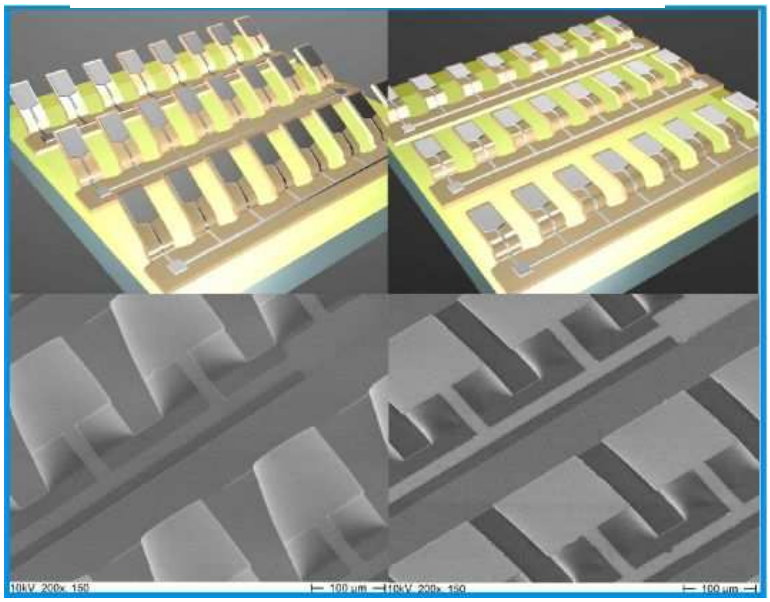

Figure 5.30: SEM and schematic illustration of the micro-mirror array concept by Viereck *et al.* [13]. Application of a voltage actuates the mirrors from close-to-vertical position to close-to-horizontal position.

Jäkel *et al.* , University of Kassel - 2009

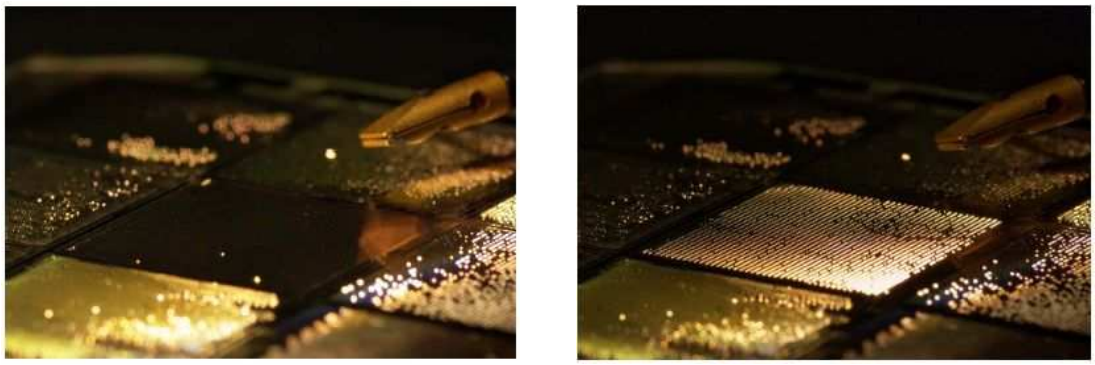

(a) (b)

Figure 5.31: Optical picture of the micromirror array by Jäkel *et al.* [14] (a) with actuation and (b) without actuation.

machining process such as SUMMiT V^{TM} is available at a competitive cost per unit area with that of a high-efficiency PV process.

5.11 Considerations regarding the operation of ALAR tiles

Discussions so far have left out detailed investigation of many issues regarding the operation of the ALAR tiles such as environmental considerations, determination of position and orientation of the tile with respect to the tower, control of the phase of the reflected wavefront, wireless ad-hoc sensor and actuator networks of ALAR tiles and its security, health and architectural considerations, cleaning of the tiles and so on. Only the first of these topics is discussed in this section.

5.11.1 Environmental considerations:

Development of ALAR tiles is a multi-disciplinary effort: electrical drive, mechanical design, tower collection efficiency optimization, wireless communication, lifetime and reliability analysis should all be considered from engineering and architectural points of view. One aspect, which is above and beyond all these points, is the environmental impact of the ALAR technology. Despite the rather shiny outlook mentioned so far about this technology, the issue about environmental implications of covering everywhere with a man-made structure is tremendous.

Extreme care should be paid on the type of the material used to build the tile; be it bio-degradable plastic or be it glass. The same holds true for the peripheral components used on the tile as well, such as actuators, motors, and batteries. For instance, if an electrolytic or radioactive battery is used, extremely strict regula-

tions must be enforced, given the possibility of the tiles being used all around us. Likewise, lead content of any motor or actuator is a key issue. U2EBA that uses PZT (lead zirconium titanate) may not be a good choice in this respect. The same can be said for the ultrasonic motors that uses PZT. Therefore, should piezoelectric materials be used in the tile, it may be necessary to consider environmentally-safer types than the ones which are most readily available or perform the best. With the same token, reassembly, reuse and recycling of the tiles must always be kept in mind.

Environmental aspects of ALAR technology are not only limited to the tile. Wide-spread use of central receiving towers is a concern for habitat. For example, hot outdoor regions of central receivers, if any[19], can be attractive for birds to nest and can get them hurt. All of these challenges and alike should be considered from the design till the end-of-lifetime of the tile, with a mindset that honors the grave nature of the environmental issues. Otherwise, *harming the environment* in the name of *saving it* could be one of the most likely pitfalls awaiting the ALAR technology.

5.12 Summary

There is a finite amount of carbon-based fuels on earth that can be used for the world energy needs. On the other hand, daily solar radiation on earth can potentially meet the demand for years. As such, the switch to renewable energies such as solar is bound to happen, unless there is a dramatic change in the patterns of global energy use. Earlier this transition happens at a larger scale, the better will

[19]In an efficient, well-insulated tower, this should not be the case.

it be for the environment and large number of people on earth whose access to electricity is limited. This transition can be much faster with pervasive, *drop & enjoy (D&E)* systems that require minimal amount of additional installation for extension.

Such a technology is proposed in this chapter by making use of All-angle, LAtchable, Reflector (ALAR) tiles incorporating micrometer to centimeter scale, steerable mirror arrays. This technology is used to redirect solar (and other forms of) radiation to a desired point in a portable, scalable, and possibly self-powered manner. *D&E* aspect of the tiles with wireless controls to position the mirror array on the tile is emphasized.

Plenty of applications for ALAR tiles, some being novel, are mentioned in the chapter. These applications include tower based concentrated solar power applications in urban areas, automatic snow melting for buildings, indoor lighting control, indoor-gardening, and reflective billboard displays.

Both MEMS technologies and mesoscale (milimeter to centimeter scale) manufacturing techniques can be used to produce ALAR tiles of different mirror dimensions. For the former approach to be feasible, development of large-area MEMS processes on low-cost substrates is required. Therefore, tiles with larger scale (milimeter to centimeter) mirror arrays looks more like a near-term goal. This is also apparent from the first prototype, which was implemented with centimeter scale mirrors.

The second prototype, which had pivoted mirror pixels, light-tracking, and wireless control capability is presented in detail. Basic modeling efforts and optical simulations of the prototype are described along with the scaling arguments for the

size of the mirrors on the tile. Some important points about the power consumption of the tiles are made. In addition, the environmental implications of covering everywhere with a man-made structure are emphasized.

CHAPTER 6

CRYSTAL OSCILLATORS AS CAPACITIVE READOUT CIRCUITS: NONLINEARITY COMPENSATION & SELF-TEMPERATURE SENSING

6.1 Introduction

6.1.1 Quartz based sensing

It is generally believed that frequency can be measured with better accuracy than any other other quantity [133]. As such, measuring the shift in resonant frequency of an oscillator under physical, chemical or electrical stimulus can deliver outstanding resolution. Quartz crystals, with their high frequency-quality factor (fQ) products, are a common choice for the frequency determining elements in these oscillators. Furthermore their exceptional intrinsic frequency stability enables use in frequency-control, time-standard applications, and sensors of various types. The ability of quartz crystals to operate with single-transistor sustaining amplifiers at low power, their low motional resistance, and numerous well-known crystal cuts to optimize their properties set very high standards for competing resonator technologies.

Sensing with quartz crystals is accomplished either with the crystal itself being exposed to the stimulus directly, or via electrical sensing of an impedance variation of another device (possibly resistor, inductor or capacitance) electrically connected to the crystal. In this chapter, the former approach is referred as *direct*, and the latter as *electrical* sensing. The direct type quartz sensors seem to be

more common in the literature, thanks to the popularity of quartz microbalance sensors. They can be used for thickness measurement in physical vapor deposition systems, viscosity measurements, absorbtion/desorbtion detection, and electrochemical sensors [134–136]. Physical, inertial sensors are also possible with quartz crystals. Norling reports on a micromachined quartz force sensor operated as a simple, sub-μg accelerometer accurate enough to detect lunar-solar gravitational fields on earth [137]. Bianchi *et al.* uses quartz oscillators as pressure and temperature sensors, which can also be classified under the direct sensing group [138].

As an example for electrically sensing quartz sensors, Matko *et al.* uses a quartz resonator to detect the capacitance shift due to a liquid-volume change in a container [139]. Tanaka *et al.* describes a vapor sensor by sensing the electrical impedance change of a parallel plate capacitor [140]. An effort in 1990's at Sandia Labs attempted to build an accelerometer using a micromachined quartz based capacitive sensor [141]. Any stimulus which shifts the resonance frequency of quartz with high signal to noise ratio (SNR), constitutes a good candidate to be sensed by a quartz resonator. Both the direct and electrical sensing methods essentially lend themselves to frequency modulation since the signal information is inherently stored in the frequency and phase as opposed to the amplitude.

The sensors with frequency modulated output can qualitatively be compared to the more conventional type of sensors with amplitude modulated output. As far as transmission across a noisy channel (White noise, gaussian, zero-mean) is concerned, signal to noise ratio performance of Frequency Modulation (FM) is better than Amplitude Modulation (AM)[1]. This advantage, of course, does not come for free. FM requires more channel bandwidth for the transmission of the same

[1]Many textbooks on communication systems include a section which compares the noise performances of FM, AM, and base-band transmission as a function of modulation parameters. See for example [142, §5.8, Figure 5.19] or [143, §7.9, Figure 7-26].

signal with the same inherent information bandwidth. The ideal system performance for a given bandwidth can be determined from Shannon's channel capacity theorem [143], that describes the tradeoff between SNR and channel bandwidth. This observation sheds some qualitative insight into why, many signal processing circuitries for capacitive read-out crave for more bandwidth than the baseband signal itself in order to improve SNR. In the context of capacitive accelerometers, for instance, Kulah *et al.* claims sub-μg resolution using a $\Delta\Sigma$ converter that operates at much higher sampling rate than the Nyquist rate.

The challenge to get the "best" sensor has a much broader scope than maximizing sensitivity [144]. Minimum detectable signal, 3-σ variation of sensor parameters, nonlinearity, noise density, temperature or magnetic field sensitivity are also very important. Last but not the least, the cost is crucial. This list can in general be extended to include sensitivity to any environmental variable other than the one being measured. Because, overall stability is a function of all these factors. Next two subsections will give an overview of the short-term stability offered by quartz in the presence of environmental fluctuations.

6.1.2 Stability considerations in capacitive readout for sensors

When ordering a sensor, the customer is given the option of choosing the operation temperature range of the product. Going from standard to military grade, the temperature range of operation expands to include lower and higher temperatures, of course at an increased cost. Military specs for temperature can typically be from -55°C to 125°C. Given this temperature span of almost 200°C, even single

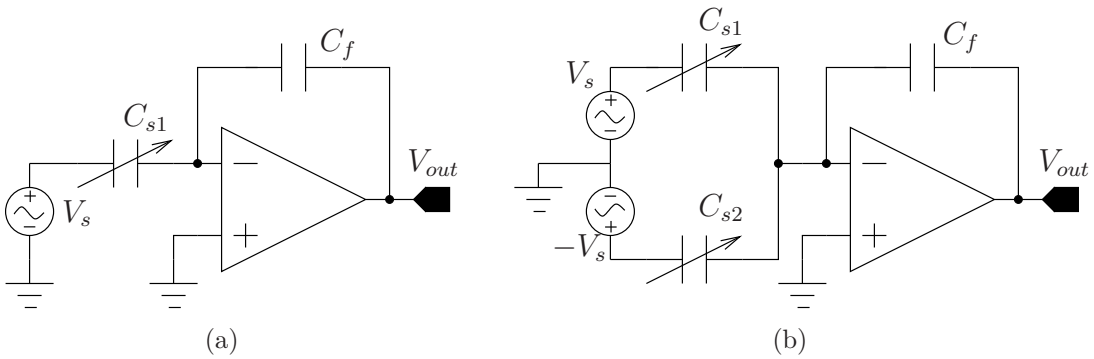

Figure 6.1: Typical opamp based capacitance readout schemes for (a) single mode and (b) differential mode.

digit ppm level sensitivities can degrade the accuracy of a capacitive sensor to unacceptable levels, depending on the ratio between the sensitivity of target entity to be measured to that of the temperature.

Transimpedance amplifier based configuration is a commonly used method of capacitive readout, and it is also the ancestor of many switched-capacitor type amplifiers [145, ch. 19], [146, ch. 5 and 11]. Single and dual mode versions are shown in Figure 6.1(a) and Figure 6.1(b), and their output voltages are expressed by Equation (6.1a) and Equation (6.1b), respectively.

$$V_{out} = -\frac{C_{s1}}{C_f} V_s = \alpha_C C_{s1} \tag{6.1a}$$

$$V_{out} = -\frac{(C_{s1} - C_{s2})}{C_f} V_s = \alpha_C (C_{s1} - C_{s2}) \tag{6.1b}$$

In Equation (6.1), the temperature stability of the proportionality constant α_C, which is the ratio of a voltage entity to a reference capacitance, needs to be understood. In the following discussion, the temperature stability of the voltage is discussed first, then that of the capacitance term follows.

If we exclude oven controlled systems, which are very power-hungry, many of the high-stability voltage references are implemented using bandgap-voltage refer-

ences. By using curvature compensation, post-fabrication trimming, and proprietary methods, 5 ppm/°C stabilities are achieved both in research and commercial VLSI chips [147, 148]. The reader can appreciate the engineering to reach single-digit ppm/°C values of temperature sensitivity much more, if (s)he considers that silicon bandgap has a much larger temperature coefficient[2] at room temperature, around 240 ppm/°C [149, p. 10].

Considering the capacitive dependence of α_c in Equation (6.1), the temperature coefficient of capacitance (TCC) of standard materials are considerably higher than the state-of-the art values mentioned above for voltage references. Both temperature coefficient of linear expansion and temperature coefficient of dielectric permittivity play a role in determination of TCC. Cockbain and Harrop describes a general relation between TCC and the relative permittivity of the dielectric valid for some cases [150]. They predict that for some materials, it is possible to get almost vanishing temperature sensitivity at a particular temperature. Silicon dioxide looks promising in this respect. However, they do not give details about the largest temperature range this behavior can be maintained. In practice, solid dielectric capacitors made out of silicon dioxide - silicon nitride insulators with TCC $\approx$ 50 ppm/°C are commercially available [151]. A paper published in 1971 reports ultra-high stability from a gas capacitor: |TCC| $<$ $\pm$2 ppm/°C over more than 200°C temperature range [152]. Despite the excellent performance, the size and the complexity of this design is not encouraging for daily applications. Toth *et al.* describes a low-cost stable reference capacitor that uses air as the dielectric with TCC$<$ 18 ppm/°C over a temperature range from -20°C to 75°C [153]. Unless some kind of cancellation is maintained, which is very challenging for large temperature ranges, the overall temperature coefficient of α_C is determined by the

[2]The reference quotes $\frac{\partial E_g}{\partial T} \approx -2.73 \times 10^{-4}$ eV/K for the temperature sensitivity of the bandgap energy at 300 K.

less stable of V_s and C_f. On the other hand, even the best stability reported above from both reference capacitors and voltage sources is almost an order of magnitude worse than the intrinsic temperature stability achievable from quartz XTLs without any compensation. Uncompensated temperature stability (averaged over -10°C to 70°C) better than 0.5 ppm/°C is common in fundamental mode of certain cuts of quartz crystals [154, 155]. This brings us to the conclusion that stability of quartz is just as invaluable for sensor applications as it is for frequency control and timing applications. Monolithic integration of a CMOS readout circuit with on-chip reference capacitors as in Figure 6.1 can be enabling for an application where miniaturization is priority. Yet, for other applications where stability is more critical than compactness, one has reasons to believe that quartz based sensing offers the state of the art.

6.1.3 Dual-mode microcomputer compensated crystal oscillators

Temperature stability of quartz based frequency references transitioned to a whole different level with the advancement of dual, c-mode, SC-cut quartz resonators [15, 156, 157]. In this mode of operation, the crystal is simultaneously resonated in fundamental and third harmonic c-modes. The beat frequency between these two modes, named as f_β, is expressed as in Equation (6.2), where f_1 and f_3 denote the fundamental and the 3rd overtone frequencies.

$$f_\beta = 3f_1 - f_3 \tag{6.2}$$

Experimental implementation described in Schodowski's work is given in Figure 6.2(a) [15].

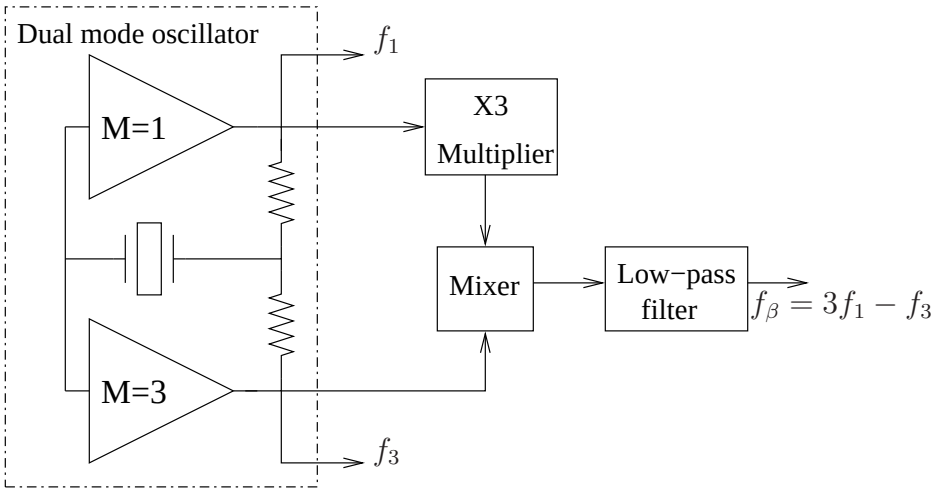

(a)

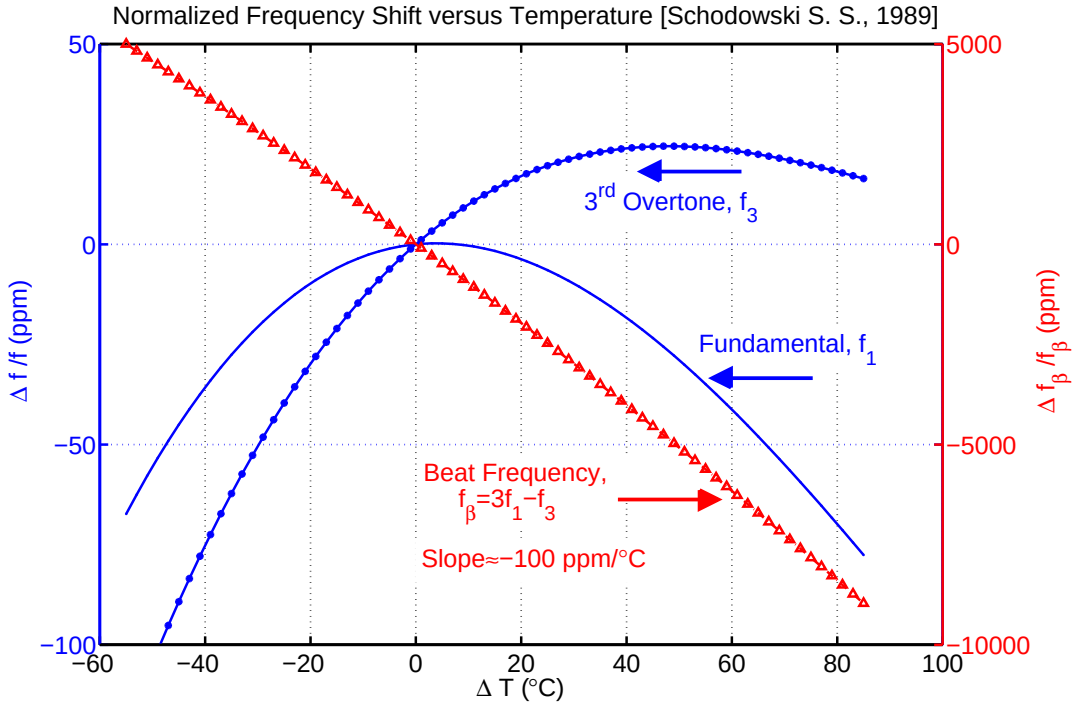

(b)

Figure 6.2: Dual mode operation block diagram and frequency versus temperature difference characteristics [15]. Reference temperature is taken as 0°C. (a) Extraction of the beat frequency, f_β from the first and 3rd overtone frequencies of a c-mode, SC-cut XTL. (b) Frequency versus temperature characteristic of the beat frequency and its components. The linear single valued nature of the beat frequency in the region of operation is used for self-thermometry of the crystal.

One of the most important advantages of dual c-mode, SC-cut oscillators is almost linear dependence of the beat frequency on temperature. Figure 6.2(b) plots the temperature dependence of the fundamental and third overtone as well as the beat frequencies from the data presented by Schodowski. Here x-axis represents the difference between the operation temperature T and the reference temperature T_0, i.e., $\Delta T = T - T_0$. The linear dependence of the beat frequency on temperature enables accurate self-temperature sensing for the XTL.

Secondly, note the orders of magnitude larger scale on the beat-frequency axis than that of the first and third harmonic frequencies in Figure 6.2(b). The relative sensitivity of the beat frequency on temperature is much larger, hence making it much more appropriate to extract temperature than the fundamental or the third harmonic modes. The latter two do not even have a one-to-one frequency versus temperature characteristic.

The detailed procedure to compensate for temperature changes in sensors and time references are described in references [133, 136, 156]. In general, if we assume that each resonance frequency of the crystal is a function of N quantities with pre-calibrated proportionality constants, then the knowledge of N frequencies allows simultaneous solution of the value of each of the N quantity. The crucial attribute of the dual mode operation is the self thermometry aspect, which eliminates the need for a separate thermistor that introduces and suffers from thermal gradients due to different time constants or spatially non-homogeneous heating. Stabilities on the order of 0.01 ppm are reported from dual c-mode SC-cut resonators over temperature ranges from -55°C to 85°C [133, 156]. Note that this stability corresponds to an average stability of 100 parts-per-trillion/°C and shows more than four orders of magnitude superiority than the best voltage references that were

described above. Pierce *et al.* lists some other advantages of SC-cut crystals including stress compensation, thermal-transient compensation, and lower number of activity dips.

6.1.4 Motivation for quartz based capacitive sensing

This chapter describes quartz based oscillators as capacitive sensors, focusing on circuit design aspects and minimum detectable signal (MDS) of capacitance and the sensed variable. Optimization of the topological connection style of the XTL resonator to the oscillator feedback loop is investigated for a given sensor capacitance range, and the implications on the circuit side are discussed. Series and parallel loading cases of the quartz crystal are analyzed and compared to each other through general models of oscillator amplifier models.

As mentioned in the previous subsections, quartz XTLs present an outstanding performance as sensors. Self temperature sensing capability offered by dual-mode microcomputer compensation and large quality factors for a given frequency are crucial in this respect. There is and there will always be room for lower power sensors and smaller packages at a given performance level. Apart from research in material science, this requires efforts in circuit design, manufacturing, and packaging.

A complication which is somewhat easier to deal-with for frequency references, but becomes an indispensable specification for sensors is *linearity*. Self-temperature sensing or external sensors in conjunction with lookup tables can be used to compensate for changes in temperature or other environments. Yet, imposing nonlinearity compensation on top of all these lookup tables is not feasible, as having an

external sensor for this purpose could defeat the purpose of trying to build a sensor to begin with.

An example will make the issue of cross-sensitivity mentioned above more clear. Let us consider the case of a quartz based capacitive sensor application, where the XTL oscillator has a capacitance and an average temperature sensitivity of 50 ppm/pF and 0.5 ppm/°C, respectively. If the temperature fluctuation in the medium is ±0.5°C, then a lower limit on the minimum detectable capacitance becomes $(1°C \times 0.5 \text{ ppm}/°C)/(50 \text{ ppm/pF}) = 10$ fF. This limitation can be eliminated, if one knows the current temperature as well as the calibrated temperature sensitivity of the output. Dual mode oscillation concept to determine temperature, as explained in the previous subsections, is an excellent solution to this problem [136]: it yields accuracy at relatively low-cost. The problem at hand is more complex, however, since the sensitivity of a typical oscillator to capacitance is also a function of capacitance, i.e., capacitance sensitivity is not constant as a function of the operating point. The consequent question, which this chapter also deals with, is the following: Is there a way of compensating for this nonlinearity? Better yet, could we do it without a dual mode oscillator?

As another means of reducing cross-sensitivity, differential capacitance structures as shown in Figure 6.3 are very useful. If one can measure both capacitors using the same resonance mode of the same crystal, the offsets in the sensed entity from interfering entities cancel during the subtraction inherent in the differential measurement. For example, with a capacitive tilt sensor, while single-ended measurements can be influenced from power supply fluctuations, differential measurement can significantly quench the adverse effect of these fluctuations up to an extent limited primarily by fabrication tolerances. Differential capacitance read-

ing is common in MEMS accelerometers [33,158,159], capacitive proximity sensors, and capacitance bridge configurations as it offers superior common-mode rejection than single capacitance reading [146, §4.5.3].

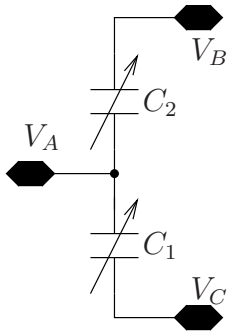

Figure 6.3: A three terminal differential capacitor sensing configuration.

Quartz XTL resonators can be (made) sensitive to many variables such as mass, temperature, and pressure. The standing of *capacitive* sensing among these variables is of concern. First of all, capacitive sensing is electrical sensing, not direct sensing. Therefore, sensing can be toggled on and off with an electrical switch if desired. This toggling operation is a completely reversible process, with no permanent change on quartz characteristics. This means quartz long term stability is limited only by aging, not the amount of usage, materials deposited, or the large-number of harsh temperature cycles that a sensor might have to go through. Additionally, electrical sensing does not impose any restrictions on the quartz package, unlike some kind of direct-loaded quartz sensors where quartz surface has to be in contact with the target medium. As the packaging of quartz is crucial for higher quality factors and better aging performance, electrically loaded quartz crystals are superior in this respect.

Next motivation is related to the large number of applications that employ capacitive sensing. For example, flow, pressure, liquid level, humidity, ice detection,

proximity, tactile, touch sensing are just a few of the applications [146].

A later section in this chapter presents a method, which can in principle compensate for the nonlinearity in capacitive sensing and also enable differential capacitive measurement using the same crystal as the reference. To substantiate equations with real-world examples and comparisons, *capacitive acceleration sensing* is chosen to be the application domain for experiments. In synch with this choice, experimental demonstration of some of the concepts through out the chapter are carried out with a hand-made large scale variable capacitor that is used for static acceleration/tilt measurement.

Although quartz crystal is always taken as the resonator in the following discussions, many circuit related arguments can be applied to other resonators such as dielectric or MEMS versions with small or no change, thanks to their topologically similar (Butterworth-Van Dyke) electrical equivalent circuits [55, 58, 160].

6.2 Oscillator circuit

6.2.1 A simple oscillator

In the application of using a capacitive acceleration sensor, the quartz XTL oscillator circuit acts as a frequency modulator with the sensor capacitance as the modulating signal. The circuit analysis in this work is centered around a single transistor Pierce oscillator along with a buffer stage, which is implemented using discrete bipolar transistors. The circuit that is shown in Figure 6.4 changes its resonant frequency based on the capacitive loading on the XTL. The sensor capac-

itance is denoted by C_{sensor} and assumed to be connected in parallel to the quartz XTL. The detailed analysis of both parallel and series loaded quartz crystals follow in later sections.

One advantage of electrical sensing over the direct sensing counterpart is that toggling the effect of the environmental factor is as simple as electrically disconnecting the sensor (e.g., capacitor) and the XTL, simply with a series switch. On the other hand, if the quartz XTL operates in direct sensing mode, switching the interaction between XTL and the quantity to be measured is not trivial. In most cases the surface absorbtion/desorption state or mass/force loading on the resonator cannot be cancelled or reversed in the presence of the environmental stimulus. In addition to this, the fact that quartz crystal and the measurement point do not have to be at the same place, introduces some flexibility during the design of measurements in harsh or moving environments. Essentially, all the information about a given environment can be sensed by just two wires carried from the point of measurement to the oscillator circuitry, without exposing quartz to the harsh environment that would introduce uncontrolled factors on the measured frequency. There are parasitic impedances that can affect the oscillation-sustaining amplifier circuit. However, later in Section 6.5, digital post-processing of the frequency measurements is shown to offer a possible solution to compensate for this unpredictability.

6.2.2 Oscillation in the presence of a capacitive sensor

A critical requirement of electrical sensing is to make sure that the circuitry can support oscillation in the presence of a largely varying capacitive load. This puts some boundaries on the component values that can be used in the basic three-point

oscillator shown in Figure 6.5(a). Vittoz *et al.* presents a theoretical treatment of the circuit in Figure 6.5(b) that uses a MOS transistor and arbitrary impedances Z_1, Z_2, and Z_3 as the feedback elements [16]. Here, the crystal is replaced by its four element Butterworth-Van Dyke (BVD) equivalent electrical circuit. This equivalence is illustrated in Figure 6.6 for the case of a crystal in parallel with a capacitive sensor, C_{sensor}.

The analysis of Vittoz *et al.* is based on the critical point of oscillation, which requires vanishing of the total impedance around the loop containing the motional branch of the crystal (XTL). The total impedance consists of the impedance of the motional branch Z_m, and the input impedance of the negative resistance amplifier seen by the motional branch, Z_c, given as:

$$Z_c = \frac{Z_1 Z_3 + Z_2 Z_3 + g_m Z_1 Z_2 Z_3}{Z_1 + Z_2 + Z_3 + g_m Z_1 Z_2}, \tag{6.3}$$

where g_m is the transconductance of the transistor.

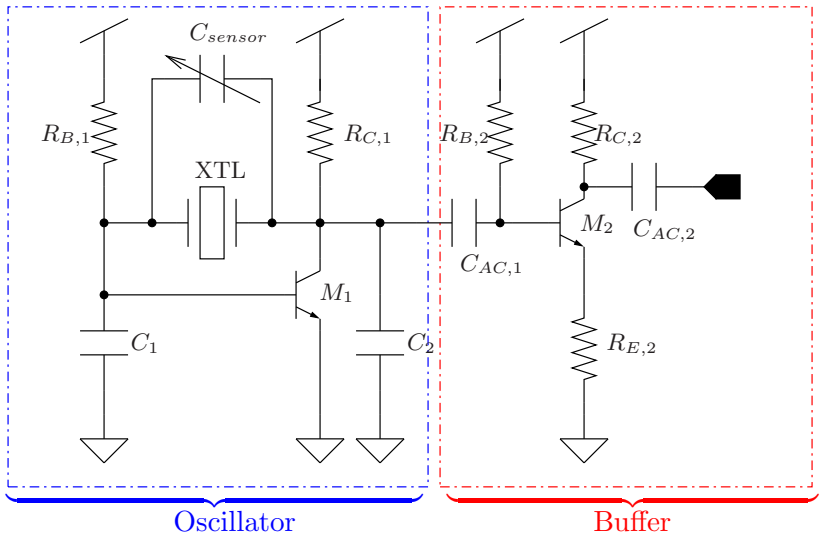

Figure 6.4: Schematic of the oscillator and the buffer stage. The capacitive accelerometer sensor is connected in parallel with the quartz crystal.

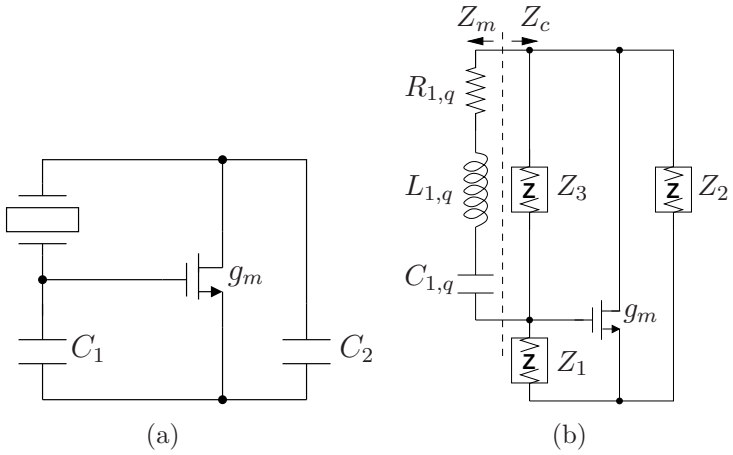

Figure 6.5: (a) Basic and (b) general forms of the three point oscillator [16].

The condition for oscillation is satisfied as long as

$$\Re(Z_c + Z_m) \leq 0, \tag{6.4}$$

where $\Re$ denotes "the real part of."

We can use Equation (6.4) to analyze the critical condition of oscillation for the oscillator in Figure 6.4. After replacing the transistors with their small signal

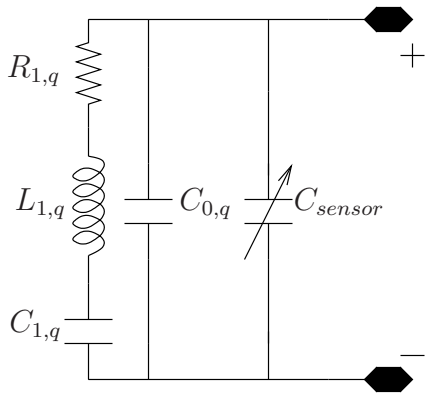

Figure 6.6: Electrical equivalent circuit of quartz in parallel with a sensor capacitor C_{sensor}.

equivalent, this circuit can be put in the form of Figure 6.5(b) provided that:

$$Z_1 = r_{\pi,1} \lVert R_{B,1} \lVert (\mathrm{j}\,\omega(C_1 + C_{BE,1}))^{-1} \tag{6.5a}$$

$$Z_2 = R_{in,buf} \lVert R_{C,1} \lVert r_{o,1} \lVert (\mathrm{j}\,\omega(C_2 + C_{in,buf})^{-1} \tag{6.5b}$$

$$Z_3 = (\mathrm{j}\,\omega(C_{0,q} + C_{sensor} + C_{BC,1}))^{-1}, \tag{6.5c}$$

where $\omega = 2\pi f$ is the angular frequency, and $r_{\pi,1}$, $r_{o,1}$, $C_{BE,1}$, $C_{BC,1}$ are the small-signal, π-equivalent circuit parameters of transistor M_1 in Figure 6.4. $R_{in,buf}$ and $C_{in,buf}$ are used to represent the input impedance (resistance and capacitance in parallel) of the buffer stage at the collector of the transistor M_1.

The values of the small signal equivalent circuit parameters can be approximated by SPICE simulation or analytical approximations. Actual component values used in the prototype of Figure 6.4 are listed in Table 6.1, which uses subscripts "1" and "2" to refer to the parameters of the transistors M_1 and M_2, respectively. The crystal equivalent circuit parameters in the table are extracted from a 16 MHz XTL via an impedance measurement, which is presented later in the experimental section. The same table also lists the small signal parameters which were used in the evaluation of Equation (6.4)[3].

The oscillator stage in Figure 6.4 was designed around three key variables: capacitances C_1, C_2, and collector current of transistor M_1, i.e., $I_{C,1} = \frac{k_B T}{q} g_{m,1}$, where k_B is the Boltzmann constant, T is the absolute temperature, and q is the elementary charge. Knowledge of the bias current value leads us to choose bias resistor values, $R_{B,1}$ and $R_{C,1}$, for DC biasing and gain control. Knowledge of the capacitor values are critical for sensitivity optimization as they affect the shunt loading on the XTL along with C_{sensor} [16]. The design space for these three variables

[3]Up to 10% mismatch was observed in the measured DC currents and SPICE simulation results. No tweaking of the model parameters was attempted to improve the match.

are better visualized under the constraints of Equation (6.4). This geometrical method can help us optimize the component values to maximize C_{sensor}, without circuit failing to oscillate. Figure 6.7 visualizes the surface where the equality in Equation (6.4) is satisfied. Inside the vase-like region the negative of the real part of the amplifier is more than the motional resistance indicated on the title of the figure. Note that, since the volume is not symmetric along the I_{C_1} axis, increasing the current does not necessarily always guarantee oscillation. This concept is well explained in [16] for the case of MOS, linear, lossless amplifiers.

Based on Figure 6.7, following values were picked for the prototype: $C_1 = 1$ nF, $C_2 = 39$ pF, and $I_{C,1} \approx 10.6$ mA. The buffer stage transistor was biased around 22 mA with a gain close to unity. The power was supplied from a 9 V regulator. As the experimental procedure targeted demonstration of basic concepts discussed throughout the chapter, not much attention was placed into minimizing the bias current of the oscillator and the buffer transistors. This resulted in a large power consumption for the XTL and the oscillator circuit.

Table 6.1: Listing of the component values of Figure 6.4 and parameters used in the evaluation of Equation (6.4).

Parameter	**Value**	**Parameter**	**Value**	**Parameter**	**Value**
$R_{B,1}$	150 KΩ	$C_{BE,1}$	103 pF	$R_{1,q}$	7.79790 Ω
$R_{C,1}$	510 Ω	$C_{BC,1}$	2.12 pF	$L_{1,q}$	7.42795 mH
$R_{B,2}$	51 KΩ	C_1	1 nF	$C_{1,q}$	13.3289 fF
$R_{C,2}$	100 Ω	C_2	39 pF	$C_{0,q}$	3.24196 pF
$R_{E,2}$	100 Ω	$R_{in,buf}$	13.109 KΩ	$C_{in,buf}$	35 pF
$r_{0,1}$	7.108 KΩ	$r_{\pi,1}$	450 Ω	$g_{m,1}$	0.4112 ℧

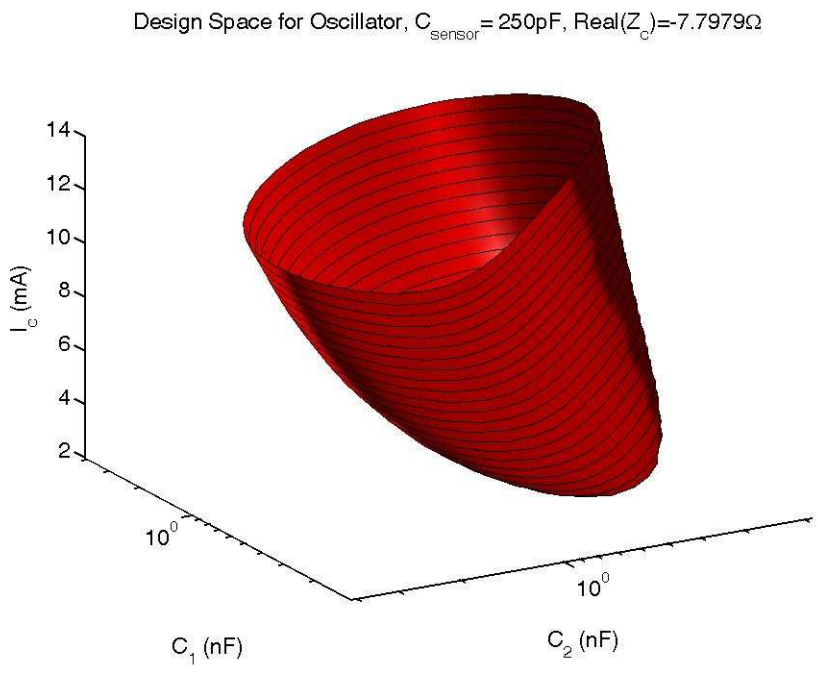

Figure 6.7: Critical oscillation surface in $\{C_1, C_2, I_{C,1}\}$ space for shunt capacitive load of $C_{sensor} = 250$ pF. The region inside the vase-like (i.e., for large bias current) region is where the inequality is satisfied.

6.3 XTL oscillator as a capacitive readout circuitry

The frequency of oscillation can in general be calculated by applying Barkhausen criteria around the main feedback loop. Therefore, any change in the impedance of elements in the loop has a finite effect on the frequency of oscillation. The corresponding change in frequency forms the basis of electrical sensing. Capacitive sensing is explained in detail in the coming sections, and an analogues treatment is possible for inductive sensing as well.

6.3.1 Series and parallel loading of XTL by a sensor capacitance

In capacitive sensing applications based on frequency modulation, sensitivity of an oscillator circuitry to changes in external capacitance is a benchmark parameter. For parallel resonant circuits as the one in Figure 6.4, the circuit operates at a frequency in between the intrinsic series and shunt resonance depending on the load impedance seen by the XTL looking into the oscillating (negative resistance) amplifier. Two ways of connecting the capacitive sensor to the oscillator are shown in Figure 6.8. Here, the *negative-resistance* amplifier circuit is represented by a series combination of a resistor and a capacitor that are labelled as R_{cir} and C_{cir}, respectively. Their values are frequency dependent, however, they can be assumed to be constant since the crystal has a high quality factor as the dominant frequency determining element.

Following the naming convention of Vittoz *et al.* [16], the frequency pulling, p, is defined as the relative spacing between the operating frequency $f = \frac{\omega}{2\pi}$ and the series resonant frequency of the crystal:

$$p = \frac{f - f_s}{f_s} = \frac{\omega - \omega_s}{\omega_s}. \tag{6.6}$$

Here, $f_s = \frac{\omega_s}{2\pi}$ is the series resonance frequency of the crystal given by Equation (6.7).

$$f_s = \frac{\omega_s}{2\pi} = \frac{1}{2\pi\sqrt{L_{1,q}C_{1,q}}} \tag{6.7}$$

Determination of the oscillation condition and the frequency for a crystal in one-port negative resistance amplifier configuration is derived in Appendix L. The results of that section are worked out below to evaluate expressions for parallel and

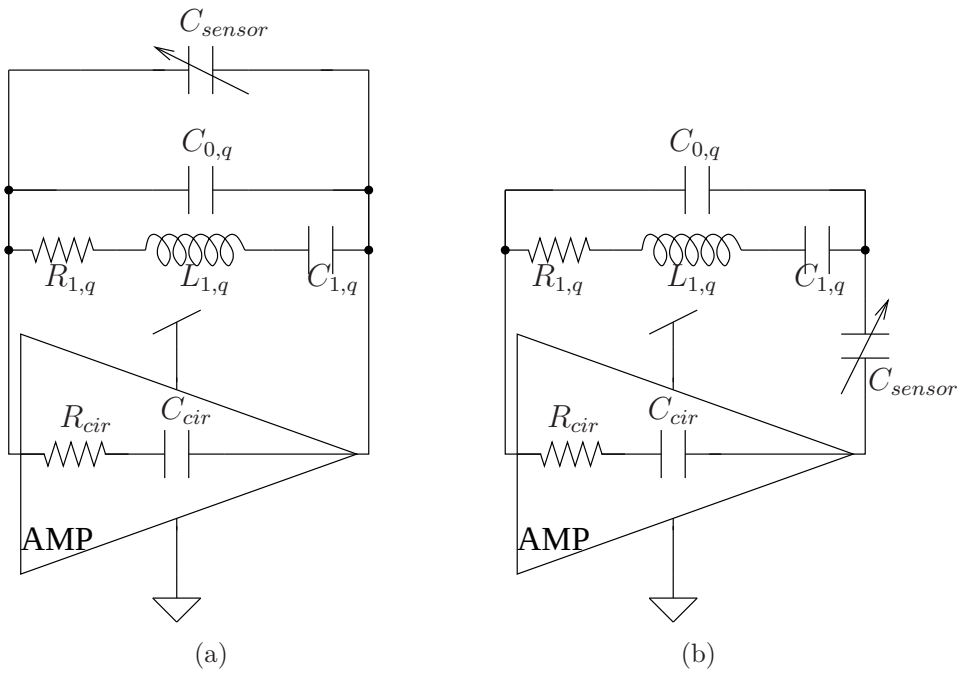

Figure 6.8: Schematic for (a) parallel and (b) series loaded XTL configurations. The negative resistance amplifier is represented by series connection of R_{cir} and C_{cir}, which are, strictly speaking, frequency-dependent.

series loaded capacitive readout. Equation (6.8) gives the necessary condition for the oscillation start-up. Equation (6.9) and Equation (6.10) give a pair of equations that need to be solved to calculate ω and R_{cir}.

Condition for oscillation:

$$\frac{\acute{C}_{cir}}{\acute{C}_{cir}+\acute{C}_{0,q}} > 2\omega R_{1,q}\acute{C}_{0,q}. \tag{6.8a}$$

or, substituting $\omega \approx \omega_s$ and $Q_q = (\omega_s R_{1,q} C_{1,q})^{-1}$ for the quality factor of the XTL yields the approximate version:

$$\frac{Q_q C_{1,q}}{\acute{C}_{0,q}} > 2\left(1+\frac{\acute{C}_{0,q}}{\acute{C}_{cir}}\right), \tag{6.8b}$$

Calculating ω and R_{cir} :

$$R_{cir} = \frac{-\acute{K}_p + \sqrt{\acute{K}_p^2 - 4\acute{K}_r^2\acute{K}_q}}{2\acute{K}_r\acute{K}_q} \tag{6.9a}$$

$$\acute{K}_p = \left(\frac{\acute{C}_{cir}}{\acute{C}_{0,q} + \acute{C}_{cir}}\right)^2 \tag{6.9b}$$

$$\acute{K}_q = (\acute{C}_{par1}\omega)^2 \tag{6.9c}$$

$$\acute{K}_r = R_{1,q} \tag{6.9d}$$

$$F_q(\omega, R_{cir}, \acute{C}_{cir}, \acute{C}_{par1}, \acute{C}_{0,q}) = \frac{\omega^2 R_{cir}^2 \acute{C}_{cir}\acute{C}_{par1} + 1}{\left(\acute{C}_{cir} + \acute{C}_{0,q}\right)\left(\omega^2 R_{cir}^2 \acute{C}_{par1}^2 + 1\right)} - \frac{\omega^2 - \omega_s^2}{C_{1,q}\omega_s^2} = 0, \tag{6.10}$$

where

$$\acute{C}_{cir} = \begin{cases} C_{cir} & \text{if parallel loaded} \\ \frac{C_{cir}C_{sensor}}{C_{cir}+C_{sensor}} & \text{if series loaded} \end{cases} \tag{6.11a}$$

$$\acute{C}_{0,q} = \begin{cases} C_{0,q} + C_{sensor} & \text{if parallel loaded} \\ C_{0,q} & \text{if series loaded} \end{cases}, \text{ and} \tag{6.11b}$$

$$\acute{C}_{par1} = \frac{\acute{C}_{cir}\acute{C}_{0,q}}{\acute{C}_{cir} + \acute{C}_{0,q}} \tag{6.11c}$$

Equations above are presented in a form that treats C_{cir} as a known parameter. One motivation for taking C_{cir} to be given as opposed to R_{cir} is because the latter is usually a stronger function of the DC operating point [161]. Indeed self-limiting of the oscillator (or gain-clipping) can qualitatively be thought as R_{cir} being less and less negative as the amplitude of oscillation increases. This argument assumes that the oscillation condition in Equation (6.8a) is satisfied so that the oscillation can start in the first place[4]. Strictly speaking, one needs to know Z_c as a function of ω for the exact solution. This gives the third equation for the calculation of $(\omega, R_{cir}, C_{cir})$ triplet in addition to Equation (6.9) and Equation (6.10).

[4]Note that oscillation condition is independent of R_{cir}.

When the oscillation condition given in Equation (6.8b) is fulfilled with high enough a margin [16], simplified expressions are available based on Equation (L.13) and Equation (L.16) of Appendix L. Table 6.2 lists these expressions for the parallel and the series loaded capacitive readout.

Table 6.2: Approximations for frequency pulling and oscillation condition for parallel and series loaded crystal configurations.

Parallel Loading	**Series Loading**
Necessary Condition for Oscillation ✠	
$\frac{Q_q C_{1,q}}{C_{0,q}+C_{sensor}} > 2\left(1+\frac{C_{0,q}+C_{sensor}}{C_{cir}}\right)$ (6.12)	$\frac{Q_q C_{1,q}}{C_{0,q}} > 2\left(1+\frac{C_{0,q}}{\grave{C}_{cir}}\right)$ (6.13)
Frequency Pulling †*(Unitless)*	
$p = \frac{C_{1,q}}{2\left(C_{0,q}+C_{sensor}+C_{cir}\right)}$ (6.14)	$p = \frac{C_{1,q}}{2\left(C_{0,q}+\grave{C}_{cir}\right)}$ (6.15)
Real part of Amplifier Impedance, R_{cir} ✠	
Use Equation (6.9) with $\omega \approx \omega_s$	
Normalized Sensitivity of Frequency to Capacitance †(Farad^{-1})	
$\bar{S}_{f/C} = -\frac{C_{1,q}}{2\left(C_{0,q}+C_{sensor}+C_{cir}\right)^2}$ (6.16)	$\bar{S}_{f/C} = -\frac{C_{1,q}C_{cir}^2}{2\left(C_{0,q}+\grave{C}_{cir}\right)^2\left(C_{sensor}+C_{cir}\right)^2}$ (6.17)

✠ Assuming $\omega \approx \omega_s$. Error introduced is extremely small, on the same order as the frequency pulling, p.

† Valid when oscillation condition is satisfied with a high margin, or likewise, when the resulting solution satisfies $\left|\omega R_{cir}\acute{C}_{par1}\right| \ll 1$ that follows from Equation (L.15).

The range of values for C_{cir} and C_{sensor} show orders of magnitude variation depending on implementation of sensor capacitance and realization of circuitry. VLSI

can easily give on-chip circuit capacitances of femtoFarad range, whereas minimum capacitance levels realized using discrete capacitances on a printed-circuit-board (PCB) are usually limited by stray capacitances. On the sensor front, while surface micromachined implementations of the capacitive accelerometers have sensor capacitances of hundreds of femtoFarad, those of bulk micromachined sensors can easily be in picoFarad range.

As the quartz oscillator serves as a capacitance readout circuitry, evaluation of its sensitivity is critical for the noise performance analysis and its comparison to other capacitive read-out techniques. Normalized sensitivity of the oscillation frequency to a unit capacitance change, which we represent by $\bar{S}_{f/C}$, is defined in Equation (6.18).

$$\bar{S}_{f/C} = \frac{1}{\omega_s}\frac{\partial \omega}{\partial C_{sensor}} = \frac{\partial p}{\partial C_{sensor}} \tag{6.18}$$

Sensitivities for parallel and series combinations can be calculated as given by Equation (6.16) and Equation (6.17), respectively, in Table 6.2. From these equations one can show that series loading yields higher sensitivities when $C_{cir} \gg C_{sensor}$, whereas parallel loading wins at the other extreme, for $C_{cir} \ll C_{sensor}$. In either case, the oscillation condition should always be kept in mind, as the sensitivity equations make sense only when the oscillation condition is satisfied.

Frequency pulling shows a different characteristic than the sensitivity to acceleration. Approximate expressions for the series loading always yield larger frequency pulling than that of the parallel loading by virtue of Equation (6.15) and Equation (6.14).

An exact analytical expression for the normalized sensitivity can be derived by a straightforward, but lengthy application of chain rule to Equation (6.9) and

Equation (6.10). The main form of the expression for the normalized sensitivity is given in Equation (6.19), yet a complete version is not included in the interest of brevity. Coming sections present a comparison between the exact and the approximate versions of sensitivity in addition to illustrating their variation as a function of C_{cir} and C_{sensor}.

$$\bar{S}_{f/C} = \frac{-M_{A2}}{\omega_s M_{A1}}, \text{ where} \tag{6.19a}$$

$$M_{A1} = \frac{\partial F_q}{\partial \omega} + \frac{\partial F_q}{\partial R_{cir}} \frac{\partial R_{cir}}{\partial \acute{K}_q} \frac{\partial \acute{K}_q}{\partial \omega}, \tag{6.19b}$$

$$\begin{aligned} M_{A2} = \frac{\partial F_q}{\partial R_{cir}} \left(\frac{\partial R_{cir}}{\partial \acute{K}_p} \frac{\partial \acute{K}_p}{\partial C_{sensor}} + \frac{\partial R_{cir}}{\partial \acute{K}_q} \frac{\partial \acute{K}_q}{\partial \acute{C}_{par1}} \frac{\partial \acute{C}_{par1}}{\partial C_{sensor}} \right) \\ + \frac{\partial F_q}{\partial \acute{C}_{cir}} \frac{\partial \acute{C}_{cir}}{\partial C_{sensor}} + \frac{\partial F_q}{\partial \acute{C}_{par1}} \frac{\partial \acute{C}_{par1}}{\partial C_{sensor}} + \frac{\partial F_q}{\partial \acute{C}_{0,q}} \frac{\partial \acute{C}_{0,q}}{\partial C_{sensor}}. \end{aligned} \tag{6.19c}$$

It should be emphasized that, in order to keep the equations simple and due to a myriad of applications [146], only capacitive sensors were investigated in this chapter. Nonetheless, an analogous treatment is straightforward for inductor or for that matter, any arbitrary complex impedance that is loaded in series or in parallel with the XTL.

Next, a parametric study of the frequency pulling and the sensitivity response is presented for both the series and the parallel loaded cases, with known values of the crystal parameters. The exact versions described by Equation (6.6) to Equation (6.11) are compared with the approximate versions given by Equation (6.14) to Equation (6.17).

6.3.2 Normalized Sensitivity, $\bar{S}_f/C$, as a function of the circuit capacitance, C_{cir}

Figure 6.9 plots the calculated sensitivities of a parallel loaded and a series loaded 16 MHZ crystal as a function of the capacitance ratio, $\xi = C_{cir}/C_{sensor}$. Sensor capacitance is fixed at 100 fF and circuit capacitance is varied in the calculation loop. Sensitivity curves are evaluated only in the region where the oscillation condition given in Table 6.2 is satisfied. The values of the capacitance ratios at which the oscillation conditions are critically satisfied are indicated by vertical, dashed lines on the plots. Both the exact solution and the approximations described in Section 6.3.1 are plotted on the same graph. The close match over orders of magnitude of capacitance change justifies the use of approximate expressions.

In general, the approximate oscillation condition is rather optimistic as compared to the exact oscillation condition. This can be observed in Figure 6.9 by noticing the difference in the critical value of C_{cir}.

Figure 6.9 is especially useful when the circuit designer has no control on the the sensor capacitance. For the component values used in the figure, large C_{cir} favors series connection, small C_{cir} favors parallel connection. If one disregards the oscillation condition, it can be shown from the expressions in Table 6.2 that the maximum absolute values of sensitivity attainable from the series and the parallel loaded configurations at the extreme values of the capacitance ratio $\xi = C_{cir}/C_{sensor}$ are equal to each other. Yet, if the oscillation condition is considered, one of the connection types can be more favorable.

One can not choose arbitrary design parameters to merely maximize the sensitivity, as the realisability of R_{cir} is an issue that can lend itself to tradeoffs. From

a circuit design point of view, the more negative R_{cir} is, higher the power consumption in the amplifier circuitry, and harder the design is, especially at higher frequencies[5]. Figure 6.10(a) shows the approximate and exact solutions of R_{cir} for the series and the parallel loadings. Almost overlapping plots from both solutions reveal even a better match than there is for sensitivity. For large C_{cir}, the series loading is much more demanding as it requires orders of magnitude of more nega-

[5]See Equation (16) and Equation (17) in reference [16] for the case of linear, lossless, MOS oscillation amplifier.

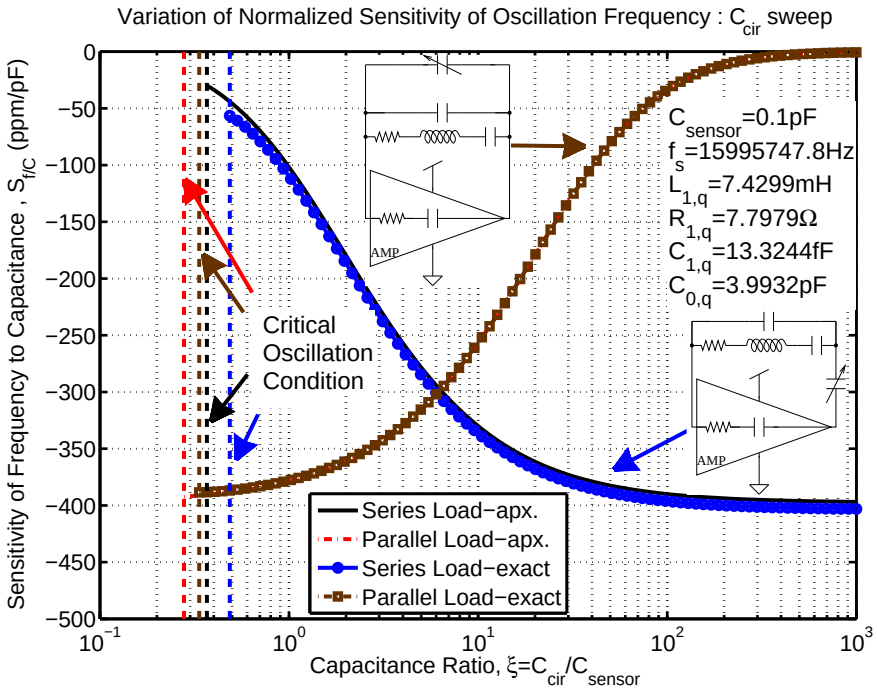

Figure 6.9: Normalized sensitivity of the parallel and the series loaded crystal oscillator. The equivalent circuit parameters for the 16 MHz crystal and the sensor capacitance ($C_{sensor} = 100$ fF) are assumed to be constant in the calculations, while C_{cir} is varied. The insets show the circuit diagrams for both loading types, where sensor (variable) capacitor, C_{sensor} is connected either in series or in parallel with the crystal. The vertical dashed lines indicate the critical point of oscillation as determined by Equation (6.8a) in the exact case, and by Equation (6.8b) in the approximate case.

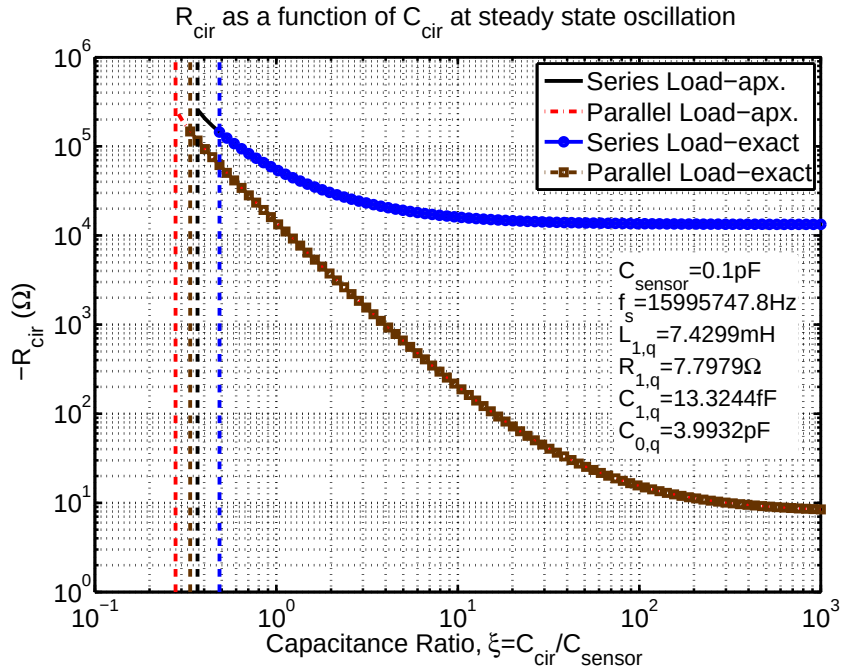

(a)

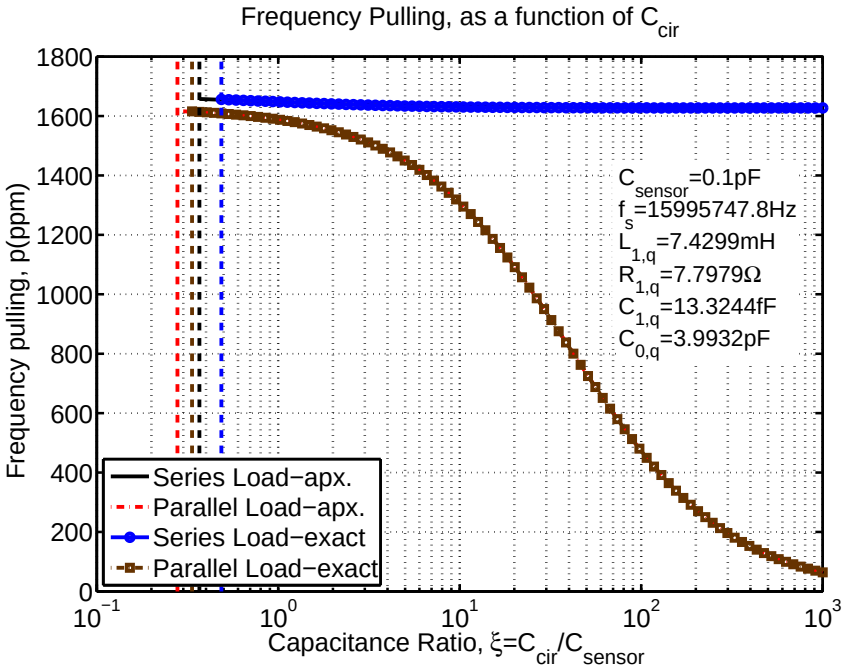

(b)

Figure 6.10: (a) Real part of the feedback amplifier impedance, $\Re Z_c = R_{cir} < 0$, and (b) normalized frequency pull, p, for the series and the parallel loading of the sensor capacitance. The graphs show the dependence on C_{cir}, when other crystal parameters listed in the insets (including C_{sensor}) are held constant.

tive R_{cir}. As such, it is left to designer's decision whether this drawback is worthy of improved sensitivity performance.

Frequency pulling comparison for the series and the parallel loading is shown in Figure 6.10(b). As in the case of R_{cir}, there is not an obvious mismatch between the approximate and the exact solutions.

6.3.3 Normalized Sensitivity, $\bar{S}_f/C$, as a function of the sensor capacitance, C_{sensor}

This section is analogues to the previous section except that all the numerical calculations are carried out at a fixed C_{cir}, while C_{sensor} is varied. As the oscillator is treated as a capacitive readout for C_{sensor}, unlike the previous section, one can comment also on the linearity of the frequency output to the sensor capacitance change.

Approximate and exact sensitivity of parallel and series connected sensor configurations are plotted in Figure 6.11. The regions of oscillation as a function of C_{sensor} are complementary; i.e., the series configuration fails to oscillate for very small C_{sensor}, while the parallel one fails for large C_{sensor}. Approaching close to the oscillation condition in the case of series connection, discrepancy between approximate and exact solutions become significant, about 20%.

As far as the linearity of sensitivity is concerned, the parallel connection is favorable for small C_{sensor} limit, as its sensitivity does not change much in the relevant regime. For 40 fF $< C_{sensor} <$ 200 fF, the series connection yields higher sensitivities (in absolute value) than the parallel connection, but it is highly non-

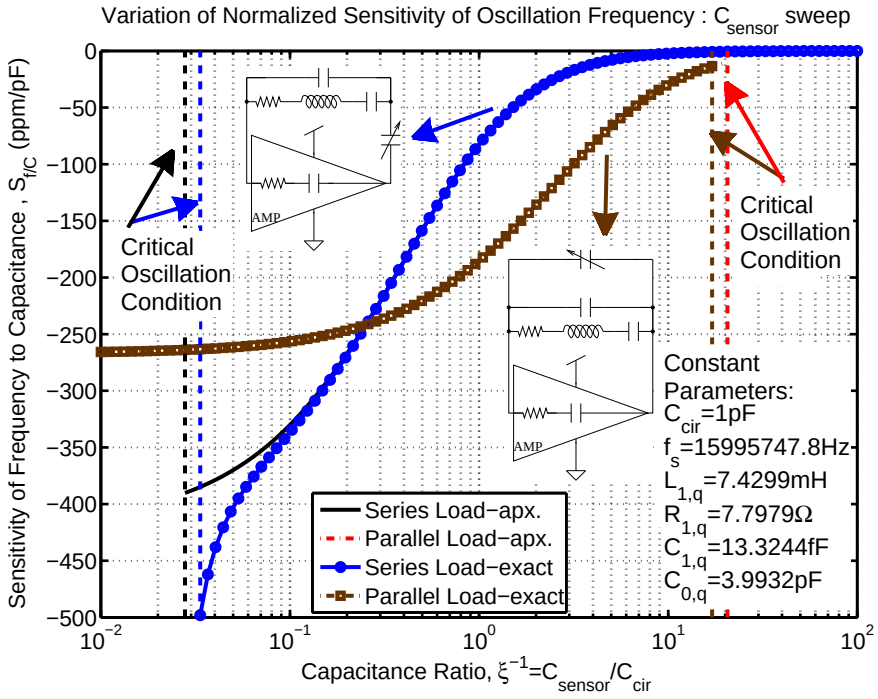

Figure 6.11: Normalized sensitivity of parallel and series loaded crystal oscillator. The equivalent circuit parameters for the 16 MHz crystal and the series circuit capacitance ($C_{cir} = 1$ pF) are assumed constant in the calculations, and C_{sensor} is varied. The insets show the circuit diagrams for both loading types, where sensor (variable) capacitor, C_{sensor} is connected either in series or in parallel with the crystal. The vertical dashed lines indicate the critical point of oscillation as determined by Equation (6.8).

linear.

R_{cir} and frequency pulling as a function of C_{sensor} are given in Figure 6.12. R_{cir} plot in Figure 6.12(a) indicates that increased sensitivity for the series connection of small C_{sensor} comes at the price of higher negative-resistance amplification. R_{cir} does not show any obvious discrepancy between the approximate and the exact solutions. Frequency pulling does show some discrepancy for small C_{sensor} in the case of series connection. Although the mismatch between the approximate and

the exact solutions is not visible at the scale of Figure 6.12(b), the sensitivity characteristics in Figure 6.11 makes it apparent for small C_{sensor} values.

It should be noted in Figure 6.12(b) that the frequency of the parallel connected XTL for very *small* C_{sensor} values approaches to the frequency of the series connected XTL for very *large* C_{sensor} values. Under these circumstances, the two circuits in Figure 6.8 for series and parallel lading become equivalent.

6.4 Comparison of the analytical model to the circuit simulations in SPICE

The performance of the model described above is tested using the oscillating amplifier of the circuit in Figure 6.4. The schematic, netlist and the BJT model parameters are detailed in Appendix M.

The frequency of the oscillation for each value of C_{sensor} was extracted from the results of the transient simulations, which were performed in the time interval from 3000 μsec to 3010 μsec at a time step of 10 psec[6]. Only the time series of the last 10 μsec was recorded and analyzed due to the large number of iterations. The frequency was extracted for each C_{sensor} value using the average time difference between peak points of the output waveform. An average of eight measurements were taken and used to calculate the frequency pulling parameter, p, using Equation (6.7) and Equation (6.6). The small time step was deemed necessary because

[6]In the case of parallel loaded configuration, the frequency extractions from SPICE simulations were performed in the interval from 15000 μsec to 15010 μsec for $C_{sensor} \geq 80$ pF, whereas the interval was from 3000 μsec to 3010 μsec for $C_{sensor} < 80$ pF. It was observed that more time was necessary in simulations for the settling of the frequency of oscillations when C_{sensor} values approached to the limit of oscillation condition for the parallel loaded configuration, i.e., close to $C_{sensor} \approx 155$ pF.

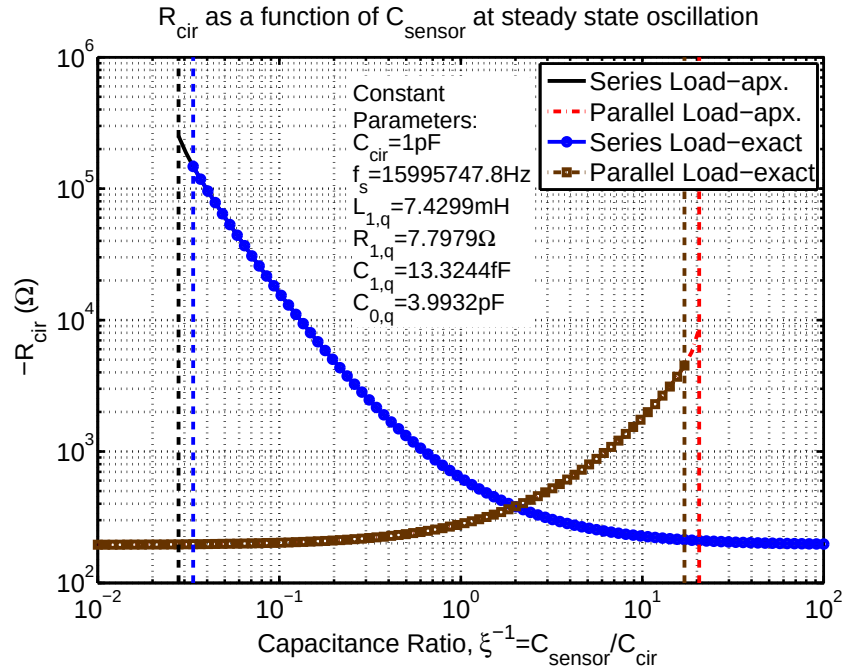

(a)

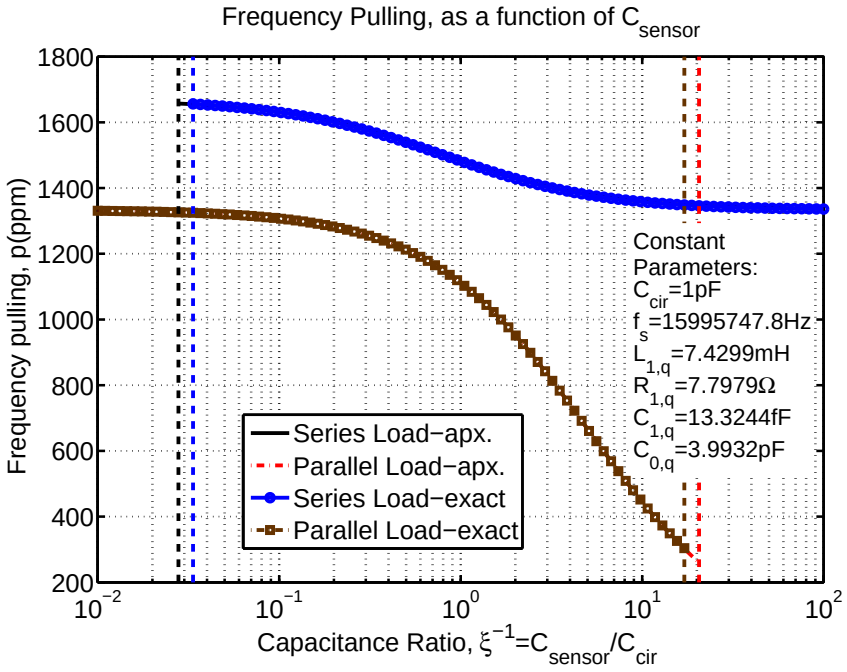

(b)

Figure 6.12: (a) Real part of the feedback amplifier impedance, $\Re Z_c = R_{cir} < 0$, and (b) normalized frequency pull, p, for the series and the parallel loading of the sensor capacitance. The graphs show the dependence on C_{sensor}, when other crystal parameters listed in the insets (including C_{cir}) are held constant.

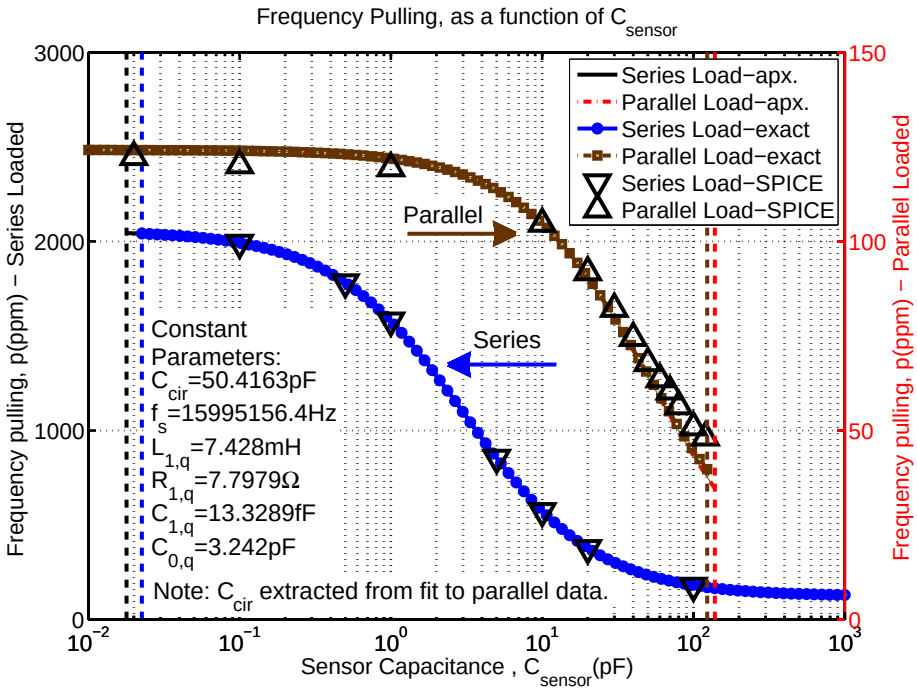

Figure 6.13: Comparison of analytical models to SPICE simulations for the series (left axis) and the parallel (right axes) loaded XTL oscillators. Due to the close match between the approximate and the exact analytical solutions, their plots almost overlap. C_{cir}, being the only unknown parameter in the model, is extracted from a least squares fit to the data of the parallel-loaded case.

of the targeted level of precision of frequency extraction, namely single digit ppm levels. Indeed the average standard deviation from the eight measurements at every C_{sensor} was around 1 ppm. The maximum standard deviation was less than 4 ppm.

Figure 6.13 compares the results of SPICE simulations to the analytical results. The only unknown model parameter for the analytical evaluation of the exact and the approximate expressions of frequency pulling (as described in Section 6.3.1) is C_{sensor}. A fit to the data of the parallel loaded case yielded its value to be $C_{sensor} = 50.41$ pF. For the series loaded case, the analytical and the simulation

results compare so well that their plots appear almost overlapping at the scale of Figure 6.13. The match is worse for the case of parallel loading, yet the results match to within 6% even in this case. Qualitative comparison results are listed in Table 6.3.

About 5.7% mean error of the parallel loaded case is more than an order of magnitude larger than that of the series loaded case. As mentioned before, the analytical model takes C_{cir} of the amplifier to be a constant parameter. Realistically, it does have a small, but non-zero dependence on the frequency of operation. As C_{sensor} is swept across four orders of magnitude, the frequency of oscillation and hence the effective value of C_{cir} changes. The assumption of constant C_{cir} becomes a better one for lower values of C_{sensor}. The significantly better match in the case of series loading than the parallel loading case is due to the small response of the series loading to changes in C_{cir}, as also apparent in Figure 6.10(b). This figure shows a much more significant response for the parallel loaded case. Another reason for large relative errors in the case of parallel loading is the low values (10's of ppm) of frequency pulling as compared to the precision at which frequencies were extracted from the simulations (ppm level). On the other hand, the series loading

Table 6.3: Mean and maximum absolute errors (%) between PSpice simulation results and the results of the analytical model presented in Figure 6.13. Both exact and approximate versions of the analytical model are considered.

		Absolute Error (%)	
		Exact Model	**Approximate Model**
Series Loading	Mean	0.4	0.4
	Max	1.7	1.7
Parallel Loading	Mean	5.7	6.6
	Max	16.2	20.4

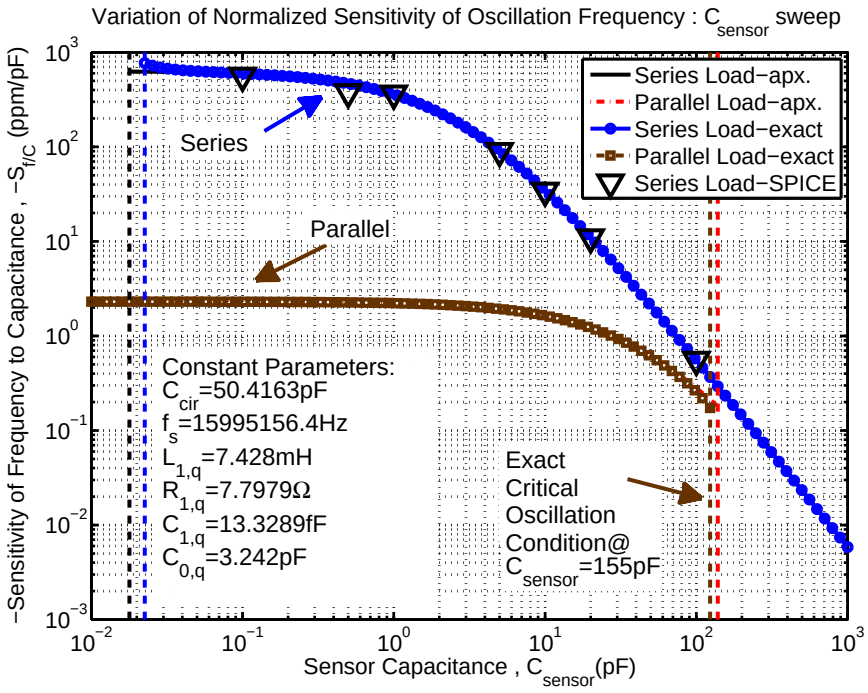

Figure 6.14: Negative of the sensitivity of oscillation frequency to sensor capacitance, -$\bar{S}_{f/C}$, as predicted by analytical calculations and SPICE simulations.

has much larger values of frequency pulling (100's of ppm). Therefore, the issue about precision of extraction is much less significant.

Extraction of sensitivity ($\bar{S}_{f/C}$) of frequency pulling to C_{sensor} from simulation results can, in principle, be calculated from the slope of the data in Figure 6.10(b). However, as the number of data points, each of which came from a time-consuming simulation[7] was not high, additional simulations had to be performed in the neighborhood of the targeted values of C_{sensor}. For example, in order to extract the sensitivity at C_{sensor} = 5 pF, simulations were performed at not only 5 pF, but also at 4.5 pF and 5.5 pF, and then an approximation to the derivative was calculated.

[7]The transient SPICE simulation for a given value of C_{sensor} took about 2.5 hour in a PC with Intel© Core 2 Duo ™, 2.66 GHz processor and 3 GB RAM.

Figure 6.14 makes a comparison between SPICE results and the analytical results of the series loaded case. As expected from the good match of frequency pulling for the series loaded case in Figure 6.10(b), the match of sensitivity between theory and simulation is also very satisfactory. However, the ppm level precision in the frequency extraction method was not good enough to extract ppm/pF level sensitivity of the parallel loaded case reliably. Hence, for the parallel loaded case, only the analytical results are reported. The comparison of the analytical results to the experimental results for the parallel case is made later in Section 6.8.1.2.

6.5 A non-linearity compensation and self-temperature sensing method

6.5.1 Introduction

Quartz sensors that work by electrical coupling to a changing capacitance do not have a constant sensitivity for different values of the sensor capacitance, C_{sensor}. Actually, as Figure 6.11 shows, the change in the sensitivity as a function of C_{sensor} can be quite significant depending on whether C_{sensor} loads the XTL in series or in parallel. For high dynamic range applications, this is not tolerable and constitutes a handicap of quartz capacitive readout as compared to the alternative capacitive readout topologies such as the one in Figure 6.1.

Lookup tables or polynomial expressions using coefficients from least square fits of calibration runs are useful tools to compensate for nonlinearity. However, in an environment where temperature can also change, the coefficients of these lookup

tables also need to be modified. This is because, as summarized in Table 6.2, the sensitivity expressions are affected by amplifier input capacitance, which are not stable over large temperature differences. Therefore, one would like to be able to express the sensor output only in terms of XTL parameters and frequency measurement results of the XTL oscillator. This form is given in Equation (6.20).

$$C_{sensor} = \Lambda_M(f_s, C_{1,q}, C_{0,q}, L_{1,q}, R_{1,q}, \{\text{frequency measurements}\}), \tag{6.20}$$

Here Λ_M is a function of only the frequency measurements of the oscillator and the calibrated parameters of quartz such as f_s, $L_{1,q}$ or $C_{1,q}$. By *calibrated* it is referred to the parameters whose variation as a function of temperature is known in advance so that they can be calculated on the fly with a precise measurement of the temperature. The dual-mode oscillator method in Section 6.1.3 was described as a very elegant way of self-temperature sensing solution that does not require any external thermometry. Elimination of thermal time constant differences and thermal gradient errors in this manner without using an oven is an outstanding attribute of dual-mode microcomputer compensation.

Even if the temperature is accurately measured, the equations that are conventionally used to express the output frequency of quartz oscillators to changes in C_{sensor} are not in the form of Equation (6.20). For example, take the approximate expression of frequency pulling for the parallel loaded case in Equation (6.14) rewritten below:

$$C_{sensor} = \frac{C_{1,q}}{2p} - C_{0,q} - C_{cir}, \tag{6.21}$$

where p is calculated from the measurement of the oscillation frequency f_{out}, as well as the operation temperature T as:

$$p = \frac{f_{out}(T) - f_s(T)}{f_s(T)}. \tag{6.22}$$

Assuming that the temperature is known accurately, one can use the calibration data to calculate the XTL parameters f_s, $C_{1,q}$, and $C_{0,q}$. However, the last term in Equation (6.21), C_{cir}, is the input capacitance of the oscillator amplifier electronics, mentioned in Section 6.3. Not only can it have significant temperature variation, but its calibration is also challenging. Because, as the real part of the amplifier input impedance, R_{cir}, is designed to have a negative resistance and cause oscillation, it is difficult to experimentally extract values of C_{cir}. Furthermore, the slight dependence of C_{cir} on frequency of operation, and hence C_{sensor}, could introduce additional errors in using Equation (6.21) when large dynamic range of operation is targeted for C_{sensor}.

Proposing a solution to the two problems mentioned above, namely non-linearity and self-temperature sensing, are among the contributions of this chapter. The linearity of the alternative capacitive readout approach shown in Figure 6.1 can be excellent in theory, as its output is described by the linear relation in Equation (6.1). However, XTL based capacitive readout, even in theory, suffers nonlinearity as illustrated by the above discussion. If XTL based capacitive readout is to be considered for high dynamic range sensing with a linearity performance comparable to that of the alternative approaches, nonlinearity issue needs to be resolved. The additional aspect of self-temperature sensing can then give some leverage to XTL based readout against the competing technologies for large size, but low power and high-precision sensor applications.

In the coming section, *Time-Multiplexed, Crystal (XTL) based Capacitive Sensing* method (TM-XCS) that offers both nonlinearity compensation and self - temperature sensing is described. Time-multiplexed nature introduces a tradeoff regarding measurement bandwidth, but it also enables differential capacitance mea-

surements using the same XTL, which, to the author's knowledge, has not been reported so far. The self-temperature sensing aspect of TM-XCS is not an alternative to dual mode oscillator approach for frequency standards, but it is predicted to serve well for sensor applications where the oscillator does not need to operate at a single frequency without interruption. Depending on the models derived in the previous sections, some of which were verified experimentally, TM-XCS enables absolute capacitance measurements. XTL calibration data and self-temperature sensing are crucial to the algorithm, which is described in detail next.

6.5.2 Time-Multiplexed, Crystal-based Capacitive Sensing (TM-XCS)

TM-XCS depends on making multiple measurements with known combinations of unknown capacitors to figure out their values in terms of only XTL parameters, in a form completely free of oscillator amplifier parameters. In order to serve just as well to differential capacitor problems, two unknown capacitors are considered and named as C_{x1} and C_{x2}. Six different ways of connections that can be created using two capacitors are illustrated in Figure 6.15. Two of them are single-capacitor configurations, the rest are series-connected, parallel-connected, short, and open configurations. Resulting C_{sensor} values for the series and the parallel connected configurations of C_{x1} and C_{x2} are named as C_{s12} and C_{p12}, respectively.

By using the six different combinations of the capacitors and two different loading types of the crystal, 12 variations are possible. However, not all of these 12 configurations are topologically different. $C_{sensor} = \infty$ (short circuit) case of the series loading is the same as $C_{sensor} = 0$ (open circuit) case of the parallel loading

case. This case is referred as the *free-running* case of the oscillator. The other extreme two cases, namely $C_{sensor} = \infty$ of parallel loading and $C_{sensor} = 0$ of series loading cannot support an oscillation. This is because of the effective decoupling of the crystal by a short circuit in the former case, and an open circuited oscillator circuit in the latter case. This observation serves as a qualitative explanation for the oscillation limits that were illustrated by Figure 6.12(b). Therefore, out of 12 combinations that can be inferred from Figure 6.15, *9* of them are valid, distinct configurations provided that they satisfy the oscillation conditions of Section 6.3.1.

The time-multiplexed nature of TM-XCS stems from the measurements of oscillator frequencies at *different* times, using the *same* crystal under different combinations of capacitive loading. Figure 6.16(a) shows the TM-XCS block diagram.

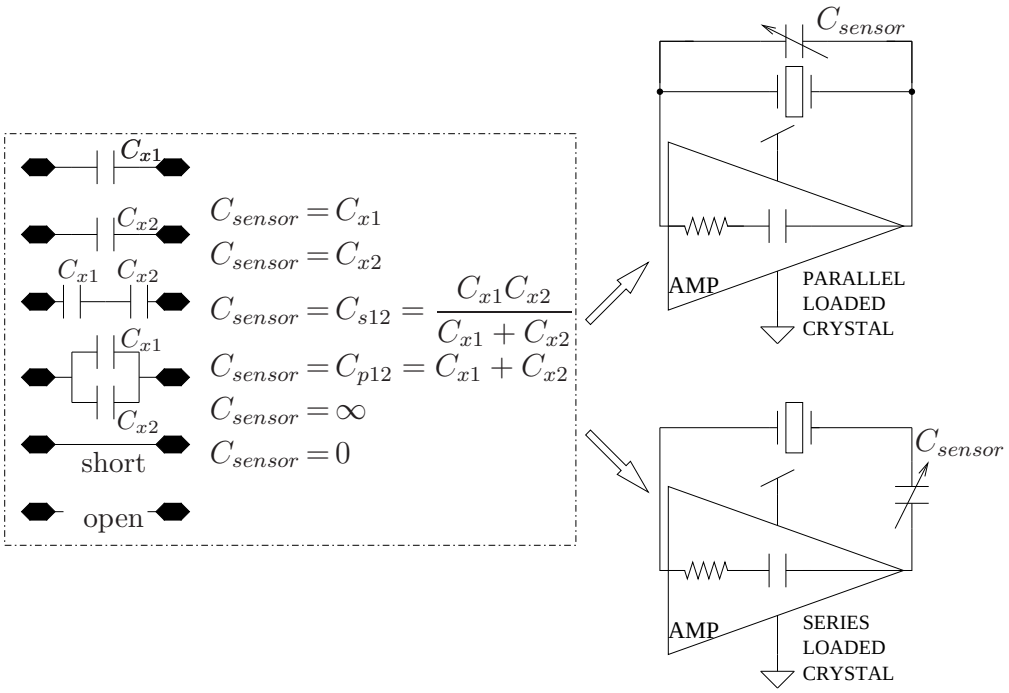

Figure 6.15: Six different connection topologies that can be made using two capacitors C_{x1} and C_{x2}. Each of them can be used in the series or parallel loaded XTL configuration, yielding 12 combinations, 9 of which are valid and topologically distinct.

The series/parallel loading of the crystal and the combinations of the capacitances (C_{sensor}) that loads the XTL are controlled by the processor core that can be either an FPGA or a μ-controller chip. This is the unit, where all the digital calculations and post-processing are performed. Control signals that are generated by the processor core, which are named as Φ_k : k=1,2,..., determine the state of the switches in the oscillator-switching block. The clock signal for the processor core is generated from the oscillator output, after passing it through an inverter in order to sharpen up the transitions. The resulting $< 1\%$ frequency modulation in the clock signal due to the sensor operation of the oscillator is not critical as the maximum speed of the processor core is chosen to be much larger than that of the XTL nominal frequency. With CPU clock speeds expressed in GHz, this is hardly a concern.

After the signal frequency is digitized using the frequency counter, its data is sent back to the processor, yielding the oscillator frequency for that set of switching signals (i.e., for particular capacitance and loading configurations). The frequency is then stored in the processor memory. At this point, the processor can repeat measurements at a different capacitor configuration by changing the control bus signals. When all the required C_{sensor} configurations are completed, calculation of the unknown capacitors and temperature is performed[8]. This completes one measurement, after which the system starts over again for the next one.

The basic flowchart of the processor core program is given in Figure 6.16(b). It is clear from the operation that a single measurement of the unknown capacitors C_{x1} and C_{x2} involves more than one measurement of frequency measurements. This reduces the maximum measurement bandwidth and is a fundamental drawback of TM-XCS. Therefore TM-XCS is more suitable for applications that favor accuracy

[8]How the temperature is calculated is detailed in a later Section 6.5.3.5.

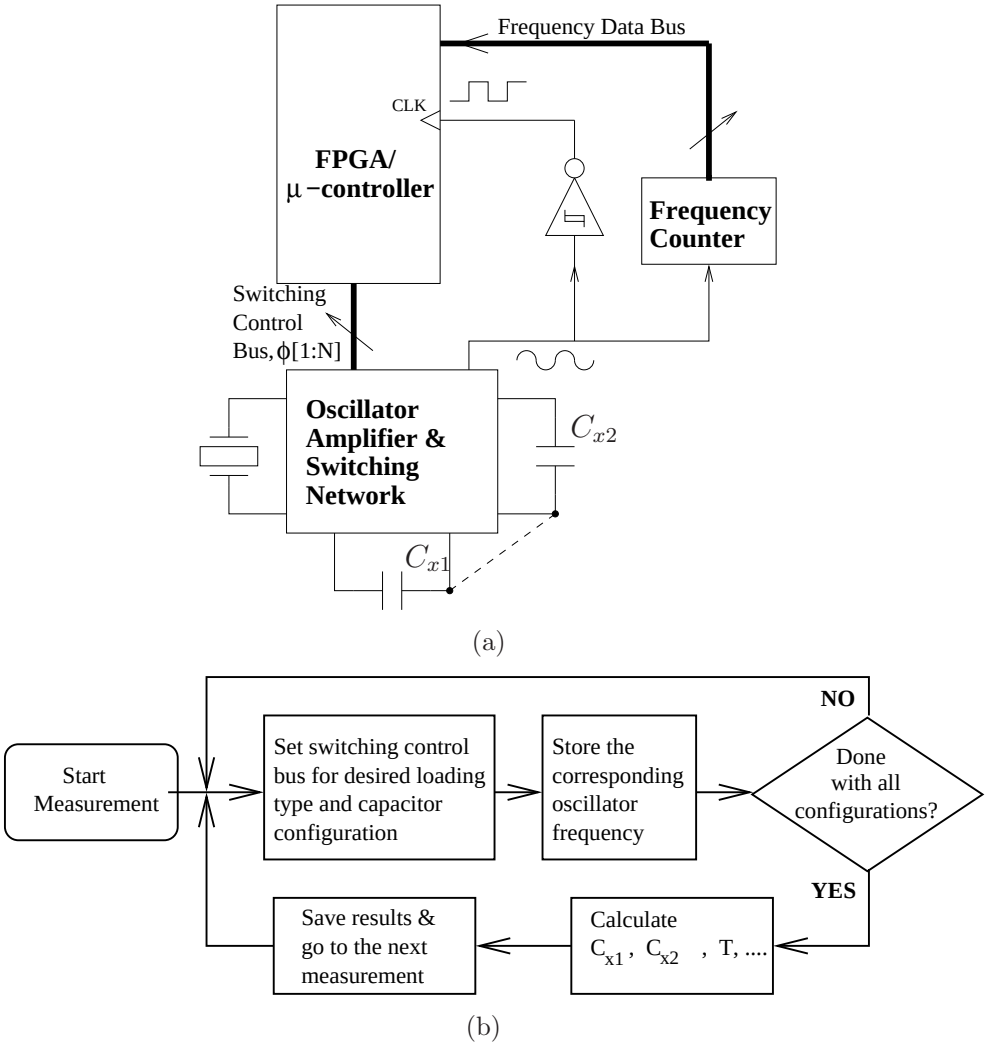

Figure 6.16: (a) Block diagram of TM-XCS. Taking the number of switches in the oscillator-switching block to be N, the control signals of the processor core are named as Φ_1 to Φ_N. The dashed line between C_{x1} and C_{x2} is reserved for differential capacitance measurements as in Figure 6.3. (b) Basic flowchart of the program run by the processor core.

over measurement speed. The number of frequency measurements necessary for a single extraction of C_{x1} and C_{x2} will be explained after the post-processing operations are detailed. But the discussion above tells us that this number, which also determines the maximum sampling rate for the measurements, is at most 9.

The oscillator-switching network shown as a block in Figure 6.16(a) is detailed in Figure 6.17. By appropriate control signals Φ_k, each of the switches are switched on and off, that determine the type of loading and effective value of C_{sensor}. Please note that, C_{x1} and C_{x2} share a common node, hence this circuit supports differential capacitance measurements. States of the switches, necessary to get 9 distinct oscillation conditions are listed in Table 6.4. Free running state is repeated for both the series and the parallel loaded XTL cases.

Implementation of the switches in the circuits is an important practical issue. The resistance of the switches needs to be minimized, as it might effect the amplifier impedance seen by the crystal, hence introducing frequency shifts. The fact that the number of the on switches is not the same between the cases listed in Table 6.4 worsens the situation. Furthermore, the switch must operate much faster than the sampling frequency so that it does not deteriorate the settling time of the oscillation frequency between the transitions. Transmission gates made using high current (i.e., high width to length ratio MOS) transistors or high-speed MEMS DC contact switches can be possible solutions.

Table 6.4: Listing of the ON (i.e., conducting) switches in the circuit of Figure 6.17 necessary for a particular capacitance combination under the series and parallel loaded XTL configurations.

XTL Loading	C_{sensor}	Switches									
		S_1	S_2	S_3	S_4	S_5	S_6	S_7	S_8	S_9	S_{10}
Series	∞ [a]						✓				
	C_{x1}			✓	✓						
	C_{x2}	✓				✓					
	C_{p12}	✓	✓							✓	✓
	C_{s12}					✓					
Parallel	0 [a]						✓				
	C_{x1}						✓		✓		✓
	C_{x2}	✓			✓			✓	✓		
	C_{p12}	✓	✓				✓	✓	✓		✓
	C_{s12}						✓	✓	✓		

[a] Free running case with no external capacitive loading.

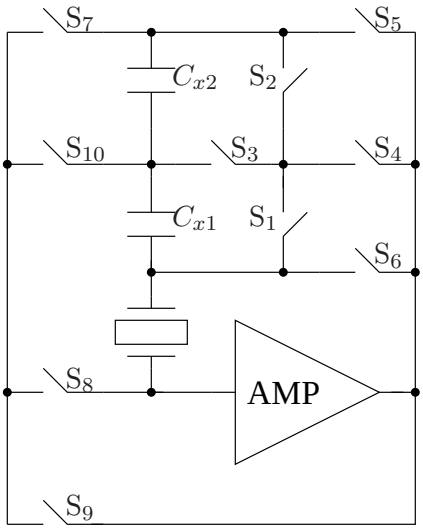

Figure 6.17: Schematic of an oscillator and a switching network to realize all of the distinct, valid configurations emanating from 6 capacitance connections and 2 crystal loading types. Each of the switch S_k, $k = 1 \ldots 10$ is controlled by the control signal Φ_k, from the processor core.

Although switch characteristics can have a formidable effect on the performance of TM-XCS, theoretical derivations in this report do not take that into consideration. Qualitatively speaking, the parasitic capacitances of the switch are more detrimental than the on-resistance of the switch. Because the approximate frequency equations derived so far are only functions of capacitors. On the other hand, significant on-resistance could require amplifiers with more negative gain, thereby consuming more power.

Before moving on to the explanation of the postprocessing in the next chapter, it should be emphasized that, by no means is the oscillator-switching circuit in Figure 6.17 is unique. Another design with a larger number of switches, but with a more structured topology is shown in Figure 6.18. The switches that need to be in the *ON* state to realize a particular capacitive loading are indicated in Table 6.5. As the configurations picked in this table reveals, switches S_7, S_8 and S_{14} in Figure 6.18 can be replaced by open, open, and short circuits, respectively, further decreasing the number of gates.

This circuit uses two additional capacitors, C_{ref1} and C_{ref2}, in addition to the circuit in Figure 6.17. These are the reference capacitors which substitute for the unknown capacitors C_{x1} and C_{x2}. Reference capacitors are in parallel to their unknown counterparts to replace them with known values of capacitors. The exact values of reference capacitors are not critical, but their main function is to make sure the oscillator can be made to oscillate when the unknown capacitors can not satisfy the oscillation condition for a particular type of XTL loading, i.e., series or parallel loading[9]. The reader can appreciate the use of seemingly unnecessary reference capacitors more, after the post-processing of frequency measurements from different capacitor loading configurations is explained.

[9]Oscillation conditions were explained in Section 6.3.1.

Table 6.5: Listing of the ON (i.e., conducting) switches in the circuit of Figure 6.18 necessary for a particular capacitance combination under the series or the parallel loaded XTL configurations.

XTL Loading		**Series**					**Parallel**				
C_{sensor}		∞	C_{x1}	C_{x2}	C_{p12}	C_{s12}	0	C_{x1}	C_{x2}	C_{p12}	C_{s12}
Switches	S_1										
	S_2		✓								
	S_3				✓					✓	
	S_4		✓		✓	✓				✓	✓
	S_5									✓	
	S_6		✓	✓	✓	✓				✓	
	S_7										
	S_8										
	S_9		✓			✓		✓			✓
	S_{10}			✓	✓				✓		
	S_{11}	✓					✓	✓	✓	✓	✓
	S_{12}							✓			
	S_{13}								✓		✓
	S_{14}	✓	✓	✓	✓	✓	✓	✓	✓	✓	✓
	S_{15}		✓		✓	✓		✓	✓	✓	
	S_{16}			✓	✓	✓			✓	✓	✓

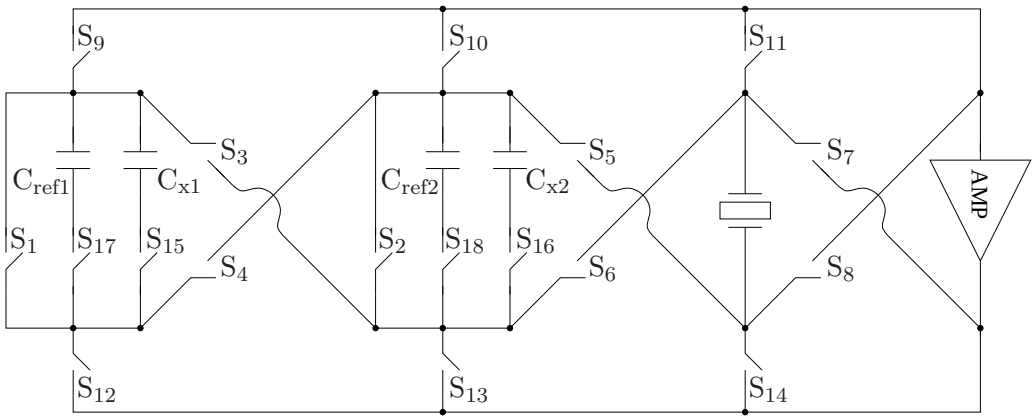

Figure 6.18: An example of an oscillator-switching network with reference capacitors, C_{ref1} and C_{ref2}, as replacements for the unknown capacitors, C_{x1} and C_{x2}.

6.5.3 TM-XCS: Postprocessing for the extraction of unknown capacitors, C_{x1} and C_{x2}

6.5.3.1 The game plan

The target of postprocessing is to yield the unknown (sensed) values of C_{x1} and C_{x2} in terms of the crystal parameters, such as f_s, $C_{1,q}$, and $C_{0,q}$. This concept was previously mentioned with the help of Equation (6.20). This section makes use of the approximate forms of the equations derived for the frequency pulling of the series and the parallel loaded crystal oscillators. The procedure consists of simply solving the unknown parameters using the results from the frequency measurements of different combinations of capacitor loadings. As will be clear from the number of the unknown parameters in the system of equations, not all of the 9 valid capacitor configurations of the previous section yield independent information. Nonetheless, this subsection shows that it is possible to express the unknown capacitors as simple algebraic functions of XTL parameters and frequency measurements. As such, the capacitance extraction can be made independent of fluctuations or complications stemming from the oscillator amplifier.

Although quartz crystal resonators can be manufactured with excellent temperature stability, its equivalent circuit parameters are in general a function of temperature. Therefore, for sensing applications that require extreme accuracy, inferring of the temperature and correction of the crystal parameters from the calibrated data is required. Dual-mode microcontroller compensated XTL solves this problem and proves very effective for frequency-control applications[10]. A possible route can be to apply this powerful method to quartz capacitive sensors as well. On

[10]See Section 6.1.3 for references.

the other hand, measurements taken during TM-XCS already contain information which can be useful to extract the temperature of the XTL, without any external temperature sensor. This topic will be covered theoretically in Section 6.5.3.5.

6.5.3.2 Different C_{sensor} configurations when XTL is *parallel* loaded

In order to make the notation easier to follow, Equation (6.14) can be rewritten as:

$$f_{out}^{(P)} = f_s + \frac{f_s C_{1,q}}{2\left(C_{0,q} + C_{sensor} + C_{cir}\right)} = A_0 + \frac{A_1}{A_2 + C_{sensor}}, \text{where} \tag{6.23}$$

$$A_0 = f_s \quad (6.24a) \qquad A_1 = \frac{f_s C_{1,q}}{2} \quad (6.24b) \qquad A_2 = C_{0,q} + C_{cir}. \quad (6.24c)$$

In Equation (6.23), $f_{out}^{(P)}$ is the measured frequency during TM-XCS when the XTL is parallel loaded with C_{sensor}. "(P)" superscript is used to refer to variables or parameters related to the parallel loaded XTL case throughout this section. Likewise, "(S)" is used for the series loaded XTL case in the next section.

Equation (6.23) can be evaluated for all the C_{sensor} configurations given in Figure 6.15. **For the sake of clear representation of equations, this chapter associates, within meaningful context, the subscripts "1", "2", "s12", "p12", "OC", "SC" with C_{sensor} values of C_1, C_2, $C_{s12} = \frac{C_{x1}C_{x2}}{C_{x1}+C_{x2}}$, $C_{p12} = C_{x1} + C_{x2}$, 0 (open circuit) , and ∞ (short circuit), respectively**. The resulting equations for parallel loaded XTL then takes the form given by Equation (6.25). Note that all the variables on the left hand side of Equation (6.25) can be measured during TM-XCS.

$$f_{out,1}^{(P)} = A_0 + \frac{A_1}{A_2 + C_{x1}} \tag{6.25a}$$

$$f_{out,2}^{(P)} = A_0 + \frac{A_1}{A_2 + C_{x2}} \tag{6.25b}$$

$$f_{out,p12}^{(P)} = A_0 + \frac{A_1}{A_2 + (C_{x1} + C_{x2})} \tag{6.25c}$$

$$f_{out,s12}^{(P)} = A_0 + \frac{A_1}{A_2 + \frac{C_{x1}C_{x2}}{C_{x1}+C_{x2}}} \tag{6.25d}$$

$$f_{out,OC}^{(P)} = A_0 + \frac{A_1}{A_2} \tag{6.25e}$$

C_{x1} and C_{x2} in Equation (6.25a) and Equation (6.25b) can be substituted in Equation (6.25d) to get the ratio A_1/A_2, which is referred as β.

$$\beta = \frac{A_1}{A_2} = \Delta f_{s12}^{(P)} \left[\frac{\Delta f_{s12}^{(P)}}{\Delta f_2^{(P)}} \left(1 + \frac{\Delta f_2^{(P)}}{\Delta f_1^{(P)}} \right) - 1 \right]^{-1} \tag{6.26}$$

In Equation (6.26), $\Delta f^{(P)}$ is the frequency difference between the free running frequency of the oscillator and the measured frequencies when the XTL is parallel loaded. It can be expressed as:

$$\Delta f_k^{(P)} = f_{out,OC}^{(P)} - f_{out,k}^{(P)}, \quad k \in \{1, 2, \text{s12}, \text{p12}, \text{OC}, \text{SC}\} \tag{6.27}$$

The right hand side of equation Equation (6.26) uses only the results of measurements from TM-XCS, hence β can be extracted from the measurements. It is straightforward to prove that β is a positive and finite number for non-zero capacitances C_{x1} and C_{x2} [11]. Once β is known, one can extract the series resonant frequency f_s of the XTL as:

$$f_s = f_{out,OC}^{(P)} - \beta = A_0. \tag{6.28}$$

[11] Since ${f_{out}}^{(P)}$ is a monotonic function of C_{sensor} and also $C_{s12} < C_{x1}$, $C_{s12} < C_{x2} \Rightarrow {f_{out,s12}}^{(P)} > {f_{out,1}}^{(P)}$ and ${f_{out,s12}}^{(P)} > {f_{out,2}}^{(P)}$. Therefore, both the numerator and denominator terms in Equation (6.26) are both positive, hence proving our claim that β is a positive and finite number.

Equation (6.28) proves that by making only four measurements from a network with unknown capacitors, we can extract the series resonance frequency of the XTL. Most importantly, now we can express the unknown capacitors in terms of $C_{1,q}$ as follows:

$$C_{x1} = \left[\frac{f_s}{2}\left(\left(f_{out,1}^{(P)} - f_s\right)^{-1} - \beta^{-1}\right)\right] C_{1,q}, \tag{6.29a}$$

$$C_{x2} = \left[\frac{f_s}{2}\left(\left(f_{out,2}^{(P)} - f_s\right)^{-1} - \beta^{-1}\right)\right] C_{1,q}. \tag{6.29b}$$

A similar expression can be written for the sum of capacitances $A_2 = C_{0,q}+C_{cir}$. Yet, C_{cir} is not known, hence, there is really not a way to extract the ratio $C_{0,q}/C_{1,q}$ from the parallel loaded measurements of TM-XCS only. The series loaded case to be analyzed in the next section turns out to have the additional information for the prediction of this ratio.

6.5.3.3 Different C_{sensor} configurations when XTL is *series* loaded

Similar to the parallel loaded case, the treatment on the series loaded case starts by rewriting the relevant approximate expression for the frequency pulling:

$$f_{out}^{(S)} = f_s + \frac{f_s C_{1,q}}{2\left(C_{0,q} + \frac{C_{sensor}C_{cir}}{C_{sensor}C_{cir}}\right)} = A_3 + \frac{A_4}{A_5 + \frac{A_6 C_{sensor}}{A_6 + C_{sensor}}}, \text{where} \tag{6.30}$$

$$A_3 = f_s \tag{6.31a}$$

$$A_4 = \frac{f_s C_{1,q}}{2} \tag{6.31b}$$

$$A_5 = C_{0,q} \tag{6.31c}$$

$$A_6 = C_{cir}. \tag{6.31d}$$

Despite the close relation between the "A" parameters of the previous and this section[12], different subscripts are used so that it is immediately obvious what type

[12] $A_0 = A3$, $A_4 = A_1$, $A_2 = A_5 + A_6$

of loading a given equation refers to. Working the different capacitance configurations of Figure 6.15 in place of C_{sensor}, one obtains the following equations:

$$f_{out,1}^{(S)} = A_3 + \frac{A_4}{A_5 + \frac{A_6 C_1}{A_6 + C_1}} \tag{6.32a}$$

$$f_{out,2}^{(S)} = A_3 + \frac{A_4}{A_5 + \frac{A_6 C_2}{A_6 + C_2}} \tag{6.32b}$$

$$f_{out,p12}^{(S)} = A_3 + \frac{A_4}{A_5 + \frac{A_6 C_{p12}}{A_6 + C_{p12}}} \tag{6.32c}$$

$$f_{out,s12}^{(S)} = A_3 + \frac{A_4}{A_5 + \frac{A_6 C_{s12}}{A_6 + C_{s12}}} \tag{6.32d}$$

$$f_{out,SC}^{(S)} = A_3 + \frac{A_4}{A_5 + A_6} \tag{6.32e}$$

After solving the first three of the relations given in Equation (6.32), Equation (6.33) is obtained. This equation serves as the definition of K_1, a parameter that can be calculated fully from TM-XCS measurements.

$$K_1 = \frac{1}{\Delta f_1^{(S)}} + \frac{1}{\Delta f_2^{(S)}} - \frac{1}{\Delta f_{p12}^{(S)}} = \frac{A_5 \left(A_5 + A_6\right)}{A_4 A_6} = \frac{A_5}{A_6 \left(f_{out,SC}^{(S)} - A_3\right)} \tag{6.33}$$

The subscript and the superscript notations used above were explained in the previous section. In Equation (6.33), $\Delta f^{(S)}$ is the difference between the measured frequencies and the free running frequency of the oscillator for the series loaded case. It can be expressed as:

$$\Delta f_k^{(S)} = f_{out,k}^{(S)} - f_{out,SC}^{(S)}, \quad k \in \{1, 2, \text{s12}, \text{p12}, \text{OC}, \text{SC}\}. \tag{6.34}$$

The $f_{out,SC}^{(S)} - A_3$ term in the denominator of Equation (6.33) is labelled as $\eta_{SC}^{(S)}$ with the help of the definition:

$$\eta_k^{(S)} = f_{out,k}^{(S)} - A_3, \quad k \in \{1, 2, \text{s12}, \text{p12}, \text{OC}, \text{SC}\}. \tag{6.35}$$

Then the ratios of A_4/A_5 and A_5/A_6 can simply be expressed from Equation (6.32e) and the definition of K_1 in Equation (6.33) as:

$$\frac{A_4}{A_5} = \frac{f_s C_{1,q}}{2C_{0,q}} = \eta_{SC}^{(S)} + \frac{1}{K_1}. \tag{6.36}$$

$$\frac{A_5}{A_6} = K_1 \eta_{SC}^{(S)}. \tag{6.37}$$

The unknown capacitors, C_{x1} and C_{x2}, follow from Equation (6.32a), Equation (6.32b), and Equation (6.33). They are given as:

$$C_{x1} = \left[\frac{A_4 A_6^2}{(A_5+A_6)}\frac{1}{\Delta f_1^{(S)}} - A_5 A_6\right]\frac{1}{(A_5+A_6)} = \left[\left(K_1 \Delta f_1^{(S)}\right)^{-1} - 1\right] A_{par} \tag{6.38a}$$

$$C_{x2} = \left[\frac{A_4 A_6^2}{(A_5+A_6)}\frac{1}{\Delta f_2^{(S)}} - A_5 A_6\right]\frac{1}{(A_5+A_6)} = \left[\left(K_1 \Delta f_2^{(S)}\right)^{-1} - 1\right] A_{par}, \tag{6.38b}$$

where A_{par} can be expressed in terms of either of the crystal capacitors, namely $C_{1,q}$ or $C_{0,q}$:

$$A_{par} = \frac{A_5 A_6}{A_5+A_6} = \frac{C_{0,q}C_{cir}}{C_{0,q}+C_{cir}} = \frac{A_5}{\left(K_1 \eta_{SC}^{(S)} + 1\right)} = \frac{C_{0,q}}{\left[K_1\left(f_{out,SC}^{(S)} - f_s\right) + 1\right]} \tag{6.39a}$$

$$= \frac{A_4 K_1}{\left(K_1 \eta_{SC}^{(S)} + 1\right)^2} = \frac{f_s C_{1,q} K_1}{2\left[K_1\left(f_{out,SC}^{(S)} - f_s\right) + 1\right]^2} \tag{6.39b}$$

The capacitance ratio of the crystal, which is named as K_r, is found from Equation (6.36):

$$K_r = \frac{C_{1,q}}{C_{0,q}} = \frac{2\left(f_{out,SC}^{(S)} - f_s + K_1^{-1}\right)}{f_s}. \tag{6.40}$$

6.5.3.4 Summary of TM-XCS postprocessing: Series and parallel loaded cases

From the derivations presented in the last two subsections, we can conclude the following:

1. Processing of TM-XCS Parallel loading frequency measurement results can yield f_s by Equation (6.28) as well as the unknown capacitors C_{x1}, C_{x2} in terms of $C_{1,q}$ by Equation (6.29). However, no independent information regarding $C_{0,q}$ and C_{cir} is obtained as the parallel loaded frequency equations employ only their sum, $A_2 = C_{0,q} + C_{cir}$. Both β and f_s can be determined from *four* measurements of different C_{sensor} configurations in the case of parallel loaded XTL, namely $f^{(P)}_{out,1}$, $f^{(P)}_{out,2}$, $f^{(P)}_{out,s12}$, and $f^{(P)}_{out,OC}$. These four parameters are also sufficient for the determination of unknown capacitances in terms of C_{1q} according to Equation (6.29).
2. Processing of TM-XCS series loading frequency measurement results can yield us the ratio $K_r = C_{1,q}/C_{0,q}$ by Equation (6.40) as as well as the unknown capacitors C_{x1}, C_{x2} in terms of f_s and either $C_{1,q}$ or $C_{0,q}$ by Equation (6.38) and Equation (6.39). Both K_1 and $\eta^{(S)}_{SC}$ can be determined from *four* measurements of different C_{sensor} configurations in the case of series loaded XTL, namely $f^{(S)}_{out,1}$, $f^{(S)}_{out,2}$, $f^{(S)}_{out,p12}$, and $f^{(S)}_{out,SC}$. These four parameters are also sufficient for the determination of unknown capacitances in terms of f_s, and either C_{1q} or $C_{0,q}$ according to Equation (6.38).

Note that the results of the series loading only, does not yield a direct value for the unknown capacitances in terms of $C_{1,q}$ or $C_{0,q}$, but it requires the knowledge of f_s. On the other hand, the parallel loaded TM-XCS can yield f_s. So using the

results of both the series and the parallel loaded configurations, one can get the unknown capacitors, C_{x1} and C_{x2} in terms of either $C_{0,q}$ or $C_{1,q}$.

The critical question, at this stage is *how stable are the XTL capacitances* $C_{0,q}$ *and* $C_{1,q}$ *with respect to the temperature?* Are these parameters as stable as f_s, for which the quartz is matchless for, or do they have large temperature coefficients to require accurate knowledge of the temperature and subsequent temperature compensation? The answers to these questions are discussed in the next section, which investigates the self-temperature sensing capability from the frequency measurements of TM-XCS.

6.5.3.5 Self-temperature sensing using TM-XCS

$C_{1,q}$ and $C_{0,q}$ need to be known at the measurement conditions for TM-XCS to function as a temperature independent measurement method. In a capacitive sensing application targeted towards measuring C_{x1} and C_{x2}, it would only make sense to use a calibration based approach to determine XTL capacitors. For this purpose, one needs to know the temperature of operation, and then using the known dependence on temperature through polynomial expansion coefficients, $C_{1,q}$ and $C_{0,q}$ can be calculated.

Ideally speaking, if the knowledge of f_s versus temperature is one-to-one, temperature can be determined from the knowledge of f_s. This parameter can be calculated from the parallel-loaded TM-XCS data. However, depending on the range of temperatures considered and the cut of the XTL, frequency versus temperature is not one-to one in general. Furthermore, the sensitivities of frequency to temperature can be very low, causing large errors in temperature predictions from small errors in frequency measurements. These points were discussed in Sec-

tion 6.1.3 on dual-mode μ-computer compensated oscillators, which successfully implements the idea of approximating a certain variable as a polynomial function of temperature [136, 156].

Temperature dependence of AT-cut crystals can be described by a three-term power series over a wide temperature range [17].

$$\frac{f_s(T) - f_s(T_0)}{f_s(T_0)} = \frac{\Delta f_s}{f_{s0}} = a_{fs}\Delta T + b_{fs}\Delta T^2 + c_{fs}\Delta T^3 \tag{6.41}$$

Here, $\Delta T = T - T_0$ is the difference between the operation temperature T and the reference temperature T_0. Assuming a similar power series expansion is also valid for both $C_{1,q}$ and $C_{0,q}$, we have:

$$\frac{C_{1,q}(T) - C_{1,q}(T_0)}{C_{1,q}(T_0)} = \frac{\Delta C_{1,q}}{C_{1,q0}} = a_{C1q}\Delta T + b_{C1q}\Delta T^2 + c_{C1q}\Delta T^3 \tag{6.42a}$$

$$\frac{C_{0,q}(T) - C_{0,q}(T_0)}{C_{0,q}(T_0)} = \frac{\Delta C_{0,q}}{C_{0,q0}} = a_{C0q}\Delta T + b_{C0q}\Delta T^2 + c_{C0q}\Delta T^3 \tag{6.42b}$$

Despite the large amount of literature on frequency versus temperature characteristic of XTLs, the temperature dependence of Butterworth - Van Dyke circuit parameters, namely $C_{1,q}$ and $C_{0,q}$, is harder to find. Holbeche and Morley investigated this problem by their experiments on approximately 70 AT-cut XTL's with fundamental frequencies ranging from 4 to 20 MHz [18]. They measured first-order temperature coefficient of $C_{1,q}$ to be about 230 ppm/°C with a standard deviation smaller than 30 ppm/°C. This temperature coefficient is two to three orders of magnitude larger than that of f_s for typical AT-cut quartz. Therefore, they concluded that:

> "In AT-cut crystals the temperature variation in C_1(i.e., $C_{1,q}$) must be compensated by a more or less equal and opposite change in motional

inductance L_1(i.e., $L_{1,q}$). The familiar cubic-frequency/ temperature curves result from small imbalances between these two quantities."

Other important findings of the authors include a nonlinearity of less than 2% in $C_{1,q}$ versus temperature characteristic. In addition they also report temperature coefficients of motional capacitance to be rather independent of the resonant frequency and the angle of cut.

They have not reported considerable change in $C_{0,q}$ down to three digit resolution. This observation is in agreement with the reported first order temperature coefficient as small as 30 ppm/°C by Ballato [17].

Following the example in [17], the calculations in this section are based on the parameters and temperature coefficients as listed below:

$$a_{fs} = -0.386 \times 10^{-6}\ /\mathrm{K}, \quad b_{fs} = +0.038 \times 10^{-9}\ /\mathrm{K}^2, \quad c_{fs} = +108 \times 10^{-12}\ /\mathrm{K}^3,$$

$$a_{C0q} = +30 \times 10^{-6}\ /\mathrm{K},$$

$$C_{1,q}(T_0)/C_{0,q}(T_0) = 1/240\ @\ T_0 = 25°\mathrm{C}.$$

For the first order temperature coefficient of $C_{1,q}$, the approximate value given by [18] is taken, i.e., $a_{C1q} = 230$ ppm/°C. Lastly, the second and third order temperature coefficients of both the static and motional capacitances are neglected: $b_{C0q} \approx c_{C0q} \approx 0$, $b_{C1q} \approx c_{C1q} \approx 0$. Then, from Equation (6.42), the temperature dependence of the capacitance ratio K_r can be expressed as

$$\frac{K_r}{K_{r0}} = \bar{K_r} = \frac{1 + a_{C1q}\Delta T}{1 + a_{C0q}\Delta T}, \tag{6.43}$$

where K_{r0} is the value of $C_{1,q}/C_{0,q}$ at $T = T_0$, and $\bar{K_r}$ is the normalized form. The calculation of K_r from TM-XCS measurements is given by Equation (6.40). *If we*

assume that the series and parallel loaded XTL measurements of different configurations of TM-XCS are done much faster than the changes in temperature, then the temperature during the series and the parallel measurements can be assumed to be the same. In this case, $f_{out,SC}^{(S)} = f_{out,OC}^{(P)}$. So Equation (6.40) can be rewritten as

$$K_r = \frac{C_{1,q}}{C_{0,q}} = \frac{2\left(\beta + K_1^{-1}\right)}{f_s} = \frac{2\left(\beta + K_1^{-1}\right)}{f_{out,OC}^{(P)} - \beta}. \tag{6.44}$$

Therefore, theoretically speaking, TM-XCS, requires *seven* measurements to yield an absolute capacitance measurement, namely $f_{out,1}^{(P)}$, $f_{out,2}^{(P)}$, $f_{out,s12}^{(P)}$, $f_{out,1}^{(S)}$, $f_{out,2}^{(S)}$, $f_{out,p12}^{(S)}$, and either $f_{out,SC}^{(P)}$ or $f_{out,SC}^{(S)}$. As the difference in the last two measurements is a good indication of the validity of the "assumption of constant temperature among measurements of series and parallel loaded XTL cases", an extra measurement is not fully redundant. Hence, TM-XCS measurement overhead is estimated to be *eight* times the standard frequency measurement approaches. This number will be used in the discussion of the maximum sampling rate. Note that both the circuit in Figure 6.17 and Figure 6.18 are capable of performing all of the eight measurements with appropriate switching cycles. If the unknown capacitors do not satisfy either the series or the parallel loaded XTL oscillation conditions[13], then the circuit in Figure 6.17 is no more useful, since both the series and the parallel loaded configurations are necessary for the determination of unknown capacitors and temperature. In order to circumvent this situation, Figure 6.18 uses reference capacitors that can be included as desired to guarantee operation at a particular loading type. These reference capacitors can be used to calculate f_s in the case of parallel loading, and K_r in the case of series loading. Their temperature coefficients are completely insignificant since their absolute values are never used during TM-XCS.

[13] See Section 6.3.1.

Figure 6.19 compares the theoretical estimates of the dependence of series frequency f_s and capacitance ratio K_r on temperature T, using the values assumed above.

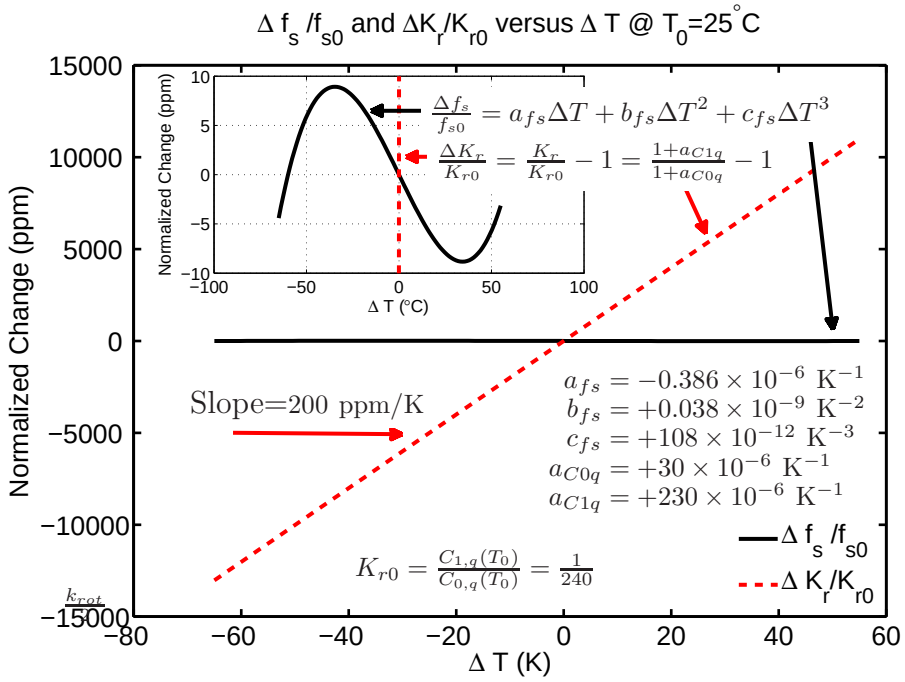

Figure 6.19: Calculated values of normalized variation in the series frequency of the crystal and the capacitance ratio, $K_r = C_{1,q}/C_{0,q}$. The temperature coefficients for f_s and $C_{0,q}$ are taken from [17]. The first order temperature coefficient for $C_{1,q}$ is taken from [18]. The inset shows a close-up of the frequency-temperature characteristic, revealing the common third order characteristics in AT-cut crystals.

In Figure 6.19, linearity, one-to-one characteristics, and three orders of magnitude difference in temperature sensitivity make the capacitance ratio K_r a much better quantity to track than frequency to extract the operation temperature of the XTL. However, it should be emphasized that the linearity of K_r over large temperature changes such as the one in Figure 6.19 is a result of neglecting second and third order temperature coefficients of XTL. Although theoretical estimates

based on the results of the reference [18] are promising, the superiority of K_r versus temperature characteristic needs dedicated experimental verification, before TM-XCS can practically come out as a self-temperature sensing method, as did dual mode microcomputer compensation.

6.5.4 Summary and discussion on TM-XCS

TM-XCS can provide a method of absolute capacitance measurement if the temperature variation of either of the capacitances of the XTL, $C_{1,q}$ or $C_{0,q}$, is well known. TM-XCS can compensate for the nonlinearity that many alternative, op-amp based capacitive read-out methods do not suffer from. However, the alternative approaches need a separate, precise temperature sensor to compensate for the variation in the reference capacitor and supply voltage values[14]. The advantage of TM-XCS is to offer a self-temperature sensing and nonlinearity compensation algorithm to reap the benefits of high precision oscillator frequency measurements in case of operation over large temperature differences and sensor capacitance changes.

As explained in the previous section, TM-XCS requires eight measurements to determine the temperature and the value of the unknown capacitance given that XTL Butterworth-Van Dyke model is precisely known as a function of temperature. The implicit assumption in the TM-XCS postprocessing calculations is that the temperature is constant during the eight measurements. Otherwise, the unknown parameters such as f_s, and C_{x1} are no longer constants, and they can not be solved by only using the information from different capacitor configuration measurements. If the switching time between different capacitance configurations

[14]See Equation (6.1).

is much smaller than the smallest thermal time constant in the system, taking the temperature to be constant during the eight measurements is a reasonable approximation. Making the situation more complex is the intrinsic power consumption of the XTL. As C_{sensor} changes between different configurations of Figure 6.15, the power dissipated in the XTL is inevitably going to change, as the impedance of the motional branch changes. To unveil the exact analytical conditions necessary for the validity of the constant temperature assumption, the thermal response of the XTL in the oscillator circuit is studied next.

6.5.5 Thermal response and self-heating effects of the XTL under different capacitive loadings

The average power in the crystal due to a harmonic voltage of amplitude $V_{XTL,p}$ is calculated in Appendix L and rewritten below.

$$PWR_{XTL} = \Re < P_{XTL} > \approx \frac{|V_{XTL,p}|^2}{2R_{1,q}\left[1 + 4\left(pQ_q\right)^2\right]} \tag{6.45}$$

High performance oscillators commonly operate the crystals with very low power levels such as 2–10 μW [162, 163]. Corresponding temperature differences are also small, so it often suffices to consider only the first order temperature coefficient in Equation (6.41). Then from the definition of the frequency pulling,

$$f = f_s(T)(1+p) \approx f_s(T_0)(1 + a_{fs0}\Delta T_{SH})(1+p), \tag{6.46}$$

where

$$a_{fs0} = \frac{1}{f_s(T_0)}\frac{\partial f_s}{\partial T}\bigg|_{T=T_0} \tag{6.47}$$

is the first order temperature coefficient at the reference temperature T_0.

ΔT_{SH} is the temperature change due to self-heating effect on the XTL and is expressed in Equation (6.48) using the thermal conductance of the XTL, $G_{th,XTL}$.

$$\Delta T_{SH} = \frac{PWR_{XTL}}{G_{th,XTL}}. \tag{6.48}$$

A second order approximation to the output frequency, which considers the effects of self-heating using Equation (6.46) and Equation (6.45), takes the following form:

$$f = f_s(T_0)\left[(1+p)\left(1+\frac{\beta_{th}}{\left[1+4\left(pQ_q\right)^2\right]}\right)\right], \tag{6.49}$$

where

$$\beta_{th} = a_{fs0}\left(\frac{V_{XTL,p}^2}{2R_{1,q}G_{th,XTL}}\right). \tag{6.50}$$

It is apparent from Equation (6.49) and Equation (6.50) that if either

$$\beta_{th} \ll 1 \quad \text{or} \quad \frac{\beta_{th}}{\left[1+4\left(pQ_q\right)^2\right]} \ll 1,$$

then effects of self heating can be neglected.

Next, a numerical example is presented to give a rough idea about the magnitudes of some of the parameters related to the thermal response of the XTL. Let us consider a $h_{XTL} \approx 100$ μm thick, circular (radius $r_1 = 10$ mm), 16 MHz AT-cut, thickness-shear mode resonator with a circular electrode region (radius $r_2 = 5$ mm). A back of the envelope approximation to the thermal conductance is $G_{th,XTL} = 2\pi\kappa_{th,XTL}h_{XTL}/\ln(r_1/r_2)$, where $\kappa_{th,XTL}$ is quartz thermal conductivity [164]. Taking $\kappa_{th,XTL} = 6.2$ W/Km yields $G_{th,XTL} = 5.62$ mW/K. Thermal capacitance of the XTL is found as $C_{th,XTL} = 65.3$ mJ/K assuming a heat capacity per unit volume of $c_{th} = 2.08$ J/(Kcm^3). This gives a thermal time constant of $\tau_{th} = C_{th,XTL}/G_{th,XTL} = 11.6$ sec.

At a nominal XTL power consumption of $PWR_{XTL} = 10\ \mu$W, if we take 100% power modulation due to C_{sensor} variations[15], temperature change due to self heating becomes $\Delta T_{SH} \approx 1.8$ mK. At ppm/K temperature sensitivities, mK level temperature difference yields normalized errors on the order of $parts - per - billion$.

Switching of the oscillator can happen at a much faster rate than the thermal time constant of the XTL. In this case the magnitude of the temperature ripple will be smaller, as the switching cycle is complete long before the exponential temperature transient is over, which would take about 5 times τ_{th}. If the switching is done at 10 Hz, yielding a switching period of $T_{switch} = 100$ msec, the error due to self-heating between TM-XCS measurements would be multiplied[16] by a factor of $T_{switch}/\tau_{th} = 0.1$ sec/11.6 sec $\approx 10^{-2}$. In other words, normalized error of 10^{-9} that was calculated above for a fully settled thermal transient would be reduced down to 10^{-11} for the fast switching case.

Despite the improved error levels in case of faster switching, it also leaves less integration time for the frequency measurement at different C_{sensor} configurations during TM-XCS. Typically, error stemming from the frequency measurement unit increases at smaller integration times. This tradeoff should be considered carefully to minimize the final error in the measurements.

Maximum sampling frequency of a TM-XCS system such as the one in Figure 6.18 is dictated by the switching frequency of the switches. This frequency depends on the oscillator settling time and the switch characteristics. TM-XCS requires eight measurements for each determination of the triplet (C_{x1}, C_{x2}, T). *Leaving some room for postprocessing, setup and hold time complications, an up-*

[15]Full modulation of the nominal power is a rather unrealistic assumption, but it is on the conservative side.

[16]The factor of five mentioned above is disregarded to be on the conservative side.

per bound for maximum capacitive sampling rate is about an order of magnitude slower than the switching frequency.

In order to avoid oscillation quenching that would severely and unnecessarily lengthen the settling time of the oscillator, it is very crucial that even during intermediate states between the configurations of Table 6.5, oscillation is always maintained.

6.6 Estimation of the best performance for the capacitive readout using crystal oscillator

6.6.1 Minimum detectable value of capacitance

Minimum detectable signal or resolution of any sensing system based on quartz is dictated by the largest of the stability deteriorating factors. The list of such environmental factors is not a short one [165]. In a 1995 paper, Walls and Vig cite flicker noise in frequency as the fundamental limit of accuracy at the time of their writing [163]. Allan deviation due to flicker noise in frequency is given as a *phenomological* [166] relation by Equation (6.51) for measurement times of order Q_q/f.

$$\sigma_y(\tau) \approx \frac{C_{flicker}}{Q_q}, \text{where} \tag{6.51}$$

$$C_{flicker} = \begin{cases} 2.8 \times 10^{-7} & : \quad \text{by Walls, in 1988 [166]} \\ 2.0 \times 10^{-7} & : \quad \text{by Vig } \textit{et al.} \text{ , in 1996 [167]} \\ 1.0 \times 10^{-7} & : \quad \text{by Vig and Walls, in 2000 [144]} \end{cases} .$$

Here, f is the oscillation frequency, and τ is the measurement time. Vig and Walls also cite the maximum frequency - quality factor product for bulk-acoustic wave (BAW) devices as:

$$(Q_{max} f)_{BAW} = 1.6 \times 10^{13} \text{ Hz, for AT- and SC-cuts.} \tag{6.52}$$

Combining Equation (6.52) with Equation (6.51) for the best case yields [144]:

$$\sigma_y(\tau, f) > 6 \times 10^{-21} f, \tag{6.53}$$

for a BAW device.

Consistent with the notation of sensitivity used in Section 6.3, let us define the normalized first order sensitivity of a dependent(output) variable υ to an independent (input) variable φ in the following manner:

$$\bar{S}_{\upsilon/\varphi}(\upsilon_0, \varphi_0) = \frac{1}{\upsilon_0} \frac{\partial \upsilon}{\partial \varphi} = \frac{1}{\upsilon_0} S_{\upsilon/\varphi}, \tag{6.54}$$

In Equation (6.54), υ_0 and φ_0 are the operating point values of the dependent and independent variables, respectively. Furthermore, minimum detectable signal (MDS) of the sensed variable φ, from the observation of the monitored variable υ, can be expressed as in Equation (6.55). The ratio of $\sigma_y(1sec)$ to sensitivity, which is MDS at 1 sec measurement time, is a possible figure-of-merit for sensor systems [144].

$$\text{MDS}_{\varphi}(\tau, \upsilon_0, \varphi_0) = \frac{\sigma_{y,\upsilon_0}(\tau)}{\bar{S}_{\upsilon/\varphi}} \tag{6.55}$$

In order to numerically estimate the minimum detectable capacitance in case of capacitive sensing by XTL oscillators, we assume a typical sensitivity value from the results of the Section 6.3.2 and 6.3.3. Considering Figure 6.9 and Figure 6.11, which were plotted with no optimization in mind, a normalized sensitivity, $\bar{S}_{f/C}$ of 50 ppm/pF is a conservative value. This is approximately the value that can be

extracted from the results of Matko *et al.* , who use a crystal that is serially loaded with a capacitive liquid volume measurement sensor[17] [139]. The same author has reported more than 110 ppm/pF sensitivity, making the choice of 50 ppm/pF a rather conservative one [154].

Using the above value of normalized sensitivity and Equation (6.51), the minimum detectable sensor capacitance that can be resolved with XTL based capacitive sensors for τ *on the order of* Q_q/f takes the following form:

$$\tau \approx Q_q/f \Rightarrow \mathrm{MDS}_C(\tau, f, C)\Big|_{\bar{S}_{f/C}=50 \text{ ppm/pF}} > 1.2 \times 10^{-28} f, (\text{ in Farad}). \quad (6.56)$$

Specifications from experimental works reported in the literature or from commercial products are used to estimate the performance in the following discussion. This should make our findings more realistic as opposed to directly using Equation (6.51) that predicts a lower limit on the minimum detectable signal.

A commercial oven controlled crystal oscillator (OCXO-8607) from Oscilloquartz claim $\sigma_y(\tau) \approx 3 \times 10^{-13}$ for measurement times as low as 0.2 sec [168]. Their design uses an SC-cut, 3$^{\text{rd}}$ overtone crystal. On the other hand, for an experiment performed *without* any special environment control, Besson [162] reports $\sigma_y(0.36sec) = 1.2 \times 10^{-11}$. His results are from a 5 MHz, fifth overtone, AT-cut XTL. Both Oscilloquartz and Besson used a so-called electrodeless BVA design that eliminates an important source of instability. Please note that even the result from the oven-controlled XTL oscillator satisfies Equation (6.51) with a safety margin of an order of magnitude.

A more conservative estimate for MDS_C based on the values and experimental

[17] See Figure 2 in the reference.

conditions reported in the papers referenced above are then:

$$\mathrm{MDS}_C(\tau)\Big|_{\bar{S}_{f/C}=50\ \mathrm{ppm/pF}} > \begin{cases} 6\times10^{-21}\ \mathrm{F} & : \begin{array}{c}\tau = 0.2\ \mathrm{sec},\\ \textit{controlled}\ \text{env. [168]}\end{array} \\ 2.4\times10^{-19}\ \mathrm{F} & : \begin{array}{c}\tau = 0.36\ \mathrm{sec},\\ \textit{uncontrolled}\ \text{env. [162]}\end{array} \end{cases} \tag{6.57}$$

The important question at this stage, before capacitive sensor attributes and related sensitivity comes into the picture, is about the standing of Equation (6.57) as compared to the state of the art capacitive detection. Capacitive readout circuitry of a surface micromachined accelerometer ADXL-150, from Analog Devices, is a commercially available, high-resolution implementation. Therefore capacitive accelerometers are chosen as the case study for comparison. ADXL-150's unofficial specifications are known very well despite being a commercial product[18], thanks to Senturia's calculations in his case study of the accelerometer [145, §19.4.4, p. 524]. He estimates the sensitivity of ADXL-150 to be,

$$S_{C/acc} \approx \frac{1.0\times10^{-18}\ \mathrm{F}}{32\ \mathrm{mg}} = 3.13\times10^{-17}\ \mathrm{F/g}, \tag{6.58}$$

where $\mathrm{g} = 9.81\ \mathrm{m/(sec^2)}$, and *acc* represents acceleration.

Input referred noise density (IRND) of ADXL-150 is specified as 1 $\mathrm{mg}/\sqrt{\mathrm{Hz}}$ [169]. There are two main contributions to IRND, namely electrical (readout) noise and mechanical (Brownian) noise. Total IRND is found as a root-mean-square average of both contributions [33]. Expressions for total-rms IRND is given by Equation (6.59). The forthcoming expressions use subscripts "el" and "mec" to distinguish between different components of noise.

$$\mathrm{IRND}_{acc} = \sqrt{[\mathrm{IRND}_{acc}]^2_{el} + [\mathrm{IRND}_{acc}]^2_{mec}} \tag{6.59}$$

$$[\mathrm{IRND}_{acc}]_{mec} = \sqrt{\frac{4\mathrm{k_B}T\omega_{0,sensor}}{m_{sensor}Q_{sensor}}} \tag{6.60}$$

[18]This model is now obsolete and replaced by another model from iMEMS© series.

Equation (6.60) gives the mechanical contribution to the MDS in terms of sensor mass m_{sensor} [kg], temperature T [K], Boltzmann constant k_B, angular resonance frequency of the sensor $\omega_{0,sensor}$, and quality factor of the sensor Q_{sensor} [145, §19.2]. Using the values that are given by Senturia, as well as Equation (6.59), and Equation (6.60), mechanical and electrical contributions to IRND of ADXL-150 can be calculated to be[19] [145, §19]:

$$[\text{IRND}_{acc}]_{mec} = 155.8\ \mu\text{g}/\sqrt{\text{Hz}} \tag{6.61}$$

$$[\text{IRND}_{acc}]_{el} = 987.8\ \mu/\sqrt{\text{Hz}} \approx 1\ \text{mg}/\sqrt{\text{Hz}} \tag{6.62}$$

Then IRND of the capacitive readout (i.e., only electrical contribution) of ADXL-150 can be estimated as:

$$[\text{IRND}_C]_{el} = 1\ \text{mg}/\sqrt{\text{Hz}} \times 3.13 \times 10^{-17}\ \text{F/g} = 3.13 \times 10^{-20}\ \text{F}/\sqrt{\text{Hz}}$$

Ignoring flicker noise and assuming that the measurement bandwidth BW is 3 Hz $\approx 1/0.3$ sec, ADXL-150 minimum detectable signal would be[20]:

$$[\text{MDS}_C(0.3\ \text{sec})]_{el} = [\text{IRND}_C]_{el}[BW] \approx 5.42 \times 10^{-20}\ \text{F} \tag{6.63}$$

Comparing MDS values for quartz and ADXL in Equation (6.57) and Equation (6.63), a conservative estimate of quartz in a controlled environment can show almost an order of magnitude better performance than the leading-edge, capacitive

[19] Senturia's list is as follows: $m_{sensor} = 2.2 \times 10^{-10}$ kg, $\omega_{0,sensor} = 2\pi \times 24.7$ krad/sec, $Q_{sensor} = 5$. Unlike Senturia however, who calculates $[\text{IRND}_{acc}]_{mec}$ to be 500 $\mu\text{g}/\sqrt{\text{Hz}}$, we calculate it to be 155.8 $\mu\text{g}/\sqrt{\text{Hz}}$. Irrelevant of what value is right, the difference would change Equation (6.62) by only 13% and therefore it comes no way near to changing the forthcoming conclusions in this report.

[20] 3 Hz is picked to make sure we compare the CMOS noise and quartz noise at similar measurement times, τ, to those that are reported in the references used for comparison. In other words: $\tau = 0.3$ sec is close to the average of integration times quoted in Equation (6.57).

readout based on amplitude modulation at similar measurement times. Furthermore, this statement is true even when we neglect the flicker noise of the latter. Controlled environment made for quartz, however, is a rather unrealistic assumption for low-power and low-cost sensor market. The same is also true for commercial products as well. The most important nuisance is temperature fluctuations. For instance the datasheet of a more recent accelerometer that costs about 14 US dollars from Analog Devices, ADXL-103, indicate an average voltage output change[21] of 1 mV/2.5 V = 400 ppm over the temperature range from -10°C to 70°C. On the other hand, a quartz XTL that costs about 80 US cents, shows a normalized frequency sensitivity of ±50 ppm in the same temperature range [170]. Therefore, as far as the stability goes, any alternative to quartz has a very tough rival to beat, thanks to the decades of research on precision frequency control.

6.6.2 Minimum detectable value of the sensed entity

For capacitive sensor applications, the final sensitivity to the measured variable and minimum detectable signal can be found using the chain rule. If we have dependent variables υ, γ, independent variables φ; and all dependence of υ on φ is via γ, then normalized sensitivity of υ to φ and MDS take the following forms:

$$\bar{S}_{\upsilon/\varphi}(\upsilon,\gamma(\varphi)) = \frac{1}{\upsilon_0}\frac{\partial\upsilon}{\partial\varphi} = \frac{1}{\upsilon_0}\frac{\partial\upsilon}{\partial\gamma}\frac{\partial\gamma}{\partial\varphi} = \left[\bar{S}_{\upsilon/\gamma}(\upsilon_0,\gamma_0)\right]\left[S_{\gamma/\varphi}(\gamma_0,\varphi_0)\right] \tag{6.64a}$$

$$\mathrm{MDS}_{\varphi}(\tau,\upsilon,\gamma(\varphi)) = \frac{\sigma_y(\tau,\upsilon)}{\bar{S}_{\upsilon/\varphi}} = \frac{\sigma_y(\tau,\upsilon)}{\bar{S}_{\upsilon/\gamma}S_{\gamma/\varphi}} = \frac{\mathrm{MDS}_{\gamma}(\tau,\upsilon,\gamma)}{S_{\gamma/\varphi}}. \tag{6.64b}$$

For example, in case of a capacitive acceleration sensor, one takes, in Equation (6.64), φ as acceleration, γ as C, and υ as the measured oscillator frequency.

[21] Based on the variation of the self-test output response of ADXL-103.

6.6.3 Estimation of quartz capacitive readout performance in comparison to a commercial CMOS capacitive readout

So far the discussion of performance of a capacitive accelerometer was limited to prediction of MDS due to capacitive readout noise, i.e., due to electronic noise. Brownian noise is another contribution for capacitive accelerometers relying on a moving proof mass. Distinguishing between different components of electrical and mechanical noise with "el" and "mec" subscripts, respectively, we express the total MDS for capacitance as:

$$\mathrm{MDS}_C = \sqrt{[\mathrm{MDS}_C]_{el}^2 + [\mathrm{MDS}_C]_{mec}^2} \tag{6.65}$$

A similar equation can be written also for MDS_{acc}. Considering only Brownian noise, Equation (6.66) gives the mechanical contribution to MDS_{acc} in terms of sensor mass m_{sensor} [kg], temperature T [K], Boltzmann constant $\mathrm{k_B}$, angular resonance frequency of the sensor $\omega_{0,sensor}$, quality factor of the sensor Q_{sensor}, and the measurement bandwidth BW [145, §19.2].

$$[\mathrm{MDS}_{acc}]_{mec} = [\mathrm{IRND}_{acc}]_{mec}\sqrt{BW} = \sqrt{\frac{4\mathrm{k_B}T\omega_{0,sensor}[BW]}{m_{sensor}Q_{sensor}}} \tag{6.66}$$

To summarize and quantify all the discussion in this section, Table 6.6 lists estimated MDS of capacitance as a function of readout circuit type and capacitive sensor technology. It unveils the typical bottlenecks for the improvement of MDS as a function of sensor and electronics implementations.

Table 6.6: Minimum detectable acceleration (MDS_{acc}) estimate of quartz based capacitive readout and a commercial CMOS capacitive readout, based on typical sensitivities from two sensor technologies: bulk and surface-micromachining. [a]

		Capacitive Sensor					
		Bulk-Micromac. [158] $S_{C/acc} = 8$ pF/g $[\text{IRND}_{acc}]_{mec} = \ldots$ 700 ng/$\sqrt{\text{Hz}}$			**Surface Micromac./ Post-CMOS** [145, 169] $S_{C/acc} = 31.3$ aF/g $[\text{IRND}_{acc}]_{mec} = \ldots$ 155.8 μg/$\sqrt{\text{Hz}}$ [d]		
		el.	mech.	Σ_{rms}	el.	mech.	Σ_{rms}
Capacitive Readout	**XTL, Controlled env.** [b] $[\text{MDS}_C]_{el} = 6 \times 10^{-21}$ F @ $\tau = 0.2$ sec [168]	0.75 ng	1.2 μg	1.2 μg	192 μg	270 μg	331 μg
	XTL, Uncontrolled env. [b] $[\text{MDS}_C]_{el} = 2.4 \times 10^{-19}$ F @ $\tau = 0.36$ sec [162]	30 ng	1.2 μg	1.2 μg	7667 μg	270 μg	7671 μg
	CMOS [c] $[\text{MDS}_C]_{el} = 5.42 \times 10^{-20}$ F @ $\tau = 0.3$ sec [145]	6.78 ng	1.2 μg	1.2 μg	1732 μg	270 μg	1753 μg

[a] A bandwidth of 3 Hz is assumed in the calculation of the mechanical contribution.
[b] $S_{f/C} = 50$ ppm/pF. See Equation (6.57).
[c] Electrical bandwidth is taken to be about 3 Hz. See Equation (6.63).
[d] See Equation (6.58) and Equation (6.61).

It is clear from Table 6.6 that, even bulk micromachining cannot provide the large proof-mass to stiffness ratio for the current state-of-the-art MEMS sensors [33] to fully exploit the capacitance resolution of both the quartz and CMOS-leading edge capacitive readout systems.

Subjectively speaking, at the moment, MEMSIC's solution, turns out to be the optimum solution for low bandwidth, low resolution, low cost edge of the market. Unlike capacitive detection, their solution requires only a monolithic CMOS process, and they do not suffer from some of the constraints due to having moving

parts as in other post-CMOS processing approaches [158]. Beating the cost of a CMOS-only sensor is unlikely for other approaches that require extra components like quartz XTLs or special processes like MEMS-on-CMOS in addition to CMOS itself.

However, if ultimate resolution is required, quartz based capacitive readout systems offer an advantage provided that the detection is not limited with the Brownian noise of the sensor. The subnano-g acceleration sensitivity in Table 6.6 is outstanding and stands very well in terms of resolution/cost as compared to other high performance accelerometers that are on the market[22]. As such, accelerometers relying on quartz based capacitive detection can be a strong contender for high-resolution, high-stability, low bandwidth side of the inertial-sensor market.

6.7 Experimental work

The calculation of important XTL based sensing parameters and concepts such as sensitivity, frequency pulling, minimum detectable signal, and intrinsic sensitivity of the XTL to the quantity being measured are demonstrated in this section. Capacitive accelerometers are chosen as sensors for demonstration purposes, since they can easily be constructed and characterized. XTL characterization and Allan deviation measurements on the prototype oscillator both with and without the sensor are also given to support the claims made during the discussions related to the experimental and simulation work done.

It should be mentioned that the goal of the experiments was not to show a

[22]See for instance ACC797 from Omega → piezoelectric 5 $\mu g/\sqrt{Hz}$@100 Hz for 315 US$ in Jan-2009, or 8330A from Kistler Instrument Corporation → bulk - micromachined 0.4 $\mu g/\sqrt{Hz}$@100 Hz for 970 US$ in Jan-2009.

leading edge capacitive sensor, but to demonstrate the concepts introduced in the theory section of this chapter and verify some of the analytical models within. Experimentally, oscillator is always operated with its XTL parallel loaded, but comparisons are made to serial loaded case where applicable.

6.7.1 Crystal characteristics

Experimentally, equivalent circuit is calculated from the impedance characteristics of the same model crystal (ECS Inc, Part no: 160ECSXR, HC-49US series, 16 MHz) as the one used in the circuit of Figure 6.4. The measured impedance (using an HP-4194A impedance analyzer) of a crystal of the same type as the one used in the experiments is given in Figure 6.20. It indicates the desired resonance dip around 16 MHz along with a secondary one slightly past the first one. The secondary peak is ignored in the model extraction process.

All of the SPICE simulations reported in Section 6.4 use the equivalent circuit of the crystal extracted from this measurement, and the parameters are listed in Figure 6.20.

6.7.2 A hand-made capacitive sensor

A large scale capacitive sensor is manually assembled using a cantilever beam structure with a mass at the tip. The sensor picture and its schematic side-view are shown in Figure 6.21.

A standard 3×1 inch, 1 mm thick microscope slide is used as the base for the sensor. The same is used as the spacer between the electrodes. Both of the

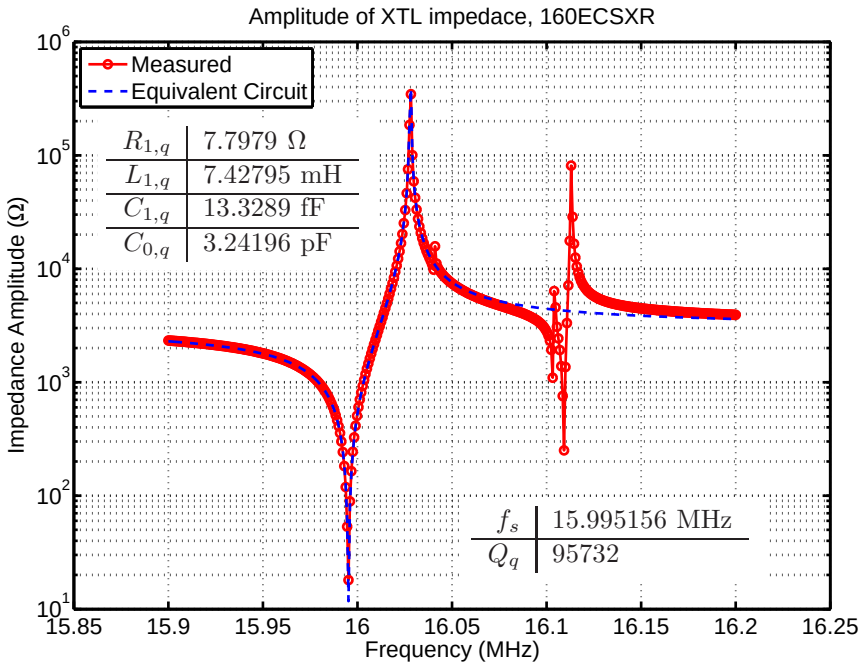

Figure 6.20: Impedance amplitude of the crystal model used in the experiments. The equivalent circuit only models the fundamental resonance. Parameters of the equivalent circuit, series resonance, and quality factor are indicated in the insets.

electrodes used were Cu/polyiminde[23] laminate to prevent a possible short circuit in case of touchdown of the top electrode. The mass used was either a SR23 watch battery ($mass_{bat} \approx 2.3$ gr), or a hexagonal nut ($mass_{nut} \approx 3.2$ gr). Although not performed rigorously, preliminary dynamic tests indicated a damped resonance frequency in the range from 0.5 Hz to 3 Hz for both the battery-mass and the nut-mass sensor.

[23]The Cu–polyimide (1 oz/ft^2 – 1 mil) laminate is from ROGERS Co. P/N:1100L110 x18.

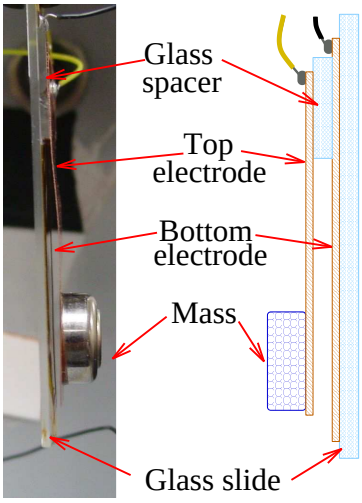

Figure 6.21: Optical picture and illustration of the sensor structure. Both of the electrodes are made of the same polyimide/Cu laminate to provide insulation between the electrodes under touchdown conditions. Watch battery or hex-nuts are used for the mass at the tip of the beam.

6.7.3 Measurement setup

The characterization of the oscillator-readout circuit was performed using a setup similar to the one shown in Figure 6.22.

Static acceleration was applied as a tilt with a manually controlled rotation stage (Newport , RSP-2). The value of the tilt angle and the static acceleration are related as :

$$\text{static acceleration} = acc = g\sin(\theta - \theta_0),$$

where g is the gravitational acceleration and θ_0 is the vertical reading on the θ-stage when the ADXL-103 acceleromter indicates zero acceleration[24]. The resolution of the stage was $\pm 2°$. The DC output of ADXL was measured using a $6\frac{1}{2}$-digit multimeter (Agilent 34401A). Sampling time was set to be ten times the wall

[24]Corresponding zero-acceleration nominal ADXL output is 2.5 V.

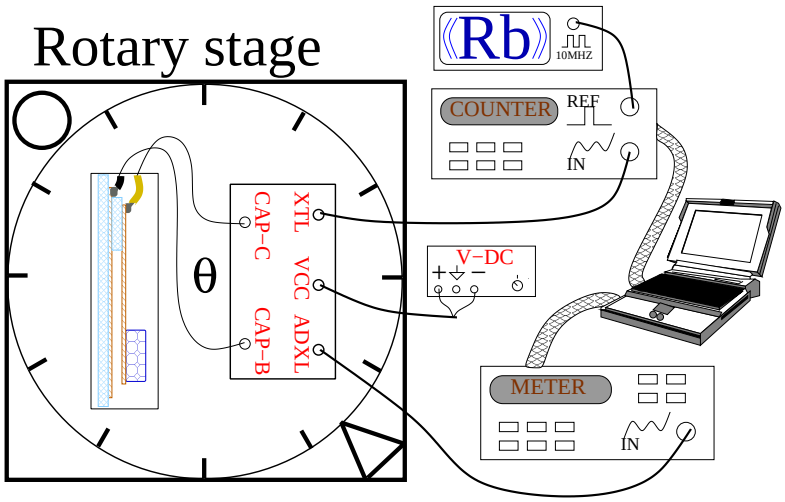

(a)

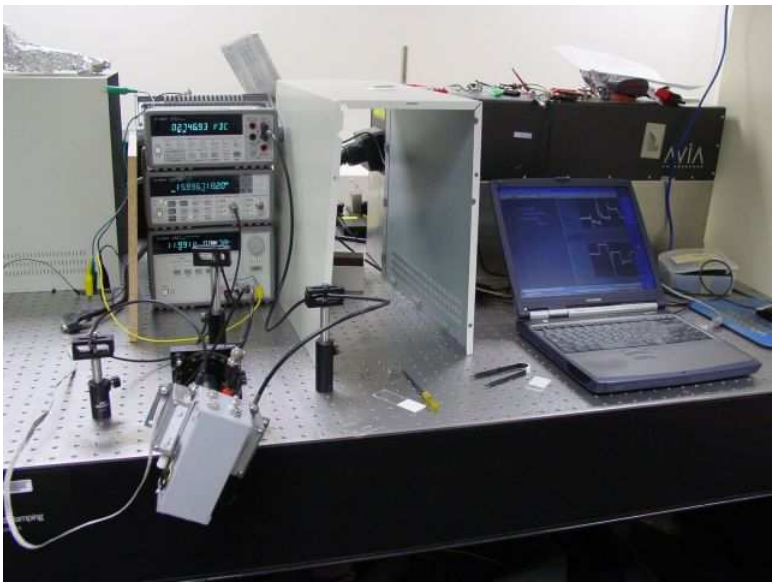

(b)

Figure 6.22: (a) Schematic view and (b) optical picture of the typical experimental setup that is used in many experiments reported. Frequency of the XTL is measured using a 12-digit, rubidium (Rb)-atomic clock-locked, frequency counter. The voltage output of the ADXL sensor is measured using a $6\frac{1}{2}$ digit multimeter.

power line frequency. The frequency of the oscillator circuit was recorded using a 12-digit universal frequency counter (Agilent 53131A) locked to a RB-frequency standard (Frequency Electronics Inc.). Although the experiments were carried out on an optical table, the table was non-floating only giving a degree of vibration damping due to its mass.

The rotation of the tilt stage was measured using ADXL-103, a commercial surface micromachined accelerometer from Analog Devices[25] [159]. Unless otherwise reported, all the results are from the device with hex-nut as the proof mass.

The oscillator circuit in Figure 6.4, which is intended for *parallel loading* of the sensor is assembled on a circuit board and cased with ADXL sensor. Due to the large size of the custom-assembled capacitive sensor, it is contained in a separate box. In order to minimize the wiring between the circuit and the sensor boxes, both of them were mounted on the rotating (θ) stage in all the experiments that involved rotation.

The operating power of the crystal was estimated to be around 2 mW, roughly 4 times the rated power. This was a result of not paying great attention to the XTL power issues at the design stage, since the goal was mostly model verification, rather than low power design. Typical precision XTL oscillators operate with a few μWatts of power [16, 162]. Overloading the XTL is known to increase aging and risk of damaging the crystal. As such, presented results can be considered on the worse (i.e., conservative) side.

[25]The choice of the commercial acceleromter was based on the superior noise performance in its class with a vendor specified input referred noise density (INRD) of 110 $\mu g/\sqrt{(}$Hz).

6.8 Capacitive sensor response

Static readout of the capacitance is measured using HP4194 for different values of tilt. Tilt angle, which is usually reported as an equivalent static acceleration, was calculated from the averaged ADXL-103 output on the circuit box. The alignment of the device-under-test (DUT) was such that when the gravitational vector was parallel to the electrodes in Figure 6.21, the static acceleration was zero. This point was calibrated by ensuring that ADXL measures zero tilt; in other words, its output is close to 2.5 V. The capacitance measurements were done at 100 kHz. This is much smaller than the crystal frequency, 16 MHz, and actual capacitance seen by the crystal can be less due to inductance of the wires. This complication is ignored in the calculations.

Figure 6.23 gives measured results of the capacitance for different values of static acceleration. Two cycles of rotation are performed to quantify any hysteresis involved. High nonlinearity and an obvious touchdown point in the plots are not surprising. However, considerable hysteresis observed between "cycle-1" and "cycle-2" is not expected. The time difference between these two measurement cycles was about 14 hrs. The offset between the "cycle-1" and "cycle-2" curves is not uniform, so it cannot merely be explained by temperature difference or change in air permittivity due to ambient humidity or temperature. One likely reason is that the polyimide/Cu electrode goes through plastic bending due to high mass to stiffness ratio. This property was used to actually tweak the undisplaced capacitance of the DUT. Another reason could be the contact related hysteresis as after touchdown, the restoring spring forces and gravity has to overcome capillary and other adhesion forces if they are significant.

The sensitivity of the capacitance to static acceleration can be calculated from

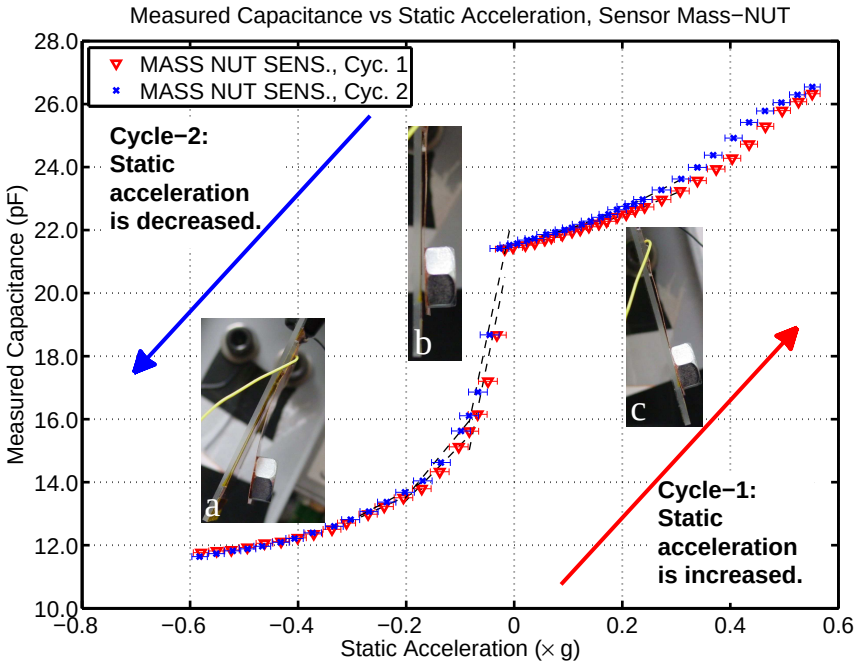

Figure 6.23: Measured capacitance of the sensor with mass NUT @ 100 kHz. Two cycles are done to quantify any hysteresis involved. "Cycle-1" is an ascending, "Cycle-2" is a descending sweep in terms of static acceleration. The sensor is highly nonlinear and the touchdown is obvious as a sharp change in slope. The insets show the pictures of the device taken approximately at (a)−0.44 g, (b)0 g, and (c)0.24 g.

the local derivative of the capacitance versus acceleration curve in Figure 6.23. Figure 6.24 plots a few data points obtained this way. Maximum sensitivity calculated is about 82 pF/g.

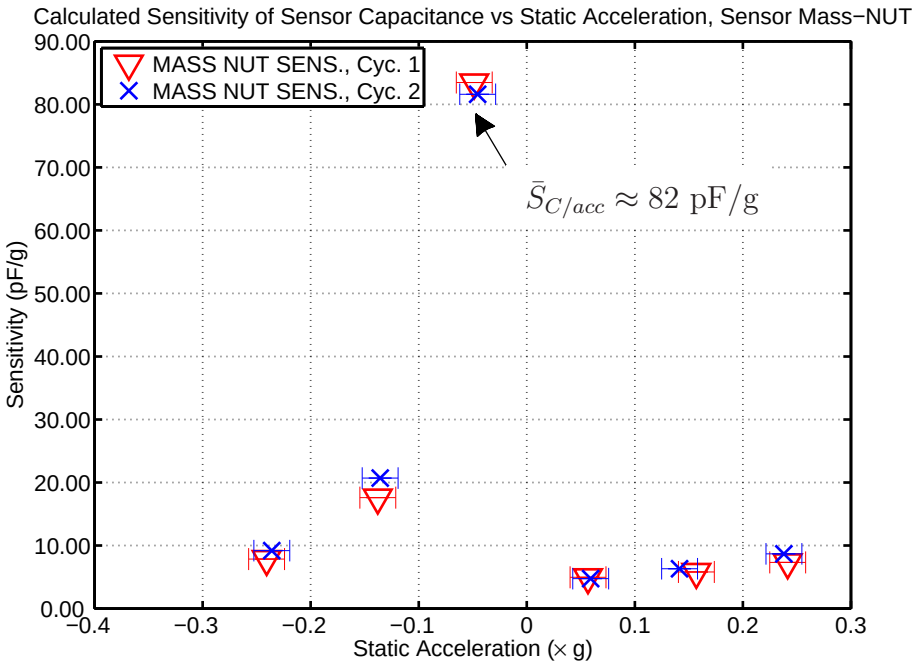

Figure 6.24: Sensitivity of capacitance to static acceleration change is calculated from the local slope of the capacitance versus static acceleration plot in Figure 6.23

6.8.1 Response of the capacitive readout circuit

6.8.1.1 Transient Waveforms at the Oscillator Output

Figure 6.25 plots the 16 MHz output of the oscillator without any sensor capacitance connected and also with $C_{sensor} = 0$ pF. SPICE simulation in the latter case is given as well. The simulations were carried out with nominal crystal values reported in Section 6.7.1, without modelling the oscilloscope input impedance, parasitics, and without any optimization of the standard discrete bipolar models. As such, there is a considerable difference between the transient waveforms. On the other hand, the matching in frequency between the experiment and the simulation is better than 1000 ppm.

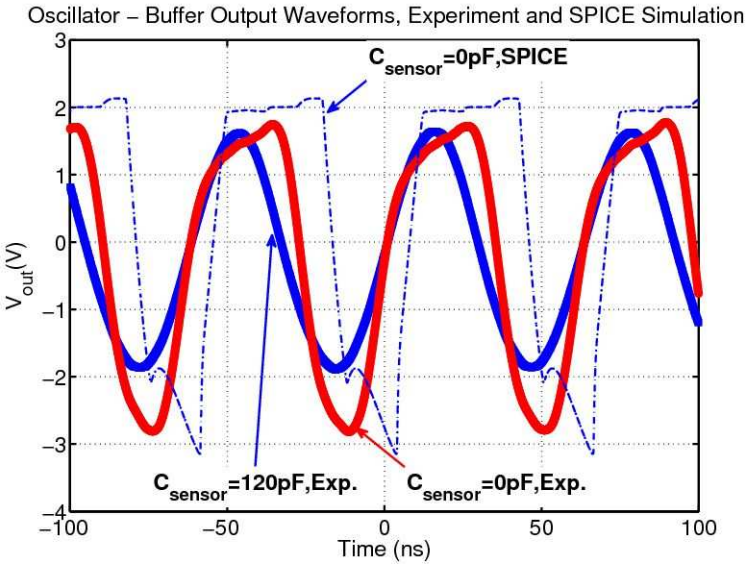

Figure 6.25: Captured waveform from the oscillator output without C_{sensor} and with C_{sensor} = 120 pF, which is realized by a ceramic capacitor. The data from the SPICE simulation with approximate model parameters and without taking parasitics into consideration are also shown.

6.8.1.2 Change of frequency due to varying discrete capacitors

In order to characterize the frequency change due to a known value of capacitance, the DUT was disconnected, followed by frequency measurements for different values of externally connected ceramic capacitors. The gate time of the frequency counter was set at 0.2 sec, and average frequency and standard deviation of the measurements were calculated from 100 consecutive measurements. The measured frequency is plotted as a function of the capacitor value in Figure 6.26. As first defined in Section 6.2.2; $L_{1,q}$, $C_{1,q}$, and $C_{0,q}$ of the crystal equivalent circuit, as well as $C_{in,buf}$ are extracted using a least-square fit of the form given in Equation (6.14). Extracted values are: $L_{1,q}$ = 7.43 mH, $C_{1,q}$ = 13.32 fF, $C_{0,q}$ = 3.99 pF. These values are given as insets in Figure 6.26 and match very well to the parameters of another XTL of the same model characterized and reported in Section 6.7.1. The

good match constitutes an experimental verification for the parallel-loaded case of the analytical model presented earlier in the chapter.

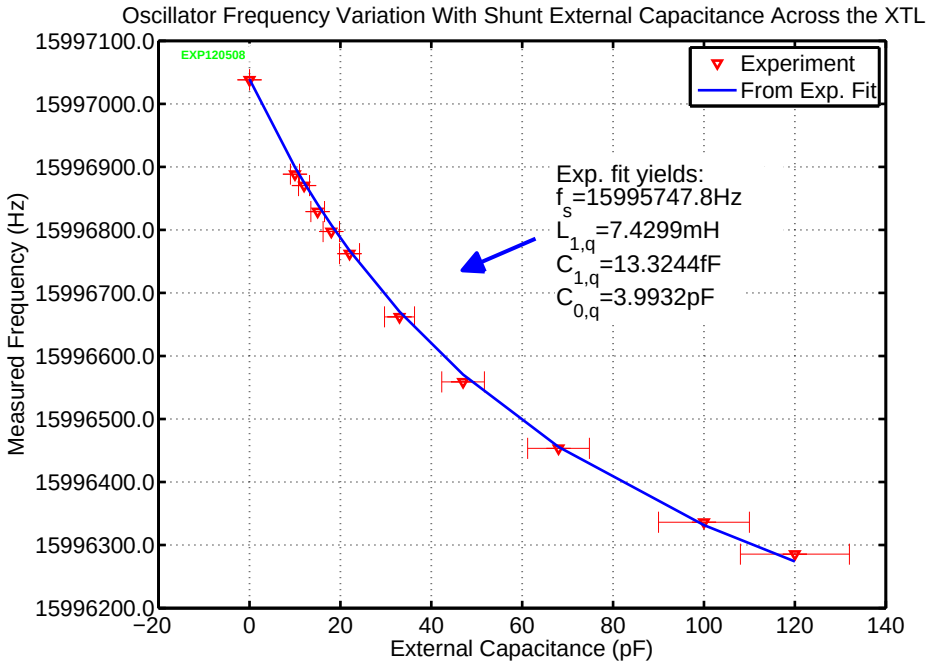

Figure 6.26: Measured and simulated values of the oscillation frequency as a function of external capacitors. The horizontal error bars in measurements were calculated assuming ±10% tolerance around the vendor specified ceramic capacitor values. Least square fit to the experimental data in the form given in Equation (6.14) is plotted as a solid line.

Calculation of the normalized frequency pulling and sensitivity is straightforward by using the extracted value of the series resonance frequency. The calculation results are given in Figure 6.27. The same graph also highlights the range of sensitivity expected from the sensor with mass-nut whose capacitance characteristic is given Figure 6.24. Calculated values of frequency, normalized frequency pulling, and sensitivity are listed in Table 6.7.

The comparison of the SPICE results to exact and analytical versions of the

theoretical model were presented in Section 6.4. The circuit modelled was schematically the same as the experimentally tested, but the parasitic capacitance and inductors were not modelled in the SPICE model. Furthermore, it also neglected the loading effect of the oscilloscope probe used in the experiments. The XTL equivalent circuit parameters used in the SPICE simulations were extracted in Section 6.7.1 from a different XTL that is of the same model as used in the capacitive-loading experiments. Therefore, it is expected that the analysis of capacitive loading experiments should lead to different values than the ones used in SPICE, but presumably within the vendor's tolerance limits[26].

[26]For HC-49US from ECS frequency tolerance at 25°C is ±30 ppm [170].

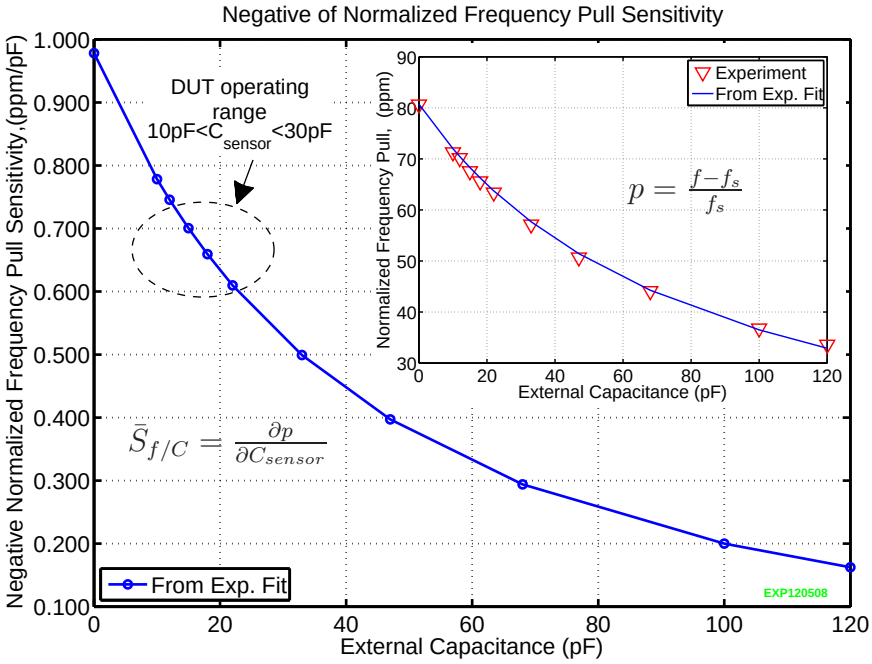

Figure 6.27: Normalized sensitivity of the frequency of oscillation to the change in sensor capacitance. The inset shows the normalized frequency pulling as calculated from the fit to the experimental data of Figure 6.26. Normalized sensitivity is simply the derivative of the frequency pulling with respect to the sensor capacitance. DUT capacitance regime and corresponding sensitivity is indicated on the graph.

Figure 6.28 plots the sensitivity $\bar{S}_{f/C}$ data from theory, experiment, and simulation all in one plot. It is essentially overlapping of Figure 6.27 and Figure 6.14. The table in the figure lists the parameters extracted from experiments or used in the analytical calculations and SPICE simulations. The simulations use XTL parameters extracted in Section 6.7.1. The value of C_{cir} for simulations is the same as the one used in Figure 6.14[27]. All of the model parameters in the second column of the table in the inset were extracted by fitting the parallel loaded experiment results to the analytical model. The match between the fit function and the experimental measurement results can be more clearly seen in Figure 6.26. Despite the excellent match in values of $L_{1,q}$ and $C_{1,q}$ for the SPICE and experimental results,

[27] C_{cir} in Figure 6.14 was extracted from a fit of parallel loaded simulation data to the analytical model.

Table 6.7: Listing of the measured and calculated values of the oscillation frequency, frequency pulling, and sensitivity of frequency pulling to sensor capacitance change.

External Capacitance (pF)	**Frequency** (Hz)	**Frequency Pulling,** p (ppm)	**Sensitivity,** $\bar{S}_{f/C}$ (ppm/pF)
0	15997038.11925	80.731	-0.978
10	15996888.43277	72.005	-0.778
12	15996870.35450	70.482	-0.746
15	15996829.10605	68.314	-0.700
18	15996797.44739	66.275	-0.659
22	15996762.30561	63.739	-0.610
33	15996662.05517	57.670	-0.499
47	15996558.88408	51.436	-0.397
68	15996453.38721	44.260	-0.294
100	15996336.13191	36.500	-0.200
120	15996285.51845	32.896	-0.162

significantly larger values of C_{cir} extracted from the experiments is mostly a result of not including parasitic capacitances in the SPICE simulations. Improving match between the experiments and simulations at larger values of C_{sensor} is another implication of negligence of parasitic capacitances in simulations by virtue of Equation (6.16). This is due to the reduced relative effect of parasitic capacitances at larger values of C_{sensor}.

On the other hand, the mismatch in f_s is around 40 ppm, therefore within the vendor specified tolerance of ±30 ppm. Likewise, the excellent match between the extracted value of $C_{1,q}$ from one XTL, and the measured $C_{1,q}$ of another XTL of the same type, is a verification of the analytical model used for calculations.

An important conclusion from Figure 6.28 is that capacitive sensing using a parallel loaded XTL was a poor design choice for the implemented circuit. As Figure 6.23 shows, the device under test (DUT) has a capacitance range of 10 – 30 pF. In this range of C_{sensor}, Figure 6.28 shows that loading the XTL in series should yield more than an order of magnitude larger sensor sensitivity.

The transient waveforms in Figure 6.25 show the effects of loading due to increased sensor capacitance in parallel. As Figure 6.11 illustrates, for parallel loading, it is typical that the oscillation halts once the sensor capacitance exceeds a certain value. For the experimental setup, the oscillation was supported for $C_{sensor} = 120$ pF, but not for $C_{sensor} = 150$ pF. Amplitude change was also accompanied by a change in the waveform owing to the nonlinear operation of the bipolar transistors. The peak-to-peak amplitude of the waveform was recorded using a digital oscilloscope, and Figure 6.29 plots the results. In addition, one can deduce from Figure 6.25 that the higher order harmonics of the output waveforms decrease when the sensor capacitance is increased.

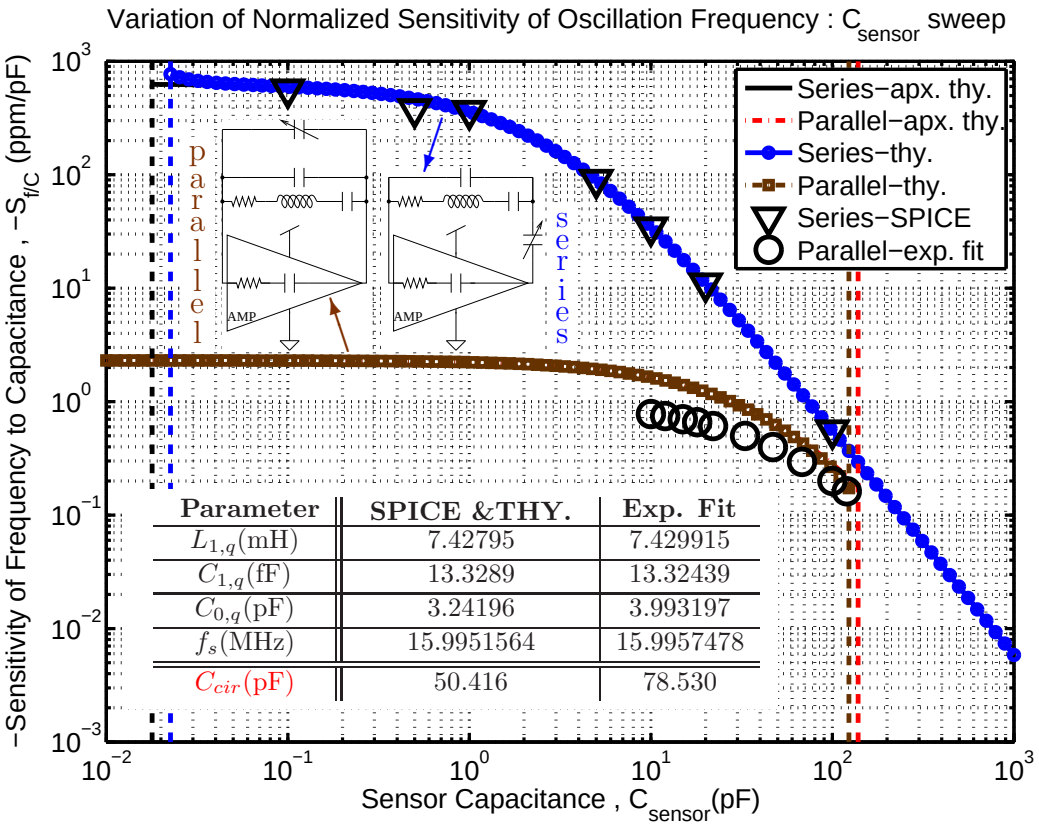

Figure 6.28: Sensitivity of the oscillator frequency to C_{sensor}. Analytical calculation results are compared to the simulations and the experimental findings for the cases of series and parallel loading, respectively. The inset shows the parameters used in simulations and extracted values from the experimental data. The extracted values of C_{cir} vary more than 50% despite less than 40 ppm mismatch in the extracted values of f_s. This is mainly a result of negligence of the parasitic capacitances in the circuit simulations.

6.8.1.3 A note about the setup-time

For the experiments that involved a frequency change due to a change in tilt with the manual rotation stage, it was noticed that during the course of the measurement of 100 samples used typically for averaging and data statistics calculations, there was a considerable drift unless one waited long enough before starting the acquisition. This "setup-time" was as high as 5 mins to ensure that output frequency settled down with an accepted level of drift.

Figure 6.30 illustrates the settling time issue after an experiment in which the frequency of the oscillator is changed. This data was taken without any sensor connected to the oscillator, so the change in the output frequency is believed to be mostly due to the acceleration sensitivity of the quartz crystal itself. The

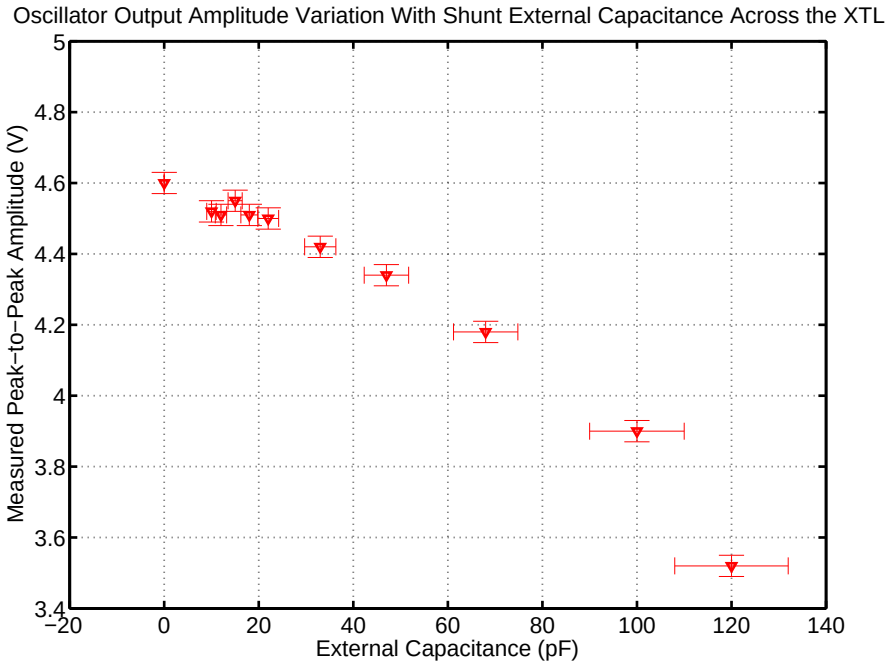

Figure 6.29: Measured peak-to-peak amplitude of the waveform at the output of the oscillator.

experiment involved tilting the XTL and the oscillator circuitry four times as shown in the inset to the same figure. Each cycle was about 40 to 60 min long. Although the output frequency was stable to within 70 mHz for about 5 min before the experiment, it varied more than 2.5 Hz within the same period of time after the experiment.

Due to the long time constants involved, it is likely that the settling process is

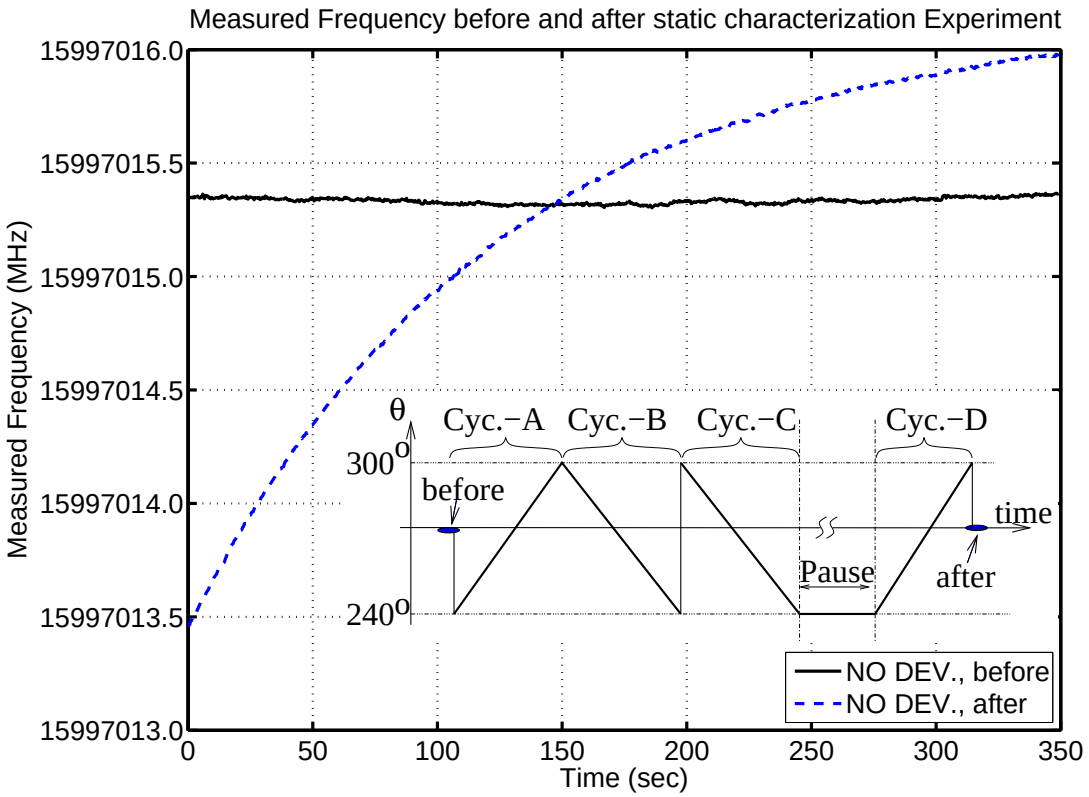

Figure 6.30: Frequency versus time data measured before and after an experiment in which angular position of the rotation stage was manually changed four times for about 60°, with no sensor connected to the oscillator. The inset shows a sketch of the variation of the rotation angle. Both measurements were done around the same tilt angle and they are indicated as "before" and "after" in the inset. The long settling time compelled us to use long setup-times before the experiments for which the measurement accuracy was critical.

of thermal nature. A rough estimate for the thermal time constant of a 16 MHz AT-cut XTL was calculated to be 11 sec in Section 6.5.5. As such, thermal settling times on the order of minutes as in Figure 6.30 is not surprising. It was also observed that the polarity of the long-time constant response was the same as the most recent large change in the frequency due to manual rotation of the stage, i.e., change in static acceleration. This can be inferred from a careful investigation of Figure 6.23, Figure 6.26, and Figure 6.30.

6.8.2 Allan deviation and stability

Frequency fluctuations were characterized for the oscillator both with and without the sensor-capacitance connected. The sensor used had a watch battery as the proof mass, and the experiments were performed with acceleromter axis parallel to the optical table. Figure 6.31 plots the measured results, all of which were taken with a gate time of 0.2 sec.

Due to the dead time in the measurement, sampling period was $\tau_0 \approx 0.349$ sec. Large difference in the long time stability of two experiments carried out with sensor disconnected indicates the poor environmental control or aging related variations in the oscillator. Approximately speaking, the data for 3 hr long, sensor-connected measurement does not show much difference from the data taken without sensor, measured for 3 hr long. In order to be more quantitative, one needs to calculate the two sample variance of the series as a function of the averaging time.

Allan deviation is conventionally used to quantify the time-domain stability of oscillators [134]. Figure 6.32 calculates the Allan deviation for the three sets of data in Figure 6.31. In calculations, no drift cancellation was performed, and the

dead-time during sampling was ignored. The close performance of the two 3 hr long measurements taken with and without sensor supports the qualitative observation made from Figure 6.31. The inset gives values of σ_y for some measurement times τ. The minimum measured deviation with sensor is $\sigma y(\tau = 2\tau_0) = 1.73 \times 10^{-10}$.

The closeness of $\sigma_y(\tau = \tau_0)$ for all the tree curves reported in Figure 6.32 brings up the issue of minimum stability that can be resolved by the measurement setup.

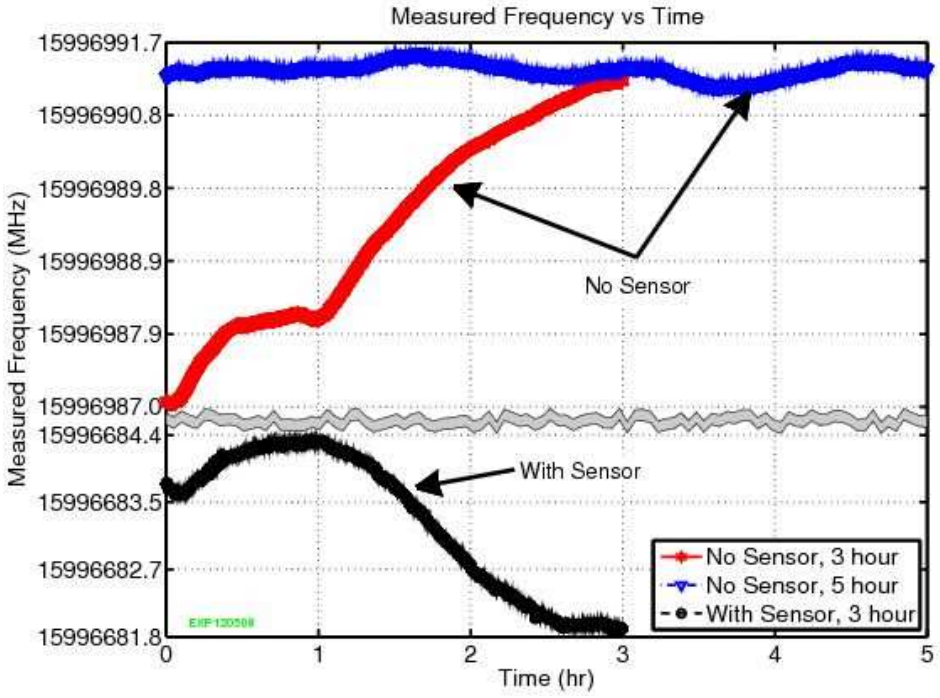

Figure 6.31: Measured frequency from three different runs, two of which were performed without any sensor connected, and the other with sensor having battery as the proof-mass. The large difference between the long-term stabilities of the two measurements without sensor reveal rather poor control of temperature, aging, or other possible environmental disturbances. The circuit-box and sensors were mounted in parallel to the optical table during this experiment. Although the gate-time of the frequency counter was set to 0.2 sec, sampling period for a single acquisition was 0.349 sec, indicating about 45% dead time.

For this purpose, the reference rubidium atomic clock was connected to the input port of the frequency counter, as well as the reference port. Figure 6.33 plots results from a day long experiment. The results from the oscillator *without* any sensor connected are also plotted for comparison. Measured σ_y of atomic clock shows τ^{-1} dependence, indicating white noise in frequency. However, at the shortest measurement time $\tau = \tau_0$, Allan deviations from both XTL and atomic clock are very close. As such, the reported stability measurements might be setup-limited for short measurement times.

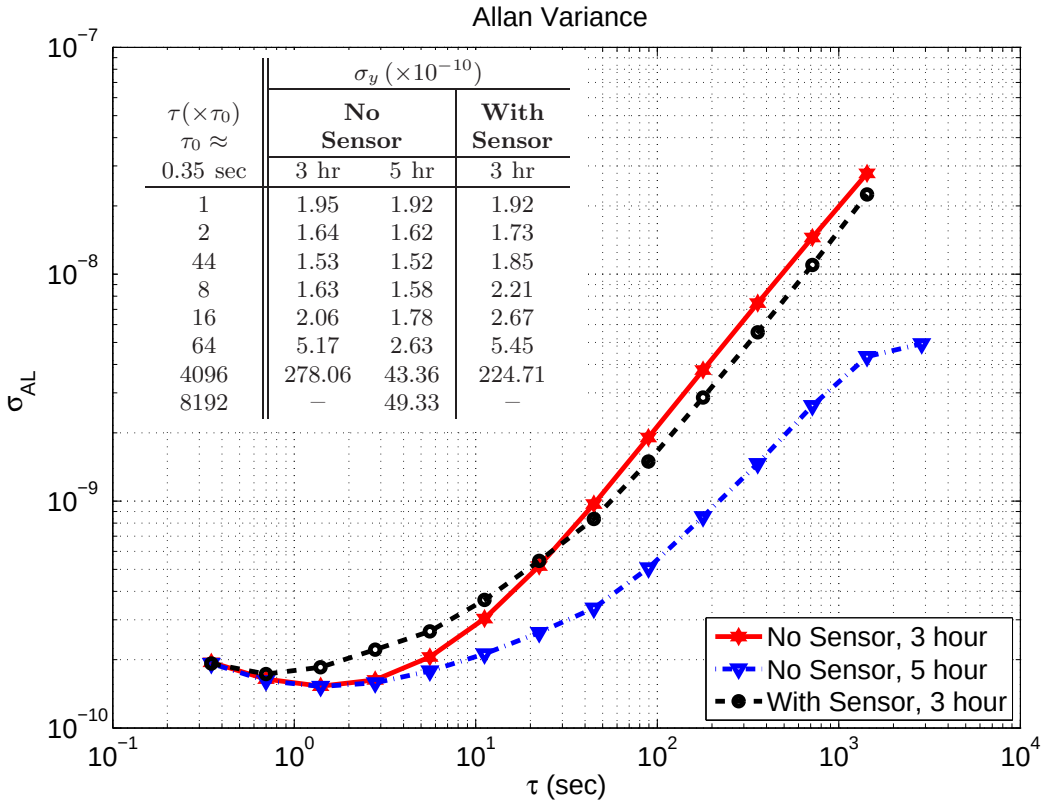

Figure 6.32: Allan deviation calculated from the data of Figure 6.31. The inset lists the values for some τ. No drift subtraction/cancellation was performed, and the deadtime was ignored in the calculations.

6.8.3 Static characterization of the capacitive sensor

Static characterization results for the DUT with mass sensor are described in this section. All the recordings are done with 5 min setup time. Two opposite polarity sweeps are performed to test for repeatability and hysteresis.

The equations governing the bandwidth and the rms noise level of acceleration for ADXL-103 are [159]:

$$BW_{-3\text{dB}} = \left(2\pi(32\ \text{k}\Omega)C_{out,ADXL}\right)^{-1} \tag{6.67a}$$

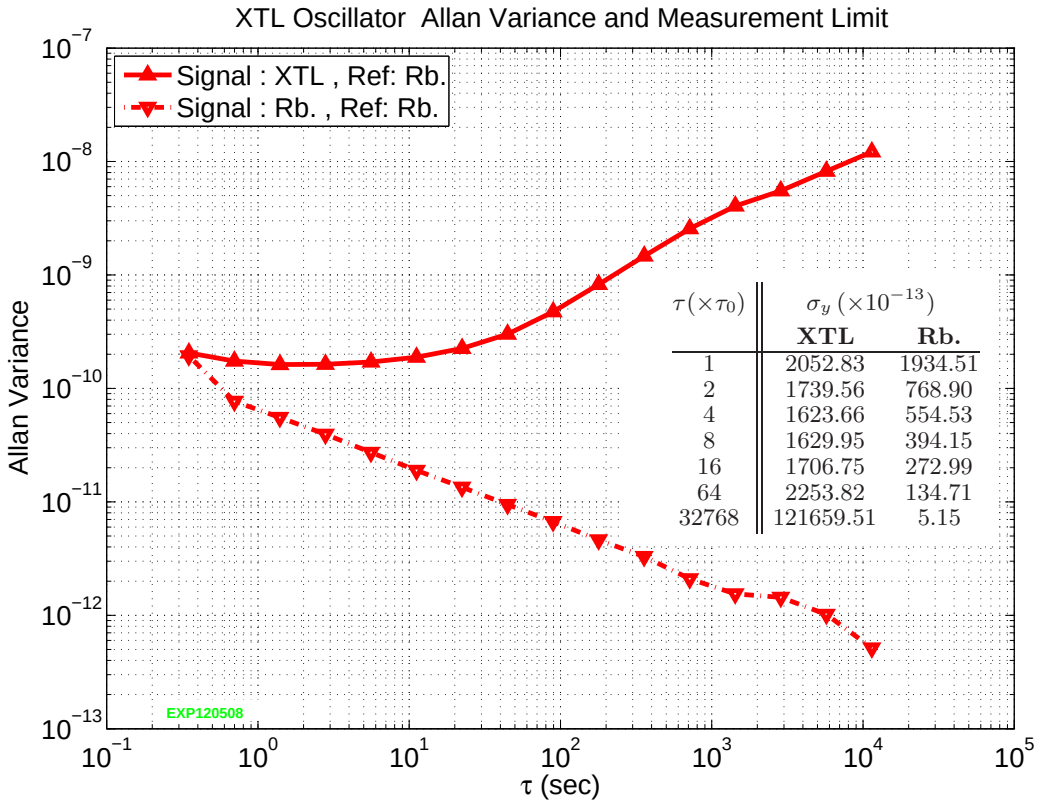

Figure 6.33: Stability limits of the experimental setup is characterized by measuring the stability of the Rb. atomic clock (bottom curve), as it is used as the reference in all of the measurements reported. A typical measurement from the XTL oscillator with no sensor connected (top curve) is given for comparison. The inset lists some of the Allan deviation values.

$$ACC_{n,rms} = (110\ \mu\text{g}/\sqrt{\text{HZ}}) \times \sqrt{1.6 \times BW_{-3\text{dB}}}, \tag{6.67b}$$

where $C_{out,ADXL}$ is the low-pass filter capacitance at the output. Unless otherwise told, electrical bandwidth of the ADXL-103 was set to about 3 Hz with an integration capacitance of $C_{out,ADXL} = 1.5\ \mu$F at the output[28]. In this case, Equation (6.67b) predicts the minimum value of acceleration to be $[\text{MDS}_{\text{acc}}]_{\text{ADXL}} = 254\ \mu$g.

6.8.3.1 Acceleration sensitivity: Sensor Connected

Measurement and analysis results for $f(C_{sensor}(acc))$ and $\bar{S}_{f/acc}$ are plotted in Figure 6.34(a). The nonlinearity in the capacitance versus acceleration characteristics in Figure 6.23 carries itself to the frequency versus acceleration characteristic in Figure 6.34(a). The same can NOT be said for the smoothness. Therefore, it is plausible that small frequency jumps are more crystal related than sensor related. The crystal operating around a few mWatt, i.e., 4-5 times its rated power, can be a contributor to this irregularity. Larger power consumption is also a source of large temperature fluctuations as the changing frequency also changes the power dissipation of the crystal. These fluctuations are definitely not acceptable when the oscillator is considered for a real sensor application.

The derivative of Figure 6.34(a) yields the sensitivity $\bar{S}_{f/acc}$, and it is given in Figure 6.34(b). The largest measured sensitivity is about 1000 Hz/g around $acc = 0$ g.

The standard deviation at each measurement was calculated from 100 measurements, and Figure 6.35(a) reports the local average in root-mean-square (rms)

[28]Note that this is not the mechanical bandwidth as that is fixed by the sensor stiffness and mass.

sense at seven acceleration values from −0.3 g to 0.3 g. These are the values used in the calculation of MDS_{acc}, which is reported in Figure 6.35(b). ADXL is observed to have a very uniform MDS_{acc} response as a function of the input acceleration, at about 155 μg. Note that this value is slightly lower than the expected value calculated by Equation (6.67), 254 μg, indicating the reliability of measurements despite the lack of vibration isolation during the measurements.

The values reported from the DUT are, for some values, more than 10 times lower than those from ADXL, going down to 13 μg. Yet, non-uniformity between cycle-A and cycle-B are not good signs of repeatability. This mismatch originates in part from the quartz frequency fluctuations mentioned above and needs to be solved for quartz based capacitive sensors. Inherent hysteresis in the capacitive sensor that is apparent in Figure 6.23 might also have an effect.

6.8.3.2 Acceleration sensitivity of quartz and others: Sensor unconnected

Quartz XTL itself, is sensitive to acceleration to begin with [165]. It is therefore critical in XTL based capacitive sensing applications to compensate for the response of the XTL to the sensed entity, unless the XTL is kept at a different environment than the capacitive sensor (i.e., only electrically connected to the sensor).

After disconnecting the sensor capacitance, the change of the frequency of the oscillator in response to the rotation of the tilt stage was measured. Four sweeps were made to unveil the repeatability and hysteresis characteristics. The measurements were done with a setup time of 10 sec. This is an important difference from other measurements reported so far with 5 min setup time.

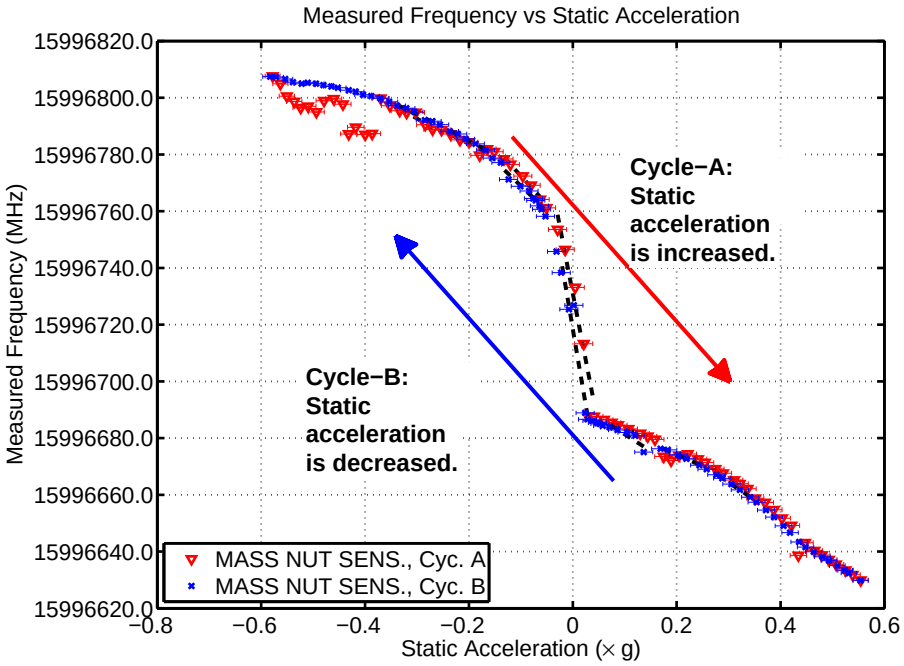

(a)

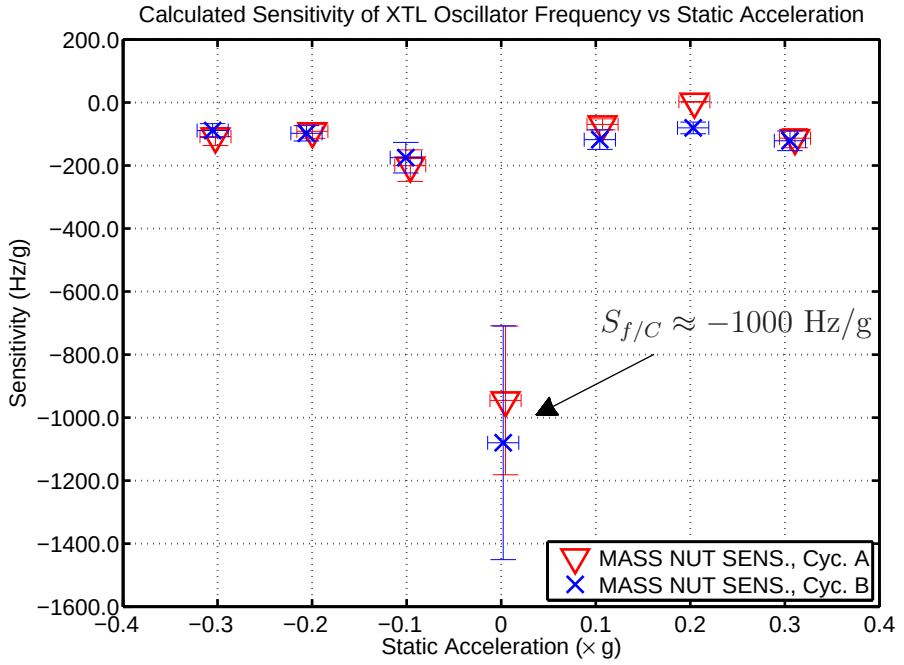

(b)

Figure 6.34: (a) Frequency versus static acceleration characteristic of the DUT with mass-nut. Theoretically speaking, this characteristic is related to Figure 6.23 via Equation (6.14). (b) Sensitivity of output frequency to acceleration ($\bar{S}_{f/acc}$). Maximum sensitivity measured is around 1000 Hz/g.

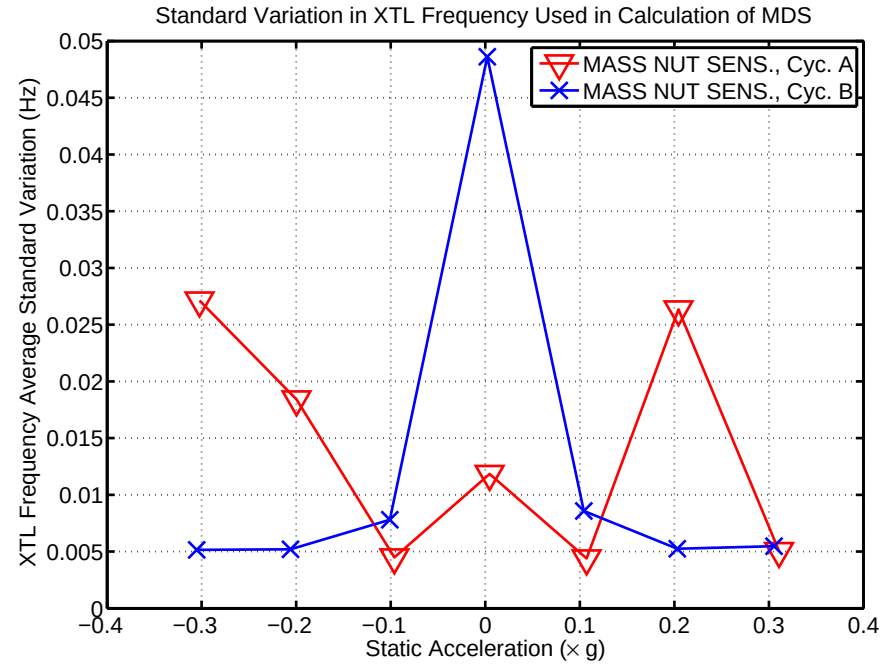

(a)

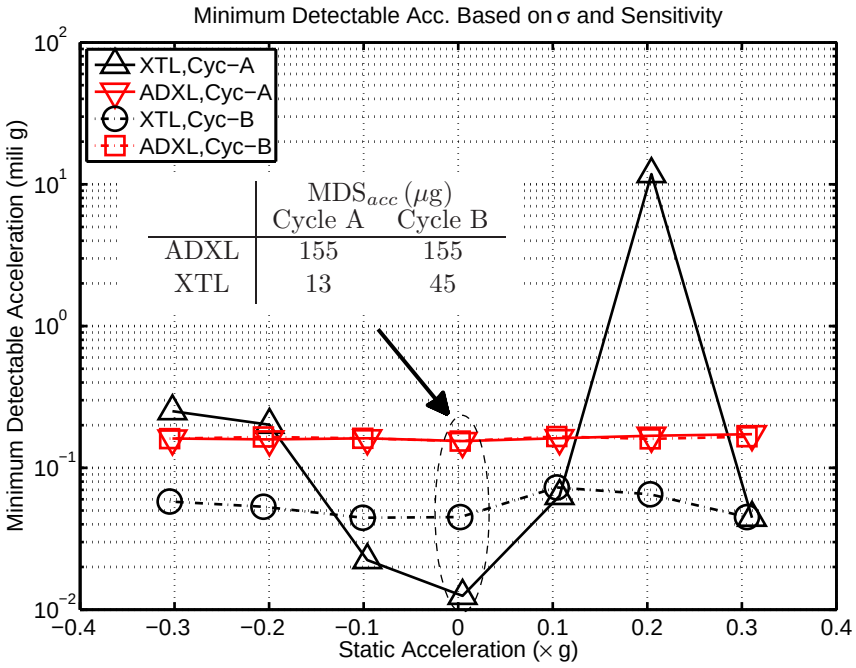

(b)

Figure 6.35: (a) Measured standard variation σ_y, as averaged locally from 100 measurement points after 5 min setup time. (b) Minimum detectable acceleration amplitude calculated from $\mathrm{MDS}_{acc} = \sigma_y / \bar{S}_{f/acc}$ using the data of (a) and Figure 6.34(b). The inset shows the values around $acc = 0$ g.

The plot of the manually controlled theta stage rotation as a function of time, and measured frequency as a function of the static acceleration are given in Figure 6.36. It is unexpected that the frequency versus acceleration response is asymmetric with the negative acceleration region of the response being quite spiky for all the cycles. A transition region can be observed if one looks at the positive acceleration region (i.e., start) of cycle-C. It can be explained by not having enough setup time for measurements after the sudden change between cycle-B and cycle-C. This was explained in Section 6.8.1.3. The overall frequency change between four cycles is close to 8 Hz. At the reported sensitivity of $S_{f/acc} = 1000$ Hz/g for the same device, 8 Hz variation would limit MDS_{acc} to 8 mg. Therefore, the acceleration sensitivity of quartz should be very well controlled in sensor applications, if it cannot be eliminated.

6.8.4 Dynamic characterization

Dynamic tests of the sensor mass-NUT was performed at three different operating regimes that can be identified in Figure 6.23, with reference to high gain transition region. These are labelled as:

- before contact: accelerations more negative than the transition region (see inset (a) in Figure 6.23),
- around contact: accelerations in the transition region (see inset (b) in Figure 6.23),
- after contact: accelerations more positive than the transition region (see inset (c) in Figure 6.23).

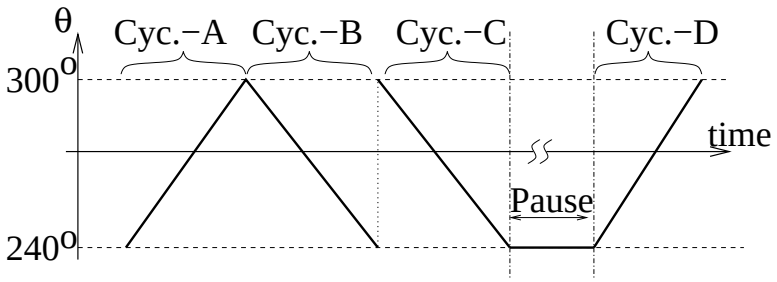

(a)

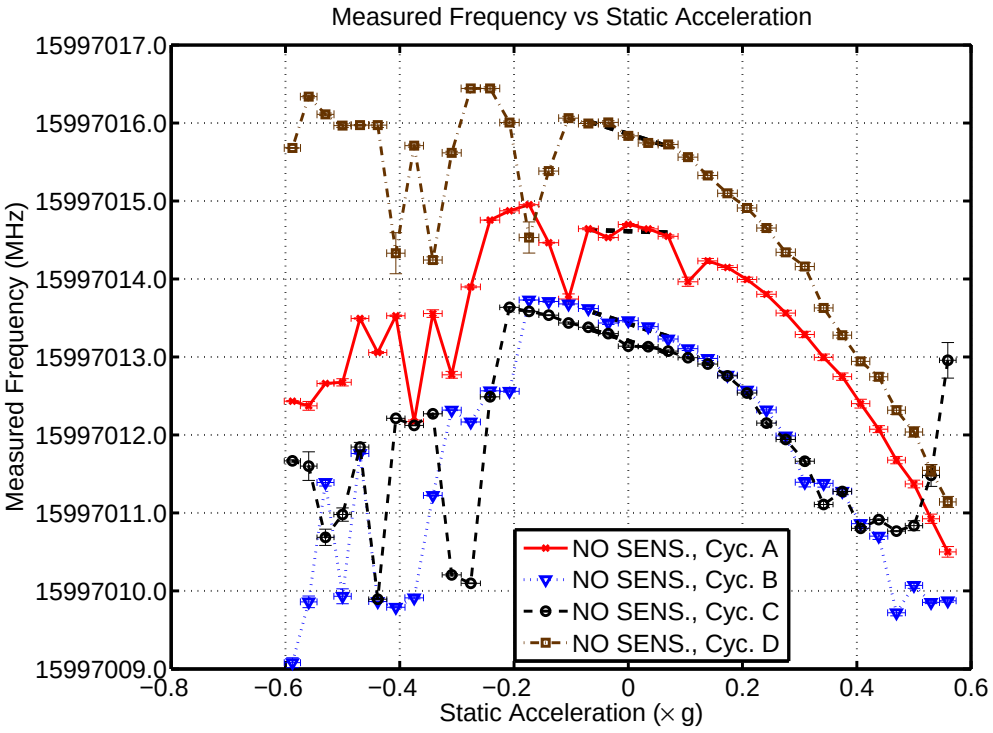

(b)

Figure 6.36: (a) Sketch of manually controlled tilt variation as a function of time. Each cycle was about 40–60 min, and there was approximately 3 hr between cycle-C and cycle-D. (b) The response of the oscillator to static acceleration without any acceleration sensor. All the measurements were performed with 10 sec setup time.

The dynamic test consisted of applying two pulses of acceleration change with opposite polarity using the manual rotation stage. The duration of pulses were kept longer than 5 min in general due to the long setup times required. The starting tilt value for each of the three regions were picked such that $acc = -66$ mili g, $acc = -46$ mili g, and $acc = 66$ mili g, respectively for before, around, and after contact regions. The most sensitive region is expected, from the static measurement result given in Figure 6.34(b), to be around the contact region with about $S_{f/acc} = 1000$ Hz/g of sensitivity.

Figure 6.37 presents an approximate sketch of the acceleration stimulus applied and the output waveforms measured from both XTL and ADXL accelerometers. Despite very symmetric pulse shapes from ADXL, which has excellent linearity, XTL output pulse amplitudes are not symmetric for approximately equal but opposite polarity input pulses. The major contributor to this is of the nonlinearity of the DUT, characterized in Figure 6.23. The contribution due to the nonlinearity of the parallel loaded capacitive readout, which was characterized in Figure 6.26, is secondary.

The signal to noise ratio analysis of the devices were calculated in the following manner: First the data were separated into five time-windows, two for signal sampling of the two pulses, and three for background sampling at either side of the pulses. Signal level of the pulses were calculated from the difference between the average values of the signal and the background sampling regions. Noise levels were calculated as the rms of standard variation in the background regions, hence noise levels were taken to be the same for both pulses. Amplitude pulses were taken from the ADXL reading assuming its nominal sensitivity.

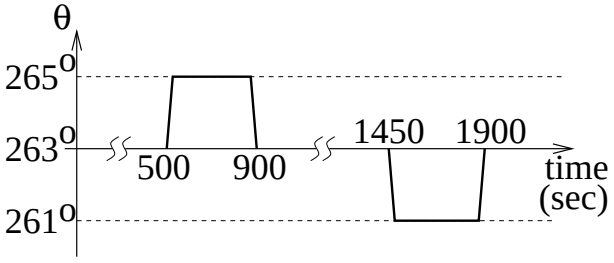

(a)

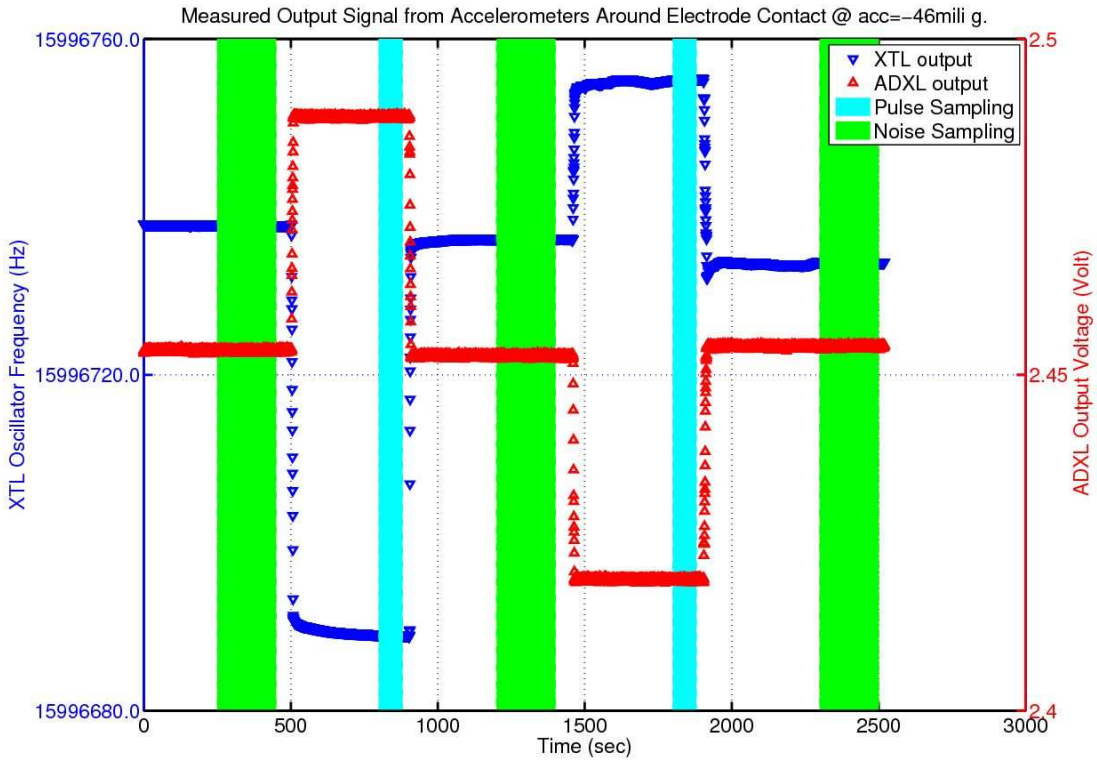

(b)

Figure 6.37: (a) Sketch of manually controlled tilt pulses applied during the dynamic experiment around the contact region. The time-axis tick labels are approximate. (b) Measured response from XTL and ADXL outputs. The shaded regions show the sections of data which were used in SNR calculations. Due to the long settling time required for XTL, a few minutes at the beginning of the pulses were discarded.

Table 6.8. lists the results of the data analysis for dynamic experiment results carried out in the three regions. SNR of the DUT was larger than that of ADXL in all three regions. This SNR improvement is due to the extremely floppy sensor in DUT as compared to that of the ADXL, and hence extremely low bandwidth of the sensor in DUT. By no means, is it a result of better capacitive sensing resolution of our sensor; to the contrary, ADXL capacitive readout has orders of magnitude superior capacitive sensing resolution as to be detailed in the coming section.

The best minimum detectable value of acceleration from dynamic measurements was calculated as 22 μg for close to contact operation. This value compares well to the results of the static measurements in Figure 6.35(b), that yielded a value of 13 μg. One can still get another value based on the average sensitivity of DUT, from the definition of MDS_{acc} in the form of Equation (6.55). Variance is on the order of $\sigma_y = 2 \times 10^{-10}$ from Figure 6.33. Using a normalized value of sensitivity of $\bar{S}_{f/C} = (1000 \text{ Hz/g})/(16 \text{ MHz}) = 62.5$ ppm/g from Figure 6.34(b) yields a theoretical estimate of $\text{MDS}_{acc} = 3.2$ μg.

6.8.5 Minimum detectable acceleration versus integration time

The bandwidth of ADXL can be made smaller to improve its resolution, as described by Equation (6.67). All the experiments mentioned so far used an ADXL output capacitor of 1.5 μF that yields a bandwidth of 3.33 Hz. If the capacitance is increased to 100 μF, the bandwidth reduces to 50 mHz. Minimum value of acceleration of ADXL for these two bandwidths are plotted in Figure 6.38. The same is also plotted for the XTL oscillator with the assumption of sensitivities typical in

the DUT characterized, namely 1000 Hz/g and 100 Hz/g. As was the case in previous results, a slightly smaller value of MDS_{acc} was measured than what datasheet predicted. It is interesting that ADXL variation with very different bandwidths converge to a common MDS_{acc} of about 20 μg for 30 sec $< \tau <$ 3000 sec. The reason is unclear to the author at the time of writing. It might be connected to some kind of a background vibration from the building[29].

6.8.6 Minimum detectable capacitance and a comparison

Table 6.9 summarizes the capacitive readout performance of the tested oscillator and compares it to the others that were mentioned in Section 6.6.

The oscillator presented in this chapter has about 300 aF resolution, a good

[29] As mentioned before, the optical table was non-floating during the experiments.

Table 6.8: Results of the dynamic experiments in three different operating regimes of the DUT: before, around, and after contact.

		Before Contact		**Around Contact**		**After Contact**	
		XTL	**ADXL**	**XTL**	**ADXL**	**XTL**	**ADXL**
	Tilt Angle(°)	262		263		270	
	Acc.(mg)	−66		−46		66	
	σ	39.19 mHz	158 μV	30.62 mHz	161 μV	9.34 mHz	162 μV
Pulse-1	**Pulse Amp.**	33.2 mg		34.8 mg		34.7 mg	
	Signal	−28.9 Hz	33.2 mV	−43.8 Hz	34.8 mV	−2.1 Hz	34.7 mV
	$\lvert\text{MDS}_{acc}\rvert$	45 μg	158 μg	22 μg	161 μg	154 μg	162 μg
	$\lvert\text{SNR}\rvert$	737	210	1595	216	225	214
	$\left\lvert\frac{\text{SNR}_{XTL}}{\text{SNR}_{ADXL}}\right\rvert$	3.51		7.40		1.05	
Pulse-2	**Pulse Amp.**	−34.4 mg		−33.3 mg		−31.8 mg	
	Signal	17.10 Hz	−34.4 mV	19.0 Hz	−33.3 mV	1.86 Hz	−31.8 mV
	$\lvert\text{MDS}_{acc}\rvert$	79 μg	158 μg	54 μg	161 μg	160 μg	162 μg
	$\lvert\text{SNR}\rvert$	436	218	621	206	199	196
	$\left\lvert\frac{\text{SNR}_{XTL}}{\text{SNR}_{ADXL}}\right\rvert$	2.00		3.01		1.01	

50,000 times more than the best value in the table, that is from a double oven controlled commercial XTL oscillator. Despite this extreme difference, it is interesting and assuring to note the relation between the experiment results of this work and an estimation based on the literature data. The second column of the table is for a crystal oscillator in an uncontrolled environment from reference [162]. This oscillator is assumed to be operated as a capacitive sensor with a sensitivity of 50 ppm/pF. Its resolution is roughly three orders of magnitude better than that of this work. Explaining this large difference is not as difficult as it first sounds.

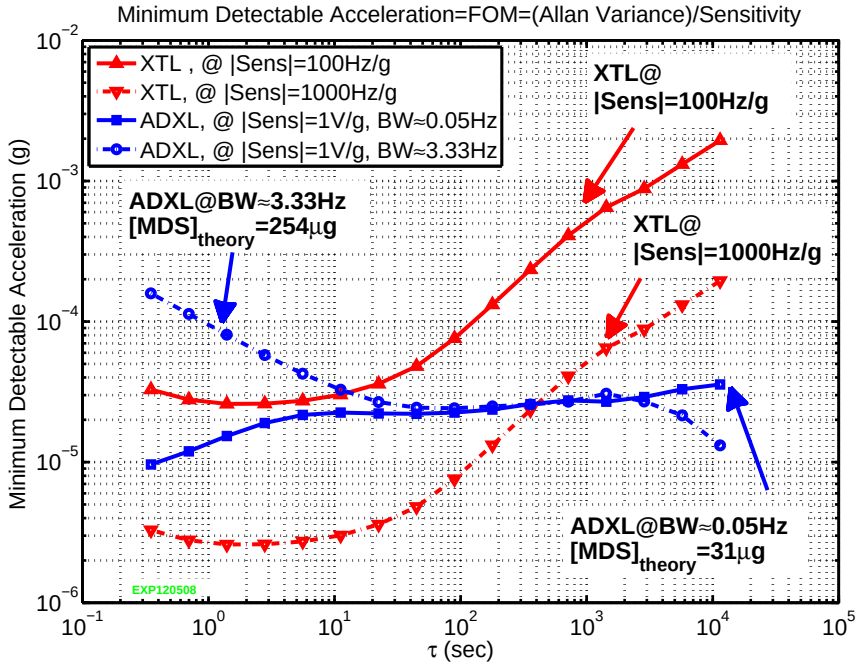

Figure 6.38: Minimum detectable acceleration, MDS_{acc}, as calculated from the ratio of Allan deviation and sensitivity. Expected noise levels from ADXL, using the rms noise formula specified in its datasheet are indicated. Allan deviation characteristic for XTL is the same as the one given in Figure 6.33. Two curves are plotted for XTL assuming sensitivities of 100 Hz/g and 1000 Hz/g for the sensor. The sensor was not connected to the oscillator during the measurements.

Firstly, note the two orders of magnitude of difference in sensitivity. The other order of magnitude difference is mostly contributed by the similar difference in the fQ-products of the XTLs used.

The performance of the ADXL capacitive readout in terms of minimum detectable signal is somewhere between the controlled and uncontrolled XTL readout estimates. In the above paragraph, three orders of magnitude in performance was explained between experimental results in this work and one entry from the literature. Assured by this verification of the performance estimate, Table 6.9 also estimates the performance of a capacitive sensor using an oven-controlled crystal oscillator. This estimation of the controlled environment performance in case of the XTL based capacitive sensor yields about nine times better resolution than a commercial capacitive readout, with quite a conservative assumption of sensitivity. This is a sign of the superiority of XTL based capacitive sensing for high-resolution, low-speed applications[30]. These theoretical estimations justifies the future work on XTL based capacitive sensing.

[30]To the author's knowledge one of the best capacitive sensing resolutions is reported as 0.01 aF @ 1 Hz in a paper by Jones and Richards in 1973 with a readout circuit that employs transformers [146, pp206].

Table 6.9: Summary of the important capacitive sensor parameters of the experimented oscillator and its comparison to other possible implementations based on literature and a commercial product.

	Capacitive Readout			
	XTL based			**ADXL-150** [a]
	controlled env. (OCXO) [b]	**uncontrolled env.**		
	[168]	[162]	[This work]	[145, 169]
$\tau(sec)$ ♯	0.2	0.36	0.34	0.3
Allan Deviation σ_y	3×10^{-13}	1.2×10^{-11}	2×10^{-10}	—
Frequency(MHz)	5	5	16	—
Quality factor Q_q	—	2.45×10^6	≈ 95700	—
fQ product (Hz)	—	12.25×10^{12}	1.53×10^{12}	—
Cut and mode	SC-cut , 3rd	AT-cut, 5th	AT-cut, 1st	—
Sensitivity ($\bar{S}_{f/C}$ or $S_{V/C}$)	50 ppm/pF [c]	50 ppm/pF [c]	0.6593 ppm/pF (@18 pF)	1.21 V/fF [d]
Min. Detectable Signal $[MDS_C(\tau)]_{el}$ ($\times 10^{-21}$F)	6	240	300,000	54

♯ Integration times are chosen close so that the comparison is fair.
[a] Based on estimations from the publicly available data.
[b] Double oven controlled XTL oscillator.
[c] $\bar{S}_{f/C} = 50$ ppm/pF is a nominal sensitivity value assumed to extend the literature work to capacitive sensor. It is indeed a conservative value since a value as high as $\bar{S}_{f/C} = 140$ ppm/pF is reported in the literature [154].
[d] This sensitivity is calculated using $S_{V/acc} = 38$ mV/g [169] and $S_{C/acc} = 3.13 \times 10^{-17}$ F/g from Equation (6.58).

6.9 Summary

This chapter presented a detailed investigation of capacitive sensing based on XTL oscillators. The widely used equations of XTL frequency pulling under capacitive loading were revisited by modelling the oscillating amplifier as a series combination of a resistor and a capacitor. This modelling approach allows one to compare

the performance of the series and the parallel loaded XTL configurations under operation with a given fixed oscillation amplifier. In addition, the modelling of the oscillator uses the Butterworth-Van Dyke equivalent circuit of the XTL. Therefore, it is also applicable to many other oscillators that use different resonator elements such as surface micromachined resonators and thin-film piezoelectric resonators.

Transient circuit simulations using SPICE were used to compare the frequency of oscillation between numerical and analytical approaches. For the specific values of parameters analyzed, the agreement between simulations and the theory was less than 0.5% in the case of series loading, and 7% in the case of parallel loading for over more than three orders of magnitude variation in C_{sensor}.

Experimentally, a Pierce oscillator with buffer amplifier was built and tested under parallel loading conditions. The parameter extraction resulted in less than 1000 ppm discrepancy in the value of motional capacitance. The experimental parameter extraction also revealed the effect of parasitic capacitances that were not included in the circuit simulations.

Plots showing the sensitivity of the oscillation frequency to changes in sensor capacitance based on both the approximate and exact analytical models were presented. Numerical examples showed that the approximate solution matched very well with the exact solution, except around close to the boundary of oscillation. The same plots also quantified the nonlinearity issues that should be overcome for high-dynamic range applications.

Later in the chapter, Time-Multiplexed Crystal based Capacitive Sensing (TM-XCS) is introduced as a way of nonlinearity compensation. The idea behind TM-XCS is to make multiple frequency measurement using the same oscillator and

XTL, under different configurations of capacitive loading using the unknown capacitors. The capacitive loading between configurations is changed using elegant switching networks around the oscillating amplifier. The TM-XCS postprocessing then reveals the unknown capacitors in terms of motional or shunt capacitances of the XTL. The processing necessary in TM-XCS only involves four basic algebraic operations and can easily be implemented with an FPGA or μ-processor. TM-XCS also yields the motional to shunt capacitance ratio of the XTL. It is claimed that this capacitance ratio can be useful in determination of the temperature of the XTL without using any external temperature sensor. While no experiments are performed to verify TM-XCS in this work, two possible circuits are proposed to implement the switching network.

CHAPTER 7

LOCALIZED OFF-CHIP TRANSDUCTION FOR MEMS USING ULTRASONIC ARRAYS

Piezoelectric transduction for microsystems has received an increasing attention over the past decade at both research and commercial level. Low power consumption, low voltage operation, built-in reciprocity between electrical and mechanical domain, and fast time-domain response are aspects to this high level of research activity. In spite of piezoelectric materials' poor reputation for ease of integration with CMOS, the application space is nevertheless large. Medical ultrasonic imaging [19,171], microphones [40], ultrasonic motors [45], microassembly [76], microfluidic pumps [28], flow sensors [172], particle manipulators [173] can be realized using piezoelectric transduction[1].

Piezoelectric layers with thicknesses less than a few microns are usually fabricated using sol-gel deposition [174, 175] or sputtering [40, 176]. The applications which require large forces at large strokes usually benefit from use of thicker piezoelectric films in the range from $2 - 50$ μm. Silk-screen printing [177, 178] and successive sol-gel [179, 180] depositions of lead zirconium titanium oxide (PZT, $Pb(Zr_{1-x}, Ti_x)O_3$) are common methods used to fabricate thick PZT films on a silicon substrate without any bonding. However, high sintering temperatures of 1100–1300°C often employed in bulk-PZT ceramics are not suitable for silicon based MEMS due to severe reaction and diffusion between PZT and the silicon substrate [177,178,181]. The sintering temperatures for thick PZT films are therefore done at temperatures less than 950°C. Further limitations on sintering temperature can result from the temperature budget of any circuitry or microsystem

[1]A longer list can be found in reference [43].

components on the target substrate. As a result of lower sintering temperatures than their bulk-counterparts, on-wafer sintered thick PZT films often yield low-density films with inferior dielectric and piezoelectric properties [177, 178].

The alternative method of using a bulk-PZT[2] eliminates all of the temperature limitations mentioned above since the fabrication of the piezoelectric ceramic is carried out separately. However, high-quality bulk piezoelectric materials come with the key challenge of bonding them to the target wafer in desired patterns.

Some examples of methods used to bond bulk-PZT to the host wafer are: using solders of AuIn [183] and AuSn [184], low-temperature surface activation [185], bonding using intermediate layers such as epoxy [181], parylene [183], and cyanoacrylate [45]. In addition, some of these methods that have sufficient bond strength can be used to get thinner (as low as 10 μm) piezoelectric films by lapping, without compromising PZT quality as in other thick film deposition methods on silicon [183].

In general, two requirements are crucial for microsystems to fully reap the benefits of bulk-PZT actuation. First is the *localization of transduction*, which is equivalent to minimizing the area of interaction of the bulk-PZT with the microsystem. Second is the *large-scale integration*, which is to have a large number of localized actuation points at desired locations, without significant crosstalk with each other. Both of these issues are also crucial to ultrasonic imaging applications that depend on localized interaction with a distant biological target (such as a fetus or a tissue) via ultrasonic pulse-echo measurements. One type of enabling device for imaging is a 2-D PZT array of pillars, each of which ideally works like a

[2]Although one can put certain limits on the thickness to distinguish between thick and bulk PZT [182], the main distinctions of bulk-PZT emphasized throughout this chapter are the additional bonding and external sintering attributes.

Davidsen *et al.* , 1998

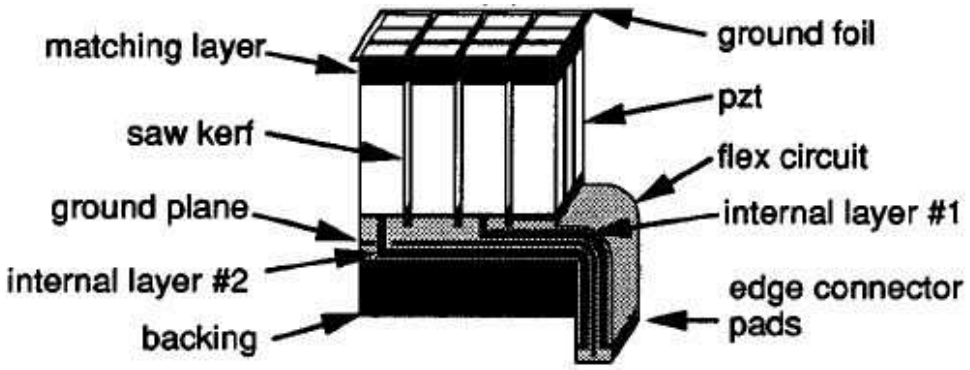

Figure 7.1: Cross section of the 2-D array transducer fabricated by Davidsen and Smith [19].

piston to send and receive ultrasonic waves. Figure 7.1 and Figure 7.2 give pictures of PZT array fabricated by Davidsen and Smith [19]. Their manufacturing process involves bonding of PZT to a circuit board for electrical connections, followed by dicing of the bulk-PZT by a wafer-saw into small rectangular pillars to form a 2-D array.

The work to be presented in this chapter pursues a 2-D bulk-PZT array as a localized transduction platform for microsystems. This effort is motivated in large by the application of ultrasonic imaging arrays to control near-field displacement as opposed to far-field. Such a platform can generate arbitrary displacement or vibration patterns on the target microsystem die at the desired frequency, when individual PZT array elements (i.e., PZT pillars) are driven with proper amplitude and phase [186].

Following attributes for the actuator platform were adapted in pursuit of a CMOS-friendly bonding process:

Davidsen *et al.* , 1998

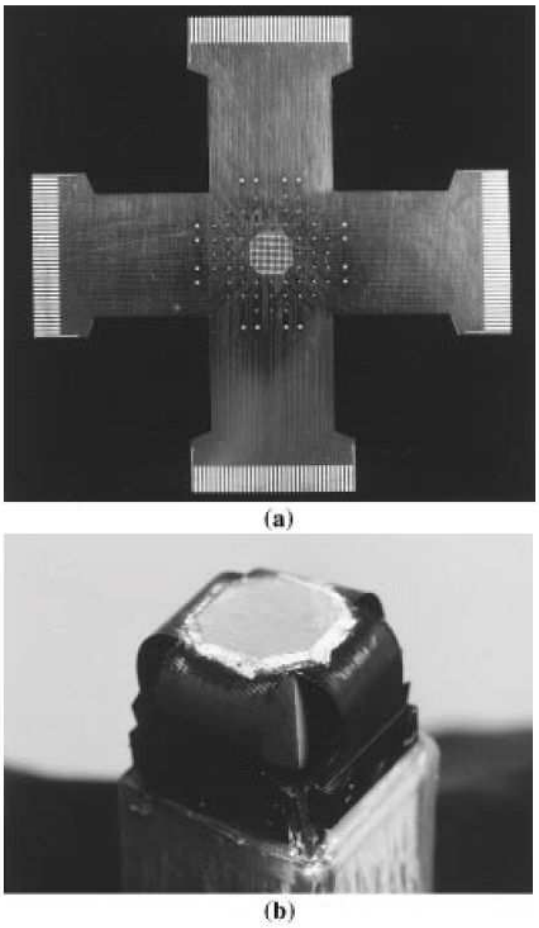

Figure 7.2: Optical picture of the 2-D array transducer for ultrasonic imaging fabricated by Davidsen and Smith [19].

1. the use of low-temperature *flip-chip bonding (FCB)* [187, 188] to minimize electrical parasitics to individual PZT pixels and to enable large spatial density of interconnects,
2. the demonstration of a membrane film as a sample MEMS platform,
3. the integration of a VLSI die that can have CMOS circuits.

An illustration of the 2D ultrasonic actuator platform is shown in Figure 7.3. It is

composed of three parts, each of which addresses one of the three points itemized above, namely from bottom to top: a VLSI die, PZT pillars, and a MEMS die. In practice, the MEMS die can contain any microsystem such as surface micromachined assembly structures or bulk micromachined membrane or diaphragms.

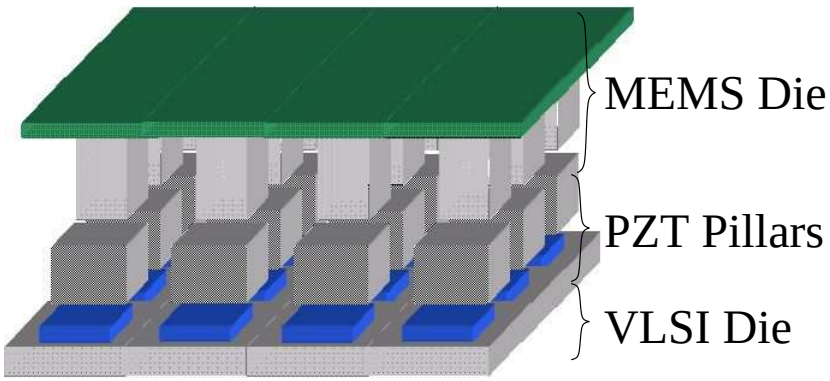

Figure 7.3: An illustration of the diagram of the microsystem showing the stacking of the three main parts: i) VLSI die ii) PZT pillars iii) MEMS die.

One can imagine applications related to piezoelectric ink-jet printing, microfluidic pumps with 2-D programmable pumping direction, micro-particle transport, localized off-chip microassembly [10], or actuation of large arrays of ultrasonic motors [45] with an application specific MEMS die. Furthermore, all these applications can potentially be implemented by only modifying the MEMS die, with little or no change to the VLSI die and the PZT pillar layer.

Given a desired vibration distribution on the MEMS die, a matrix based approach can be used to approximate necessary amplitude and phase drive for every pixel, if the frequency response of each of the pixel is known [186].

The next section summarizes the experimental effort towards an ultrasonic array based actuation platform. It starts with the fabrication of 1-D arrays and their applications to microfluidic actuation. This is followed by the fabrication and

assembly of the 2-D actuator array.

7.1 Fabrication of 1-D PZT arrays and microfluidic actuation

A linear 1-D PZT actuator and an array of membranes were assembled on top of a circuit board. Figure 7.4(a) shows the device structure, and the picture is given in Figure 7.4(b).

The square shaped membranes were made out of low-stress, LPCVD silicon nitride (SiN). Single mask lithography on the back side, etching of the SiN layer, and consequent wet anisotropic etching in KOH completed the fabrication of the membrane die. The pitch of the array was designed to be 2.54 mm as determined by that of the circuit board holes underneath the PZT array. The circuit board, functioning as a primitive version of the VLSI die, is used for electrical connections to PZT electrodes.

The microfluidic channel was made by curing PDMS [189] on a wafer that had patterned SU8 resist to serve as a mold. After peeling PDMS off of the mold, it was immediately bonded to the silicon die housing the membrane with rough alignment. The dimensions of the PDMS channel on the membranes were 0.5 mm $\times$ 90 μm $\times$ 2.55 cm.

The membrane die was fabricated with 12 membranes, but the first and the last membranes had different dimensions than the interior ones which were typically 1.7 mm on one side. The first and the last membranes were pierced with a sharp object to accommodate the inlet and outlet ports to the microchannel. Silicone

tubing was later inserted to these ports via grommets that were attached to the back of the MEMS using cyanoacrylate. The same was used to bond the silicon die to the PZT, which was partially diced through the thickness using a wafer saw. The attachment of the PZT pillars to the circuit board was established using a conductive epoxy. The wiring to individual pixels were soldered to a connector on the circuit board. The top electrode of the PZT ceramic was grounded separately.

Bulk-PZT actuation of the membrane array was tested using fluorescent microscopy (Carl Zeiss, AXIOPLAN2, AttoArc®2) on polystyrene beads ($5 - 10$ μm diameter) in DI water. Figure 7.4(c) pictures the device being tested under the microscope. The image in Figure 7.4(d) was captured during excitation of two pixels on a different device with 4 V_{pp}[3] sinusoidal signal at 333 kHz. The collection of the beads in stripes as in the picture at particular frequencies was observed to be a common result in experiments performed on membranes of varying sizes. Vortex and continuously rotating agglomeration of beads along different closed paths were among other results that were observed.

Figure 7.5 gives snapshots of different regions along the microchannel when one of the pixels was excited with 20 V_{pp} at 362 kHz[4]. The image labelled 'f' is closer to the excited pixel and is an example of beads' both rotating and forming stripes. Actuation is observed not only in the vicinity of the excited pixel, but all through out the channel (i.e., images labelled 'a' to 'e') due to the mechanical coupling in the system.

The regions where particles are rather uniformly and randomly dispersed on the left of images 'a', 'b', 'd', and 'e' in Figure 7.5 are noteworthy. The bead

[3] 2 V_{pp} @50 Ω.

[4] All the fluorescent microscopy images with bright background have gone through and/or contrast enhancement and color inversion to make them printer friendly. Figure 7.4(d) is not modified.

distribution in these regions are not much different than the distribution at the beginning of the experiment, i.e., before the application of any ultrasound. This observation suggests that most of the actuation happens in the highly compliant membrane regions, where displacement amplitudes are much higher than the non-membrane regions.

As a last stop in the discussion of 1-D devices, an experiment is described in which the phase of excitation among two pixels is changed while keeping the drive amplitude the same. Figure 7.6 shows the snapshots of an experiment in which a membrane close to excited two pixels is monitored. The position of the device

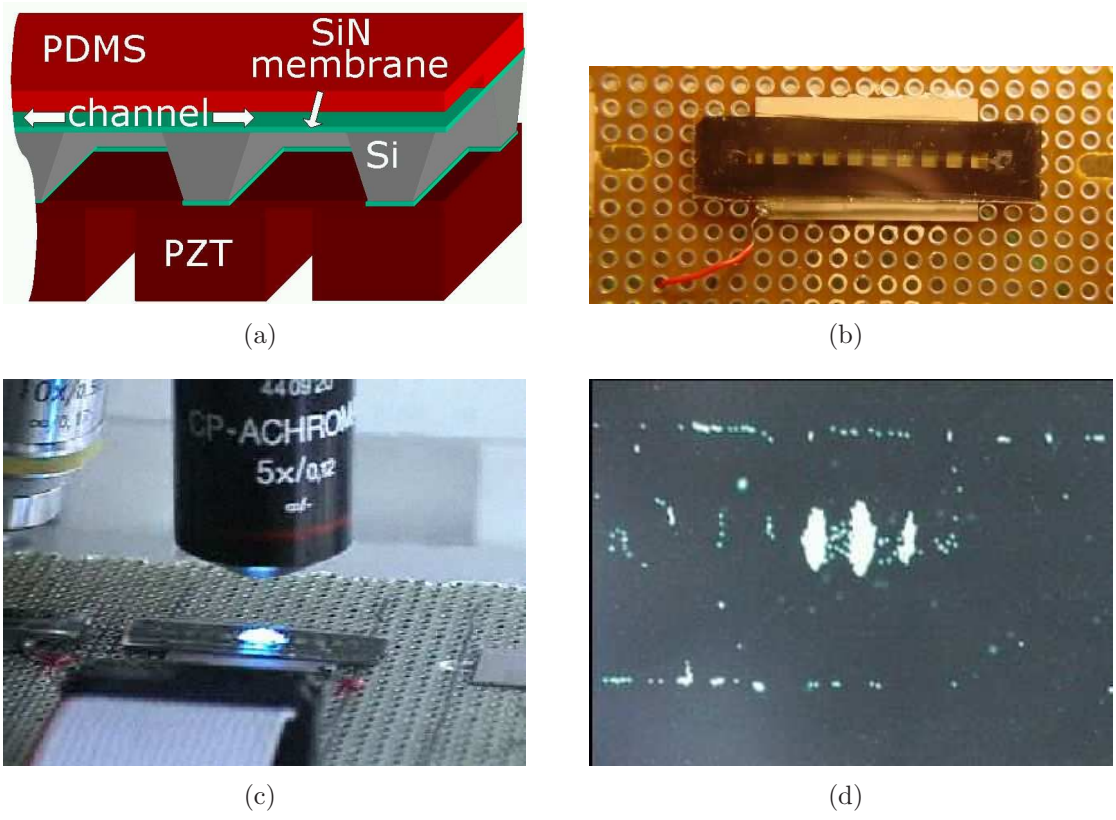

Figure 7.4: 1-D device (a) illustration, (b) optical picture, (c) picture under fluorescent microscope, and (d) a sample experimental result showing the collection of fluorescent micro beads inside the channel on the membrane.

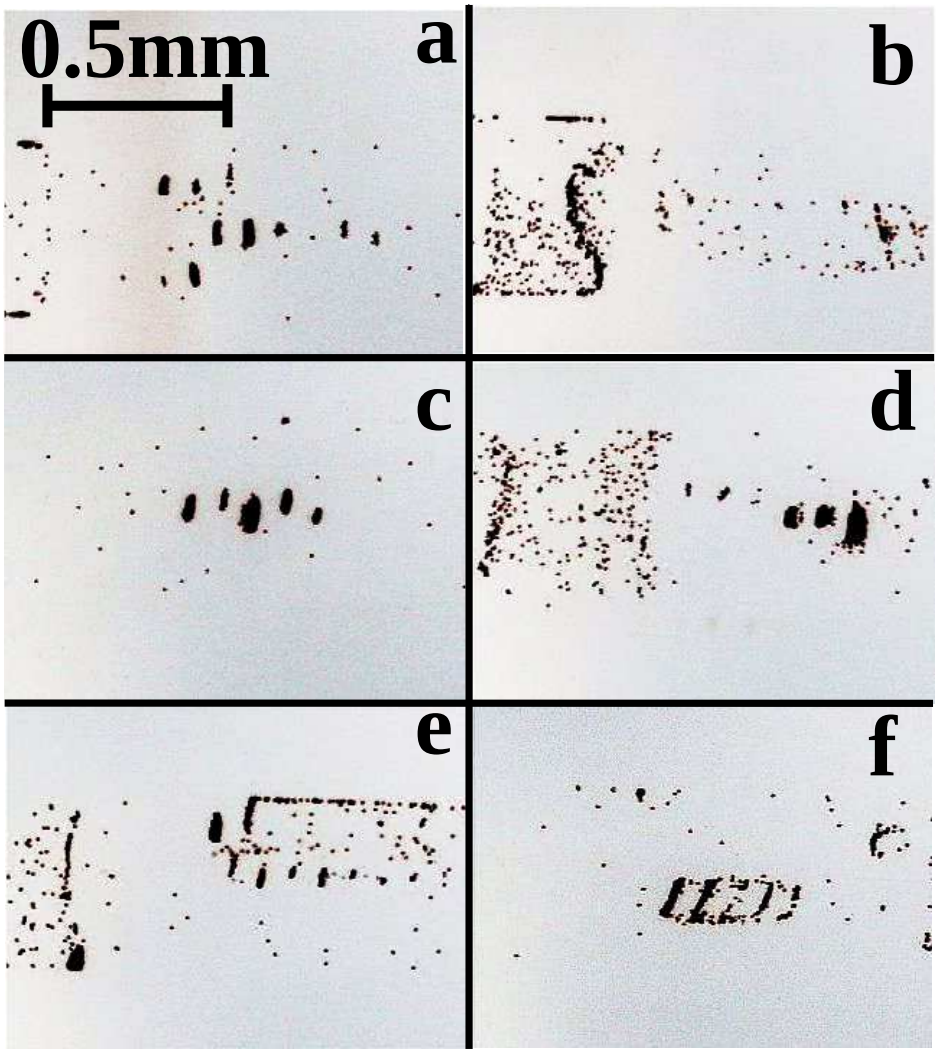

Figure 7.5: Snapshots from different regions along the channel when only one of the pixels was driven with 20 V_{pp}. The image labelled 'f' was taken close to the excited PZT pillar. Despite excitation of only single pixel, the mechanical coupling causes similarly strong actuation in neighboring pixels.

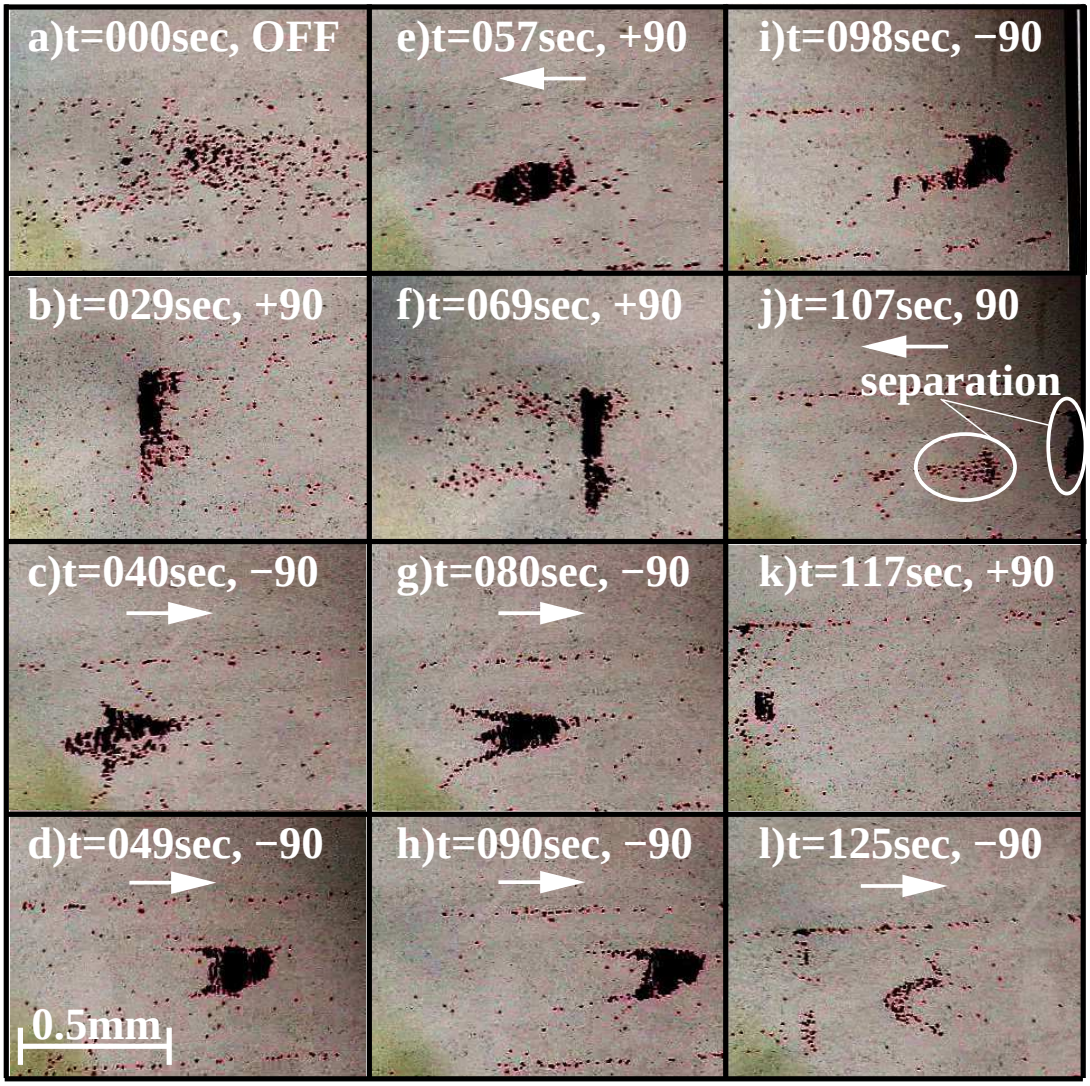

Figure 7.6: Snapshots from the two-pixel excitation of a linear nitride membrane array. Two adjacent pixels are excited with varying phases of $\pm 90°$. The time and the phase difference between the excited pixels are indicated at the top of each snapshot. The direction of the flow, when significant, is shown with an arrow.

under the microscope is adjusted manually during the experiment in order to keep moving particles under the objective, but, the magnification and the focus of the microscope are not changed. The times at which the snapshots are taken, and the phase between the drive signals of PZT pixels are noted on top of each snapshot. The amplitude and frequency of excitation are 20 V_{pp} and 333 kHz, respectively. When there is a fast moving visible motion of a concentrated set of beads, an arrow showing the direction of beads is added on top of the image as another annotation.

In Figure 7.6 $t = 000$ sec(image 'a') depicts the case before any voltage is applied on the system. Upon excitation of two pixels (image 'b') with a phase difference of +90° between them, most of the beads in the region gets collected towards the left boundary of the membrane. When the phase is reversed to -90°, the packet of beads start moving toward the right boundary of the membrane (image 'c'). After the packet travels a certain distance, the speed decreases (image 'd'), yet the packet keeps moving. At this point, if the phase is reversed again to +90°, the packet starts moving to the left boundary of the membrane (image 'e'). It stops moving after a distance, possibly indicating arrival at the membrane boundary (image 'f'). At this point the shape of the packet is similar to the previous case at $t = 29$ sec (image 'b'). As before, reversal of the phase to -90° causes the packet to start moving to right again (image 'g' and 'h'). In about 20 sec, the packet comes to an apparent stop, presumably close to the right boundary of the membrane (image 'i').

If the phase is reversed to 90° to move the packet towards the left boundary of the membrane, an unusual incident occurs. The packet is separated into two pieces, one smaller than the other (image 'j'). While the small packet moves toward the left boundary as expected, the large one moves very slowly towards right. One

explanation for this can be the packet's being on the membrane boundary before the separation. Then small part of the packet that is on the membrane starts moving as expected, while the rest of the packet that is on the non-membrane region gets very little actuation, and separation into two pieces occur.

The rest of the motion of the small packet is predictable, namely it comes to a halt (image 'k') after moving to left. Finally, when the phase is switched to -90° it starts moving to right (image 'l').

The ±90 degree phase difference is reminiscent of the operation principle of unidirectional travelling wave devices generated using interdigitated transducers [190, 191] that are spaced one quarter of an acoustic wavelength and driven in quadrature. Nonetheless, phase differences of 130° and 210° between the pixels also resulted in opposite flow velocities across a membrane around the excited pixels. So the problem at hand is more complex, although the basic idea of phased drive is common to both.

A 20 V_{pp} actuation voltage can be considered to be large. Particle motion at voltages as low as 4 V_{pp} was observed as well, but the speed of the motion was much lower.

In general, the response of the beads to ultrasonic actuation shows much variety depending on the membrane position along the arrays. The manual bonding of the PDMS channel causes a misalignment between the center of the membrane and the symmetry axis of the microchannel. The bonding between the MEMS die and the PZT array is another source of misalignment. Given all these problems, fabrication of a 2-D array to be described in the next section follows a more structured line of attack towards the assembly of the main components, VLSI die, PZT array, and

MEMS die.

A rigorous or quantitative explanation for the operation of the 1-D device is not attempted, but the results presented here show that bulk-PZT actuation can be used to generate micro-particle motion with voltages as low as 4 V_{pp}. Furthermore, near field displacement control of micro-particles in a microchannel by phased drive of PZT pillars was also demonstrated.

7.2 Fabrication of 2-D PZT arrays

In order to fabricate a prototype for the stacked structure shown in Figure 7.3 at the chip level, a manual flip-chip bonding process was developed [186]. To pursue this approach, a 20×20 array of PZT pillars at a 250 μm pitch was made from a 0.5 mm thick plate of bulk-PZT by dicing. The MEMS die consists of a silicon nitride-silicon oxide membrane that is formed by backside deep reactive ion etching (DRIE). In addition, silicon protruding islands were formed over the membrane to engage the motion of PZT pillars to the membrane. VLSI die at the bottom of the stack did not include any transistors for the prototype. Therefore, from now on it will be called as *PAD die*. Its main function was to provide electrical connections to individual PZT pillars and solder bumps for them to be bonded. However, all the fabrication to be described can easily be adapted as a post-CMOS process, without compromising transistor characteristics as the temperatures stay below 225°C.

Another important consideration is the Curie temperature of the PZT. It is in the range 320–325°C for the PZT types employed in this work[5]. So the bond-

[5]Some PZT types and their properties are listed in Table N.4 in Appendix N.1.

ing operation does not affect the PZT characteristics negatively. This point is experimentally verified in Appendix N.2.

Fabrication of the PAD die, PZT pillars, and the MEMS die are illustrated in Figure 7.7, Figure 7.8, and Figure 7.9, respectively. Detailed description for each follows next.

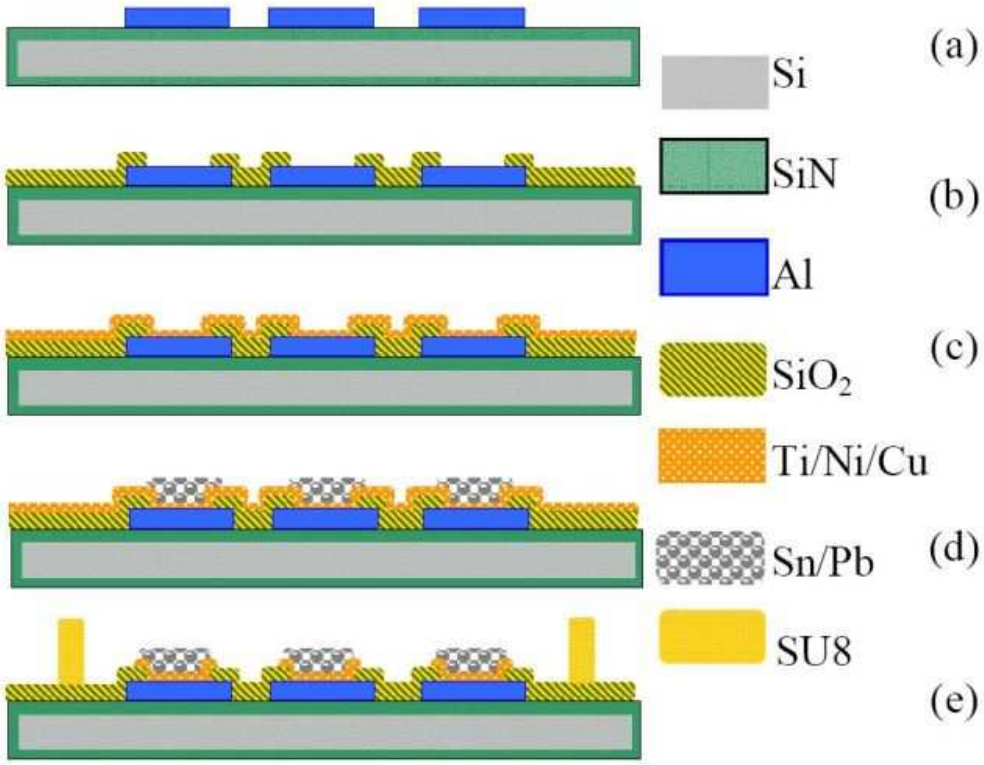

Figure 7.7: Process flow for the PAD die: (a) SiN deposition and aluminum patterning, (b) oxide deposition and etching of contact holes, (c) e-beam evaporation of the seed layer, Ti/Ni/Cu, (d) solder electroplating and stripping of the photoresist mold, (e) wet etching of the seed layer and SU8 lithography to form the alignment pillars.

7.2.1 Fabrication of the PAD die

The fabrication for the PAD die starts on a 4 inch silicon wafer with SiN insulation layer on top. First, 0.75 μm of aluminum is sputtered and patterned using a wet etchant. Next, 0.5 μm of PECVD oxide is deposited as a passivation layer that is later patterned to realize contact to the pads and the bumping sites. A multilayer sandwich of Ti/Ni/Cu is evaporated as a seed layer for the electroplated eutectic Sn/Pb solder. This layer stack along with Al underneath constitutes the under bump metallurgy (UBM) layer. A thick positive photoresist, AZ4903, is used as a mould to define the regions to be filled with solder. After pulsed electroplating of about 30 μm solder, the photoresist is stripped in acetone. Next UBM layer is wet etched. Finally, 220 μm thick SU8 lithography is performed to form the pillars that aid in manual alignment during the bonding of the PZT pillars to the

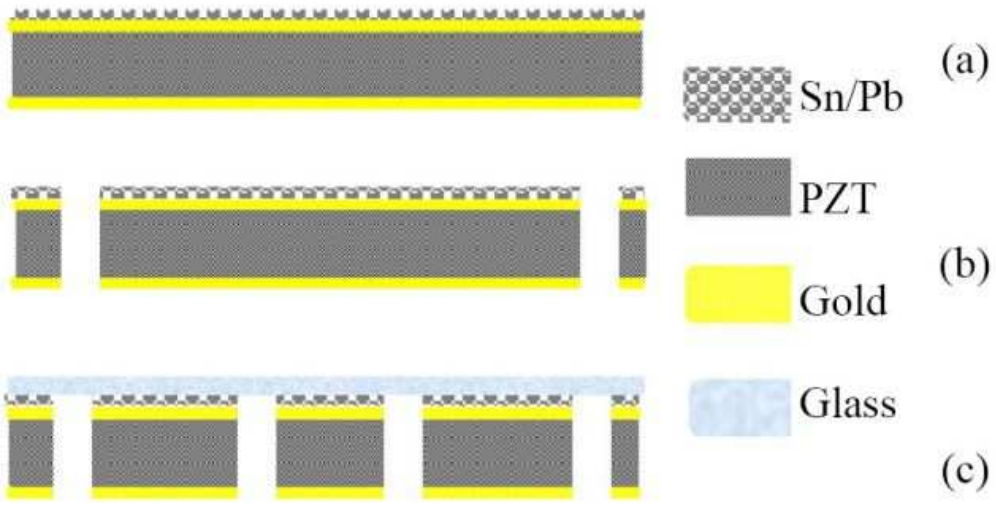

Figure 7.8: Bulk-PZT processing: (a) 0.5 mm thick PZT plates with gold electrodes are solder electroplated on one side, (b) the alignment marks and holes are laser drilled, (c) a dummy glass die with spin-on adhesive on the surface is bonded to the pillars to later transfer them from the dicing tape to the PAD die.

PAD die. These structures are not needed if a flip-chip bonder with alignment capabilities is available. Step by step process flow for PAD die, with suggested improvements for the future runs, is given in Appendix O. Optical picture of part of the array is shown in Figure 7.10.

SEM pictures of a PAD die before and after reflow of the solder are shown in Figure 7.11 and Figure 7.12, respectively. The reflow is performed by heating up the sample to around 220°C.

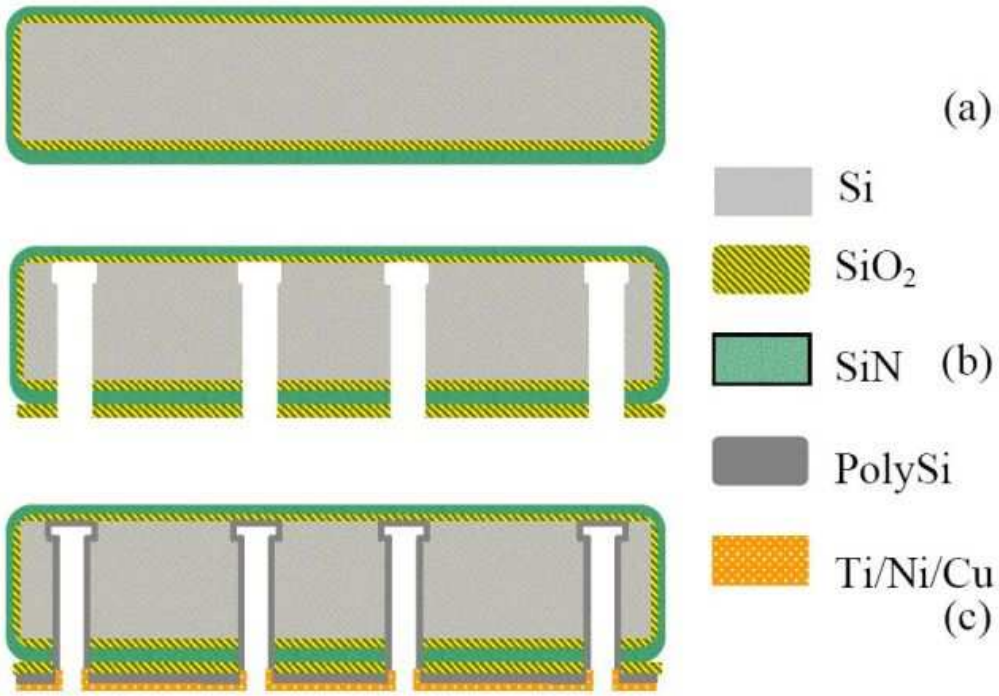

Figure 7.9: MEMS die processing: (a) grow thermal oxide and deposit SiN on 350 μm thick, double-side-polished, silicon wafer, (b) deposit PECVD oxide on the backside. Pattern DRIE mask and do etch till stopping at the oxide on the front layer.

7.2.2 Fabrication of the PZT pillars

Both PZT-4 and PZT-5A[6] bulk plates are used in the process shown in Figure 7.8. The plates are 0.5 mm thick with gold electrodes for good solder wetting properties. One side of this plate is solder electroplated under similar conditions as described for the PAD die. Then, alignment holes and marks are laser drilled using a diode

[6]Staveley NDT technologies

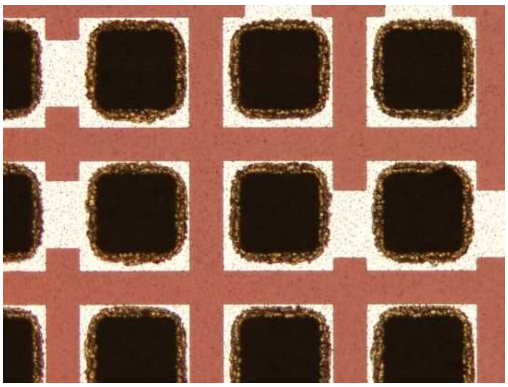

Figure 7.10: An optical picture of a subarray on the PAD die.

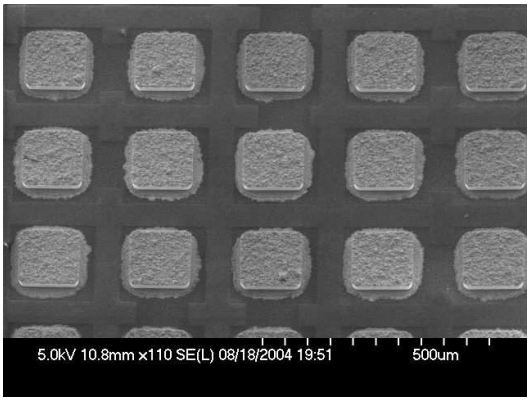

(a)

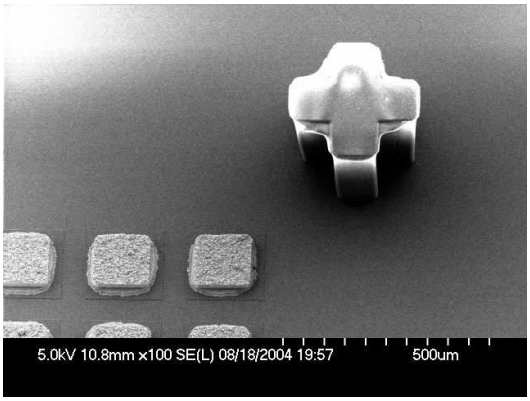

(b)

Figure 7.11: SEM picture of a PAD die before reflow. (a) Array of solder bumps at 250 μm pitch, interconnected by Al metallization. (b) SU8 pillars placed symmetrically at the four corners of the bump array facilitate alignment during bonding.

pumped, solid-state, pulsed laser (Coherent Inc., Avia 355-1500, 355 nm). The SU8 alignment pillars on the PAD die, one of which is visible in Figure 7.11(b), interface through these alignment holes to ensure coarse manual alignment. After laser drilling, the PZT die is diced at 250 μm pitch using K&S 7100 wafer saw with a blade kerf width of 35 μm. The dicing recipe is detailed in Appendix N.1. At the end of the dicing process, the PZT pillars are separated from each other and attached to the dicing tape. Images from two different PZT arrays that are laser-machined and diced are shown in Figure 7.13.

A dummy glass die with spin-on adhesive (3M, Pronto CA-100) on top is used in order to transfer the pillars onto the PAD die. The pillars are bonded to the glass die with a force of 5 N. After waiting for 6–7 hours at room temperature for the curing of the adhesive, the dicing tape is peeled off, leaving all of the pillars on the glass die with their gold electrode available for PAD die bonding.

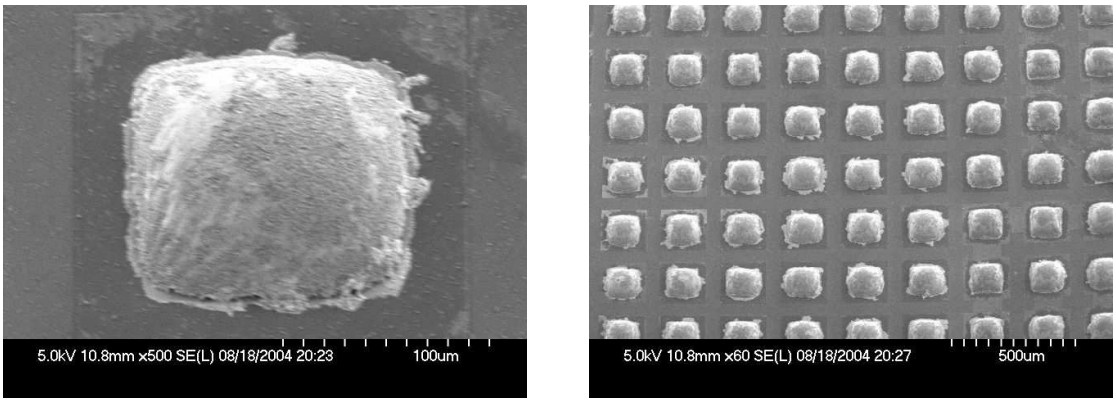

(a) (b)

Figure 7.12: SEM picture of (a) a single bump and (b) a subarray on the PAD die after reflow. Surface tension cause the reflowed solder to take a spherical form.

7.2.3 Fabrication of the MEMS die

The MEMS die for the prototype consisted of a large SiN membrane with a 2-D array of silicon pillars over it. In general, this die can include any microsystem manufactured by surface or bulk micromachining.

The fabrication procedure, outlined in Figure 7.9, starts by growing 0.5 μm oxide on a 4 inch, 350 μm thick, double-side-polished silicon wafer, followed by a 0.9 μm deposition of low stress LPCVD silicon nitride. A 1.8 μm of PECVD oxide is deposited on the back side to serve as a mask for the long backside DRIE. After patterning of the oxide-nitride-oxide layer on the backside, the wafer is etched until the oxide layer on the front side is reached. At the end of this step, a membrane with an array of protruding silicon pillars is formed. These pillars are used to engage the vibrations of individual PZT pillars to the membrane, hence providing

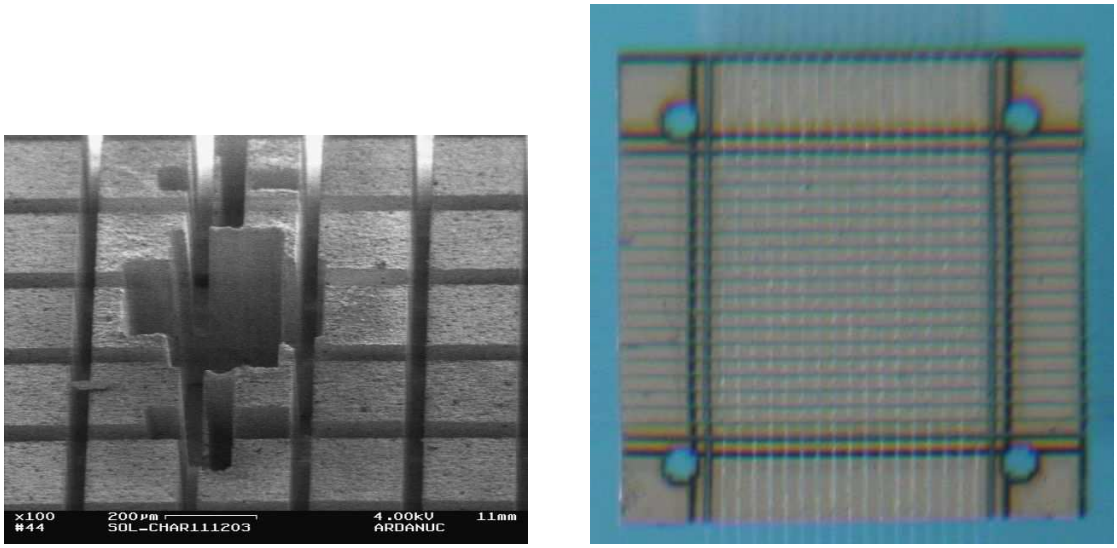

(a) (b)

Figure 7.13: (a) An SEM picture of the marks engraved on a PZT array with laser. These marks are used both for alignment during subsequent dicing and manual bonding. (b) An optical picture of a fully-cut PZT array on the sticky tape used for dicing.

local actuation of the membrane. A conductive coating needs to be deposited on the backside of the MEMS die for it to serve as a common ground for all of the pillars. However, the large aspect ratio of the etched silicon pillars and undercutting that occurs right after DRIE reaching to the stop later, necessitate the deposition tool to be very conformal. LPCVD deposition of polysilicon is chosen for this purpose. First the wafers are annealed at 1050°C for 30 min to burn out C_4F_8 passivation from DRIE. This is followed by p+ polysilicon deposition at 650°C with expected thickness of around 1 μm. Lastly, Ti/Ni/Cu is evaporated to serve as a solder wetting layer during bonding with solder electroplated PZT array.

Figure 7.14 shows SEM and optical pictures of the MEMS die. In order to avoid dicing of the wafer with delicate membrane structures, cleaving paths are etched around the die boundary as shown in Figure 7.14(a). The negative slope observed on the pillars in Figure 7.14(b) and Figure 7.14(c) can be optimized by modifying the DRIE etch recipe. Figure 7.14(d) shows some MEMS dies at different stages of the fabrication. The die on the south side of the picture, which is presented at a larger scale in Figure 7.14(e), shows the membrane after DRIE etching is complete. The die on the north side of the picture in Figure 7.14(d) pictures membrane from back side after metal deposition. The flatness of the membrane and transparency is lost after high temperature anneal and polysilicon deposition. The resulting curvature of the membrane is visible in Figure 7.14(f).

7.2.4 Assembly and packaging

There are two bonding stages, both of which include solder reflow. Firstly, bonding of PZT pillars on the dummy glass slide to solder bumped PAD die is done at 225°C,

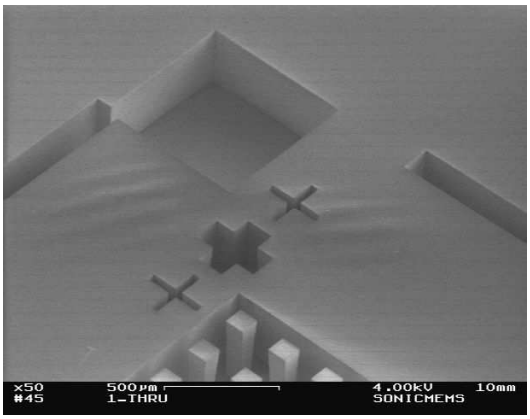

(a)

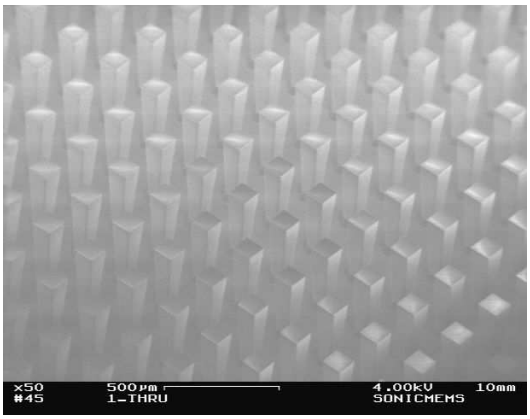

(b)

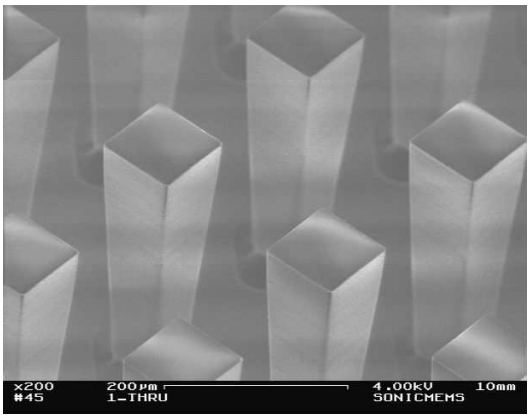

(c)

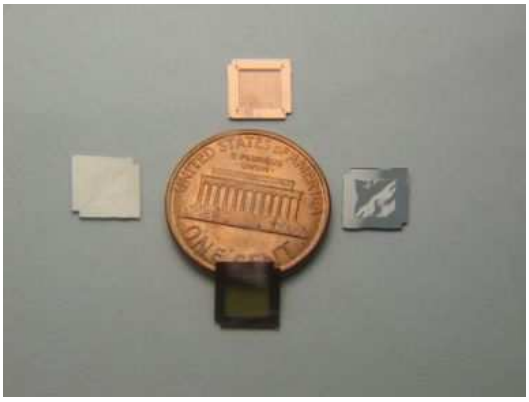

(d)

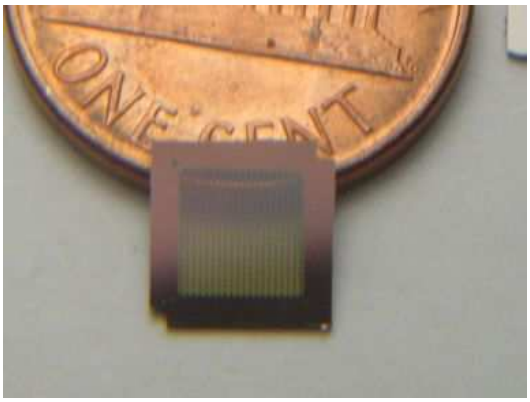

(e)

(f)

Figure 7.14: SEM pictures of the MEMS die after DRIE etching showing (a) the die boundary, (b), (c) pillar structures protruding from the membrane. (d), (e), (f) Optical pictures of some MEMS dies taken from front and back at different stages of fabrication.

on a hot-plate, in a N_2 ambient. After this step, the dummy glass slide is removed by leaving the device in acetone for 24 hours. Figure 7.15(a) and Figure 7.15(b) give the optical and SEM pictures of the device at this stage. It is noticed that about 5-10% of the PZT pillars are shorted with the neighboring pillars via their merged solder layer on the top electrode. This problem should be avoided in the future runs, and plating the backside of the MEMS die rather than the PZT plate can be helpful.

The second reflow, which bonds the MEMS die to the top of the PZT pillars is also done under the same conditions as the first bonding. A picture of a fully bonded stack of PAD die, PZT pillar and MEMS die is shown in Figure 7.15(c).

It was not possible to wire bond to the electroplated electrode on the PZT plate. Therefore, some misalignment during the MEMS die bonding had to be introduced in order to ground the PZT pillars. A sticky copper tape was used to ground the array via connecting it to the bottom of the MEMS die. Figure 7.15(d) gives a picture of a device packaged in this manner. Its electrical characterization is described in the following section.

7.2.5 Electrical characterization results and discussion

Figure 7.16 plots the amplitude and phase of the impedance measured from two neighboring pixels using an HP4194 impedance analyzer. While the matching between the impedance characteristics of two pixels seems to be acceptable, the quality factor of the strong resonance around 2 MHz is less than 20. One reason can be the large series resistance between the rim of the membrane and the individual pillars, that was measured to be 300–1000 Ω. This can be due to the decreased

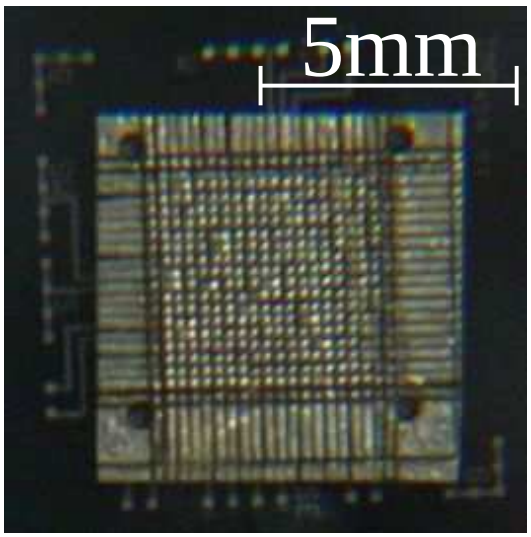

(a)

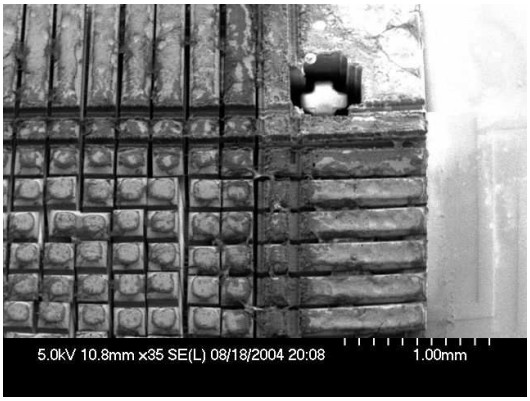

(b)

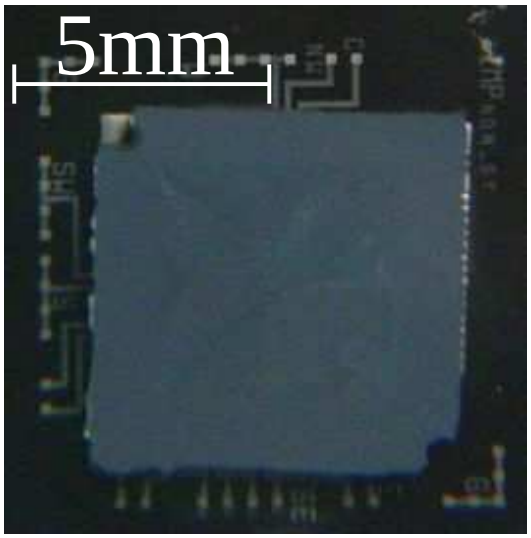

(c)

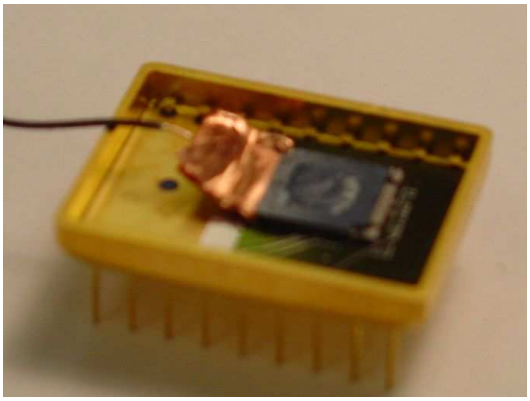

(d)

Figure 7.15: (a) Picture of the actuator platform after the first flip-chip bonding, which bonds the PZT pillars to the PAD die. (b) An SEM image of the device after the first bonding, showing the SU8 alignment pillar in the alignment marks engraved in the PZT plate. Pictures taken (c) after the second bonding, and (d) after packaging for electrical testing.

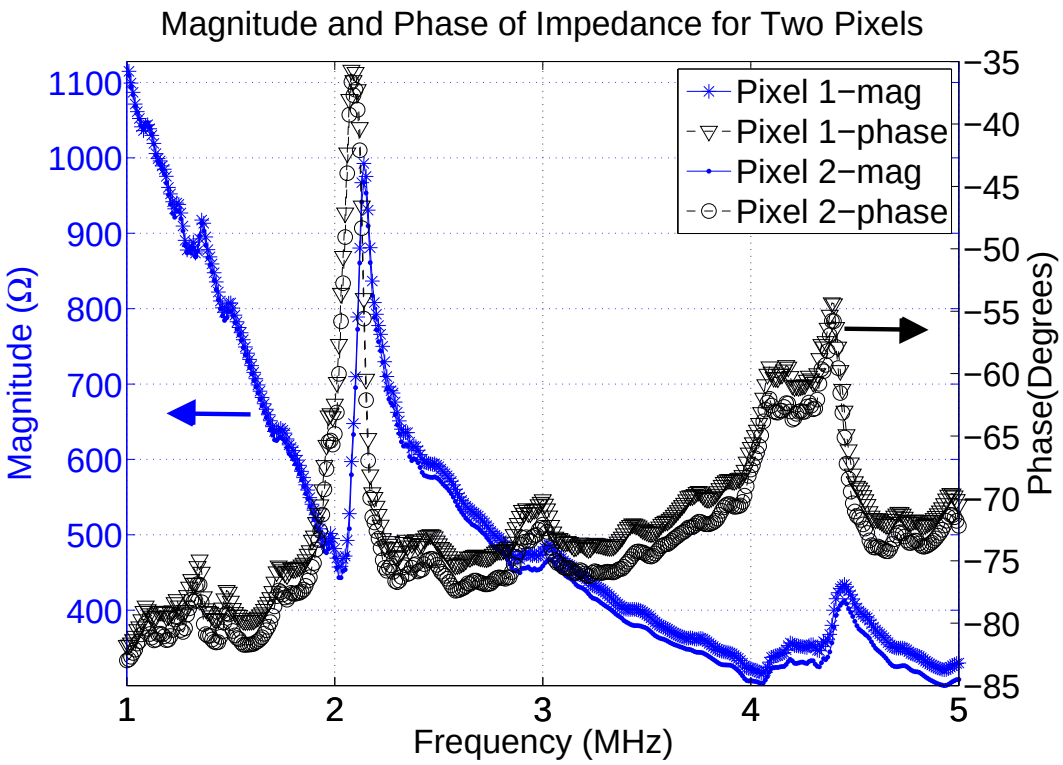

Figure 7.16: Amplitude and phase of the measured impedance from two pixels in the array.

rate of polysilicon deposition in the undercut regions that are formed once the DRIE hits the stop layer. Another complication is the amplitude of impedance, which is more than two orders of magnitude less than what is expected from the capacitance of a single pillar. This indicates the possibility of shorting on the PAD die.

Given all the above problems, future runs require a characterization of solder overflow versus applied pressure and electroplated solder volume. It was realized that performing two soldering processes that have similar reflow temperature is not a robust process. This is because the solder bumps on the PAD die that reflowed during the first bonding, reflows also during the second bonding between the PZT pillars and the MEMS die. A solution can be transient liquid phase bonding,

in which all solder is transformed into intermetallic compounds that have higher melting points than the solder itself [192].

Finally, it should be noted that Pb containing solders used in this work are known to have health and environmental risks. There is a promising and fast growing trend in the industry to eliminate the use of Pb containing compounds. Therefore future bulk-PZT bonding studies that use solder should investigate Pb-free alternatives. Transient liquid phase bonding using Au/In solder [183, 192], with rather low bonding temperatures ($< 200°C$), seems to be very promising for bulk-PZT integration and large scale, localized actuation of microsystems.

CHAPTER 8

CONCLUSIONS AND FUTURE WORK

The integration of bulk-PZT to a given microsystem comes usually with a unique elastic/acoustic problem, as well as circuit design, fabrication and packaging considerations. This multidisciplinary nature is also apparent in the diversity of the material presented in this thesis, where different aspects of bulk-piezoelectric sensing and actuation are considered theoretically and experimentally. Some of the important results are summarized below.

The energy transfer between a bulk-PZT actuated, surface micromachined beam is investigated and experimental results are shown to satisfy the reciprocity relation to within 45%. The discrepancy is ascribed to nonlinear operation of the resonant beams that had to be incurred in consideration of low signal levels in some part of the experiments. To the author's knowledge, this was the first time that electrostatic and bulk-piezoelectric actuation are compared by measurements on the same beam in the vicinity of its resonance. Piezoelectric coupling coefficient amplitudes of 0.3×10^{-7} N/V and 0.1×10^{-7} N/V were extracted for two of the tested beams. Electrostatic actuation caused larger displacements than piezoelectric actuation for the tested range of operation. It is also noted that for two beams of very similar electrostatic actuation characteristics, piezoelectric actuation can yield considerably different results. This is explained, qualitatively, by the position dependence of the piezoelectric actuation, i.e., the relative position of the beam anchors as compared to nodes and antinodes of the standing wave pattern on the die surface.

The above results were all obtained under conditions for which the resonant frequency of the beam was away from the frequencies of the structural bulk modes

of the bonded PZT-silicon die. Investigation of the co-resonant regime, which is expected to increase PZT actuation of the beam by the relative quality factor of that particular mode (ignoring nonlinearity), can very well complement the work presented in this thesis. Studying the position dependence of PZT actuation using a 2-D array of identical beams can also prove beneficial. Along this line, studies of correlations among the piezoelectric actuation efficiency of micro-beams, quality factor, anchor loss, and the vibration patterns on the substrate are intriguing research efforts.

Later in the thesis, Ultrasound Enhanced Electrostatic Batch Assembly (U2EBA) is proposed as a low-cost method to assemble microstructures. Here, electrostatic field due to a global top electrode is used to assemble structures, while PZT actuation helps to reduce the stiction to the substrate. Important advantages of this method are in-air operation and off-chip attribute requiring no electrical wiring or on-chip actuators. Yield rates reaching up to 100% are reported on certain types of micromirror arrays. For the reported devices, the DC voltages used were very large, on the order of kV. Nonetheless, future attempts made with more compliant structures are expected to require smaller voltages. A point of concern is the damage on the devices due to large amplitude vibrations, which on the positive side, is a good indication of the power of bulk-PZT actuation. The resulting damage can be minimized, if not eliminated, by monitoring the device assembly yields during the experiment and subsequently changing the PZT drive parameters. U2EBA is suitable especially for one-time assembly of high density, large aspect ratio micro-structures that are otherwise very hard to fabricate. Take for example a large array of a pillar array with a very sharp tip, but relatively large base on the substrate side for mechanical rigidity. Such a structure can work as a thermionic emission cathode. These structures can first be fabricated in 2-D by

e-beam or optical lithography with arbitrary cross section and extreme sharpness. Subsequent application of U2EBA, then yields the desired high-aspect ratio tip array in 3-D.

The use of novel latching designs with U2EBA is shown to yield semi-permanent positioning with zero idle-power. Stepped operation at intermediate angles between parallel and vertical positions is demonstrated. The duration of steps of angular displacements is shown to be approximately equal to the period of frequency sweep applied on the PZT actuator. Semi-permanent latching at seven angles between 45° and 72° is obtained from one of the good devices without much effort on optimizing the drive parameters.

One of the motivations behind the work on semi-permanent latching structures described above is the possibility of using very small mirrors over large areas for energy redirection and focusing. This energy can be due to *microwave*, *acoustic*, or *solar* radiation, with the last type getting the most attention at the time of writing of this thesis. This type of redirection is named as All-angle LAtchable Reflector (ALAR) technology and is proposed as a tile-level solution to make solar energy pervasive and built-in, as opposed to a costly addition to the buildings with aesthetic and structural concerns of wind stability and loading. Tile-level integration aspect offered by ALAR not only introduces a new breath to the exponentially growing concentrated solar power market, but also makes many interesting applications mentioned in this thesis possible. The prospective arguments of ALAR technology mentioned above are substantiated by the demonstration of a working prototype. This prototype houses an array of centimeter scale mirrors, which are wirelessly controlled and can automatically track the brightest spot in the ambient.

Although the chapter about the ALAR technology is related to U2EBA efforts

for the assembly of micromirrors, it may appear to be rather off the main theme of this thesis, namely bulk-piezoelectric transduction in microsystems. The author, however, believes that it is probably one of the most interesting chapters for a random reader of this thesis, given the potential impact of the ALAR vision and the importance of the sun, our ultimate energy source, on our daily lives.

The sensing part of the thesis regarding bulk-piezoelectricity use in microsystems is centered around capacitance measurement using oscillators based on quartz resonators, i.e., one of the most common bulk-piezoelectric crystals in the market today. In order to reap the benefits of the well-known frequency stability of quartz for large dynamic range measurements, a nonlinearity compensation and self thermometry method is proposed for capacitive sensing applications. This method, named as Time-Multiplexed Crystal based Capacitive Sensing (TM-XCS), requires data-processing on measurements of oscillator frequency under different loading configurations with possibly unknown capacitors. The postprocessing described in the thesis reveals the unknown capacitors in terms of Butterworth-Van Dyke (BVD) equivalent circuit parameters. Self thermometry aspect then lets determination of the unknown capacitors only from calibrated values of the BVD circuit, making the capacitance measurements independent of oscillator amplifier parameters. Although dedicated testing of this method has not yet been done, some of the relations used in derivation of the algorithm were experimentally tested to give errors less than 6%. The future work towards experimental verification of TM-XCS can involve design of an application-specific integrated circuit or programming of a microcontroller unit to perform the required sequential switching operations and postprocessing.

As a final stop in the application arena of bulk-piezoelectric actuation, mi-

crofluidic particle transport is considered. A 1-D SiN membrane array on a silicon chip is ultrasonically actuated inside a PDMS channel, and fluorescent microscopy is used to picture the motion of μm sized beads due to bulk-PZT excitation. Results on both single pixel excitation and phased drive excitation of two pixels are presented.

APPENDIX A

THE EQUIVALENT CIRCUIT OF PARALLEL PLATE ELECTROSTATIC ACTUATORS

This section gives the summary of the equivalent circuit of a parallel plate electrostatic actuator in a notation convention that facilitates the analysis in Chapter 2. [55,56]. The model is based on the assumption of a single degree-of-freedom, lumped, mass-spring-damper (MSD) system with an undeformed electrostatic gap of g_0, and with no fringing capacitance. This system is illustrated in Figure A.1. The displacement of the body from its reference position is shown by

$$z_t = z_0 + z, \tag{A.1}$$

where z_t, z_0 and z are the total, DC and small-signal displacements. Voltage, current and force variables are also named similarly and are listed in Table A.1 along with other parameters. The static part of the voltage, v_0, causes the static capacitance and the system spring constant to change from their no-displacement values of C_0 and k to C_0^* and k^*, respectively. This is governed by the following:

$$C_0^* = \frac{\epsilon_0 A_e}{g_0 - z_0} = \frac{C_0 g_0}{g_0 - z_0} \tag{A.2}$$

$$k^* = \frac{k(g_0 - 3z_0) - 2F_0}{g_0 - z_0}. \tag{A.3}$$

It is assumed that the static part of the voltage is determined by a DC voltage source of V_p, whereas the static part of external force is zero, i.e. $v_0 = V_p$ and $F_0 = 0$. With this notation, the turns ratio of the transformer in Figure A.1(b), which is the electromechanical transduction factor, takes the form:

$$\eta_{\text{es}} = \frac{\partial^2}{\partial v \partial z}\left(\frac{C_0^* v^2}{2}\right) = \frac{V_p \epsilon_0 A_e}{(g_0 - z_0)^2}. \tag{A.4}$$

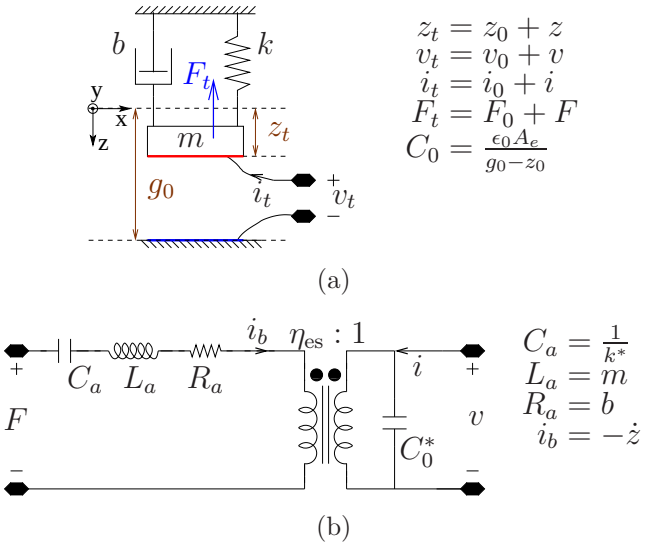

Figure A.1: The parallel plate capacitor modelled as a mass-spring-damper (MSD) system of constants $m\,(kg)$, $k\,(N/m)$, and $b\,(Nsec/m)$, respectively: (a) the mechanical model (b) the small signal equivalent circuit.

Finally, equating the static forces, one can also show that $\eta_{es} = \frac{2kz_0}{V_p}$ and

$$k = \frac{\epsilon_0 A_e V_p^2}{2z_0(g_0 - z_0)^2}. \tag{A.5}$$

Table A.1: Nomenclature for the MSD model.

Symbol	Description	Unit
A_e	Area of the beam where uniform electrostatic pressure is applied	m^2
b	System damping constant	$(\mathrm{N\,sec})/\mathrm{m}$
i, i_0, i_t	Small-signal, large-signal (bias) and total current	A
ϵ_0	Permittivity of free space	F/m
F, F_0, F_t	Small-signal, large-signal (bias) and total applied mechanical force	m
k	Mechanical spring constant of the MSD system	N/m
k^*	Effective (system) spring constant modified due to electromechanical coupling	N/m
C_0	Parallel plate electrical capacitance at zero bias (undeformed)	F
C_0^*	Parallel plate electrical capacitance modified due to elastic deformation due to bias of v_0	F
m	Mass of the MSD system	N/m
v, v_0, v_t	Small-signal, large-signal (bias) and total voltage	V
z, z_0, z_t	Small-signal, large-signal (bias) and total displacement of the moving electrode towards the stationary electrode in the MSD system	m
g_0	Parallel plate capacitance gap as fabricated	m
γ	$\gamma = \frac{g_0}{z_0}$	—

APPENDIX B

MEASUREMENT OF OUT-OF-PLANE DISPLACEMENTS ON THE SUBSTRATE SURFACE BY INTERFEROMETRY

The surface vibrations are measured using a Polytec Doppler Laser Vibrometer (Sensor Head: OFV-511, Controller:OFV-2700, Microscope Adapter: OFV-074). It has two demodulator options: one for position (OVD-30) and the other for velocity (OVD-05) output. The setup is shown in Figure B.1. A lock-in amplifier (Stanford Research Systems, SR844) is used to enhance the resolution for linear measurements. We could resolve down to 50 fm displacements with this setup. For experiments that require spatial scan at a particular frequency, the setup uses a position controller (Newport , ESP300) and XYZ stage. All the equipment is controlled by a PC using Labview© software.

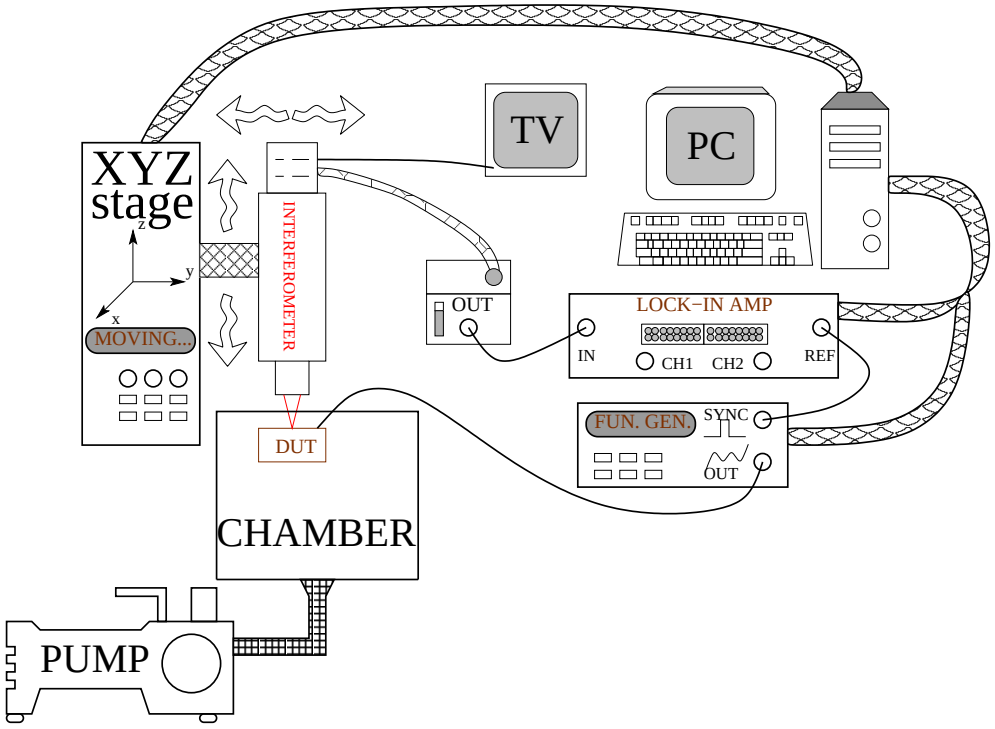

Figure B.1: Schematic of the Doppler interferometry setup for measurement of vibrations above 25 kHz. The system is equipped with two replaceable signal processor modules that can give position or velocity output.

APPENDIX C

RESULTS ON SUBSTRATE DISPLACEMENT MEASUREMENTS

C.1 Substrate vibrations due to PZT actuation

The complexity of die level vibrations is another reason, besides packaging, that hinders the usage of bulk PZT actuation for well controlled actuation of MEMS structures. The force simply cannot be localized due to the whole silicon die getting actuated. This is valid for the devices studied in Chapter 2 as well. Although the displacement pattern is not controllable, its visualization is important in investigating the position dependence of piezoelectric coefficients.

A Doppler laser vibrometer (Polytec, OFV-501, OFV-2700) is used to measure the amplitude and phase response of the out-of-plane vibrations of the silicon surface close to the resonant frequency of *FBT-200*, at 200 kHz[1].

Figure C.1 presents the spatial picture of amplitude and phase of the vibrations with 'y-axis' roughly aligned with the long side of the PZT bar. A straightforward observation from this figure is that the points lying on a line parallel to the longitudinal axis of the PZT have about the same amplitude and phase of vibration. This implies that the overhang parts of the silicon over PZT acts much like a wide cantilever. Such a behavior is plausible also from Figure 2.2. We measured the fundamental mode resonance frequency of this wide silicon cantilever to be 64.8 kHz[2]. Figure C.2 investigates the amplitude of vibration of two points on the die surface as a function of frequency. The inset in the same figure shows the location of these

[1]The setup is explained in Appendix B.

[2]Due to poor manual bonding, the die is not symmetric on the 5 mm wide PZT bar, but one part of the overhang is about 3 mm while the other side is close to 2 mm.

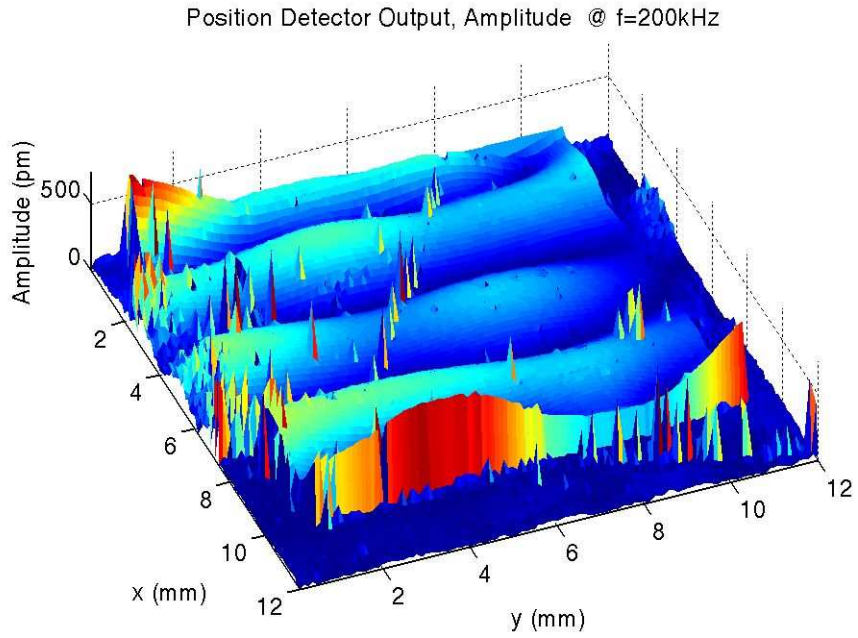

(a)

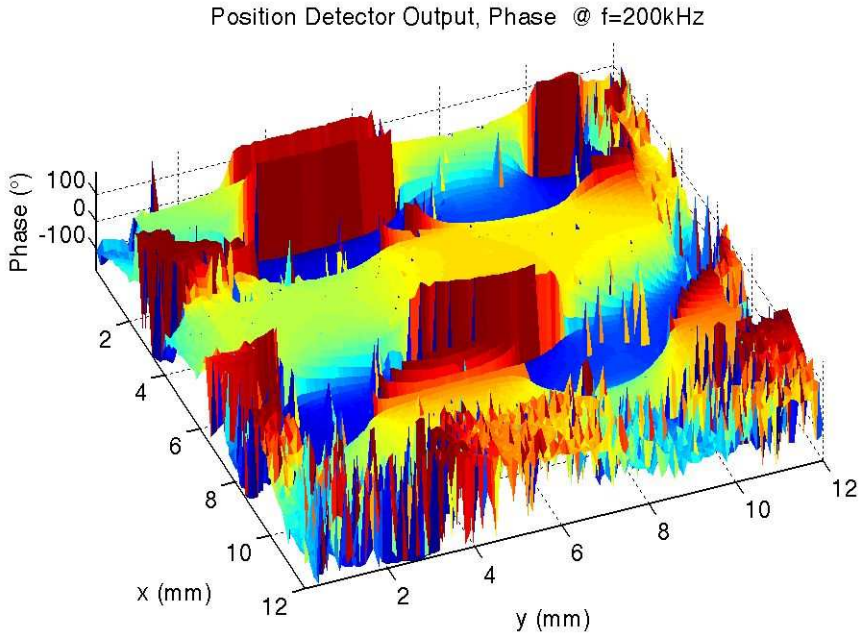

(b)

Figure C.1: (a) Amplitude and (b) phase response measured on the silicon die interferometrically at 200 kHz with 50 mV_{pp} drive. The long side of the PZT bar is roughly aligned with the 'y-axis'.

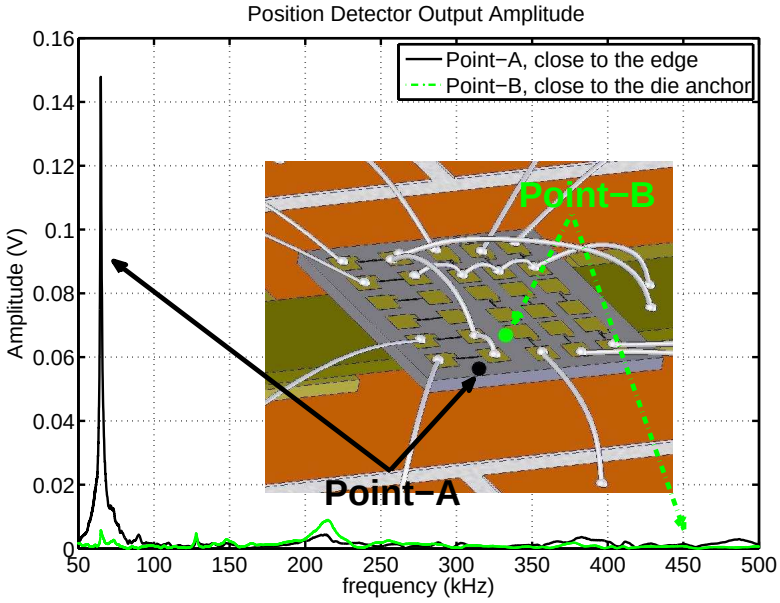

Figure C.2: The vibration amplitude on the die measured by interferometry. The inset shows the two points of measurement on the die surface. Point A is close to the edge of the die, hence picks up the first harmonic component of the cantilever vibration. On the other hand Point B, being close to the anchor, has negligible vibration at this frequency.

two points, one being at the tip of the cantilever-like silicon region on the PZT bar, and the other being closer to the anchor of the same region. Figure C.2 shows that two close points on the die can have a large difference in vibration amplitude at certain frequencies, as determined by the boundary conditions formed after the bonding of the silicon die to the PZT. As such, any microsystem implementation that aims to have a good control of localization of actuation using bulk-PZT actuation needs a repeatable bonding process.

C.2 Substrate vibrations due to electrostatic excitation

The data presented in this section shows the out-of-plane displacements at the anchor of surface-micromachined beams when they are electrostatically (ES) excited. Doppler interferometry was used to quantify the out-of-plane components of these vibrations as in the previous section.

Two sets of measurements were done on 200 μm long, fixed-fixed Beam-F as it is electrostatically excited. In the first one, the variation of the substrate vibration was monitored at three different points using the laser beam of the interferometer. The spot size of the beam was around 10 μm. In order to ensure that no edge reflections from the anchor interfered with the measurement, the laser beam was not brought closer than $\approx$ 20 μm to the anchor. The results are plotted in Figure C.3. The peak at 284.6 kHZ decays steeply in about 10 μm as the points get further away from the beam.

As expected all curves present one peak, around 284 kHz. There is a second peak in each curve, around 287 kHz, for which we lack an explanation.

Second set of measurements were done at a fixed point for varying V_p. Our experimental setup was able to measure 290 fm peak displacement at $V_p = 2$ V. The results are presented in Figure C.4.

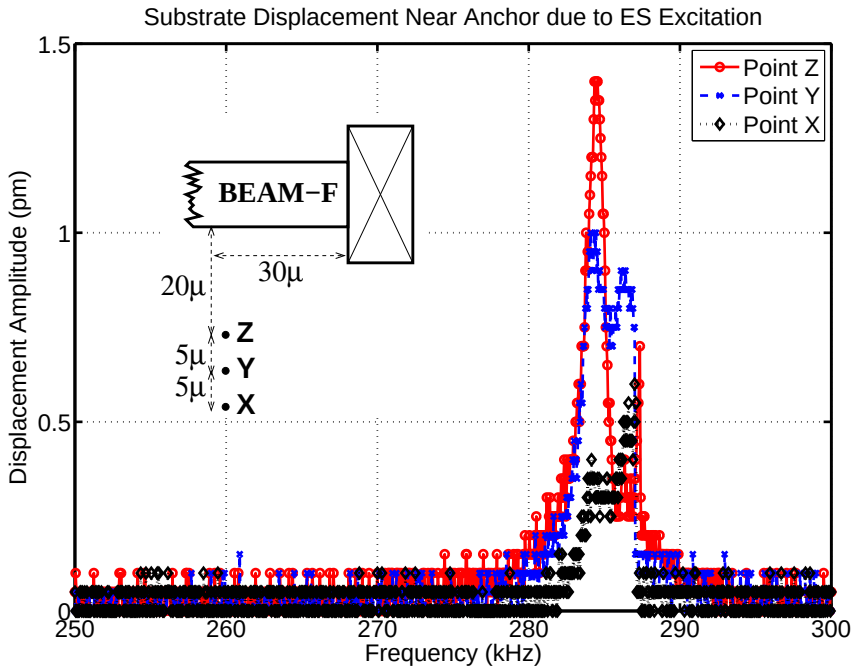

Figure C.3: Out of plane substrate vibration measured near anchor at three different positions. AC excitation amplitude was 50 $\mathrm{mV_{pp}}$ (50 Ω) and polarization voltage was $V_p = 20$ V. The inset shows the approximate positions of the points relative to the anchor.

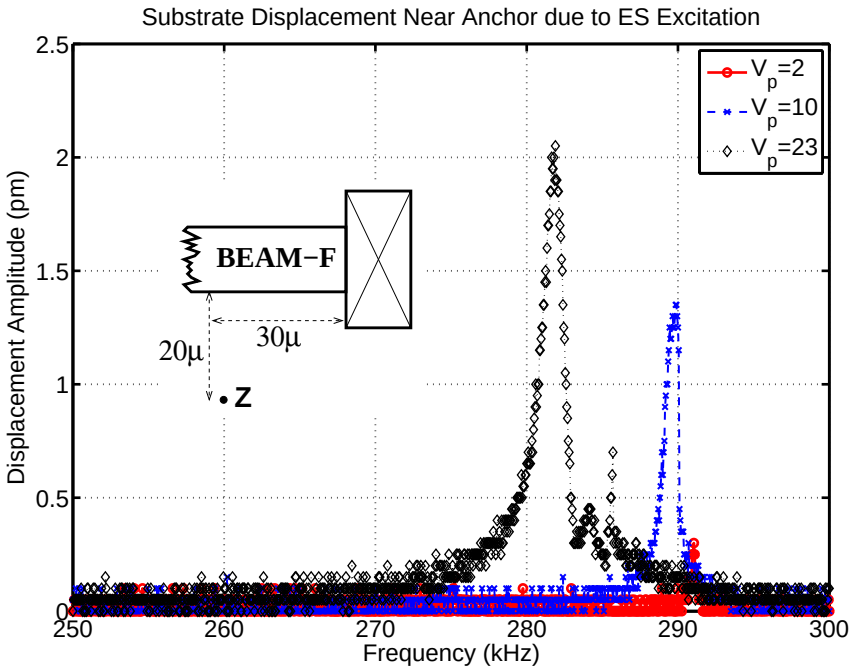

Figure C.4: Out of plane substrate vibration measured at a point with approximate position as indicated in the inset from the 200 μm long fixed-fixed Beam-F.

APPENDIX D

ELECTRICAL FEEDTHROUGH CONCERNS DURING BULK-PZT AND SURFACE-MICROMACHINED BEAM INTERACTIONS

The motional branch of the electrical equivalent circuit (Figure 2.9(b)) of the beam goes to a minimum at the series resonance. Specific to the devices and setup of Chapter 2 shown in Figure 2.2, the bottom of the silicon die is only partially in touch with the grounded top electrode of the PZT. Unless the bottom layer of the beam is a low impedance ground, the signal transmission to the bottom electrode of the PZT and hence to the TIA can yield a maximum near the resonance frequency via the fringing air capacitance. This electrical feedthrough is a concern during the calculation of coupling coefficients in Section 2.4.3, since it can interfere with the signal measured across the terminals of PZT due to elastic waves. This appendix describes the experiments and analysis performed to make sure that neglecting the contribution from the electrical feedthrough is a reasonable assumption.

Experimentally, we modified the wiring for Beam-C as illustrated in Figure D.1. This figure shows the switching of top and bottom electrodes of the beam. In this way, the effective crossection of the feedthrough for the parasitic substrate capacitances is reduced, hence also decreasing the feedthrough via series combinations of substrate parasitics and air capacitances. In the figure, all of the parasitic couplings are modelled by lumped elements with their descriptive subscripts, whereas beam is modelled by its R_x again with the assumption of high Q and operation close to the resonance of the beam.

The parameter extraction described in Section 2.4.3 is then repeated in this low feedthrough wiring configuration in order to see if the low amplitude backward gain signal still existed. Backward gain signal shown in Figure D.2 is still on the

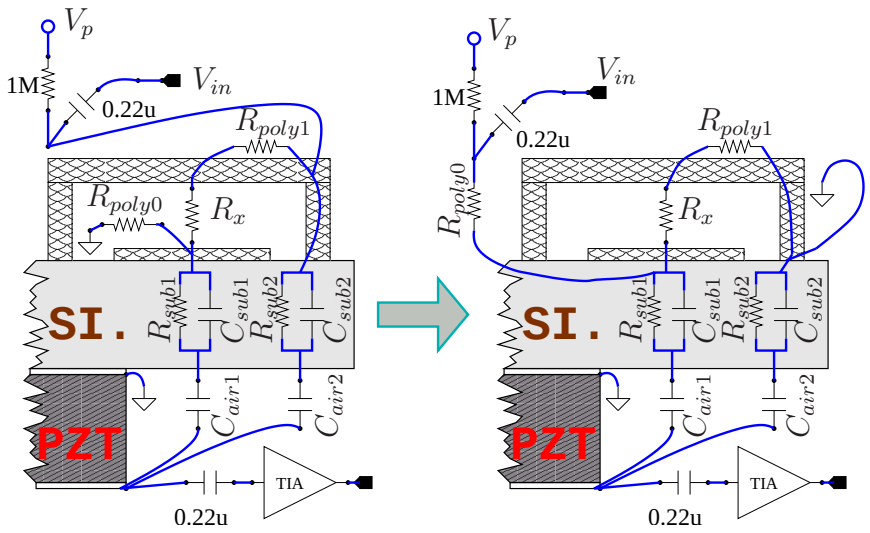

Figure D.1: Diagram showing the change in the wiring from the experiments on Beam-B (left) to the experiments on Beam-C (right).

same order of magnitude as that in Figure 2.7. This observation shows that the signal obtained is not just an electrical feedthrough. All of the extracted coupling coefficients of Beam-C are summarized in Figure 2.23 along with that of Beam-B for comparison.

Next, we describe another experiment performed on the same beam to qualitatively compare the amplitude of feedthrough to that of the backward-gain signal.

D.1 Measured signal versus electrical feedthrough

Given the very low levels of the measured reverse gain signals from Beam-B in Figure 2.7 and Figure D.2, a very important concern is the possibility that it being not the stress waves from the anchor of the resonating beam, but electrical feedthrough due to frequency dependent electrical impedance of the beam. To explain this issue, we will refer to Figure D.3, which shows the experimental set-up

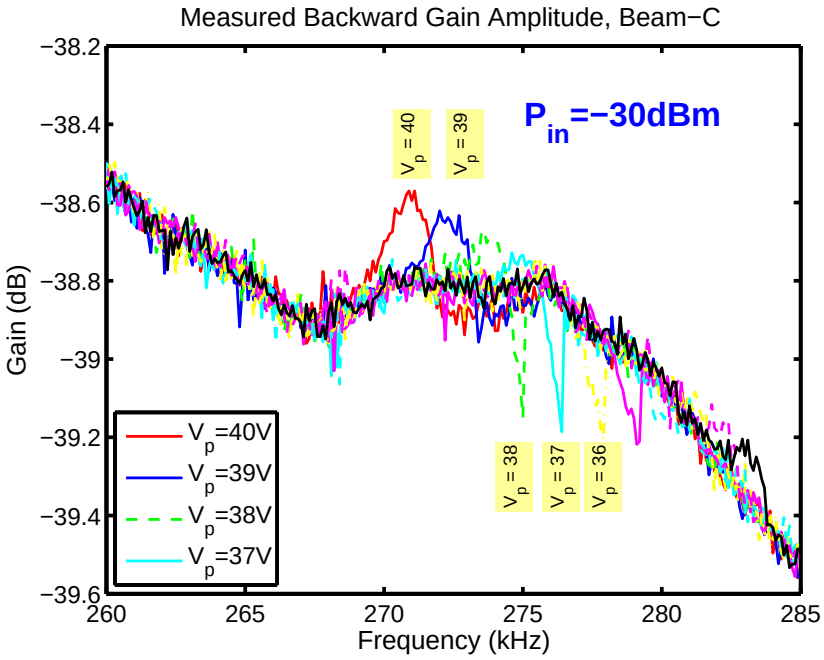

Figure D.2: Measured reverse gain from *FB-200*.

used for signal to interference comparison. It is a slightly modified version of the standard backward gain wiring setup of Figure 2.5(b) with DC bias tee removed, but parasitic electrical elements shown. R_{sub1}, R_{sub2}, C_{sub1}, C_{sub2}, and C_{air1}, C_{air2} are lumped resistors and capacitors between their indicated nodes. Since they are lumped elements between two points in space, the physical volumes and areas they model may not be disjoint. R_{poly0} (R_{poly1}) represents the resistance between the beam bottom (top) electrode and the respective wirebond pad on the die.

The feedthrough experiments were done on 150 μm long cantilever beams D and E, which are situated close to Beams A, B and C mentioned in Chapter 2. Therefore, it is reasonable to assume that the parasitics associated with all of these beams are similar. First step was to isolate the electrical feedthrough by making sure that the beam did not vibrate at the fundamental resonance mode due to electrical excitation. This was ensured by removing the DC polarization,

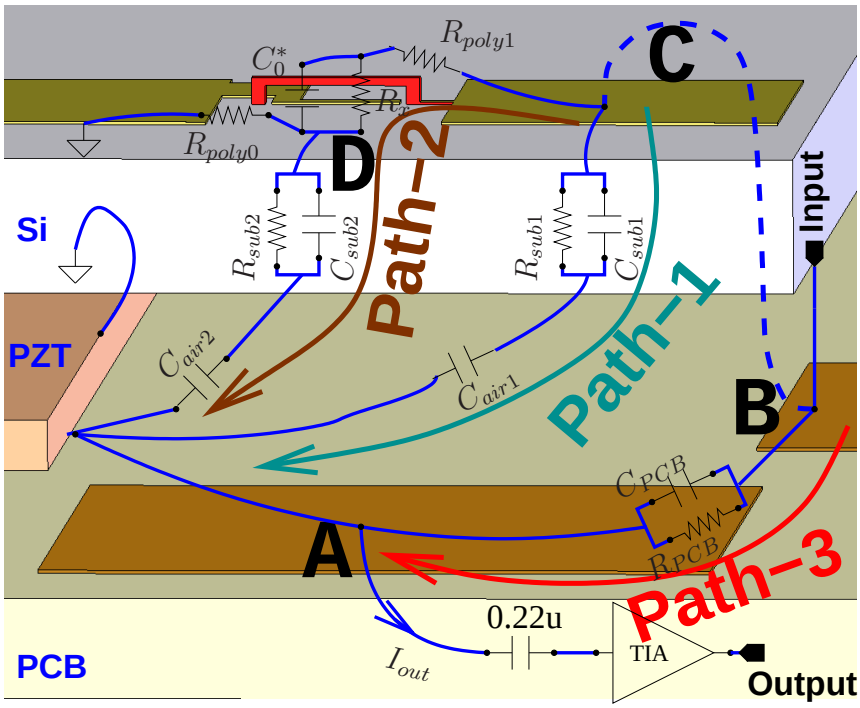

Figure D.3: Schematic of the electrical connections overlayed with parasitics modelled by lumped elements. The resonance conductance of electrostatic gap is modelled by the motional impedance R_x in parallel with C_0^*. The figure also shows the PCB connections and associated parasitics between input and output pads. Furthermore, the drawing illustrates the three possible paths through which electrical conductance occurs from the input to the output by contributing to the input current of the TIA.

essentially eliminating R_x and leaving it with only $C_0^* = C_0$ in Figure D.3.

One can write the conductance between the input pad, node-B, and the TIA input pad, node-A, as a sum of conductance along three paths. These paths are shown in Figure D.3, and they have admittance Y_{pi}, $i \in \{1, 2, 3\}$, given by Equation (D.1):

$$Y_{total}(\mathbf{s}) = \frac{I_{out}}{V_{in}} = Y_{p1}(\mathbf{s}) + Y_{p2}(\mathbf{s}) + Y_{p3}(\mathbf{s}) \tag{D.1a}$$

$$Y_{p1}(\mathbf{s}) = \left[\left(R_{sub1} \parallel \frac{1}{\mathbf{s}C_{sub1}} \right) + \frac{1}{\mathbf{s}C_{air1}} \right]^{-1} \tag{D.1b}$$

$$Y_{p2}(\mathbf{s}) = \frac{R_{poly0}}{(R_{poly1} + R_x + R_{poly0} \lVert Z_{b2})\,(Z_{b2} + R_{poly0})} \tag{D.1c}$$

$$Y_{p3}(\mathbf{s}) = \left(R_{PCB} \lVert \frac{1}{\mathbf{s}C_{PCB}}\right)^{-1}, \tag{D.1d}$$

where $a \lVert b = (ab)(a+b)^{-1}$ and

$$Z_{b2} = \left(R_{sub2} \lVert \frac{1}{\mathbf{s}C_{sub2}}\right) + \frac{1}{\mathbf{s}C_{air2}}.$$

The values of C_{sub1} and R_{sub1} were estimated by making two measurements using an HP4194 impedance analyzer; first with the wirebond connection shown dashed in Figure D.3, and then without the wirebond. The first type of measurement yields Y_{total}, whereas the second one yields Y_{p3}. Note that Y_{p3} of path-3 involves a resistor R_{PCB} and a capacitor C_{PCB} in parallel, both of which originate from the parasitics between the node-A and node-B of the circuit board. The impedance measurements were done in the range 200–205 kHZ, close to the resonance frequency of Beam-B[1]. The measurements yielded mostly capacitive admittance with phase angles larger than 87°. Therefore, the parasitic resistances can be ignored in the frequency of interest.

The difference in admittance between these two measurements is named as

$$Y_{diff} = Y_{total} - Y_{p3} = Y_{p1} + Y_{p2}.$$

Since the pad area is much larger than the bottom electrode area for any given beam we tested, an upper limit for the feedthrough via path-1 can be obtained by assuming $C_{sub2} = C_{sub1}$, $R_{sub2} = R_{sub1}$, and $C_{sub2} = C_{sub1}$. We do have other useful information regarding the component values along path-2. An upper limit of 500 Ω for R_{poly0} and R_{poly1} was extracted using PolyMUMPs$^{\text{TM}}$ process specifications and the layout of the design. Absence of a polarization voltage allows us to discard R_x.

[1]The reverse signal of Beam-B is later used for comparison of measured signal to electrical feedthrough.

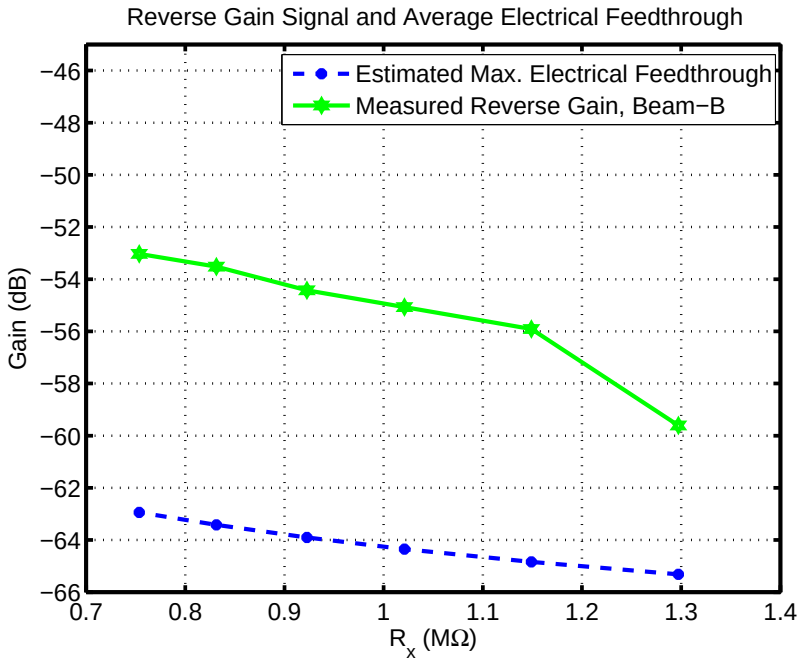

Figure D.4: Comparison of the reverse gain signal from Beam-B and the estimated maximum electrical feedthrough. More than 12 dB difference in amplitude indicates that the measured signal is indeed due to stress waves rather than being due to electrical feedthrough.

Furthermore, C_0^* is known to be less than 10 fF from Figure 2.21. If these findings are substituted in Equation (D.1), it follows that

$$|Y_{p2}(\mathrm{s})| \ll |Y_{p1}(\mathrm{s})|. \tag{D.2}$$

Consequently $Y_{diff} \approx Y_{p1}$. Average of two measurements at 202.5 kHz yielded an admittance value of

$$Y_{p1} \approx Y_{diff} = 0.18 + 6.51\mathrm{j} \;\; \mu\mho,$$

which is well represented by a capacitor of 5.12 pF.

With non-zero V_p, it was shown in Figure 2.21 that 0.5 MΩ $< R_x <$ 25 MΩ. Going by the above worst case scenario and using Equation (D.1b), an upper limit

for the amplitude of electrical feedthrough can be calculated as in Equation (D.3).

$$|A_{ft,max}| = \frac{R_{poly0}|Y_{p1}||Z_{TIA}|}{R_x \lVert 10^6\ \Omega}. \tag{D.3}$$

Here, the input current to the TIA is taken to be due to path-2 in parallel with 1 MΩ biasing resistor used in the experiments in Chapter 2.

Equation (D.3) is plotted in Figure D.4 with $|Z_{TIA}| \approx 100$ kΩ[2] for the relevant range of R_x. The same figure shows the amplitude of the reverse gain signal for Beam-B from Figure 2.7 for comparison. The signal measured is larger than the estimated value of maximum feedthrough, suggesting that the signal measured cannot be due merely to electrical feedthrough. This is further supported by their different slopes that is an indication of different underlying physics rather than simple electrical feedthrough.

[2]100 kΩ represents an upper worst case limit, as gain of the TIA can be significantly less during the backward gain experiments as described in Section 2.3.3.

APPENDIX E

AN ANALYTICAL EXAMPLE FOR THE CALCULATION OF ULTRASOUND INDUCED REPULSION OF AN OBJECT RESIDING ON A VIBRATING SUBSTRATE

Examination of the an AFM tip in contact with a vibrating tip gives valuable insight to understand the effect of ultrasound in U2EBA of Chapter 3. A simplified, lumped mechanical model for the interactions of an AFM tip and the surface it stands on are given in Figure E.1 [20,80]. The spring model in Figure E.1(a) depicts the AFM tip as an object suspended at the end of a cantilever beam of spring constant k_c. The displacement of the tip is named as z_c, and that of the substrate bottom is z_s. The surface interactions are modelled only by considering repulsive contact forces, i.e., when the substrate is in compression. As such, it is modelled by a nonlinear spring k_{nl}. The force-displacement characteristic of this spring, shown in Figure E.1(b), does not support tensile stress. In other words, force applied on the tip by the surface, F_{rep}, vanishes when $z_s < z_c$. This relation is expressed in Equation (E.1),

$$F_{rep} = k_s \mathrm{R}(z_s - z_c) = \begin{cases} k_s(z_s - z_c): & z_s - z_c > 0 \\ 0: & z_s - z_c \leq 0 \end{cases}, \tag{E.1}$$

where k_s is the contact stiffness of the surface in contact, and $\mathrm{R}(z)$ is the ramp function.

If the system is initially under a static compressive stress due to gravitational or external forces, then the operating point in Figure E.1(b) shifts from origin to the point O_p on the curve. At this point the compression in the substrate is z_{s0}-z_{c0}, where z_{s0} and z_{c0} are the static displacements of the substrate bottom and the tip

along z-direction, respectively. They are related to each other by:

$$z_{s0} = (K+1)z_{c0} \quad \text{and} \quad K = \frac{k_c}{k_s}, \tag{E.2}$$

where K represents the ratio of cantilever spring constant k_c to contact spring constant k_s.

Hertzian contact theory can be used to estimate contact stiffness when a surface is intended with a spherical object as pursued commonly in ultrasonic force microscopy analysis [193, 194]. Pharr *et al.* shows that a general relationship of the form [195]:

$$k_s = \frac{2}{\sqrt{\pi}}\sqrt{A_{contact}}\frac{E_s}{1-v_s^2}, \tag{E.3}$$

exists for the elastic contact problem with axisymmetric indenters. Here $A_{contact}$ is the contact area, v_s is the Poisson's ratio, and E_s is the Young's modulus. In particular, for spherical indenter case, Equation (E.3) agrees with Hertzian analysis. If one takes the surface to be silicon with $E_s = 170$ GPa, $v_s = 0.22$, and (s)he assumes a contact radius of $r_{contact} = 20$ nm then Equation (E.3) yields a value of 7.15 kN/m. Typical AFM cantilevers are much less stiff, resulting K in Equation (E.2) to lie somewhere between 10^{-4} and 10^{-3} [20].

Figure E.1(b) shows the superimposed ultrasonic vibration of amplitude a on top of the static operating point. One can see from the same figure that the system will be in linear region as long as the ultrasonic vibration amplitude is less than the compression of the substrate, namely $z_{s0} - z_{c0}$.

It is important to note that the resonance frequency of the cantilever in contact with a surface is higher than the free running resonance frequency of the cantilever, F_0. The effect of coupling becomes more pronounced for smaller values of K, and is explained very well in reference [196]. For the rest of the discussion, this modified

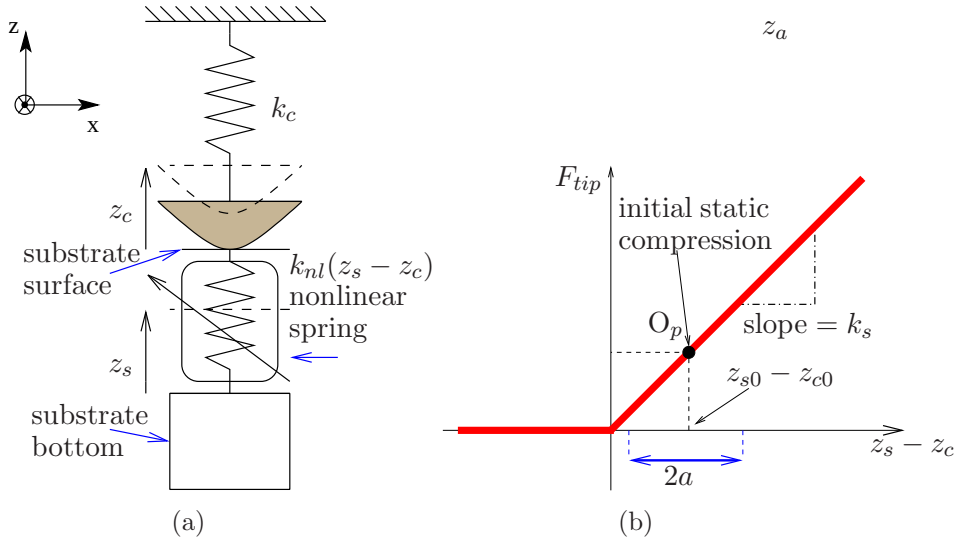

Figure E.1: (a) A simple mechanical model for the interaction of an AFM tip that is in contact with a surface. Surface interactions are modelled with a nonlinear spring that is described by the characteristic in (b). Adhesion forces are neglected, and the surface is only assumed to apply contact forces to the tip body. The static compression of $z_{s0} - z_{c0}$ and the ultrasonic peak-to peak vibration amplitude of $2a$ are shown in the figure.

resonance frequency of the tip is referred as *surface-coupled resonance frequency* of the tip and denoted by F_0^*.

Let us assume that the vibration frequency $f = \omega/(2\pi)$ of the substrate is much less than the surface coupled resonance frequency of the cantilever (i.e., $f \ll F_0^*$). Then, as long as the object stays in the first quadrant of the plot in Figure E.1(b), Equation (E.2) can be used to relate the tip displacement to substrate-bottom displacement. For a substrate-bottom vibration amplitude of a, the cantilever vibration amplitude is $a/(1+K)$. Since $K \ll 1$, the substrate bottom and the tip moves almost together in this low frequency, linear regime.

At vibration frequencies much higher than the surface coupled cantilever resonance (i.e., $f \gg F_0^*$), the tip fails to follow, and vibration amplitude of the

cantilever becomes much smaller than the initial base excitation from the substrate [20]. In this high frequency regime, as long as the vibration amplitude is small so that the operation never occurs in the zero-force region of Figure E.1(b), the tip only experiences negligible vibration at the excitation frequency. Time average of the position of the cantilever stays the same as the static case, namely at $z_c = z_{c0}$. This observation is in agreement with Section 3.4.1.2, that pointed to the fact that linear interactions alone between the objects and the underlying surfaces cannot result in a time-averaged net force on the object due to ultrasonic actuation.

On the other hand, if the vibration amplitude goes beyond the static substrate compression, $z_{s0} - z_{c0}$, then the surface and the cantilever tip starts to separate from each other for part of the ultrasonic vibration cycle due to nonlinear operation. This situation is illustrated in Figure E.2, which pictures the case of a sinusoidal vibration $g(t) = a \sin \omega t$ superimposed on the static operating point.

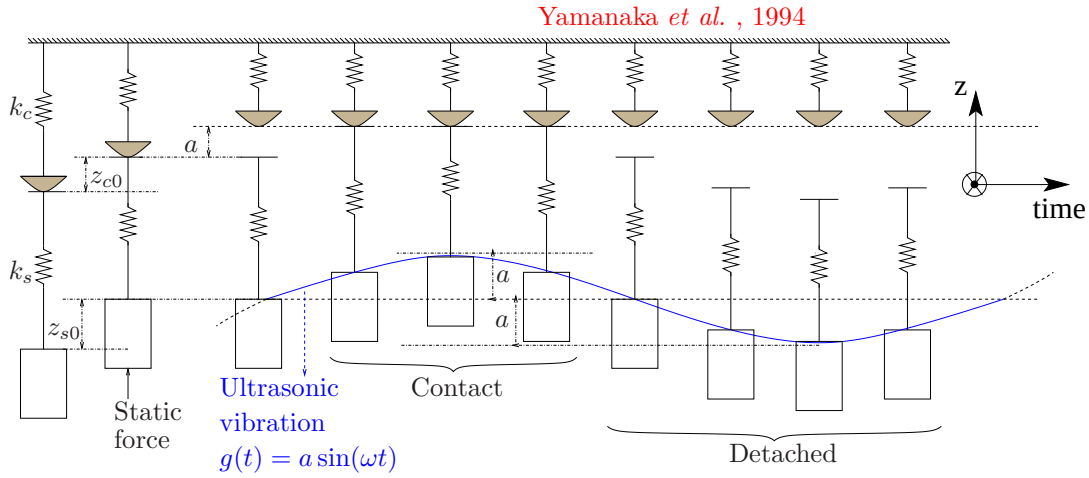

Figure E.2: Time evolution of a spring model of the tip-surface interactions as the substrate vibrates with an ultrasonic vibration amplitude of $g(t)$. An initial compression of $z_{s0} - z_{c0}$ is assumed, and the adhesion forces are neglected so that the substrate only supports compression but not tension.

Considering the force exerted on the object by the substrate during the time the substrate is in contact with the tip, the time averaged net force in the z direction is more than what is necessary to keep it at $z = z_{c0}$ against the linear spring force of the cantilever. This time-averaged force causes an extra static displacement of z_a in addition to z_c, as shown in Figure E.2 [20]. Therefore, cantilever and substrate-bottom displacements can be expressed as:

$$z_s = z_{s0} + g(t), \qquad \text{(E.4a)} \qquad\qquad z_c = z_{c0} + z_a + h(t), \qquad \text{(E.4b)}$$

where $g(t)$ is the ultrasonic vibration component of the substrate at the angular frequency of $\omega = 2\pi f$, and $h(t)$ is the corresponding vibration of the tip at the same frequency. As mentioned before, when $f \gg F_0^*$, the system is excited at a much higher frequency than the coupled resonance frequency, rendering $h(t)$ to be negligible.

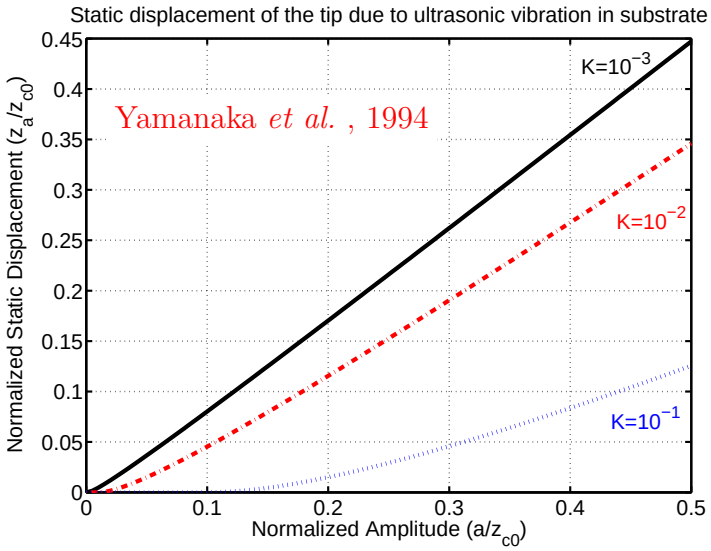

Figure E.3: Analytical calculation of the static displacement of an AFM tip on a substrate surface that vibrates at a much higher frequency than the coupled system resonant frequency [20]. The calculation assumes a triangular vibration amplitude a, and both of the axes are normalized to the initial static displacement z_{c0}.

The expression for z_a when $g(t)$ is a *triangular wave* of amplitude a and frequency $f \gg F_0^*$ is calculated by Yamanaka *et al.* . The solution for z_a for all values of a and K can be expressed in the form of Equation (E.5). This variable is plotted in Figure E.3 in normalized form for different values of K. As Equation (E.5) suggests, the linear to nonlinear transition creates a threshold value in amplitude, below which the static tip displacement is zero. This threshold is easily distinguishable in the plots for $K = 0.1$.

$$z_a = \begin{cases} Kz_{c0} + a + 2aK - 2\sqrt{Ka(1+K)(a+z_{c0})} & : \quad a \geq Kz_{c0} - z_a \\ 0 & : \quad a < Kz_{c0} \end{cases} \tag{E.5}$$

If one attempts to model the case of batch assembly of hinges described in Section 3.4.1.2 using the model above, (s)he has $z_{c0} = k_c = K = 0$. Then Equation (E.5) results in a static displacement same as the vibration amplitude, i.e., $z_a = a$. On the other hand, much more realistic approximations can be possible by including the adhesion forces instead of using the simple force-displacement characteristic in Figure E.1(b).

APPENDIX F

APPROXIMATE ELECTROMECHANICAL ANALYSIS OF A TORSIONAL, ELECTROSTATIC ACTUATOR FORMED BY TWO RIGID, PLANAR ELECTRODES

When a surface micromachined, hinged plate is subjected to an electric field that stems from a voltage difference between a top electrode and the substrate surface, it experiences an electrostatic moment pulling it away from the substrate surface. The geometry of the problem and its electromechanical model are illustrated in Figure 3.13. The situation here is basically the same as the one for on-chip torsional electrostatic actuators [90, 197]. However, many on-chip torsional actuator cases have gaps on the order μm. So cited works had no reason to investigate the response of the model for gaps around mm and for large rotation angles, which are typical for the assembly method described in Chapter 3. It is the scope of this section to investigate the uncommon territory of large gap to paddle length ratios and decide whether the models are still applicable.

In Figure 3.13, neglecting the electrostatic attraction on the moment arm region and assuming infinite rigidity for the structural layers, the capacitance of the paddle region C_p can be expressed as an integral sum of differential parallel plate capacitors:

$$C_p = \frac{\epsilon_0 b_p}{g_0} \int_{L_0\cos(\phi)}^{L_1\cos(\phi)} \frac{\mathrm{d}x}{(1 - x\tan(\phi)(g_0)^{-1})} = -\frac{b_p \epsilon_0}{\tan(\phi)} \log\left(f_\Upsilon(\phi)\right), \tag{F.1}$$

where ϵ_0 is the permittivity of air, and

$$f_\Upsilon(\phi) = \frac{g_0 - L_1\sin(\phi)}{g_0 - L_0\sin(\phi)}. \tag{F.2}$$

The canonical conjugate of ϕ, namely the moment M_ϕ in Figure 3.13 can be calculated from the stored electrostatic energy as

$$M_\phi = \frac{1}{2} V_a^2 \frac{\partial C_p}{\partial \phi}.$$

Next, the capacitance and the moment are normalized in the following manner:

$$\bar{C}_p = \frac{C_p}{\epsilon_0 b_p} = -\frac{\log(f_\Upsilon)}{\tan(\phi)} \tag{F.3a}$$

$$\bar{M}_\phi = \frac{M_\phi}{\frac{1}{2}\epsilon_0 b_p V_a^2} = \frac{\partial \bar{C}_p}{\partial \phi}, \tag{F.3b}$$

where the bar symbol on the variable name refers to the normalized version. The value of $\bar{M}_\phi$ at $\phi = 0$ can either be calculated as a limiting operation or directly from the product of force and moment arm to be:

$$\bar{M}_\phi(\phi = 0) = \frac{L_p \left(L_0 + 0.5 L_p\right)}{g_0^2}. \tag{F.4}$$

Normalized capacitance and moment are plotted in Figure F.1 for substrate to gap spacings of 0.55, 1, and 1.55 mm. The decreasing trend in capacitance shown in Figure F.1(a) after a certain value of ϕ, and the corresponding negative moment in Figure F.1(b) would indicate electric field acting as a repelling force source. This is not realistic for two conducting surfaces that are at different potentials and do not have any charge trapping. Therefore the plots in Figure F.1 reveal the unacceptable performance of the theoretical model at large rotation angles. As such, approximating the electric field between the paddle and the top electrode as a sum of differential parallel plate capacitors is a bad assumption for large rotation angles. What is more, the assumption gets even worse at increasing gaps as the transition value of ϕ, for which capacitance starts decreasing and the moment becomes negative, gets closer to zero. In summary, theoretical model that is used for surface micromachined torsional actuators with μm level gaps is far from being applicable to the situation encountered in U2EBA in Chapter 3.

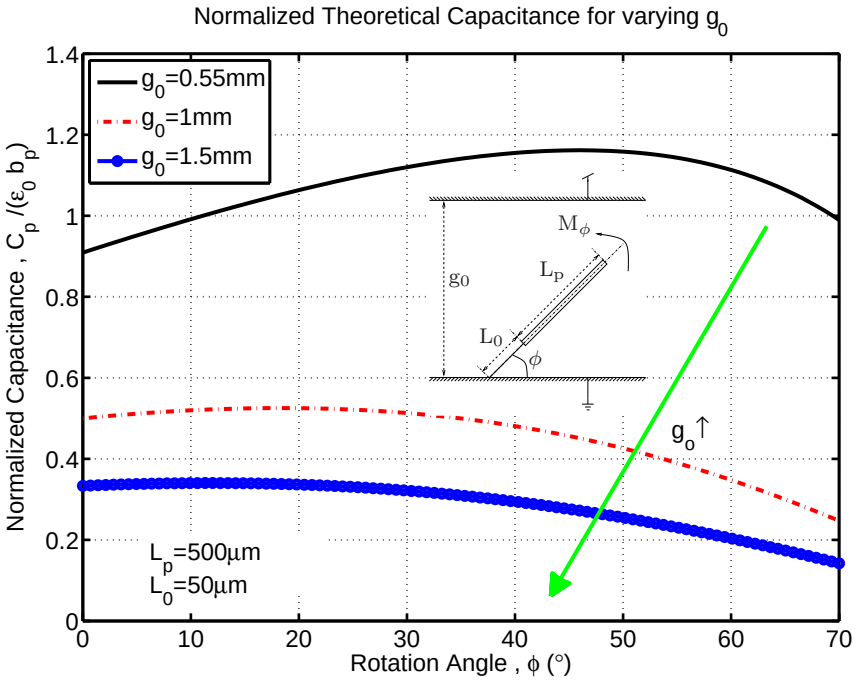

(a)

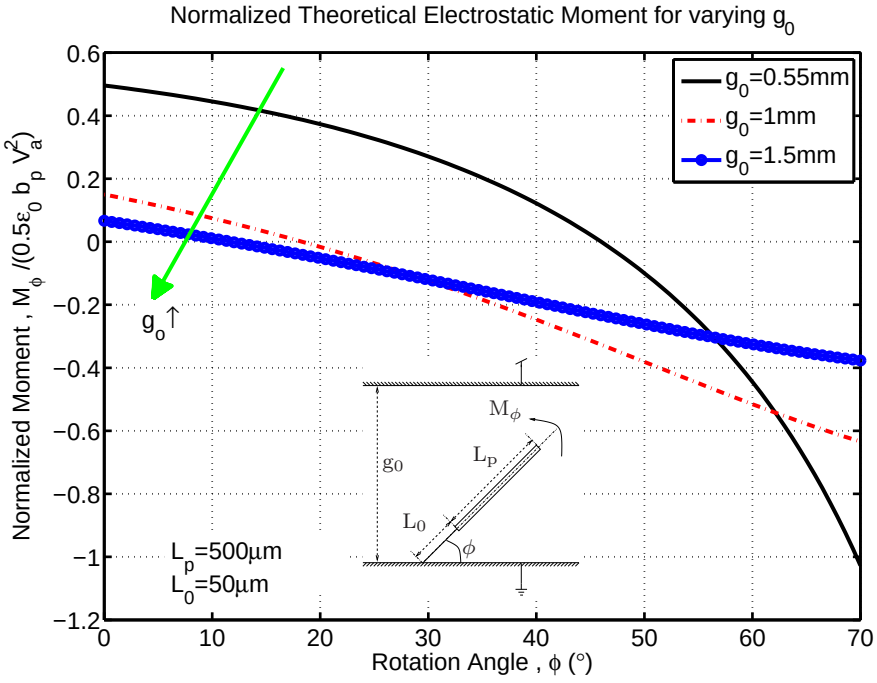

(b)

Figure F.1: Theoretical predictions of the (a) normalized capacitance and (b) normalized electrostatic moment on a plate that is rotated to an angle of ϕ from horizontal.

It is necessary to solve the 3-D Laplace equation iteratively with morphing boundary conditions of the compliant paddle in order to calculate the static electrostatic moment. This can be done by FEM approaches that are pursued in Chapter 3 to reveal electrostatic moment on infinitely stiff paddles at varying rotation angles.

The electrostatic pull-down voltage associated with Figure 3.13 can be calculated to illustrate that the special case of the above model for $L_0 = 0$ reduces to the often used small-signal model for torsional electrostatic actuators [90, 197]. This is done by equating the electrostatic moment to the torsional spring restoring moment in a way analogous to the parallel plate case [145, §6.4.3].

$$\begin{aligned} \frac{1}{2}\epsilon_0 b_p \left(V_a^2\right) \frac{\partial \bar{C}_p(\phi)}{\partial \phi} &= k_{rot}\phi \\ \frac{\partial^2 \bar{C}_p}{\partial \phi^2} - \frac{1}{\phi}\frac{\partial \bar{C}_p}{\partial \phi} &= 0 \end{aligned} \tag{F.5}$$

Substituting $L_0 = 0$ in Equation (F.2) and working Equation (F.5), one can show that the expressions for voltage pulldown reduce to those in references [90, 197]. Calling the value of ϕ and V_a at the voltage pull-down point as ϕ_{PDV} and $V_{a,PDV}$, respectively, then the numerical solution yields:

$$\phi_{PDV} \approx 0.441\frac{g_0}{L_p} \tag{F.6}$$

$$V_{a,PDV}^2 \approx 0.827\frac{k_{rot}{g_0}^3}{{L_p}^3\epsilon_0 b_p}. \tag{F.7}$$

APPENDIX G

FINITE ELEMENT MODELLING OF A RIGID PADDLE IN ELECTRIC FIELD FOR U2EBA IN ANSYS©

```
FINISH
/CLEAR

/TITLE, ELECTROSTATIC ASSEMBLY

/CWD,'E:\Users\public\ardanuc'
/FILNAME,file,0                          ! Not to change filename_each time

/COM, Sweep Phi and record Capacitance using CMATRIX
/COM, UNDER dc VOLTAGE WITH GAP "d_gap"
/COM,
/COM, DATE:11-28-06
/COM, FILE:ES_assembly_CAP_SweepPhi_Static
/COM, AUTHOR: Serhan ARDANUC

!/COM   SEE ANSYS NOTES page 4 dated 11/23/06,
!/COM   OR REGULAR NOTES 8.8.06 page 1, (Stuff you did when you were in XEROX) ,
!/COM   just before PI meeting
!/COM   DRAWING for phi=45 degrees
!/COM
!/COM                SIDE VIEW


!/COM          <----------------2* x_hle+l_0+L_pdl------------------>
!/COM        ____________________________________________________
!/COM       \\\\\\\\\\\\\\\\\\\\\\\\\\\\\\\\\\\\\\\\\\\\\\\\\\\\\\|  h_paddle    y5
!/COM         ____________________________________________________|          y4
!/COM                                V_a
!/COM         ^                 y
!/COM         |                 ^
!/COM         |               1 /   |
!/COM         |              / /    |
!/COM       d_gap           / /     ____>x
!/COM         |     l_0+L_pdl  / /
!/COM         |           / /-
!/COM         |          / /  \   phi
!/COM         v         L _    |
!/COM         ____________________|_|____|_____________________GND                  y3
!/COM         \\\\\\\\\\\\\\\\\\\\\\\\\\\\\\\\\\\\\\\\\\\\\\\\\\\\\\\\\\\\\\\\\ |           y2
!/COM        ____________________________________________________  |  h_paddle y1
!/COM
!/COM         <-x_hle----------> x=0               x=x_hle+l_0+L_paddle
!/COM
```

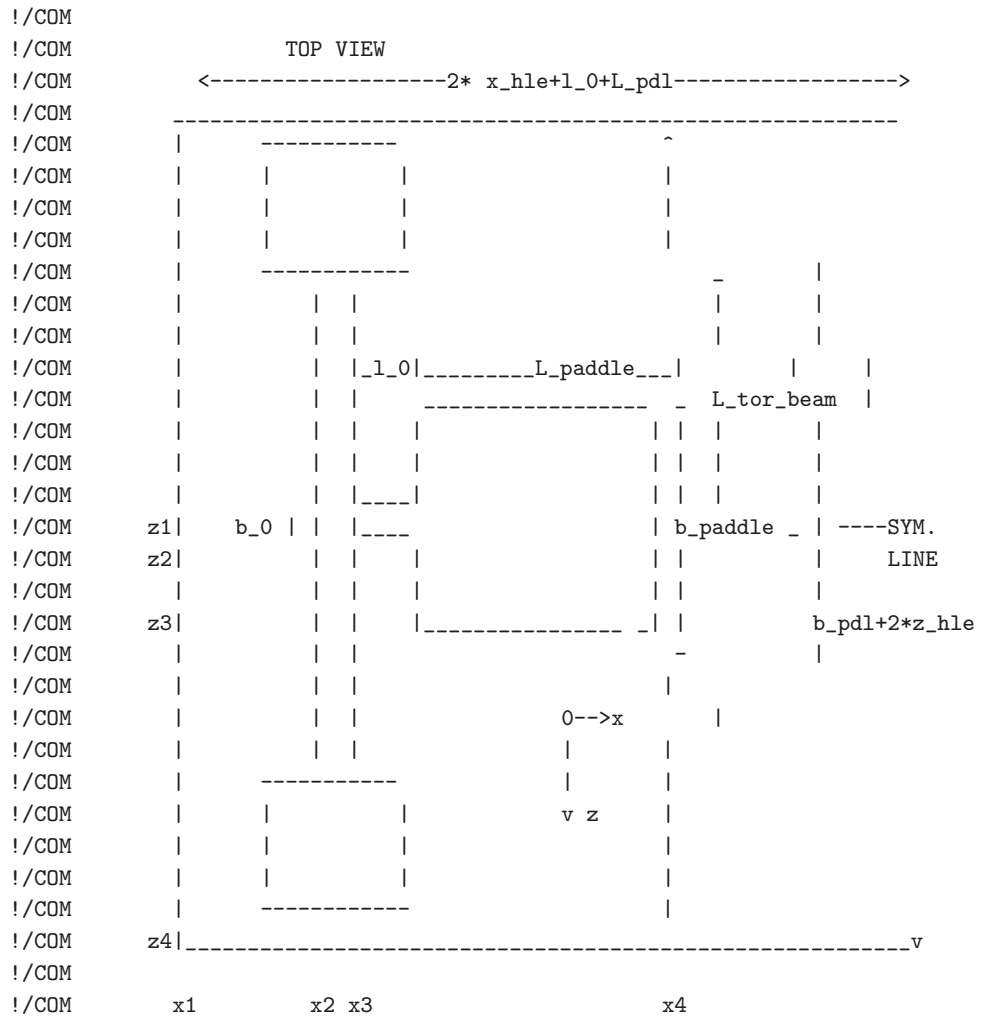

```
!/COM
!/COM                 TOP VIEW
!/COM          <-------------------2* x_hle+l_0+L_pdl------------------>
!/COM        ----------------------------------------------------------
!/COM        |      -----------                     ^
!/COM        |      |          |                    |
!/COM        |      |          |                    |
!/COM        |      |          |                    |
!/COM        |      ------------                        _       |
!/COM        |          |  |                            |       |
!/COM        |          |  |                            |       |
!/COM        |          |  |_l_0|_________L_paddle___|        |     |
!/COM        |          |  |     __________________  _  L_tor_beam  |
!/COM        |          |  |    |                  | |  |       |
!/COM        |          |  |    |                  | |  |       |
!/COM        |          |  |____|                  | |  |       |
!/COM      z1|    b_0 | |  |____                   | b_paddle _ | ----SYM.
!/COM      z2|          |  |    |                  | |          |     LINE
!/COM        |          |  |    |                  | |          |
!/COM      z3|          |  |    |________________ _| |          b_pdl+2*z_hle
!/COM        |          |  |                         -          |
!/COM        |          |  |                        |
!/COM        |          |  |                0-->x       |
!/COM        |          |  |                |       |
!/COM        |      -----------             |       |
!/COM        |      |          |            v z     |
!/COM        |      |          |                    |
!/COM        |      |          |                    |
!/COM        |      ------------                    |
!/COM      z4|__________________________________________________________v
!/COM
!/COM        x1         x2 x3                       x4


!/COM    UNITS in MKS

   !define constants  in mikroMKSv unit system
UM=1              !in micrometer
UM_M1= 1
PA=1e-6           !convert to MPA
PA_M1=1e6     !convert to 1/MPA
KGM_M3=1e-18      !convert to kg/(micrometer^3)
```

```
CN_M1 = 1e6       !convert to (pico Coulomb)/(micro Newton)
PI=ACOS(-1)       !Yes, it is what you think.

INV_MESH_DENSITY=5    ! Smart Size INV_MESH DENSITY
WICKED_NO=-99.99  ! A Wicked number

THIS_FILE_NAME='ES_MSHR2_F_M_SweepPhi_Static_SAVEIMAGE_d1500_071709.txt'

/COM Define Geometry
h_paddle           =25*UM               ! PLATE THICKNESS ALONG Y
l_paddle           =500*UM              ! PLATE Length ALONG x
b_paddle           =1000*UM             ! PLATE Length ALONG x
b_0                 =25*UM              ! BRIDGE WIDTH (ALONG Y)
l_0                 =25*UM              ! BRDGE LENGTH, MOMENT ARM (ALONG X)

d_gap              =1500*UM             ! AIR GAP
X_hle              =l_paddle            ! HALF of EXTRA LENGTH
                                        ! to the END of THE BOUNDARY (X-AXIS)
z_hle              =l_paddle            ! HALF of EXTRA LENGTH
                                        ! to the END of THE BOUNDARY (Z-AXIS)

eps=1e-3                                ! SELECTION RESOLUTION

!get the cur_wall_time
*get,cur_wall_time ,ACTIVE, , TIME, WALL        ! As a file label

cur_wall_time=NINT(mod((cur_wall_time*1e8),1e5))
rand_string=CHRVAL(cur_wall_time)

phi_D_start=0
phi_D_end=90
phi_D_step=1
n_steps=(phi_D_end-phi_D_start)/phi_D_step +1
endcondition=1

number_par=11                           ! number of parameters
                                        ! to be stored in the final

*DIM,par_array,ARRAY,n_steps,number_par,1
*DIM,par_array_FP,ARRAY,n_steps,number_par,1
*DIM,par_array_HP,ARRAY,n_steps,number_par,1
*DIM,par_array_MAXEFIELD,ARRAY,n_steps,6,1
index=0                                 ! To count the sweep index


*DO, phi_D_sweep, phi_D_start,phi_D_end,phi_D_step

*if ,index,NE,0,THEN
PARSAV, ALL, parfile       !clear everything before doing a new simulation
/CLEAR, NOSTART
PARRES, NEW,parfile
*endif
```

```
/PREP7
! WORKING in microMKS , so change the unit of permeability
EMUNIT, EPZRO,  8.854e-6
ANTYPE, STATIC
/TRIAD, OFF                         ! TURN OF THE ANNOYING VECTORS
index=index+1                       ! increment index

ET,1,SOLID123                       ! 3D ELectrostatic ELEMENT for
                                    ! electromagnetic force using SOLID123
SMRTSIZE,INV_MESH_DENSITY           ! USE smartsizing for meshing


phi_D=phi_D_sweep                    ! phi in Degrees
phi_R=phi_D*PI/180                   ! phi in Radians

/COM,%%%%%%%%%%%%%%%
/COM, PHI is %phi_D% Degrees
/COM,%%%%%%%%%%%%%%%

V_app=1                           ! Applied Voltage to top electrode

/TITLE, ELECTROSTATIC ASSEMBLY,phi=%phi_D% Deg.

! MATERIAL 1 is air
! MATERIAL 2 is silicon

!air
res_air=1e7                                ! Resistivity of air
per_air=1
EPS_air=per_air*8.854e-6

MP,PERX,1,per_air
MP,PERY,1,per_air
MP,PERZ,1,per_air
MP,RSVX,1,res_air                       ! MIcroMKS
MP,RSVY,1,res_air                       ! MIcroMKS
MP,RSVZ,1,res_air                       ! MIcroMKS


!silicon
per_si=11.8
res_si=20e-6
MP,PERX,2,per_si
MP,RSVX,2,res_si                     ! MIcroMKS
MP,RSVY,2,res_si                     ! MIcroMKS
MP,RSVZ,2,res_si                     ! MIcroMKS



! GEOMETRICAL BOUNDARIES AS SHOWN in the FIGURE and your notes
x1=-x_hle                         ! left end of outer boundary
```

```
x2=0                            ! start of paddle is taken as origin
x3=h_paddle                     ! right end of the ANCHOR
x4=x_hle+l_0+l_paddle                  ! RIGHT end of outer boundary

y1=-3*h_paddle                  ! bottom surface of the bottom plate
y2=-2*h_paddle                  ! top surface of the bottom plate
y3=0                            ! top surface of the paddle
y4=d_gap                        ! bottom surface of the top plate
y5=d_gap+h_paddle               ! top surface of the bottom plate

z1= 0                           ! SYMMETRY AXIS
z2= b_0/2                       ! HALF WIDTH of the BRIDGE
z3=b_paddle/2                   ! HALF WIDTH of the paddle
z4=b_paddle/2+z_hle             ! HALF WIDTH of the BOUNDARY (Z-AXIS)

local_x_momarm_start=0                     ! Local MOMENT ARM START, X value
local_x_momarm_end=l_0+(x3-x2)*cos(phi_R)  ! Local MOMENT ARM END, X value
local_x_pdl_start=local_x_momarm_end       ! Local PADDLE START, X value
local_x_pdl_end=local_x_momarm_end+l_paddle! Local PADDLE END, X value

local_y_paddle_start=-h_paddle        ! LOCAL PADDLE START, Y value
local_y_paddle_end=0                  ! LOCAL PADDLE END, Y value


! DEFINE A LOCAL COORDINATE SYSTEM ROTATED by (right hand along z Ax0s by phi_D)
LOCAL,11,0,0,0,0,phi_D             ! THIS BECOMES THE ACTIVE csYS
WPCSYS, 1, 11                      ! ALIGN WORKING PLANE with ACTIVE CSYS

VSEL,NONE
   ! PADDLE REGION
block, local_x_pdl_start,local_x_pdl_end,local_y_paddle_start,local_y_paddle_end,-z3,z3
CM,PADDLE_VOL,VOLU                  ! CREATE PADDLE_VOL COMPONENT

VSEL,NONE
  ! MOMENT ARM REGION
block, local_x_momarm_start,local_x_momarm_end,-h_paddle,0,-b_0/2,b_0/2
CM,MOM_ARM_VOL,VOLU                 ! CREATE MOM_ARM_VOL COMPONENT

CSYS,0                          ! CHANGE BACK to GLOBAL CSYS and WP
WPCSYS, 1, 0                                        !

VSEL,NONE                       !
block, x2,x3,y2,y3,-z2,z2       ! CREATE THE ANCHOR WHICH
                                ! JOINS IT TO THE BOTTOM PLATE
CM,ANCHOR_VOL,VOLU              ! CREATE ANCHOR_VOL COMPONENT

CMSEL,S,ANCHOR_VOL
cMSEL,A,MOM_ARM_VOL                 !
CMDELE,ANCHOR_VOL
cMDELE,MOM_ARM_VOL
VADD,ALL                       ! Now the moment arm  and
                               ! the anchor are all one volume
```

```
CM,ANCHOR_MOM_ARM_VOL,VOLU     ! Rename the merge component after
                               ! deleting the others
ASLV,S
ASEL,R,LOC,Z,z2        ! DO some trimming after the  Volume addition
AADD,ALL
ASLV,S                 ! DO some trimming after the  Volume addition
ASEL,R,LOC,Z,-z2
AADD,ALL
VSEL,ALL
CM, PADDLE_ARM_ANCHOR,VOLU  ! Name the rotated paddle  and its moment arm

VSEL,NONE
! CREATE THE  THE BOTTOM PLATE of THICKNESS h_paddle
block, x1,x4,y1,y2,-z4,z4
CM,BOT_ELE,VOLU

CMSEL,S,BOT_ELE
CMSEL,A,PADDLE_ARM_ANCHOR

CM,BOT_ELE_PADDLE,VOLU     ! This includes, Bottom Electrode, ANCHOR,
                           ! MOM_ARM,PADDLE


VSEL,NONE
! CREATE THE  THE TOP PLATE of THICKNESS h_paddle
block, x1,x4,y4,y5,-z4,z4

CM,TOP_ELE,VOLU
CMSEL,A,BOT_ELE_PADDLE
VATT,2,,1                          ! ASSIGN THEM to be SILICON




! CREATE THE UNIVERSAL SPACEAIR REGION

VSEL,NONE
block,x1,x4,y2,y4,-z4,z4      ! Bottom Plate to the bottom of the top plate
CM,UNIV_AIR,VOLU              ! Create Universal air


CMSEL,A,PADDLE_ARM_ANCHOR
!CMSEL,A,BOT_ELE_PADDLE     ! Unselect bot_electrode since universal air region
                           ! Does not include that
!CMSEL,U,BOT_ELE
BOPTN,KEEP,YES             ! I DO NOT want my inputs to be deleted


VOVLAP,ALL                 ! Create the real air region
BOPTN,DEFA                 ! Turn back to default
```

```
CMSEL,S,UNIV_AIR            ! Now I can delete the universsal air
CMDELE,UNIV_AIR
VDELE,ALL


! Still the paddle needs to be removed from inside  since a copy  of it
! is created at the Vovlap command.

VSEL,S,MAT,,2                       ! Select silicon
VSEL,INVE                           ! NOW I have air in my hands
VATT, 1, ,1                         ! A GOOD TIME to call it air
ASEL,S,LOC,Y,Y2                     ! I will drop the greater air volume
                                    ! with the help of y=y2 area
VSLA,U, 0
VDELE,ALL                           ! Finally Delete the  extra air region

NUMMRG,ALL
NUMCMP,VOLU                         ! GET RID of the unnecessary index

! SELECT AIR
VSEL,S,MAT,,1                       ! AIR
CM,AIR_VOL,VOLU                     ! CREATE the AIR REGION
NUMCMP,AREA

!!!!!!!!!!!!!!!!GEOMETRY DEFINITION IS COMPLETE!!!!!!!!!!!!!!!111

VSEL,S,MAT,,2

! DELETE ALL THE COMPONENTS since after addition they will no longer exist
CMDELE,PADDLE_VOL
CMDELE,MOM_ARM_VOL
CMDELE,ANCHOR_VOL
CMDELE,ANCHOR_MOM_ARM_VOL
CMDELE,PADDLE_ARM_ANCHOR
CMDELE,BOT_ELE
CMDELE,BOT_ELE_PADDLE
CMDELE,TOP_ELE

VADD,ALL
VATT,2,,1              ! MAKE SURE OUTPUT VOLUME is also silicon

ASEL,S,LOC,Y,y5
VSLA,S,0
CM,TOP_ELE,VOLU        ! CREATE TOP ELECTRODE AGAIN

ASEL,S,LOC,Y,y1
VSLA,S,0
CM,BOT_ELE_PADDLE,VOLU  ! ALL the bottom electrode anchor mom arm and paddle

VSEL,ALL
vmesh,ALL               ! mesh everything
ALLSEL,ALL
```

```
FINISH

/SOLU
ALLSEL,ALL
CMSEL,S,TOP_ELE         ! SELECT TOP ELECTRODE
NSLV,S,1
D,ALL,VOLT,V_app        ! APPLY V_app to TOP ELECTRODE

CMSEL,S,BOT_ELE_PADDLE  ! SELECT BOTTOM ELECTRODE
NSLV,S,1                !
D,ALL,VOLT,0            ! APPLY 0V to BOTTOM ELECTRODE

ALLSEL,ALL
SOLVE
FINISH

/POST1
! STORE ALL THE DESIRED PARAMETERS
par_array(index,1)=phi_D
par_array(index,2)=WICKED_NO
par_array(index,3)=d_gap
par_array(index,4)=l_paddle
par_array(index,5)=b_paddle
par_array(index,6)=h_paddle
par_array(index,7)=l_0
par_array(index,8)=b_0
par_array(index,9)=V_app
par_array(index,10)=x4-x1
par_array(index,11)=2*z4

/PNUM,MAT,1
RSYS,0               ! REPORT ALL THE RESULTS in CARTESIAN COORDINATE
                     ! SYSTEM
/TYPE,1,8
/CPLANE,1            ! CUTTING plane is the WORKING PLANE
/TYPE,1,5            !  Q SLICE DISPLAY


!  COMPArison tables have the following format
!
! /COM            TARGET       ANSYS          RATIO
! /COM    F_x
! /COM    F_y
! /COM    F_z
! /COM    F_sum
! /COM    M_x
! /COM    M_y
! /COM    M_z
! /COM    M_sum
!
```

```
! /COM    MAX_E_Field have the following format

!
! /COM            TARGET       ANSYS          RATIO
! /COM    E_x
! /COM    E_y
! /COM    E_z
! /COM    E_sum


! FORCE CALCULATION USING EMFT for the whole paddle
! SELECT THE NODES on the PADDLE
CMSEL,S,BOT_ELE_PADDLE
NSLV,s,1

!WPCSYS, -1, 11                              ! ALIGN WP with ROTATED LOCAL CS
CSYS,11                                ! GO to rotated coordinate frame
NSEL,R,LOC,Y,local_y_paddle_start,local_y_paddle_end
NSEL,R,LOC,X,local_x_pdl_start,local_x_pdl_end
NSEL,R,LOC,Z,-z3,z3
!WPCSYS, -1, 0                          ! ALIGN WP with GLOBAL CS
CSYS,0                                 ! GO back to global CS

EMFT,1                                 ! Summarize the electrostatic
                                       ! force and moment on the paddle
NSEL,ALL

! GET the MAximum E-Field
nsort,EF,SUM,,,                        ! Default is descending order
*get,MAX_E_NODE_INDEX,sort,0,IMAX

! NOW FILL UP the E_Field_Max array
par_array_MAXEFIELD(index,1)=phi_D
par_array_MAXEFIELD(index,2)=V_app

*get,par_array_MAXEFIELD(index,3),NODE,MAX_E_NODE_INDEX,EF,X
*get,par_array_MAXEFIELD(index,4),NODE,MAX_E_NODE_INDEX,EF,Y
*get,par_array_MAXEFIELD(index,5),NODE,MAX_E_NODE_INDEX,EF,Z
*get,par_array_MAXEFIELD(index,6),NODE,MAX_E_NODE_INDEX,EF,SUM

! FINALY FILL UP THE FORCES  for FULL PADDLE
par_array_FP(index,1)=phi_D
par_array_FP(index,2)=V_app
par_array_FP(index,3)=_fxsum
par_array_FP(index,4)=_fysum
par_array_FP(index,5)=_fzsum
par_array_FP(index,6)=_fssum
par_array_FP(index,7)=_txsum
par_array_FP(index,8)=_tysum
par_array_FP(index,9)=_tzsum
par_array_FP(index,10)=_tssum
```

```
! FORCE CALCULATION USING EMFT for the center part
! SELECT THE NODES on the PADDLE

! Local CNT_PADDLE START, X value
local_x_CNTpdl_start=(3*local_x_pdl_start+local_x_pdl_end)/4
! Local CNT_PADDLE END, X value
local_x_CNTpdl_end=(local_x_pdl_start+3*local_x_pdl_end)/4

CMSEL,S,BOT_ELE_PADDLE

NSLV,s,1

CSYS,11                   ! GO to rotated coordinate frame
!WPCSYS, -1, 11           ! ALIGN WP with ROTATED LOCAL CS
NSEL,R,LOC,Y,local_y_paddle_start,local_y_paddle_end
NSEL,R,LOC,X,local_x_CNTpdl_start,local_x_CNTpdl_end
NSEL,R,LOC,Z,-z3/2,z3/2

CSYS,0                    ! GO back to global CS
EMFT,1

! FINALY FILL UP THE FORCES  for HALF PADDLE
par_array_HP(index,1)=phi_D
par_array_HP(index,2)=V_app
par_array_HP(index,3)=_fxsum
par_array_HP(index,4)=_fysum
par_array_HP(index,5)=_fzsum
par_array_HP(index,6)=_fssum
par_array_HP(index,7)=_txsum
par_array_HP(index,8)=_tysum
par_array_HP(index,9)=_tzsum
par_array_HP(index,10)=_tssum

! BELOW IS ORNAMENTS
! GET RID OF ANSYS LOGO AND STUFF

/PLOPTS,INFO,3
/PLOPTS,LEG1,1
/PLOPTS,LEG2,1
/PLOPTS,LEG3,1
/PLOPTS,FRAME,1
/PLOPTS,TITLE,1
/PLOPTS,MINM,1
/PLOPTS,FILE,0
/PLOPTS,LOGO,0
/PLOPTS,WINS,1
/PLOPTS,WP,0
/PLOPTS,DATE,0
/TRIAD,OFF
/REPLOT

CMSEL,S,AIR_VOL
```

```
/REPLOT

ESLV,S          ! SELECT THE ELEMENTS IN AIR REGION
/POST1
PLESOL,EF,SUM,

! Scale the data to show regular contours
/CONT,1,8,0, ,par_array_MAXEFIELD(index,6)
/REPLOT

/ANG,1
/REP,FAST
/VIEW,1,1,2,3
/ANG,1
/REP,FAST
/AUTO,1
/REP,FAST
/AUTO,1
/REP,FAST

PNGR, DEFAULT   ! DEFAULT SETTINGS FOR PNG IMAGE SAVING

FINISH
IMAGE_SAVE_DIR='E:\Users\public\ardanuc\im_del'
/CWD, IMAGE_SAVE_DIR
/FILNAME,d_%d_gap%micron_phi_% phi_D_sweep%_,0
/ui,copy,save,png,graph,color,reverse,portrait,yes
/CWD,'E:\Users\public\ardanuc'
/FILNAME,file,0               ! Not to change filename_each time
FINISH
FINISH

*ENDDO                      ! DOne with the loop


/POST1

! SAVE FULL PADDLE
/COM
/OUT,Z:\ANSYS_simulations\ES_assembly_Cap_F_M_112306\..-->.
..<--..TEXT_OUT\full_paddle_ForceTorquevsPHI_%cur_wall_time%,txt
/COM,         By: Serhan ARDANUC
/COM, CREATED BY THE ANSYS FILE:
/COM, %THIS_FILE_NAME%
/COM,
/COM
*VWRITE,INV_MESH_DENSITY
('Smart Size Inverse Mesh Density',F18.2,'  ')
/COM
/COM
/COM
/COM,
```

```
/COM, %Header Line COunt=27 on 11/30/2006
/COM,
/COM,UNITS MIKROMKS, FULL_PADDLE, FORMAT
/COM,               TARGET       ANSYS          RATIO
/COM,    1)phi_D 2)V_app 3)F_x  4)F_y   5)F_z
/COM,
/COM,
/COM,    6)F_sum 7)M_x 8)M_y 9)M_z  10)M_sum
/COM,
/COM,
/COM,
/COM,
/COM,
/COM, %%%%%%%%%%%%%% FULL PADDLE %%%%%%%%%%%%%%%%%%%%%%%%%%%%
/COM,
/COM,
/COM,

*VWRITE,par_array_FP(1,1),par_array_FP(1,2),par_array_FP(1,3),par_array_FP(1,4),..-->.
..<--..par_array_FP(1,5),par_array_FP(1,6),par_array_FP(1,7),..-->.
..<--..par_array_FP(1,8),par_array_FP(1,9),par_array_FP(1,10)
(1X,E15.8,'  ',E15.8,'  ',E15.8,'  ',E15.8,'  ',E15.8,'  ',E15.8,' ..-->.
..<--.. ',E15.8,'  ',E15.8,'  ',E15.8,'  ',E15.8,'  ')

/NOPR
/OUT

! SAVE FULL PADDLE
/COM
/OUT,Z:\ANSYS_simulations\ES_assembly_Cap_F_M_112306\\..-->.
..<--..TEXT_OUT\center_paddle_ForceTorquevsPHI_%cur_wall_time%,txt
/COM,         By: Serhan ARDANUC
/COM, CREATED BY THE ANSYS FILE:
/COM, %THIS_FILE_NAME%
/COM,
/COM
*VWRITE,INV_MESH_DENSITY
('Smart Size Inverse Mesh Density',F18.2,'  ')
/COM
/COM
/COM
/COM,
/COM, Header Line COunt=27 on 12/30/2006
/COM,
/COM,UNITS MIKROMKS, Center_PADDLE, FORMAT
/COM,               TARGET       ANSYS          RATIO
/COM,    1)phi_D 2)V_app 3)F_x  4)F_y   5)F_z
/COM,
/COM,
/COM,    6)F_sum 7)M_x 8)M_y 9)M_z  10)M_sum
/COM,
/COM,
```

```
/COM,
/COM,
/COM,
/COM, %%%%%%%%%%%%%% CENTER PADDLE %%%%%%%%%%%%%%%%%%%%%%%%%%%%
/COM,
/COM,
/COM,

*VWRITE,par_array_HP(1,1),par_array_HP(1,2),par_array_HP(1,3),par_array_HP(1,4),..-->.
..<--..par_array_HP(1,5),par_array_HP(1,6),par_array_HP(1,7),..-->.
..<--..par_array_HP(1,8),par_array_HP(1,9),par_array_HP(1,10)
(1X,E15.8,'  ',E15.8,'  ',E15.8,'  ',E15.8,'  ',E15.8,'  ',E15.8,' ..-->.
..<--.. ',E15.8,'  ',E15.8,'  ',E15.8,'  ',E15.8,'  ')
/NOPR
/OUT


! SAVE ELEctrical Field VECTOR where the Electric Field Magnitude is Maximum

/COM
/OUT,Z:\ANSYS_simulations\ES_assembly_Cap_F_M_112306\..-->.
..<--..TEXT_OUT\E_FIELD_at_MAX_E_SUM_NODEvsPHI_%cur_wall_time%,txt
/COM,         By: Serhan ARDANUC
/COM, CREATED BY THE ANSYS FILE:
/COM, %THIS_FILE_NAME%
/COM,
/COM, 1)phi_D 2)V_app 3)E_x  4)E_y   5)E_z  6)E_sum
/COM,UNITS MIKROMKS, FULL_ FORMAT
/COM,
/COM,Header Line COunt=12 on 11/28/2006
/COM, %%%%%%%%ELECTRIC FIELD COMPONENTS at the NODE with LARGEST E_SUM VALUE%%%%%%
/COM,
/COM,
/COM,

*VWRITE,par_array_MAXEFIELD(1,1),par_array_MAXEFIELD(1,2),..-->.
..<--..par_array_MAXEFIELD(1,3),par_array_MAXEFIELD(1,4),..-->.
..<--..par_array_MAXEFIELD(1,5),par_array_MAXEFIELD(1,6)
(1X,E18.8,'  ',E18.8,'   ',E18.8,'     ',E18.8,'  ',E18.8,'   ',E18.8,'     ')
/NOPR
/OUT

! DUE to fringin EFFETS CENTER PADDLE matches much bettter than the FULL paddle


! SAVEPARAMETER FILE  !

/COM
/OUT,Z:\ANSYS_simulations\ES_assembly_Cap_F_M_112306\..-->.
..<--..TEXT_OUT\FMvsPHI_otherpars_%cur_wall_time%,txt
/COM,         By: Serhan ARDANUC
/COM, CREATED BY THE ANSYS FILE:
```

```
/COM, %THIS_FILE_NAME%
/COM,
/COM,UNITS MIKROMKS, FULL_PADDLE, FORMAT
/COM,   1)phi_D(Degrees)  2)CAP(pF)   3)d_gap(micron)
/COM,   4)l_paddle(micron) 5)b_paddle(micron)  6)h_paddle(micron)
/COM,  7)l_0(micron)  8) b_0(micron)  9) V_app(V)   10)Total_x_length((micron))
/COM   11)   Total_z_length(micron)
/COM
*VWRITE,INV_MESH_DENSITY
('Smart Size Inverse Mesh Density',F18.2,'  ')
/COM
/COM
/COM
/COM,
/COM, %%%%%%%%Parameters of the Cap vs Phi using CMATRIX macro (v_APP , dummy)%%
/COM, %Header Line COunt=19 on 11/28/2006
/COM,
/COM,

*VWRITE,par_array(1,1),par_array(1,2),par_array(1,3),par_array(1,4),..-->.
..<--..par_array(1,5),par_array(1,6),par_array(1,7),par_array(1,8),..-->.
..<--..par_array(1,9),par_array(1,10),par_array(1,11)
(1X,E15.8,'  ',E15.8,'  ',E15.8,'  ',E15.8,'  ',E15.8,'  ',E15.8,'..-->.
..<--..  ',E15.8,'  ',E15.8,'  ',E15.8,'  ',E15.8,'  ',E15.8,'  ')
/NOPR
/OUT

/COM, By Serhan ARDANUC
FINISH
```

APPENDIX H

CHARACTERIZATION OF THE POWER AMPLIFIER USED IN U2EBA EXPERIMENTS

Although the function generator used in U2EBA experiments can produce sinusoidal waveforms up to 10 MHz, its output amplitude is limited to 10 V_{pp} at 50 Ω load. Many experiments presented in Section 3.5 require drive amplitudes as large as 40 V_{pp} across the terminals of the PZT. The power amplifier used for high-voltage drive experiments was EPA-102 from Piezo Systems Inc. Its specified voltage gain is 20 in the frequency range from DC to 300 kHz.

The frequency response performance of the power amplifier was tested and compared to that of the function generator using a digital oscilloscope as a broadband amplitude measurement tool. The results are plotted in Figure H.1. Function generator has a 3-dB bandwidth in excess of 4 MHz when loaded with PZT. However, low impedance of PZT at a resonance around 200 kHz causes a dip in the gain amplitude characteristics. On the other hand, if a power amplifier is used at the output of the function generator, this dip disappears and lends itself to a flat low frequency response. As expected, the power amplifier output is not affected much from the loading of the PZT, unlike the case when output is taken directly from the function generator. However, using a power amplifier reduces the 3-dB bandwidth to 0.8 MHz.

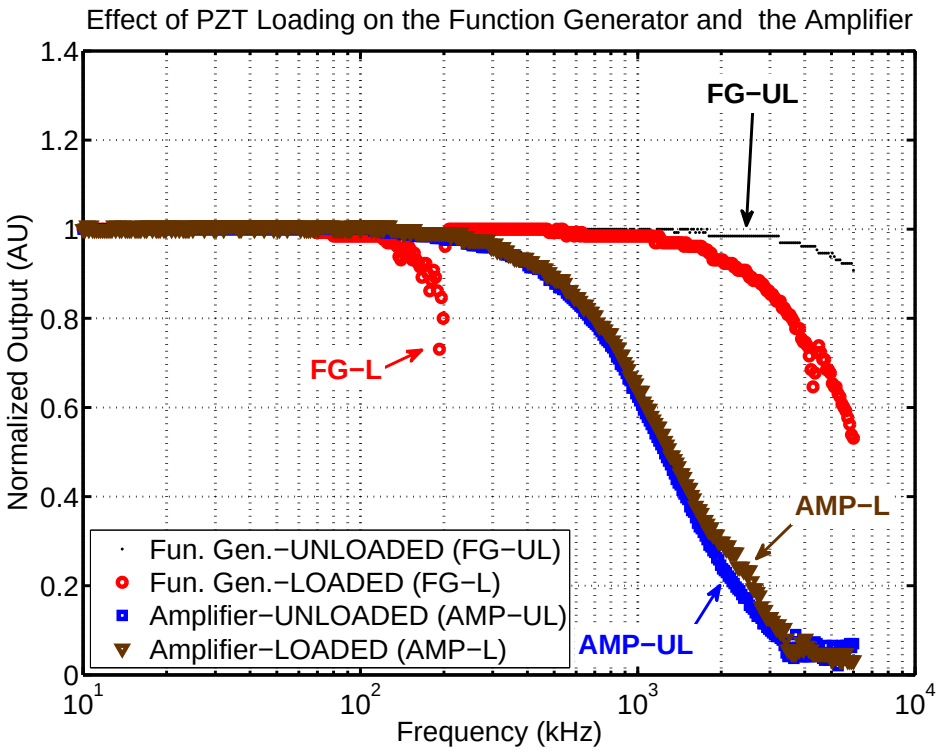

Figure H.1: Normalized gain amplitude for the function generator and the power amplifier. Two plots are indicated for each case one with PZT ceramic of the U2EBA assembly setup, and one without any load.

APPENDIX I

ASSEMBLY FIXTURE CHARACTERIZATION

I.1 Surface velocity measurements and comparison of the assembly fixture with PZT-on-top to the fixture with chuck-on-top

In order to measure the effectiveness of the actuation when PZT is above or below the vacuum chuck, the apparatuses shown in Figure I.1 were built, and their vibration characteristics due to PZT excitation were characterized.

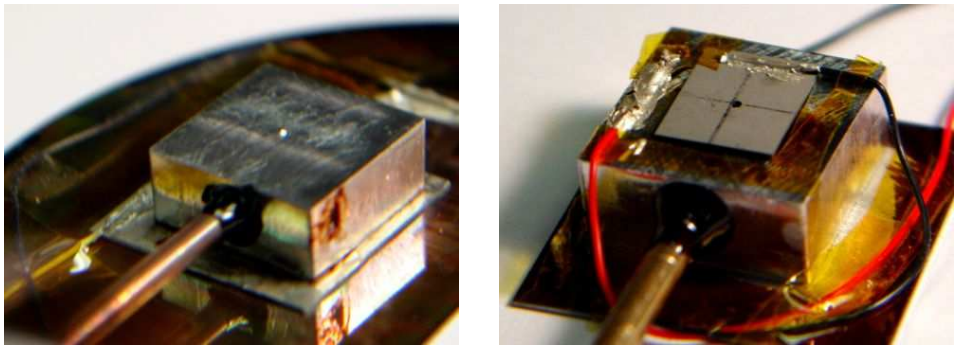

(a) (b)

Figure I.1: Two different experimental fixtures for comparison: (a) Chuck-on-top (COT) (b) PZT-on-top (POT)

The out-of-plane vibration velocity on the top surface of the fixtures, where the assembly die would be placed, was performed with an interferometric setup as described in Appendix B. The results, plotted in Figure I.2, indicate that the fixture with PZT-on-top (POT) has higher displacements for higher frequencies than the fixture with chuck-on-top (COT). This can qualitatively be reasoned as follows: the chuck is a massive and stiff load which quenches a rich variety of

piezoelectric plate modes that would happen strongly if there was no chuck on top. Moreover, the peak amplitude of vibration obtained from POT fixture (at a frequency slightly below 100 kHz) is larger than that of COT fixture.

At low frequencies, however, the COT fixture shows slightly better performance in a limited bandwidth. Given that U2EBA needs a high bandwidth of actuation to sweep across varying resonances of microstructures stuck to the substrate, high bandwidth of POT fixture is still much more favorable. This statement was also justified by experiments. Successful assemblies were achieved with the COT fixture, but its performance did not match that of the POT fixture. For this reason, the POT fixture was used in most of the experiments reported in Chapter 3.

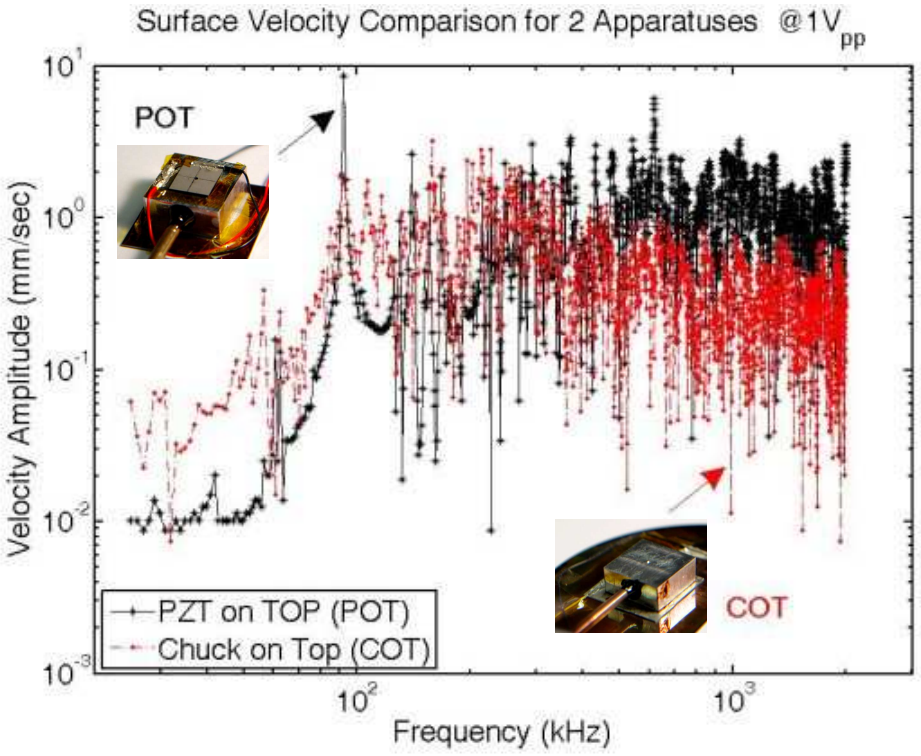

Figure I.2: Measurement of the out-of-plane, surface velocity as a function of frequency from two possible stacking schemes for the apparatuses: PZT-on-top (POT) and chuck-on-top (COT).

I.2 Impedance of the PZT actuator at different temperatures

The impedance of the PZT-4 rectangular plate measured using HP4194A from 10 kHz to 6 MHz is plotted in Figure I.3. Three data sets are plotted. The solid (black) curve is taken from a bare-PZT before bonding to the fixture. The dashed (blue) and dot-marked (red) curves are measured after bonding at room temperature and 200°C, respectively. The high temperature of operation that is common to many U2EBA experiments does not cause a significant loss of actuation capability. On the other hand, bonding causes a clear decrease in the sharpness of the resonance peaks.

The thickness resonance mode of the actuator can be calculated from the manufacturer specified frequency constants that are given in Table N.4. It is calculated to be around 4 MHz and highlighted in Figure I.3.

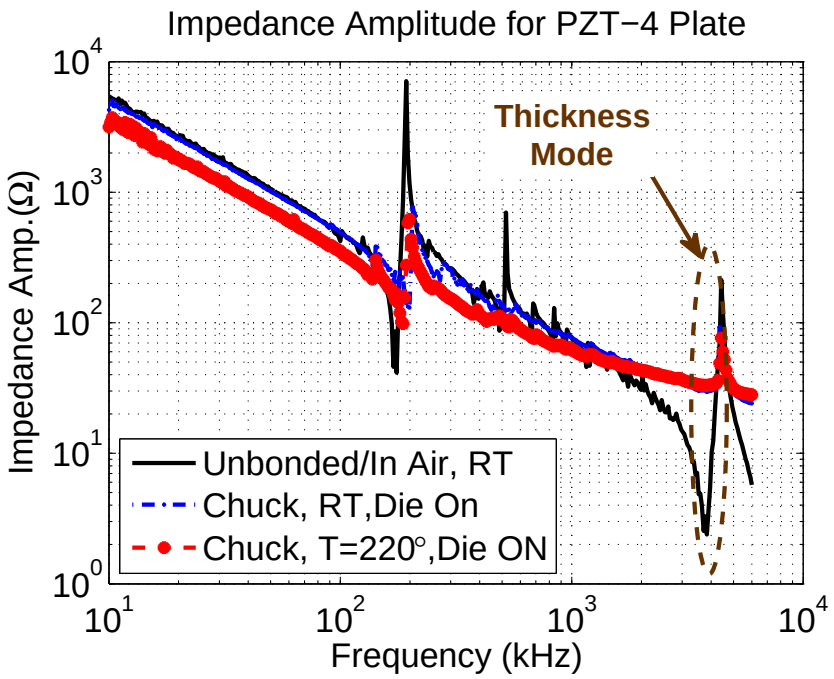

Figure I.3: Measured impedance amplitude of the 12.5 mm×10 mm×0.5 mm PZT-4 slab. "Die On" term in the legend indicates that a silicon die is placed on top during the measurement.

APPENDIX J

BACKGROUND FOR CONCENTRATED SOLAR POWER

Following two sections present theoretical and experimental arguments about efficiency of thermal and PV converters under concentrated sun light.

J.1 Efficiency of an ideal thermal solar generator

Figure J.1 is used to derive the efficiency of a thermal concentrated solar converter following Fletscher and Moen's work [21, 198]. Here, sun light incident on a collector with area A_c is concentrated on a central absorber with effective aperture area A_a. This process, whose efficiency is referred as η_1, forms the first energy transfer process in the system. The second process is due to an idealized Carnot heat engine, which generates an output power P_{out} by operating between the high-temperature absorber region and a low-temperature region. Temperatures of the absorber and the low-temperature regions are $T_H = T_a$ and T_L, respectively.

The incident solar irradiance on the collector is denoted by I (units: W/m^2). Using the the input power P_{in} to the absorber, and the blackbody radiation from the absorber $P_{a,BB}$, the efficiency of heat transfer to the absorber during the first process is

$$\eta_1 = \frac{P_{in} - P_{a,BB}}{P_{in}} = \frac{A_c I \eta_a \alpha_c - A_a e \sigma T_a^4}{A_c I}, \tag{J.1}$$

where η_a is an optical efficiency correction factor, α_c and e are the absorbtance and emissivity of the absorber, and σ is the Stefan-Boltzmann constant [21]. If one assumes idealized operation at the Carnot efficiency for the second process and also takes (idealized) values of 1 for η_a, α_c, and e, then the system efficiency can

be expressed as

$$\eta_{system} = \eta_1 \eta_2 = \left(\frac{A_c I - A_a \sigma T_a^4}{A_c I} \right) \left(\frac{T_H - T_L}{T_H} \right) = \left(1 - \frac{\sigma T_a^4}{C_{geom} I} \right) \left(1 - \frac{T_L}{T_a} \right), \tag{J.2}$$

where $C_{geom} = A_c / A_a$ is the geometrical concentration factor.

Figure J.2 plots Equation (J.2) as a function of T_a for different concentration factors, with $T_L = 300$ K and $I = 1$ kW/m^2. It can be seen that when the operation of the thermal solar-converter is assumed to be ideal, *the maximum possible efficiency increases with increasing optical concentration factors*. In practice, however, the melting temperatures of materials and alloys commonly used in these systems limit the absorber temperature. For example, iron melts at 1538°C.

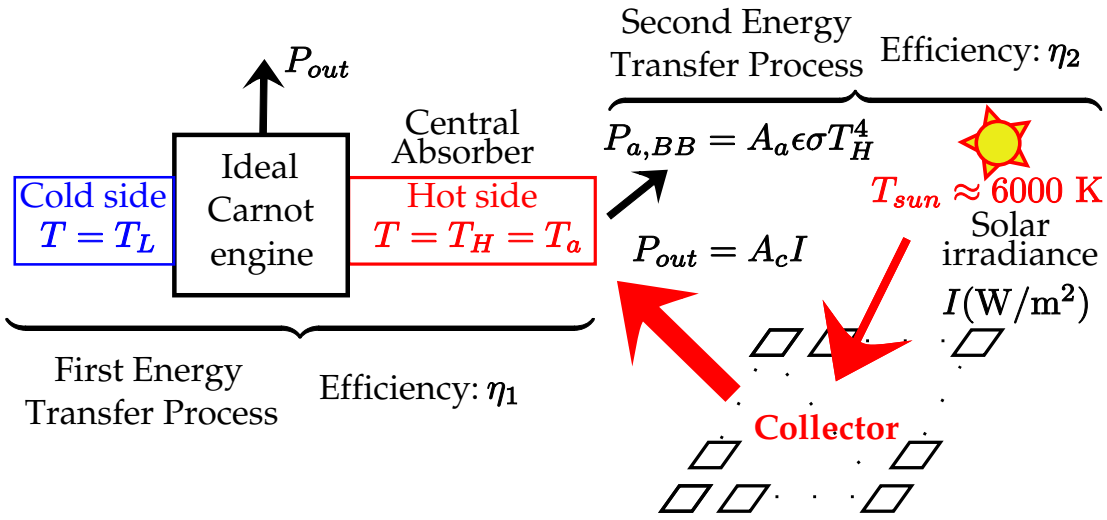

Figure J.1: Illustration of two energy transfer processes for the calculation of the efficiency of an idealized thermal solar converter.

J.2 Efficiency of concentrated photovoltaics (PV)

As for the effect of concentration on photovoltaic (PV) systems; best photovoltaic efficiencies are reported under concentrated sun-light [101, 199, 200]. Figure J.3 plots the evolution of research-level, efficiencies obtained from PV cells over the years [22, 23]. In line with the theoretical predictions of efficiency for thermal systems presented in the previous section, PV technology have been showing highest efficiencies at higher concentrations. In addition, the highest rate of increase in efficiency over the years (i.e., highest slope in Figure J.3) has also come from the concentrated cells.

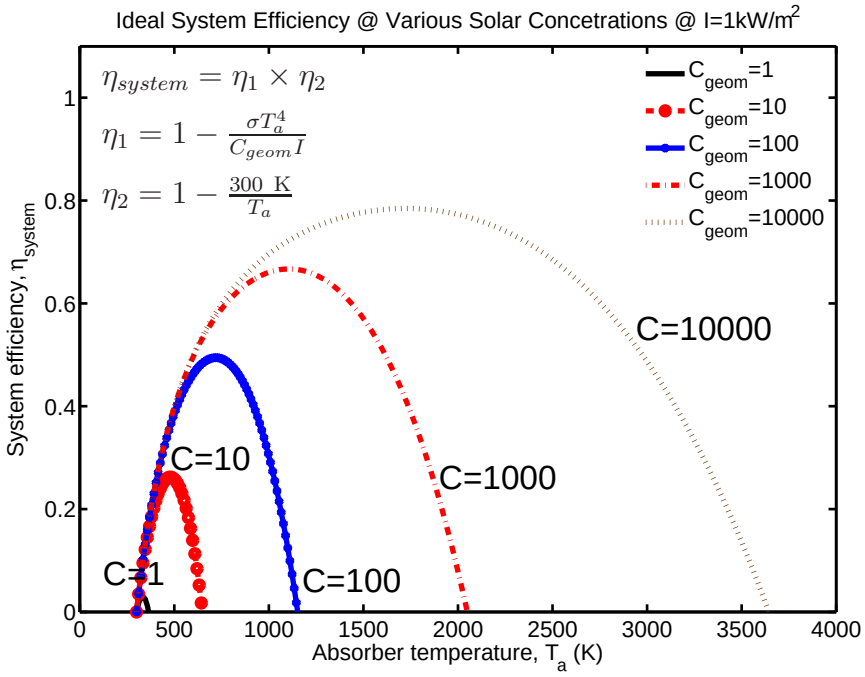

Figure J.2: Theoretical system level efficiency of a solar thermal converter as a function of temperature, at different concentration factors [21]. Maximum attainable efficiency increases at increased concentration factors, and it occurs at higher temperatures.

One of the main issues with concentrated PV is that an increase in temperature has a negative effect on the efficiency of the system. Concentrated cells might lead to higher efficiencies at a given temperature. However, overall system efficiency, which is the real yardstick, is based on how the excess heat from the PV cell is removed. For instance a dedicated refrigeration system would hamper efficiency as it would reduce the available generated- electricity output. Passive heat sinks are an option, but the question remains about how effective can they be at removing the heat from the PV. More aggressive approaches to increase efficiency can harness the temperature difference between the PV cell and the ambient as usable electrical energy, adding yet a second electrical output to the system. Heat engines or thermoelectric converters can be feasible for this route of excess heat removal. See the patent for instance by Bell R. L., titled "Solar energy converter with waste heat engine" [201]. Theoretical investigations of other high efficiency conversion methods such as *thermophotovoltaic* and *thermophotonic* converters are described in [117, §4.5].

Carnot efficiency associated with the temperature of the sun $T_{sun} \approx 6000$ K and the room temperature $T_{room} = 300$ K can give an idea for the maximum theoretical efficiency of any solar converter system operating on earth. This efficiency is $\eta_{Carnot,sr} = 1 - 300/6000 = 95\%$. More detailed calculations indicate a theoretical limit for maximum efficiency to be 93.3% [117, §4.6], [200]. The historical trends in Figure J.3, in conjunction with the fact that state of the art PV efficiencies being much less than the theoretical maximum limit, might be signs of improving efficiencies for a few more decades.

Both Figure J.2 and Figure J.3 make a case for the use of concentrating solar generators. They indicate that *concentrated solar systems*, be it thermal, photo-

voltaic or be it a hybrid combination of thermal and photovoltaic technologies, will play a central role in increasing the efficiency of the solar energy systems of the future.

J.3 Thermodynamic limit of solar concentration

The solar constant, which is the power density of light outside the atmosphere for the zero air mass spectrum (AM0), is $I_0 = 1373$ W/m^2 [118, Equation 2.1.1]. Part of this irradiance is absorbed by the atmosphere as a function of the air-mass through which the light travels to the surface of the earth. Under standard test conditions, direct normal irradiance (DNI) and global normal irradiance (GNI) are taken as 850 W/m^2 and 1000 W/m^2, respectively [119]. DNI involves only beam irradiance coming directly from the solar disc without significant scattering, whereas GNI involves diffuse irradiance scattered via the atmosphere.

Concentrated solar power systems allows us to magnify the beam irradiance. There is, however, a thermodynamical limit on how much the solar energy can be concentrated [118, §5.3.2]. This claim can qualitatively be understood by realizing that maximum concentrated solar irradiance on earth's surface can not be more than that predicted by Stefan-Boltzman law for an object at sun's temperature. Otherwise, it would be a violation of energy conversation. The maximum limit can therefore, be calculated from the the ratio of solar radiation at sun to that on earth. As such, the maximum concentration factor is simply the square of the ratio of the earth-sun distance ($\approx 1.495 \times 10^{11}$ m) to solar-disc radius ($\approx 6.95 \times 10^8$ m), yielding a value close to $46,000$. This would translate into concentrated power density in excess of $>$ MW/m^2 even after losses of more than 10X due to nonidealities.

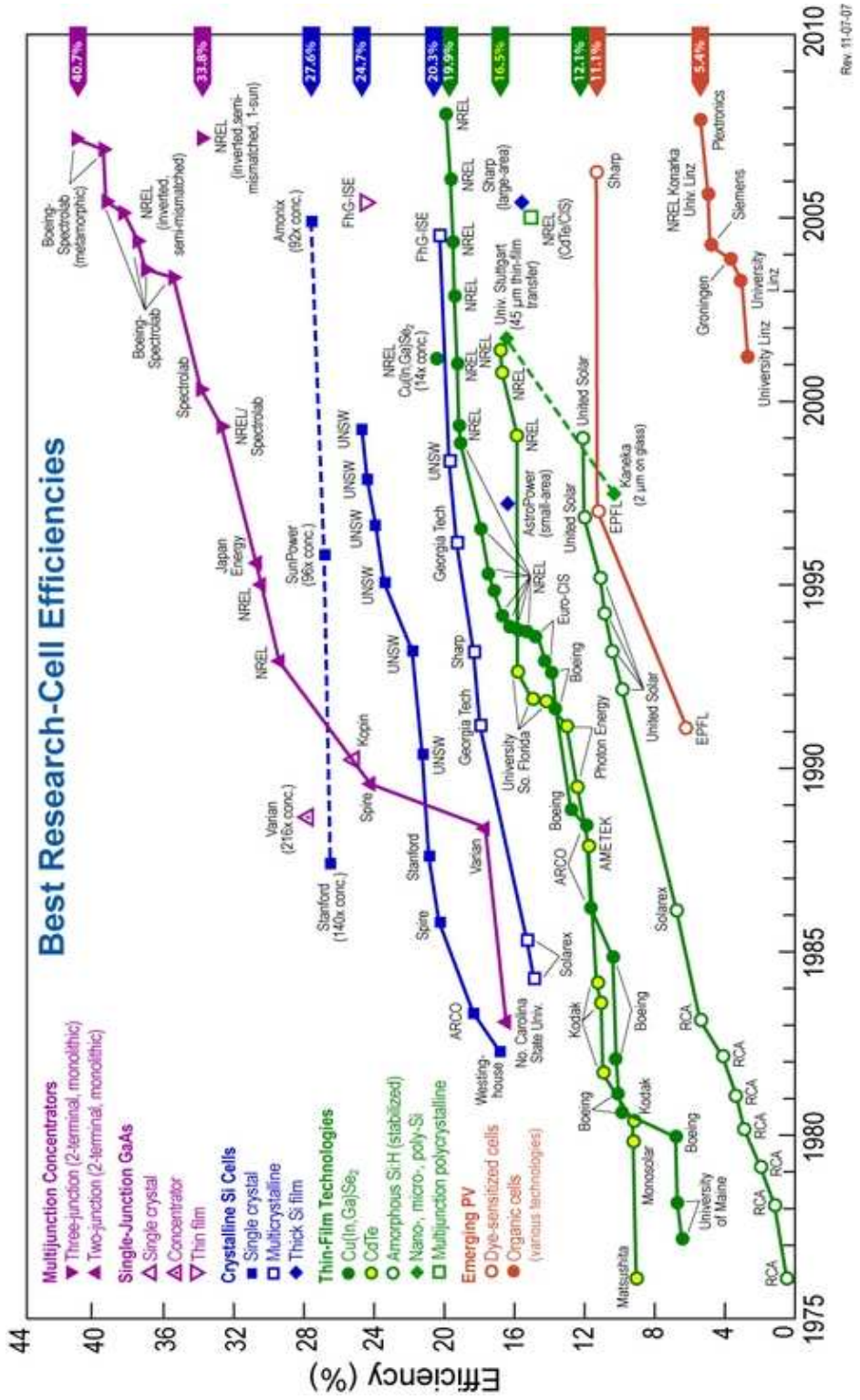

Kazmerski *et al.* , NREL

Figure J.3: Efficiency of the best research level photovoltaic cells [22, 23].

MW/m^2 is on the order of the heat flux density that would be available at the nozzle of a commercial, heavy-duty heat gun. 1 MW/m^2 incident on 1 m^2 surface area can bring 100 kg of water at room temperature to the edge of boiling (i.e., to 100°C) in about 33.5 sec. Likewise, if 10% of 1 MW/m^2 is absorbed by 1 gr of ice ($\approx$ 1 cm thick) at -5°C over 1×1 cm^2 area, it can turn it into water at 5°C in about 36.4 sec.

APPENDIX K

CALCULATION OF REFLECTOR NORMAL FOR PIVOTED-PIXEL DESIGN WITH GIVEN SOURCE AND TARGET LOCATIONS

This section describes the calculation of rotation angle necessary for a pivoted, mirror pixel to reflect light coming from a source point $\boldsymbol{F_s}$ to a target point $\boldsymbol{F_t}$ as pictured in Figure 5.15. It is assumed that source and target points are on the same side of the half-space produced by the plane of the reflector. The problem is trivial if the length of the pivot-rod is zero, i.e., $L_z = 0$. This case was described in Section 5.5.1.

In order to calculate the polar angle γ of the mirror normal for nonzero L_z, Figure K.1 is used. Here, the inner (the first) circle plots the trajectory of the center point of the mirror as it is rotated. It is a circle centered at $\boldsymbol{C}$ with a radius $|\boldsymbol{CD}|$. The outer (the second) circle is used to calculate the image of $\boldsymbol{F_s}$, which is indicated as point $\boldsymbol{F_{si}}$. The center and the radius of the second circle are $\boldsymbol{D}$ and $|\boldsymbol{F_sD}|$, respectively. Point $\boldsymbol{D}$ can be expressed in terms of the point $\boldsymbol{C}$ and the length of the pivot-rod $\overline{\boldsymbol{CD}}$.

$$\boldsymbol{D} = \boldsymbol{C} + L_z\hat{\boldsymbol{n}}. \tag{K.1}$$

Equation (K.1) implies the following:

$$D_x = C_x + L_z\cos(\gamma) \tag{K.2a}$$

$$D_y = C_y + L_z\sin(\gamma) \tag{K.2b}$$

Here D_x, D_y are the x, y components of $\boldsymbol{D}$, and C_x, C_y are the x, y components of $\boldsymbol{C}$, respectively. The same subscript convention is used to decompose points and vectors into their x and y components throughout this section. It can be seen from Figure K.1 that $\boldsymbol{F_{si}}$ is at the intersection of outer circle and $\overline{\boldsymbol{F_tD}}$. The equation

of the outer circle can be written as:

$$|\boldsymbol{r} - \boldsymbol{D}| = |\boldsymbol{F_s} - \boldsymbol{D}|\,, \tag{K.3}$$

where $\boldsymbol{r} = x\hat{\boldsymbol{e}}_{\boldsymbol{x}} + y\hat{\boldsymbol{e}}_{\boldsymbol{y}}$ represents an arbitrary position on the xy-plane. The last equation can be put into the form of Equation (K.4) after substituting:

$$\boldsymbol{r} = \boldsymbol{F_{si}} = F_{six}\hat{\boldsymbol{e}}_{\boldsymbol{x}} + F_{siy}\hat{\boldsymbol{e}}_{\boldsymbol{y}}.$$

$$(F_{six} - D_x)^2 + (F_{siy} - D_y)^2 = (F_{sx} - D_x)^2 + (F_{sy} - D_y)^2 \tag{K.4}$$

Since $\boldsymbol{F_{si}}$ is on the line passing through points $\boldsymbol{F_t}$ and $\boldsymbol{D}$:

$$\frac{F_{six} - F_{tx}}{D_x - F_{tx}} = \frac{F_{siy} - F_{ty}}{D_y - F_{ty}}. \tag{K.5}$$

Also, $\overline{\boldsymbol{F_s F_{si}}}$ is parallel to $\hat{\boldsymbol{n}}$, therefore

$$(F_{sx} - F_{six})\sin(\gamma) = \cos(\gamma)\,(F_{sy} - F_{siy})\,. \tag{K.6}$$

Solving Equation (K.5) and Equation (K.6), one can express F_{six} and F_{siy} in terms of γ, D_x, D_y, and known components of source and target points.

$$F_{six} = \frac{(\tan(\gamma)F_{sx} - F_{sy} + F_{ty})\,(D_x - F_{tx}) - F_{tx}\,(D_y - F_{ty})}{R_1} \tag{K.7a}$$

$$F_{siy} = \frac{F_{ty}\tan(\gamma)\,(D_x - F_{tx}) + (D_y - F_{ty})\,[\tan(\gamma)\,(F_{sx} - F_{tx}) - F_{sy}]}{R_1}, \tag{K.7b}$$

where

$$R_1 = \tan(\gamma)\,(D_x - F_{tx}) - D_y + F_{ty}. \tag{K.8}$$

Equation (K.7) can be rewritten after substitution of Equation (K.2) as follows:

$$F_{six} = \frac{R_2}{R_1} \tag{K.9a}$$

$$F_{siy} = \frac{R_3}{R_1}, \tag{K.9b}$$

where

$$R_1 = K_1 \tan(\gamma) + K_2 \tag{K.10a}$$

$$R_2 = F_{sx} K_1 \tan(\gamma) + L_z \left(K_3 \cos(\gamma) - K_4 \sin(\gamma)\right) + K_5 \tag{K.10b}$$

$$R_3 = K_6 \tan(\gamma) + \sin(\gamma) \left(K_3 L_z - L_z K_4 \tan(\gamma)\right) + K_2 F_{sy}, \tag{K.10c}$$

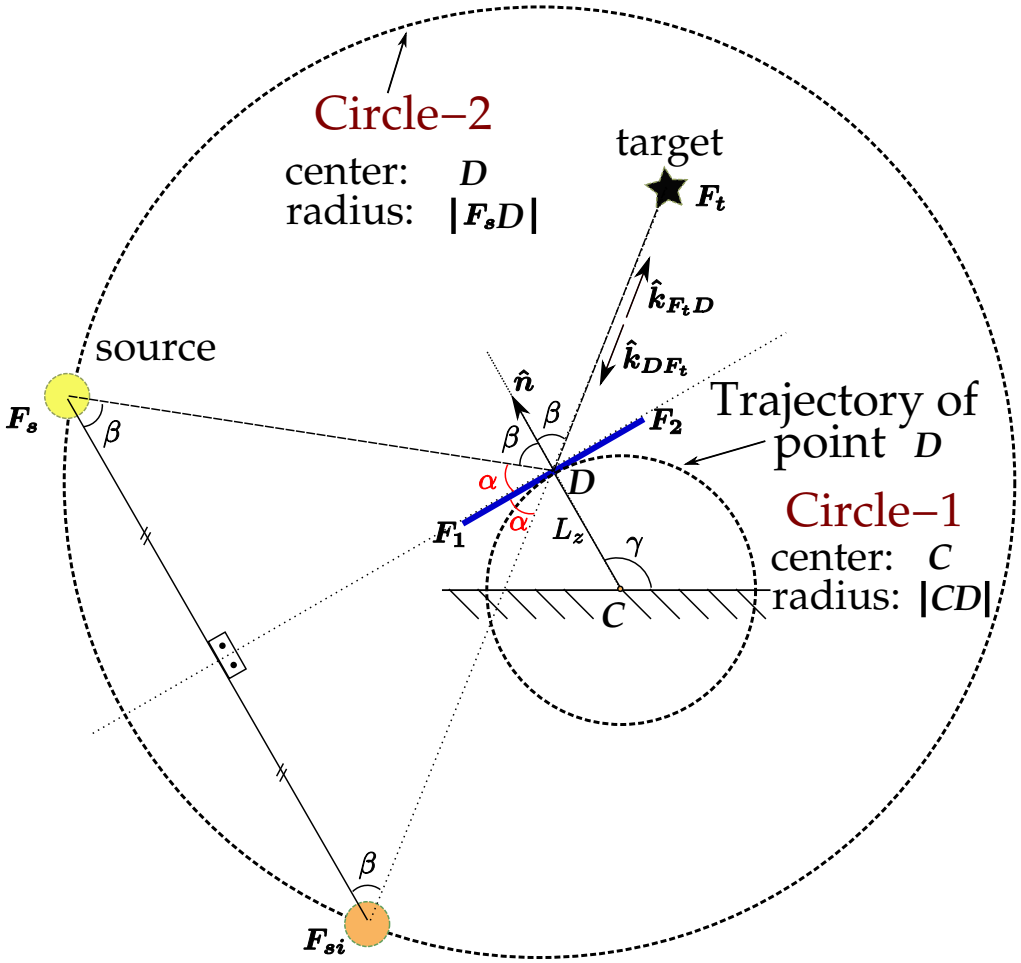

Figure K.1: Pivoted pixel design with arbitrary pivot-bar length L_z. Points $\boldsymbol{C}$ and $\boldsymbol{D}$ indicate the pivotal center of the pixel and mid-point of the mirror segment $\overline{\boldsymbol{F_1 F_2}}$, respectively.

and

$$K_1 = C_x - F_{tx} \tag{K.11a}$$

$$K_2 = F_{ty} - C_y \tag{K.11b}$$

$$K_3 = F_{ty} - F_{sy} \tag{K.11c}$$

$$K_4 = F_{tx} - F_{sx} \tag{K.11d}$$

$$K_5 = K_3 K_1 + F_{tx} K_2 \tag{K.11e}$$

$$K_6 = K_1 F_{ty} + K_2 K_4 \tag{K.11f}$$

Note that all of the K_m variables where $m = 1, 2, \ldots$ are known since $\boldsymbol{C}$, $\boldsymbol{F_s}$, and $\boldsymbol{F_t}$ are given for the problem being analyzed. Finally, substitution of Equation (K.9) into Equation (K.4) yields the following equation:

$$R_2^2 + R_3^2 - 2R_1 R_4 + R_1^2 R_5 = 0. \tag{K.12}$$

Here, R_4 and R_5 are defined as:

$$R_4 = R_2 D_x + R_3 D_y \tag{K.13a}$$

$$R_5 = 2F_{sx} D_x + 2F_{sy} D_y - F_{sx}^2 - F_{sy}^2 \tag{K.13b}$$

Equation (K.12) can be solved together with Equation (K.2) to calculate γ and the mirror rotation from the initial state, $\theta = \gamma - \pi/2$.

The procedure to calculate mirror rotation is performed using MATLAB® for a pivoted mirror array of five pixels. Figure K.2 shows the two computer-generated sketches of the mirror arrays and the locations of the source and the target points. Two cases are considered, one for a free-latticed array with pixels moving independently to optimize reflection of light rays from the source to the target point. The second case considers a parallel-latticed array, where all the mirrors in the array move in parallel to each other. In the parallel-latticed case,

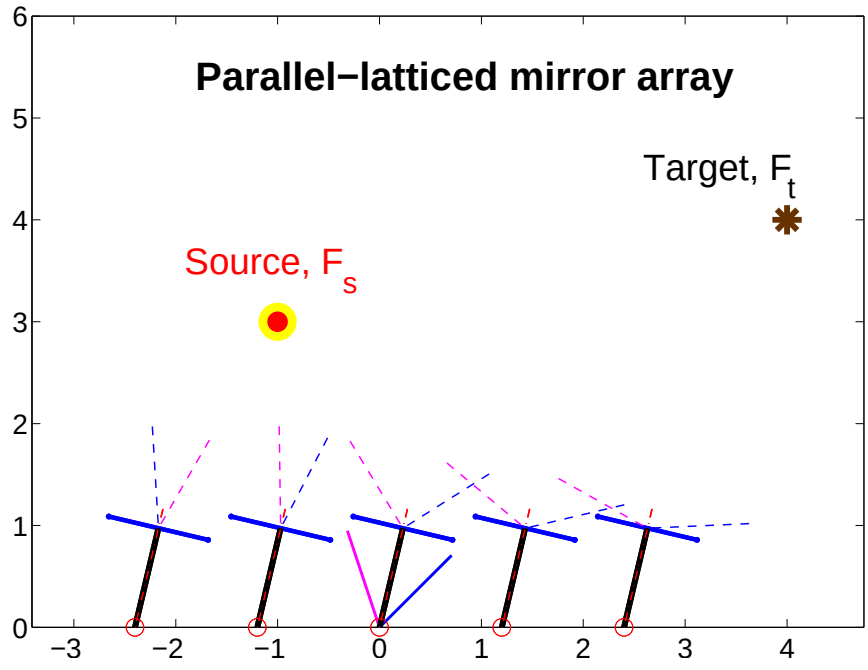

(a)

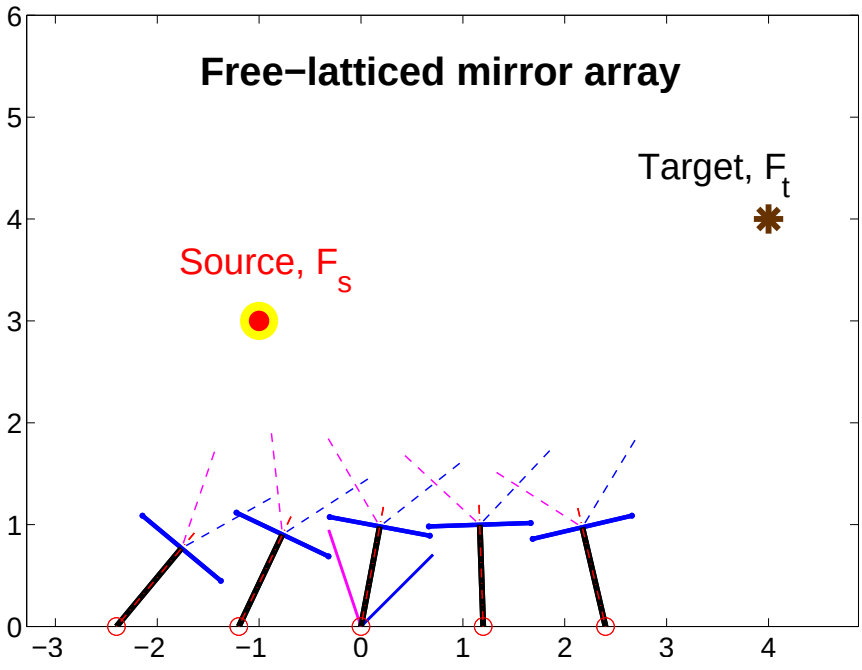

(b)

Figure K.2: A sketch of numerically calculated mirror orientations in mirror arrays of (a) parallel-latticed, and (b) free-latticed tiles. Incident and reflected ray directions from the center of the mirror are also shown in the figure.

the required rotation angle calculation is done only for one point on the tile, which is chosen as the pivot point of the central pixel on the tile. More details about the simulation program used to generate Figure K.2 are given in Section 5.6.

APPENDIX L

OSCILLATION FREQUENCY OF A CAPACITIVELY LOADED CRYSTAL

Following Vittoz *et al.* [16], we can approximate the oscillation frequency of a loaded crystal using Figure L.1 given that the motional branch sees a capacitive input impedance looking into the circuit. The necessary condition for oscillation is [16]:

$$Z_c + Z_m = 0. \tag{L.1}$$

Here Z_m is the motional impedance,

$$Z_m = R_{1,q} + \frac{j}{\omega_s C_{1,q}} \left(\frac{\omega}{\omega_s} - \frac{\omega_s}{\omega} \right). \tag{L.2}$$

The normalized frequency pulling, p is defined by:

$$p = \frac{f - f_s}{f_s} = \frac{\omega - \omega_s}{\omega_s} \ll 1. \tag{L.3}$$

Then Equation (L.2) can be approximated as:

$$Z_m \approx R_{1,q} + j \frac{2p}{\omega C_{1,q}}, \tag{L.4}$$

and average real power consumed on the crystal becomes:

$$PWR_{XTL} = \Re < P_{XTL} >= \frac{1}{2} \left| \frac{V_{XTL}}{Z_m} \right|^2 R_{1,q} = \frac{|V_{XTL}|^2}{2R_{1,q} \left[1 + 4 \left(\frac{p}{\omega C_{1,q} R_{1,q}} \right)^2 \right]}. \tag{L.5}$$

If we make the approximation $\omega \approx \omega_s$ and use the expression for the XTL quality factor, $Q_q = (\omega_s R_{1,q} C_{1,q})^{-1}$, then Equation (L.5) becomes simpler.

$$PWR_{XTL} = \Re < P_{XTL} >\approx \frac{|V_{XTL}|^2}{2R_{1,q} \left[1 + 4 \left(pQ_q \right)^2 \right]}. \tag{L.6}$$

For Figure L.1 we have:

$$\Re(Z_c) = \frac{R_{cir}}{\left[(R_{cir}C_{par1}\omega)^2 + 1\right]}\left(\frac{C_{cir}}{C_{cir}+C_{0,q}}\right)^2 \tag{L.7a}$$

$$\Im(Z_c) = -\frac{\omega^2 R_{cir}^2 C_{cir} C_{par1} + 1}{\omega\left(C_{cir}+C_{0,q}\right)\left[(R_{cir}C_{par1}\omega)^2 + 1\right]}, \text{ where} \tag{L.7b}$$

$$C_{par1} = \frac{C_{cir}C_{0,q}}{C_{cir}+C_{0,q}}. \tag{L.8}$$

Equation (L.1) implies:

$$-\Re(Z_c) = \Re(Z_m) \tag{L.9a}$$

$$-\Im(Z_c) = \Im(Z_m) \tag{L.9b}$$

Here $\Re$ and $\Im$ represent "real part of" and "imaginary part of", respectively. Equation (L.9a) yields a quadratic equation for R_{cir}. Fortunately, the more negative of the roots does not lead to a stable oscillation [16]. The other (less negative) root yields the value of R_{cir} necessary for steady state oscillation, and it is expressed in Equation (L.10).

$$R_{cir} = \frac{-K_p + \sqrt{K_p^2 - 4K_r^2 K_q}}{2K_r K_q} \tag{L.10a}$$

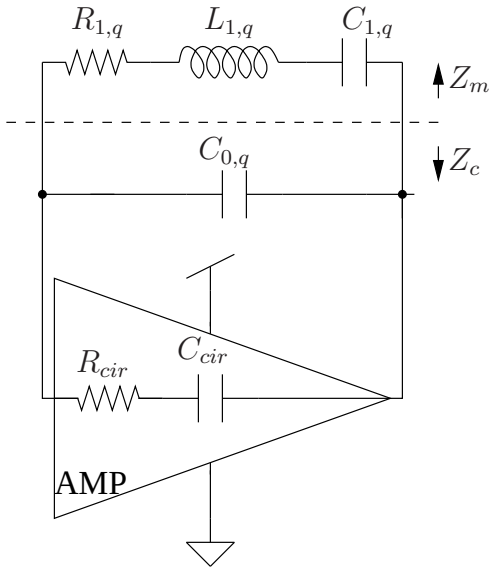

Figure L.1: Schematic of the XTL in the feedback loop with an amplifier that presents an input impedance of $R_{cir} + (\mathrm{j}\,\omega C_{cir})^{-1}$.

$$K_p = \left(\frac{C_{cir}}{C_{0,q} + C_{cir}}\right)^2 \quad \text{(L.10b)} \qquad K_q = (C_{par1}\omega)^2 \quad \text{(L.10c)} \qquad K_r = R_{1,q} \quad \text{(L.10d)}$$

A necessary condition for oscillation is obtained by calculating the largest value of negative resistance, $-\Re(Z_c)$, treated as a function of R_{cir}. $-\Re(Z_c)$ takes its maximum value for

$$R_{cir,m} = -\frac{1}{C_{par1}\omega}. \tag{L.11}$$

Substituting Equation (L.11) in Equation (L.7a) and imposing that it is larger than $R_{1,q}$ of the motional branch, yields the condition of oscillation. This calculation yields *without* any approximations to:

$$\frac{C_{cir}}{C_{cir} + C_{0,q}} > 2\omega R_{1,q} C_{0,q}. \tag{L.12}$$

It is handy to associate oscillation capability of any resonator, i.e., crystal in our case, with its quality factor. As such, Equation (L.12), can be expressed in terms of the quality factor in light of Equation (L.3), if we take $\omega \approx \omega_s$ as before. A good approximation for the oscillation condition is then

$$\frac{Q_q C_{1,q}}{C_{0,q}} > 2\left(1 + \frac{C_{0,q}}{C_{cir}}\right). \tag{L.13}$$

The oscillation frequency is calculated by equating the negative of the imaginary part of Z_c given in Equation (L.7b) to the imaginary part of the motional branch impedance [16]:

$$-\Im(Z_c) = \frac{\omega^2 R_{cir}^2 C_{cir} C_{par1} + 1}{\omega\left(C_{cir} + C_{0,q}\right)\left(\omega^2 R_{cir}^2 C_{par1}^2 + 1\right)} = \frac{\omega^2 - \omega_s^2}{C_{1,q}\omega\omega_s^2} \approx \frac{2p}{\omega C_{1,q}}, \tag{L.14}$$

XTL equivalent circuit can be determined separately, so there are three remaining unknowns in Figure L.1. These are ω, R_{cir}, and C_{cir}. Two of the three equations required for the solution are given by Equation (L.10) and Equation (L.14).

The third (and the last one) is dictated by the amplifier input impedance as a function of ω. One approach at this stage is to use small signal analysis and computer simulation to calculate the input impedance [161]. In order to avoid limiting the discussion to a particular amplifier topology, we assume C_{cir} is known and is relatively constant as a function of frequency. Under these circumstances, Equation (L.10) and Equation (L.14) can numerically be solved for ω and R_{cir}. This solution is referred as the *exact* solution throughout the text.

A very well known and simplified analytical form for ω, is possible if the oscillation condition in Equation (L.13) is, as Vittoz *et al.* states, "fulfilled with a large enough margin." Qualitatively speaking, this high margin ensures that Equation (L.15) is valid once the amplitude of oscillation is stabilized. The expression for p then becomes as in Equation (L.16).

$$|\omega R_{cir} C_{par1}| \ll 1 \Rightarrow \tag{L.15}$$

$$\frac{\omega - \omega_s}{\omega_s} = p \approx \frac{C_{1,q}}{2\left(C_{0,q} + C_{cir}\right)}. \tag{L.16}$$

It is possible to proceed with a similar derivation if we take the negative resistance circuit in Figure L.1 to present an inductive input impedance as opposed to capacitive. In that case, one can show that the crystal can oscillate both below and above the series resonance frequency as determined by the component values. Below series frequency operation is mentioned for a bridge oscillator in [202]. However, operation frequency is more commonly in between the series and the shunt resonance frequency, and the amplifier circuitry presents a capacitive input impedance as depicted in Figure L.1 [16, 140, 161].

APPENDIX M

NETLIST AND MODEL PARAMETERS OF THE OSCILLATORS USED IN CIRCUIT SIMULATIONS

Figure M.1 shows the parallel loaded version of the oscillators used in some of the simulations of Chapter 6. The series loaded version of the circuit follows from Figure 6.8. The listing of the netlist and BJT model parameters as generated by OrCAD Capture v10 and PSpice, where the simulations were performed, are given on page 398. The power consumption of the circuit is excessive, and the same goes for the power consumed by the XTL since power consumption was not a major design criteria. The scope of simulations and experiments were to test the validity of the analytical model derived in Section 6.2.2 and to demonstrate the calculation of some of the parameters defined in the main text.

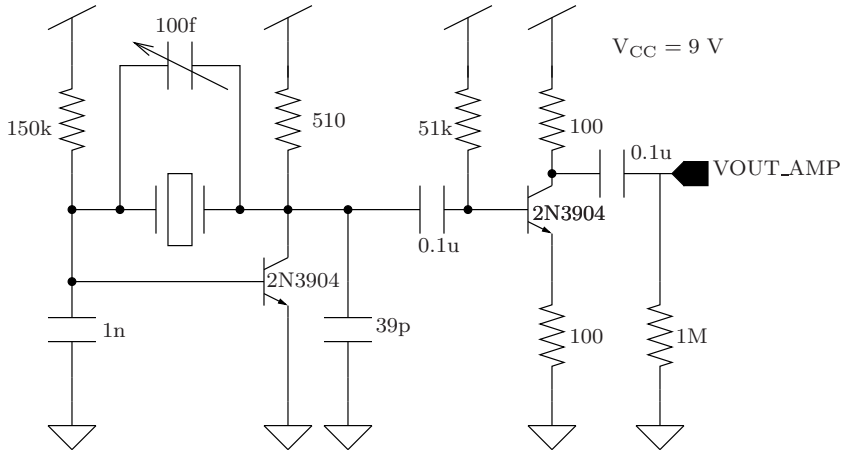

Figure M.1: Schematic of the parallel loaded version of the simulated circuit. C_{sensor} = 100 fF is chosen as an example, but varied during simulations. Supply voltage is V_{CC} = 9 V. The series version of the simulated circuit uses the same component values, with only the connection of XTL and C_{sensor} differing as illustrated by Figure 6.8 in the main text.

In the simulations the crystal is replaced by its equivalent circuit as in Figure 6.6 with the values as listed in Table 6.1. The netlist includes an extra damped sinusoidal voltage source, which is not shown in Figure M.1. This voltage is included in series with the motional branch of the XTL and has no effect in steady state solution. It is used to get the oscillator circuit started [203].

```
*Analysis directives:
.TRAN  0 15010u 15000u 10p
.OPTIONS RELTOL= 1e-4
.PROBE V(alias(*)) I(alias(*)) W(alias(*)) D(alias(*)) NOISE(alias(*))
.INC "..\exp120508sch_with_buffer.net"


**** INCLUDING exp120508sch_with_buffer.net ****
* source EXP120508_CIRCUIT

C_C2         0 VOUT_OSC  39e-12
V_V4         VCC_BAR 0 9
R_RC1         VOUT_OSC VCC_BAR  510
Q_Q3         VOUT_BUF N41766 N43311 Q2N3904
R_RC2         VOUT_BUF VCC_BAR  100
C_C_AC_1         N41766 VOUT_OSC  1e-7
R_RL2         0 VOUT_AMP  1e6
C_C_sensor         VOUT_OSC N41678  0.1e-12
C_C1         0 N41678  1000e-12
R_RE2         0 N43311  100
R_RB1         N41678 VCC_BAR  150K
V_V5         N41678 N41844
+SIN 0 700 15.996e6 100n 016000000 00
C_C_AC_2         VOUT_AMP VOUT_BUF  1e-7
R_RB2         N41766 VCC_BAR  51K
C_C0_q         VOUT_OSC N41678  3.24196e-12
Q_Q2         VOUT_OSC N41678 0 Q2N3904
C_C1_q         N41682 N41844  13.3289e-15
L_L1_q         N41682 N416441  7.42795e-3
R_R1_q         VOUT_OSC N416441  7.7979

**** RESUMING for_epoxy.cir ****
.END
**** 06/02/09 16:43:42 ************** PSpice Lite (Jan 2005) ****
 ** Profile: "exp120508sch_with_buffer-for_epoxy"
 ****     BJT MODEL PARAMETERS
******************************************************************
               Q2N3904
               NPN
       LEVEL    1
          IS    6.734000E-15
          BF  416.4
```

```
          NF    1
         VAF   74.03
         IKF     .06678
         ISE    6.734000E-15
          NE    1.259
          BR     .7371
          NR    1
         ISS    0
          RB   10
          RE    0
          RC    1
         CJE    4.493000E-12
         VJE     .75
         MJE     .2593
         CJC    3.638000E-12
         VJC     .75
         MJC     .3085
        XCJC    1
         CJS    0
         VJS     .75
          TF  301.200000E-12
         XTF    2
         VTF    4
         ITF     .4
          TR  239.500000E-09
         XTB    1.5
          KF    0
          AF    1
          CN    2.42
           D     .87

**** 06/02/09 16:43:42 ************** PSpice Lite (Jan 2005) *****************
 ** Profile: "exp120508sch_with_buffer-for_epoxy"
 ****     INITIAL TRANSIENT SOLUTION       TEMPERATURE =   27.000 DEG C
********************************************************************************
 NODE   VOLTAGE     NODE   VOLTAGE     NODE   VOLTAGE     NODE   VOLTAGE
(N41678)     .7253 (N41682)    4.2952 (N41766)    2.7682 (N41844)     .7253
(N43311)    2.0191 (N416441)    4.2952                  (VCC_BAR)    9.0000
(VOUT_AMP)    0.0000                 (VOUT_BUF)    6.9932
(VOUT_OSC)    4.2952

    VOLTAGE SOURCE CURRENTS
    NAME         CURRENT
    V_V4        -2.947E-02
    V_V5         0.000E+00

    TOTAL POWER DISSIPATION   2.65E-01  WATTS
```

APPENDIX N

DETAILS ON PZT-ARRAY FABRICATION

N.1 Dicing and bonding characterization

Material properties, plate thickness, and aspect ratio of the pillars need to be considered in the design of the PZT array. From a process point of view, PZT type is important because the ceramic is to be exposed to rather high temperatures (225°C) during FCB. Therefore, Curie temperature of the PZT needs to be higher than the bonding temperature with as large a safety margin as possible. Coupling factor and d_{33} coefficient are among other important parameters. The vendor specified properties of some PZT types are listed in Table N.4. PZT-5A (EBL-#2) is the PZT of choice in this work, mainly due to its high Curie temperature.

In Section 7.2, it was mentioned that the dicing of the PZT array was performed on a tacky tape that is part of the standard dicing procedure. It was later found that the addition of a dummy die under the PZT during the dicing allowed higher aspect ratio pillars and improved the dicing yield significantly. The dicing procedure with a dummy die is illustrated in Figure N.1. The dicing process was optimized to give pitch sizes as low as 150 μm on a 500 μm thick PZT plate[1].

Among different substrates used for realizing the dummy die, it was found that the substrate same as the one being diced, namely PZT, yielded the best results. A good match between the acoustic impedance of the dummy and actual PZT plates is believed to reduce the stress and vibration at the bonding interface during dicing. Additionally, surface roughness of the surfaces can be important for the quality

[1]Given a blade kerf-width of ≈ 35 μm, PZT thickness of 0.5 mm, and an array pitch size of 150 μm, the aspect ratio is calculated to be greater than four.

of the bond formed using a cyanoacrylate based glue of certain viscosity. When a silicon piece that has typically nm level average surface roughness was used as a dummy bonding die, it gave worse results than using PZT that has μm level average surface roughness.

For the reasons described above, suggested dicing procedure starts with two PZT plates of similar sizes that are preferably gold coated for solder wettability. The smaller plate is the *actual plate* to be diced, whereas the larger one is the *dummy plate* for handling the actual array during the rest of the assembly process. The dummy plate can be discarded at the end of the process or it can be used again as a dummy die for the second time. For the samples presented in this section, the actual plate is 7.4×7.4 mm^2, and the dummy plate is 10×10 mm^2.

The bonding between dummy and actual plates has to fulfill the following requirements:

1. **Strong shock and vibration resistance:** Dicing of especially high aspect ratio pillars (i.e. with large thickness to array-pitch ratio) require a very strong bond. Furthermore this bond must be resistant to DI water or possibly any other cooling liquid used during dicing.
2. **Easy removal after the high temperature reflow process:** As its name implies, dummy plate is discarded after the boding of the actual array on the VLSI die. So the bonding process should be reversible without damaging surfaces or leaving residues. High temperatures involved in FCB makes the latter condition more challenging since the adhesives above certain temperatures can go through phase transitions or chemical reactions leaving burnt residues behind.
3. **Allow application on the surface with uniform thickness in a re-**

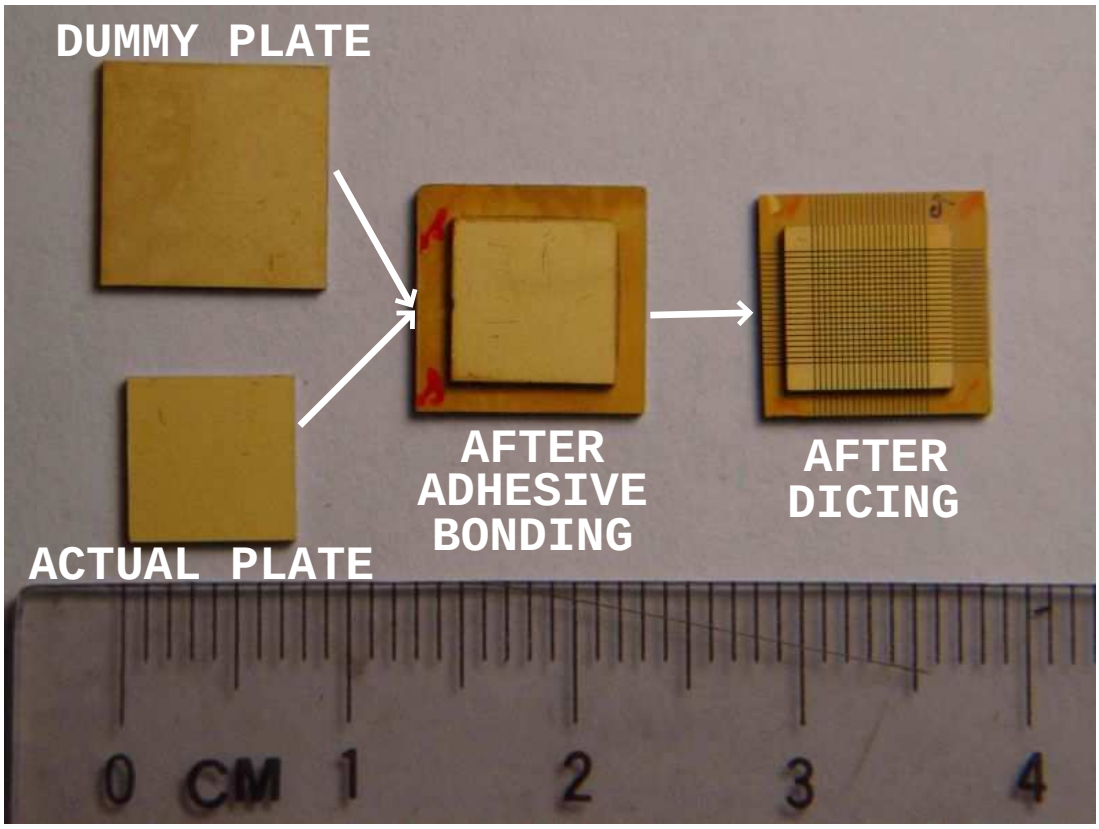

Figure N.1: Illustration of the PZT array fabrication steps. After the adhesive bonding of the dummy and the actual PZT plates, the stack is diced all through the actual plate, and partially through the dummy plate.

peatable manner: Dicing occurs partially through the dummy wafer. The depth of dicing into dummy plate needs to be minimized in order to make the process softer on the bonded stack. On the other hand, one needs to make sure that there is always some penetration into the dummy to guarantee the formation of fully separated pillars out of the actual PZT plate. Any nonuniformity in the adhesive layer thickness translates into extra dicing thickness, i.e., more shock and vibration during dicing that limits the maximum achievable aspect ratio of the pillars.

First and second items in the above list are rather conflicting, since a high quality bond is also hard to remove. 3M-Pronto CA-100, a cyanoacrylate based glue, was used as a bonding agent in the experiments. There are also adhesives known as dicing wax as well as other types used in the optoelectronic industry. However, CA-100 gave satisfactory results, after process optimization, even at pitch lengths of 150 μm, i.e., significantly less than the nominal value of 250 μm. A procedure that removed the glue residues satisfactorily was also developed[2].

Main steps of the PZT array dicing is illustrated in Figure N.1. Both surfaces needs to be cleaned to render them free of any grease, dust or oxide, before adhesive bonding with cyanoacrylate glue. Steps for the cleaning procedure are listed in Table N.1. Bonding is done by spinning the glue at 6 kRPM on a table top spinner (Laurell, Model: WS-400A-6NPP/LITE, single step spinning, time=40 sec, ACC=007). The dummy and the actual PZT plates are brought to contact after spinning, and the adhesive is set to dry for 12–24 hr under 10 N force. Next, the bonded stack is diced in a commercial wafer saw (Kulicke & Soffa -7100) using a diamond blade (K&S, Semitec brand diamond hub blade , S1235). The thickness of the cut is critical. The depth is calibrated before each batch of dicing so that the blade completely cuts through the actual plate, but barely touches to the dummy plate. This makes sure that pillars formed by the actual plate are attached to the dummy plate only via the glue layer. The dicing recipe is summarized in Table N.2.

After the dicing, the PZT stack is ready to be aligned and bonded on the solder-bumped die. This bonding process is based on the reflow of the solder bumps and is known as *flip-chip bonding (FCB)*. Application of pressure during bonding is also possible. Unlike the manual bonding procedure described in Section 7.2, a

[2]A sequential application of: (1) oxygen plasma, (2) sonicated acetone dip for an hour, (3) immersion in boiling DI water for 4 hr, (4) immediately followed by an acetone dip removed residues to a sufficient extent.

Table N.1: Cleaning procedure before adhesive bonding.

1	Rinse the samples in acetone for	$\approx$ 1 minute
2	Rinse the samples in IPA for	$\approx$ 1 minute
3	DI water rinse	$\approx$ 1 minute
4	1:10 (volume)Sulfuric Acid:DI	$\approx$ 15 seconds
5	DI	$\approx$ 1 minute
6	Dry on hotplate 50–70°C	typically 10–15 minute

flip-chip bonder machine (Research Devices M8) was used in the characterization experiments. The recipe used for a typical bonding operation is given in Table N.3. Programmed temperature versus time characteristics and its measured values according to the above recipe are plotted in Figure N.2. The first horizontal region along the measured curve indicates *tack*, and the second one indicates the *reflow* stage.

Table N.2: The dicing recipe used in PZT array fabrication.

***Cut* Pitch**(μm)	250
Depth(μm)	490-535 [a]
Wafer Diameter(inch)	1
***Spindle* Entry Speed**(mm/sec)	3.81
Exit Speed(mm/sec)	5.08
Cut Speed(mm/sec)	5.08
Rotation Speed(kRPM)	30
***Blade* Model**	Semitec - S1235

[a] Exact value needs to be characterized at each batch of dicer run so that the blade barely touches the dummy die, fully cutting the actual plate.

Table N.3: Flip-chip bonder recipe used during bond characterization.

STAGE	***PARAMETER***	***VALUE***
Setup	**Upper Temperature**	60°C
	Lower Temperature	62°C
	Pitch & Roll	HOLD
	Contact Method	PRESSURE
	Contact	1000 g
	Pressure Maintenance	YES
	Contact Hold Time	00 : 30 (mm : ss)
Tack	**Pitch & Roll**	HOLD
	Vacuum Release	NONE
	Contact	1000 g
	Pressure Maintenance	YES
	Ramp Time	05 : 30 (mm : ss)
	Upper Tack Temperature	200°C
	Lower Tack Temperature	200°C
	Hold Time	01 : 00 (mm : ss)
Reflow #1	**Pitch & Roll**	HOLD
	Vacuum Release	NONE
	Contact	1000 g
	Pressure Maintenance	YES
	Ramp Time	01 : 00 (mm : ss)
	Upper Reflow Temperature	225°C
	Lower Reflow Temperature	227°C
	Hold Time	01 : 00 (mm : ss)
Reflow #2	**Pitch & Roll**	HOLD
	Vacuum Release	NONE
	Contact	1000 g
	Pressure Maintenance	YES
	Ramp Time	00 : 30 (mm : ss)
	Upper Reflow Temperature	225°C
	Lower Reflow Temperature	227°C
	Hold Time	00 : 05 (mm : ss)
Cool-Down	**Vacuum Release**	UP & LOW
	Ramp Time	05 : 00 (mm : ss)
Bonding Program Identifier		213

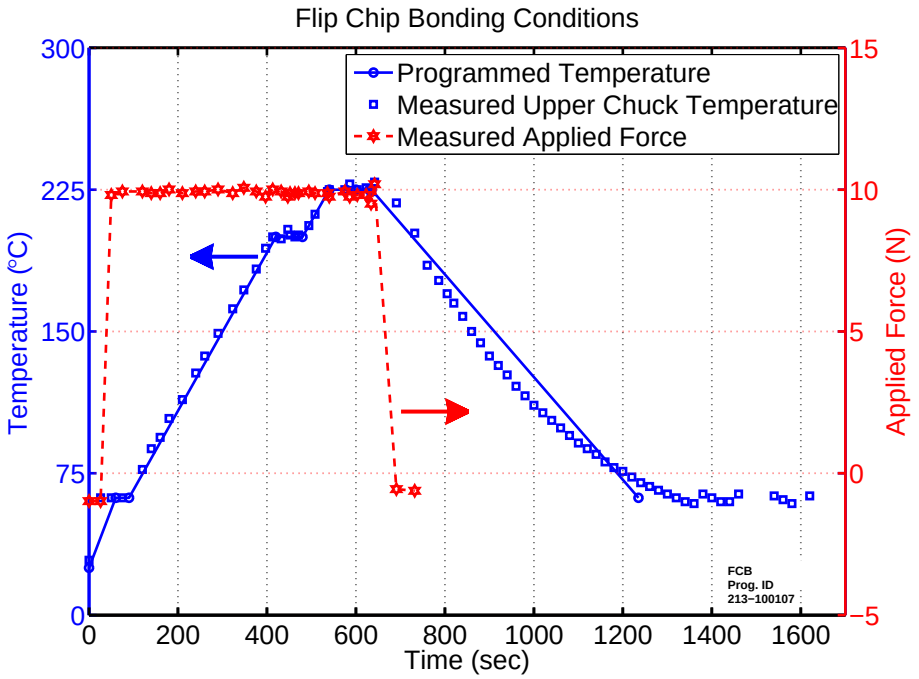

Figure N.2: Programmed temperature, measured temperature, and measured force applied during a typical FCB recipe.

N.2 Effect of reflow temperature on PZT characteristics

Flip-Chip Bonding (FCB) recipe developed here uses temperatures as high as 225°C with simultaneous application of pressure. As such, going above or close to the Curie temperature of the PZT becomes a concern since that could result in reduction of piezoelectric properties. The characterization assessing this aspect of the bonding process is explained below.

The experiments are performed on mm 7.4×7.4 mm rectangular PZT slabs of both PZT5-A(EBL#2) and PZT8(EBL#4)[3]. Conductive adhesives and epoxies are not used in order to avoid complications due to temperature related variations in these materials. The electrical contact is obtained by constraining the PZT slabs

[3]Staveley NDT

under a metal coated substrate[4] and a probe tip. In other words, the electrical contact is obtained via a mechanical contact, without any solid state bond.

The electrical measurements were done using an HP4194 impedance analyzer and a probe station. Stray capacitances and resistances were accounted for via a 'deembedding' operation involving measurements of open and short circuit impedances without the device under test.

The test samples went through electrical measurement both before and after FCB. The recipe used in bonding was a generic one that involved highest set temperature of 225°C and a pressure of approximately 0.18 MPa. The amplitude and phase of the two types of PZT samples tested are given in Figure N.3. The curves both before and after FCB closely match each other for both types. There is also not a considerable degradation in sharpness of the peaks, which indicate that piezoelectric coefficients are not adversely affected. Focusing on the low frequency impedance amplitude as highlighted in Figure N.3(a), the parallel plate capacitance of the samples before FCB are extracted as $C_{PZT5A} = 1.81$ pF and $C_{PZT8} = 1.07$ pF. These values increase to $C_{PZT5A} = 1.91$ pF and $C_{PZT8} = 1.26$ pF after FCB. This is equivalent to: 5.8% change for PZT5-A versus 17.6% change for PZT8. For low frequencies, at which the capacitance extraction is done, deembedding has negligible effect while at higher frequencies it changes the impedance considerably. This is illustrated in the inset. Phase response given in Figure N.3(b) shows even a closer match than its amplitude counterpart for the measurements taken before and after FCB. The inset in the figure emphasizes this match.

It is concluded, from the above results, that the temperature and the pressure used during FCB bonding (around ($T \approx 225°\text{C}, P \approx 0.2$ MPa) do not introduce

[4]Metal coated substrate was Ti/Ni/Cu (Ti at the bottom) silicon wafer.

significant degradation in the bulk transducer performance for PZT5-A. This claim is also verified by Doppler interferometry measurements of the transverse surface velocity on PZT samples before and after FCB, which did not indicate a degradation after the high-temperature bonding process.

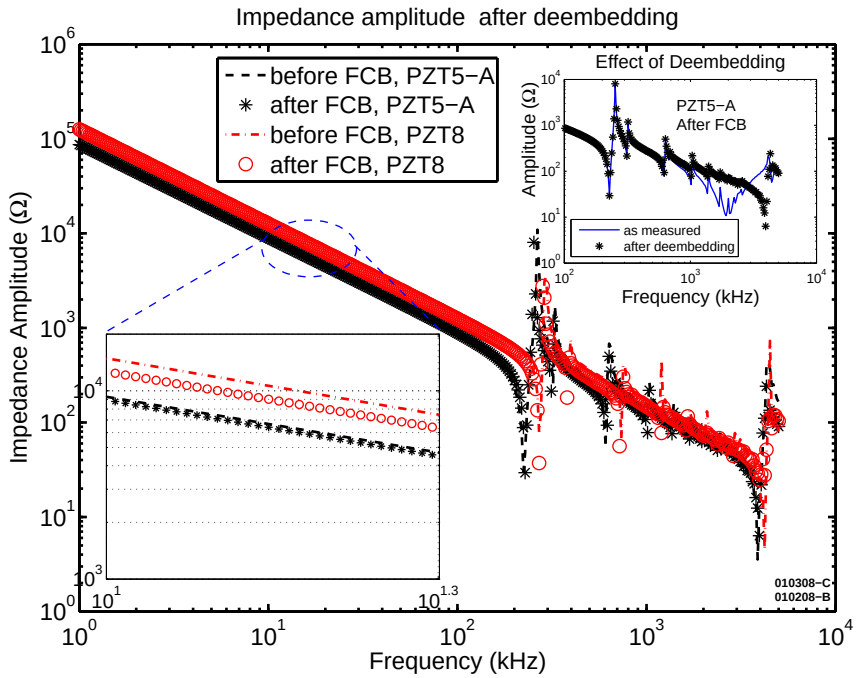

(a)

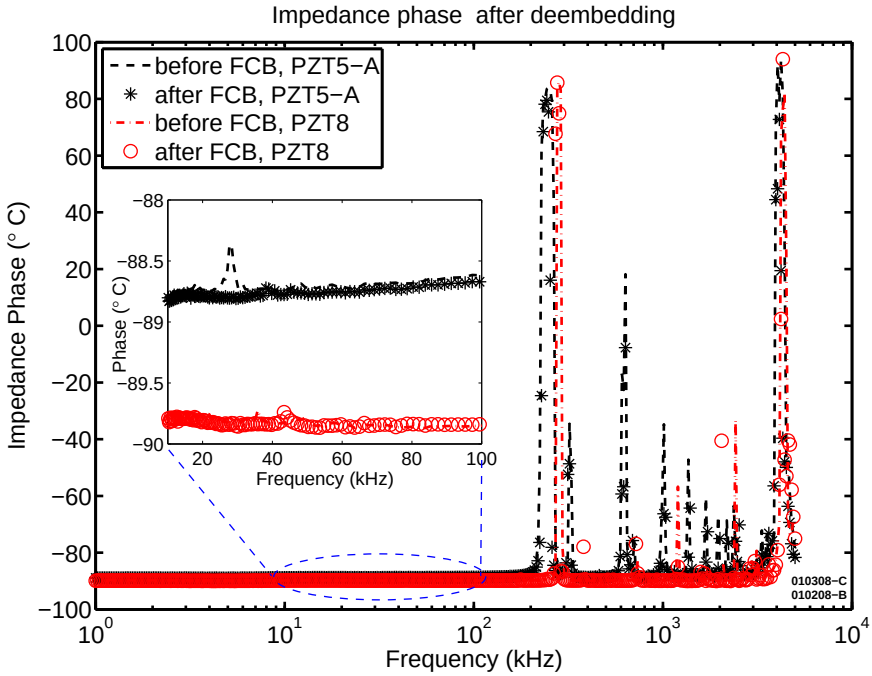

(b)

Figure N.3: (a) Amplitude and (b) phase of the impedance measured before and after FCB with deembedding performed on the raw data. The top figure has an inset to show the effect of deembedding at high frequencies.

Table N.4: EBL lead zirconate titanate characteristics.
Source: http://www.eblproducts.com/leadzirc.html

Material Properties	**EBL**									
	#1	**#2**	**#3**	**#4**	**#5**	**#6**	**#7**	**#9**	**#23**	**#25**
Density (g/cm^3)	7.5	7.5	7.45	7.5	7.7	7.45	7.5	7.6	7.8	7.7
Dielectric Constant $\epsilon_{33}^{\mathrm{T}}/\epsilon_0$	1300	1725	3450	1050	425	2750	1100	1450	3800	1800
Mechanical Q	400	100	65	960	600	75	900	600	30	80
Dissipation %@ 1 kHz	0.4	2.0	2.0	0.4	2.5	2.0	0.3	0.4	2.4	1.8
Curie Temperature °C	320	350	190	300	350	220	300	320	250	350
d constant m/V $\times 10^{-12}$										
d_{33}	295	380	583	220	150	480	240	315	650	350
d_{31}	-127	-173	-262	-95	-60	-260	-107	-135	-320	-179
d_{15}	506	584	730	330	360	670	360	—	—	—
g constant Vm/N $\times 10^{-3}$										
g_{33}	25.0	25.0	19.1	24.5	41.0	20.9	24.8	24.6	19.0	24.2
g_{31}	-10.7	-11.5	-8.6	-10.5	-16.0	-9.8	-10.9	-10.5	-9.0	-11.0
g_{15}	39.8	38.2	28.9	28.9	50	35.0	28.7	—	—	—
Coupling Coefficients										
k_p	0.60	0.62	0.64	0.52	0.52	0.63	0.56	0.60	0.75	0.63
k_{33}	0.69	0.72	0.75	0.62	0.67	0.74	0.66	0.71	0.75	0.7
k_{31}	0.36	0.36	0.38	0.31	0.30	0.37	0.33	0.34	0.44	0.30
k_{15}	0.72	0.69	0.68	0.55	0.68	0.67	0.59	—	0.68	—
Frequency Constants Hzm										
Thickness	2026	1778	1765	2181	2050	1727	2141	1990	2030	2050
Planar	2149	1994	1981	2311	2340	1943	2269	2110	—	2020
Transverse	1321	1092	1105	1415	1750	1058	1333	—	—	—
Industry Types	PZT-4	PZT-5A	PZT-5H	PZT-8	PZT-7A	PZT-5J	—	PZT-4D	—	–

APPENDIX O

PROCESS FLOW SUMMARY FOR FLIP-CHIP BONDING USING SU-8 PILLARS FOR ALIGNMENT

Following steps were performed mostly at Cornell Nanofabrication Facilities (CNF).

1. Start with a 4 inch silicon wafer with an insulation layer of nitride.
2. Sputter $0.75 - 0.8$ μm Al + 1% Si + 4% Cu 2 KW @ 1.6 mT with 12.sccm Argon for 35 min. CVC Sputtering tool, with ion beam clean and presputtering. Note for next run: Sputter pure aluminum, because silicon in aluminum can be responsible for the residues on nitride after wet aluminum etching. So sputtering metal and parameters are as follows: pure Al, 1.6 mT @ 40 sccm Ar, 35 min.
3. Anneal in % 5 H_2/N_2 at 400°C for 30 min.
4. Lithography using S1813.
5. Wet etch aluminum in Transene Type A aluminum etchant.
6. Strip resist in 1165. If not available, use acetone, IPA, and then DI water rinse. But do not use AZ-300T with Al.
7. PECVD oxide in GSI, n1.46 recipe, 2 min, target 0.5 μm @ 400°C. This oxide has an etch rate of about $390 - 400$ Å/min in BOE 1:30.
8. Oxide lithography with S1827.
9. Etch pad and solder contacts in BOE 1:30 for $14 - 15$ min. 500 nm/390 nm$\times$1.1 = 14.1 min so etching for 15 min is fine. Al attack in BOE is tolerable; its attack is estimated to be 10 nm/min. However, BOE makes the surface of Al a bit rough. So you have the option of using dry etch here, since pure Al is allowed in Oxford etcher. Alternatively, pad etch can be tried as well.
10. Evaporation of Ti/Ni/Cu: 200/2000/6000 Å using electron-gun. Next time consider Ti/Ni/Cu 200/2000/8000 Å to make sure you have more Cu against intermetallic compound formation. Otherwise you can also use Cu electroplating for a few microns, before solder electroplating without any extra patterning. See the reference [204].

    Make sure you do a 20 second BOE 30:1 dip just to remove residual oxide over aluminum before evaporation. This is very critical to get good contact resistance.
11. AZ4903 lithography for 30 μm thickness.
12. Electroplate at 10.2 mA/137 mm^2 for 84 min. This results in $25 - 30$ μm of bump height. Pulsed electroplating done at %75 duty cycle (on for 7.5 ms and off for 2.5 ms).

    - Make sure the beaker is very clean. Getting rid of contamination in the plating solution is important for repeatable results in electroplating.
    - Do not hardbake the AZ4903 before electroplating. It causes cracks on the photoresist.

- Make sure you do a $15 - 20$ sec dip in $5 - 10\%$ H_2SO_4 in DI water to remove copper oxide.
- Clean anode in 10% HCL for at least an hour.
- Apply strong stirring at $400 - 500$ rpm.

13. Strip the resist in acetone (> 4 hr) then 3 min in IPA, and 5 min in DI. Blow dry in N_2.
    CAUTION: Do not use 1165 or AZ-300T stripper at this stage to strip the AZ 4903. It is not nice on solder and leaves some residues between the pixels. Use acetone to strip photoresist on top of the seed layer.
14. UBM etch using the following recipe.
    - Prepare 50 ml of DI water,
    - Add 60 ml H_2SO_4,
    - Wait until the solution gets warm, and the wild reaction gets mild (about an hour).
    - Add 20 ml of 30% H_2O_2.
    - Wait for 20–25 mins. Etch the wafer for about a minute, until both Cu and Ni are etched. Inspect for the residues. Ti will act as an etch stop and will protect the aluminum pads.
    - 1:30 BOE etch to remove Ti, it must take about 60–70 sec.[1]
15. SU8-100 lithography for $200 - 250$ μm (only necessary if alignment is done manually):
    - Dehydrate the wafer @ 115°C for > 5 min.
    - Spin in 2 steps follows.
      - Speed: 500 rpm acceleration: 100 rpm/sec time: 15 sec
      - Speed: 300 rpm acceleration: 300 rpm/sec time: 35 sec
    - Pre-Exposure Bake: 20 min @ 65°C on hotplate. Then set the temperature of the hotplate to ramp to 95°C in about 4 min. Bake at 95°C for 75 min.
    - Expose the wafer in EV-620 (without any optical filter). Exposure dose is 105 sec $\times$ 9.8 mW/cm^2.
    - Post-Exposure Bake: Start at 65°C. Immediately set to ramp up to 95°C in 4 min. Keep an additional $14 - 16$ min @ 95°C.
    - Develop in two baths using fresh SU8 developer, $25 + 5$ mins. Rinse in IPA. Measured heights of SU8: 223, 245, 230 μm.

[1]Minimum bump width is limited by the undercut incurred during UBM etching. For aggressive scaling, ion milling can be a favorable option for UBM etching.

BIBLIOGRAPHY

[1] M. Wu, "Micromachining for optical and optoelectronic systems," *Proceedings of the IEEE*, vol. 85, no. 11, pp. 1833 – 1856, 1997.

[2] D. Reyes, E. Schildkraut, J. Kim, R. Connors, P. Kotidis, and D. Cavicchio, "A novel method of creating a surface micromachined 3-D optical assembly for MEMS-based, miniaturized FTIR spectrometers," *Proceedings of SPIE - The International Society for Optical Engineering*, vol. 6888, 2008.

[3] R. Chen, H. Nguyen, and M. Wu, "A high-speed low-voltage stress-induced micromachined 2×2 optical switch," *IEEE Photonics Technology Letters*, vol. 11, no. 11, pp. 1396 – 1398, 1999.

[4] L. Lin, E. Goldstein, and R. Tkach, "Free-space micromachined optical switches for optical networking," *IEEE Journal of Selected Topics in Quantum Electronics*, vol. 5, no. 1, pp. 4 – 9, 1999.

[5] L. Fan and M. Wu, "Two-dimensional optical scanner with large angular rotation realized by self-assembled micro-elevator," in *1998 IEEE/LEOS Summer Topical Meeting. Digest. Broadband Optical Networks and Technologies: An Emerging Reality. Optical MEMS. Smart Pixels. Organic Optics and Optoelectronics (Cat. No.98TH8369)*, 1998, pp. 107 – 108.

[6] N. Dechev, W. L. Cleghorn, and J. K. Mills, "Microassembly of 3-D microstructures using a compliant, passive microgripper," *Journal of Microelectromechanical Systems*, vol. 13, no. 2, pp. 176 – 189, 2004.

[7] V. Lubecke, B. Barber, E. Chan, D. Lopez, M. Gross, and P. Gammel, "Self-assembling MEMS variable and fixed RF inductors," *IEEE Transactions on Microwave Theory and Techniques*, vol. 49, no. 11, pp. 2093 – 2098, 2001.

[8] H. Storck, W. Littmann, J. Wallaschek, and M. Mracek, "The effect of friction reduction in presence of ultrasonic vibrations and its relevance to travelling wave ultrasonic motors," *Ultrasonics*, vol. 40, no. 1-8, pp. 379 – 383, 2002.

[9] O. Kolosov and K. Yamanaka, "Nonlinear detection of ultrasonic vibrations in an atomic force microscope," *Japanese Journal of Applied Physics, Part 2 (Letters)*, vol. 32, no. 8A, pp. 1095 – 1098, 1993.

[10] S. Ardanuc, A. Lal, and D. Reyes, "Process-independent, ultrasound-enhanced, electrostatic batch assembly," in *TRANSDUCERS '07 &; Eurosensors XXI. 2007 14th International Conference on Solid-State Sensors, Actuators and Microsystems*, Lyon, France, 2007, pp. 407 – 410.

[11] "Concentrating solar power: From research to implementation," Tech. Rep., 2007, European Commision Publication.

[12] M. R. Douglass, "DMD reliability: A MEMS success story," *Proceedings of SPIE - The International Society for Optical Engineering*, vol. 4980, pp. 1 – 11, 2003.

[13] V. Viereck, J. Ackermann, Q. Li, A. Jakel, J. Schmid, and H. Hillmer, "Sun glasses for buildings based on micro mirror arrays: Technology, control by networked sensors and scaling potential," in *Proceedings of INSS 2008 - 5th International Conference on Networked Sensing Systems*, Kanazawa, Japan, 2008, pp. 135 – 139.

[14] A. Jakel, Q. Li, V. Viereck, and H. Hillmer, "Development of electrostatically driven micromirror arrays for daylight guiding on large areas," in *Optical MEMS and Nanophotonics, 2009 IEEE/LEOS International Conference on*, Aug. 2009, pp. 41 – 42.

[15] S. Schodowski, "Resonator self-temperature-sensing using a dual-harmonic-mode crystal oscillator," in *Proceedings of the 43rd Annual Symposium on Frequency Control 1989 (Cat. No.89CH2690-6)*, New York, NY, USA, 1989, pp. 2 – 7.

[16] E. A. Vittoz, M. G. R. Degrauwe, and S. Bitz, "High-performance crystal oscillator circuits: Theory and application." *IEEE Journal of Solid-State Circuits*, vol. 23, no. 3, pp. 774 – 783, 1987.

[17] A. Ballato, "Frequency-temperature-load capacitance behavior of resonators for TCXO application," *IEEE Transactions on Sonics and Ultrasonics*, vol. SU-25, no. 4, pp. 185 – 191, 1978.

[18] R. Holbeche and P. Morley, "Investigation into temperature variation of equivalent-circuit parameters of AT-cut quartz crystal resonators," *IEE Proceedings A: Physical Science. Measurement and Instrumentation. Management and Education. Reviews*, vol. 128, no. 7, pp. 507 – 510, 1981.

[19] R. E. Davidsen and S. W. Smith, "Two-dimensional arrays for medical ultrasound using multilayer flexible circuit interconnection," *IEEE Transactions*

on Ultrasonics, Ferroelectrics, and Frequency Control, vol. 45, no. 2, pp. 338 – 348, 1998.

[20] K. Yamanaka, H. Ogiso, and O. Kolosov, "Ultrasonic force microscopy for nanometer resolution subsurface imaging," *Applied Physics Letters*, vol. 64, no. 2, pp. 178 – 180, 1994.

[21] E. Fletcher and R. Moen, "Hydrogen and oxygen from water," *Science*, vol. 197, no. 4308, pp. 1050 – 1056, 1977.

[22] L. Kazmerski, D. Gwinner, and A. Hicks, "Best research cell efficiencies," Nov 2007. [Online]. Available: http://en.wikipedia.org/wiki/File:PVeff%28rev110707%29d.png

[23] L. Kazmerski, "Best research cells." [Online]. Available: http://www.nrel.gov/pv/thin_film/docs/kaz_best_research_cells.ppt

[24] M. Lutz, A. Partridge, P. Gupta, N. Buchan, E. Klaassen, J. McDonald, and K. Petersen, "MEMS oscillators for high volume commercial applications," in *Proc. TRANSDUCERS '07; 14th International Conference on Solid-State Sensors, Actuators and Microsystems*, Lyon, France, 2007, pp. 49 – 52.

[25] R. Ruby, P. Bradley, D. Clark, D. Feld, T. Jamneala, and K. Wang, "Acoustic FBAR for filters, duplexers and front end modules," in *2004 IEEE MTT-S International Microwave Symposium*, vol. 2, Fort Worth, TX, USA, 2004, pp. 931 – 934.

[26] G. Piazza, P. Stephanou, J. Porter, M. Wijesundara, and A. Pisano, "Low motional resistance ring-shaped contour-mode aluminum nitride piezoelectric micromechanical resonators for UHF applications," in *18th IEEE International Conference on Micro Electro Mechanical Systems*, Miami Beach, FL, USA, 2005, pp. 20 – 23.

[27] J. W. Judy, T. Tamagawa, and D. L. Polla, "Surface-machined micromechanical membrane pump," in *Proc. IEEE International Workshop on Microelectromechanical Systems (MEMS'91)*, Nara, Japan, 1991, pp. 182 – 186.

[28] J. Smits, "Piezoelectric micropump with three valves working peristaltically [for insulin delivery]," *Sensors and Actuators A (Physical)*, vol. 21, no. 1-3, pp. 203 – 206, Feb. 1990.

[29] F. Filhol, E. Defay, C. Divoux, C. Zinck, and M.-T. Delaye, "Resonant micro-

mirror excited by a thin-film piezoelectric actuator for fast optical beam scanning," *Sensors and Actuators A (Physical)*, vol. 123-124, pp. 483 – 489, 2005.

[30] J. Zara, J. Izatt, K. Divakara Rao, S. Yazdanfar, and S. Smith, "Scanning mirror for optical coherence tomography using an electrostatic MEMS actuator," in *2002 IEEE International Symposium on Biomedical Imaging*, Washington, DC, USA, 2002, pp. 297 – 300.

[31] O. Oralkan, A. Ergun, C.-H. Cheng, J. Johnson, M. Karaman, T. Lee, and B. Khuri-Yakub, "Volumetric ultrasound imaging using 2-D CMUT arrays," *IEEE Transactions on Ultrasonics, Ferroelectrics and Frequency Control*, vol. 50, no. 11, pp. 1581 – 1594, Nov. 2002.

[32] S. Smith and E. Light, "Two-dimensional array transducers using thick film connection technology," *IEEE Transactions on Ultrasonics, Ferroelectrics and Frequency Control*, vol. 40, no. 6, pp. 727 – 734, Nov. 1993.

[33] J. Chae, H. Kulah, and K. Najafi, "A monolithic three-axis micro-g micromachined silicon capacitive accelerometer," *Journal of Microelectromechanical Systems*, vol. 14, no. 2, pp. 235 – 242, Apr. 2005.

[34] L.-P. Wang, R. A. Wolf Jr., Y. Wang, K. K. Deng, L. Zou, R. J. Davis, and S. Trolier-McKinstry, "Design, fabrication, and measurement of high-sensitivity piezoelectric microelectromechanical systems accelerometers," *Journal of Microelectromechanical Systems*, vol. 12, no. 4, pp. 433 – 439, 2003.

[35] S. Kamisuki, M. Fujii, T. Takekoshi, C. Tezuka, and M. Atobe, "A high resolution, electrostatically-driven commercial inkjet head," in *Proc. IEEE 13th Annual International Conference on Micro Electro Mechanical Systems*, Miyazaki, Japan, 2000, pp. 793 – 798.

[36] U. Demirci, G. Yaralioglu, E. Haeggstrom, and B. Khuri-Yakub, "Femtoliter to picoliter droplet generation for organic polymer deposition using single reservoir ejector arrays," *IEEE Transactions on Semiconductor Manufacturing*, vol. 18, no. 4, pp. 709 – 715, Nov. 2005.

[37] B. Piekarski, D. DeVoe, M. Dubey, R. Kaul, and J. Conrad, "Surface micromachined piezoelectric resonant beam filters," *Sensors and Actuators A (Physical)*, vol. 90, no. 3, pp. 313–320, 2001.

[38] G. Piazza, R. Abdolvand, and F. Ayazi, "Voltage-tunable piezoelectrically-transduced single-crystal silicon resonators on SOI substrate," in *Proc. IEEE 16th Annual International Conference on Micro Electro Mechanical Systems*, Kyoto, Japan, 2003, pp. 149–152.

[39] J. Weigold, T. Brosnihan, J. Bergeron, and X. Zhang, "A MEMS condenser microphone for consumer applications," in *Proc. IEEE International Conference on Micro Electro Mechanical Systems*, Istanbul, Turkey, 2006, pp. 86 – 89.

[40] S. Lee, R. Ried, and R. White, "Piezoelectric cantilever microphone and microspeaker," *Journal of Microelectromechanical Systems*, vol. 5, no. 4, pp. 238 – 242, Dec. 1996.

[41] D. DeVoe, "Piezoelectric thin film micromechanical beam resonators," *Sensors and Actuators A (Physical)*, vol. 88, no. 3, pp. 263–272, Mar. 2001.

[42] H. Tilmans, D. IJntema, and J. Fluitman, "Single element excitation and detection of (micro-)mechanical resonators," in *Proc. TRANSDUCERS '91; International Conference on Solid-State Sensors and Actuators*, San Francisco, CA, USA, 1991, pp. 533–537.

[43] S. Ardanuc and A. Lal, "Two-port electromechanical model for bulk-piezoelectric excitation of surface micromachined beam resonators," *Microelectromechanical Systems, Journal of*, vol. 18, no. 3, pp. 626 – 640, June 2009.

[44] K. Yamada and T. Kuriyama, "A novel asymmetric silicon micro-mirror for optical beam scanning display," in *Proc. MEMS 98; IEEE 11th Annual International Workshop on Micro Electro Mechanical Systems*, 1998, pp. 110 – 115.

[45] V. Kaajakari, S. Rodgers, and A. Lal, "Ultrasonically driven surface micromachined motor," in *Proc. IEEE 13th Annual International Conference on Micro Electro Mechanical Systems*, Miyazaki, Japan, 2000, pp. 40 – 45.

[46] S. Baglio, V. Ferrari, A. Ghisla, V. Sacco, N. Savalli, and A. Taroni, "Optical SOI micro-gravimeters with bulk PZT excitation," in *Proc. IEEE Sensors 2004*, vol. 1, Vienna, Austria, 2004, pp. 264 – 267.

[47] W. Wong and A. Street, "Novel acoustic techniques for microelectronic failure analysis and characterization," in *Proc. 12th International Symposium*

on the Physical and Failure Analysis of Integrated Circuits, Singapore, 2005, pp. 14 – 19.

[48] S. Ardanuc and A. Lal, "Bulk detection of sound waves launched by surface micromachined beam resonators," in *Proc. IEEE Ultrasonics Symposium*, vol. 2, Rotterdam, Netherlands, 2005, pp. 1171 – 1174.

[49] W.-K. Wong and M. Palaniapan, "Phonon-mediated characterization of microelectromechanical resonators," *Applied Physics Letters*, vol. 89, no. 6, p. 064102, 2006.

[50] A. Churenkov, "Self-excitation of microresonators," *International Journal of Optoelectronics*, vol. 8, no. 2, pp. 99 – 103, 1993.

[51] W.-K. Wong, C.-L. Wong, M. Palaniapan, and F. Tay, "Non-destructive functionality and reliability assessment of dynamic MEMS using acoustic phonon characterization," in *Proc. TRANSDUCERS '07; 14th International Conference on Solid-State Sensors, Actuators and Microsystems*, Lyon, France, 2007, pp. 371 – 374.

[52] U. Rabe and W. Arnold, "Acoustic microscopy by atomic force microscopy," *Applied Physics Letters*, vol. 64, no. 12, pp. 1493 – 1495, 1994.

[53] K. Takata, T. Hasegawa, S. Hosaka, S. Hosoki, and T. Komoda, "Tunneling acoustic microscope," *Applied Physics Letters*, vol. 55, no. 17, pp. 1718 – 1720, 1989.

[54] D. Koester, A. Cowen, R. Mahadewan, M. Stonefield, and B. Hardy, *PolyMUMPs Design Handbook*, MEMSCAP, 2003, revision 10.0.

[55] H. Tilmans, "Equivalent circuit representation of electromechanical transducers: I. lumped-parameter systems [micromechanical systems]," *Journal of Micromechanics and Microengineering*, vol. 6, no. 1, pp. 157 – 176, 1996.

[56] C. T.-C. Nguyen, "Micromechanical signal processors," Ph.D. dissertation, University of California at Berkeley, 1994.

[57] R. Pratt, G. Johnson, R. Howe, and J. Chang, "Micromechanical structures for thin film characterization," in *Proc. TRANSDUCERS '91. 1991 International Conference on Solid-State Sensors and Actuators*, San Francisco, CA, USA, 1991, pp. 205 – 208.

[58] G. S. Kino, *Acoustic Waves*. New Jersey: Prentice-Hall, 1987.

[59] J. W. Nilsson and S. A. Riedel, *Electric Circuits*, 6th ed. Prentice-Hall, 2001.

[60] M. Kobayashi and T. Sugita, "Complex reciprocity theorem for multiregions with piezoelectric media and surface impedance," *IEEE Transactions on Microwave Theory and Techniques*, vol. MTT-27, no. 4, pp. 343 – 345, 1979.

[61] B. Auld, "Application of microwave concepts to the theory of acoustic fields and waves in solids," *IEEE Transactions on Microwave Theory and Techniques*, vol. MTT-17, no. 11, pp. 800–811, 1969.

[62] Y.-H. Park and K. Park, "High-fidelity modeling of MEMS resonators - Part I: Anchor loss mechanisms through substrate," *Journal of Microelectromechanical Systems*, vol. 13, no. 2, pp. 238 – 247, 2004.

[63] S. Humad, R. Abdolvand, G. K. Ho, G. Piazza, and F. Ayazi, "High frequency micromechanical piezo-on-silicon block resonators," in *Technical Digest - International Electron Devices Meeting*, Washington, DC, United States, 2003, pp. 957–960.

[64] S. Hutcherson and W. Ye, "On the squeeze-film damping of micro-resonators in the free-molecule regime," *Journal of Micromechanics and Microengineering*, vol. 14, no. 12, pp. 1726 – 1733, 2004.

[65] M. Bao and H. Yang, "Squeeze film air damping in MEMS," *Sensors and Actuators A (Physical)*, vol. 136, no. 1, pp. 3 – 27, May 2007.

[66] M. Andrews, I. Harris, and G. Turner, "A comparison of squeeze-film theory with measurements on a microstructure," *Sensors and Actuators A (Physical)*, vol. 36, no. 1, pp. 79 – 87, Mar. 1993.

[67] A. Corney, "Capacitor microphone reciprocity calibration," *Metrologia*, vol. 11, no. 1, pp. 25 – 32, 1975.

[68] J. D. Achenbach, *Reciprocity In Elastodynamics*, 1st ed. Cambridge University Press, 2003.

[69] J. Kuypers, M. Schmidt, S. Tanaka, and M. Esashi, "Monolithic phase shifter based on mechanically tunable SAW delay line," in *Proc. TRANSDUCERS*

'07; 14th International Conference on Solid-State Sensors, Actuators and Microsystems, Lyon, France, 2007, pp. 161 – 164.

[70] K.-F. Bohringer, K. Goldberg, M. Cohn, R. Howe, and A. Pisano, "Parallel microassembly with electrostatic force fields," *Proceedings - IEEE International Conference on Robotics and Automation*, vol. 2, pp. 1204 – 1211, 1998.

[71] K. Saitou, D.-A. Wang, and S. J. Wou, "Externally resonated linear microvibromotor for microassembly," *Journal of Microelectromechanical Systems*, vol. 9, no. 3, pp. 336 – 346, 2000.

[72] C. King, L. Lin, and M. Wu, "Out-of-plane refractive microlens fabricated by surface micromachining," *IEEE Photonics Technology Letters*, vol. 8, no. 10, pp. 1349 – 1351, 1996.

[73] R. R. A. Syms, "Surface tension powered self-assembly of 3-D micro-optomechanical structures," *Journal of Microelectromechanical Systems*, vol. 8, no. 4, pp. 448 – 455, 1999.

[74] Y. Yi and C. Liu, "Mechanically-stable micro assembly using magnetic actuation," *International Conference on Solid-State and Integrated Circuit Technology Proceedings*, pp. 939 – 942, 1998.

[75] K. W. Lai, P. Chung, M. Li, and W. J. Li, "Automated micro-assembly of optical mems structure by centrifugal force," *Proceedings of the World Congress on Intelligent Control and Automation (WCICA)*, vol. 6, pp. 5624 – 5628, 2004.

[76] V. Kaajakari and A. Lal, "Thermokinetic actuation for batch assembly of microscale hinged structures," *Journal of Microelectromechanical Systems*, vol. 12, no. 4, pp. 425 – 432, 2003.

[77] K. Pister, M. Judy, S. Burgett, and R. Fearing, "Microfabricated hinges," *Sensors and Actuators, A: Physical*, vol. 33, no. 3, pp. 249 – 256, 1992.

[78] http://www.mems.sandia.gov/tech-info/summit-v.html. [Online]. Available: http://www.mems.sandia.gov/tech-info/summit-v.html

[79] S. Ardanuc and A. Lal, "Off-chip actuation for angular position control of MEMS mirrors," in *TRANSDUCERS '09 &; Eurosensors XXII. 2009 15th International Conference on Solid-State Sensors, Actuators and Microsystems*, Denver, USA, 2009, pp. 1766 – 1769.

[80] F. Dinelli, S. Biswas, G. Briggs, and O. Kolosov, "Ultrasound induced lubricity in microscopic contact," *Applied Physics Letters*, vol. 71, no. 9, pp. 1177 – 1179, 1997.

[81] R. Maboudian and R. Howe, "Critical review: Adhesion in surface micromechanical structures," *Journal of Vacuum Science &; Technology B (Microelectronics and Nanometer Structures)*, vol. 15, no. 1, pp. 1 – 20, 1997.

[82] Y.-P. Zhao and J.-G. Guo, "Dynamic stability of electrostatic torsional actuators with van der Waals effect," *International Journal of Solids and Structures*, vol. 43, no. 3-4, pp. 675 – 85, 2006.

[83] W. Littmann, H. Storck, and J. Wallaschek, "Sliding friction in the presence of ultrasonic oscillations: Superposition of longitudinal oscillations," *Archive of Applied Mechanics*, vol. 71, no. 8, pp. 549 – 554, 2001.

[84] Y. Zhuang and A. Menon, "On the stiction of MEMS materials," *Tribology Letters*, vol. 19, no. 2, pp. 111 – 117, 2005.

[85] C. Mastrangelo and C. Hsu, "A simple experimental technique for the measurement of the work of adhesion of microstructures," in *Technical Digest-IEEE Solid-State Sensor and Actuator Workshop*, Hilton Head Island, SC, USA, 1992, pp. 208 – 212.

[86] K. Yamanaka and S. Nakano, "Ultrasonic atomic force microscope with overtone excitation of cantilever," *Japanese Journal of Applied Physics, Part 1*, vol. 35, no. 6B, pp. 3787 – 3792, 1996.

[87] K. Yamanaka, H. Ogiso, and O. Kolosov, "Analysis of subsurface imaging and effect of contact elasticity in the ultrasonic force microscope," *Japanese Journal of Applied Physics, Part 1: Regular Papers and Short Notes and Review Papers*, vol. 33, no. 5 B, pp. 3197 – 3203, 1994.

[88] W. C. Young, *Roark's Formulas for Stress &; Strain*, 6th ed. Mc Graw Hill, 1989.

[89] J. I. Seeger and B. E. Boser, "Charge control of parallel-plate, electrostatic actuators and the tip-in instability," *Journal of Microelectromechanical Systems*, vol. 12, no. 5, pp. 656 – 671, 2003.

[90] R. Sattler, F. Plotz, G. Fattinger, and G. Wachutka, "Modeling of an electro-

static torsional actuator: Demonstrated with an RF MEMS switch," *Sensors and Actuators, A: Physical*, vol. 97-98, pp. 337 – 346, 2002.

[91] D. M. Pozar, *Microwave Engineering*, 2nd ed. John Wiley & Sons, 1998, ch. 3, p. 165, eq. 3.211.

[92] N. Allen, N. Lam, and D. Greaves, "Tests on the breakdown of air at elevated temperatures in non-uniform electric fields," *IEE Proceedings-Science, Measurement and Technology*, vol. 147, no. 6, pp. 291 – 295, 2000.

[93] C. Powell and H. Ryan, "Breakdown characteristics of air at high temperatures," 2^{nd} *International Conference on Gas Discharges*, pp. 285 – 287, 1972.

[94] T. Akiyama, D. Collard, and H. Fujita, "Scratch drive actuator with mechanical links for self-assembly of three-dimensional MEMS," *Journal of Microelectromechanical Systems*, vol. 6, no. 1, pp. 10 – 17, 1997.

[95] T. Ono, D. Y. Sim, and M. Esashi, "Micro-discharge and electric breakdown in a micro-gap," *Journal of Micromechanics and Microengineering*, vol. 10, no. 3, pp. 445 – 451, 2000.

[96] *SUMMiT* V^{TM} *Five Level Micromachining Technology Design Manual*, Sandia National Labs, 2005, version 1.3 09/22/2005.

[97] R. Johnstone and M. Parameswaran, "Self-assembly of surface-micromachined structures using electrostatic attraction," *Proceedings of the SPIE - The International Society for Optical Engineering*, vol. 4561, pp. 66 – 76, 2001.

[98] V. Kaajakari and A. Lal, "Pulsed ultrasonic actuation of polysilicon surface micromachines," in *Proceedings of the IEEE Ultrasonics Symposium*, vol. 1, Caesars Tahoe, NV, USA, 1999, pp. 643 – 646.

[99] E. E. Hui, R. T. Howe, and M. Rodgers, "Single-step assembly of complex 3-D microstructures," *Proceedings of the IEEE Micro Electro Mechanical Systems (MEMS)*, pp. 602 – 607, 2000.

[100] L. Stoddard, J. Abiecunas, and R. O'Connell, "Economic, energy, and environmental benefits of concentrating solar power in California, NREL/SR-550-39291," Overland Park, Kansas," National Renewable Energy Laboratory Subcontractor Report, 2006.

[101] M. Yamaguchi and A. Luque, "High efficiency and high concentration in photovoltaics," *IEEE Transactions on Electron Devices*, vol. 46, no. 10, pp. 2139 – 2144, 1999.

[102] A. Leitner and B. Owens, "Brighter than a hundred suns: Solar power for the southwest, NREL/SR-550-33233," Boulder, Colorado," National Renewable Energy Laboratory Subcontractor Report, 2003.

[103] V. Viereck, Q. Li, J. Ackermann, A. Schwank, S. Araujo, A. Jakel, S. Werner, N. Dharmarasu, J. Schmid, and H. Hillmer, "Novel large area applications using optical MEMS," in *2007 IEEE/LEOS International Conference on Optical MEMS and Nanophotonics, OMENS*, Hualien, Taiwan, 2007, pp. 55 – 56.

[104] B. Hälg, "On a nonvolatile memory cell based on micro-electro-mechanics," in *Proceedings. IEEE Micro Electro Mechanical Systems. An Investigation of Micro Structures, Sensors, Actuators, Machines and Robots (Cat. No.90CH2832-4)*, Napa Valley, CA, USA, 1990, pp. 172 – 176.

[105] M. Daneman, N. Tien, O. Solgaard, A. Pisano, K. Lau, and R. Muller, "Linear microvibromotor for positioning optical components," in *Proceedings of the IEEE Micro Electro Mechanical Systems*, Amsterdam, Neth, 1995, pp. 55 – 60.

[106] C. J. D., *Gaseous Conductors*. McGraw-Hill Book Company Inc., 1941.

[107] "Electricity access database in 2008, International Energy Agency, (IEA)," 2008. [Online]. Available: http://www.iea.org/weo/electricity.asp

[108] "SolarPACES no. III - 1/00: Catalog of solar heliostats," Tech. Rep., 2000. [Online]. Available: http://www.fika.org/jb/resources/Heliostat%20Catalog.pdf

[109] G. J. Kolb, S. A. Jones, M. W. Donnelly, D. Gorman, and R. Thomas, "Heliostat cost reduction study," Sandia National Laboratories, United States, Tech. Rep., 2007, SAND2007-3293.

[110] S. Patil, V. Chu, and J. Conde, "Performance of thin film silicon MEMS on flexible plastic substrates," *Sensors and Actuators, A: Physical*, vol. 144, no. 1, pp. 201 – 206, 2008.

[111] "mirasol®; display technology (iMoD) by Qualcomm." [Online]. Available: http://www.mirasoldisplays.com

[112] "iMoD™ display overview." [Online]. Available: http://www.qualcomm.com/common/documents/white_papers/iMoD_Display_Overview.pdf

[113] G. J. Kolb, "2008 solar annual review meeting," Sandia National Laboratories, Tech. Rep., 2008. [Online]. Available: http://www1.eere.energy.gov/solar/review_meeting/pdfs/prm2008_kolb_sandia.pdf

[114] T. H. Kim and S. H. Baek, "Variable focal length lens comprising micromirrors with two degrees of freedom rotation and one degree of freedom translation," August 2005, US Patent no: 6,934,072.

[115] J. J. Allen, "Erected mirror optical switch," June 2005, US Patent no: 6,903,861.

[116] J. A. Ayers, W. C. Tang, and Z. Chen, "360° rotating micro mirror for transmitting and sensing optical coherence tomography signals," *Proceedings of IEEE Sensors*, vol. 1, pp. 497 – 500, 2004.

[117] A. Luque and S. Hegedus, Eds., *Handbook of photovoltaic science and engineering*. John Wiley & Sons Ltd., 2002.

[118] A. Rabl, *Active Solar collectors and their applications*. Oxford University Press, 1985.

[119] D. Myers, S. Kurtz, C. Whitaker, and T. Townsend, "Preliminary investigations of outdoor meteorological broadband and spectral conditions for evaluating photovoltaic modules and systems," in *NCPV Program Review Meeting*, 2000, pp. 69 – 70.

[120] "Geoengineering the climate: science, governance and uncertainty," Royal Society, Tech. Rep., September 2009.

[121] M. R. Dokmeci, A. Pareek, S. Bakshi, M. Waelti, C. D. Fung, K. H. Heng, and C. H. Mastrangelo, "Two-axis single-crystal silicon micromirror arrays," *Journal of Microelectromechanical Systems*, vol. 13, no. 6, pp. 1006 – 1017, 2004.

[122] E. J. Garcia, "Pivoting micromirror designs for large orientation angles,"

Sandia National Laboratories, United States, Tech. Rep., 2000, SAND2000-0865C.

[123] V. Aksyuk, F. Pardo, D. Carr, D. Greywall, H. Chan, M. Simon, A. Gasparyan, H. Shea, V. Lifton, C. Bolle, S. Arney, R. Frahm, M. Paczkowski, M. Haueis, R. Ryf, D. T. Neilson, J. Kim, C. R. Giles, and D. Bishop, "Beam-steering micromirrors for large optical cross-connects," *Journal of Lightwave Technology*, vol. 21, no. 3, pp. 634 – 642, 2003.

[124] M. Adrian Michalicek and V. M. Bright, "Flip-chip fabrication of advanced micromirror arrays," *Sensors and Actuators, A: Physical*, vol. 95, no. 2-3, pp. 152 – 167, 2002.

[125] T. Kudrle, C. Wang, M. Bancu, J. Hsiao, A. Pareek, M. Waelti, G. Kirkos, T. Shone, C. Fung, and C. Mastrangelo, "Electrostatic micromirror arrays fabricated with bulk and surface micromachining techniques," in *Proceedings of the IEEE Micro Electro Mechanical Systems (MEMS)*, Kyoto, Japan, 2003, pp. 267 – 270.

[126] D. J. Dagel, W. D. Cowan, O. B. Spahn, G. D. Grossetete, A. J. Grine, M. J. Shaw, P. J. Resnick, and B. Jokiel Jr., "Large-stroke mems deformable mirrors for adaptive optics," *Journal of Microelectromechanical Systems*, vol. 15, no. 3, pp. 572 – 583, 2006.

[127] L. J. Hornbeck, "Active yoke hidden hinge digital micromirror device," July 1996, US Patent no: 5,535,047.

[128] V. Milanovic, G. A. Matus, and D. T. McCormick, "Gimbal-less monolithic silicon actuators for tip-tilt-piston micromirror applications," *IEEE Journal on Selected Topics in Quantum Electronics*, vol. 10, no. 3, pp. 462 – 471, 2004.

[129] L. Wu and H. Xie, "124° rotation angle electrothermal micromirror with integrated platinum heater," *IEEE Journal of Selected Topics in Quantum Electronics*, vol. 13, no. 2, pp. 316 – 321, 2007.

[130] D. J. Dagel, O. B. Spahn, J. J. Allen, S. A. Kemme, G. D. Grossetete, and F. R. Gass, "Out-of-plane, rotary micromirrors for reconfigurable photonic applications," *Proceedings of SPIE - The International Society for Optical Engineering*, vol. 4983, pp. 114 – 121, 2003.

[131] V. Viereck, "Large-area applications of optical MEMS: micromirror arrays

guide daylight, optimize indoor illumination," *Photonik*, vol. 2, pp. 48 – 49, Feb. 2009.

[132] Q. Li, A. Jakel, V. Viereck, J. Schmid, and H. Hillmer, "Design and fabrication of self-assembling micromirror arrays," *Proceedings of SPIE - The International Society for Optical Engineering*, vol. 7362, pp. SPIE Europe; GMM VDE/VDI Gesellschaft Mikroelektronik, Mikro– und Feinmechanik –, 2009.

[133] J. Vig, "Temperature-insensitive dual-mode resonant sensors-a review," *IEEE Sensors Journal*, vol. 1, no. 1, pp. 62 – 68, 2001.

[134] J. Barnes, A. Chi, L. Cutler, D. Healey, D. Leeson, T. McGunigal, J. Mullen, J.A., W. Smith, R. Sydnor, R. Vessot, and G. Winkler, "Characterization of frequency stability," *IEEE Transactions on Instrumentation and Measurement*, vol. IM-20, no. 2, pp. 105 – 120, 1971.

[135] R. Bucur, V. Mecea, and J.-O. Carlsson, "EQCM with air-gap excitation electrode. calibration tests with copper and oxygen coatings," *Electrochimica Acta*, vol. 48, no. 23, pp. 3431 – 3438, 2003.

[136] D. Pierce, Y. Kim, and J. Vig, "A temperature insensitive quartz microbalance," *IEEE Transactions on Ultrasonics, Ferroelectrics and Frequency Control*, vol. 45, no. 5, pp. 1238 – 1245, 1998.

[137] B. L. Norling, "Precision gravity measurement utilizing accelerex vibrating beam accelerometer technology," in *Record - IEEE PLANS, Position Location and Navigation Symposium*, Piscataway, NJ, USA, 1990, pp. 509 – 515.

[138] N. Bianchi, J.-M. Karam, and B. Courtois, "ALC crystal oscillators based pressure and temperature measurement integrated circuit for high temperature oil well applications," *IEEE Transactions on Ultrasonics, Ferroelectrics and Frequency Control*, vol. 47, no. 5, pp. 1241 – 1245, 2000.

[139] V. Matko, D. Donlagic, and J. Koprivnikar, "Measurement of 0-1 ml volumes using the procedure of capacitive dependent crystals," in *Asia-Pacific Workshop on Advances in Motion Control Proceedings (Cat. No.93TH0541-3)*, New York, NY, USA, 1993, pp. 57 – 62.

[140] H. Tanaka and Y. Kanno, "Quartz crystal capacitive sensor with inductance-capacitance resonance circuit for vapor sensing," *Japanese Journal of Applied Physics*, vol. 46, no. 11, pp. 7509 – 7511, 2007.

[141] D. R. Koehler, S. H. Kravitz, and P. T. Vianco, "Ultraminiature resonator accelerometer," 1996, eDB/440800;.

[142] S. Haykin, *Communication Systems*, 3rd ed. John Wiley & Sons, Inc., 1994.

[143] L. W. Couch, *Digital and analog communication systems*, 5th ed. Prentice-Hall, Inc., 1997.

[144] J. Vig and F. Walls, "A review of sensor sensitivity and stability," in *Proceedings of the 2000 IEEE/EIA International Frequency Control Symposium and Exhibition (Cat. No.00CH37052)*, Piscataway, NJ, USA, 2000, pp. 30 – 33.

[145] S. D. Senturia, *Microsystem Design*. Kluwer Academic Publishers, 2001.

[146] L. K. Baxter, *Capacitive Sensors: Design and Applications*. IEEE Press, 1996.

[147] K. N. Leung, P. K. Mok, and C. Y. Leung, "A 2-V 23-μA 5.3-ppm/°C curvature-compensated CMOS bandgap voltage reference," *IEEE Journal of Solid-State Circuits*, vol. 38, no. 3, pp. 561 – 564, 2003.

[148] *ADR280:* 1.2 V *Ultralow Power High PSRR Voltage Reference Datasheet*, Rev c ed., Analog Devices, Apr 2007. [Online]. Available: http://www.analog.com/static/imported-files/data_sheets/ADR280.pdf

[149] Y. Taur and T. H. Ning, *Fundamentals of modern VLSI devices*. Cambridge University Press, 1998.

[150] A. Cockbain and P. Harrop, "The temperature coefficient of capacitance," *British Journal of Applied Physics (Journal of Physics D)*, vol. 1, pp. 1109 – 1115, 1968.

[151] *SC Series:MIS Chip Capacitors*, Rev d ed., Skyworks, January 2008.

[152] E. Haran, "Stable gas capacitor with low temperature coefficient over a wide range of temperatures," *Journal of Physics E (Scientific Instruments)*, vol. 4, no. 12, pp. 987 – 989, 1971. [Online]. Available: http://dx.doi.org/10.1088/0022-3735/4/12/015

[153] F. Toth, D. Bertels, and G. Meijer, "A low-cost, stable reference capacitor

for capacitive sensor systems," *IEEE Transactions on Instrumentation and Measurement*, vol. 45, no. 2, pp. 526 – 30, 1996.

[154] V. Matko and D. Donlagic, "Sensor for high-air-humidity measurement," *Sensors and Actuators A (Physical)*, vol. A61, no. 1-3, pp. 331 – 334, 1997.

[155] *Quartz Crystal Ceramic F6/FX SMD - Datasheet*, Rev 2008-oct16 ed., Pericom, Oct 2008. [Online]. Available: http://www.pericom.com/pdf/datasheets/se/F6_FX.pdf

[156] A. Benjaminson and S. Stallings, "A microcomputer-compensated crystal oscillator using a dual-mode resonator," in *Proceedings of the 43rd Annual Symposium on Frequency Control 1989 (Cat. No.89CH2690-6)*, New York, NY, USA, 1989, pp. 20 – 26.

[157] R. Filler and J. Vig, "Resonators for the microcomputer compensated crystal oscillator," in *Proceedings of the 43rd Annual Symposium on Frequency Control 1989 (Cat. No.89CH2690-6)*, New York, NY, USA, 1989, pp. 8 – 15.

[158] H. Luo, G. Zhang, L. Carley, and G. Fedder, "A post-CMOS micromachined lateral accelerometer," *Journal of Microelectromechanical Systems*, vol. 11, no. 3, pp. 188 – 195, 2002.

[159] *ADXL103:Precision ±1.7g Single Axis iMEMS® Accelerometer Datasheet*, Rev. a ed., Analog Devices, Mar 2006.

[160] H. A. Tilmans, "Equivalent circuit representation of electromechanical transducers: II. distributed-parameter systems," *Journal of Micromechanics and Microengineering*, vol. 7, no. 4, pp. 285–309, 1997.

[161] T. Adachi, M. Hirose, and Y. Tsuzuki, "Computer analysis of Colpitts crystal oscillator," in *Proceedings of the 39th Annual Frequency Control Symposium 1985 (Cat. No.85CH2186-5)*, New York, NY, USA, 1985, pp. 176 – 182.

[162] R. Besson, "A new piezoelectric resonator design," in *Proceedings of the 30th Annual Symposium on Frequency Control*, 1976, pp. 78 – 83.

[163] F. Walls and J. Vig, "Fundamental limits on the frequency stabilities of crystal oscillators," *IEEE Transactions on Ultrasonics, Ferroelectrics and Frequency Control*, vol. 42, no. 4, pp. 576 – 589, 1995.

[164] P. Kao and S. Tadigadapa, "Micromachined quartz resonator based infrared

detector array," *Sensors and Actuators, A: Physical*, vol. 149, no. 2, pp. 189 – 192, 2009.

[165] F. Walls and J.-J. Gagnepain, "Environmental sensitivities of quartz oscillators," *IEEE Transactions on Ultrasonics, Ferroelectrics and Frequency Control*, vol. 39, no. 2, pp. 241 – 249, 1992.

[166] F. Walls, "The influence of pressure and humidity on the medium and long-term frequency stability of quartz oscillators," in *Proceedings of the 42nd Annual Frequency Control Symposium 1988 (IEEE Cat. No.88CH2588-2)*, New York, NY, USA, 1988, pp. 279 – 283.

[167] J. Vig, R. Filler, and Y. Kim, "Uncooled IR imaging array based on quartz microresonators," *Journal of Microelectromechanical Systems*, vol. 5, no. 2, pp. 131 – 137, 1996.

[168] "OCXO 8607 datasheet from Oscilloquartz," online, Sep 2008. [Online]. Available: http://www.oscilloquartz.com/file/pdf/8607.pdf

[169] *ADXL150:* 5 g *to* 50 g*, Low-Noise, Low-Power, Single/Dual Axis iMEMS® Accelerometers Datasheet*, Analog Devices.

[170] *HC-49US Quartz crystal datasheet*, ECS Inc. International. [Online]. Available: http://www.ecsxtal.com/store/pdf/hc_49us.pdf

[171] K. Erikson, A. Hairston, A. Nicoli, J. Stockwell, and T. White, "A 128x128 ultrasonic transducer hybrid array," *1997 IEEE Ultrasonics Symposium Proceedings. An International Symposium*, vol. 2, pp. 1625 – 1629, 1997.

[172] *Transonic Flow Probes*, Transonic Systems Inc.©. [Online]. Available: http://www.transonic.com/flowprobes.shtml

[173] T. Kozuka, T. Tuziuti, H. Mitome, and T. Fukuda, "Acoustic micromanipulation using a multi-electrode transducer," *Proceedings of the International Symposium on Micro Machine and Human Science*, pp. 163 – 170, 1996.

[174] K. Yamashita, H. Katata, M. Okuyama, H. Miyoshi, G. Kato, S. Aoyagi, and Y. Suzuki, "Arrayed ultrasonic microsensors with high directivity for in-air use using PZT thin film on silicon diaphragms," *Sensors and Actuators, A: Physical*, vol. 97-98, pp. 302 – 307, 2002.

[175] P. Muralt, D. Schmitt, N. Ledermann, J. Baborowski, P. K. Weber, W. Steichen, S. Petitgrand, A. Bosseboeuf, N. Setter, and P. Gaucher, "Study of PZT coated membrane structures for micromachined ultrasonic transducers," in *Proceedings of the IEEE Ultrasonics Symposium*, vol. 2, Atlanta, GA, United states, 2001, pp. 907 – 911.

[176] G. Percin, A. Atalar, F. Levent Degertekin, and B. T. Khuri-Yakub, "Micromachined two-dimensional array piezoelectrically actuated transducers," *Applied Physics Letters*, vol. 72, no. 11, pp. 1397 – 1399, 1998.

[177] T. Kwon, Y. Kim, K. Eom, D. Yoon, H. Lee, and T. Kim, "Fabrication of stabilized piezoelectric thick film for silicon-based mems device," *Applied Physics A: Materials Science and Processing*, vol. 88, no. 4, pp. 627 – 632, 2007.

[178] B. Xu, D. White, J. Zesch, A. Rodkin, S. Buhler, J. Fitch, and K. Littau, "Characteristics of lead zirconate titanate ferroelectric thick films from a screen-printing laser transfer method," *Applied Physics Letters*, vol. 87, no. 19, pp. 1 – 3, 2005.

[179] Q. Zhou, K. Shung, and Y. Huang, "Fabrication of sol-gel modified piezoelectric thick films for high frequency ultrasonic applications," in *Proceedings - IEEE Ultrasonics Symposium*, vol. 3, Montreal, Que., Canada, 2004, pp. 1958 – 1961.

[180] Y.-C. Hsu, K.-C. Kuo, and L.-S. Jang, "Development and characterization of PZT thick films fabricated by an improved sol-gel method," in *2005 IEEE International Conference on Robotics and Biomimetics, ROBIO*, vol. 2005, Shatin, N.T., China, 2005, pp. 778 – 782.

[181] X.-H. Xu and J.-R. Chu, "Preparation of a high-quality PZT thick film with performance comparable to those of bulk materials for applications in MEMS," *Journal of Micromechanics and Microengineering*, vol. 18, no. 6, 2008.

[182] Z. Wang, J. Miao, C. W. Tan, and T. Xu, "Fabrication of piezoelectric MEMS devices-from thin film to bulk PZT wafer," *Journal of Electroceramics*, 2008. [Online]. Available: http://www.springerlink.com/content/4703682476386472

[183] E. E. Aktakka, H. Kim, and K. Najafi, "Wafer level fabrication of high performance MEMS using bonded and thinned bulk piezoelectric substrates,"

in *TRANSDUCERS '09 &; Eurosensors XXII. 2009 15th International Conference on Solid-State Sensors, Actuators and Microsystems*, Denver, USA, 2009, pp. 849 – 852.

[184] K. T. Turner, R. Mlcak, D. C. Roberts, and S. M. Spearing, "Bonding of bulk piezoelectric material to silicon using a gold-tin eutectic bond," in *Materials Research Society Symposium - Proceedings*, vol. 687, Boston, MA, United states, 2002, pp. 49 – 54.

[185] H. Takagi, R. Maeda, N. Hosoda, and T. Suga, "Room-temperature bonding of lithium niobate and silicon wafers by argon-beam surface activation," *Applied Physics Letters*, vol. 74, no. 16, pp. 2387 – 2389, 1999.

[186] S. Ardanuc and A. Lal, "PZT driven micromachined 2-D membrane arrays," in *Proc. IEEE Ultrasonics Symposium*, vol. 1, Montreal, Que., Canada, 2004, pp. 509–512.

[187] E. K. Yung and I. Turlik, "Electroplated solder joints for flip-chip applications," *IEEE transactions on components, hybrids, and manufacturing technology*, vol. 14, no. 3, pp. 549 – 559, 1991.

[188] S.-Y. Jang, J. Wolf, O. Ehrmann, H. Gloor, H. Reichl, and K.-W. Paik, "Pb-free Sn/3.5 Ag electroplating bumping process and under bump metallization (ubm)," *IEEE Transactions on Electronics Packaging Manufacturing*, vol. 25, no. 3, pp. 193 – 202, 2002.

[189] M. Maghribi, J. Hamilton, D. Polla, K. Rose, T. Wilson, and P. Krulevitch, "Stretchable micro-electrode array [for retinal prosthesis]," in 2^{nd} *Annual International IEEE-EMBS Special Topic Conference on Microtechnologies in Medicine and Biology. Proceedings (Cat. No.02EX578)*, Piscataway, NJ, USA, 2002/, pp. 80 – 83.

[190] C. Bradley, J. Bustillo, and R. White, "Flow measurements in a micromachined flow system with integrated acoustic pumping," in *Proceedings of the IEEE Ultrasonics Symposium*, vol. 1, Seattle, WA, USA, 1995, pp. 505 – 510.

[191] J. McLean and F. L. Degertekin, "Directional Scholte wave generation and detection using interdigital capacitive micromachined ultrasonic transducers," *IEEE Transactions on Ultrasonics, Ferroelectrics, and Frequency Control*, vol. 51, no. 6, pp. 756 – 764, 2004.

[192] W. Zhang and W. Ruythooren, "Study of the Au/In reaction for transient

liquid-phase bonding and 3D chip stacking," *Journal of Electronic Materials*, vol. 37, no. 8, pp. 1095 – 1101, 2008.

[193] G. Yaralioglu, F. Degertekin, K. Crozier, and C. Quate, "Contact stiffness of layered materials for ultrasonic atomic force microscopy," *Journal of Applied Physics*, vol. 87, no. 10, pp. 7491 – 7496, 2000.

[194] Z. Parlak and F. Levent Degertekin, "Contact stiffness of finite size subsurface defects for atomic force microscopy: three-dimensional finite element modeling and experimental verification," *Journal of Applied Physics*, vol. 103, no. 11, pp. 114 910 – 1, 2008.

[195] G. Pharr, W. Oliver, and F. Brotzen, "On the generality of the relationship among contact stiffness, contact area, and elastic modulus during indentation," *Journal of Materials Research*, vol. 7, no. 3, pp. 613 – 617, 1992.

[196] U. Rabe, K. Janser, and W. Arnold, "Vibrations of free and surface-coupled atomic force microscope cantilevers: theory and experiment," *Review of Scientific Instruments*, vol. 67, no. 9, pp. 3281 – 3293, 1996.

[197] J.-G. Guo and Y.-P. Zhao, "Influence of van der Waals and Casimir forces on electrostatic torsional actuators," *Journal of Microelectromechanical Systems*, vol. 13, no. 6, pp. 1027 – 1035, 2004.

[198] W. A. Weimer, "Solar-thermal production of renewable fuels," Mar 2008, SolarPACES 2008, plenary talk.

[199] M. A. Green, K. Emery, D. L. King, S. Igari, and W. Warta, "Solar cell efficiency tables (version 26)," *Progress in Photovoltaics: Research and Applications*, vol. 13, no. 5, pp. 387 – 392, 2005.

[200] C. Henry, "Limiting efficiencies of ideal single and multiple energy gap terrestrial solar cells," *Journal of Applied Physics*, vol. 51, no. 8, pp. 4494 – 4500, 1980.

[201] R. L. Bell, "Solar energy converter with waste heat engine," 1975, US Patent no: 4,002,031.

[202] R. Karlquist, "New type of balanced-bridge controlled oscillator," *HP Laboratories Technical Report*, no. HPL-1999-6, pp. 1 – 27, 1999, balanced-bridge controlled oscillators;.

[203] A. Chen, "Kick start a crystal oscillator in SPICE," *EDN*, vol. 44, no. 11, pp. 110 – 111, 1999.

[204] S.-Y. Jang and K.-W. Paik, "Eutectic Pb/Sn solder bump and under bump metallurgy interfacial reactions and adhesion," in *Proceedings of 2nd Electronics Packaging Technology Conference (Cat. No.98EX235)*, Piscataway, NJ, USA, 1998, pp. 69 – 75.